



Development of the Future Rail Freight System to Reduce the Occurrences and Impact of Derailment

D-RAIL

Grant Agreement No.: 285162 FP7 – THEME [SST.2011.4.1-3]

Project Start Date: 01/10/2011

Duration: 36 Months

D3.2

Analysis and mitigation of derailment, assessment and commercial impact

Due date of deliverable: 31/03/2013

Actual submission date: 03/06/2013

(15/11/2013 rev after int & ext review)

Work Package Number: WP3

Dissemination Level: PU

Status: Final after review and revision

	<u>Name</u>	<u>Organisation</u>
Leader of this deliverable:	Francesco Braghin	PoliMi
Prepared by:	Anders Ekberg	Chalmers
	Björn Pålsson	Chalmers
	Dimitri Sala	Lucchini
	Dirk Nicklisch	DB
	Elena Kabo	Chalmers
	Francesco Braghin	PoliMi
	Paul Allen	UoH
	Philip Shackleton	UoH
	Tore Vernersson	Chalmers
Verified by:	Michel Pineau	SNCF

Dissemination Level		
PU	Public	√
PP	Restricted to other programme participants (including the Commission Services)	
RE	Restricted to a group specified by the consortium (including the Commission Services)	
CO	Confidential, only for members of the consortium (including the Commission Services)	

D-RAIL consortium

1.	UNIVERSITY OF NEWCASTLE UPON TYNE	UNEW	United Kingdom
2.	UNION INTERNATIONALE DES CHEMINS DE FER	UIC	France
3.	RAIL SAFETY AND STANDARDS BOARD LIMITED	RSSB	United Kingdom
4.	TECHNISCHE UNIVERSITAET WIEN	VUT	Austria
5.	PANTEIA BV	PANTEIA	Netherlands
6.	CHALMERS TEKNISKA HOEGSKOLA AB	CHALM	Sweden
7.	POLITECNICO DI MILANO	POLIM	Italy
8.	THE MANCHESTER METROPOLITAN UNIVERSITY	MMU	United Kingdom
9.	LUCCHINI RS SPA	LUCC	Italy
10.	MER MEC SPA	MERM	Italy
11.	FAIVELEY TRANSPORT ITALIA SPA	FAIV	Italy
12.	TELSYS GMBH	TELS	Germany
13.	OLTIS GROUP AS	OLT	Czech Republic
14.	VYZKUMNY USTAV ZELEZNICNI AS	VUZ	Czech Republic
15.	DEUTSCHE BAHN AG	DB	Germany
16.	HARSCO RAIL LIMITED	HARS	United Kingdom
17.	SCHWEIZERISCHE BUNDESBAHNEN SBB AG	SBB	Switzerland
18.	OBB-Infrastruktur AG	OBB	Austria
19.	SOCIETE NATIONALE DES CHEMINS DE FER FRANCAIS	SNCF	France
20.	TRAFIKVERKET - TRV	TRV	Sweden

Document History

Version	Date	Authors / Contributors	Description of additions / modifications
v1	29/03/2013	all	Draft for review among partners
V2	09/04/2013	all	For technical review
V3	24/05/2013	all	With additional results following joined WP3, WP4, WP5 and WP6 meeting
V4	31/05/2013		Full version
F1	03/06/2013		Text revisions and complementing material
F3	15/11/2013		Revisions after review

Executive Summary

The aim of this deliverable is to assess through numerical simulations the critical parameters of both vehicle and track range, their variation range and their combination for different derailment scenarios based on conclusions by WP1 and WP3.1:

- derailments in straight and curved tracks
- derailments in switches and crossings (S&C) that are an extremely crucial and sensitive component in all railway systems
- derailments due to sloshing that, according to track geometry and vehicle speed, may lead to critical wheel unloading
- derailments due to wheel and rail failures

A bottom-up approach is adopted, i.e. through numerical simulation a detailed technical investigation encompassing a multitude of influencing parameters is carried out with the aim of defining the threshold operational conditions (which implies also parametric combinations) as precisely as possible. This requires a detailed knowledge of which parameters have an influence, how significant this influence is, and how the influencing parameters interact.

Thus, the influence of a broad variety of parameters, such as vehicle suspension, track geometry and condition etc, on the risk of derailment has been investigated, especially considering operational conditions known to be prone to derailment (e.g. asymmetrical loading, tank wagons, etc).

In deliverable D1.1 derailment data were collected from safety databases in the USA, Russia, and several European countries, as well as UIC and ERADIS and classifies derailments into five main categories: Infrastructure, Rolling Stock, Operation, Weather and Unspecified.

A shortlist with eight European main line derailment causes (ranking with respect to cost and number) was derived:

1. axle ruptures
2. excessive track width
3. wheel failure
4. skew loading
5. excessive track twist
6. track height/cant failure
7. rail failures
8. spring & suspension failure

For the purpose of the D-Rail project and the current deliverable, the eight European main derailment causes have been re-grouped as follows:

- derailments induced by poor track geometry
 - o excessive track width
 - o excessive track twist

- track height/cant failure
- derailments induced by poor vehicle conditions
 - skew loading
 - spring & suspension failure
- derailments due to failures
 - axle ruptures
 - wheel failures
 - rail failures

Axle ruptures are already being addressed by another EU-project (EURAXLES) and won't therefore be studied in D-RAIL. Note that excessive track width is intended as "very excessive track width" due to rail support failure or rail roll over and is thus not covered in this report.

In order to assess derailment due to flange climbing (basically the first two groups in the re-ordered list) there is the need for a definition of limit conditions in a vehicle dynamics simulation. Moreover, since simulation codes adopted by the partners differ (SIMPACT, VAMPIRE, GENSYS), an initial "benchmark phase" was carried out to check and compare simulation results even in extreme conditions (derailment) and set limit conditions for the identification of a derailment. Focus was placed on the Y25 bogie, which is the most common bogie design in Europe.

For derailment causes related to crack growth and fracture of wheels and rails, numerical simulations featuring stress/strain analysis and fatigue & fracture assessment have been carried out. Also in these cases lot of efforts were put on assuring correct input data in terms of realistically poor operational conditions.

This report provides a *very* detailed account of the background for the analyses, input data, presumptions and modelling choices made, operational scenarios considered, results obtained *etc.* It also includes a discussion on the results including discussions on their implications e.g. in terms of operational recommendations.

Due to the massive scope of the current deliverable, it is not feasible to summarize the results and their implications in an executive summary: The result would either be overly simplistic or too lengthy. Instead this summary is extracted in a dedicated report D3.3 "Guidelines on derailment analysis and prevention". The reader is encouraged to start off with that report and then return to the current report for details on analyses / results of interest.

Table of Contents

1	Introduction.....	10
2	Common vehicle.....	11
	2.1 Model parameters	11
	2.2 Benchmark.....	11
	2.2.1 Benchmark track case	11
	2.2.2 Benchmark results.....	12
	2.2.3 The influence of chassis torsional flexibility.....	15
3	Derailment due to flange climbing in line operations.....	18
	3.1 Influence of vehicle parameters on derailment	19
	3.1.1 Simulation analyses.....	19
	3.1.2 Configuration of vehicle models	20
	3.1.3 Results – Influence of vehicle parameters on derailment.....	26
	3.1.4 Conclusions – Influence of vehicle parameter variation on derailment	67
	3.2 Influence of suspension failure and faults on derailment	73
	3.2.1 Simulation analyses.....	73
	3.2.2 Configuration of vehicle models	73
	3.2.3 Results – Suspension Failure and faults	77
	3.2.4 Conclusions – Suspension Failure and faults.....	90
	3.3 Influence of isolated track defects on derailment.....	91
	3.3.1 Study on existing track defect amplitudes in dependency on defect length	91
	3.3.2 Influence of IAL track defects and their length on the derailment risk.....	93
	3.3.3 Conclusions – Isolated track defects	104
	3.4 Concluding remarks	105
	3.4.1 Identified main affecting parameters.....	105
	3.4.2 Recommendations	108
	3.5 References	109
4	Derailments in switches & crossings	110
	4.1 Background	110
	4.2 Literature survey	110
	4.2.1 Derailment in turnouts.....	110
	4.2.2 Other literature	111
	4.2.3 Standards.....	111
	4.3 Studied derailment scenario	111
	4.3.1 Motivation of derailment scenario.....	111
	4.3.2 Delimitations	112
	4.4 Simulation Procedure	113
	4.4.1 Task 1 Sensitivity studies to find key influencing parameters	113
	4.4.2 Task 2 Evaluation of current standards	113
	4.4.3 Task 3 Limit state as a function of key influencing parameters.....	113
	4.4.4 Task 4 Comparison to standard rails.....	113
	4.4.5 Task 5 Vehicle parameter limits.....	113
	4.5 Numerical simulations	114
	4.5.1 Simulation model	114
	4.5.2 Investigated parameters.....	115
	4.5.3 DOE methodology	117
	4.5.4 Objectives.....	119
	4.5.5 Load Ratios	119
	4.5.6 Overview of parameter study	122

4.5.7	DOE 1.....	122
4.5.8	DOE 2.....	123
4.5.9	DOE 3 skew loading.....	126
4.5.10	DOE 4 track irregularities.....	132
4.5.11	Summary of parameter studies.....	142
4.5.12	Bad case.....	144
4.5.13	Vehicle parameter limits.....	149
4.5.14	Vehicle configuration and observed load imbalances.....	151
4.5.15	Load imbalance criteria.....	155
4.5.16	Discussion and conclusions for vehicle parameter limits.....	161
4.6	References.....	164
5	Derailments due to sloshing.....	165
5.1	Background.....	165
5.1.1	Literature survey.....	165
5.2	CFD analysis.....	166
5.2.1	Description of the model of the fluid.....	166
5.2.2	Results.....	167
5.2.3	Damping.....	171
5.3	Equivalent mechanical model.....	172
5.4	Multi-body model of the tank vehicle.....	181
5.5	Results of the parametric analysis.....	188
5.5.1	Non-dimensional relation.....	188
5.5.2	Effect of the length of the intermediate straight.....	191
5.5.3	Effect of the curve radius.....	195
5.5.4	Effect of the fill level.....	197
5.5.5	Effect of the length of the counter-curve.....	198
5.6	Concluding remarks.....	200
5.6.1	Identified main affecting parameters.....	200
5.6.2	Estimation of commercial impact of preventive measures.....	201
5.7	References.....	201
6	Derailments due to wheel failures.....	202
6.1	Derailment scenarios.....	202
6.2	Studied wheel designs.....	203
6.3	Numerical simulations.....	203
6.3.1	Numerical models.....	204
6.3.2	Parametric studies.....	214
6.4	Results.....	215
6.4.1	Mechanical loading from wheel-rail contact.....	215
6.4.2	Thermomechanical loading from tread braking.....	220
6.4.3	Wheel web fatigue due to track brakes.....	230
6.4.4	Wheel web fatigue due to combined mechanical and thermomechanical loading.....	233
6.4.5	Cracks in wheel rim and web.....	237
6.5	Derailments caused by mechanical wheel tread cracking.....	243
6.5.1	Studied derailment scenarios.....	243
6.5.2	Influencing parameters.....	244
6.5.3	Prevention of wheel breaks caused by RCF.....	245
6.6	Concluding remarks.....	245
6.7	References.....	248
7	Derailments due to rail failures.....	250
7.1	Studied derailment scenarios.....	250

7.2 Numerical simulations	250
7.2.1 Model for numerical analysis of dynamic interaction between wheel and rail	250
7.2.2 Model for numerical analysis of crack loading, risk of fracture and crack growth	254
7.2.3 Influence of main parameters – definition of a “bad case scenario”	258
7.3 Operational conditions resulting in high risk of rail breaks	259
7.3.1 Nominal track conditions	259
7.3.2 Influence of hanging sleepers	260
7.3.3 Influence of lateral rail bending	262
7.4 Crack growth and pertinent inspection intervals	262
7.4.1 Influence of temperature	263
7.4.2 Influence of crack geometry.....	263
7.4.3 Load cycles for head crack growth prediction.....	264
7.5 Wöhler curve based prediction	268
7.6 Validation of predictions	268
7.7 Other rail break mechanisms	270
7.8 Concluding remarks	270
7.8.1 Identified main affecting parameters.....	270
7.8.2 Estimation of commercial impact of preventive measures.....	271
7.9 References	271
8 Conclusions.....	273
8.1 Derailment due to flange climbing in line operations	273
8.1.1 Limits to lateral load imbalance	273
8.1.2 Bogie suspension variation.....	274
8.1.3 Suspension failure and faults	275
8.1.4 Isolated track defects	275
8.2 Derailments in switches & crossings	275
8.2.1 The most influential parameters	276
8.2.2 Bad vehicle-turnout case.....	276
8.2.3 Vehicle parameter limits	277
8.2.4 Implementation strategy.....	279
8.3 Derailments due to sloshing.....	279
8.4 Derailments due to wheel failures.....	280
8.4.1 Identified main affecting parameters.....	281
8.4.2 Estimation of commercial impact of preventive measures.....	281
8.5 Derailments due to rail failures	282
8.5.1 Identified main affecting parameters.....	282
8.5.2 Estimation of commercial impact of preventive measures.....	283
Appendices	284
Common model for WP3.2.....	284
Vehicle Parameters of the Benchmark Y25 Box Wagon	284
Track Parameters	287
Dynamic Simulation Environment	288
Results table for influence of vehicle parameters on derailment resistance	291
Comparison of EN 14363 and GM/RT 2141 – with respect to resistance to derailment, in the context of D-Rail simulation cases.....	295
Overview of the methods	295
Equivalentents between the standards	296
Differences between the equivalent methods	297

1 Introduction

The report sets out with a description of a common vehicle to be employed in the subsequent vehicle dynamics simulations. The common vehicle description has been used for benchmarks to assure that output from the numerical codes employed by the project partners is consistent.

This is followed by in-depth analyses of the risk of derailment due to flange climbing on the line, in switches and crossings where the derived vehicle models are used. To complement these analyses, chapter 5 provides a detailed analysis of the influence of sloshing loads.

Fracture of wheels and rails are investigated in chapters 6 and 7, respectively.

Finally chapter 8 summarizes conclusions from the analyses.

Additional material is placed in appendices.

2 Common vehicle

In order to limit the extent of the simulation workscope and form commonality between the simulation partners, a single bogie type was agreed for use in the project. The selected bogie was the Y-series type, which forms a large population of the freight fleet running in Europe.

To ensure that each partner's bogie model was functionally correct, a benchmark vehicle and simulation environment was defined for use by all partners. This subjected the vehicle models to a closely controlled validation process, with the primary aim of demonstrating the correct derailment response prior to application within WP 3.2.

2.1 Model parameters

To facilitate the model benchmarking exercise, a detailed list of vehicle and track parameters were defined. These are listed in Appendix 0. The parameter values were distributed to the simulation partners and used to create the benchmark models. Vehicle parameters included a full definition of the Y-series bogie setup, including spring stiffness, friction levels, clearances, pre-loads – all values expected for a detailed vehicle dynamics study.

The track model, which can also influence the forces predicted within the simulations was also fully defined. This included degrees of freedom, track system components and the linear stiffness and damping terms used to define the dynamic behaviour. (Appendix 0)

In addition to the parameters themselves, a dynamic simulation environment was also defined. This dictated the required wheel and rail profile shape and inclination. Wheel-rail friction, numerical integration settings and output channels were also defined. (Appendix 0)

2.2 Benchmark

2.2.1 Benchmark track case

With the primary aim of ensuring the correct prediction of derailment performance, a track case was generated to create high levels of wheel lift relative to the rail and promote flange climb derailment. The philosophy of the track geometry was to impose significant curvature and twist, thereby increasing lateral forces (Y) and reducing vertical forces (Q), thereby creating high Nadal derailment quotients (Y/Q). To further promote a flange climb response, a rail dip fault was also added to the high rail. An overview of the track geometry is shown in Figure 1 and Figure 2 below.

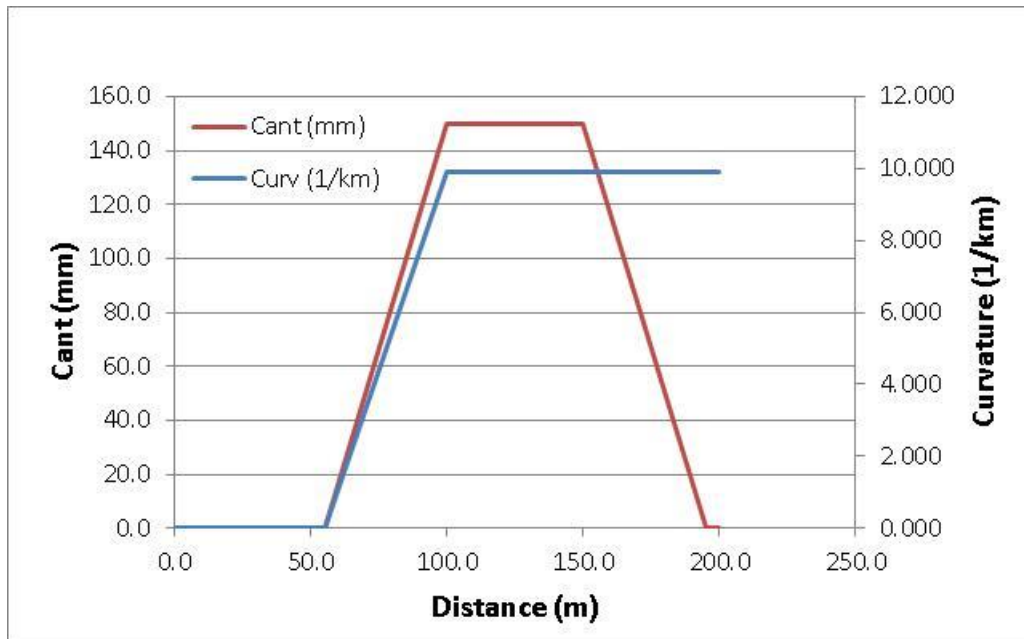


Figure 1 Track geometry.

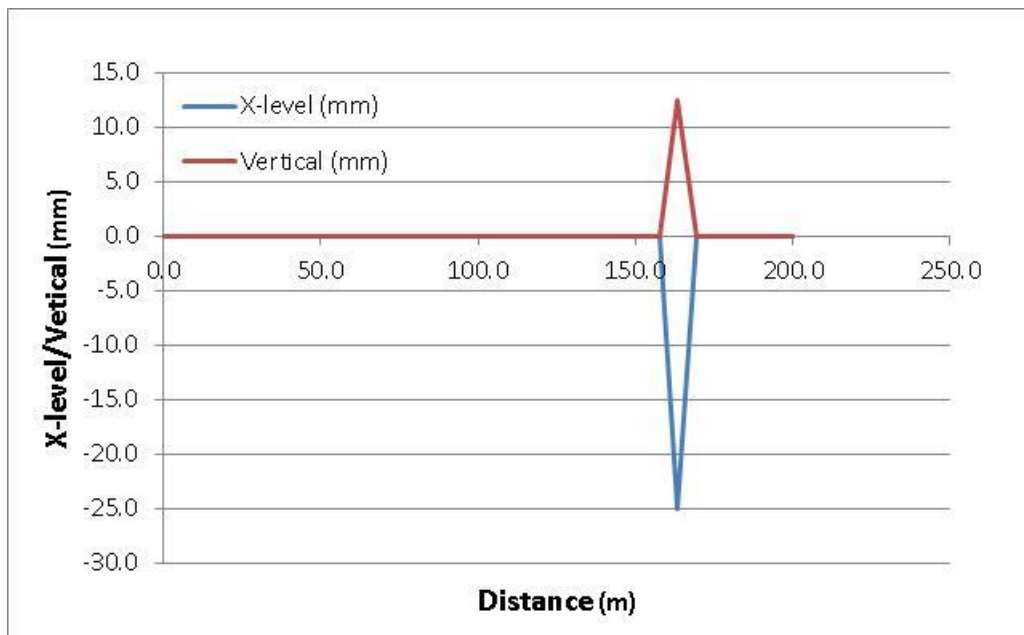


Figure 2 Dip geometry.

With reference to the above figures; a curve radius of 101m (9.9 km⁻¹), with 150mm of cant was combined with a 25mm dip. The dip semi-span was 6m. The curvature and cant transitions were 45m in length. All simulations were carried out at a trundle speed of 4m/s.

2.2.2 Benchmark results

This section presents results from the benchmark simulation case. The benchmark exercise has been performed by University of Huddersfield (UoH), Deutsche Bahn (DB), Politecnico di Milano (PoliMi) and Chalmers University of Technology. To compare the different simulation models, a set of output results relevant for the estimation of derailment risk or derailment limit were selected. The output quantities compared are plotted in Figure 3-8. All results are for the leading outer wheel or leading wheel as indicated on top of each figure. The

agreement isn't perfect, but good enough to provide confidence that the models used by the D-rail partners are qualitatively similar and provides reasonable results. All results are filtered with a 2m sliding window average.

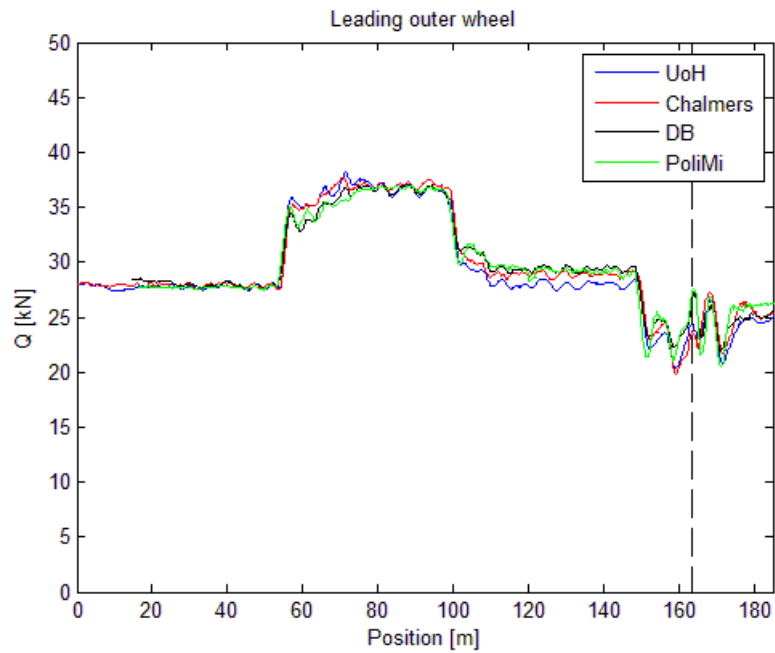


Figure 3 Vertical wheel force Q as function of position along the track for the leading outer wheel

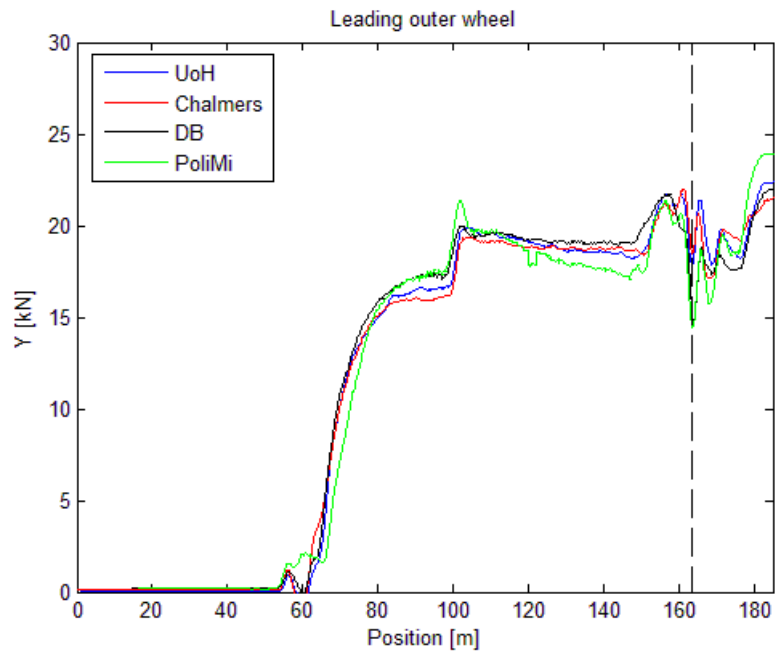


Figure 4 Lateral wheel force Y as function of position along the track for the leading outer wheel

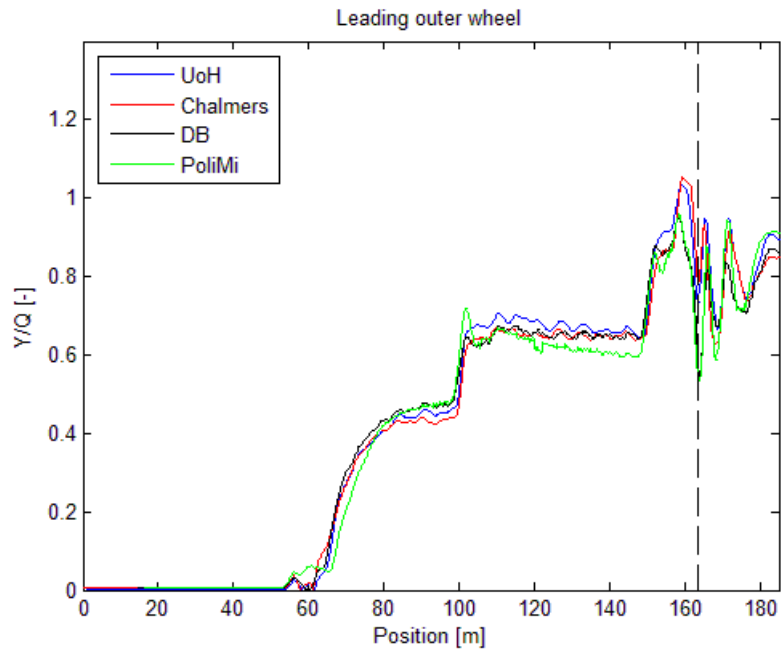


Figure 5 Y/Q ratio as function of position along the track for the leading outer wheel

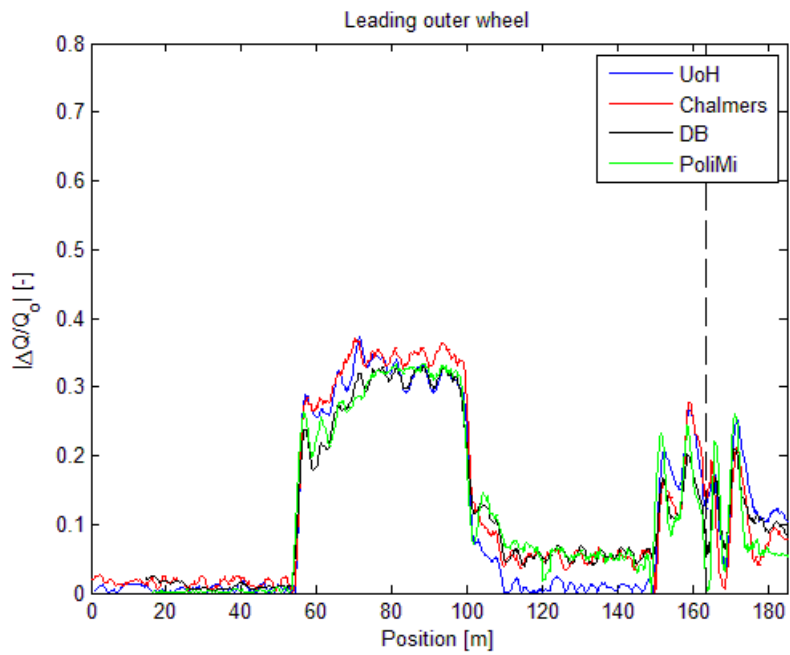


Figure 6 Magnitude of change in Q over the static Q value as function of position along the track for the leading outer wheel

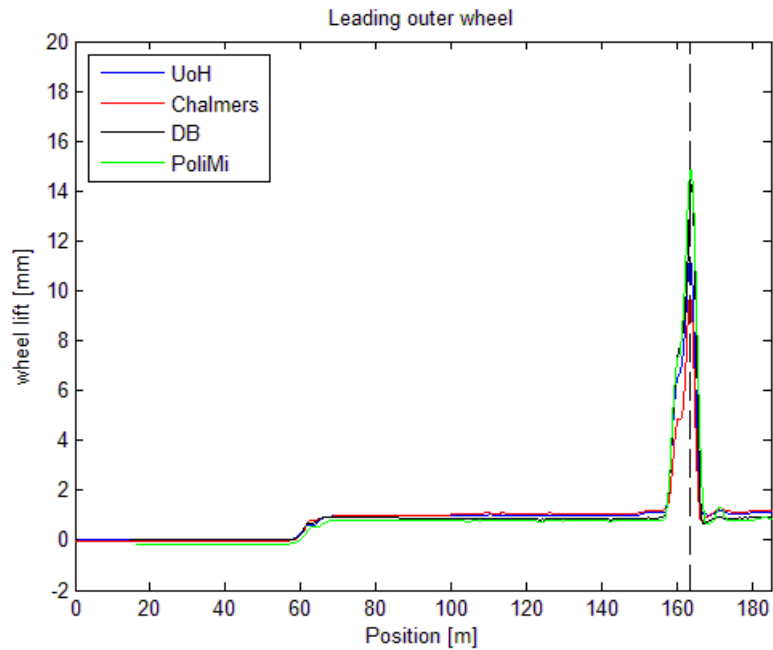


Figure 7 Wheel lift as function of position along the track for the leading outer wheel

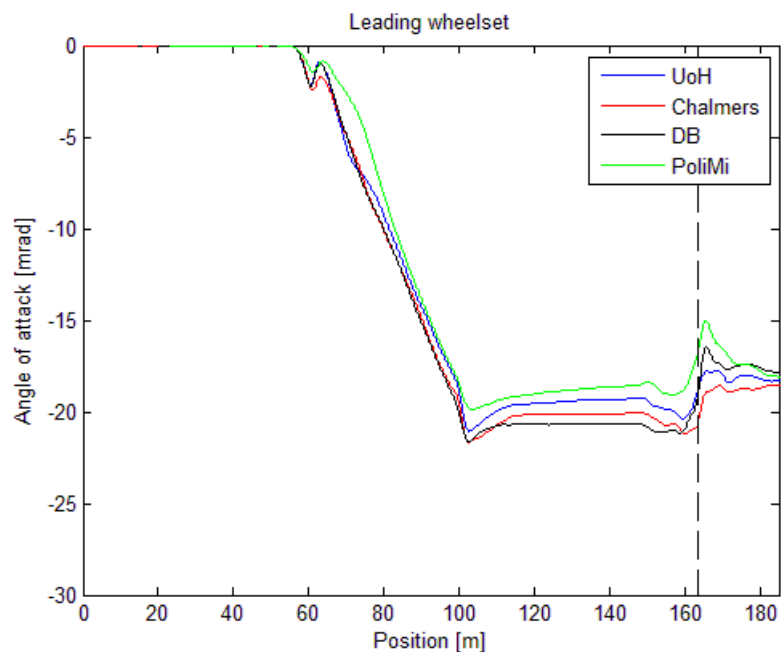


Figure 8 Yaw rotation for leading wheel set as a function of position along the track

2.2.3 The influence of chassis torsional flexibility

The influence of chassis torsional flexibility on the results for the benchmark simulation case has been studied by Chalmers. A car body torsional stiffness property has been implemented by splitting the carbody into two identical parts, one for each end, and reconnecting them by the introduction of a bushing element with a prescribed torsional stiffness and very high stiffness in all other directions.

Simulations are run for the tare and laden states for three different levels of torsional stiffness. In addition to a rigid car body, the investigation also includes two stiffness levels provided by UoH. The simulations are summarised in Table 1.

Table 1 Specification of simulation runs for the investigation of car body torsional stiffness.

Simulation	Load state	Chassis torsional stiffness	Type of vehicle
1	Tare	Rigid	Idealized
2	Tare	18.1MN/rad (stiff)	Hopper wagon
3	Tare	0.5 MN/rad (weak)	Container flat wagon
4	Laden	Rigid	Idealized
5	Laden	18.1MN/rad (stiff)	Hopper wagon
6	Laden	0.5 MN/rad (weak)	Container flat wagon

The outputs compared are Y/Q , wheel lift and torsional rotation in the bushing element providing the chassis torsional flexibility. The results are presented in Figure 9, Figure 10 and Figure 11. Maybe the most interesting results regarding derailment prediction is that the wheel lift is drastically reduced for the laden case also for the stiff torsional flexibility as seen in Figure 10. Thus, the rigid car body model is a conservative approach. All results are filtered with a 2m sliding window average.

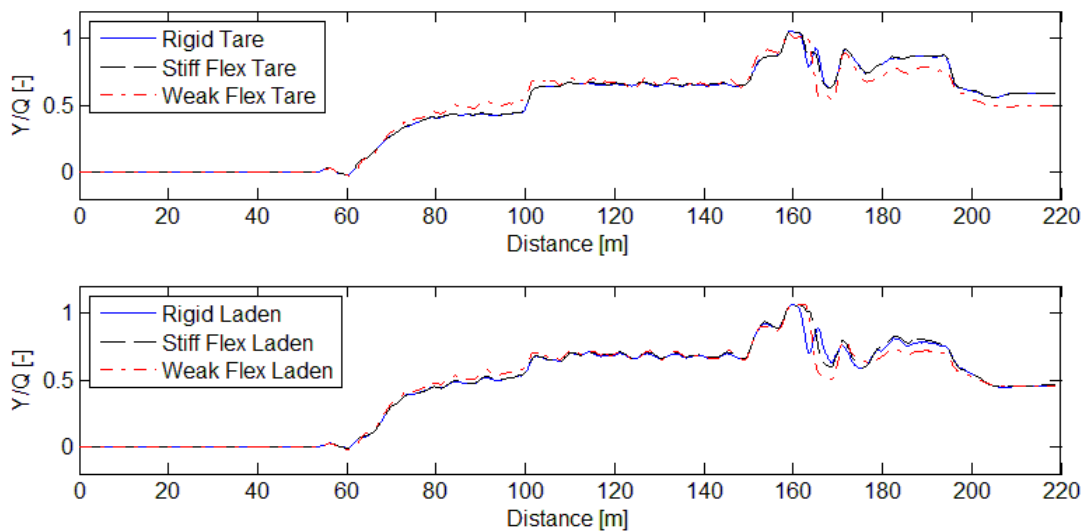


Figure 9 Y/Q_{2m} output from the benchmark simulation for three different levels of chassis torsional stiffness at two different load states

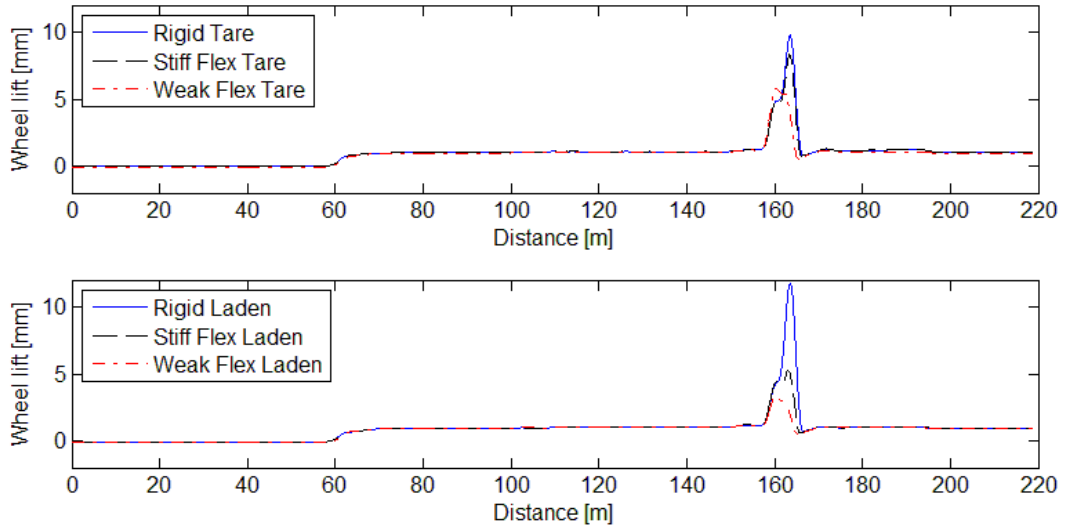


Figure 10 Wheel lift output from the benchmark simulation for three different levels of chassis torsional stiffness at two different load states

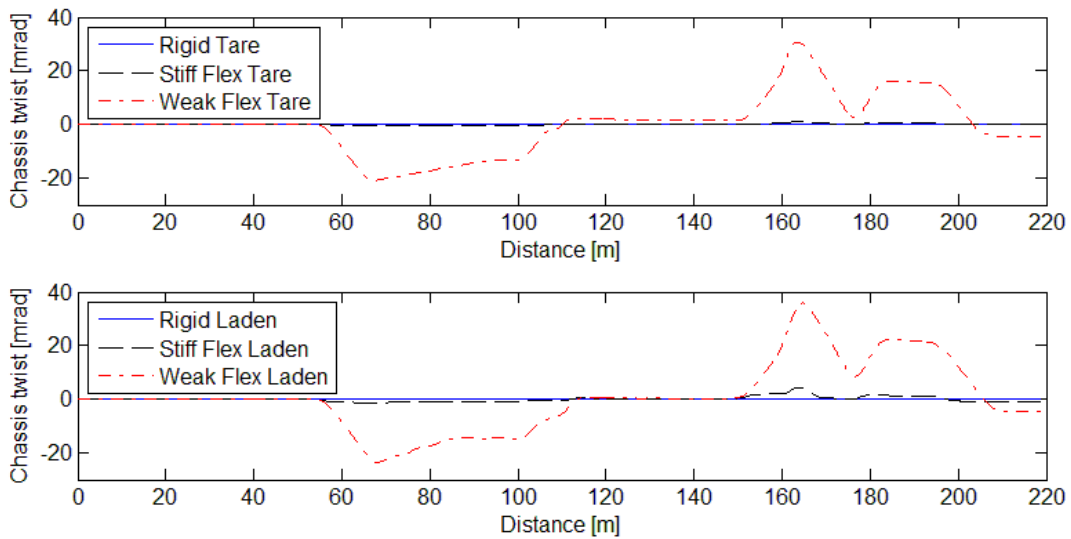


Figure 11 Chassis torsional rotation output from the benchmark simulation for three different levels of chassis torsional stiffness at two different load states

3 Derailment due to flange climbing in line operations

This section considers the influence of vehicle condition on the resistance to flange climb derailment in plain line operations. The section is split into two categories. The first considers controllable vehicle parameters, which might be determined during a vehicle's design process or affected by in-service conditions and maintenance regimes. The second considers various failure modes of a number of key suspension components; the likelihood or mechanism of the failure is not studied, just the influence the failure might have on derailment resistance.

The vehicle parameters included in the study were:

- Skew loading – primarily in the scope of container vehicles
- Both lateral and longitudinal skew loading (and combinations thereof were considered)
- Primary spring nest
 - Tare spring rate
 - Laden spring rate
 - Tare to laden spring clearance
- Primary damping – through manipulation of the coefficient of friction in the primary suspension system
- Bogie yaw resistance – through manipulation of the coefficient of friction in the secondary suspension system

The failure modes included in the study were:

- A failed Lenoir link
- A failed primary spring
- A failed side bearer unit
- Bogie frame twist

A number of derailment measures were used to assess the resistance to flange climb derailment. These were:

- $\Delta Q/Q$ – the quotient of the change in static wheel load and the nominal static wheel load. The measure quantifies the degree of wheel unloading which might arise on twisted track.
- Y/Q – the quotient of the lateral and vertical forces at a given wheel. The measure quantifies the likelihood the flange will ride up over the gauge corner of the rail when high lateral forces (e.g. from curving) are coupled with wheel unloading (e.g. track twist or dip).
- Wheel lift – the height (in mm) which a given wheel is lifted from its nominal height when the wheelset is positioned centrally on the track. The measure provides a similar indication as the Y/Q ratio; however it can also give an indication of how close a vehicle came to derailment.

- X-factor – a measure of the yaw resistance between the bogie and the vehicle body. The measure aims to provide an indication of the likelihood for high bogie angle of attack (and excessive lateral wheel rail forces) on tight curves.
- Peak counting – counts the number of acceleration peaks of given amplitude from ride test data. The philosophy of the assessment is that a much larger number of small acceleration peaks may be tolerated than high accelerations. A limit line is provided by the GB Railway Group Standard GM/RT 2141 in both the lateral and longitudinal directions.

3.1 Influence of vehicle parameters on derailment

This section addresses the influence of vehicle load conditions and bogie suspension parameters on the propensity for a vehicle to derail through flange climb.

3.1.1 Simulation analyses

A number of vehicle parameteric studies have been carried out to understand their relationship to derailment propensity within plain line operations. The detailed configurations of the vehicle models are defined within Section 3.1.2. This was also supplemented by analysis of in-track wheel load measurements in the context of skew loading. This and the parameter variation tasks are summarised below:

- Skew loading (longitudinal and lateral load offset)
- Analysis of measured wheel load data with respect to skew loading
- Bogie suspension variation:
 - Tare spring rate
 - Laden spring rate
 - Tare-laden spring clearance
- Bogie yaw resistance variation

A base vehicle model was configured using nominal parameters for a Y-series freight vehicle. The relevant parameters of the base vehicle were then modified as necessary to generate the derivatives for the parameter variation studies identified above.

For each set of parameters simulations of the derailment cases detailed below were carried out. Where deemed necessary additional simulations were undertaken to better understand notable trends in the results of the derailment assessments. Details of these cases are presented in the discussion of results (Section 3.1.3) where applicable.

A number of derailment assessments were used to establish the influence of parameter variation on flange climb derailment. To provide a reference framework and also to include a review of the current industry standards, the assessments were based on the Euro Norm EN 14363 and on the GB Railway Group Standard GM/RT 2141. All the assessments were simulated using the Vampire vehicle dynamic simulation software. The scenarios, and relevant track geometry and simulations of lab tests studied were as follows:

- EN 14363 $\Delta Q/Q$ test – Simulation of a static laboratory test.

- GM/RT 2141 $\Delta Q/Q$ Appendix A – Simulation of a static laboratory test.
- X-factor test (common to both standards) – Simulation of a static laboratory test.
- EN 14363 Y/Q test – Simulation of an on track flange climb assessment.
- GM/RT 2141 Appendix C, Y/Q simulations – Suite of transient simulations to assess flange climb.
- GM/RT 2141 Appendix D, Assessment of on-track ride; vertical and lateral body accelerations

Note that the conditions used to determine the $\Delta Q/Q$ quotient in GM/RT 2141 and EN 14363 are dissimilar, while the limit values imposed are the same. This is discussed further under the review of relevant standards in Appendix 0.

3.1.2 Configuration of vehicle models

The following section describes the vehicle models used in each of the simulation scenarios used in the derailment studies undertaken. These include offset loading cases, bogie parameter variations and failure modes.

3.1.2.1 Base vehicle model

A base vehicle model was developed in the Vampire modelling environment, using parameters extracted from the benchmarking exercise. The vehicle featured Y-series bogies with a bogie semi-spacing of 7 m.

The parameters of this base vehicle were then varied to produce a suite of vehicles for each parameter study. For traceability each vehicle was given a unique number which can be used to cross-reference the vehicle parameters used in Section 0.

3.1.2.2 Skew loading parameters

Loading cases were required to ascertain the influence of asymmetric loading (both laterally, longitudinally and combined), a range of loadings from tare to laden and combined high loads with a high centre of gravity.

For the purpose of the plain line derailment simulations, asymmetric loading conditions which have been found to be contributory causes to past derailments in the UK were used as a starting point to define plausible loading conditions. Container vehicles and bulk carriers were considered separately due to the differing scope for asymmetrically loading the two freight types.

Container vehicles

A range of plausible asymmetric loading conditions for container vehicles were specified based on: the Rail Accident Investigation Branch (RAIB) investigation into the derailment of a FEA(B) container wagon at Duddleston Jn.[1]; Freightliner's permissible loading configurations for those vehicles (contained within the RAIB report); and the UIC RIV limit for wheel and axle load imbalance [2]. The loading configurations are shown in Table 2 which includes the appropriate container weights required to achieve the load conditions. This is relevant to the derivation of the plausible loading configurations and does not mean that the cases are irrelevant to other wagon/cargo types. For the general case, and for input into the dynamic

simulations, it is the longitudinal and lateral offsets of the centre of gravity (CoG) which are of interest. The sign of the CoG offsets in Table 2 will generate the worst case for the leading left wheel of the vehicle when traversing a right hand curve using the Vampire coordinate system.

Table 2 Summary of Asymmetric Loading Conditions Applicable to Container Vehicles.

	40' Container Weight (t)	20' Container Weight (t)	Resultant Mass (t)	Longitudinal CoG Offset (m)	Lateral CoG Offset (m)
Best Case	35	17.5	52.5	0.00	0
	30	19	49	-0.50	0.04
	26	20	46	-0.93	0.08
	23	20.5	43.5	-1.26	0.12
	20	21	41	-1.64	0.16
	17	21.5	38.5	-2.06	0.2
	14	22	36	-2.54	0.24
	11	22.5	33.5	-3.09	0.28
	8	23	31	-3.74	0.32
	5	23.5	28.5	-4.49	0.36
Worst Case	3.8	24	27.8	-4.85	0.4

The range of CoG offsets in Table 2 represent the reality that a heavily laden container vehicle with a large lateral load offset is unlikely: for this to be the case both/all containers on the vehicle would need to have a significant load offset, and both need to be loaded with the offset to the same side. However, as the range of load offsets does not include independent longitudinal and lateral variation in load offset, it will not be possible to subsequently identify which is the most influencing factor (the longitudinal offset or the lateral offset).

Consequently four longitudinal and lateral offset cases were selected from Table 2 and combined to produce 16 vehicles, where the offsets vary independently of each other. To improve resolution around the lower range of lateral offset, two additional lateral offsets were also defined. The resulting 24 load combinations are summarised in Table 3.

The matrix of lateral and longitudinal load offsets deviates from the logic used to identify suitable limit conditions in that significant lateral offsets are combined with high pay loads. The combinations in Table 3 have therefore been colour coded: green for plausible, orange for less plausible and red for unlikely. For reference Figure 12 shows the distribution of the longitudinal and lateral load imbalances with respect to the RIV loading limits (red).

Table 3 Pay Load for Varying Longitudinal and Lateral Load Offsets. Green indicates plausible load cases, orange are less plausible and red are unlikely.

		Longitudinal Offset (m)			
		0.00	-1.64	-3.74	-4.85
Lateral Offset (m)	0.00	52.5	41	31	27.8
	0.05	52.5	41	31	27.8
	0.10	52.5	41	31	27.8
	0.16	52.5	41	31	27.8
	0.32	52.5	41	31	27.8
	0.40	52.5	41	31	27.8

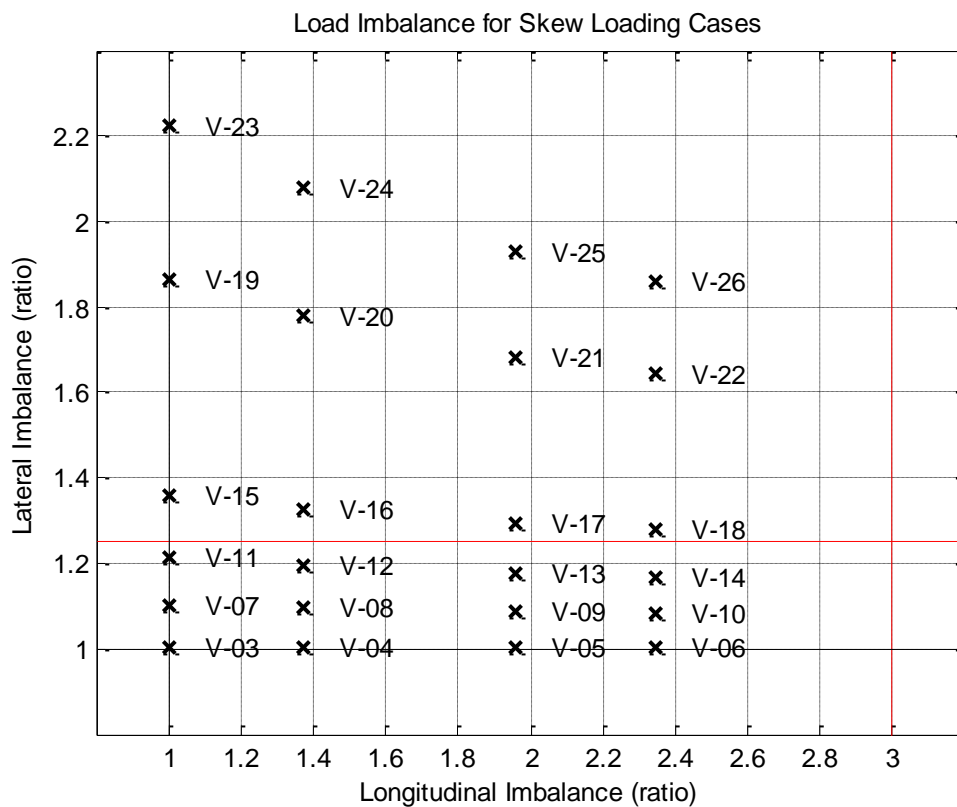


Figure 12 Distribution of Load Imbalance Cases with respect to the RIV Loading Limits (red lines).

The payload parameters were combined with the base tare vehicle body parameters to produce the overall load, centre of gravity offsets and inertias for the laden vehicle bodies.

Bulk carriers

Bulk carriers nearly always travel either fully laden or tare, this is with the possible exceptions of engineering vehicles, ballast hoppers and other specialist traffic. The loading cases considered here aim to be applicable to the majority of bulk carriers and is therefore focussed on either fully laden or tare laden conditions, where there is limited scope for asymmetrical loading.

When investigating a derailment of an HHA coal hopper wagon near the Foreign Ore Branch [3] the RAIB identified the longitudinal and lateral offset of the load as a causal factor in the derailment. The RAIB report found the imbalance in wheel load to be skewed 1 : 1.32 laterally and 1 : 1.04 longitudinally to the rear. As this degree of asymmetry was identified as being causal to the derailment it provides an indication of the appropriate range of asymmetry to be used for these cases.

Based on a bogie centre pivot spacing of 14.1 m and a contact patch spacing of 1.52 m, the load imbalance relates to a CoG positioned at -0.141 m longitudinally and at 0.106 m laterally (unloading the leading left wheel in a right hand curve). These levels of asymmetry are significantly less than those derived for container vehicles in the previous section. The wagon in the Foreign Ore Branch case study was loaded with 57 t of coal, compared to the maximum permissible load of 74 t (approx.) for a HHA wagon. The RAIB report refers to a normal load being 70 t.

In addition to the possibility for the load to be offset longitudinally and laterally, depending upon the asymmetry of the load and the angle of repose for the bulk material, the vertical distribution of the load may also vary. This will have an impact on the inertia of the vehicle and affect the dynamic unloading of the critical leading wheel through certain track irregularities. The angle of repose for industrial coal [4] is between 35° and 38°. From this a number of loading conditions were defined.

Initially a typical loading volume for a coal hopper wagon was defined which represents the general shape and nominal dimensions of wagons operating in the UK, such as the HHA, HTA, HYA and HXA. The loading volume also has a similar cross-section to that of stone hopper wagons (such as the HIA, HOA etc.) but is somewhat longer. The loading volume was then reduced from the top down to provide a volume which corresponded to a mass of 74 t when assuming a density of 850 kg/m³ for loose bulk coal. The volume was reduced in four manners in order to provide: a level symmetrical load; a heaped symmetrical load; a heaped laterally offset load; and a heaped longitudinally and laterally offset load. For the heaped cases the angle of repose was assumed to be 38°. For the lateral offset, the load was assumed to be heaped against one side of the volume, with the surface of the load falling at the angle of repose towards the opposite side. For the longitudinal offset a gradient of 3° was assumed for the surface of the load in the longitudinal direction.

Subsequently the position of the centre of gravity for the load was calculated along with the inertia values in the three principle directions through the CoG. These values were then combined with those for a hopper body in tare conditions, resulting in the mass, CoG and inertia values for the laden cases. An additional set of loading configurations were also calculated using a lower density to represent low-density coal (or other less dense bulk materials, but the loaded volume remained the same. These cases are of interest for the influence of suspension failure modes on derailment, as the reduced axle load may make the vehicle more susceptible to friction lock-ups, or higher friction break-out limits.

The loading cases are summarised in Table 4 where the offset values will tend to lead to an unloading of the leading left wheel when traversing a right hand curve. The longitudinal and lateral CoG offsets are with respect to the geometrical vehicle centre, while the vertical offset is specified by the height above the rails.

It should be noted that no attempt was made to directly replicate the conditions of the Foreign Ore Branch derailment with these cases, other than the general concept of an offset

bulk load. It is therefore interesting to note that the longitudinal and lateral CoG offsets derived here are similar to those stated in the RAIB report, which were measured by the WheelChex system prior to the derailment.

Table 4 Summary of Asymmetric Loading Conditions Applicable to Bulk Carriers

Case	Mass (kg)	CoG Offset			Inertia (Through CoG)			
		X (mm)	Y (mm)	h (m)	I _{xx} (Mg.m ²)	I _{yy} (Mg.m ²)	I _{zz} (Mg.m ²)	
High Density Coal (850 kg/m ³)	Load Levelled	90800	0	0	2.154	130.4	1155.6	1151.3
	Load Heaped	90800	0	0	2.172	128.6	1165.5	1150.2
	Load Heaped Laterally Offset	90800	0	100	2.183	132.1	1171.2	1154.4
	Load Heaped Long. and Lat. Offset	90800	-136	98	2.185	132.5	1168.4	1151.6
Low Density Coal (650 kg/m ³)	Load Levelled	73400	0	0	2.124	107.2	967.2	962.8
	Load Heaped	73400	0	0	2.141	105.9	974.8	961.9
	Load Heaped Laterally Offset	73400	0	95	2.152	108.7	979.3	965.2
	Load Heaped Long. and Lat. Offset	73400	-129	92	2.153	109.0	977.2	963.1

Skew loading measurements

An analysis of measured wheel loads from the DB and GB networks is presented in Section 3.1.3.3 which corroborates the skew loading imbalances chosen for the simulation cases (which were devised prior to the measured wheel load data becoming available). Figure 36 shows that the extreme lateral imbalances devised (greater than approximately 1.5) do not appear to occur, while longitudinal imbalance can be greater than the devised cases, and can be as high as the limit of 1:3.

3.1.2.3 Bogie suspension variation

For the Y-Series bogie used here, the following suspension parameters were identified as being potentially influential to derailment resistance: primary tare spring rate, primary laden spring rate, tare-laden spring clearance (in tare state) and damping rate (coefficient of friction). A matrix of parameters was constructed based on a nominal value (taken from the base vehicle model), and a high and low value representing the realistic extremes of the parameters. It is well understood that the load state of the vehicle is also influential to derailment resistance, consequently three load cases were also defined, based on the tare laden base vehicle, the fully laden base vehicle and a part laden vehicle with a mass sufficient to just bring the laden spring into contact.

The variation of the primary spring characteristics (tare rate, laden rate and clearance) were considered separately to the damping rate. In order to reduce the resulting 81 parameter combinations for the spring characteristics (shown in Table 5) to a more manageable number, the extreme values for the suspension characteristics were matched against each

other and the three load states (providing $3 \times 2^3 = 24$ combinations). In addition, the nominal suspension parameters were also matched to the three load cases to form a point of reference. This resulted in 27 vehicle models to be assessed.

Table 5 Summary of the primary spring parameter variation values.

Parameter	Low	Nominal	High
Tare Spring Rate (MN/m)	0.399	0.499	0.624
Laden Spring Rate (MN/m)	0.623	0.779	0.974
Clearance (mm)	8.8	11.0	13.8
Sprung Mass (t)	17.5	26.4	83.9

The variation in damping rate was achieved through the nine parameter combinations shown in Table 6.

Table 6 Summary of the primary damping variation values

Parameter	Low	Nominal	High
Damping friction coefficient	0.2	0.4	0.6
Sprung Mass (t)	17.5	26.4	83.9

3.1.2.4 Bogie yaw resistance variation

The bogie yaw resistance on the Y-Series vehicle design is provided by three friction surfaces: the centre bowl and the left and right hand side bearers. The side bearers are supported by comparatively soft springs (0.572 MN/m was used in the models here) which provide a nominal pre-load of approximately 16 kN per side. The preload is dictated by the relative position of the centre bowl surface and the unloaded side bearers. Therefore the preload is, to the most part, unaffected by the body mass (other than reacting roll torque for asymmetrically loaded vehicles). Therefore, frictional resistance provided by the side bearers can be considered equal for all symmetrically laden vehicles with a body weight greater than 64 kN (all cases considered here). The centre bowl carries the remainder of the vertical load from the vehicle body, and its influence on yaw resistance is therefore related to the body mass.

While the aim here is to investigate the effects of bogie yaw resistance, altering the coefficient of friction at the centre bowl will also have affect the bogie pitch and roll resistance. These other modes of movement will have an influence on the performance of the vehicle through twisted track, and specifically the resistance to wheel unloading ($\Delta Q/Q$). In the simulations undertaken here it would be possible to use differing friction coefficients in the yaw, roll and pitch directions. However, this is far less feasible in reality and therefore the decision was taken to use the same coefficient of friction in the three directions.

The base vehicle was modified to represent conditions of low ($\mu = 0.1$), normal ($\mu = 0.3$) and high ($\mu = 0.5$) coefficients of friction at the centre bowl and side bearers, giving 9 combinations of yaw resistance in total. To determine the combined non-linear influence of the side bearers and centre bowl three symmetrical load cases were also defined to represent high (178 kN axle load), medium (112 kN axle load) and low load (64 kN axle load) conditions. For simplicity these are referred to later as fully laden, part laden and tare laden.

3.1.3 Results – Influence of vehicle parameters on derailment

The following section presents the results of parameter variations carried out based on dynamic simulations to investigate derailment propensity of Y-series bogied railway freight vehicles. This includes analysis of the following cases, assessed in curved track sections and against relevant standards:

- Skew loading
- Analysis of GB Gotcha data with respect to skew loading
- Bogie suspension variation
- Bogie yaw resistance variation

The graphical data presented for each of the numbered vehicle variants is supplemented by tabular output of simulation values within Appendix O. The assessments have been referenced to the EN standard 14363 and the UK standard GM/RT2141. The key differences between the two are described in more detail within Appendix O.

3.1.3.1 Skew loading

Asymmetric or skew loading is a well-documented contributory factor to flange climb derailment. In this section results are presented for simulations of vehicle models with differing extents of skew loadings. The primary aim of the analysis is to investigate the influence of skew loading on the likelihood of derailment. This has been achieved by applying the existing vehicle acceptance standards of EN 14363 and the UK standard GM/RT2141. These are briefly described below. The changes made to the base vehicle model to achieve the skew loading variation cases were described previously in Section 3.1.2.2.

Results for the effect of skew loading on vehicle derailment risk are presented within this section in relation to the following acceptance tests, each of these assessments are described in further detail within Appendix O:

1. EN 14363 Quasi-static Assessment of Wheel Unloading ($\Delta Q/Q$)
2. GM/RT 2141 Quasi-static Assessment of Wheel Unloading ($\Delta Q/Q$)
3. GM/RT 2141 and EN 14363 bogie rotational resistance (X-factor test)
4. EN 14363 Low speed flange climb assessment (Y/Q)
5. GM/RT 2141 Low speed flange climb assessment (Y/Q)

In order to improve the transferability of the skew loading results to other vehicle and loading types, the various derailment resistance assessments have been plotted against the ratio of the wheel loads as used in the UIC RIV limits. For the lateral dimension this was obtained by dividing the mean wheel load on the right side of the vehicle by the mean wheel load on the left side. The UIC RIV limit for lateral variation in wheel loads is 1:1.25 (subsequently referred to as 1.25). In the longitudinal dimension the ratio was obtained by taking the mean axle load on the trailing bogie and dividing it by the mean axle load on the leading bogie. The UIC RIV limit for longitudinal wheel load imbalance is 1:3 (subsequently referred to as 3).

These calculations are summarised in Equations (1) and (2) for the lateral and longitudinal dimensions respectively. The following nomenclature is used: Q is the quasi static wheel load

at the left wheel (L) or right wheel (R) of wheelset 1, 2, 3 or 4 (where 1 is leading and 4 is trailing).

The quasi-static wheel loads were calculated by taking the mean of the dynamic wheel load from a transient analysis with straight and level track with light irregularities. This was to ensure that locked in friction did not affect the wheel loads, as might be the case for a static calculation.

The effects of skew loading offsets are presented only for shifts which unload the leading high rail wheel, i.e. a rearwards longitudinal shift and a lateral shift towards the inside of the curve.

$$\text{Lateral imbalance} = 1 : \frac{\Sigma Q_{R(1,2,3,4)}}{\Sigma Q_{L(1,2,3,4)}} \quad (1)$$

$$\text{Longitudinal imbalance} = 1 : \frac{\Sigma Q_{L+R(3,4)}}{\Sigma Q_{L+R(1,2)}} \quad (2)$$

EN 14363 Quasi-static Assessment of Wheel Unloading ($\Delta Q/Q$)

A quasi-static wheel unloading assessment involves lifting the vehicles wheels by a prescribed amount to simulate traversing track twist. The change in static load as a ratio of the original static load ($\Delta Q/Q$) is then used to gauge likely derailment resistance performance on the basis that high wheel unloading promotes flange climb through low Q values.

The $\Delta Q/Q$ values from the EN 14363 simulations are shown in Figure 13, plotted against longitudinal and lateral wheel load offset. To aid the visualisation of the trends in the data, a surface has been fitted to the data set using a cubic approximation.

The $\Delta Q/Q$ limit is set to 0.6 in both the Euro Norm and the GB RGS. The vehicles with a calculated $\Delta Q/Q$ value within this limit are denoted by a blue ring, while those above are denoted by a red ring.

As would be expected, it can be seen that increasing the load offset in either the lateral or longitudinal directions increases the calculated $\Delta Q/Q$ value. Increasing the longitudinal loading offset alone, up to the accepted loading ratio offset of 3, increases $\Delta Q/Q$ value to close to the limit of 0.6.

Increasing the lateral load offset has a greater influence on the $\Delta Q/Q$ value than longitudinal offset, on a like-for-like basis: the lateral offset having approximately 2.7 times greater influence on the $\Delta Q/Q$ ratio than the longitudinal offset.

Whilst the analysis presented is to an extent vehicle specific, it is clear that lateral loading offset has a significant influence on the quasi-static wheel unloading due to track twist. In this area the applicable standards are not prescriptive regarding the level of offset load which should be considered for acceptance testing and are also not specifically aligned to the UIC RIV loading limits (1.25 lateral and 3.0 longitudinal) which have been widely adopted throughout Europe.

However, the simulations presented in Figure 13 demonstrate that with a lateral load offset at the limit value of 1.25, combined with a high longitudinal load offset approaching 3.0, the vehicle marginally remains within the limit value of 0.6. This result suggests that when considering quasi-static wheel unloading due to track twist the UIC RIV loading limits are

appropriate. This suggests that the key factor in minimising derailment risk in this case is the effective measuring and monitoring of wheel loads in traffic to ensure that vehicles remain within the UIC RIV loading limits.

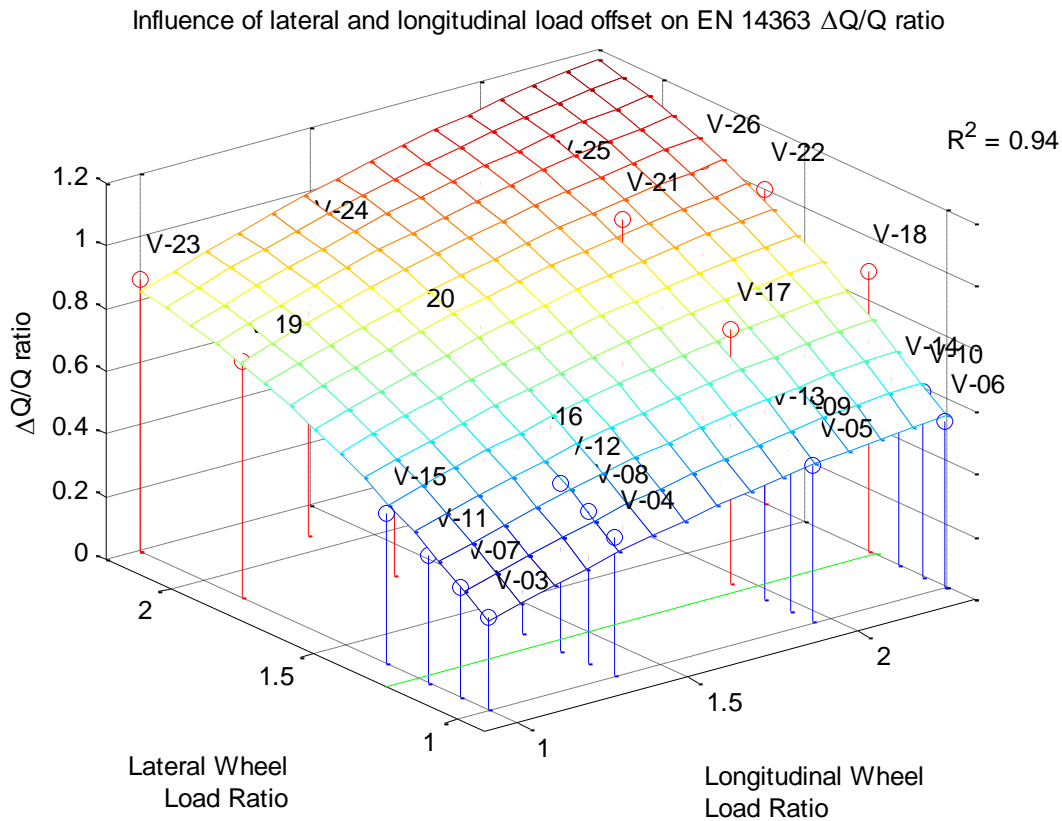


Figure 13 Influence of lateral and longitudinal load offset on EN 14363 $\Delta Q/Q$ ratio.

GM/RT 2141 Quasi-static Assessment of Wheel Unloading ($\Delta Q/Q$)

The $\Delta Q/Q$ values from the GB acceptance standard GM/RT 2141 simulations are shown in Figure 14, plotted against longitudinal and lateral wheel load offset. Whilst the GM/RT 2141 test procedure specifies different twist parameters than EN 14363 the calculated $\Delta Q/Q$ values are similar for both standards. Consequently the same observations can be made for the GM/RT 2141 $\Delta Q/Q$ results as can be made for the EN 14363 results in the previous subsection.

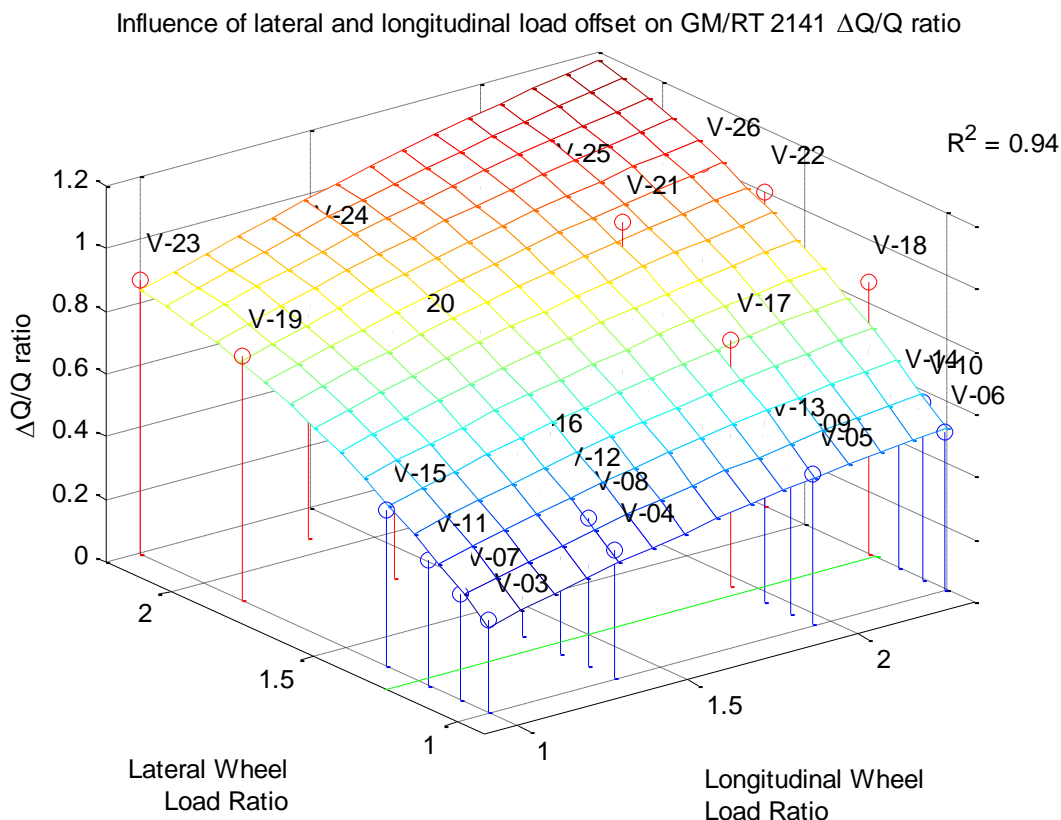


Figure 14 Influence of lateral and longitudinal load offset on GM/RT 2141 $\Delta Q/Q$ ratio.

GM/RT2141 and EN14363 bogie rotational resistance (X-factor test)

A bogie rotational resistance assessment is a quasi-static test which rotates the bogie beneath the vehicle and the body-bogie torque is then measured. The X-factor is derived based on the wheelbase of the bogie and its axle load. A high x-factor is considered a higher derailment risk as it promotes increased lateral wheel-rail forces (Y). The direct influence of bogie x-factor on Y/Q values is presented in Section 3.1.3.4.

The bogie X-factor values calculated for the skew laden vehicles are plotted in Figure 15 against longitudinal and lateral wheel load offset. To aid the visualisation of the trends in the data a surface has been fitted to the data set using a quadratic approximation. It can be seen that the longitudinal wheel load offset has little influence on the bogie X-factor. In contrast, any degree of lateral wheel load offset greater than approximately 1.3 is predicted to lead to a bogie X-factor in excess of the limit value of 0.1, for the vehicle model analysed here.

The influence of lateral load offset on bogie X-factor can be explained by the way in which the standard UIC side bearers of the Y-series bogies influence bogie yaw torque (X-factor being a function of bogie yaw torque, as per equation (1)). The side bearers provide friction damping between the vehicle body and the bogie in the yaw direction. The side bearers carry a component of the body vertical load and are in turn supported on relatively soft springs. The springs allow roll compliance between the body and bogie and also accommodate wear in the friction surfaces. The body roll torque produced by a lateral load offset must be reacted by the side bearers. Where the body roll torque is small there is no net change in the load on the side bearers: as the load on the more 'laden' side increases the load on the opposite side decreases. However this is not the case when the relatively soft support spring

becomes coil bound or the side bearer reaches a metallic bump stop. When the travel of the more 'laden' side bearer is limited in this way the roll displacement of the vehicle body is also limited, which in turn restricts the extension of the side bearer support spring on the opposite side. This situation leads to an increase in the effective body roll torque which must be reacted by the side bearer on the more laden side. Compared to the symmetrically laden case there is a greater net load on the side bearers and consequently an increase in the frictional body to bogie yaw resistance.

For the skew loading cases considered here the side bearer travel on the more laden side was limited by the bumpstop clearance in all laterally asymmetric cases which exceed the UIC RIV limit ratio of 1.25.

Initial simulations suggests that if bumpstop contact can be prevented (by increasing the allowable deflection of the side bearer support spring) the X-factor can be reduced by 20% (based on vehicle V-07 – 0.1 reduces to 0.08). Further analysis of the impact of these changes on vehicle gauging (body sway and drop) would also be required if sidebearer vertical clearance were to be increased.

$$X - \text{Factor} = \frac{\text{Body/bogie yaw torque}}{\text{wheel base} \times \text{axle load}} \quad (3)$$

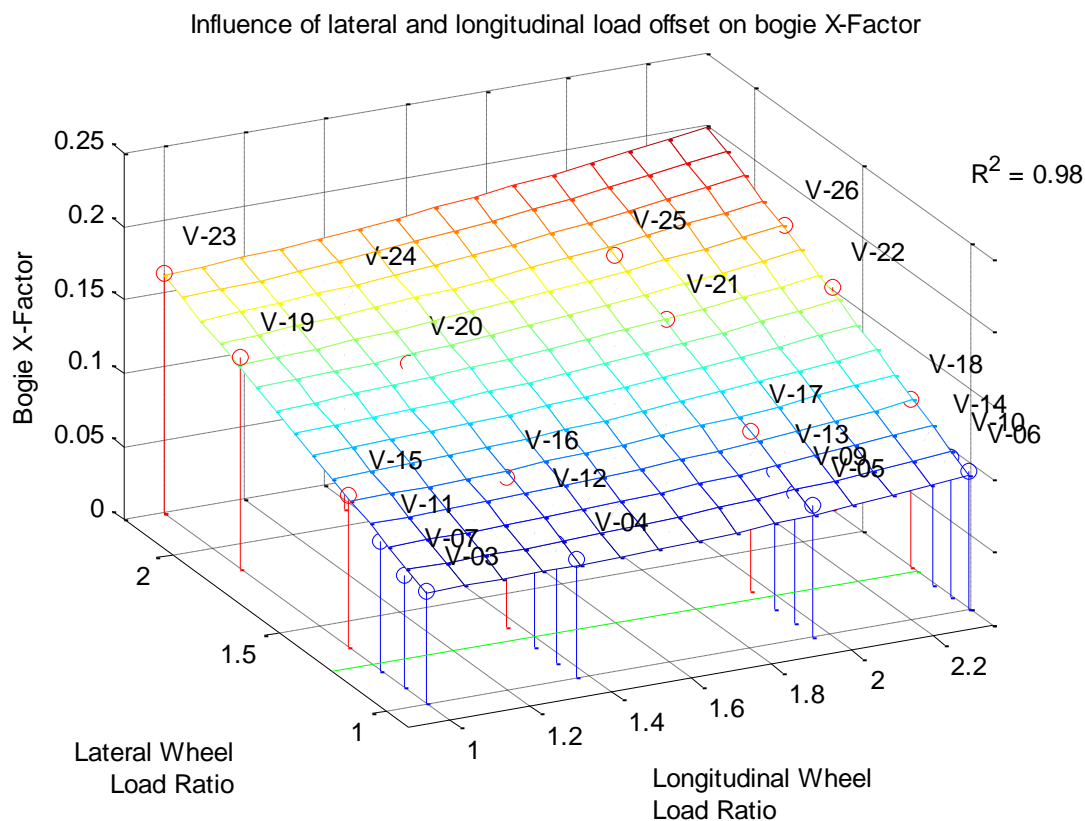


Figure 15 The influence of lateral and longitudinal load offset on bogie X-factor.

EN 14363 Low speed flange climb assessment (Y/Q)

The EN low speed flange climb assessment is used to assess both the steering and twist performance of a vehicle. The vehicle must negotiate a small radius curve with applied cant and track twist without the Nadal derailment quotient exceeding 1.2.

The Y/Q ratios calculated at the leading outer wheel of the vehicles during the EN 14363 Y/Q simulations are plotted in Figure 16. It should be noted that vehicles which produced Y/Q values in excess of 2 are not included so that focus may remain on the vehicles which gave plausible results. EN 14363 states a limit to the maximum Y/Q ratio of 1.2 for a flange angle of 70°. Data points within this limit are presented as blue circles, while values in exceedance are shown as red circles. During the transient simulations a number of vehicles derailed: these are denoted by a suffix '-D' appended to the relevant data labels.

From Figure 16 it can be seen that both the longitudinal and lateral wheel load offsets affect the calculated Y/Q ratio. As seen in the quasi-static $\Delta Q/Q$ analysis the lateral load offset presents the highest influence. Significant exceedance of the lateral offset limit results in failure against the standard without any longitudinal offset loading, However, values close to the lateral offset limit of 1.25 only result in significant exceedance of the Y/Q limit value if longitudinal offset is also present.

Conversely high levels of longitudinal offset without any lateral offset does not present a significant increase in derailment risk.

In summary, the EN low speed flange climb assessment follows the trends seen in the wheel unloading assessment – excessive lateral load offset has a significant effect on the derailment risk. However, if the vehicle remains within the UIC RIV limit of 1.25 then this risk can be reduced.

The maximum wheel lift recorded during the Y/Q assessments are plotted in Figure 17 . It can be seen that tolerance to lateral skew loading reduces with increasing longitudinal load imbalance. For reference, the highest non-derailed wheel lift recorded (Vehicle V-16) was 5.0 mm.

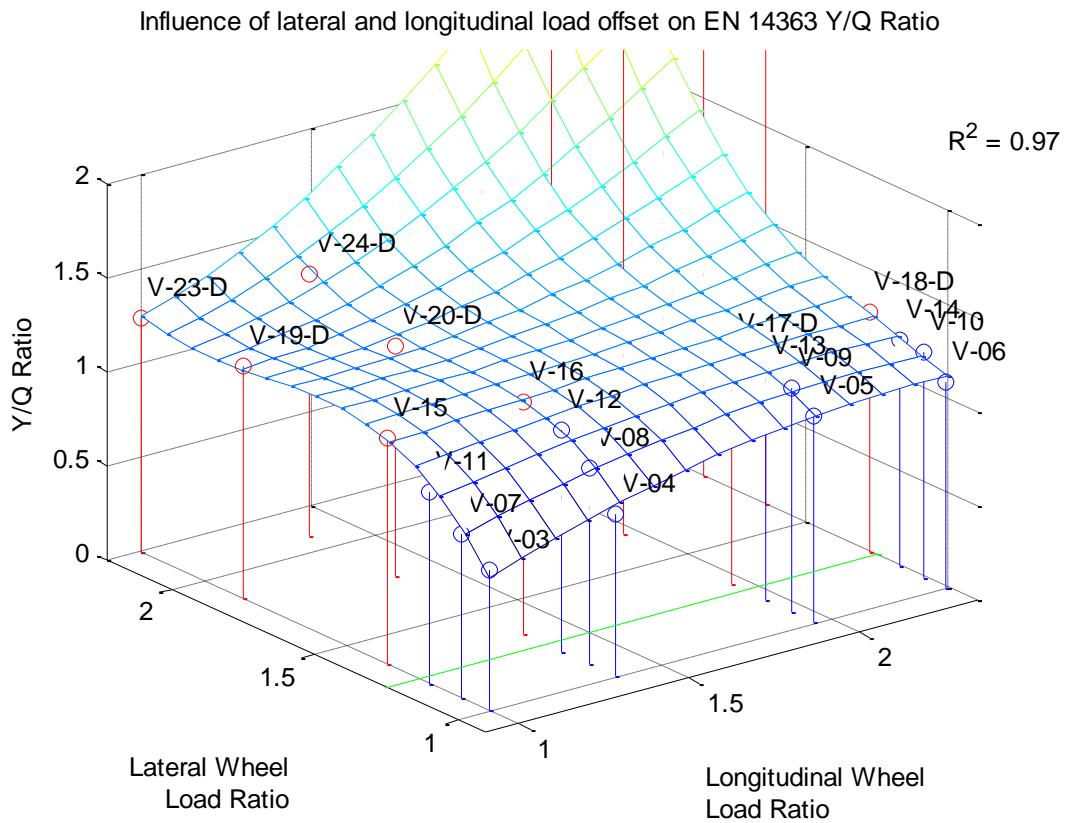


Figure 16 The influence of lateral and longitudinal load offset on EN 14363 Y/Q ratio.

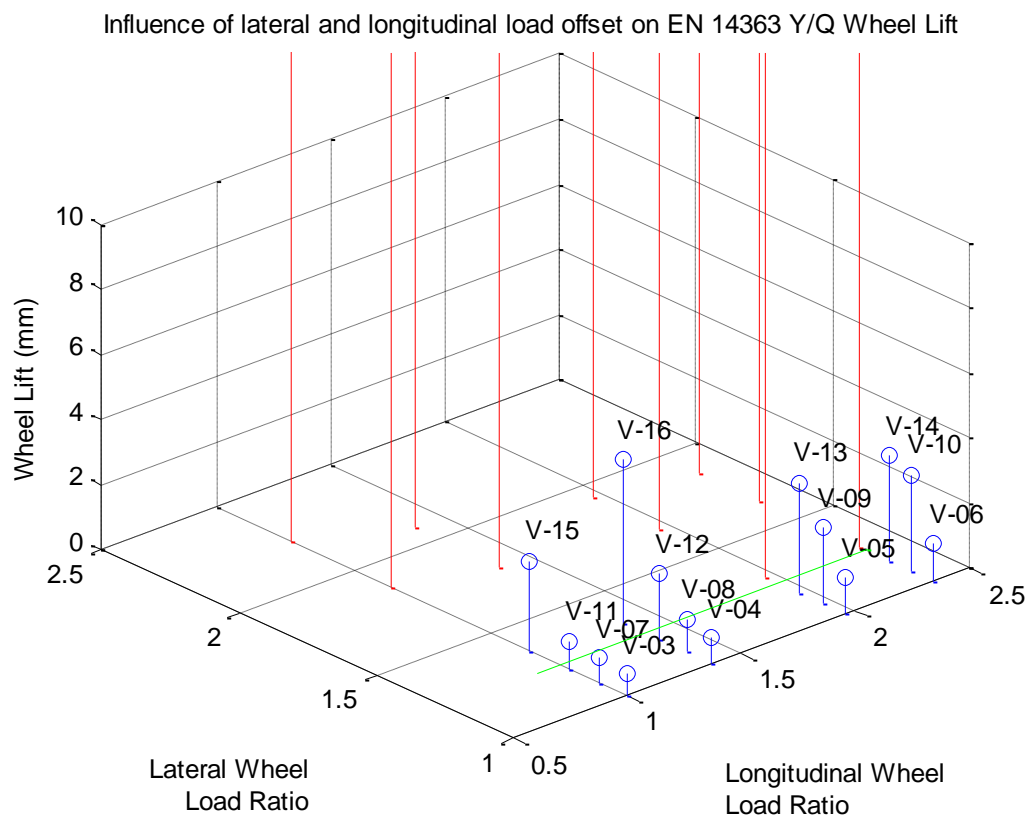


Figure 17 The influence of lateral and longitudinal load offset on wheel lift

GM/RT 2141 Low speed flange climb assessment (Y/Q)

The GB low speed flange climb assessment of GM/RT2141 is similar to that of the EN standard in that it subjects the vehicle to high levels of twist and curvature. However, rather than a single case of curvature and track twist, the GB method applies a range of test track cases with varying levels of track twist and curvature. The philosophy is to present the vehicle with geometry which can lead to high Y/Q values due to low Q or low Y values. It is a more comprehensive assessment of vehicle flange climb risk than the EN equivalent.

The Y/Q ratios from the GM/RT 2141 Y/Q analyses are shown in Figure 18. The Y/Q values plotted in this figure are the maximum values calculated from the range of test track cases defined by the GB method.

A linear surface has been fitted to the Y/Q ratios above a value of 2 as these are not of great relevance. In contrast to the results from the Euro Norm, the GB RGS results show that the lateral load offset is much more influential than the longitudinal load offset. This result emphasises the more severe test conditions of the GB low speed flange climb method. The combination of much greater twist levels, high cant excess cases and smaller curve radii result in the much greater sensitivity to lateral load offset.

It is also interesting that only two of the vehicles were found to pass the GMRT 2141 Y/Q analysis for all test tracks, with the remaining vehicles generating Y/Q ratios in excess of the limit in at least one case. The vehicles which derailed during the assessment are indicted by the appended '-D' in the data labels.

In order to provide a clearer image of the relative vehicle's performance on the GM/RT 2141 Y/Q test suite, the number of track cases on which a vehicle derailed are plotted in Figure 19. The plot might be thought of as an indicator of the propensity for derailment. The derailment count shows that all the vehicles with a lateral load imbalance below the UIC RIV limit of 1.25 negotiated all the test tracks without derailling (despite most generating Y/Q ratios in excess of the limit). Only two vehicles with load imbalance above the limit line negotiated all test tracks without derailment.

The above result presents further evidence that, with the exception of consideration against the GB low speed flange climb assessment, the UIC RIV limits appear to be appropriate and provide an effective mitigation against increased flange climb list due to skew loading.

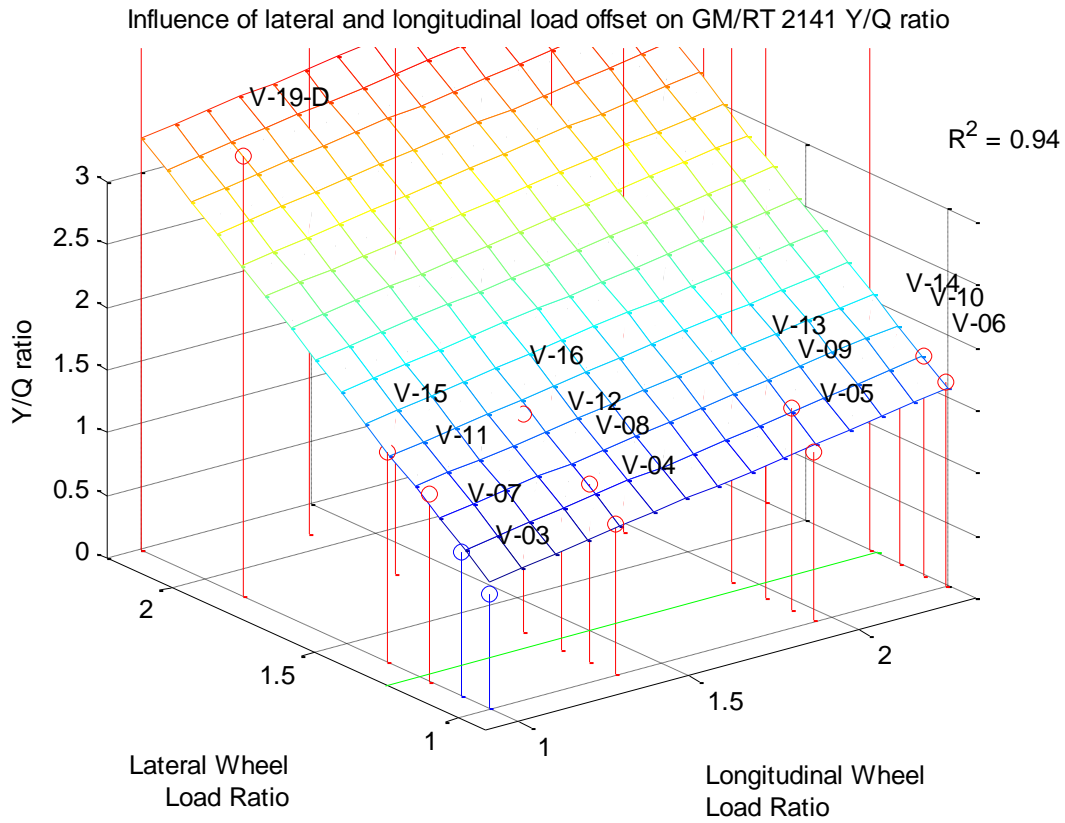


Figure 18 The influence of lateral and longitudinal load offset on GM/RT 2141 Y/Q ratio.

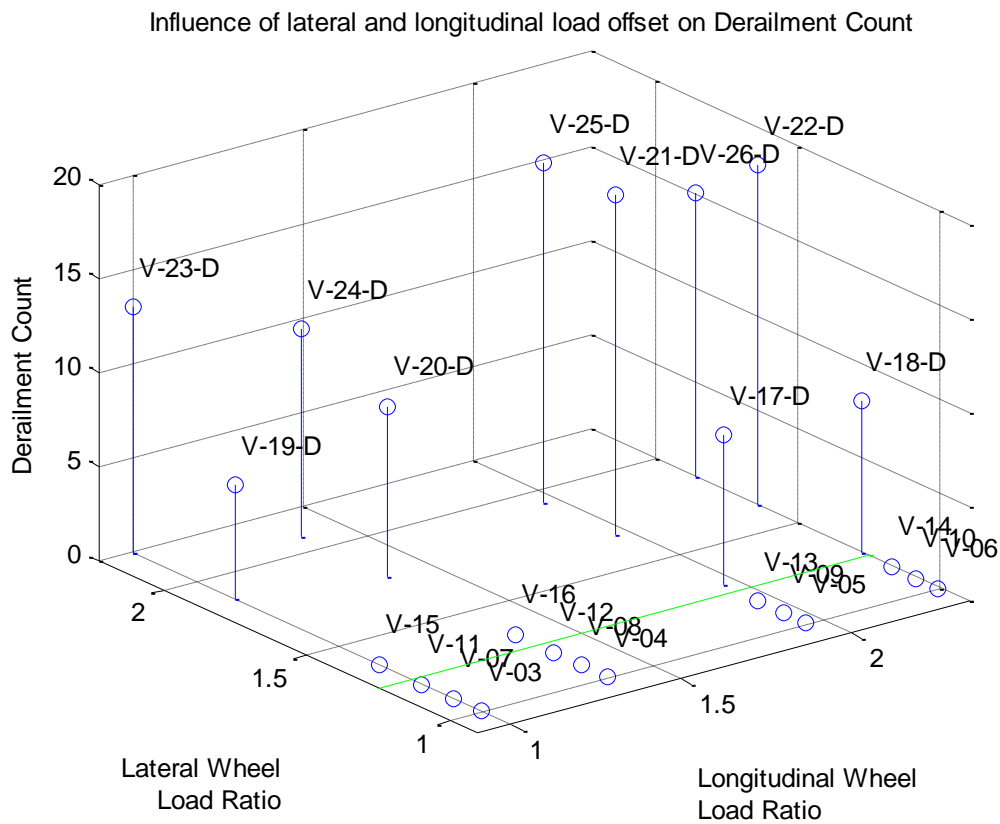


Figure 19 The influence of lateral and longitudinal load offset on derailment count.

Skew loading for bulk carriers

The scope for skew loading is reduced for bulk carriers as they almost always travel fully laden or tare, with the exceptions of engineering vehicles, ballast hoppers and other specialist traffic. To investigate the relative importance of loading configuration for bulk carriers on derailment the base vehicle was modified as described in Section 3.1.2.2.

The results from the derailment assessments are presented in Table 7. The first point of interest is that it is not possible to achieve significant longitudinal load imbalance for bulk carriers. The maximum longitudinal imbalance, with the load skewed to the side and to the rear, was 1.04. However significant lateral imbalances can be achieved when the load is piled to the angle of repose against one side of the hopper (resulting in a lateral imbalance of 1.28).

Table 7 Summary of derailment results for bulk skew loading cases

Vehicle ID	Sprung Mass	Lateral Skew	Long. Skew	GMRT 2141 $\Delta Q/Q$	EN 14363 $\Delta Q/Q$	GMRT 2141 YQ	EN 14363 YQ	X-factor
V-27	94.07	1.00	1.00	0.21	0.24	0.97	0.66	0.07
V-28	94.07	1.28	1.00	0.42	0.40	1.47	0.99	0.09
V-29	94.07	1.27	1.04	0.41	0.39	1.46	1.01	0.09
V-30	76.67	1.01	1.00	0.27	0.27	1.06	0.71	0.07
V-31	76.67	1.25	1.04	0.40	0.40	1.46	1.00	0.09

The derailment measures for bulk carrier case V-28 (lateral load imbalance only) are plotted along with the derailment measures for 3 of the container vehicle cases with similar lateral load imbalances. It can be seen that the derailment resistance for the bulk case is similar to that predicted for the container cases. The higher mass of the bulk case leads to a lower effective stiffness of the vertical suspension system, and reduced wheel unloading ($\Delta Q/Q$); this is also reflected in the EN 14363 Y/Q results. For the GMRT 2141 Y/Q test there is little difference between the load categories

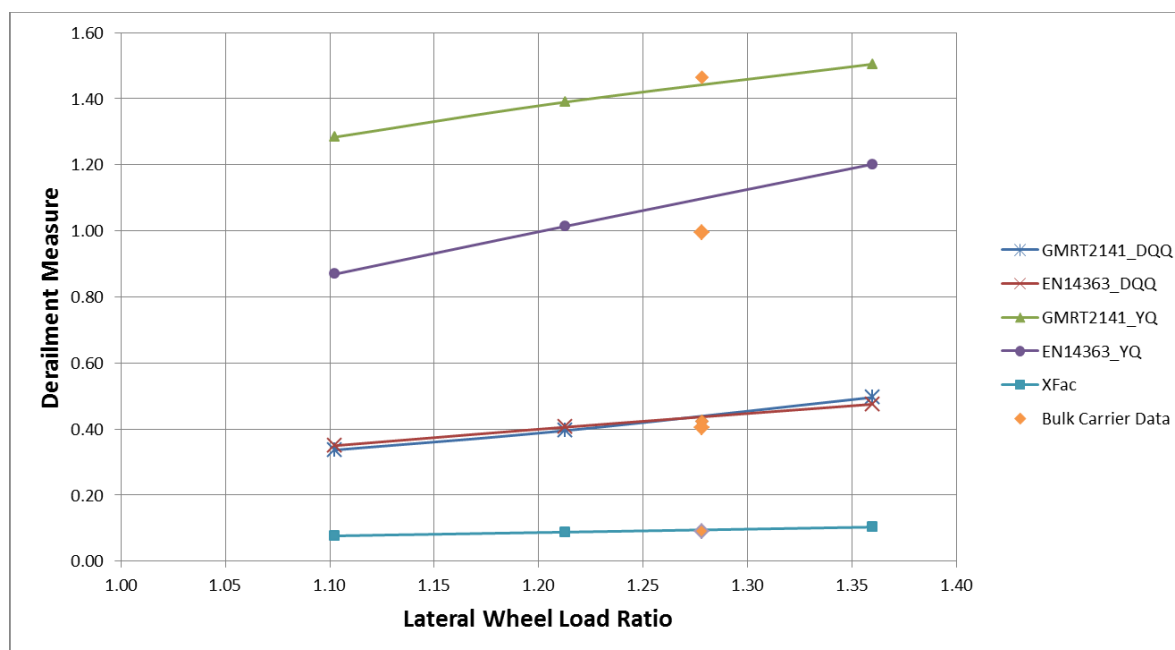


Figure 20 Correlation between lateral skew loading for bulk carrier conditions and container vehicle conditions

Relating skew loading, single axle imbalance and derailment

In the previous sub-sections the magnitude and direction of the load imbalance was described by the mean left to right and the mean front to rear wheel load imbalances. This was in order to make the observations transferable to other vehicles/vehicle configurations, as opposed to providing a centre of gravity offset or similar. Current monitoring by SBB (Swiss Federal Railways) utilises single axle imbalances to identify at risk vehicles. It is therefore useful to relate the findings of the previous skew loading analyses (based on vehicle imbalance) to equivalent single axle imbalances.

To further improve the relevance of these skew loading results, this sub-section presents the results from the derailment assessments with respect to the highest left to right wheel load imbalance of the four axles on the vehicle (the definition of the longitudinal imbalance remains unchanged). Due to the perfect symmetry in the modelled vehicle suspension and the absence of any body-bogie pitch stiffness, the quasi-static imbalance will be the same for the two axles of each bogie. However, the non-linear behaviour of the Y-series suspension, and the interaction of the leading and trailing bogies means that the lateral imbalance can differ for the two bogies.

For each vehicle simulated in the skew laden analyses the maximum quasi-static lateral imbalance was identified and used to characterise the lateral imbalance of the vehicle. The non-linear suspension of the Y-series vehicle results in the relationship between the mean and the highest lateral imbalances is also non-linear. Consequently the distribution of lateral and longitudinal imbalances was uneven, and an additional 6 vehicle models were configured to fill those ranges. The resulting range of imbalances is shown in Figure 21.

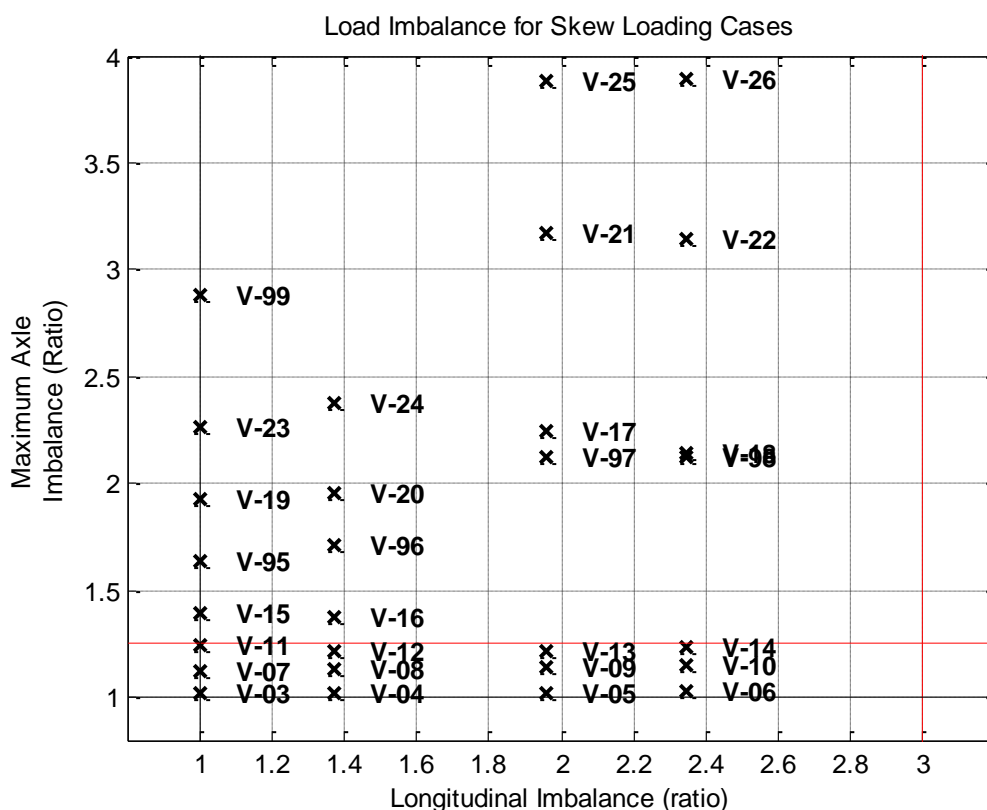


Figure 21 Maximum lateral axle imbalance for skew laden vehicles and additional cases

The non-linear influence of the Y-series suspension on the maximum axle lateral imbalance can be seen for vehicles outside the lateral RIV limit from Figure 21; the lateral offset of the payload is the same for vehicles V-15 to V-18, and likewise for vehicles V-23 to V-26 etc. The interaction of the leading and trailing bogies has a large effect on the leading wheelset lateral imbalance, and dramatically increases the axle imbalance for longitudinal imbalances greater than around 1.6 to 1.8. It is interesting to note that this effect is not apparent below the RIV limit of 1.25, where the axle imbalance appears independent of the longitudinal offset.

Figure 22 shows the influence of the maximum axle lateral imbalance and longitudinal vehicle imbalance on the EN 14363 $\Delta Q/Q$ derailment resistance measure. Vehicle V-95, with no longitudinal imbalance provides a $\Delta Q/Q$ ratio of 0.62, which corresponds to a maximum axle imbalance of 1.64. It can be seen that the tolerance for lateral imbalance reduces with increasing longitudinal imbalance, and that the lateral imbalance is significantly more important on a like-for-like basis e.g. vehicle V-14 has a $\Delta Q/Q$ ratio almost equal to that of V-95, but with a lateral imbalance of 1.23.

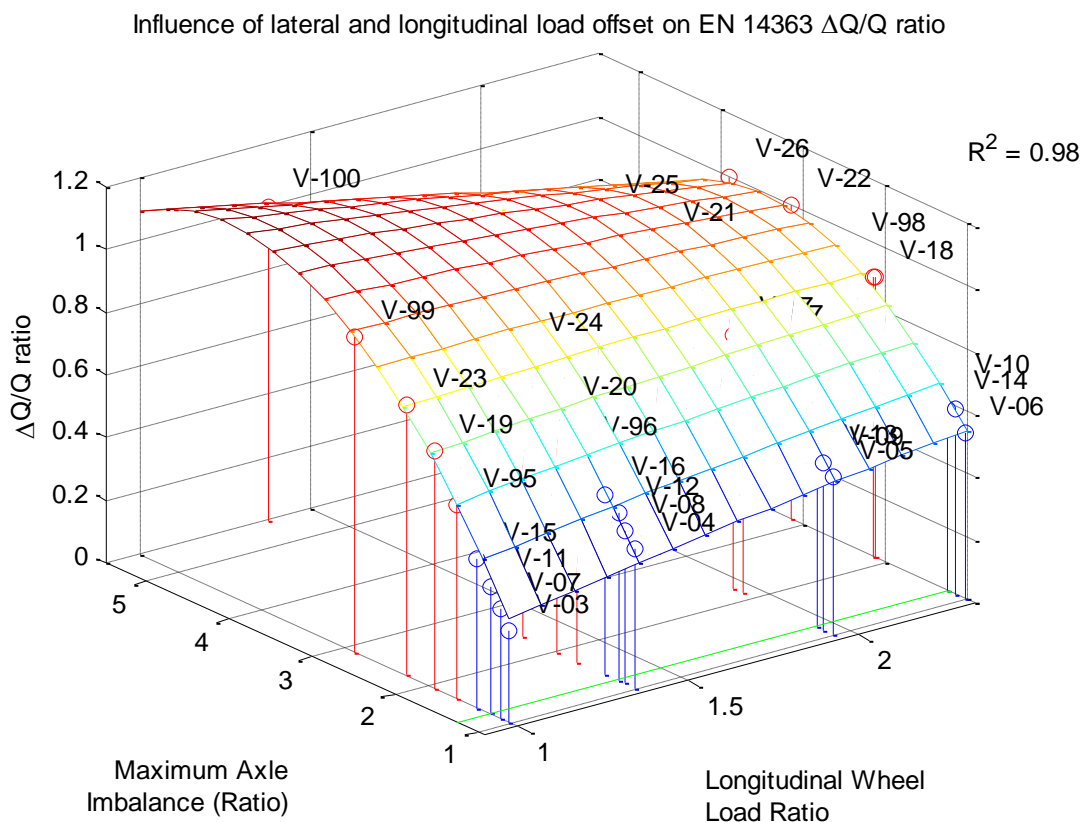


Figure 22 $\Delta Q/Q$ versus axle imbalance and vehicle longitudinal imbalance

Figure 23 shows the maximum wheel lift recorded during the EN 14363 Y/Q simulations. Values greater than 6 mm are coloured red. It can be seen that the wheel lift increases rapidly with increasing lateral axle imbalance. Here vehicle V-95 recorded a wheel lift of 8.8 mm with an axle imbalance of 1.64, while vehicle V-16 recorded a wheel lift of 5 mm with an axle imbalance of 1.38.

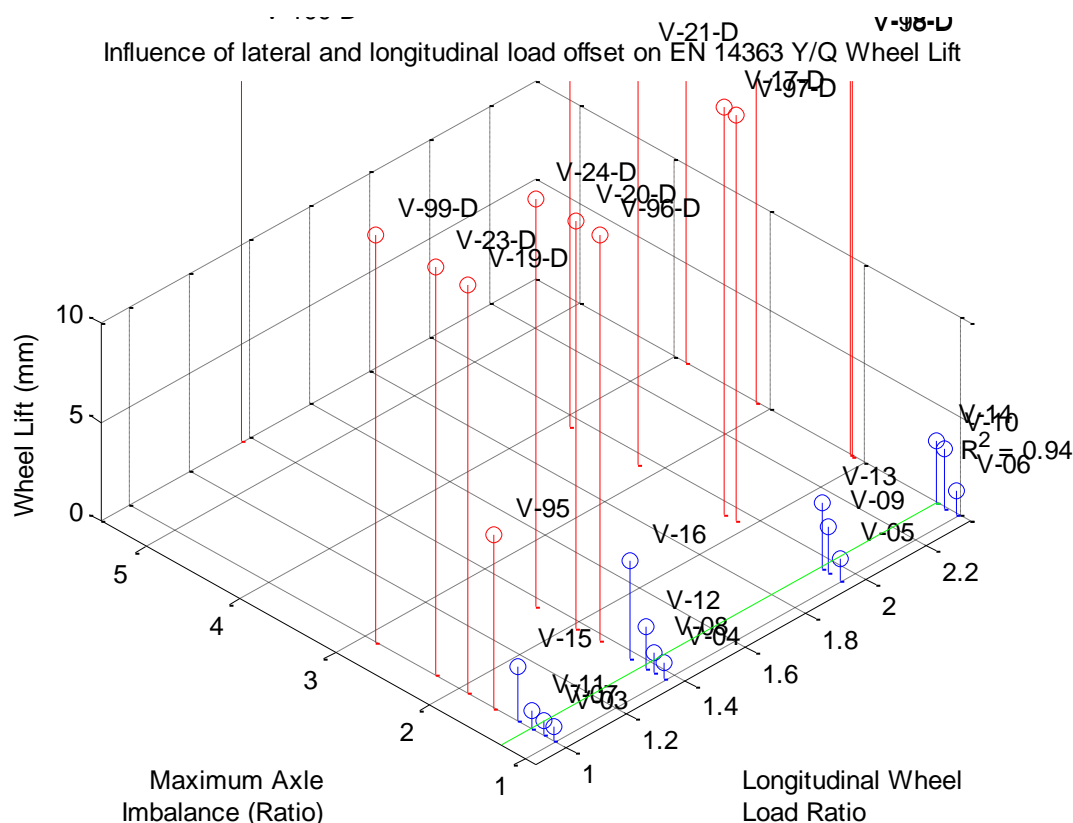


Figure 23 Wheel lift (from EN 14363 Y/Q analyses) versus axle imbalance and vehicle longitudinal imbalance

The maximum Y/Q ratios recorded are plotted in Figure 24. For low longitudinal imbalance the Y/Q ratio is dependent upon the axle imbalance, up to an imbalance of approximately 1.4. For larger longitudinal imbalance (> 2) the Y/Q ratio is to the most part independent of lateral axle imbalance and high Y/Q ratios are predicted in all cases. The exceedance of the Y/Q ratio limit and the RIV lateral imbalance limit of 1.25 seem in agreement.

The GM/RT 2141 Y/Q analysis uses a test suite of 16 track cases. The number of track cases in which the simulated vehicles derailed are shown in Figure 25 and can be considered as a measure of the propensity for derailment: the combinations of curvature, crosslevel and dip faults which are likely to result in derailment. It can be seen for longitudinal imbalances less than 1.5 none of the vehicles within the RIV limit of 1.25 derailed. The lateral axle imbalance which did not result in derailment reduced with increasing longitudinal imbalance.

For vehicle with no longitudinal imbalance the number of derailment cases increases sharply for lateral axle imbalances outside the RIV limit, with vehicle V-15 (lateral imbalance of 1.40) derailling in 2 cases, and vehicle V-95 (lateral imbalance of 1.6) derailling in 10 cases.

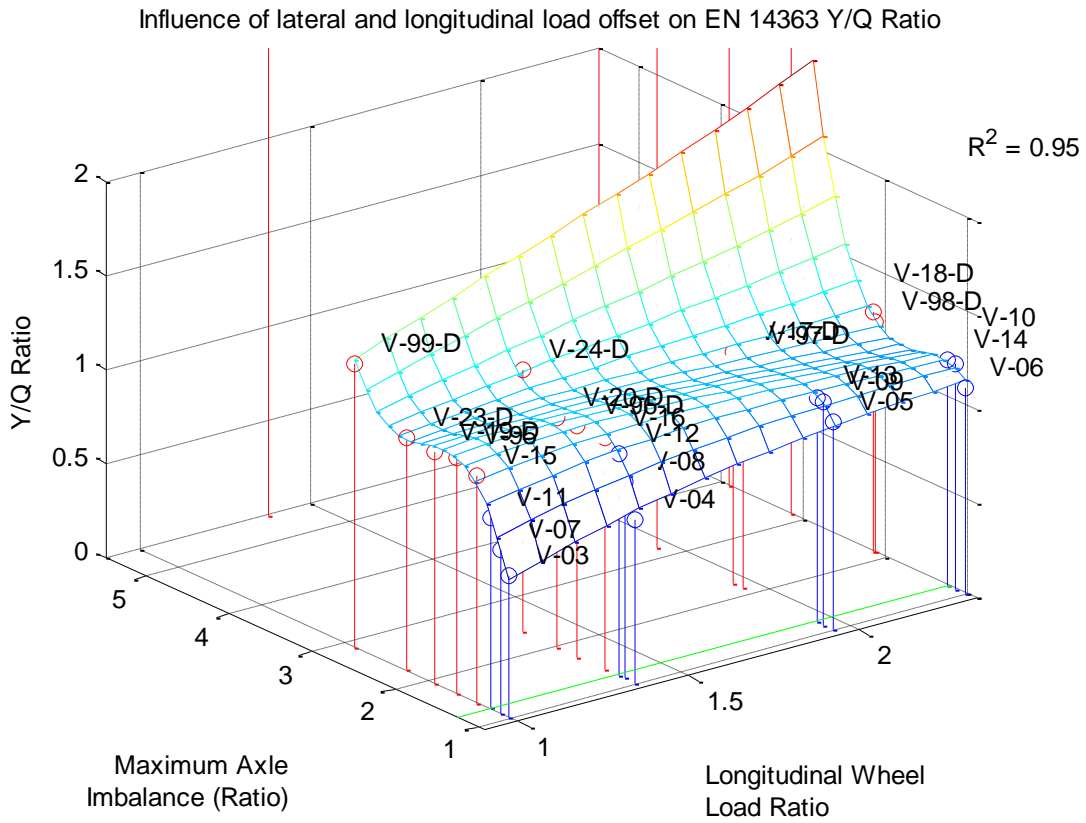


Figure 24 Y/Q versus axle imbalance and vehicle longitudinal imbalance

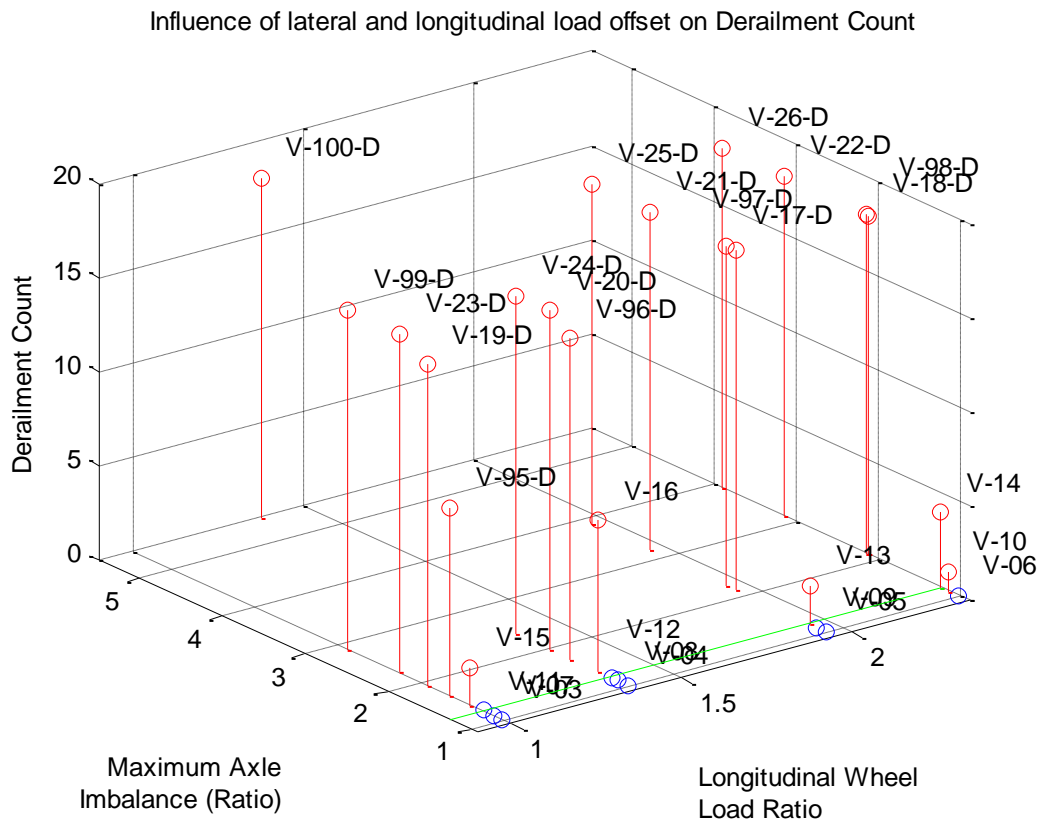


Figure 25 GM/RT 2141 Y/Q derailment count versus axle imbalance and vehicle longitudinal imbalance

The results from the bogie X-factor tests are shown in Figure 26. The bogie yaw resistance is highly dependent upon the lateral axle imbalance, and there is a slight downward trend in X-factor with increasing longitudinal imbalance between 1 and 1.4. Vehicle V-15 has an axle imbalance of 1.40, and an X-factor of 0.10 (coincident with the limit line).

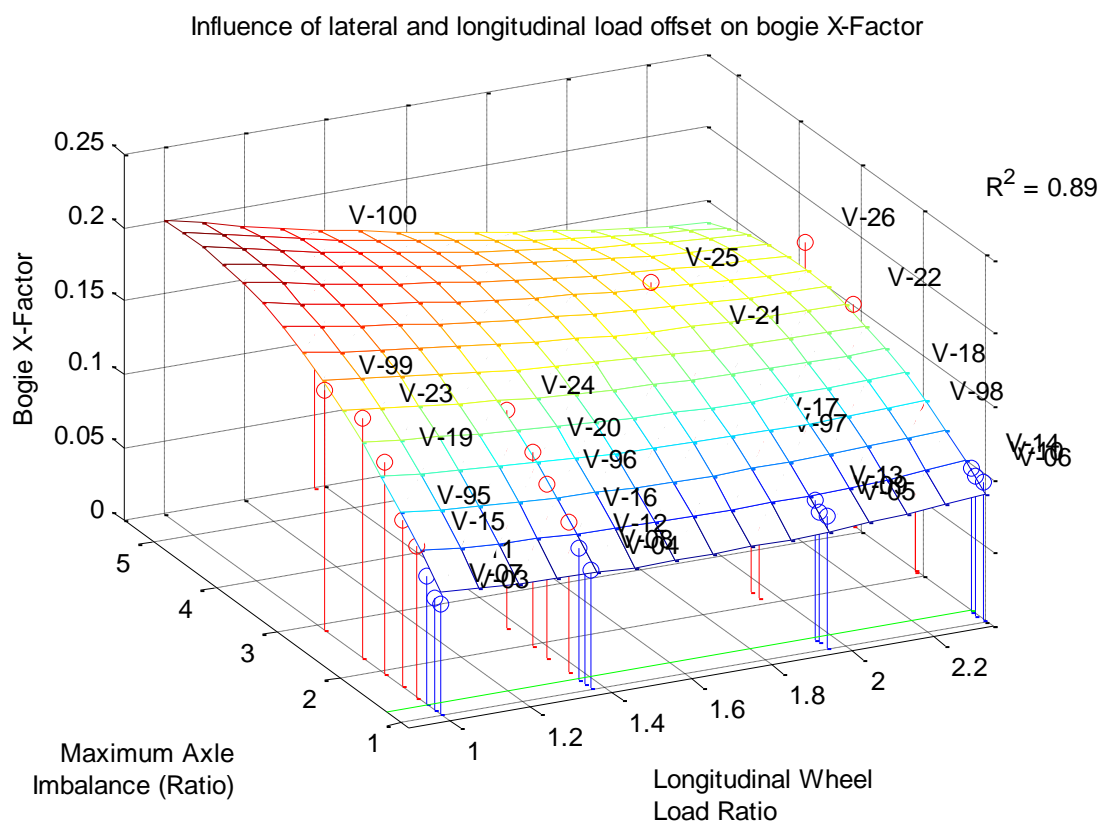


Figure 26 Bogie X-factor versus axle imbalance and vehicle longitudinal imbalance

3.1.3.2 The sensitivity of skew loading and derailment resistance to bogie spacing

A sensitivity study was carried out to determine the influence of bogie semi-spacing on the skew loading derailment risk. The aim of the study was to improve the transfer of conclusions from other analyses where a shorter bogie spacing was used. It did not aim to be a complete parameter variation study for the bogie spacing.

The vehicle models derived for the container vehicle skew loading simulations (Section 3.1.2.2) were modified to have a bogie semi-spacing of 5.89 m (reduced from 6.97 m). The load states of the vehicles remained unchanged. Results for the same load states of the two bogie spacings cannot be directly compared as the wheel load imbalances arising differ due to the different bogie spacing; however comparisons may be made by interpolating equal wheel load imbalances from the two data sets. The modified vehicle numbers were pre-fixed with the number 4, so for example vehicle V-23 correlates to V-423. The various derailment assessment cases were then re-simulated.

Figure 27 compares the $\Delta Q/Q$ ratios for the vehicles with only longitudinal load imbalance. It can be seen that the longer bogie spacing results in higher $\Delta Q/Q$ values, which can be attributed to the greater vehicle twist prescribed for those vehicles by the test standard (the vehicle twist being a function of the bogie spacing). For the shorter bogie spacing the offset

load conditions defined in Section 3.1.2.2 lead to greater longitudinal load imbalances. The trend in $\Delta Q/Q$ ratio appears to drop towards the highest longitudinal load imbalance (approximately 2.8). With this degree of imbalance the leading bogie of the corresponding vehicle is very lightly laden (near tare state) and is torsionally less stiff than the neighbouring vehicle with longitudinal imbalance equal to approximately 2.25.

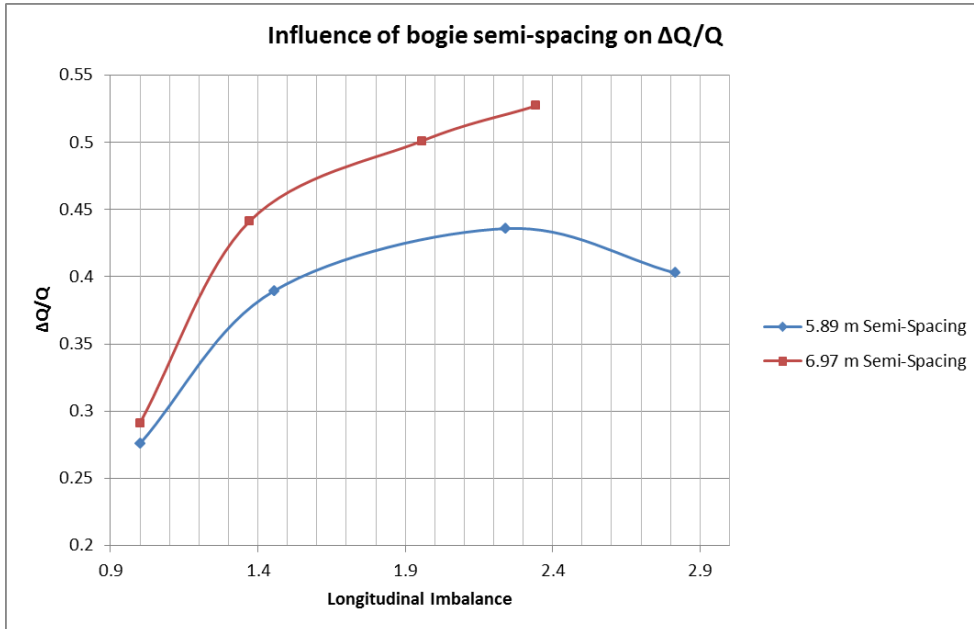


Figure 27 Influence of bogie spacing and longitudinal load imbalance on $\Delta Q/Q$ ratio

Figure 28 below shows that there is no significant difference between the $\Delta Q/Q$ ratios for the vehicles with only lateral load imbalance, as would be expected. The small differences are a consequence of the different twist magnitude for the two cases, and the effects of differing degrees of body roll.

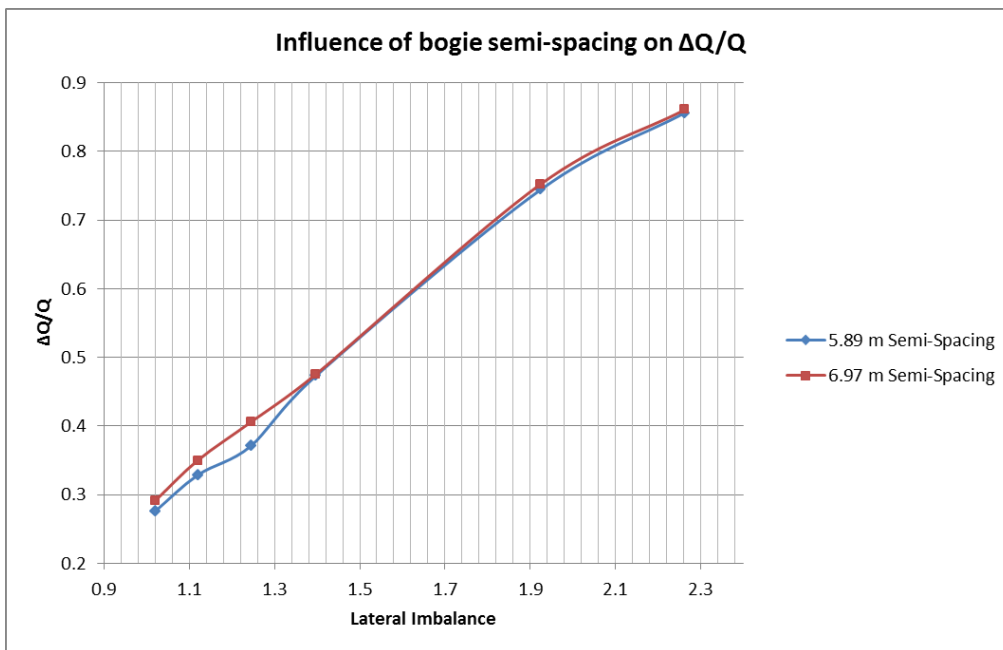


Figure 28 Influence of bogie spacing and lateral load imbalance on $\Delta Q/Q$ ratio

For combined longitudinal and lateral load offset (Figure 29) the vehicles with reduced bogie spacing were found to have higher $\Delta Q/Q$ ratios, where the longitudinal offset was greater than 2 (comparing vehicles V-409 and V-413 in Figure 29 with vehicles V-10 and V14 in Figure 13). For the shorter bogie spacing exceedances of the $\Delta Q/Q$ limit are predicted for vehicles within the RIV skew loading limits. This is a consequence of the non-linear behaviour of the Y-series vehicle.

The step increase in the $\Delta Q/Q$ values for vehicles V-409, V-413, V-417 and V-418 are associated with the side bearer support spring becoming coil bound. This effect leads to the same step increase seen for vehicles V-17 and V-18 in Figure 13. The limit of side bearer travel is reached at different load imbalances for the two bogie spacings. This is due in part to the non-linear suspension system and also in part to the differences in the load cases: for cases where the longitudinal and lateral load imbalances are comparable other factors such as payload mass and CoG height differ. For example the body mass in vehicle V-14 is 36.6 t and that of V-413 is 42.8 t, while both vehicles have a similar load imbalance. These variations are a consequence of the initial conditions defined to generate realistic load cases in Section 3.1.2.2, which were re-used in this sensitivity study. A comprehensive bogie spacing parameter variation study, which this short investigation is not, would need initial conditions which provided consistency in these other factors across differing bogie spacings.

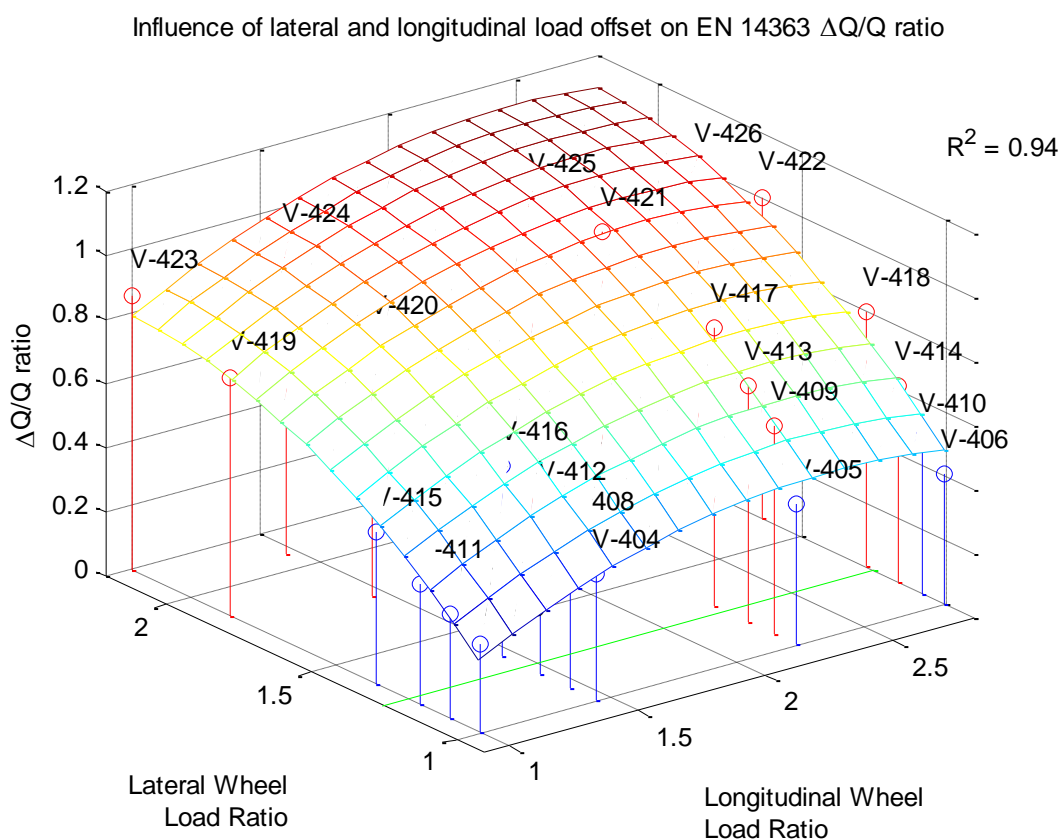


Figure 29 The influence of lateral and longitudinal load offset on EN 14363 $\Delta Q/Q$ ratio for 5.89 m bogie spacing

3.1.3.3 Analysis of measured wheel load data with respect to skew loading

This sub-section aims to provide further context to the results from skew loading simulations presented previously, by determining the skew loading distributions from measured wheel

load data. In addition the data analysis investigated the possibilities for detecting chassis and frame twist from the measured wheel loads.

A request was made to the GB infrastructure manager, Network Rail, for the provision of on-track based wheel load measurements. Unfortunately this was not made available until after the initial skew loading simulations had been defined and reported as presented above. In addition data from DB's axle load checkpoints "DafuR" was made available. Both measurement systems record the dynamic and mean vertical wheel forces of all passing vehicles with the primary aim of detecting wheel flats and high axle loads.

At present the Gotcha system does not allow for automated identification of vehicles and therefore within the analysis presented, the vehicle type may only be inferred based on loading levels and bogie/wheelbase dimensions. The GB Gotcha data was post processed to obtain the distribution in skew loadings for 8 weeks of traffic. The raw data contains measurements for all passing vehicles, which includes non-bogie freight, passenger stock and locomotives. All non-bogied vehicles were removed from the data set, along with all bogied vehicles with a wheelbase greater than 2.2 m (the majority of passenger stock). The bogie semi-spacing was then used to identify intermodal vehicles.

The DB DafuR data set contained measurements from four different locations in the DB network within a time period of one month. All the selected axle load checkpoints are situated on straight track and the investigation was restricted to freight wagons with 2-axle bogies.

In both cases, the integrity of the mean wheel load data was checked by looking at the dynamic load ratio (dynamic force/mean force), and disregarding any vehicle with a wheel reporting a dynamic ratio greater than 0.75. A high dynamic ratio indicates the likelihood of a wheel defect, which in turn has been found to be associated with outlying measured mean wheel load values. 8,597 vehicles were disregarded from the GB data set due to high dynamic ratios, leaving 22,320 vehicles for analysis, while the filtered DB data set contained 55,262 vehicles.

In Figure 30 the frequency distribution of the measured axle loads of the total 55,262 freight wagons from the DB data set is shown. As the maximum permitted axle load is 22.5 t it can be seen that nearly 3% of the measured axles are overloaded. The maximum axle load measured was 29.7 t.

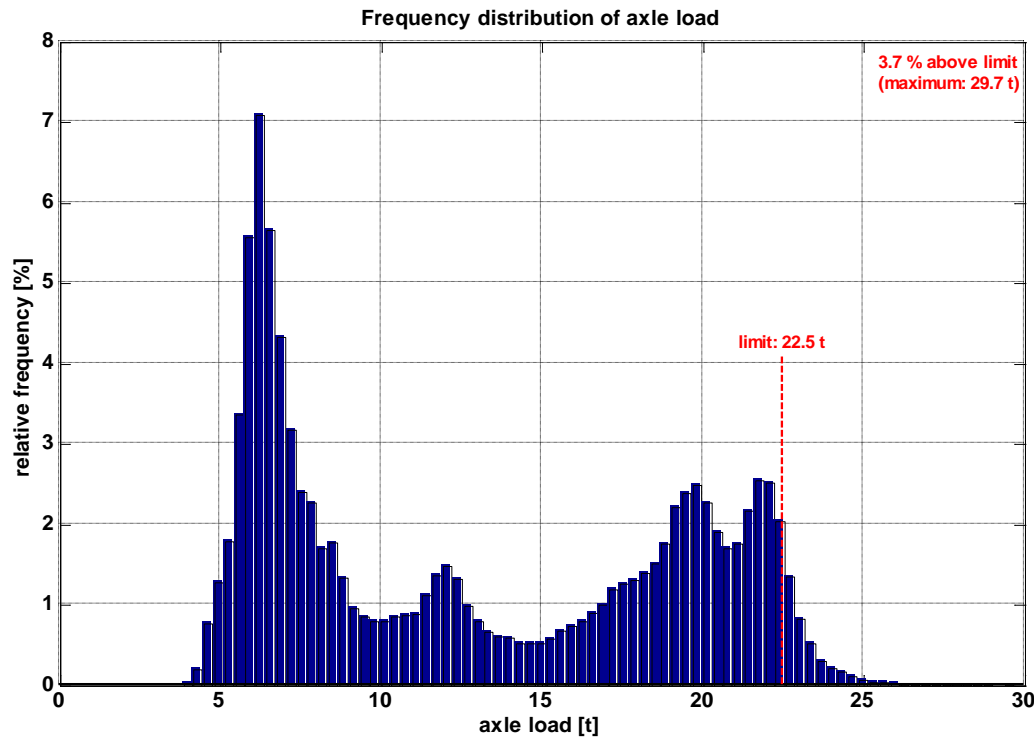


Figure 30 Frequency distribution of axle load measured on 4-axle freight wagons at four locations in the DB network (55,262 vehicles considered).

Skew Loading

According to the UIC loading guidelines [2] the asymmetric loading of freight wagons is limited in lateral as well as in longitudinal direction. For 4-axle wagons the following limits apply:

$$\begin{aligned}
 \text{lateral : } \max & \left(\frac{\sum_{i=1}^4 Q_{i1}}{4}; \frac{\sum_{i=1}^4 Q_{i2}}{4} \right) \leq 1.25 \\
 \text{longitudinal : } \max & \left(\frac{\sum_{i=1}^2 \sum_{j=1}^2 Q_{ij}}{4}; \frac{\sum_{i=3}^4 \sum_{j=1}^2 Q_{ij}}{4} \right) \leq 3
 \end{aligned} \tag{4}$$

where Q_{ij} is the vertical wheel load on wheel j ($j = 1/2$ – right/left with respect to the running direction) of wheelset i (counting the wheelsets sequentially starting at the leading wheelset of the vehicle).

The following two figures show the load ratios in lateral and longitudinal direction derived from the DB wheel load measurements mentioned above whereby only loaded vehicles (total weight greater than 30 t) are taken into account. It can be noted that a significant number of wagons do not meet the international loading requirements especially in regard to the lateral load distribution.

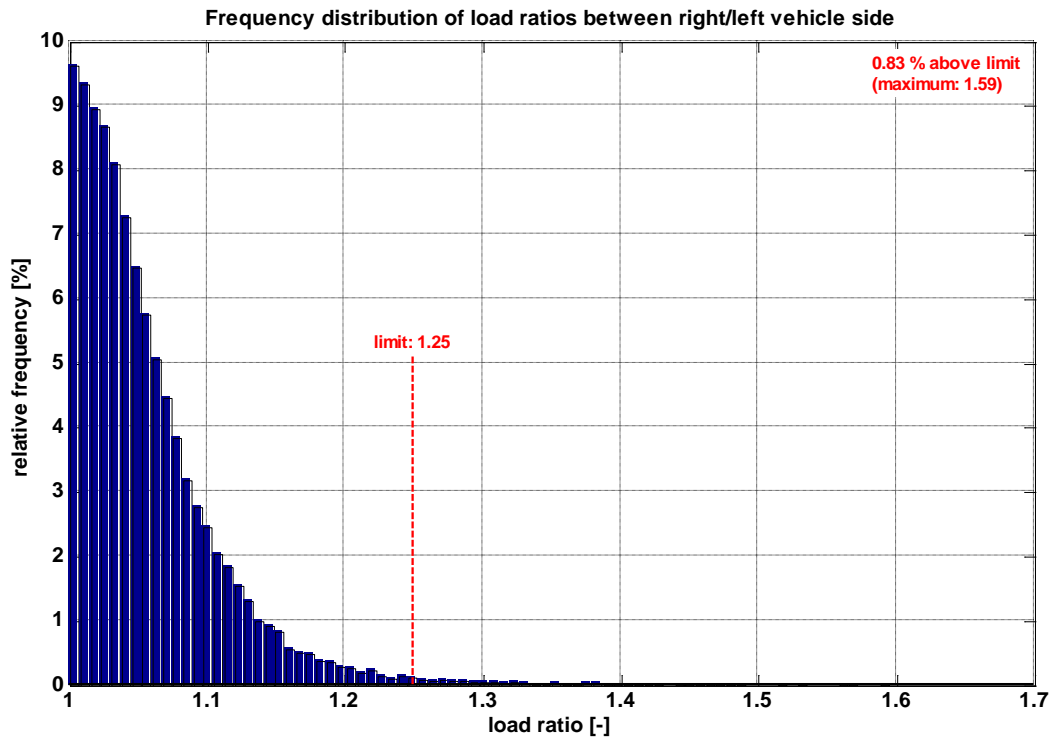


Figure 31 Frequency distribution of lateral load ratio (36,461 vehicles considered – DB data set).

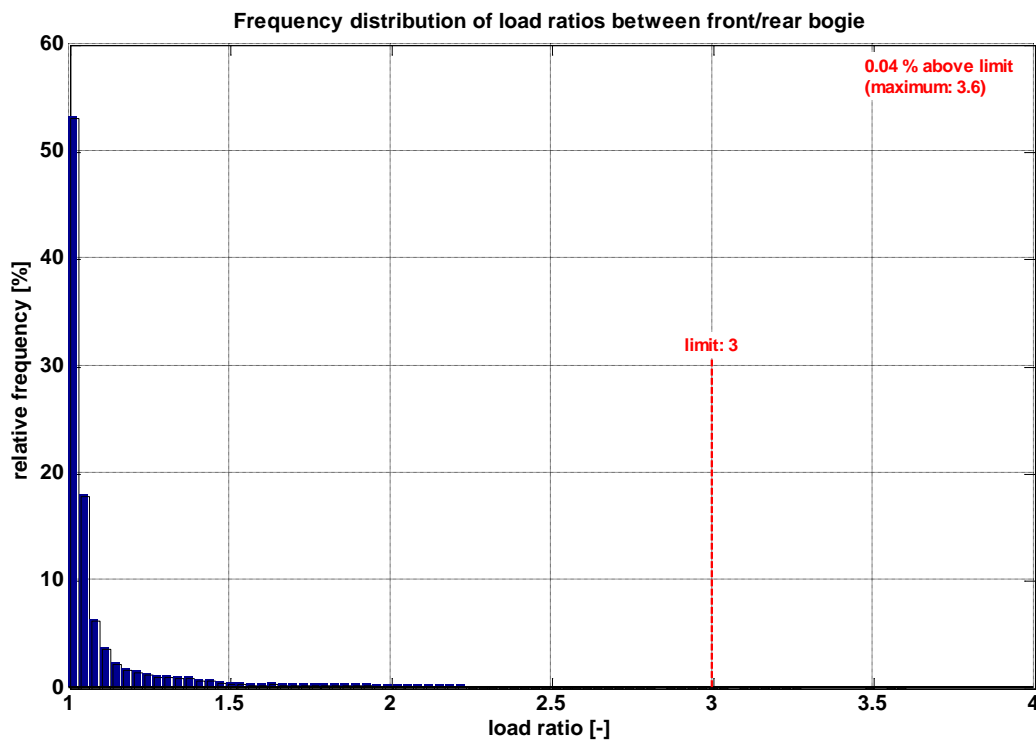


Figure 32 Frequency distribution of longitudinal load ratio (36,461 vehicles considered – DB data set).

For the same selection of loaded vehicles Figure 33 shows the normalised horizontal position of the fictitious centre of gravity calculated based on the assumption that the vehicle suspension is totally symmetrical. The UIC load limits mentioned above are transformed to normalised values and indicated in the graph by dashed lines in red. Again it can be seen that

a large number of vehicles is outside the limits especially in lateral direction, but extreme cases with superposition of lateral and longitudinal asymmetries at the same vehicle are rather rare. However, it can be concluded that the investigation of vehicle conditions with superposed lateral and longitudinal shift of the centre of gravity in accordance to the UIC limits is of high relevance.

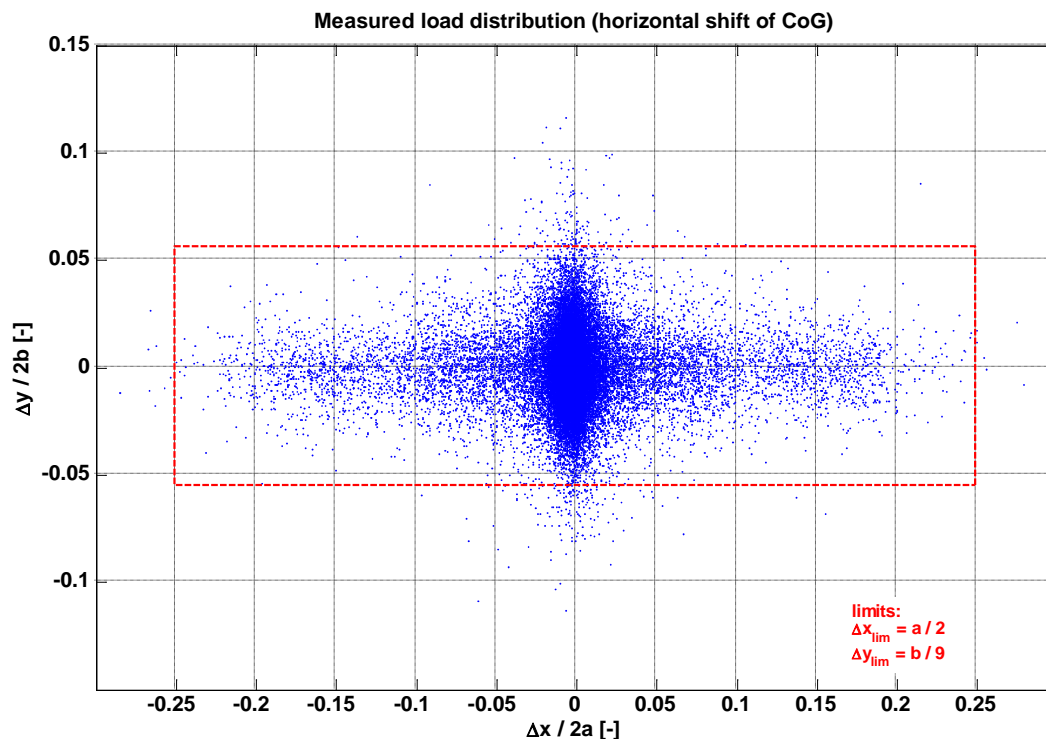


Figure 33 Measured load distribution of 4-axle freight wagons (Δx – longitudinal shift of CoG, Δy – lateral shift of CoG, $2a$ – bogie base, $2b$ – lateral wheelbase).

The distributions of lateral and longitudinal imbalances for the GB data set are shown in Figure 34. The mode of the lateral distribution is at a slight imbalance of 1.02 to 1.04, while the mode of the longitudinal distribution is closer towards equilibrium. The range of the two distributions is predominantly within the limits defined by UIC RIV, with 15 vehicles exceeding a longitudinal imbalance of 3 and 65 vehicles exceeding a lateral imbalance of 1.25 (0.29%).

For further analysis, the data set was separated into four bands of mean vehicle axle load: less than 75 kN (typical for empty/tare vehicles); 75 kN up to 125 kN (typical for lightly laden container vehicles); 125 kN up to 175 kN (typical for moderately laden container vehicles); and greater than 175 kN (typical for containers carrying bulk loads). The scatter plots in Figure 35 show the spread in load imbalance for these four bands.

As expected the lowest axle load band has little lateral spread. However longitudinal offsets of up to 1.5 appear frequently as well as lateral offsets up to 1.14 (which are significant offsets, given the low axle load).

The middle two bands of axle load show the greatest longitudinal load imbalance, which is commensurate with these axle loads being associated with container vehicles. Again there are some outlying points at both the longitudinal and lateral extremities which require further investigation. In the 125 kN to 175 kN range the vehicles with lateral offsets of around 1.43 are particularly suspect.

The highest load band shows the least longitudinal spread, which is slightly less than that for the lowest load band. Lateral imbalances up to approximately 1.175 appear to occur frequently.

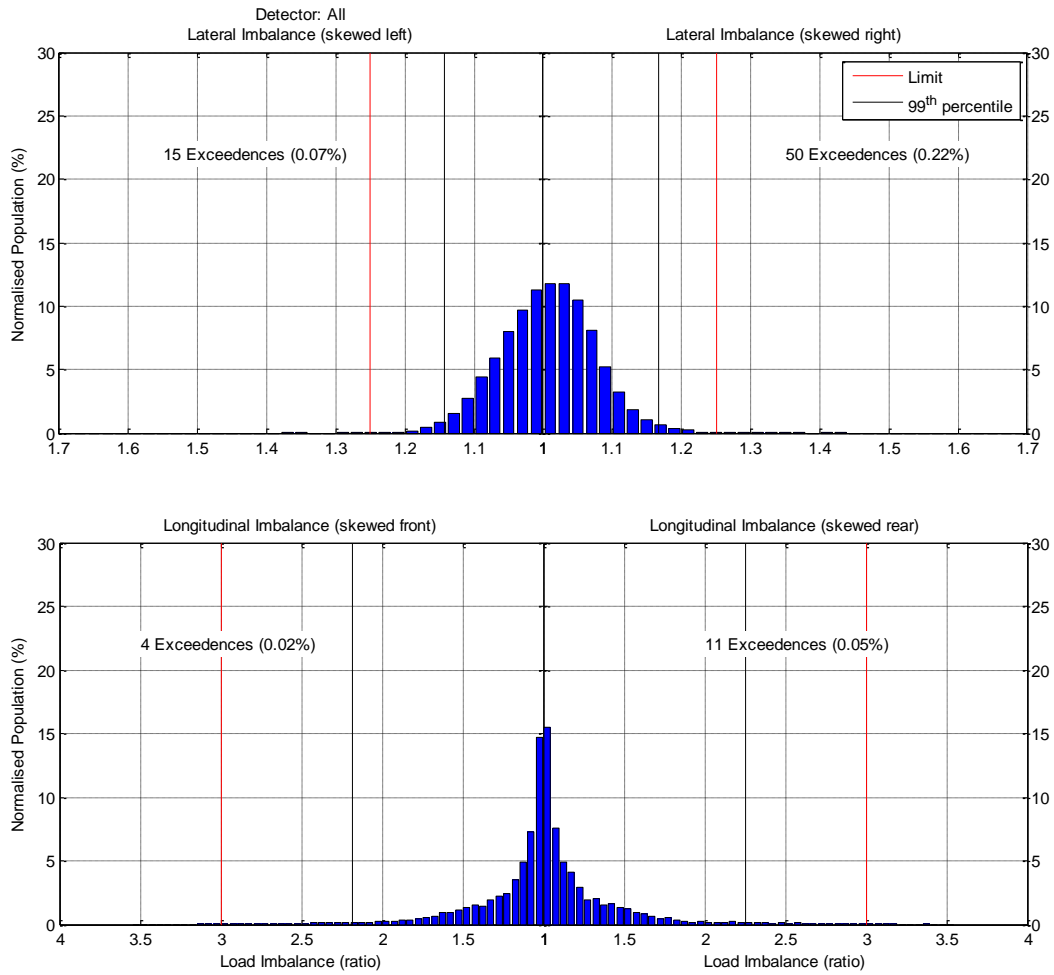


Figure 34 Distribution of Lateral and Longitudinal Load Imbalance from GB Gotcha Data.

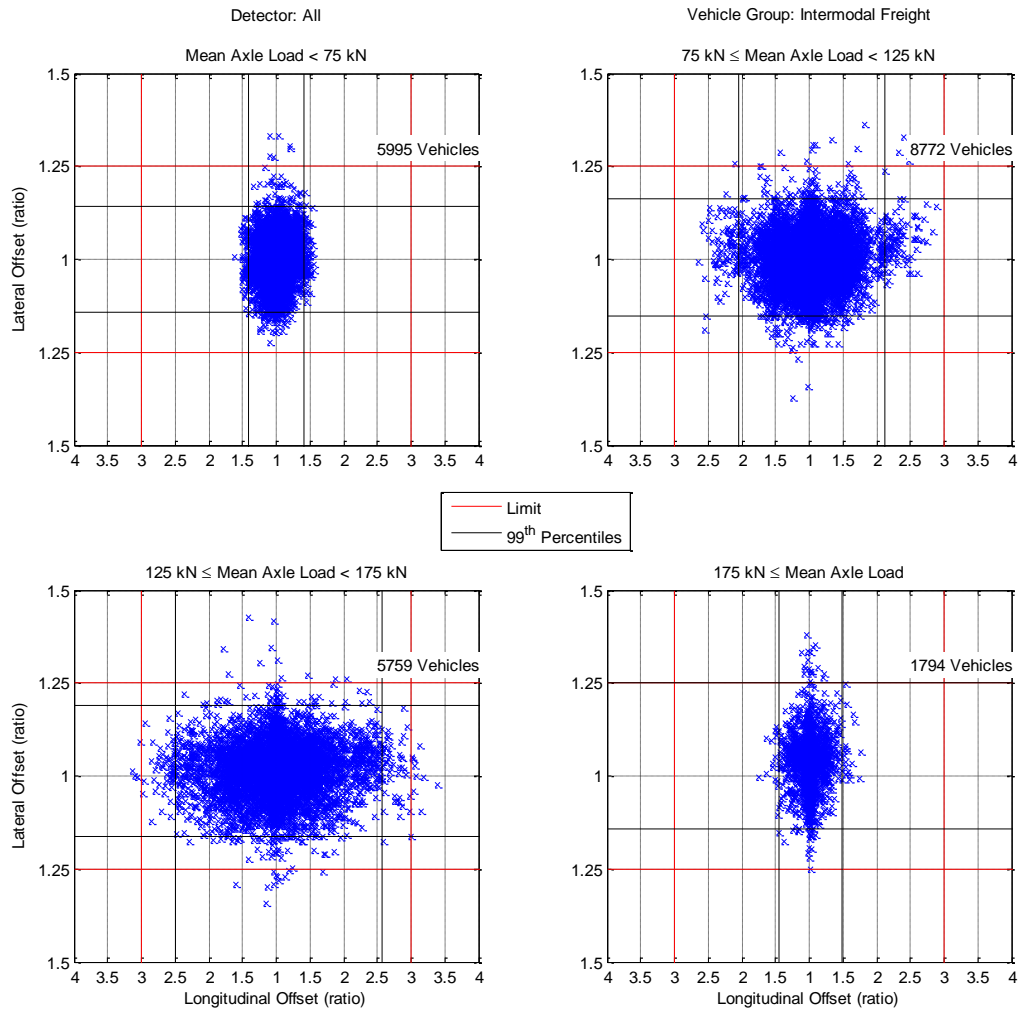


Figure 35 Scatter Plots of Load Imbalance for Four Mean Axle Load Ranges from the GB data set.

For reference the vehicle models used in the skew loading analyses are plotted over the distribution from the GB Gotcha data in Figure 36. From the 99th percentiles in Figure 34 it can be seen that vehicles V-03 to V-10 represent 99% of the lateral and longitudinal load imbalances measured from the Gotcha data set.

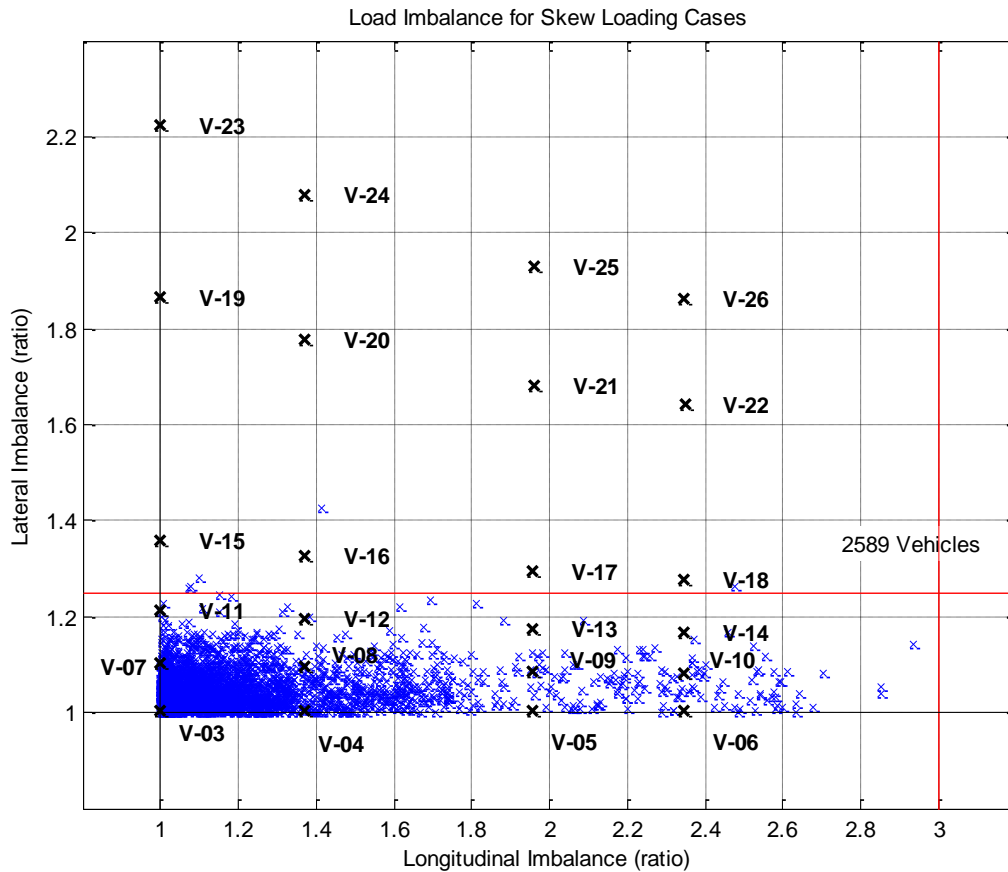


Figure 36 Scatter plot of all GB Gotcha load imbalances for bogied freight with the skew loading cases overlaid.

Cross loading/chassis twist

In addition to the analysis presented above, the available wheel load measuring data was exploited to identify chassis twist. Therefore the measuring results of empty wagons (total weight below 30 t) were selected to calculate a cross loading index which is defined as

$$\rho = \frac{\sum_{i=1}^2 Q_{i1} + \sum_{i=3}^4 Q_{i2} - \sum_{i=1}^2 Q_{i2} - \sum_{i=3}^4 Q_{i1}}{\sum_{i=1}^4 \sum_{j=1}^2 Q_{ij}} \quad (5)$$

where Q_{ij} is the quasi static vertical wheel load on wheel j of wheelset i . The coefficient thus gives a normalised value of the difference in wheel loading for one diagonal compared to the other.

The calculated cross loading indices for the DB data set are plotted in Figure 37. It can be recognised that an important number of vehicles are subject to significant chassis twist.

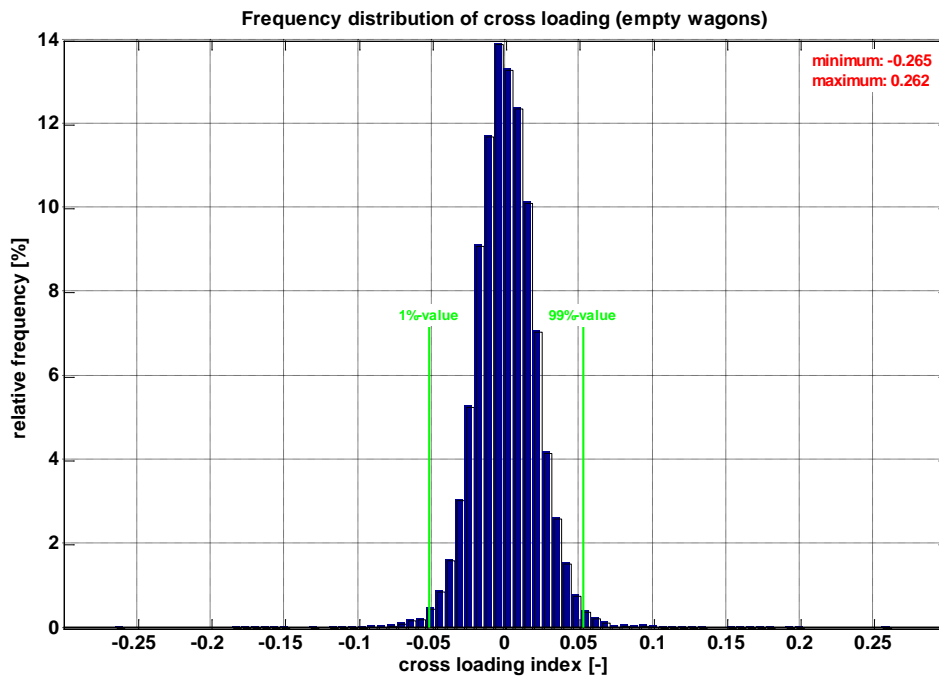


Figure 37 Frequency distribution of cross loading index.

The bogie and chassis twist was also calculated from the GB wheel load data for all vehicles with dynamic ratios less than 0.75. The calculated twist values give the imbalance between the wheel loads on the two diagonals of the vehicle or bogie (in a similar manner to the skew loading imbalances). The values were calculated so as to always provide a value greater than 1. A twist value of 1 (unity) indicates that both diagonals carry equal load and correspond to no twist.

The results are shown in Figure 38 and Figure 39. The distribution of bogie twist represents a typical bell curve distribution, but again the mode is slightly offset. The spread of the data indicates that some vehicles appear to be running with significant bogie twist of up to 1.47. It was also noticed that the majority of bogies have a longitudinal imbalance, which is unexpected due to the absence of any bogie to vehicle pitch stiffness in conventional freight vehicles. It is probable that the majority of these imbalances are due to hysteresis in the bogie to vehicle pitch damping (centre bowl). Although significant imbalances were detected (as high as 1.57) which may be indicative of a suspension malfunction or possibly erroneous measurements.

The distribution of chassis twist was found to be weighted more towards unity than a typical bell curve, and slightly offset towards one direction. The majority of chassis twists were less than 1.2, and the highest value calculated was 1.47.

The combined consequence of a chassis twist and vehicle lateral imbalance will lead to axle imbalance being increased at one end of the vehicle and reduced at the other. There is potential for significant exacerbation of axle imbalance, however this combination has not been considered in the simulations undertaken here.

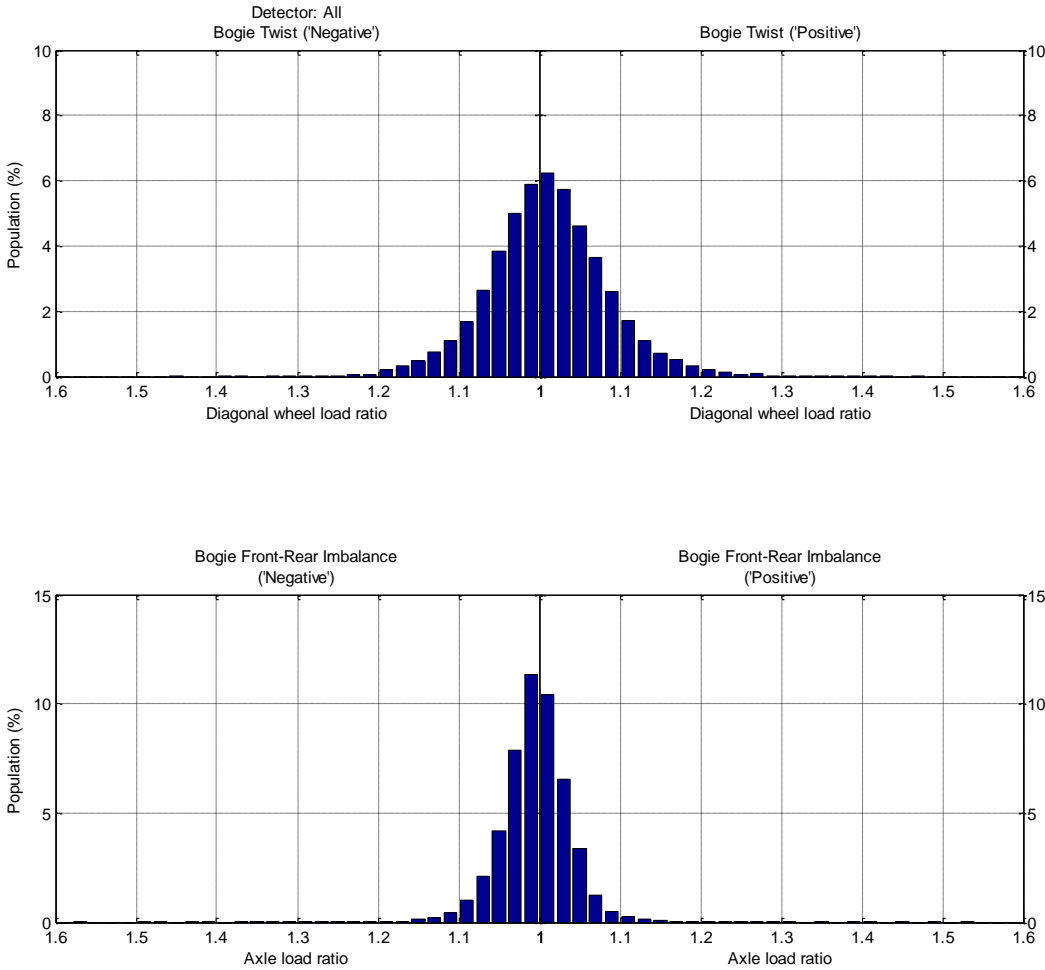


Figure 38 Distributions of bogie diagonal twist and front-rear imbalance

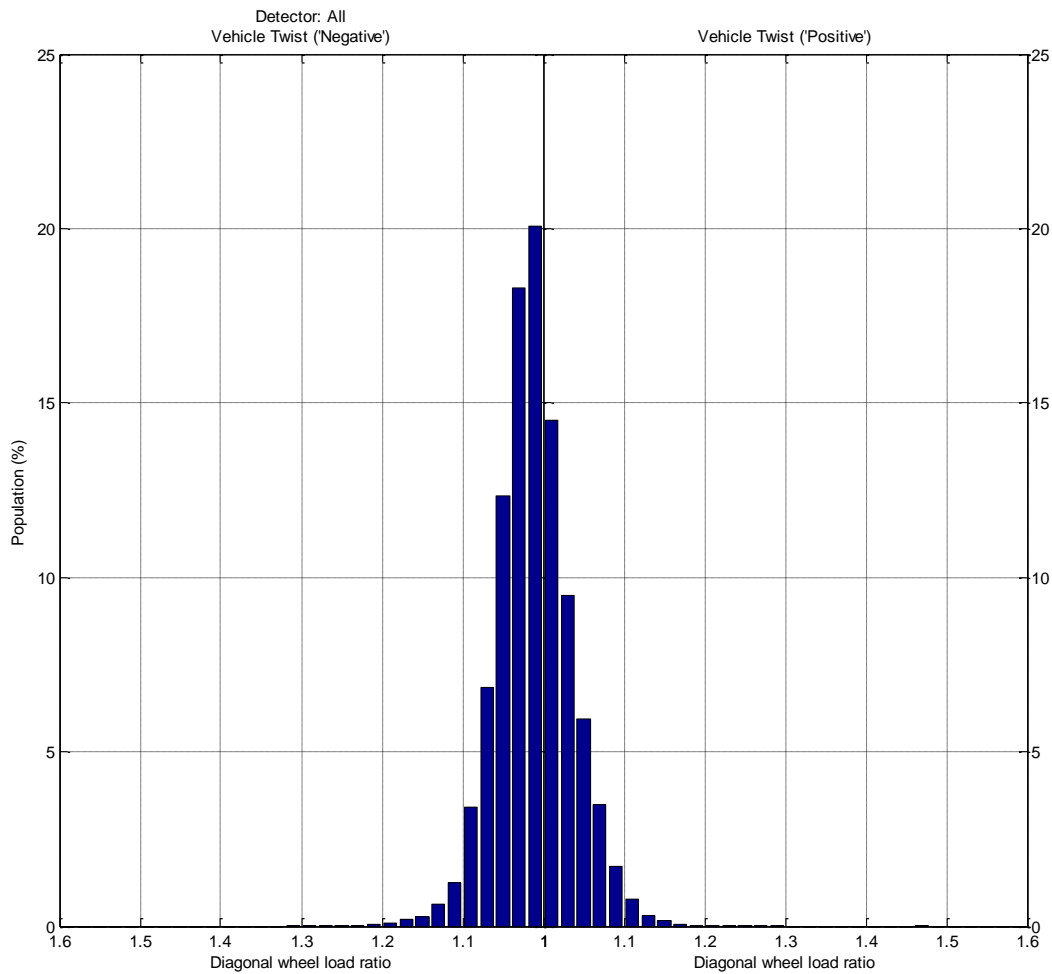


Figure 39 Distribution of vehicle chassis twist

For the GB data set, an analysis of the individual axle imbalances for the intermodal vehicles with dynamic ratio less than 0.75 revealed that 12 axles had an imbalance over 1.70 (0.013%), while 65 vehicles had a lateral imbalance greater than 1.25 (0.29%). The maximum axle imbalance in this data set was 2.12. The reference to the threshold of 1.70 is made as it is currently used as an alarm threshold by SBB in Switzerland.

If no limit to dynamic ratio is applied the number of axles exceeding 1.70 increases to 221 axles of 123668 (0.18%), which represents an increase in propensity of nearly 14 times compare to a dynamic ratio threshold of 0.75. Incidentally, the percentage of vehicles exceeding a lateral imbalance of 1.25 almost doubles (to 0.51%) when the dynamic ratio threshold is removed. The highest axle imbalance recorded here was then 7.60, with 14 vehicles having axle imbalances greater than 3.

These observations suggest that there is a relationship between wheel defects and reported axle imbalance. The question remains whether this difference should be attributed to a real characteristic of the vehicle, or limitations in the measurement system. Further investigations will be carried out in this area.

3.1.3.4 Bogie suspension variation – Primary Springs

The Y-series bogie design is widely used in the freight sector. The bogie suspension is generally configured by the vehicle manufacturer to suit the wagon body under which it runs. Within the normal design range of suspension parameters, there is the possibility that the bogie engineer creates a configuration which is not particularly optimal with respect to potential derailment risk.

The simulation studies in the following subsection analyse the effect of changes to tare and laden spring rates and tare to laden spring clearance on derailment resistance. The influence of primary friction damping levels on derailment resistance are presented in the following subsection.

The stiffness of the primary suspension in the three load conditions considered is expressed in terms of the lowest body bounce frequency ω_n . This approach has been adopted to present the results in a form which is more generic and transferrable than absolute levels of spring rate. A high body bounce frequency indicates a stiff primary suspension – the stiffest configuration occurs in the part-laden condition, in the transition between tare and laden spring contact.

The suspension parameter study has been carried out against the assessment methods within the EN and GB vehicle acceptance standards. Details of the variation in suspension parameters are listed in 3.1.2.3.

GM/RT 2141 – Assessment of low speed flange climb(Y/Q)

The 27 vehicle models for the primary spring variation analyses were simulated through the GM/RT 2141 Y/Q suite of test tracks. During the analysis of the simulation data it was hypothesised that the derailment resistance would be influenced by the effective stiffness of the primary vertical suspension system. In order to test this hypothesis the maximum Y/Q ratios from the simulations were plotted against the nominal bounce frequency of the primary suspension (ω_n) in Figure 40. For tare vehicles this is calculated from the sprung mass and the tare spring stiffness. For all other cases this is calculated from the sprung mass and the combined tare and laden spring stiffness.

It should be noted here that the use of the vehicle modal frequency is to provide an indication of the effective vertical stiffness of the primary suspension system. It is not implied that modal resonance is significantly contributing to the derailment resistance.

In Figure 40 the maximum Y/Q ratios from the GM/RT 2141 analysis are plotted against bounce frequency and colour coded according to load case: blue – tare laden; red – part laden; magenta – fully laden. Two trends can be seen, one for the tare vehicles and one for the part laden and fully laden cases. A linear trend line was fitted to the each data subset with an R^2 correlation coefficients of 0.998 for the tare cases and 0.961 for the laden cases. As anticipated, a stiffer primary suspension system results in reduced derailment resistance and higher Y/Q ratios. For the vehicle model used in this analysis it was only the least stiff, fully laden vehicles which passed the GM/RT 2141 YQ tests. The part laden vehicle with the highest natural frequency produced the highest Y/Q ratios, and the greatest spread in results, suggesting the non-linear characteristics of the suspension at this load level is significant – for the tare and laden vehicles the majority of the suspension deflection is at a single spring rate and therefore behaves more linearly than for the transitional part laden case. In the tare state, high Y/Q ratios are associated with comparatively lower natural frequencies than for

the part laden cases. The difference between the two trends is likely to be a consequence of the step change in the load versus damping rate relationship when the laden spring comes in to contact.

The tare-laden spring clearance has little to no influence on the Y/Q ratios for the tare and fully laden cases, however it is a significant influence for the transitional part laden case. It can also be seen that for a given spring rate combination greater tare-laden spring clearance results in lower Y/Q ratios.

The results from the EN 14363 Y/Q simulations (Figure 41) show the same trends as the GM/RT 2141 results. However, in the case of the Euro Norm assessment all vehicles are predicted Y/Q ratios within the limit (the highest value being 1.01).

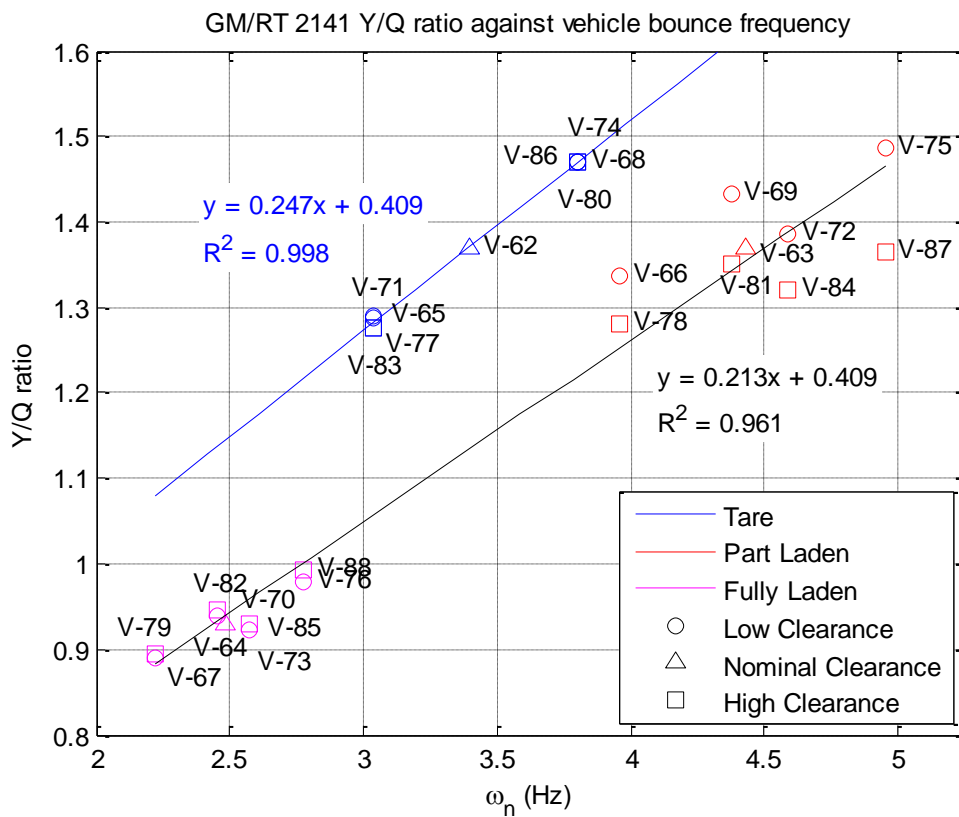


Figure 40 GM/RT 2141 Y/Q ratio against primary suspension bounce frequency.

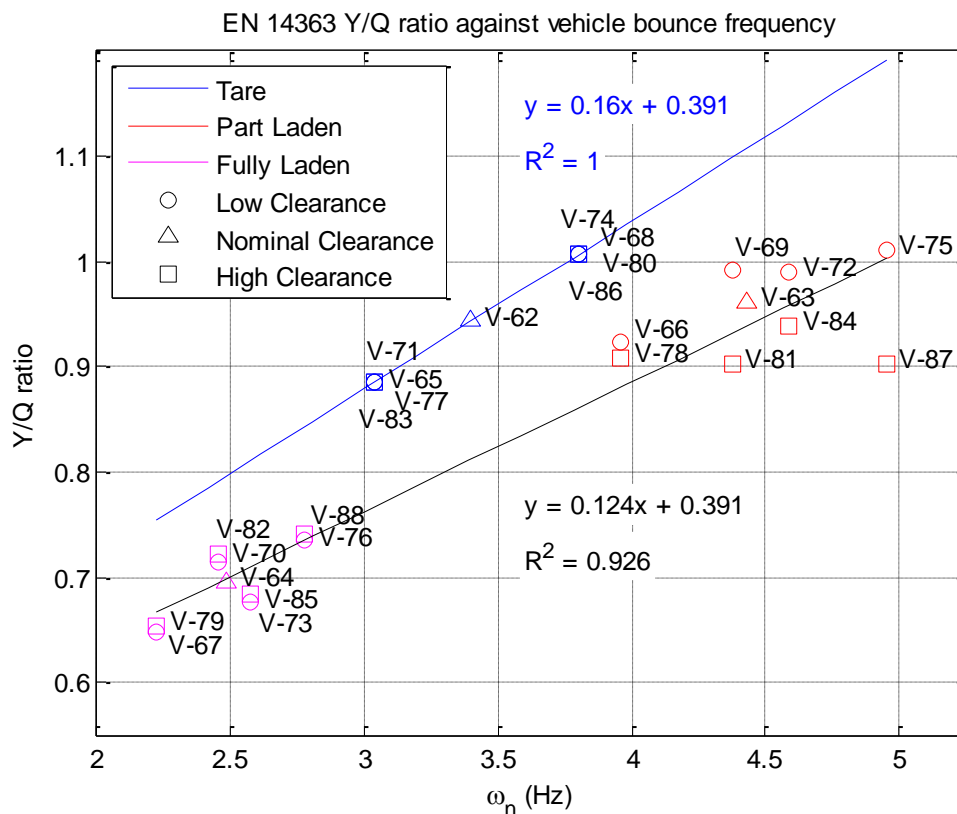


Figure 41 EN 14363 Y/Q ratio against primary suspension bounce frequency.

GM/RT 2141 Quasi-static Assessment of Wheel Unloading ($\Delta Q/Q$)

The $\Delta Q/Q$ ratios from the GM/RT 2141 static simulations are plotted in Figure 42 against the nominal bounce frequency of the primary suspension. As described previously, it is not implied that modal resonance contributes to the wheel unloading behaviour. The first natural frequency is shown only to indicate the relative stiffness of the suspension in relation to the body mass.

The data points are colour coded according to load case: blue – tare laden; red – part laden; magenta – fully laden. Two linear trend lines have been fitted to the tare and fully laden/part laden data subsets with R^2 correlation coefficients of 0.999 and 0.904 respectively. The trends indicate that as the effective vertical stiffness of the primary suspension system increases so does the wheel unloading. The difference between the two trends is likely to be due to the step change in the load versus damping rate relationship when the laden spring comes into contact.

As for the Y/Q analysis, it can be seen that the tare-laden spring clearance has a significant influence on wheel unloading for the part laden vehicles, with increased clearance leading to reduced wheel unloading. The trend is the same for the fully laden vehicles, but much less significant.

The constants for the trend line will be affected by other vehicle parameters, such as bogie semi-spacing, bogie wheelbase and bogie to body torsional resistance.

As the trend in the data series and the distribution of the data points is very similar to that from the GM/RT 2141 Y/Q analysis it can be concluded that the effect of vertical stiffness on derailment resistance is through wheel unloading, as opposed to changes in curving forces.

This is in line with the expected influence of the vertical suspension parameters on the plan view curving behaviour.

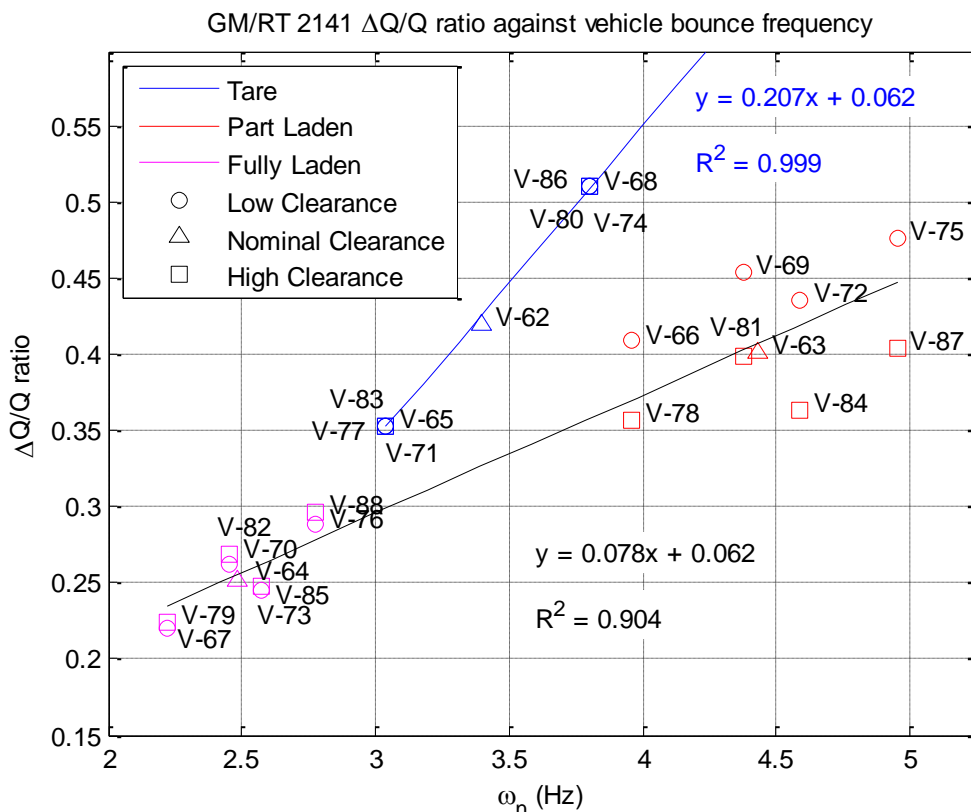


Figure 42 $\Delta Q/Q$ ratio against primary suspension bounce frequency.

The results from the above figure suggest that the vertical bounce frequency could be used as an initial design parameter to minimise wheel unloading due to track twist. The results also indicate that load cases which results in the higher natural modal frequencies should be scrutinised in derailment assessments for vehicle acceptance requirements.

1.1.1.1 Bogie suspension variation – Primary Damping

The Y-series bogie design is widely used in the freight sector. The bogie suspension is generally configured by the vehicle manufacturer to suit the wagon body under which it runs. Within the normal design range of suspension parameters, there is the possibility that the bogie engineer creates a configuration which is not particularly optimal with respect to potential derailment risk.

The simulation studies in the following subsection analyse the effect of changes to the primary friction damping levels on derailment resistance. The influence of tare and laden spring rates and tare to laden spring clearance on derailment resistance are presented in the previous subsection.

GM/RT 2141 – Assessment of low speed flange climb (Y/Q)

The nine vehicle configurations for the primary damping assessment were simulated through the GM/RT 214 Y/Q suite of test cases. The highest Y/Q ratios calculated during simulations are plotted in Figure 43 for each vehicle. Two clear trends exist, one for the tare and part laden vehicles and a second for the fully laden vehicles. In both cases increasing the

coefficient of friction in the primary damping increases the derailment risk in a relatively linear manner. The difference between the two trends represents the step change in the load-damping relationship as the laden spring comes into contact and shares more of the load.

The EN 14363 Y/Q analyses produced similar observations and, as with previous cases, the absolute Y/Q ratios predicted were consistently less than those from the GM/RT analyses.

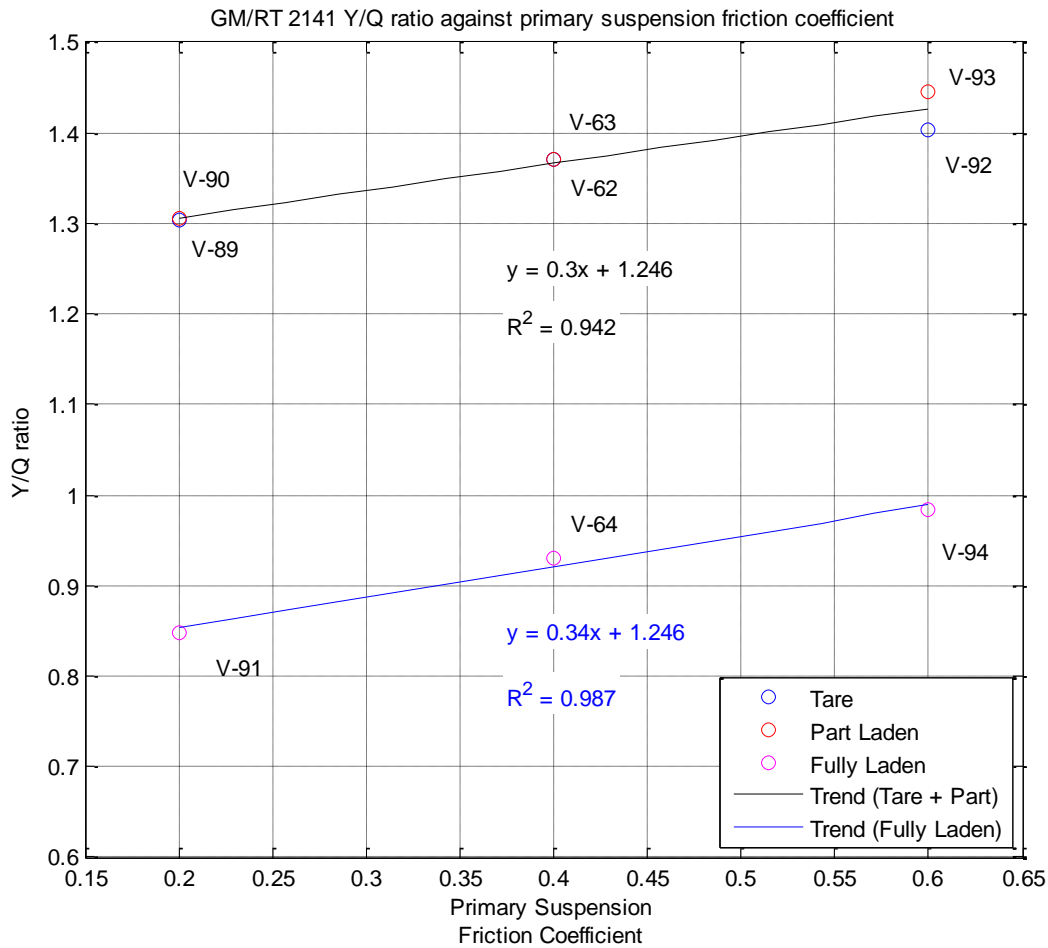


Figure 43 GM/RT 2141 Y/Q ratio against primary suspension friction coefficient

GM/RT 2141 Quasi-static assessment of wheel unloading ($\Delta Q/Q$)

The results from the GM/RT 2141 $\Delta Q/Q$ simulations are plotted in Figure 44 for the nine vehicle configurations. The data is split into two trends, one for the tare and part laden vehicles and a second for the fully laden vehicles. For both trends increasing the coefficient of friction in the primary damping leads to an increase in the calculated wheel unloading in a relatively linear manner. The increased friction leads to larger forces being required to break out the static friction. This in turn leads to reduced axle articulation and greater unloading of the leading outer wheel. The influence of the primary damping friction on wheel unloading is slightly less for the fully laden case (a gradient of 0.243 versus 0.305 for the tare/part laden trend), but in all cases the influence is significant. For the vehicles simulated here a high coefficient of friction does not lead to exceedance of the $\Delta Q/Q$ limit (0.6). However coupled

with other factors, which lead to high $\Delta Q/Q$ ratios, such as skew loading, optimal friction specification could be the difference between compliance and noncompliance.

As for the previous parameter studies the EN 14363 $\Delta Q/Q$ analyses led to the same conclusions as the GM/RT 2141 assessment.

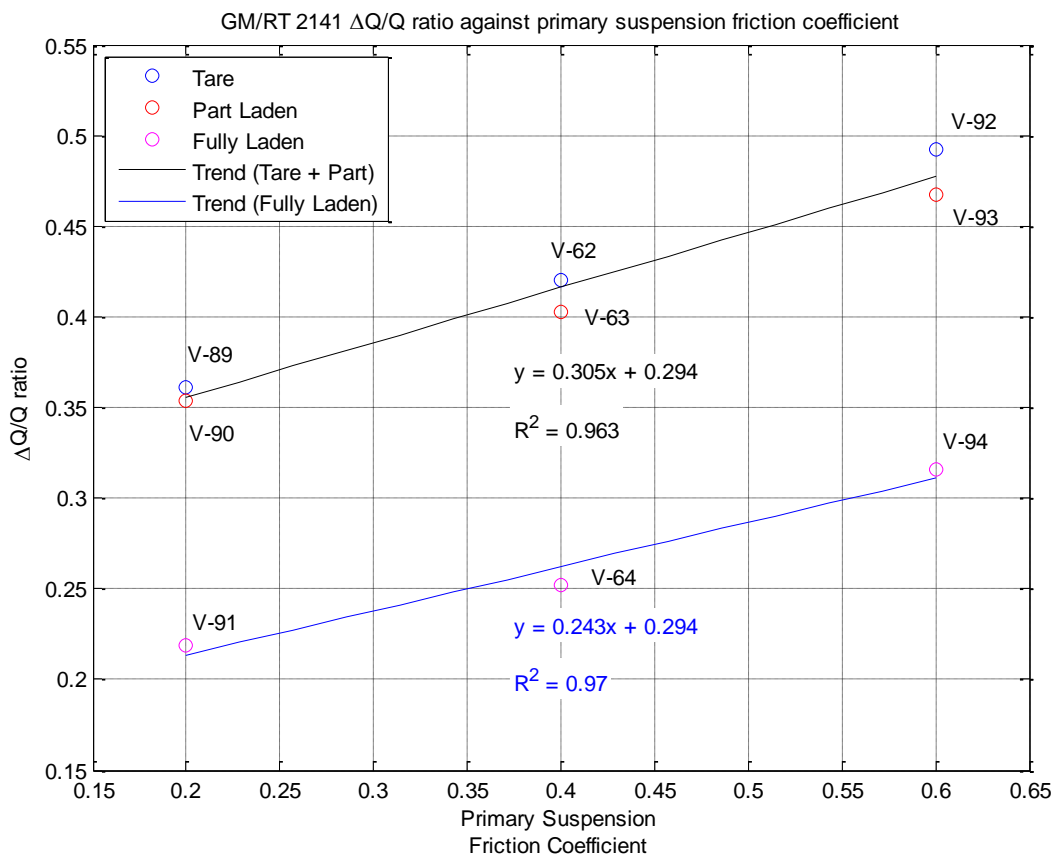


Figure 44 GM/RT 2141 $\Delta Q/Q$ ratio against primary suspension friction coefficient

Acceleration peak counting

During this investigation (of the influence of primary damping on derailment resistance) it is recognised that the principle purpose of the primary damping is to help provide acceptable ride performance. The nine vehicle variants were simulated along a straight track with vertical, lateral and crosslevel irregularities representative of 160 km/h track. The vertical and lateral accelerations at the centre of the leading bogie were then post-processed using the Vampire Peak-Counting feature. Figure 45 shows the vertical acceleration peak counting for the nine vehicles, along with the limit line from RGS GM/RT 2141. It can be seen that the lower coefficient of friction leads to a greater percentage of high acceleration peaks. Comparing the tare and part laden vehicles with nominal friction ($\mu = 0.4$) to those with low friction ($\mu = 0.2$) it can be seen that the limit line margin is significantly reduced for the low friction vehicles.

The lateral acceleration peak counting is shown in Figure 46 for the nine vehicle variants. The trend between friction level and the proximity to the limit line is less clear than for the vertical case. However it can be seen that the lowest friction levels ($\mu = 0.2$) lead to the highest accelerations in the tare and part laden load states. For the part laden case the limit line is exceeded at 0.325 g.

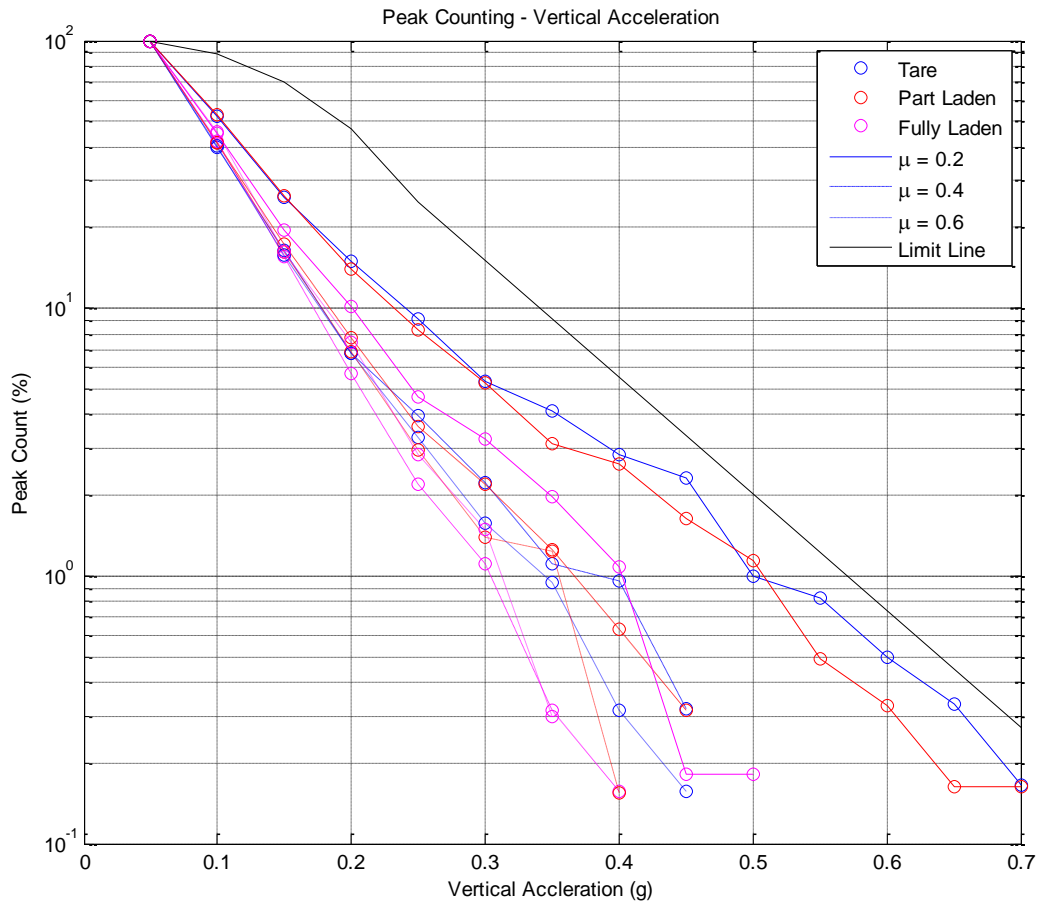


Figure 45 Vertical acceleration peak counting for differing load and primary suspension friction conditions

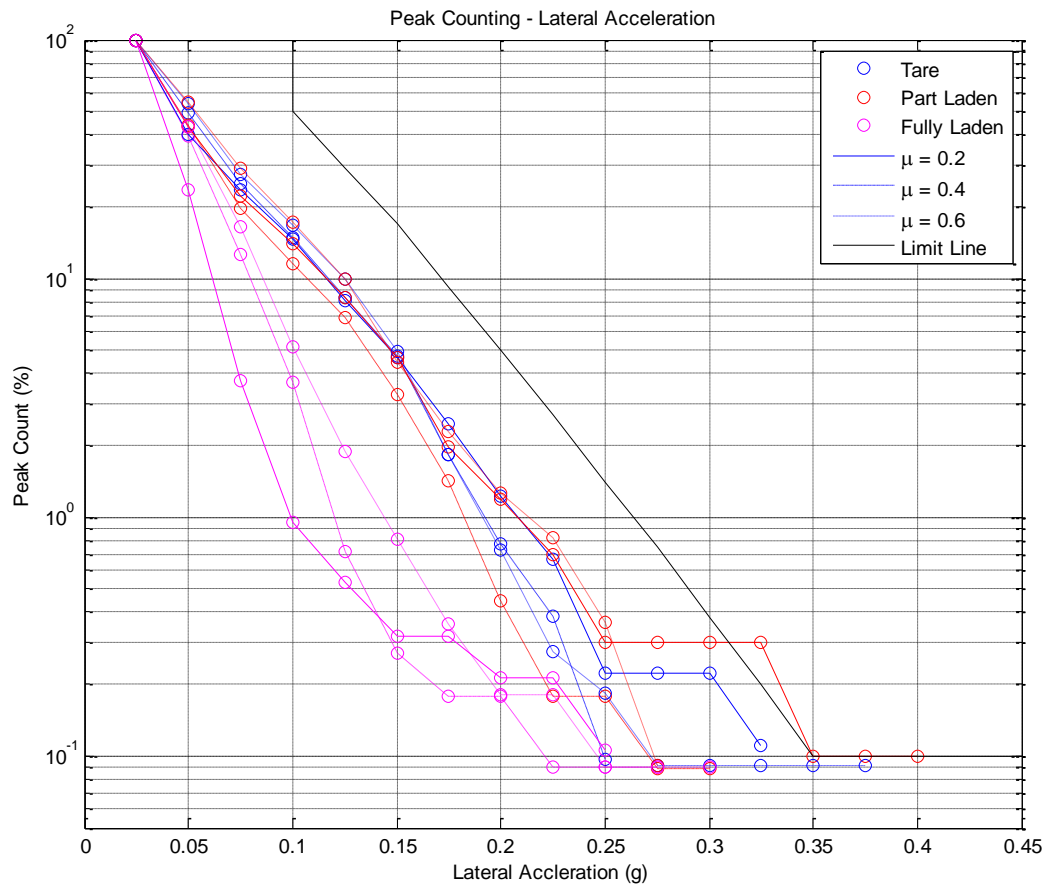


Figure 46 Lateral acceleration peak counting for differing load and primary suspension friction conditions

1.1.1.2 Bogie yaw resistance variation

The rotational resistance of the bogie beneath the vehicle body (X-factor) is a method of assessing derailment resistance which is used in both the GB and EN acceptance standards. Increased bogie rotational resistance will generally lead to an increase in lateral curving forces and hence nominally higher Y/Q ratios.

GM/RT 2141 – Low speed flange climb assessment(Y/Q)

Increasing the yaw resistance of the bogie gives rise to higher lateral forces at the leading outer wheel when negotiating a curve. It can be seen from Figure 47 that for the tare vehicle the side bearer friction coefficient is more influential than the centre bowl friction coefficient, as the centre bowl carries relatively little load. For the fully laden vehicle, the centre bowl coefficient of friction is more influential, as the centre bowl friction surfaces carry the majority of the vertical load.

For the part laden vehicle the side bearer and centre bowl coefficients of friction have minimal influence on the Y/Q ratio. This is due to the dominating factor for the part laden vehicle being wheel unloading (see the $\Delta Q/Q$ plots in Figure 49), not lateral force. Note that all the part laden cases have Y/Q ratios in excess of the limit of 1.2.

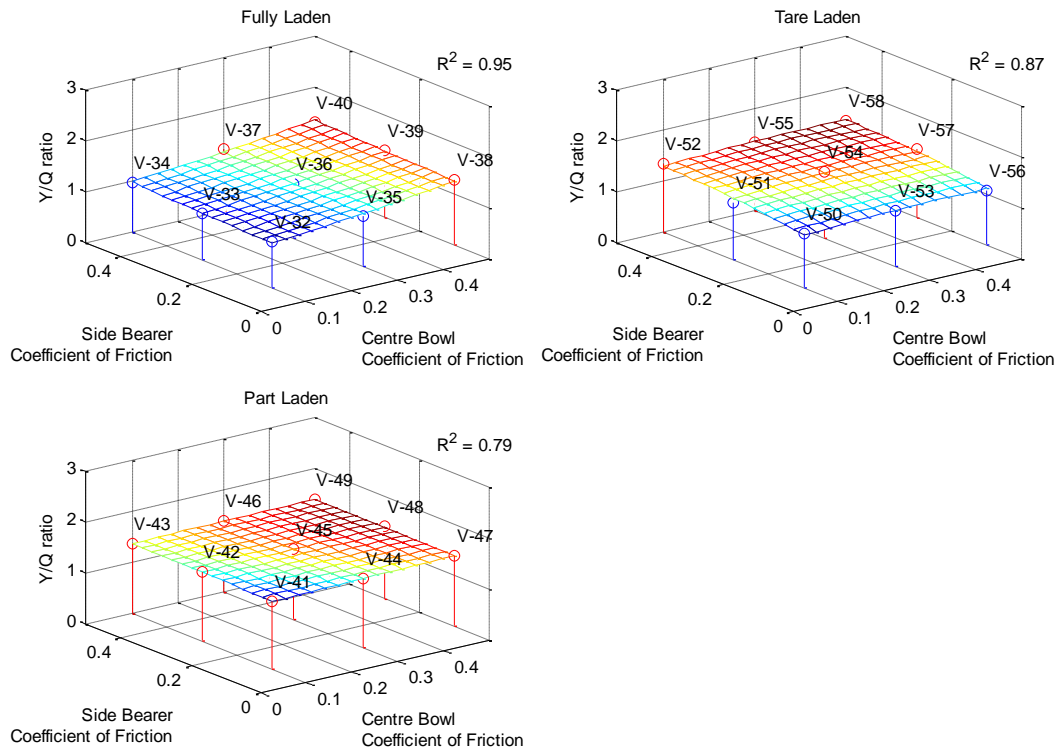


Figure 47 The influence of centre bowl and side bearer friction coefficient on GM/RT 2141 Y/Q ratio.

The maximum wheel recorded in the EN 14363 Y/Q assessments are shown in Figure 48. It can be seen that the coefficient of friction at either the centre bowl or the side bearer has little influence on flange climb. This indicates that while the increased friction leads to increased lateral forces, those lateral forces are not large enough to overcome the gravitational stiffness and cause flange climb.

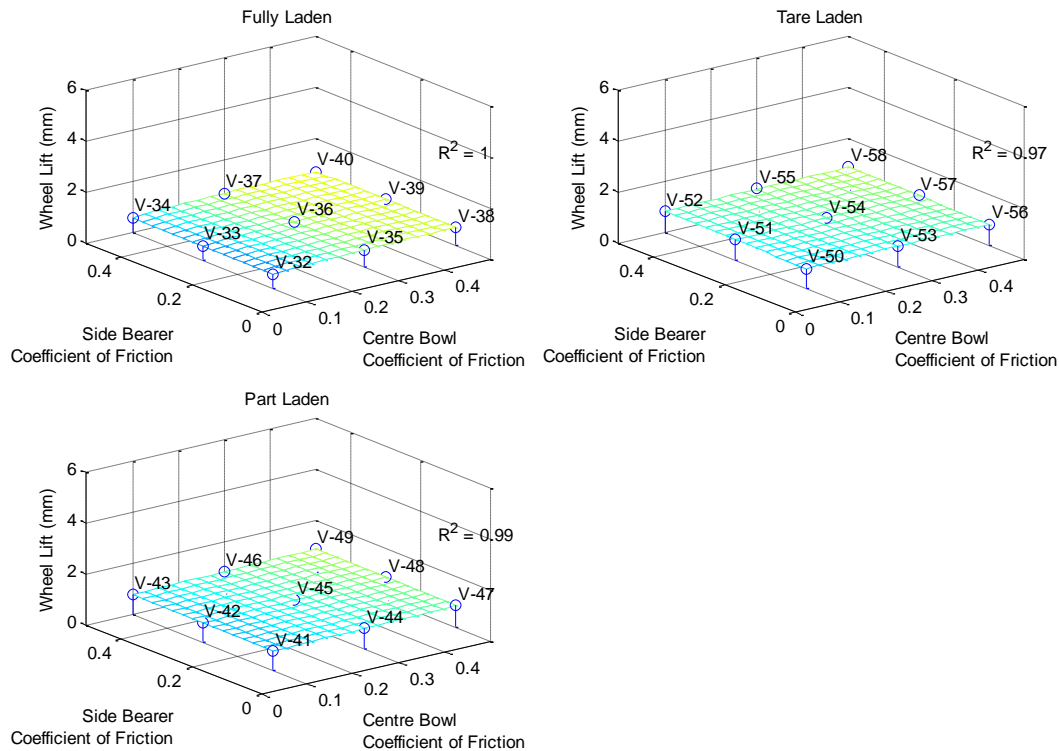


Figure 48 The influence of centre bowl and side bearer coefficient of friction on wheel lift

GM/RT 2141 Quasi-static Assessment of Wheel Unloading ($\Delta Q/Q$)

As expected the coefficient of friction in the side bearers and centre bowl have little to no influence on the $\Delta Q/Q$ ratio. Of the two friction elements it is only the centre bowl which has a direct influence on the vehicle's response to twist, via the roll and pitch resistance between the bogie and vehicle body. Figure 49 shows the results from the GM/RT 2141 $\Delta Q/Q$ analysis.

In the tare condition the centre bowl carries little load, and therefore altering the coefficient of friction has little influence on the vehicle performance. In the part laden condition the centre bowl carries more load, but still has little influence in the vehicle response: the behaviour of the primary suspension and side bearer stiffness being the more influential factors. In the fully laden case the friction coefficient at the centre bowl has a noticeable, but still small, influence on the $\Delta Q/Q$ ratio: with increased centre bowl friction coefficient leading to increased roll and pitch resistance and increased wheel unloading.

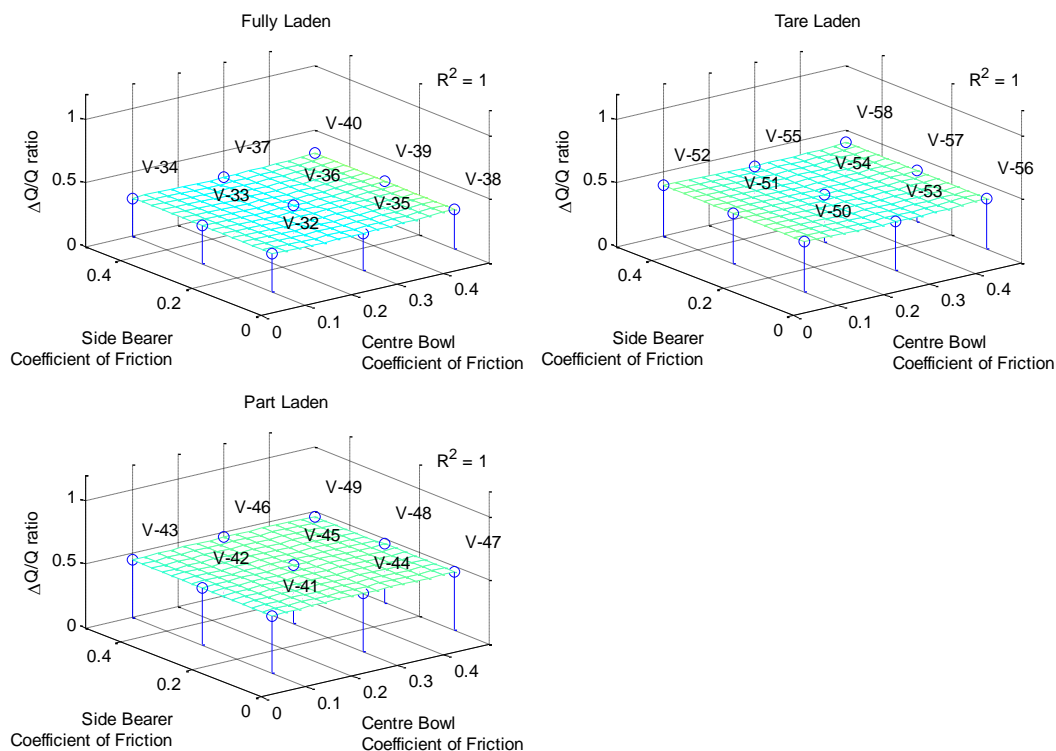


Figure 49 The influence of centre bowl and side bearer coefficient of friction on GM/RT 2141 $\Delta Q/Q$ ratio.

3.1.3.5 Bogie X-factor

As expected increasing the coefficient of friction at the centre bowl and side bearers increases the bogie X-factor. Figure 50 shows that for the tare laden vehicle the side bearer friction coefficient has greatest influence of the two parameters. This is because the centre bowl carries comparatively little load and has a smaller effective radius than the side bearers. In part laden conditions the two parameters have relatively equal influence on bogie X-factor. For the fully laden vehicle it is the centre bowl coefficient of friction which is most influential, as under this load condition the centre bowl carries most of the vertical load.

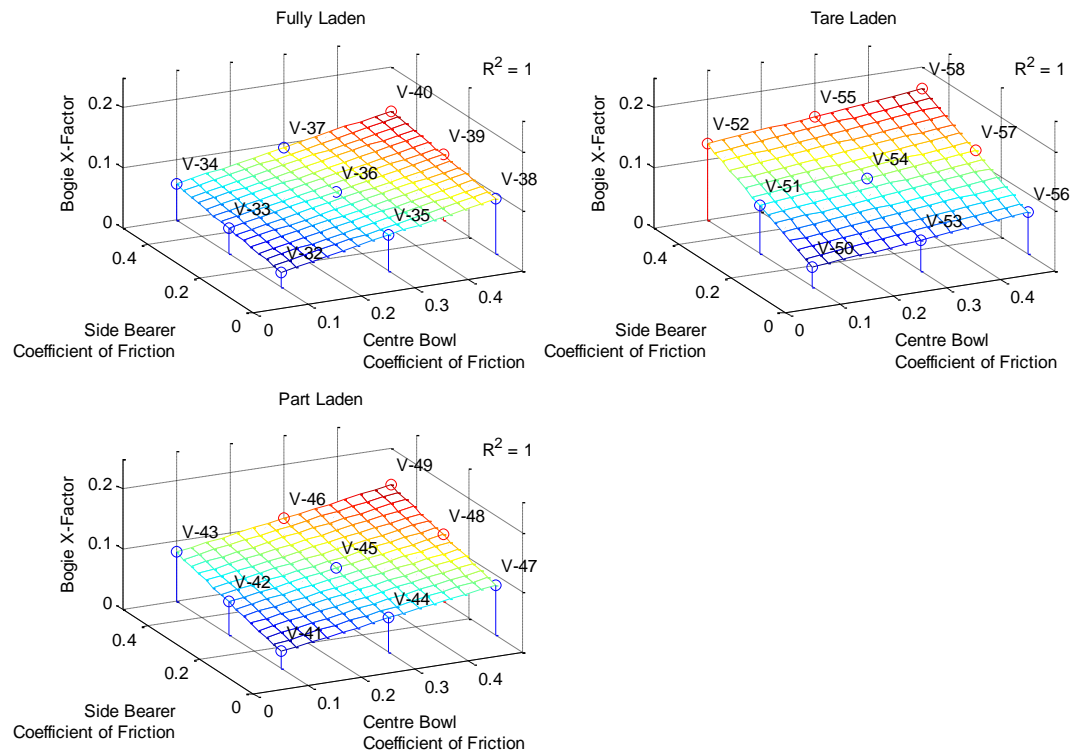


Figure 50 The influence of centre bowl and side bearer coefficient of friction on bogie X-factor.

To further understand the influence of bogie yaw resistance on derailment the results from the GM/RT Y/Q analyses have been plotted against X-factor in Figure 51. The plot contains the results for the 27 vehicles simulated in this section and the 18 test tracks used. The data has been separated by test track (coloured lines). It is clear that there is not a clear correlation between X-factor and Y/Q ratio when all the vehicles are considered in this way. This is due to other factors influencing the derailment measure, particularly the wheel lift propensity ($\Delta Q/Q$).

A clearer trend may be seen in the subplots of Figure 52. In general it can be seen that an increase in bogie X-factor leads to an increase in Y/Q ratio; however the correlation coefficients for these trends are not high (< 0.89).

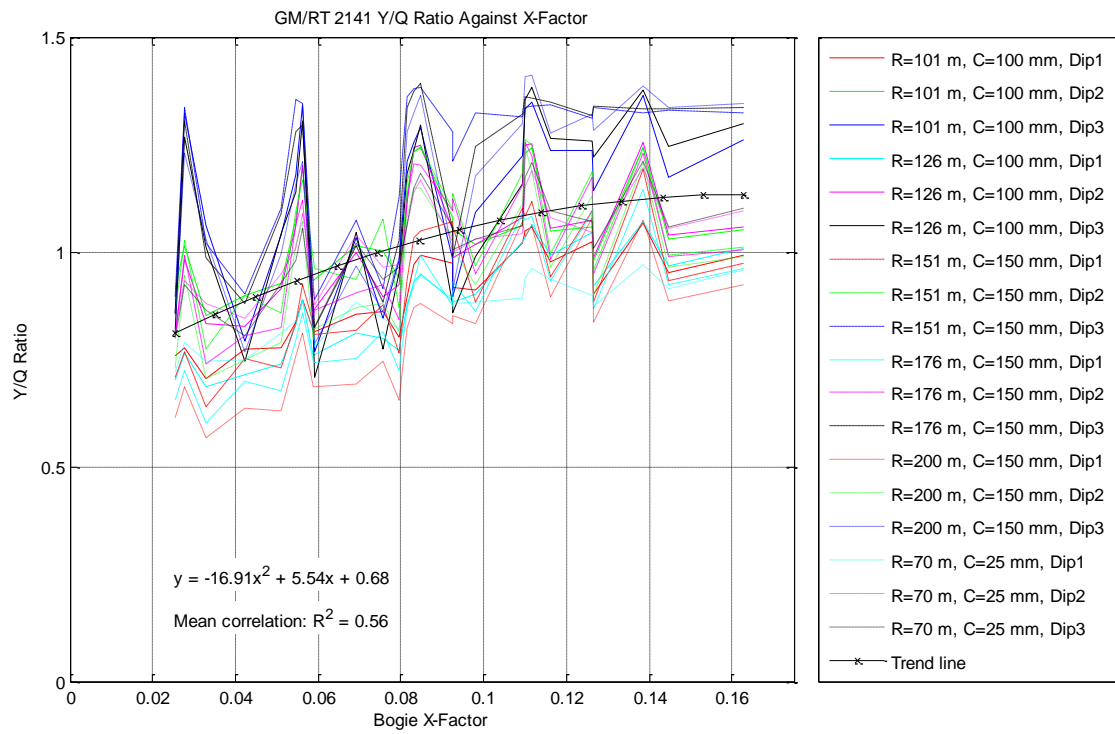


Figure 51 GM/RT 2141 Y/Q ratio against X-factor (all vehicle load conditions).

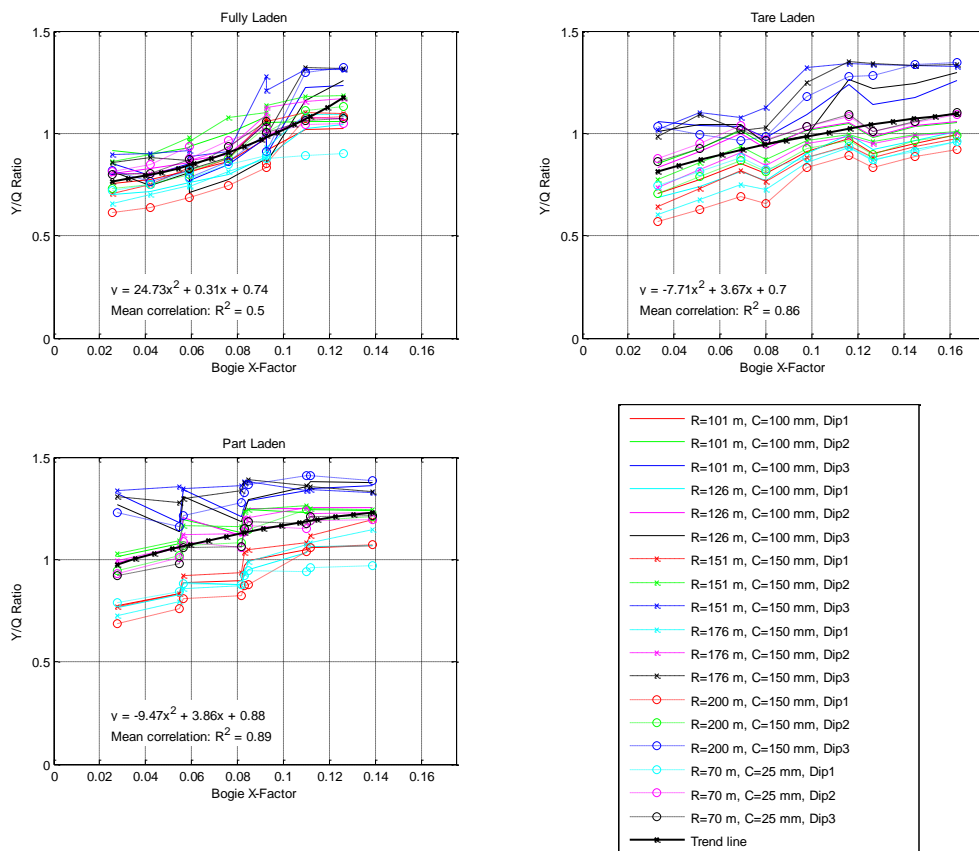


Figure 52 GM/RT 2141 Y/Q ratio against X-factor separated by vehicle load case.

The 27 vehicles were subsequently simulated through a steady curve of 150 m radius installed with 150 mm cross level and light irregularities. Quasi-static wheel load and Y/Q ratios were calculated from steady state curving, by taking the mean of the channels (Y and Q) over 25 m. Figure 53 shows these results plotted along with X-factor. It can be seen that the quasi-static wheel load (a function of the static wheel load and the cant deficiency) has little to no influence on the Y/Q ratio. This is because an increase in wheel load leads to an approximately proportional increase in lateral forces – the net effect on the Y/Q ratio is therefore practically nil.

It can also be seen that X-factor has an almost linear influence on Y/Q ratio. However as the Y/Q ratios for these cases are well within the limits it is clear that high X-factor on its own does not lead to excessive (or even borderline) Y/Q ratios; excessive Y/Q ratios can only be achieved in combination with wheel unloading.

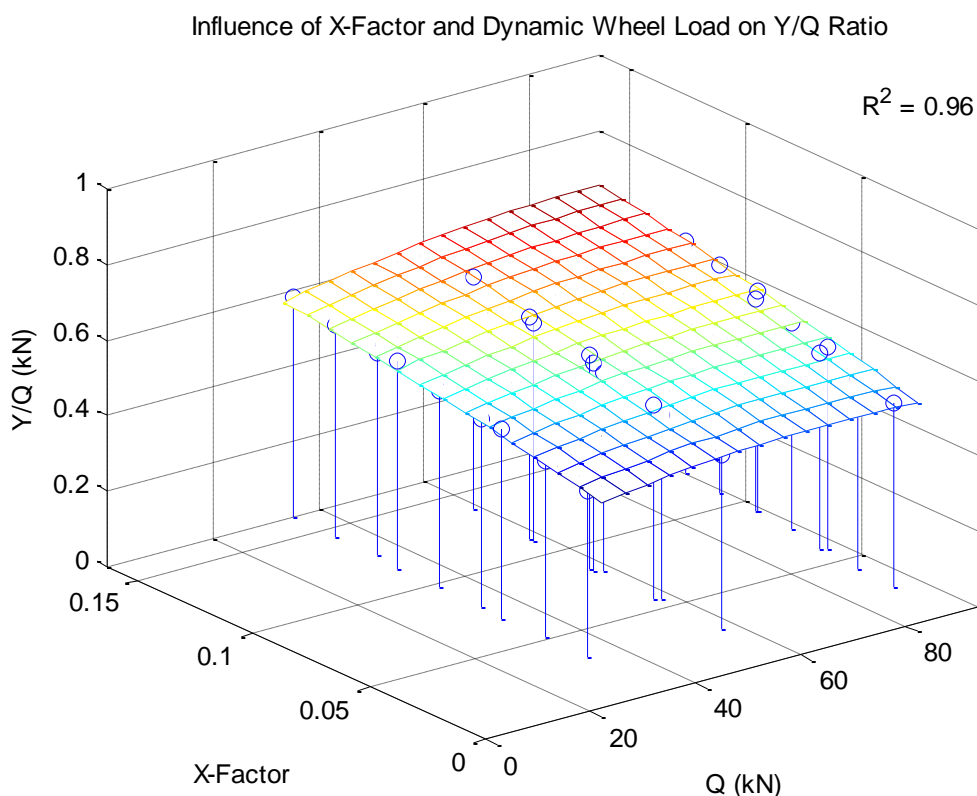


Figure 53 The influence of X-factor and dynamic wheel load on Y/Q ratio.

Figure 54 demonstrates how the increased quasi-static wheel load leads to an almost proportional increase in lateral force. The dynamic wheel load is influenced primarily by the static wheel load and secondarily by the cant (excess or deficiency) of the curve. Consequently increasing the static wheel load increases both the numerator and denominator of the Y/Q quotient and has little influence on the derailment measure. Changing the static wheel load (load state of the vehicle) has a secondary effect on the wheel unloading due to a twist ($\Delta Q/Q$ ratio) of the vehicle, which has a greater influence on derailment than the change in dynamic wheel load.

In comparison to the influence of quasi-static wheel load, X-factor has a relatively small influence on lateral force.

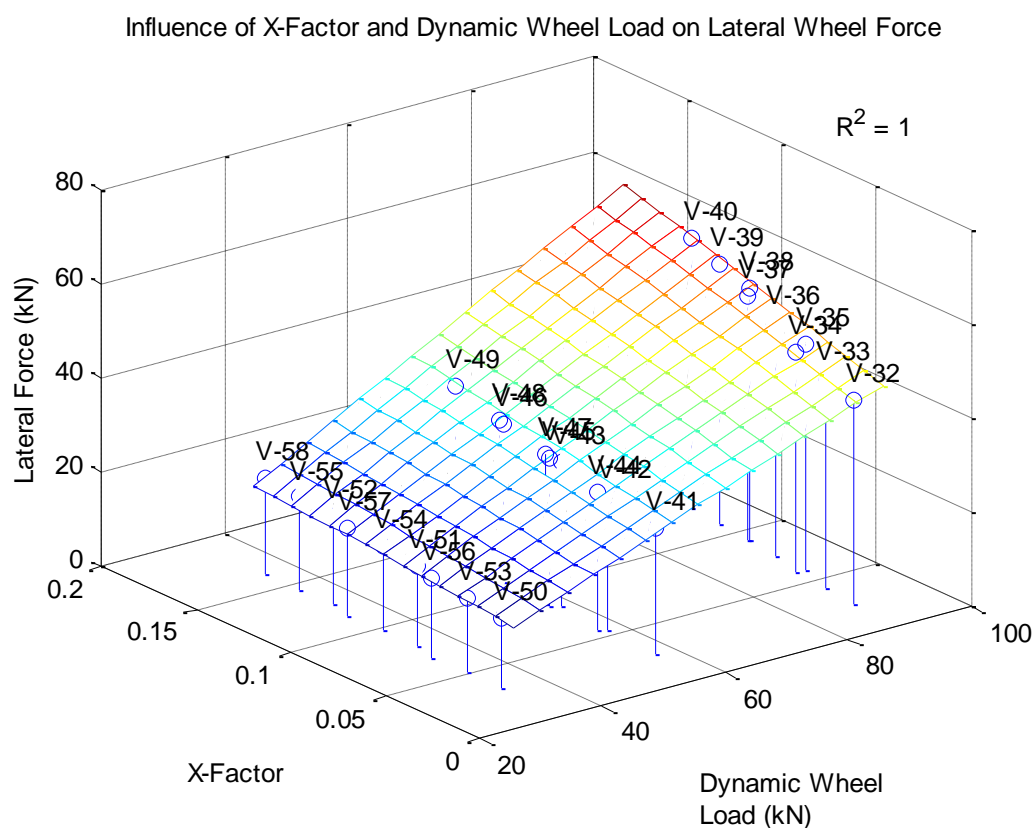


Figure 54 The influence of X-factor and dynamic wheel load on lateral wheel force.

3.1.4 Conclusions – Influence of vehicle parameter variation on derailment

1.1.1.3 Skew loading

w.r.t $\Delta Q/Q$ twist (EN 14363 and GM/RT2141)

As would be expected, it can be seen that increasing the load offset in either the lateral or longitudinal directions increases the calculated $\Delta Q/Q$ value. Increasing the longitudinal loading offset alone, up to the accepted longitudinal loading imbalance ratio of 3, increases $\Delta Q/Q$ value to close to the limit of 0.6.

Increasing the lateral load offset has a greater influence on the $\Delta Q/Q$ value than longitudinal offset, on a like-for-like basis: the lateral load imbalance having approximately 2.7 times greater influence on the $\Delta Q/Q$ ratio than the longitudinal imbalance.

Whilst the analysis presented is to an extent vehicle specific, it is clear that lateral loading offset has a significant influence on the quasi-static wheel unloading due to track twist. In this area the applicable standards are not prescriptive regarding the level of offset load which should be considered for acceptance testing and are also not specifically aligned to the UIC RIV loading limits (1.25 lateral and 3.0 longitudinal) which have been widely adopted throughout Europe.

However, the simulations presented in Figure 13 demonstrate that with a lateral load imbalance at the limit value of 1.25, combined with a high longitudinal load imbalance approaching 3.0, the vehicle marginally remains within the $\Delta Q/Q$ limit value of 0.6. This result suggests that when considering quasi-static wheel unloading due to track twist the UIC RIV loading limits are appropriate.

w.r.t. X-factor (EN 14363 and GM/RT2141)

It can be seen that the longitudinal wheel load imbalance has little influence on the bogie X-factor. In contrast, any degree of lateral wheel load imbalance greater than approximately 1.3 is predicted to lead to a bogie X-factor in excess of the limit value of 0.1, for the vehicle model analysed here.

This is due to the sidebearer spring becoming coil bound and the unit reaches a metallic bumpstop. Compared to the symmetrically laden case there is a greater net load on the side bearers and consequently an increase in the frictional body-bogie yaw resistance.

Initial simulations suggests that if bumpstop contact can be prevented (by increasing the allowable deflection of the side bearer support spring) the X-factor can be reduced by 20% (based on vehicle model V-07 – 0.1 reduces to 0.08). Further analysis of the impact of these changes on vehicle gauging (body sway and drop) would also be required if sidebearer vertical clearance were to be increased.

Low speed flange climb assessment (EN 14363 and GM/RT2141)

In terms of assessing the effect of skew loading on the low speed flange climb risk, the EN and GB standards present different sensitivities. This is due to the distinct differences in the assessment methods. The GB method is a more severe test which has relatively extreme values of curvature, twist and cant excess.

With respect to the EN method, it initially appears that increases in the longitudinal and lateral wheel load offsets affect the calculated Y/Q ratio at a similar rate.

However, significant exceedance of the lateral offset limit of 1.25 results in failure against the EN standard ($Y/Q > 1.2$) without any longitudinal offset loading. Conversely, high levels of longitudinal offset without any lateral offset, do not present a significant increase in derailment risk. It is noted that values which are close to the lateral offset limit of 1.25 only result in significant exceedance of the Y/Q limit value if longitudinal offset is also present.

In contrast to the results from the Euro Norm, the GB RGS results show that the lateral load offset is much more influential than the longitudinal load offset. Only two vehicles were found to pass the GMRT 2141 Y/Q analysis for all test tracks, with the remaining vehicles generating Y/Q ratios in excess of the limit in at least one case.

This result emphasises the more severe test conditions of the GB low speed flange climb method. In essence, a relatively low lateral or longitudinal load offset will result in failure against the GB method, although analysing the derailment count under the GB method shows that all of the vehicles with a lateral load imbalance below the UIC RIV limit of 1.25 negotiated all the test tracks without derailing (despite most generating Y/Q ratios in excess of the limit). Conversely, only two vehicles with load offset above the limit line negotiated all test tracks without derailment.

In summary, the low speed flange climb assessments follows the trends seen in the wheel unloading assessment – excessive lateral load offset has a significant effect on the derailment risk. However, if the vehicle remains within the UIC RIV limit of 1.25 then this risk can be mitigated. Furthermore, it appears the GB RGS assessment may be overly severe; it is likely that if offset loading were fully considered in the GB assessment, then many vehicles would fail the low speed flange climb assessment. However, on-track evidence suggests that such vehicles generally run with an acceptable derailment record. Conversely the EN standard shows that all vehicles at the UIC RIV limit would pass the low speed flange climb assessment. The most appropriate limit values may lie somewhere between the two standards.

To conclude, with the exception of the GB low speed flange climb assessment, the above analysis of the effects of skew loading suggests that the UIC RIV limits appear to be appropriate and provide an effective mitigation against increased flange climb list due to skew loading. Therefore, a key factor in minimising derailment risk appears to be the effective measuring and monitoring of wheel loads in traffic to ensure that vehicles remain within the UIC RIV loading limits and the establishment of possible threshold values for which vehicles should be flagged for exceeding these limits.

Relating skew loading, single axle imbalance and derailment

The maximum lateral imbalance for any given axle on the skew laden vehicle models was calculated. The derailment metrics (Y/Q, $\Delta Q/Q$, X-factor etc.) were plotted against this maximum axle imbalance and the longitudinal vehicle imbalance in order to draw out correlations between the maximum axle imbalance and derailment risk. This work supports the activities of SBB in isolating vehicles in traffic with axle imbalances greater than 1.7.

It was noted that, for vehicles with an initially longitudinally symmetrical load, but with a lateral load offset greater than 1.25, increasing the longitudinal load offset had a large influence on the maximum axle imbalance.

For longitudinally symmetrical vehicles the $\Delta Q/Q$ analysis showed that the limit value of 0.6 is coincident with an axle imbalance of approximately 1.63. For the maximum longitudinal imbalance simulated (1:2.3) the $\Delta Q/Q$ limit was coincident with an axle imbalance of approximately 1.23. When considering the maximum axle imbalance the RIV limit of 1.25 offers a margin of safety against the $\Delta Q/Q$ wheel unloading assessments. This margin reduces with increasing longitudinal imbalance. In the EN 14363 Y/Q analyses the limit value of 1.2 was coincident with an axle imbalance of approximately 1.40 for longitudinally symmetrical vehicles. For vehicles with low axle imbalance (< 1.25) the Y/Q ratio increased with increasing longitudinal offset. The Y/Q ratio did not increase significantly with axle imbalances greater than 1.4, an axle imbalance of 2.26 corresponded to a Y/Q ratio of 1.24 for example. However, despite the marginal exceedance of the Y/Q limit all the vehicles in this range derailed during the simulations. This reinforces the current philosophy that Y/Q alone does not provide a complete indication of the derailment resistance.

The maximum wheel lift measurements recorded during the EN 14363 Y/Q simulations revealed that all vehicles with axle imbalances greater than 1.40 produced excessive wheel lift (> 6 mm), with all but one of those vehicles derailed. The Y/Q simulations suggest that the RIV loading limit of 1.25 offers a small margin of safety against the limits for Y/Q ratio and

wheel lift. For the Y-series vehicles modelled here the critical imbalance appears to be at approximately 1.40.

The GMRT 2141 Y/Q suit of test track cases was used to establish a derailment propensity for each vehicle. The test suite features tight curves of various radii, crosslevel combinations and different dip locations. For approval against the standard a vehicle must not produce excessive Y/Q ratios (>1.2) on any of the track cases, and must certainly not derail. However, as has already been discussed this assessment appears to be disproportionately severe in comparison to the other derailment assessments used in this study. Due to the variety of the derailment drivers in the different test cases a vehicle with a high derailment count has a high propensity to derail – it is sensitive to a wider range of track faults. Conversely, a vehicle with a zero derailment count is unlikely to derail in even the worst combination of track geometry. None of the vehicles within the RIV loading limit of 1.25 and longitudinal imbalance less than approximately 1.5 derailed. Also, none of the longitudinally asymmetric vehicles with lateral symmetry derailed. For vehicles close to the RIV loading limit and longitudinal imbalance greater than approximately 1.8 the derailment propensity increased with increasing longitudinal imbalance. All of the vehicles beyond the RIV limit for axle imbalance had a non-zero derailment count.

For longitudinally symmetrical vehicles the derailment count increased sharply from an axle imbalance of 1.40 (with 2 derailments) to 1.64 (with 10 derailments). With combined longitudinal imbalance the derailment count also increased sharply with an axle imbalance of 1.38 and longitudinal imbalance of 1.37 corresponding to a derailment count of 8. From the GMRT 2141 Y/Q simulations it appears that the RIV loading limit has little margin of safety against prevention of derailments in a range of ‘worst case’ track conditions.

For the Y-series vehicle model used here, longitudinal imbalance was found to have a large influence on the maximum axle load imbalance, when the axle imbalance was greater than the RIV limit of 1.25 and the longitudinal imbalance exceeded approximately 1.6 or 1.8. Increasing longitudinal imbalance under these circumstances led to a step change in the axle lateral imbalance. The non-linear characteristic is due to the non-linear behaviour of the Y-series suspension and the complex interaction between the suspension systems of the two bogies. This behaviour implies that the effects of lateral load imbalance may be reduced by minimising longitudinal imbalance.

In summary of the axle imbalance investigations:

- The maximum axle imbalance can become highly dependent upon the longitudinal load offset.
- For longitudinally symmetrical vehicles the $\Delta Q/Q$ limit corresponded to an axle imbalance of 1.63, the Y/Q limit to an axle imbalance of 1.40 and a wheel lift limit of 6 mm corresponded to an axle imbalance of 1.40.
- The RIV loading limit therefore provides a margin of safety against those derailment resistance measures.
- Derailment propensity increased sharply for axle imbalances greater than 1.40 and also increased with longitudinal offset.
- Against the GM/RT 2141 Y/Q assessment, which combines a number of detrimental factors, the RIV limit provides little margin of safety.

1.1.1.4 Analysis of measured wheel load data with respect to skew loading

Initial analysis of measured wheel loads from an 8 week sample of GB Gotcha data showed that most vehicles operate within the bounds of the UIC RIV loading limits, with 65 of the 22 320 vehicles exceeding a lateral imbalance of 1.25 (0.29%) and 15 vehicles exceeding the limit for longitudinal load imbalance.

Over 97% of the Gotcha data set could be represented by the skew load cases simulated in the studies in this Section, with 69 vehicles having a greater longitudinal load offset than that simulated. If these vehicles were assumed to be the same as the generic Y-series model used in the simulations then they would be expected to pass the derailment assessments studied, with the exception of the GM/RT 2141 low speed flange climb Y/Q tests.

A key question raised by the analysis of both the skew loading and the Gotcha data is what would be an appropriate alarm value for skew loading given that 0.29% of vehicles exceeded the current limit in the data set studied. It is proposed that further analysis will be carried out in the final issue of the WP 3.2 report to investigate the level of skew loading present in vehicles which have derailed and this will be related back to the Gotcha data to establish the number of vehicles which would exceed these limits. It may be that further work outside the D-RAIL project will be required to fully establish a practical alarm value.

It is worth noting that GB Railway Group Standard, GM/RT 2141 stipulates that derailment resistance must be proven in the worst foreseeable loading configurations but this is not defined. This is also the case in the EN. It is further noted that in reality this is rarely carried out in a comprehensive manner and if it were, then it is expected that many more vehicles would fail the GB vehicle acceptance process if the low speed flange climb assessment was applied.

From the Gotcha data analysed, a hypothetical assessment of the impact of an alarm threshold may be made. If a dynamic ratio threshold of 0.75 is applied the data showed that 12 axles exceeded a lateral imbalance of 1.70. It is not known how these highly imbalanced axles were distributed amongst different vehicles or consists. However a worst case may be found by assuming that no consist/train would have no more than 1 highly imbalanced axle. The entire intermodal Gotcha data set contained 1268 consists. If an alarm threshold was implemented at an axle imbalance of 1.70, twelve of those consists would be stopped in order to remove the offending vehicle, which (in this worst case scenario) represents an impact on 0.94% of intermodal traffic. In a more optimistic scenario, where all the axle imbalances are the consequence of skew loading and four exceedance may be attributed to a single vehicle this value may be quartered (to around 0.24%). To complete the range of possibilities, a third scenario may be posed where all the offending axles are distributed amongst a single consist. In this case the alarm limit would impact 0.08% of intermodal traffic.

If no dynamic threshold were to be applied, and implementing the same logic as above, it could be expected that between 0.16%, 4.4% and 17% of intermodal consists would be affected.

This demonstrates that setting an alarm threshold even well above the stipulated limit, where simulations suggest a high derailment risk, could have a potentially catastrophic impact on rail freight. The integrity of the measurement data used to trigger such an alarm is therefore paramount.

1.1.1.5 Bogie suspension variation

The influence of the primary tare spring, laden spring and tare-laden spring clearance on derailment resistance was investigated. A correlation was found between the effective primary suspension bounce frequency and $\Delta Q/Q$ and Y/Q , with the lower frequency models returning lower Y/Q ratios.

It should be noted that the modal frequency was used as a proxy for effective stiffness of the vertical suspension, and it is not implied that the effect on $\Delta Q/Q$ or Y/Q is through resonance.

All the suspension cases simulated predicted $\Delta Q/Q$ ratios within the limit of 0.6, however only the laden vehicles (which had the lowest resonant frequencies) passed the GB low speed flange climb simulations.

These results suggest that a low effective vertical stiffness is preferable when designing for high derailment resistance. Further it indicates that the vehicle load case which provides the highest modal frequency should be included in any derailment resistance assessments.

For the tare and fully laden load cases the nominal clearance between the tare and laden spring at tare weight had little influence on the predicted $\Delta Q/Q$ and Y/Q ratios. For the part laden load case (where the load was just sufficient to bring the laden spring into contact) a trend could be seen between reducing clearance and reducing derailment resistance. This suggests that a high tare-laden spring clearance is of benefit when designing for derailment resistance, however the analysis only included the one transitional part laden load case. It is not clear what the trend would be further away from the tare-laden spring transition point in either direction.

A study of the influence of the primary damping friction level on derailment resistance revealed that minimising the coefficient of friction reduces derailment risk for low speed flange climb. It should be noted that the scope of the investigations here did not include other derailment mechanisms, such as cyclic top derailments, where the conclusion might be different.

The trend between suspension friction coefficient and derailment risk ($\Delta Q/Q$ and Y/Q) was almost linear. For the tare and part laden vehicles the gradient was approximately 0.3 for the two metrics i.e. increasing the coefficient by 0.1 leads to an increase in the derailment measures ($\Delta Q/Q$ or Y/Q) by 0.03. For the laden case the $\Delta Q/Q$ versus friction coefficient gradient was less at approximately 0.24 and the Y/Q gradient was slightly higher at 0.34.

While reducing the coefficient of friction in the primary suspension improved derailment resistance it was found to have adverse effects on the vehicle's ride performance, as measured by vertical and lateral acceleration peak counting (as per GM/RT 2141). In practice the optimisation of the primary damping should be done in conjunction with all its required roles; for low speed flange climb resistance low friction is favourable over high.

The influence of bogie yaw resistance (or bogie X-factor) on derailment resistance was assessed by altering the coefficient of friction at the centre bowl and side bearers. Due to the way in which the vertical load is distributed between the centre bowl and side bearers, the relative friction coefficient at the two locations had differing influences on yaw resistance depending upon vehicle load state. The side bearers were found to be most influential on

yaw resistance for the tare case, the centre bowl most influential for the laden case, and the two friction surfaces had approximately equal contribution in the part laden state.

Bogie X-factor was found to lead to increased Y/Q ratio in steady state curves, although the increase was insufficient to significantly reduce derailment resistance. Where a dip was included to promote higher Y/Q ratios (as per GM/RT 2141) high bogie yaw resistance led to exceedance of the Y/Q limit. For vehicles which are already close to the derailment limits an increase in bogie yaw resistance (such as increased friction in the secondary suspension) could lead to non-compliance with the Y/Q limits set in the standards.

It should be noted that the results with respect to X-factor are specific to vehicles with frictional (coulomb) rotation behaviour and would not apply to vehicles with a stiffness related rotational resistance (e.g. shear of a coil or rubber spring)

3.2 Influence of suspension failure and faults on derailment

3.2.1 Simulation analyses

The following sections detail the investigation of a number of suspension failure modes on the derailment risk of Y-series bogies. These are summarised below:

- Failed Lenoir Link
- Failed Primary Spring
- Failed Sidebearer Unit
- Bogie Frame Twist

Each of the above cases is described in further detail, together with simulation results in the following sections. The method of assessing derailment risk was based upon the following analyses from the GB RGS GM/RT2141:

1. GM/RT 2141 Quasi-static Assessment of Wheel Unloading ($\Delta Q/Q$)
2. GM/RT 2141 Low speed flange climb assessment (Y/Q)
3. GM/RT 2141 On-track ride (Acceleration Peak Counting)

As in the previous studies under section 3.1, the above assessments provide an indication of the vehicle derailment propensity.

3.2.2 Configuration of vehicle models

The base Y-series vehicle (Section 3.1.2.1) was modified in order to simulate the different failure modes, under various loading configurations as detailed in the following subsections.

1.1.1.6 Failed Lenoir Link

The Lenoir link of the common Y-series bogie type (see Figure 55) has the main function of providing load dependant vertical and lateral friction damping to the primary suspension. It does this by pushing the wheelset in a longitudinal outboard direction into the bogie frame. This pre-loads two friction faces with a force that is proportional to the suspension vertical load. Only the inner tare spring acts through the Lenoir link and prior to laden spring contact

each link supports 1/16 of the sprung mass of the vehicle. There is one Lenoir link per axlebox.

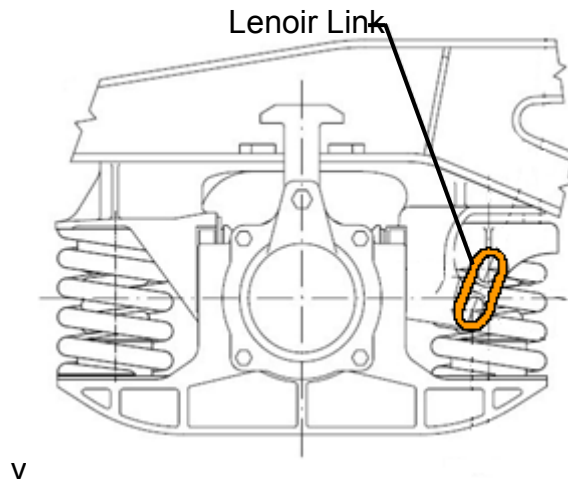


Figure 55 Schematic representation of the primary suspension of a Y25 bogie.

Failure of the Lenoir link is a realistic possibility as it is a relatively highly stressed component which suffers from wear due to sliding contact and is subject to degradation through corrosion. The failure of of one link in one bogie has been represented in the Vampire vehicle dynamics package through the following model changes:

- Modified loading element to remove the link preload on the outboard face between axlebox and bogie frame
- Modified loading element to remove the link preload on the inboard face between axlebox and bogie frame
- Modified primary spring loading element to take account of change in stiffness characteristic and change in static wheel load
- Removal of the related longitudinal 'pendulum' stiffness leaving 4mm of longitudinal clearance (zero stiffness) followed by a hardstop
- Removal of the influence of the primary spring load on outboard hornguide friction surfaces and set static preloads to zero
- Removal of the influence of the primary spring load on inboard hornguide friction surfaces and set static preloads to zero

To investigate the effect of loss of primary damping and pre-load on one wheel of the bogie, simulations were performed at high speeds on straight track. This scenario was selected as the loss of primary damping is likely to cause bogie ride and stability deterioration rather than a reduction in performance in response to track curvature or twist.

To assess the effects of the change in static wheel load and primary vertical stiffness and friction damping characteristics that result from a failed Lenoir link, $\Delta Q/Q$ and Y/Q assessments were performed.

1.1.1.7 Failed Primary Spring

Coil springs can break as a result of material fatigue which can have an impact on the derailment risk of a vehicle. A failed primary spring will result in the static wheel load

reducing on the failed corner and the corner diagonally opposite whilst the load on the other two wheels increases. This reduction in static wheel load increases the $\Delta Q/Q$ and Y/Q quotients that are used to assess derailment risk.

In addition to the change in static wheel loads, a broken spring results in a change in vertical stiffness. Depending on the location of the break, the spring may continue to carry static load or the suspension may collapse onto the hardstops. Both of these scenarios results in an increase in vertical stiffness. In the case where the spring continues to carry static load the stiffness will be higher due to the loss of active coils (fewer coils results in a stiffer spring). In the case of hardstop contact, the stiffness goes up considerably as the vertical stiffness provided by the hardstop is the metallic stiffness of the bogie frame and the axlebox.

Any increase in primary vertical stiffness results in greater wheel unloading on twisted track, thus increasing the $\Delta Q/Q$ and Y/Q quotients and the risk of derailment.

A model was developed that had a broken outboard tare spring. That is the spring that is not connected via the Lenoir link so damping is not lost, although it is varied by the change in static load.

In order to represent the effects of a broken spring, the following changes were made to the Vampire model:

- Modified primary spring loading element to take account of change in stiffness characteristic
- Modified primary spring loading element to take account of change in static wheel load
- Modified loading elements to correct the Lenoir link preloads on the outboard face between axlebox and bogie frame
- Modified loading elements to correct the Lenoir link preloads on the inboard face between axlebox and bogie frame

To assess the effects of the change in static wheel loads and primary vertical stiffness characteristic that result from a failed primary spring, $\Delta Q/Q$ and Y/Q assessments were performed.

1.1.1.8 Failed Sidebearer

The bogie secondary suspension consists of a centre bowl and two side bearers. The majority of the vertical load of the vehicle carbody is supported by the centre bowl in the middle of the bogie but this provides very little in the way of roll stiffness to keep the carbody upright, this is the role of the side bearers. They are located one either side of the bogie and provide the roll stiffness that keeps the vehicle body vertical and within gauge. Also, the top of the side bearers provide a friction surface that allows the bogie to yaw relative to the vehicle body whilst providing yaw damping to control bogie hunting. Figure 56 shows a side view of a side bearer unit. The side bearer contains two springs and various friction elements to provide vertical and horizontal damping. The vertical deflection of the side bearer is limited by a hardstop located inside the coil springs.

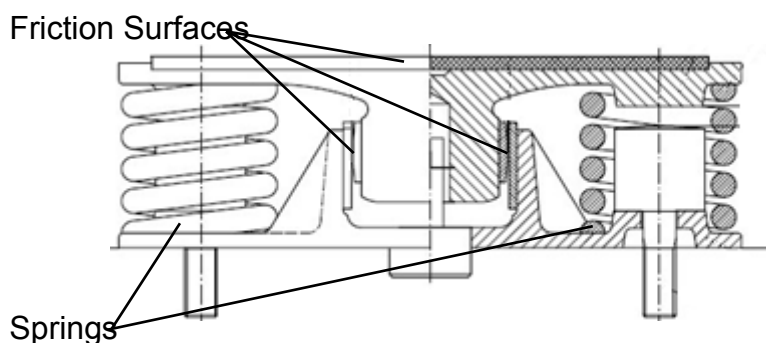


Figure 56 Side view of a Side Bearer Unit

The failure mode considered is that the both coil springs fail as a result of material fatigue causing the side bearer to sit on its hardstops resulting in a very high stiffness and a reduced vertical load. The result of this is that the weight of the carbody has to be redistributed between the centre bowl and the other side bearer of that bogie and the side bearers and the centre bowl of the other bogie in the vehicle. This does not have the same sort of effect as a failed primary spring on a bogie has where the diagonally opposite wheel loads increase or decrease accordingly; this is because the car body is supported mainly by the metallic stiffness of the centre bowls and is therefore unable to pitch. The wheel load is instead shifted laterally across each bogie such that the static loads on one side of the bogie increase and on the other side decrease.

A model was developed that had a failed side bearer. In order to represent the effects of a failed side bearer, the following changes were made to the Vampire model:

- Modified side bearer spring loading element to take account of change in stiffness characteristic
- Modified side bearer and centre bowl spring loading elements to take account of change in static load
- Modified friction elements to reflect change in static preloads

To assess the effects of the change in static wheel loads and stiffness characteristics caused by a failed side bearer, $\Delta Q/Q$ and Y/Q assessments were performed.

1.1.1.9 Bogie Frame Twist

Having equally distributed wheel loads on a bogie is very important for ensuring safety against derailment. This is because any imbalance of wheel loads means that wheels are initially unloaded whilst on level track which will increase the total unloading whilst negotiating track twists. A twisted bogie frame can cause an imbalance of static wheel loads and could be the result of fabrication, incorrect machining during manufacture, damage caused in service or poor maintenance practice during overhaul.

It is typical when assembling bogies to put packing into the suspension to correct for bogie frame manufacturing tolerances and variations in spring stiffnesses and heights. If the incorrect packing is used then this will have the same effect as a twisted frame. Incorrect packing may result from maintenance procedures where suspension is dismantled and not reassembled in the correct order or when springs are replaced without the packing being

adjusted. Incorrectly packed suspension and twisted bogie frames will be treated as the same thing in this report.

In order to represent the effects of a twisted frame or incorrect spring packing, the following changes were made to the Vampire model:

- Modified primary spring loading element to take account of change in stiffness characteristic
- Modified primary spring loading element to take account of change in static wheel load
- Modified loading elements to correct the Lenoir link preloads on the outboard face between axlebox and bogie frame
- Modified loading elements to correct the Lenoir link preloads on the inboard face between axlebox and bogie frame

To assess the effects of the change in static wheel load and primary vertical stiffness characteristics that arise due to a twisted frame, $\Delta Q/Q$ and Y/Q assessments were performed.

3.2.3 Results – Suspension Failure and faults

The following section details the investigation of a number of suspension failure modes on the derailment risk of Y-series bogies. These are summarised below:

- Failed Lenoir Link
- Failed Primary Spring
- Failed Sidebearer Unit
- Bogie Frame Twist

Each of the above cases is described in further detail, together with simulation results in the following sections. The method of assessing derailment risk for each case varies depending on the type of failure mode being investigated. The method may investigate reduced ride performance and hence potentially increased dynamic wheel unloading or may investigate changes in quasi-static response to high levels of track twist or curvature.

1.1.1.10 Failed Lenoir Link

Simulations using the vehicle models with a failed Lenoir link were used to assess the impact of the suspension fault on the derailment risk of the vehicle. The standard used for the assessment is GM/RT 2141 which covers a number of methods. The failure of the Lenoir link results in a change in static wheel loads and stiffness characteristic so the static wheel unloading ($\Delta Q/Q$) and the flange climb derailment Y/Q quotients have been assessed. Also the Lenoir link failure results in the loss of the friction damping between the bogie frame and the axlebox so the ride quality of the vehicle has been assessed using the acceleration peak counting method.

GM/RT 2141 Assessment of low speed flange climb (Y/Q)

Y/Q analysis was carried out for the worst case curves defined in GM/RT 2141. The simulations were done for nominal vehicle models and failed Lenoir link models. The worst

case curve for each loading condition was found to be 150m radius with 150mm installed cant with a 20mm dip at the least favourable location. The location of the dip changes slightly for each loading condition. A plot of the results is shown in Figure 57 and the maximum values are summarised in Table 8.

Table 8 Y/Q results for nominal and failed Lenoir link vehicle models.

Load Condition	Y/Q		
	Nominal Suspension	Broken Lenoir Link	Percentage Change
Empty Containers	1.32	1.35	+2.3%
Partly Laden	1.38	1.43	+3.6%
Laden	1.08	1.23	+13.9%

The largest change in Y/Q is for the laden vehicle. The change in Y/Q for the other load conditions is small. Looking at the raw Y and Q values it was found that the large change in Y/Q in the laden case was mainly due to the Q forces being lower for the broken Lenoir link case than the nominal case, this is because of the reduced static wheel load resulting from the broken Lenoir link. The Y force is also slightly higher, most likely due to the effect on steering that the loss of the Lenoir link has had by altering the longitudinal stiffness.

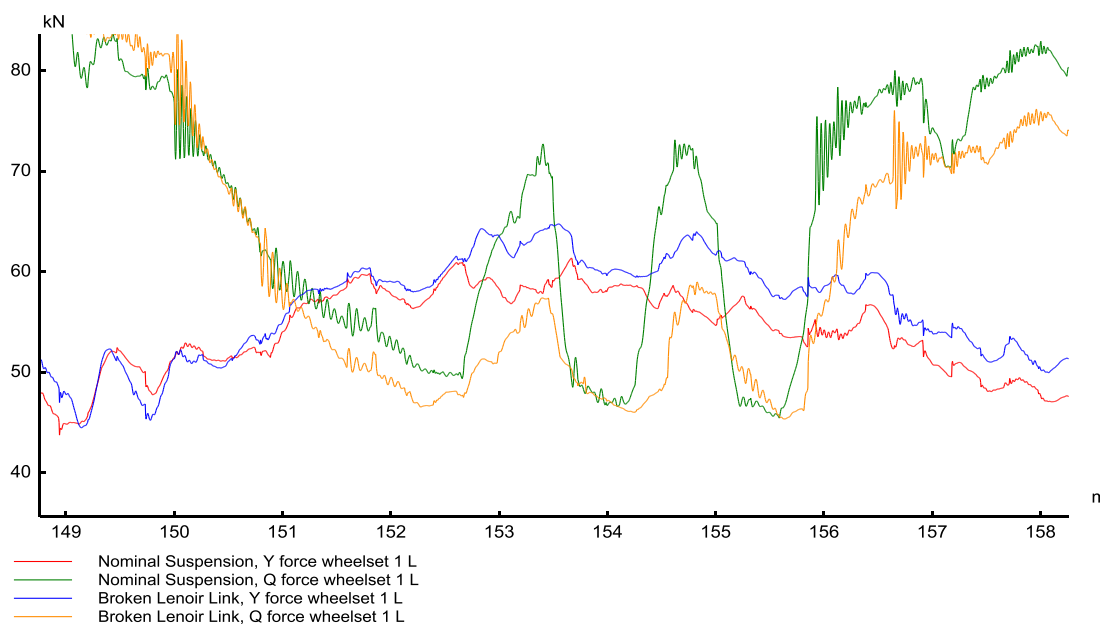


Figure 57 Y & Q forces for Nominal Suspension and Broken Lenoir Link cases in Laden condition for worst case track twist (R150, 150mm Cant, 20mm dip).

GM/RT 2141 Quasi-static assessment of wheel unloading ($\Delta Q/Q$)

Static $\Delta Q/Q$ simulations were carried out to investigate how a broken Lenoir link affects the wheel offloading performance of the vehicle. The maximum $\Delta Q/Q$ values for nominal and failed suspension are shown below.

Table 9 $\Delta Q/Q$ results for nominal and failed Lenoir link vehicle models.

Load Condition	$\Delta Q/Q$

	Nominal Suspension	Broken Lenoir Link	Percentage Change
Empty Containers	0.381	0.421	+10.5%
Partly Laden	0.460	0.524	+13.9%
Laden	0.291	0.330	+13.4%

In all cases the $\Delta Q/Q$ increases as a result of a failed Lenoir link indicating an increased propensity for derailment, however, the GM/RT2141 limit of 0.6 is not exceeded. The increase in $\Delta Q/Q$ is due to the reduction in static wheel load, Q , caused by the failure of the Lenoir link. This is illustrated in Figure 58, it can be seen that the ΔQ remains largely unchanged, this is because the stiffness of the springs remained the same for the cases considered.

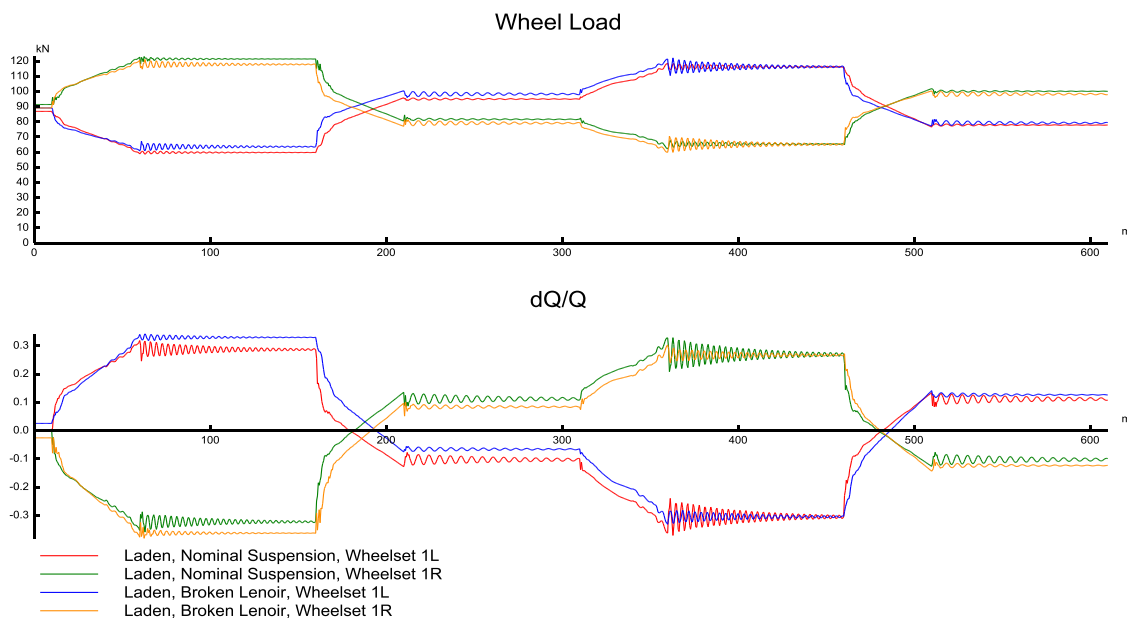


Figure 58 Q forces and $\Delta Q/Q$ for Nominal Suspension and Broken Lenoir Link cases in Laden condition.

GM/RT 2141 Assessment of on-track Ride Test

The results of the analysis are presented as vertical and lateral peak counting curves. These compare the cumulative total of acceleration peaks in the vertical and lateral direction against acceptance lines which are provided in the GB vehicle acceptance standard GM/RT2141. The curves are used to relate dynamic ride to derailment risk, if a vehicle curve crosses the acceptance line then this is deemed a failure against the standard. The acceptance lines are plotted automatically on the graphs generated using VAMPIRE, they are shown as a black line.

The peak counting method has been used here as the loss of the Lenoir link results in a loss of friction damping on one corner of the bogie which could be detrimental to the vehicle ride. Within this GB assessment vehicle ride is used as an indirect measure of derailment risk.

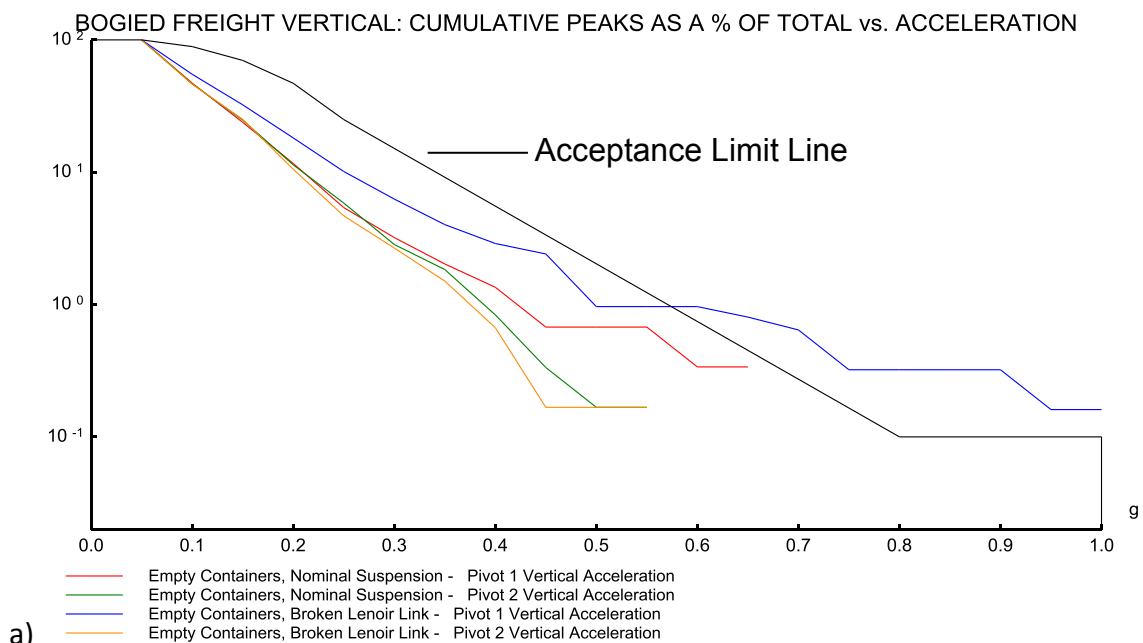
Assessment has been carried out on the following track irregularities:

- Track110 - A low speed, 110km/h (70mph) piece of GB track, typical of freight track and lower quality cross country track. Used here to assess the degradation in ride quality of the vehicle due to a failed Lenoir link.
- Track225 - Top quality GB track, 225km/h (140mph), an example of best intercity track. Used here to assess the effect of a failed Lenoir link on vehicle stability.

Accelerations in the vertical and lateral directions were processed separately, the results are discussed below.

Vertical Ride Acceptance

In all three vehicle loading conditions plotted in Figure 59, the failure of the Lenoir link leads to failure of the GB vertical ride acceptance standard for derailment on Track110 irregularity which is representative of freight track. The largest influence is in the part laden case, although a significant deterioration in ride performance is found in all cases.



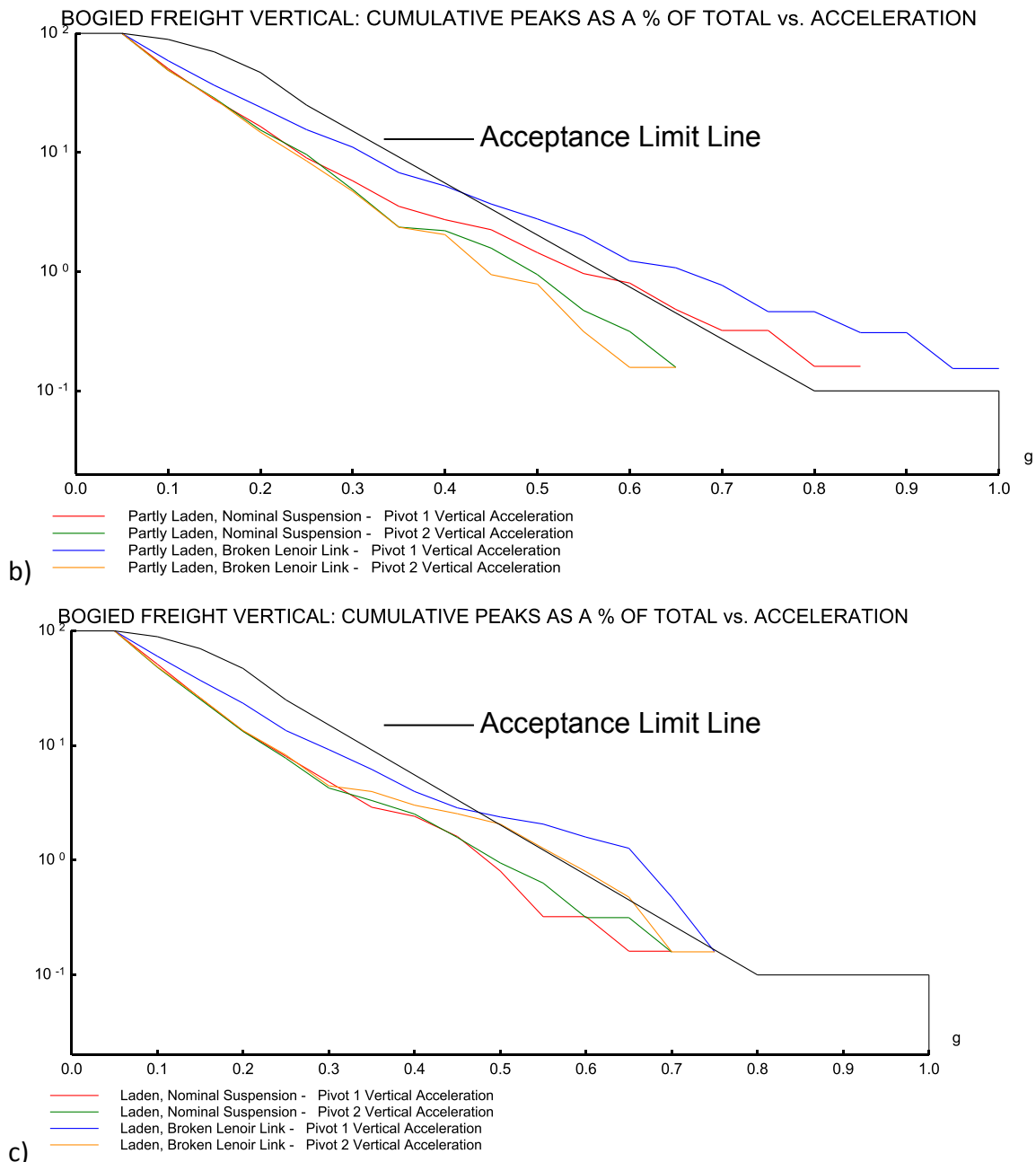


Figure 59 Vertical Ride Acceptance – a) Empty Containers, b) Partly Laden, c) Fully Laden on Track110 at 70mph.

Simulations carried out on the higher quality Track225 irregularity showed a similar trend. None of the loading conditions resulted in exceedance of the limit line but in all cases resulted in some deterioration of the ride performance but not enough to indicate that the vehicle was unstable.

As with the Track110 simulations, the partly laden case showed the largest change, this is shown in Figure 60.

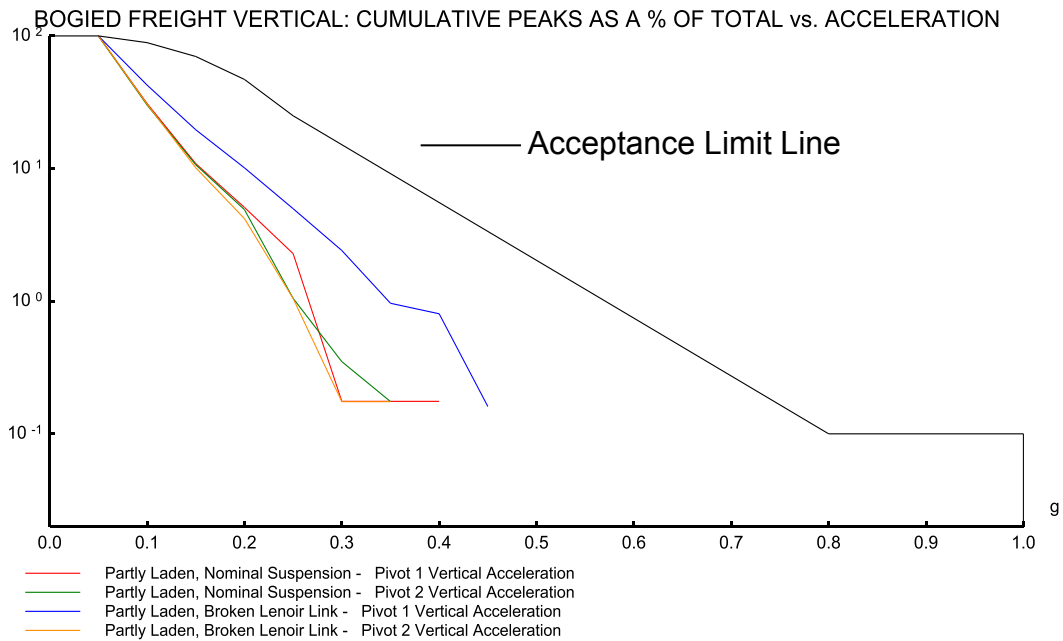
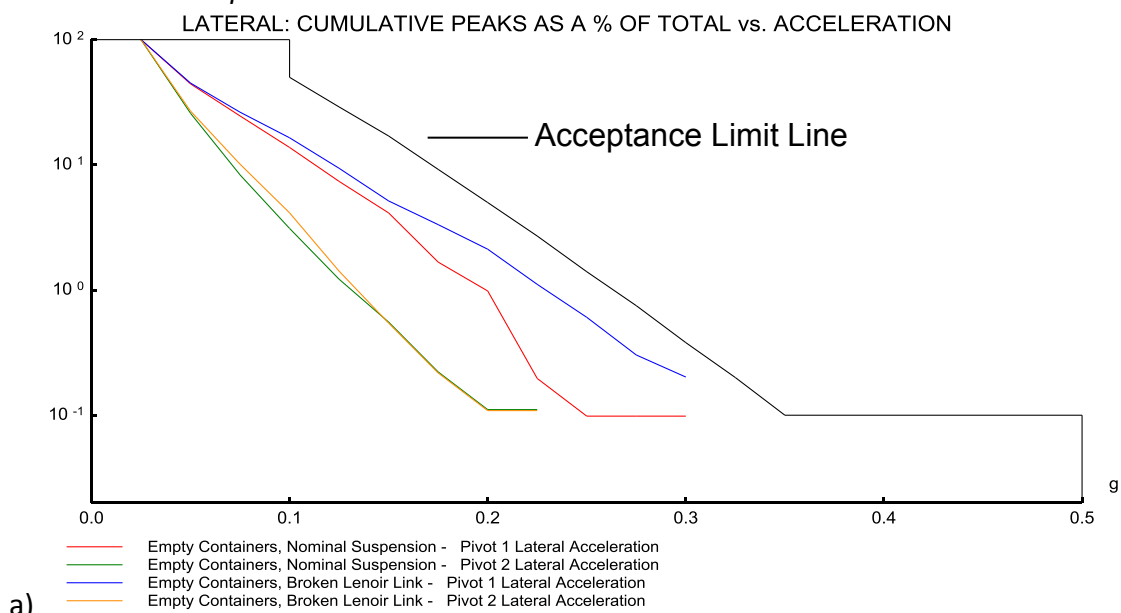


Figure 60 Vertical Ride Acceptance –Partly Laden on Track225 at 75mph.

In all three vehicle loading conditions plotted in Figure 61, the failure of the Lenoir link has a small effect on the vehicle lateral ride. The worst case is the Empty Containers loading condition but this does not lead to failure of the GB lateral ride acceptance standard for derailment.

The simulations carried out on the higher quality Track225 irregularity showed that the failed Lenoir link had a limited effect on the lateral ride quality, with none of the loading conditions resulting in exceedance of the limit line. The largest effect was in the partly laden case as shown in Figure 62.

Lateral Ride Acceptance



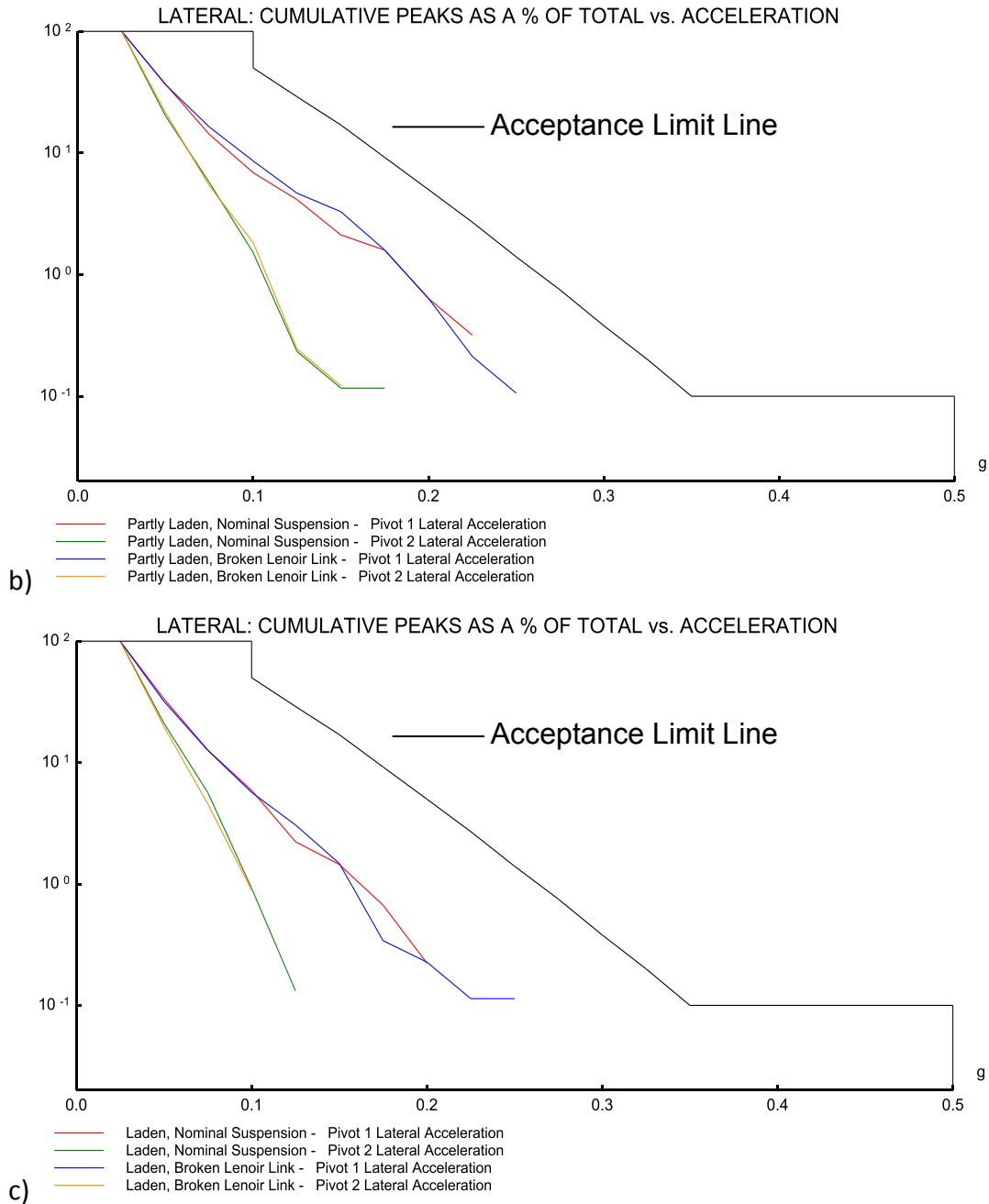


Figure 61 Lateral Ride Acceptance – a) Empty Containers, b) Partly Laden, c) Fully Laden on Track110 at 70mph.

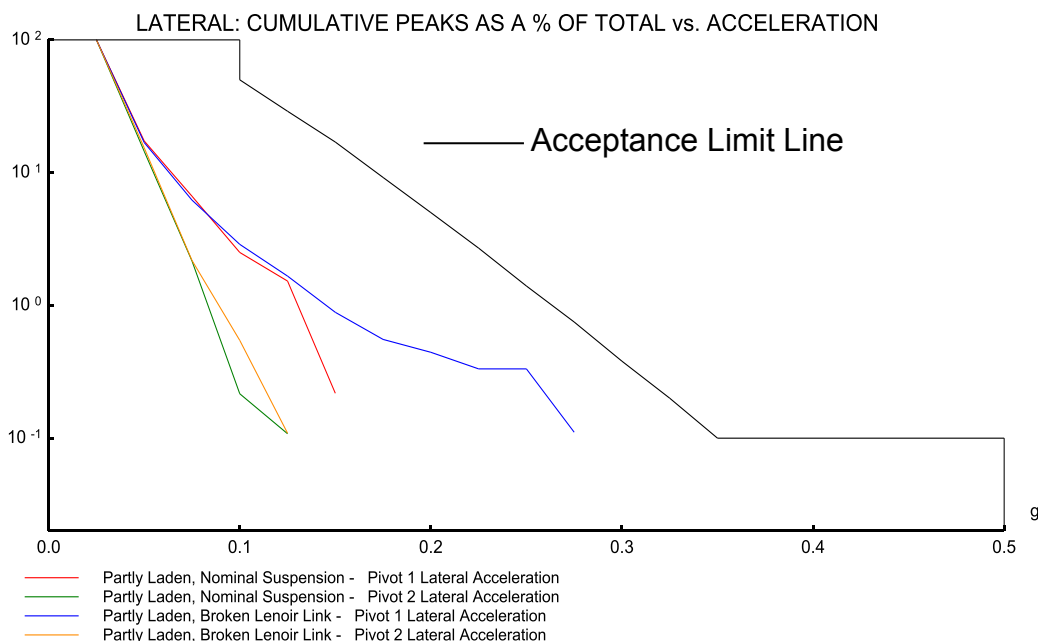


Figure 62 Lateral Ride Acceptance –Partly Laden on Track225 at 75mph.

3.2.3.1 Failed Primary Spring

Simulations using the vehicle models with a failed outboard primary spring were used to assess the impact of the suspension fault on the derailment risk of the vehicle.

The standard used for the assessment is GM/RT 2141 which covers a number of methods. A broken spring results in a change in static wheel loads as well as a change in primary vertical stiffness so the static wheel unloading ($\Delta Q/Q$) and the flange climb derailment Y/Q quotients have been assessed. A peak counting assessment has not been carried out for this suspension fault because although a broken spring will alter the Lenoir link preload and therefore the friction damping by a small amount it will not have anywhere near the same effect on the friction damping as a failed Lenoir link which has been assessed in Section 1.1.1.10.

GM/RT 2141 Assessment of low speed flange climb (Y/Q)

Low speed Y/Q analysis was carried out for the worst case curves defined in GM/RT 2141. The simulations were carried out for nominal vehicle models and a model with a failed primary spring. The worst case curve for each loading condition was found to be 150m radius with 150mm installed cant with a 20mm dip at the least favourable location. The location of the dip changes slightly for each loading condition. The results are shown in Table 10.

Table 10 Y/Q results for nominal and broken primary spring vehicle models

Load Condition	Y/Q		
	Nominal Suspension	Broken Primary Spring	Percentage Change
Empty Containers	1.32	1.36	+3.0%
Partly Laden	1.38	1.43	+3.6%
Laden	1.08	1.33	+23.1%

The largest increase in Y/Q is for the Laden vehicle. The change in Y/Q for the other load conditions is small. Looking at the raw Y and Q (Figure 63) values it was found that the large change in Y/Q in the laden case was mainly due to the Q forces being lower for broken spring case than the nominal case.

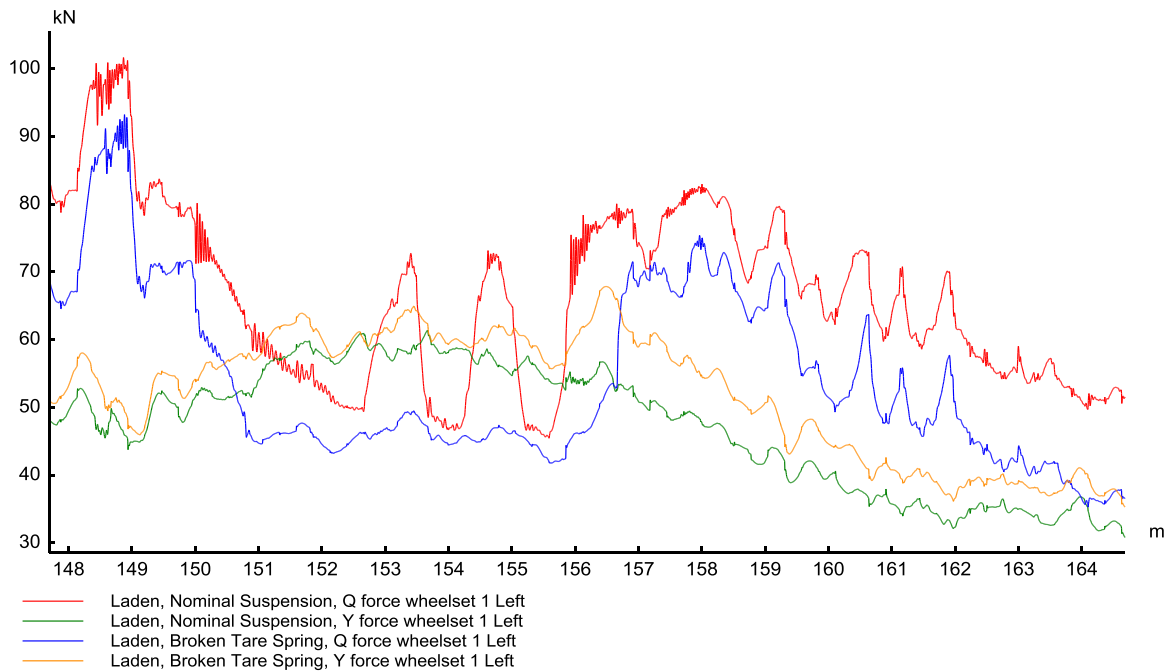


Figure 63 Y & Q forces for Nominal Suspension and Broken Primary Spring cases in Laden condition

GM/RT 2141 Assessment of quasi-static wheel unloading ($\Delta Q/Q$)

Static $\Delta Q/Q$ simulations were carried out to see how a broken tare spring affects the wheel offloading performance of the vehicle. The maximum $\Delta Q/Q$ values for nominal and failed suspension are shown below.

Table 11 $\Delta Q/Q$ results for nominal and broken primary spring vehicle models

Load Condition	$\Delta Q/Q$		
	Nominal Suspension	Broken Primary Spring	Percentage Change
Empty Containers	0.381	0.595	+56.2%
Partly Laden	0.460	0.549	+19.3%
Laden	0.291	0.423	+45.4%

In all cases the $\Delta Q/Q$ increases by an appreciable amount as a result of a failed primary tare spring which indicates an increased propensity for derailment. The GM/RT2141 limit of 0.6 is not exceeded for any of the cases. The increase in $\Delta Q/Q$ is due to the reduction in static wheel load, Q, caused by the broken spring.

3.2.3.2 Failed Side Bearer Unit

GM/RT 2141 Assessment of low speed flange climb (Y/Q)

Y/Q analysis was carried out for the worst case curves defined in GM/RT 2141. The simulations were done for nominal vehicle models and failed side bearer models. The worst case curve for each loading condition was found to be 150m radius with 150mm installed cant with a 20mm dip at the least favourable location. The location of the dip changes slightly for each loading condition. The results are shown in Table 12.

Table 12 Y/Q results for nominal and failed side bearer vehicle models

Load Condition	Y/Q		
	Nominal Suspension	Failed Side Bearer	Percentage Change
Empty Containers	1.32	1.43	+8.3%
Partly Laden	1.38	1.46	+5.8%
Laden	1.08	1.1	+1.9%

The largest change in Y/Q is for the tare vehicle. The change in Y/Q becomes less significant as vehicle loading increases. Looking at the raw Y and Q values it was found that the change in Y/Q was mainly due to the Q forces being lower for the failed side bearer case than the nominal case, this is because of the reduced static wheel load and the increase in torsional stiffness across the car body resulting from the failed side bearer. The Y force was also lower, most likely due to the reduced longitudinal friction reducing the torque between the carbody and the bogie.

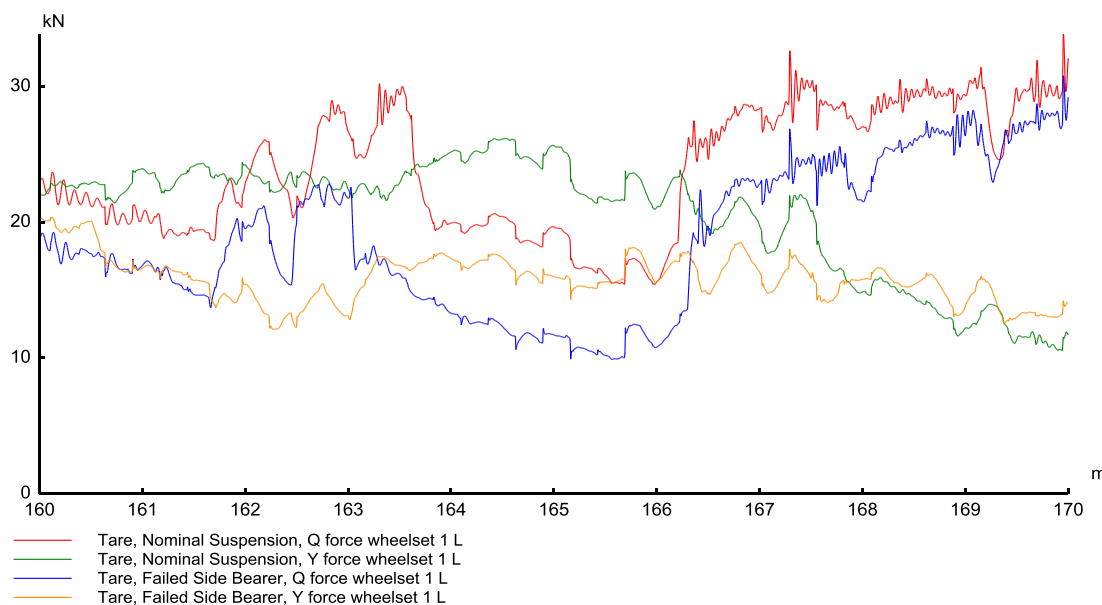


Figure 64 Y & Q forces for Nominal Suspension and Failed Side Bearer cases in Tare condition

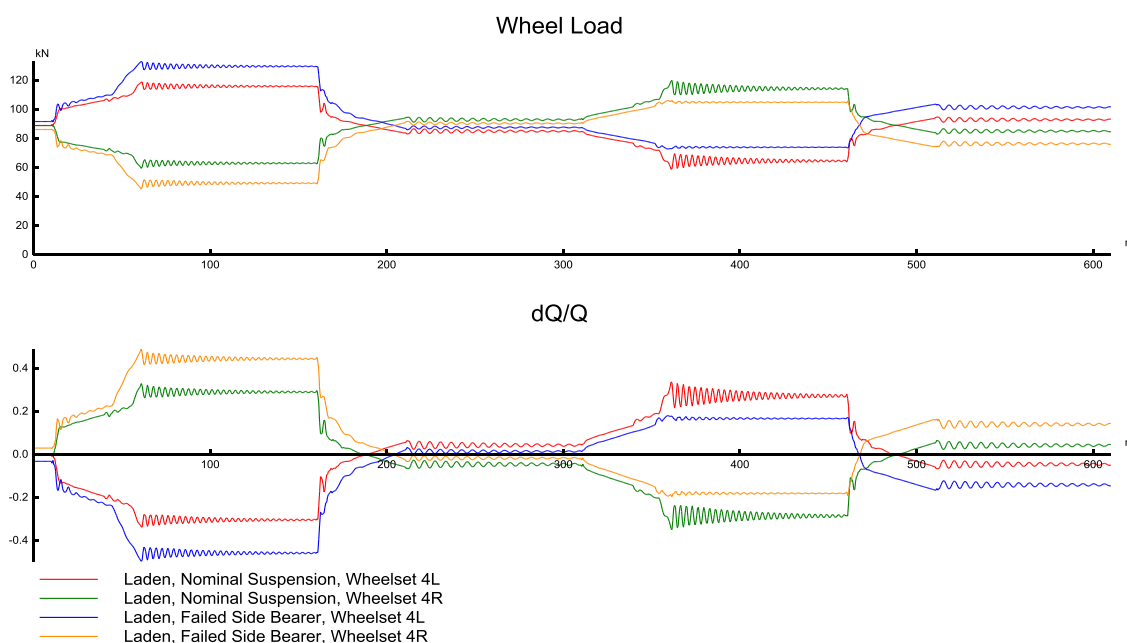
GM/RT 2141 Quasi-static assessment of wheel unloading ($\Delta Q/Q$)

Static $\Delta Q/Q$ simulations were carried out to investigate how a failed side bearer unit affects the wheel offloading performance of the vehicle. The maximum $\Delta Q/Q$ values for nominal and failed suspension are shown below.

Table 13 $\Delta Q/Q$ results for nominal and failed Lenoir link vehicle models

Load Condition	$\Delta Q/Q$		
	Nominal Suspension	Failed Side Bearer Unit	Percentage Change
Empty Containers	0.381	0.493	+29.4%
Partly Laden	0.460	0.505	+9.8%
Laden	0.291	0.446	+53.3%

In all cases the maximum $\Delta Q/Q$ increases as a result of a failed side bearer indicating an increased propensity for derailment, however, the GM/RT2141 limit of 0.6 is not exceeded. The increase in $\Delta Q/Q$ is partly due to the reduction in static wheel load, Q , caused by the failure of the side bearer but the largest contribution is from the increase in ΔQ when negotiating twisted track geometry. This increase in $\Delta Q/Q$ only occurs when the vehicle is twisted in one direction, in the other direction ΔQ is actually reduced, this is illustrated in Figure 65.

Figure 65 Q forces and $\Delta Q/Q$ for Nominal Suspension and Failed Side Bearer cases in Laden condition

The reason for the increase in ΔQ in the first track twist in Figure 65 is due to an effective increase in secondary roll stiffness on the bogie without a failed side bearer. This is because when a side bearer fails the other side bearer on that side of the vehicle has to take the static load which increases its static deflection. The increased static deflection means that the side bearer is closer to hardstop contact so that when negotiating a track twist hardstop contact occurs earlier and increases the torsional stiffness across the vehicle. When the vehicle is twisted in the other direction, the failed side bearer reduces the effective torsional stiffness and actually reduces $\Delta Q/Q$.

1.1.1.11 Bogie Frame Twist

Simulations using the vehicle models with a twisted bogie frame were used to assess the impact of the suspension fault on the derailment risk of the vehicle. In the absence of measured data, a twist of 10mm across corners (± 5 mm per axlebox) was assumed to be a worst case.

The standard used for the assessment is GM/RT 2141 which covers a number of methods. A twist across the bogie results in a change in static wheel loads so the static wheel unloading ($\Delta Q/Q$) and the flange climb derailment Y/Q quotients have been assessed. A peak counting assessment has not been carried out for this suspension fault as a twist in the bogie will have minimal effect on the primary stiffness characteristics or the friction damping.

GM/RT 2141 Assessment of low speed flange climb (Y/Q)

Low speed Y/Q analysis was carried out for the worst case curves defined in GM/RT 2141. The simulations were carried out for nominal vehicle models and a twisted bogie frame. The worst case curve for each loading condition was found to be 150m radius with 150mm installed cant with a 20mm dip at the least favourable location. The location of the dip changes slightly for each loading condition. The results are shown in Table 14.

Table 14 Y/Q results for nominal and twisted bogie frame vehicle models.

Load Condition	Y/Q		
	Nominal Suspension	Twisted Bogie	Percentage Change
Empty Containers	1.32	1.35	+2.3%
Partly Laden	1.38	1.32	-4.3%
Laden	1.08	1.32	+29.6%

The largest change in Y/Q is for the Laden vehicle. The change in Y/Q for the other load conditions is small with a slight improvement in the Partly Laden case. Looking at the raw Y and Q values it was found that the large change in Y/Q in the laden case was mainly due to the Q forces being lower for twisted frame case than the nominal case, this is mainly due to the reduced static wheel load resulting from the twisted frame.

In the Partly Laden case the small improvement is due to the non-linear primary vertical stiffness characteristic of this type of bogie, with the laden spring engaging after the tare spring has reached a certain vertical load resulting in a step change in stiffness. In the twisted frame case, the laden spring is initially offloaded and when negotiating twisted track offloads completely earlier than the Nominal case. This means only the tare spring is in use so the primary vertical stiffness is much softer and thus the ΔQ is reduced.

GM/RT 2141 Assessment of quasi-static wheel unloading ($\Delta Q/Q$)

Static $\Delta Q/Q$ simulations were carried out to see how a twist across the structure of the bogie affects the wheel offloading performance of the vehicle. The maximum $\Delta Q/Q$ values for nominal and failed suspension are shown below.

Table 15 $\Delta Q/Q$ results for nominal and failed Lenoir link vehicle models.

Load Condition	$\Delta Q/Q$		
	Nominal Suspension	Twisted Bogie	Percentage Change
Empty Containers	0.381	0.624	+63.8%
Partly Laden	0.460	0.618	+34.3%
Laden	0.291	0.455	+56.4%

In all cases the $\Delta Q/Q$ increased considerably as a result of a realistic twist in the bogie or incorrect primary spring packing, this indicates an increased risk of derailment. In the Empty Containers and Partly Laden cases the GM/RT2141 limit of 0.6 is exceeded which means that the vehicle does not comply with UK requirements. The increase in $\Delta Q/Q$ is due to the reduction in static wheel load, Q , caused by twist across the bogie frame. This is illustrated in Figure 66, it can be seen that the ΔQ remains largely unchanged, this is because the stiffness of the springs remains the same for the cases considered.

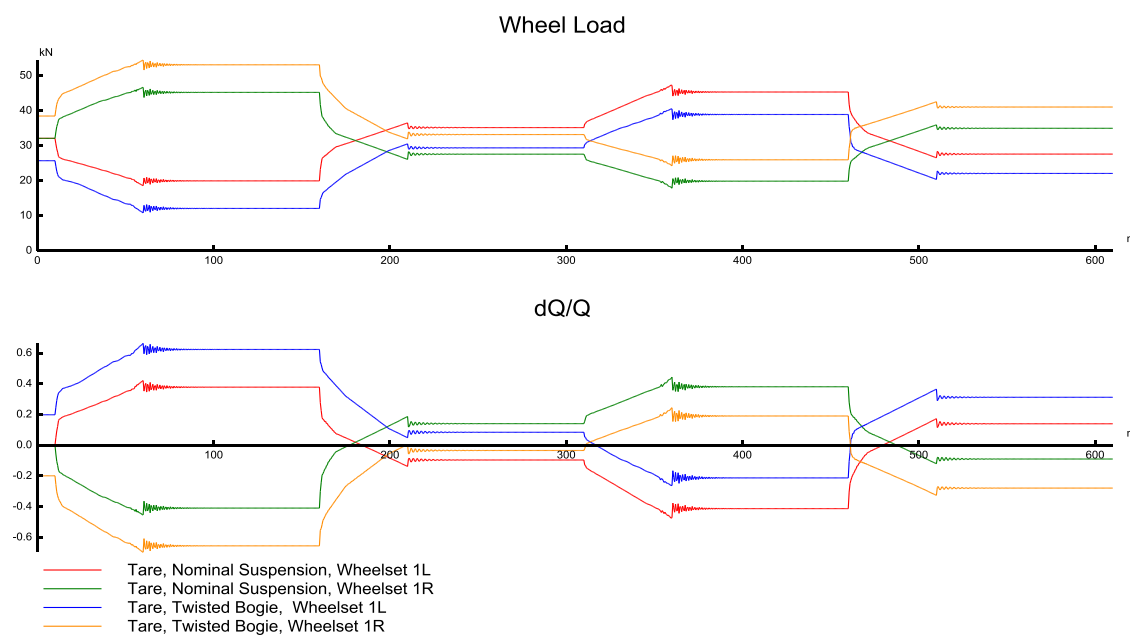


Figure 66 Q forces and $\Delta Q/Q$ for Nominal Suspension and Twisted Bogie cases in Tare condition.

3.2.3.3 The influence of suspension failures on axle imbalance

The suspension failures simulated in the previous sub-sections all increased derailment risk by increasing the axle lateral imbalance to a greater or lesser degree. The maximum axle imbalance for the suspension failure vehicles are shown in Table 16 below.

Table 16 Summary of lateral axle imbalance for suspension failure cases

Failure mode	Load condition	Mean axle load (kN)	Maximum axle imbalance
Lenoir Link	Laden	89.1	1.05

	Partly Laden	56.0	1.09
	Empty	32.1	1.08
Side bearer	Laden	89.1	1.07
	Partly Laden	56.0	1.11
	Empty	32.1	1.21
Tare Spring	Laden	89.1	1.24
	Partly Laden	56.0	1.29
	Empty	32.1	1.29
Bogie Twist	Laden	89.1	1.46
	Partly Laden	56.0	1.87
	Empty	32.1	1.52

It can be seen from Table 16 that a failed (broken) tare spring, or twisted bogie frame can produce axle imbalances in excess of the RIV limit of 1.25. In the case of bogie twist the exceedance can be large, with the partly laden vehicle resulting in an imbalance of 1.87. Clearly if these failure mechanisms were combined with other detrimental factors, such as skew loading, even higher axle imbalances could be achieved.

For all the failure modes, bar the failed Lenoir link, varying degrees of degradation are possible. In the cases of the failed tare spring and failed side bearer, the limiting case is represented here, and a weak spring (for example) might produce lower imbalances. For the bogie twist there is the possibility that even higher imbalances may be achieved with increased bogie twist (a 10 mm difference in corner height was modelled here).

3.2.4 Conclusions – Suspension Failure and faults

Several suspension failures and faults have been considered and their impact on vehicle derailment propensity assessed using suitable simulation methods from the GB standard GM/RT2141 such as wheel unloading on twisted track ($\Delta Q/Q$), low speed flange climb (Y/Q) and on-track ride Acceleration Peak Counting.

All of the suspension faults considered resulted in an imbalance of static wheel loads. This means that the vertical load on some wheels is reduced as the vehicle load is redistributed in response to a suspension failure. Any reduction in wheel load can increase the risk of derailment.

Suspension faults that increase the primary vertical stiffness also increase the derailment risk. This is because stiffer suspension increases the rate at which the wheel unloads on twisted track. This compounds the issue of static wheel load imbalance to further increase the derailment risk.

The effect of a broken Lenoir link was also considered. As well as a change in static wheel loads and a change in the primary vertical stiffness characteristic, a broken Lenoir link results in a loss of friction damping. The effect of this was assessed by looking at the ride quality for the vehicle and comparing it to limit lines defined in GM/RT 2141. It was shown that the loss

of a Lenoir link has an effect on the measured accelerations but the effect is not large. The accelerations were greater with a broken Lenoir link than the nominal case and exceed the limit line in some cases on rough track. Ride quality assessment on higher speed track showed that there were no stability issues as a result of a broken Lenoir link.

The fault with the largest effect on derailment propensity was a twisted bogie frame. Any twist in the bogie frame has a large effect on the vertical wheel loads with a lower load on one wheel posing a greater derailment risk. In the cases examined, a twisted frame resulted in up to 64% increase in $\Delta Q/Q$ and up to 30% increase in Y/Q . The results from the twisted frame analysis highlight the importance of maintaining the correct bogie geometry in manufacture, assembly and maintenance.

Analysis of the maximum axle imbalances for the suspension failure vehicle models showed that significant axle imbalances may result from suspension failures. The most significant failure modes were the failed tare spring and bogie twist, with the latter yielding axle load imbalances as high as 1.87. All of the failure modes could lead to axle imbalance beyond the RIV limit of 1.25 if combined with another detrimental factor of modest amplitude (such as skew loading).

3.3 Influence of isolated track defects on derailment

This section addresses the influence of track defects in longitudinal level and lateral alignment on the derailment risk.

As known from experience the vehicle response to geometric track defects strongly depends not only on the amplitude but also on the shape and especially the length of the defect. It is quite easy to understand that the exciting effect of a track defect with given amplitude to a passing vehicle will become more intensive the shorter the defect is. Nevertheless current track geometry standards like EN 13848 limit the defect amplitudes only whereas the defect length is taken into account very roughly by distinguishing between quite large wavelength bands for which the measured track geometry parameters are assessed. As it is very unlikely that the safety limits provided by the standards will be reached within a very short distance it is important to know which defect length is relevant for investigations regarding safety against derailment. Further the influence of isolated track defects according to the Immediate Action Limits of EN 13848-5 in lateral as well as in longitudinal direction in combination with skew loading conditions will be analysed in this chapter.

3.3.1 Study on existing track defect amplitudes in dependency on defect length

At first a study based on track geometry measurements of longitudinal level and lateral alignment was carried out to get an impression of the correlation between amplitude and length of geometric track defects. For this analysis track geometry data of about 560 km track length containing measuring results in the wavelength band 1 to 70 m was available. The measurements originate from track sections with a permitted line speed of $v \leq 120$ km/h.

In order to determine the maximum defect amplitude corresponding to a given length λ the following analysing method was applied, see Figure 67:

1. Span a virtual chord of length λ over a respective number of measuring points,
2. Calculate the distances d of each measuring point within this span perpendicular to the chord and determine the maximum d_{\max} ,
3. Move the chord forward by one measuring step and find the next maximum distance d_{\max} within the new span,
4. Repeat steps 1 to 3 until the end of the considered track is reached,
5. Calculate percentiles $p(\lambda)$ of the frequency distribution of d_{\max} ,
6. Change chord length λ and start procedure again.

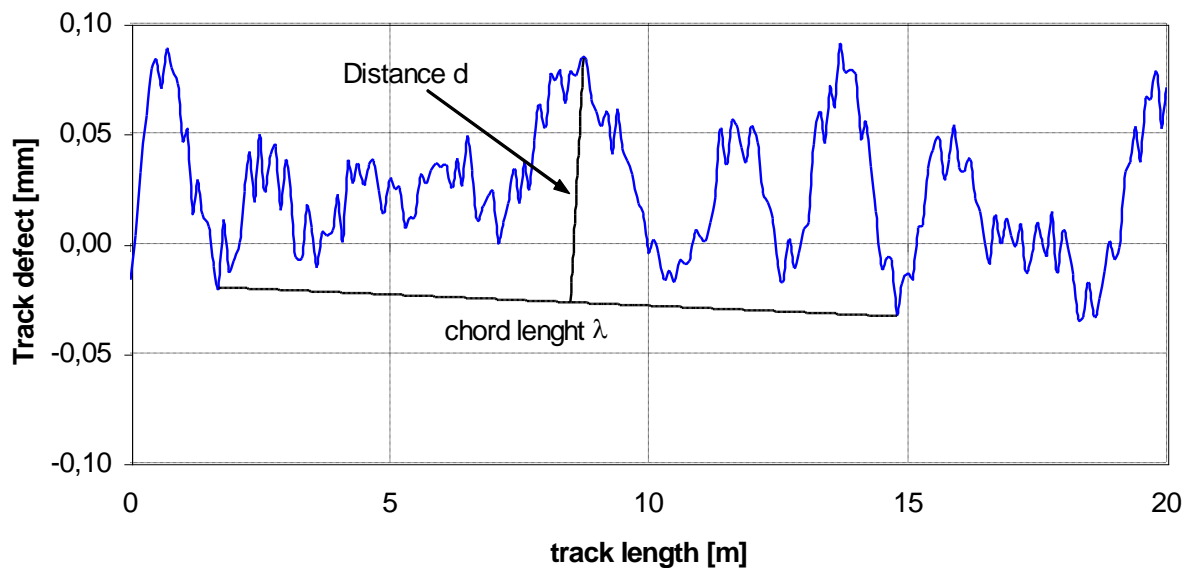


Figure 67 Determination of maximum track defect amplitude d_{\max} in dependence on the defect length λ .

In accordance to the wavelength band D1 defined in EN 13848-1 the chord length was varied within the range $3 \leq \lambda \leq 25$ m. In order to eliminate possible measuring errors the 99.85th percentiles of the defect amplitudes are used and plotted in relation to the defect length λ . The results of this analysis are presented in Figure 68 for vertical as well as lateral track defects (longitudinal level and alignment, respectively). As expected the defect amplitudes increase with defect length and the respective Immediate Action Limits (IAL) of EN 13848-5 are reached only for quite long defects of about 18 m length.

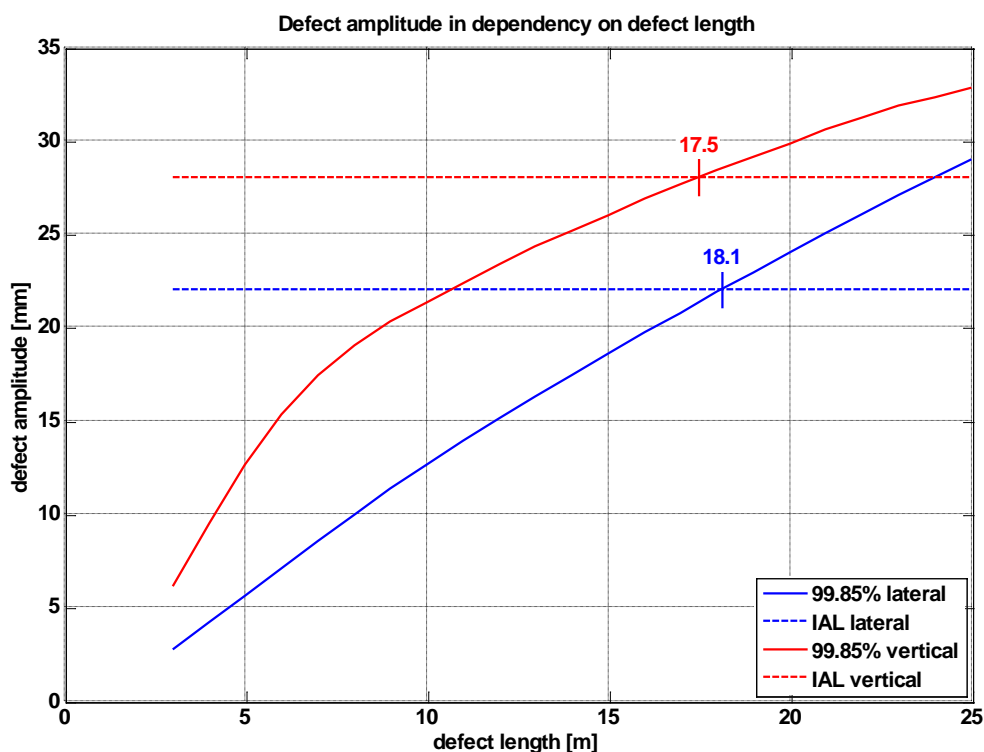


Figure 68 Track defect amplitude in dependence on the defect length.

The presented results seem to confirm the assumption that the IAL values are not relevant for very short defect length. However, the study is restricted to the available track data and the results should be verified based on a significant larger amount of measured track geometry data including track of very poor geometric quality.

3.3.2 Influence of IAL track defects and their length on the derailment risk

In order to investigate the influence of isolated track defects which are based on the IAL's according to EN 13848-5, vehicle dynamics simulations are carried out using the 4-axle wagon with Y25 bogies as specified in Appendix 0 and modelled in the commercial MBS code SIMPACK. The simulations consider runs in full curve sections of different curve radii and cant deficiencies. The selected parameter constellations as shown in Table 17 are studied for tare as well as skew loaded vehicle state. Regarding skew loading the worst situation with unloading of the leading wheel due to lateral and longitudinal load shift towards both the inner side and the trailing vehicle end is taken into account. In order to reach the skew loading limits according to the UIC RIV loading rules while respecting the maximum axle load of 22.5 t on all wheelsets the total car body mass is reduced to 54.5 t.

Table 17 Varied operational parameters.

Curve radius [m]	Speed [km/h]	Cant [mm]	Cant deficiency [m/s ²]
250	74.4	130	0.85
250	52.6	130	0.00

250	33.8	130	-0.50
500	109.2	150	0.85
500	79.9	150	0.00
500	56.0	150	-0.50
1000	105.0	0	0.85
1000	82.4	80	0.00
1000	79.2	150	-0.50

For all these simulation cases the length of an artificial sinusoidal track defect as illustrated in Figure 69 is varied. Even if probably not completely relevant for practical application, see Section 3.3.1, the range from 20 m down to 3 m defect length is investigated. The defect amplitude remains constant at IAL level of lateral alignment and longitudinal level, respectively, corresponding to the speed range $v \leq 80$ km/h. The defects are placed on the outer rail (single sided) separately in lateral and vertical direction as well as superposed with identical length at the same location. As usually existing in real track the vertical defects are always orientated downwards and the lateral defects towards the field side.

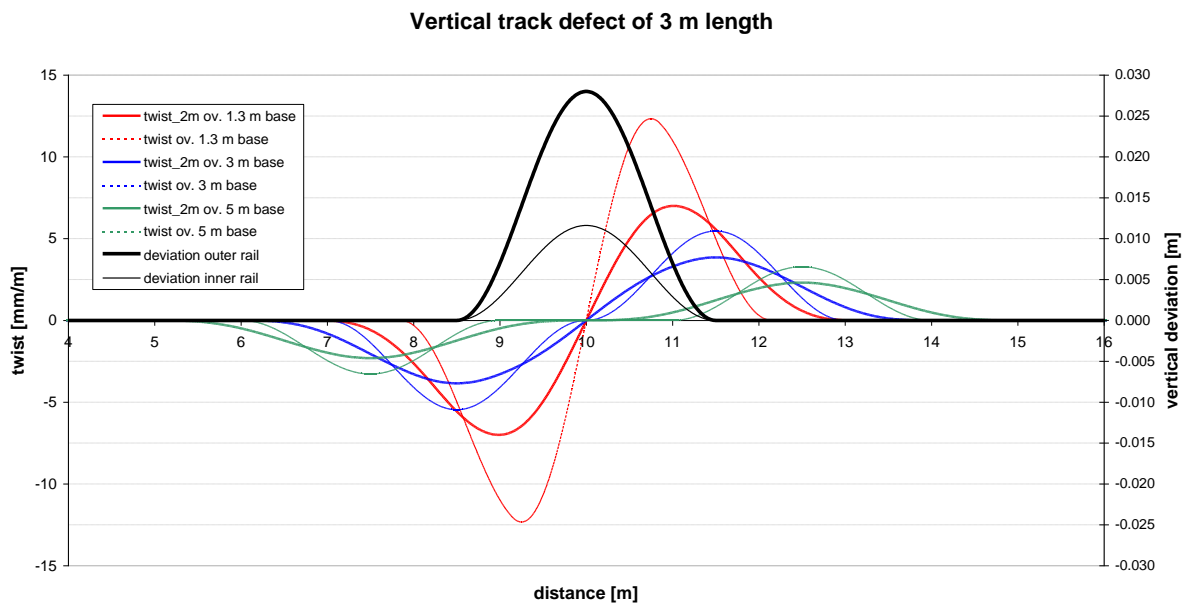


Figure 69 Example of vertical track defect and resulting twist (meeting the limit of 7 mm/m).

When defining artificial vertical track defects, attention has to be paid on the resulting track twist. In order to respect the EN twist limit curve A with a maximum of 7 mm/m (exceedance over up to 2 m), for defect lengths below 12 m it is necessary to add a downscaled vertical defect of the same length on the inner rail. The scaling factor for the inner rail defect is set such that the twist limit is met by the sliding mean over 2 m for a base length of 1.3 m. Figure 70 gives an overview of the resulting twist values for all the studied vertical track defects.

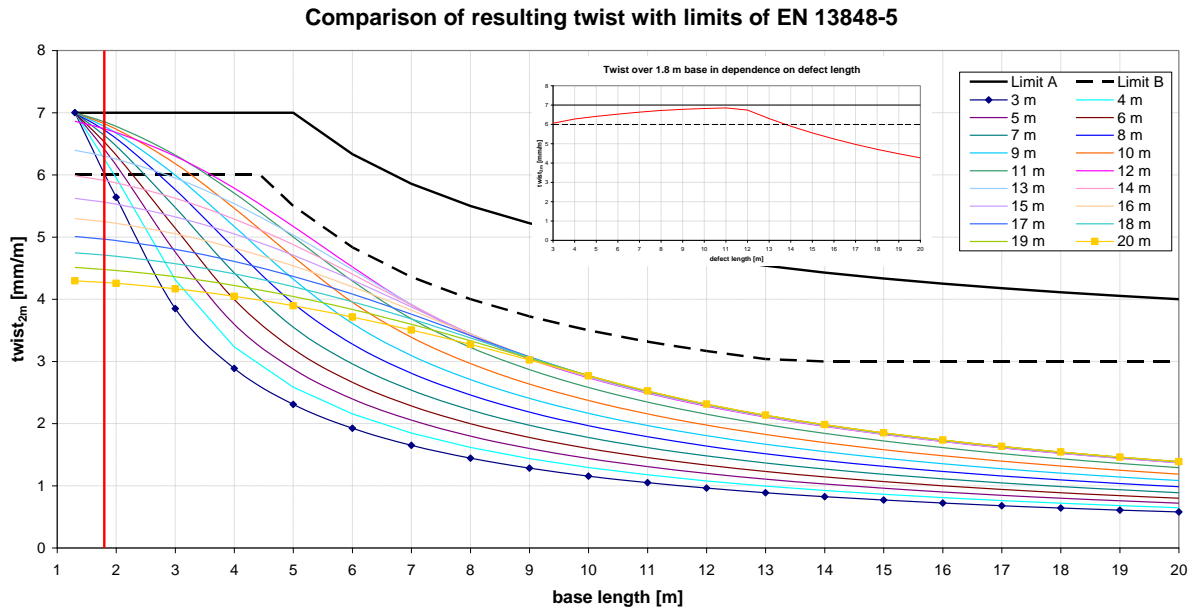


Figure 70 Track twist (sliding mean over 2 m) due to artificial vertical IAL track defects of length from 3 to 20 m.

For comparison the unfiltered track twist is shown in Figure 71. It can be observed that the limit curve A is respected by all defects down to a base length of 2.5 m. Many track measuring systems provide and assess track twist only at 3 m base length which is plausible as in practise the twist limit will not be exceeded for more than 2 m if the 3 m limit is met. Thus the defined artificial track defects can be considered marginally acceptable according to EN 13848-5.

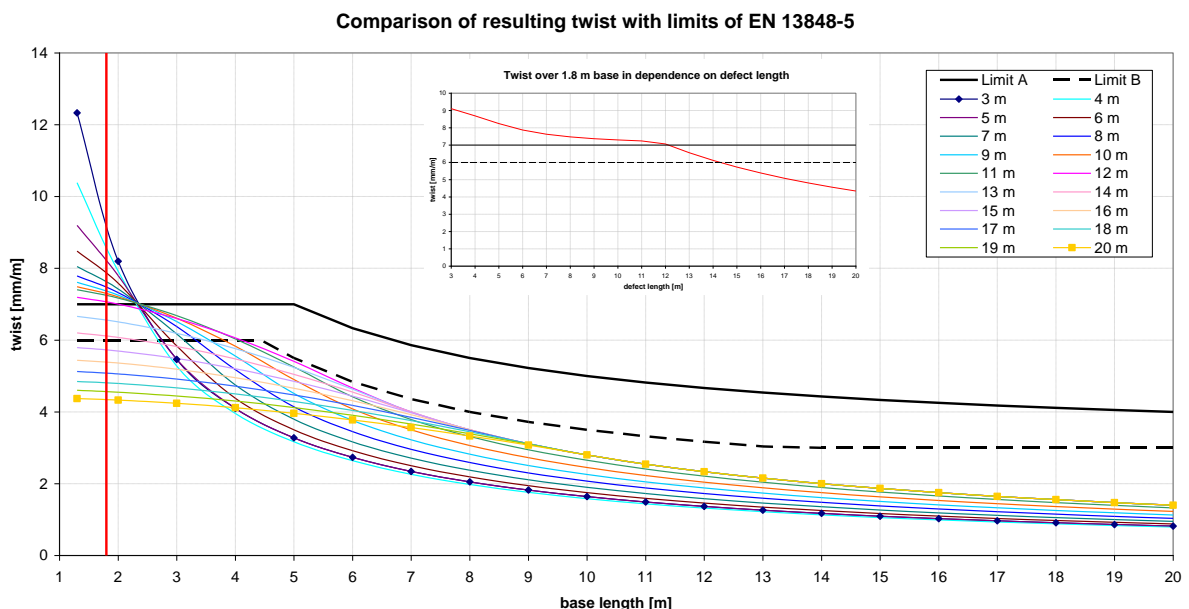


Figure 71 Track twist due to artificial vertical IAL track defects of length from 3 to 20 m.

In order to avoid unrealistic sticking of the friction elements in the vehicle suspension a slight vertical excitation is additionally applied to both rails as agreed for the benchmark described in chapter 2.2

The simulation results are evaluated in terms of derailment coefficient Y/Q and vertical wheel lift on the outer wheel of the leading wheelset. In accordance to EN 14363 [6] a low pass filtering with a cut-off at 20 Hz and a subsequent sliding mean calculation over 2 m are applied to the derailment coefficient Y/Q .

3.3.2.1 Empty wagon

In the following the simulation results for the empty vehicle are presented.

The maximum values of the Y/Q ratio obtained when passing a vertical track defect of 28 mm amplitude are shown in Figure 72. Obviously the main influencing parameter here is the curve radius with higher Y/Q for small radius curves. Regarding the defect length for long defects, as expected, the derailment risk increases with decreasing defect length, but for defects shorter than 12 m the decreasing averaged 2 m twist for the relevant bogie base of 1.8 m and the sliding averaging over 2 m of Y/Q lead to a reduction of the maximum Y/Q ratio. The derailment coefficient doesn't exceed 0.8 and no significant wheel climbing (wheel lift > 6 mm) occurs in any of the considered constellations with pure vertical excitation.

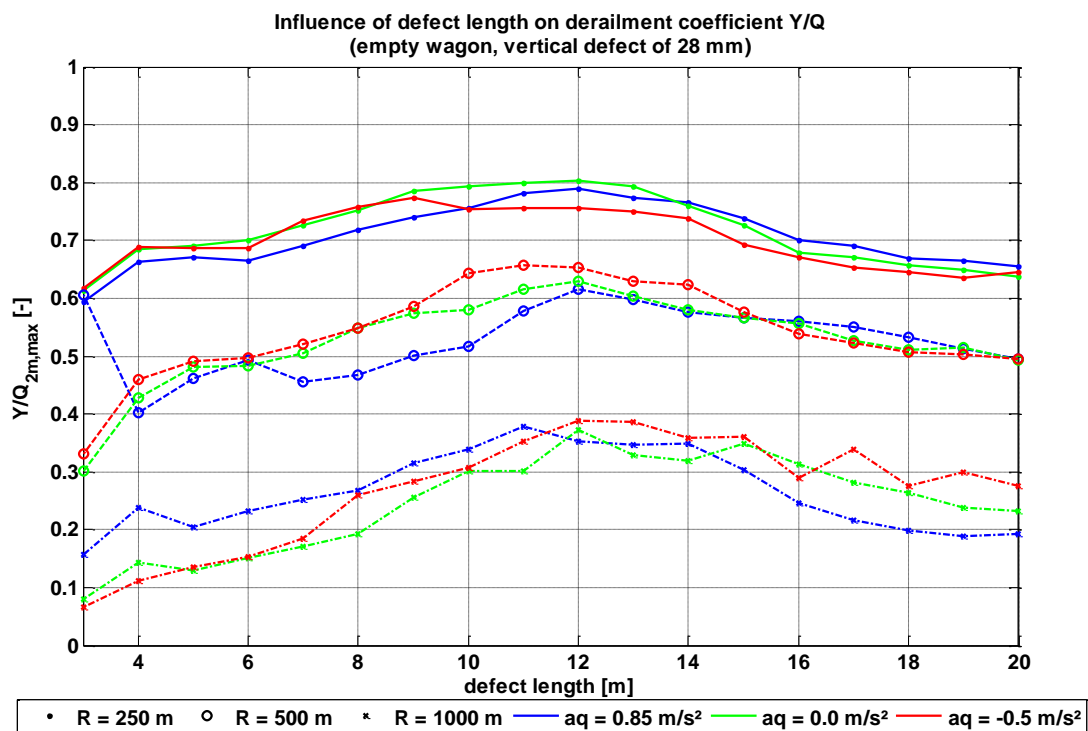


Figure 72 Maximum Y/Q in dependence on defect length and operational conditions (empty wagon with pure vertical excitation).

The results for the case with pure lateral excitation ($IAL = 22$ mm) are presented in Figure 73 and Figure 74. Also here the Y/Q values remain below 1.0, but for very short defects a wheel lift of more than 6 mm can occur in case of high cant deficiency in small radius curves. It is remarkable that just in these cases the derailment coefficient Y/Q is even lower than the dynamic limit of 0.8 according to EN 14363.

In case of combined vertical and lateral defects, see Figure 75 and Figure 76, the simulation results are quite similar to those with pure vertical excitation because the increase of lateral wheel force Y due to the rail movement towards the track centre when leaving the defect coincides with the increase of the vertical wheel force Q in the same instant. Hence the

derailment coefficient Y/Q remains moderate but contrary to the case with pure lateral excitation no significant wheel climbing can be observed here as the outer rail comes up when the leading wheel hits the gauge corner due to the lateral defect. Thus the wheel climbing is partly compensated by the vertical rail movement.

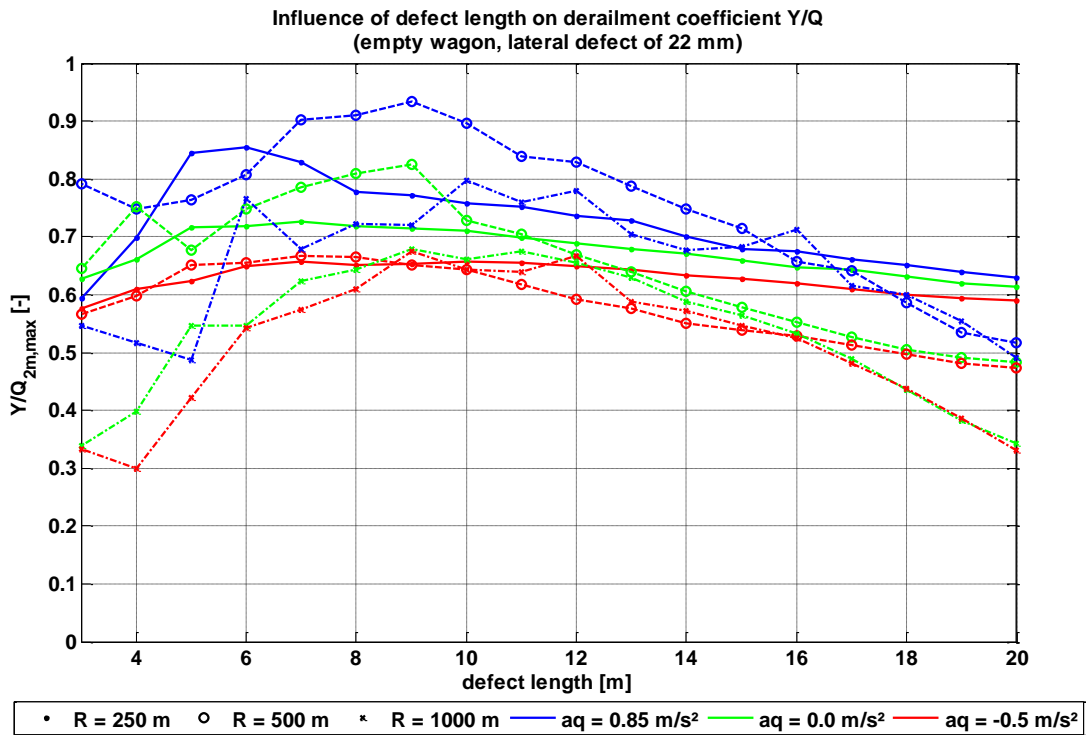


Figure 73 Maximum Y/Q in dependence on defect length and operational conditions (empty wagon with pure lateral excitation).

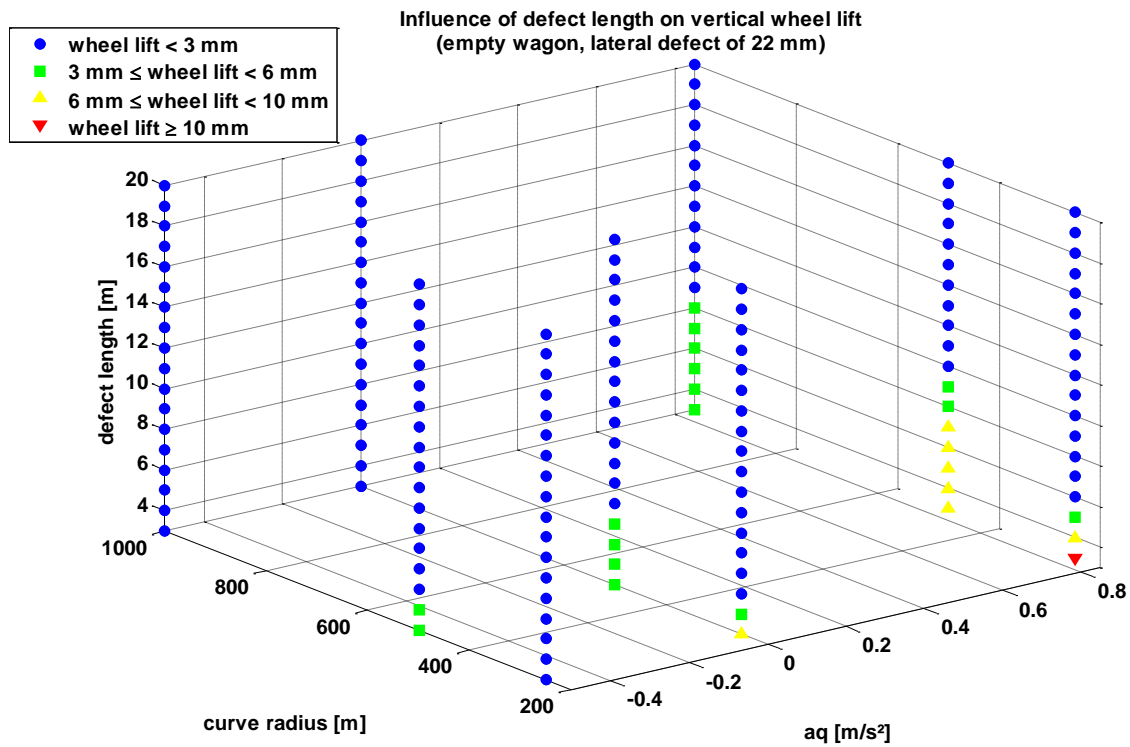


Figure 74 Maximum wheel lift in dependence on defect length and operational conditions (empty wagon with pure lateral excitation).

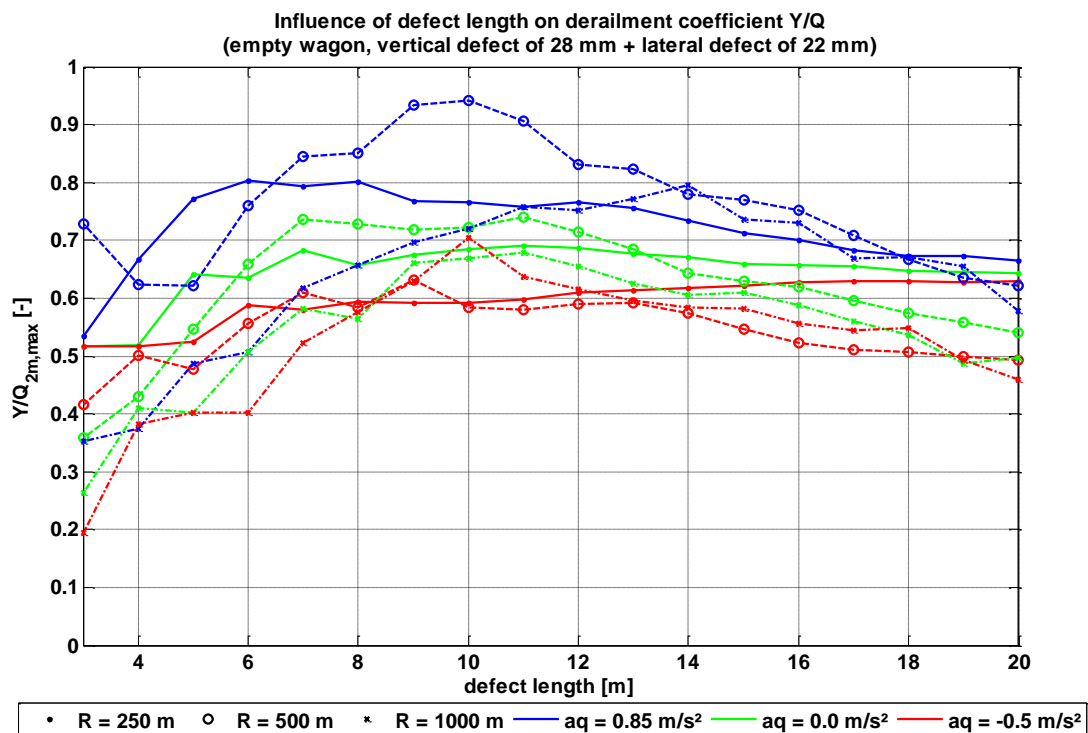


Figure 75 Maximum Y/Q in dependence on defect length and operational conditions (empty wagon with combined vertical and lateral excitation).

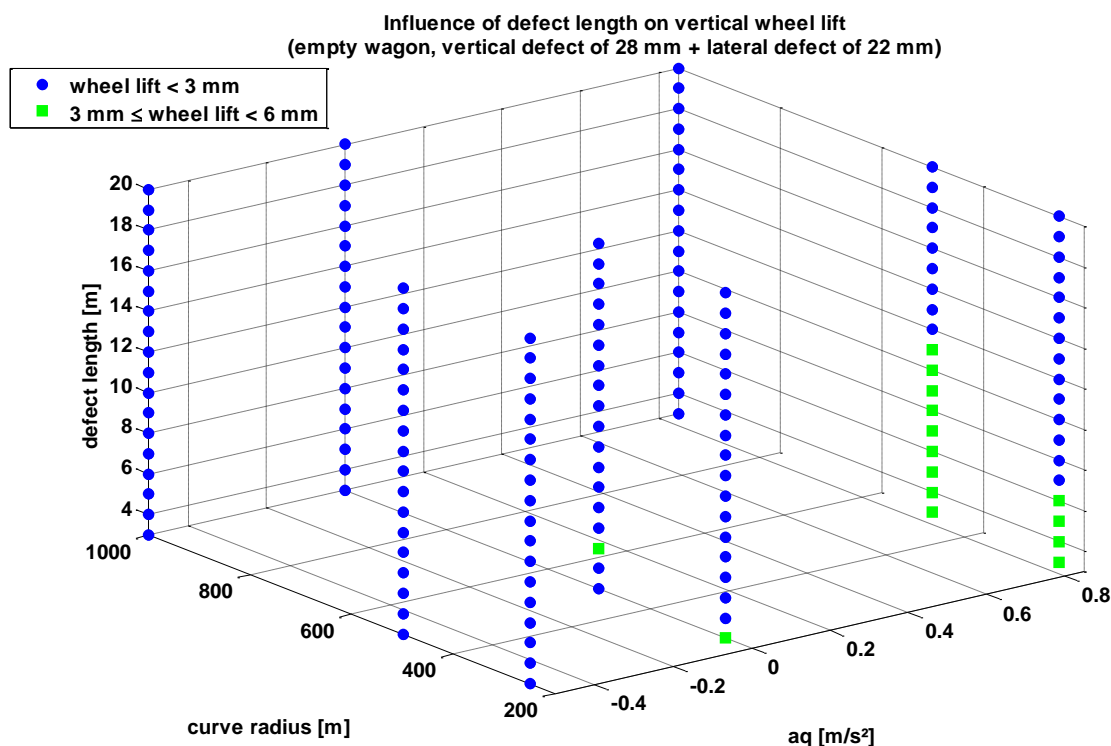


Figure 76 Maximum wheel lift in dependence on defect length and operational conditions (empty wagon with combined vertical and lateral excitation).

3.3.2.2 Skew loaded wagon

In case of skew loading at the borderline of the UIC RIV loading guidelines the behaviour in regard to derailment is significantly different compared to the empty vehicle. Here the main influencing parameter is the cant deficiency. As shown in Figure 77 for pure vertical excitation the most critical situation exists at cant excess ($a_q = -0.5 \text{ m/s}^2$) in combination with medium defect lengths of 11 to 13 m where Y/Q ratios of up to 1.7 are reached. According to Figure 70 exactly for these defect lengths the averaged 2 m twist at wheelset spacing (1.8 m base length) achieves its maximum. From Figure 78 it can be observed that in 250 m radius curves the leading outer wheel climbs up by more than 6 mm also for quite long vertical defects of up to 20 m length, whereas in many cases with higher Y/Q values of up to 1.7 but larger curve radii no critical wheel lift occurs. The reason is probably the smaller angle of attack in large radius curves.

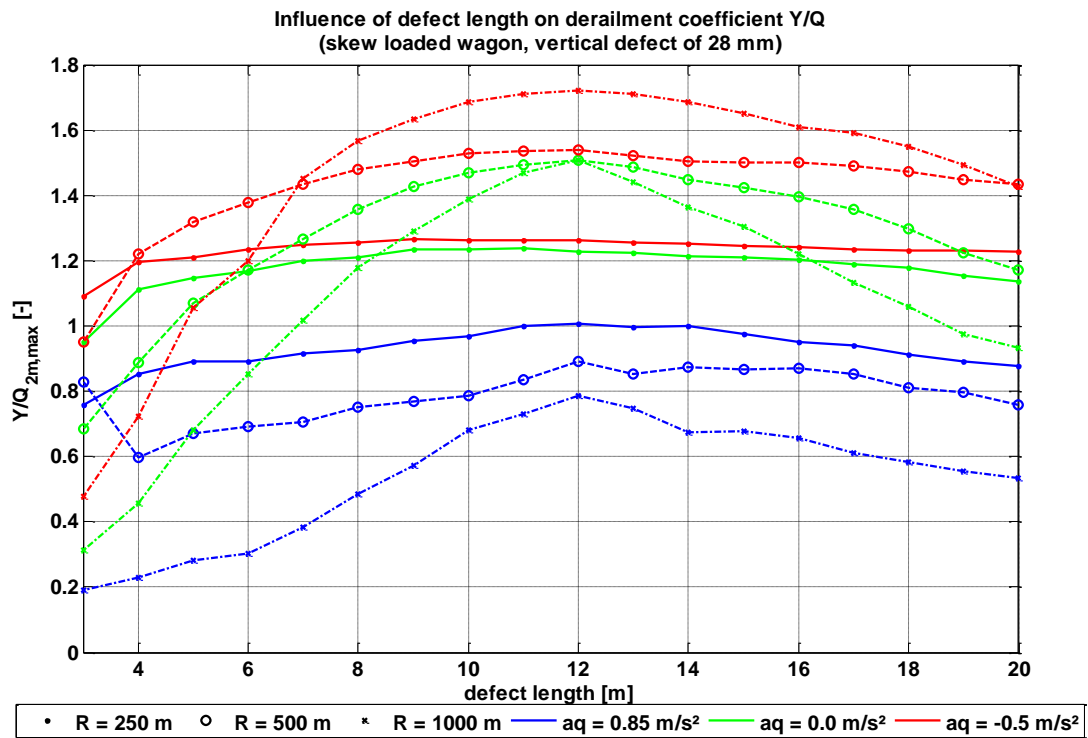


Figure 77 Maximum Y/Q in dependence on defect length and operational conditions (skew loaded wagon with pure vertical excitation).

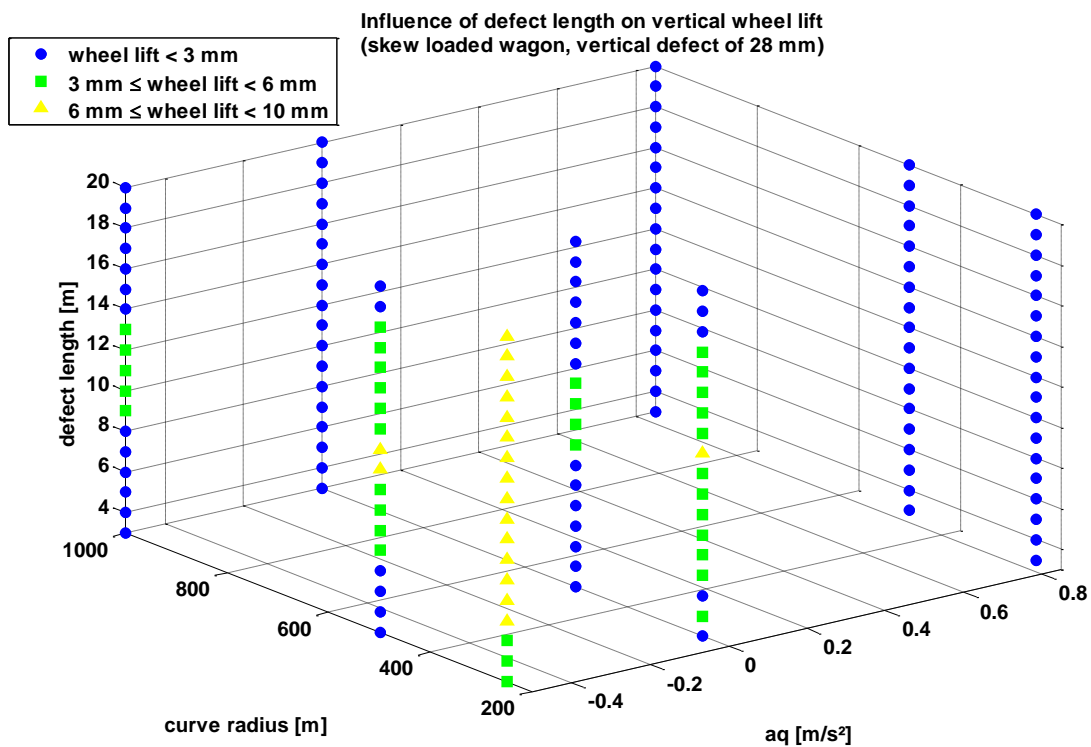


Figure 78 Maximum wheel lift in dependence on defect length and operational conditions (skew loaded wagon with pure vertical excitation).

The simulation results for pure lateral excitation are presented in Figure 79 and Figure 80. Compared to the cases with vertical excitation here the maximum values of derailment coefficient Y/Q are much smaller but for very short defects there are still cases with wheel lift of more than 6 mm.

As expected the worst situation exists if skew loading is combined with lateral and vertical track defects, see Figure 81 and Figure 82. Even if the Y/Q ratios are by far not as high as for pure vertical excitation there are a lot of simulation runs with large wheel lift, especially in case of cant excess where also for moderate curve radius and long defects 6 mm wheel lift is exceeded.

From the analysis of wheel load measurements presented in Section 3.1.3.3 it is known that a combination of lateral and longitudinal asymmetries both close to the UIC RIV borderline is very unlikely. Hence further simulations were carried out where the vehicle is only laterally skew loaded with a lateral load ratio of 1 : 1.25. The results are shown in Figure 83 and Figure 84. As expected the derailment coefficient as well as the wheel lift are considerably reduced. Critical wheel lift of more than 6 mm occurs only for defect lengths below 7 m which are supposed to be practically not relevant, see chapter 3.3.1.

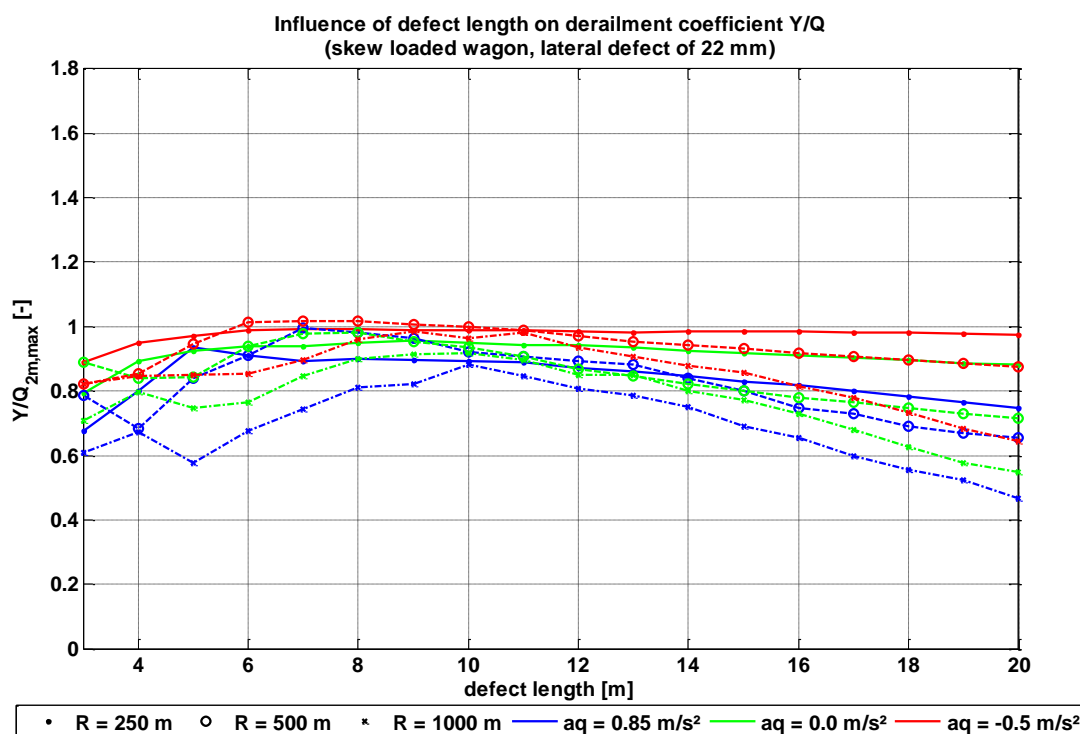


Figure 79 Maximum Y/Q in dependence on defect length and operational conditions (skew loaded wagon with pure lateral excitation).

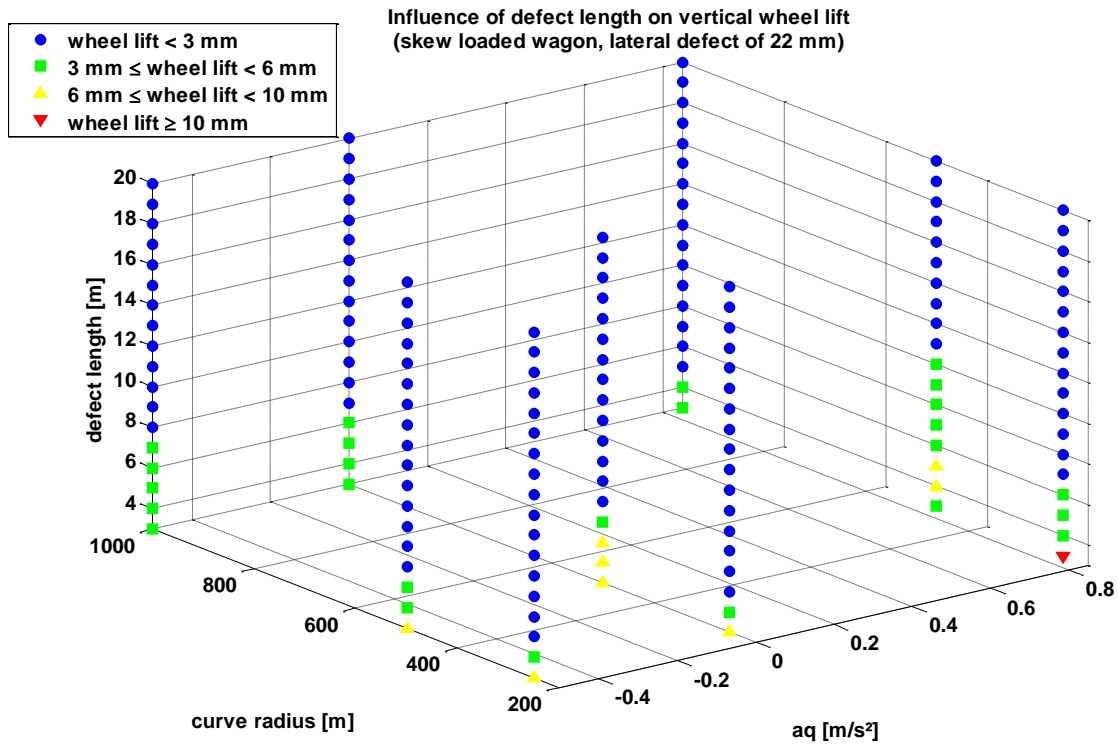


Figure 80 Maximum wheel lift in dependence on defect length and operational conditions (skew loaded wagon with pure lateral excitation).

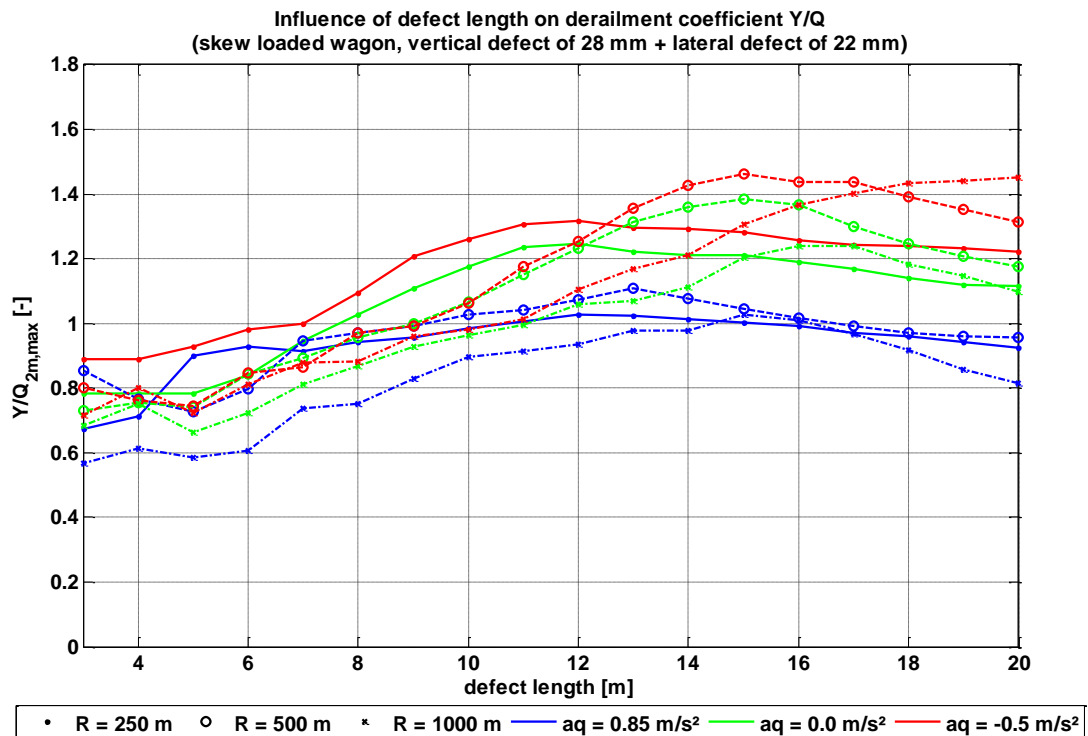


Figure 81 Maximum Y/Q in dependence on defect length and operational conditions (skew loaded wagon with combined vertical and lateral excitation).

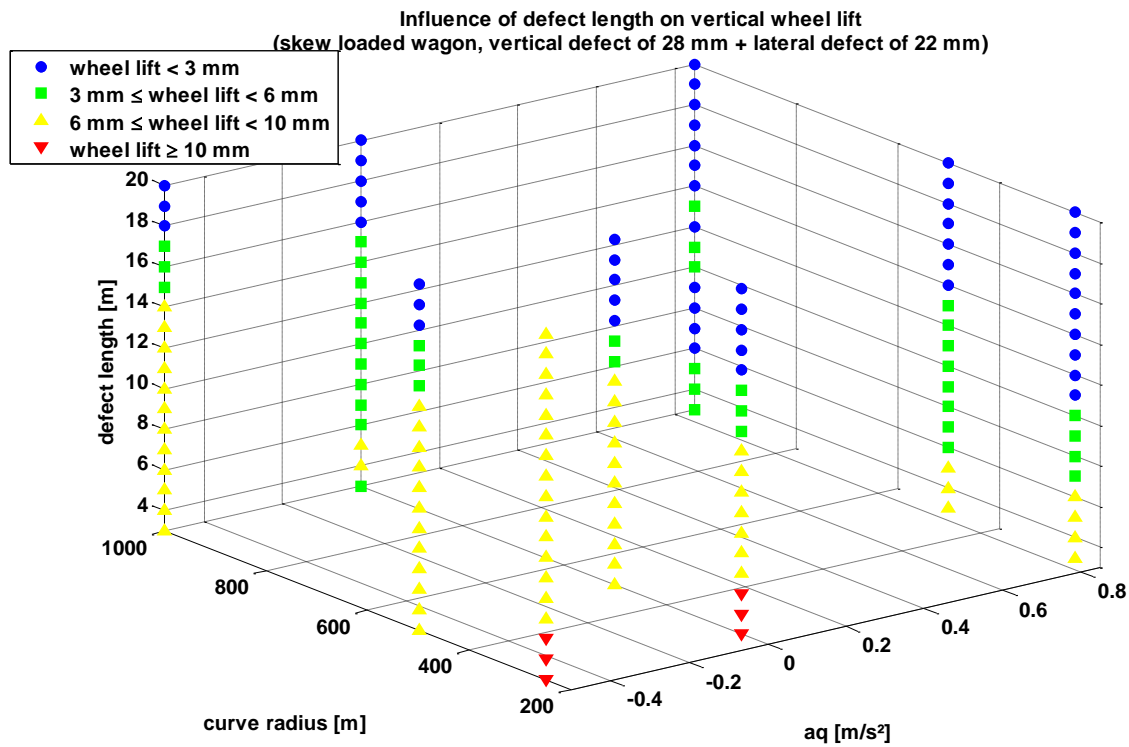


Figure 82 Maximum wheel lift in dependency on defect length and operational conditions (skew loaded wagon with combined vertical and lateral excitation).

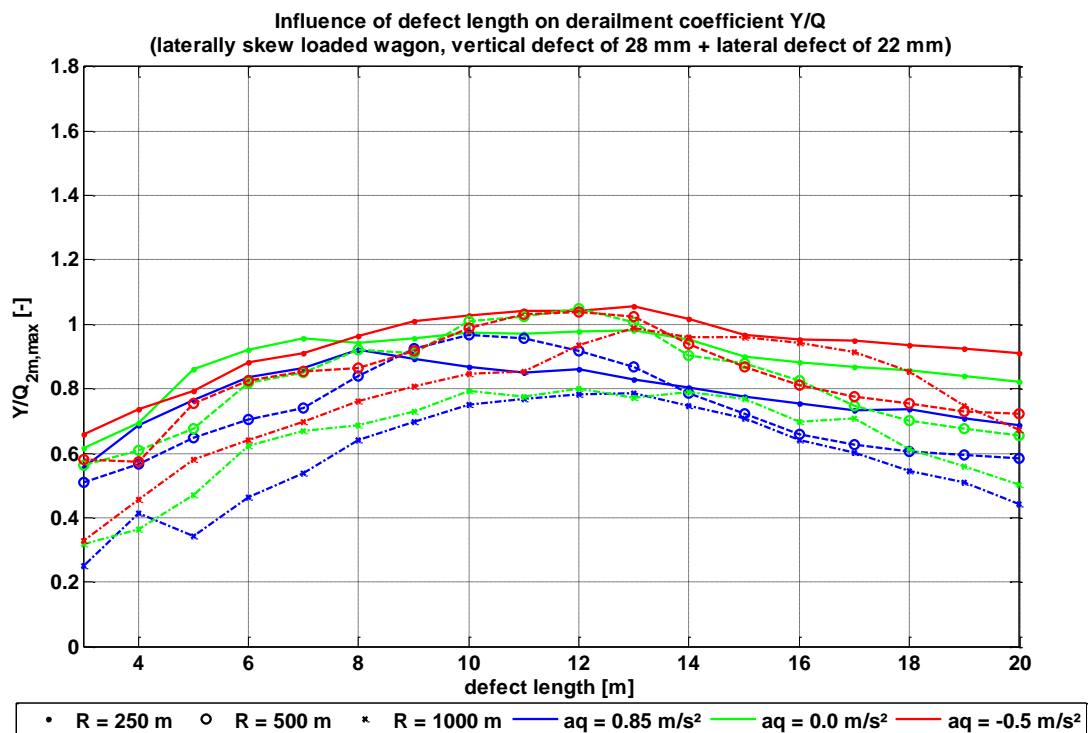


Figure 83 Maximum Y/Q in dependency on defect length and operational conditions (laterally skew loaded wagon with combined vertical and lateral excitation).

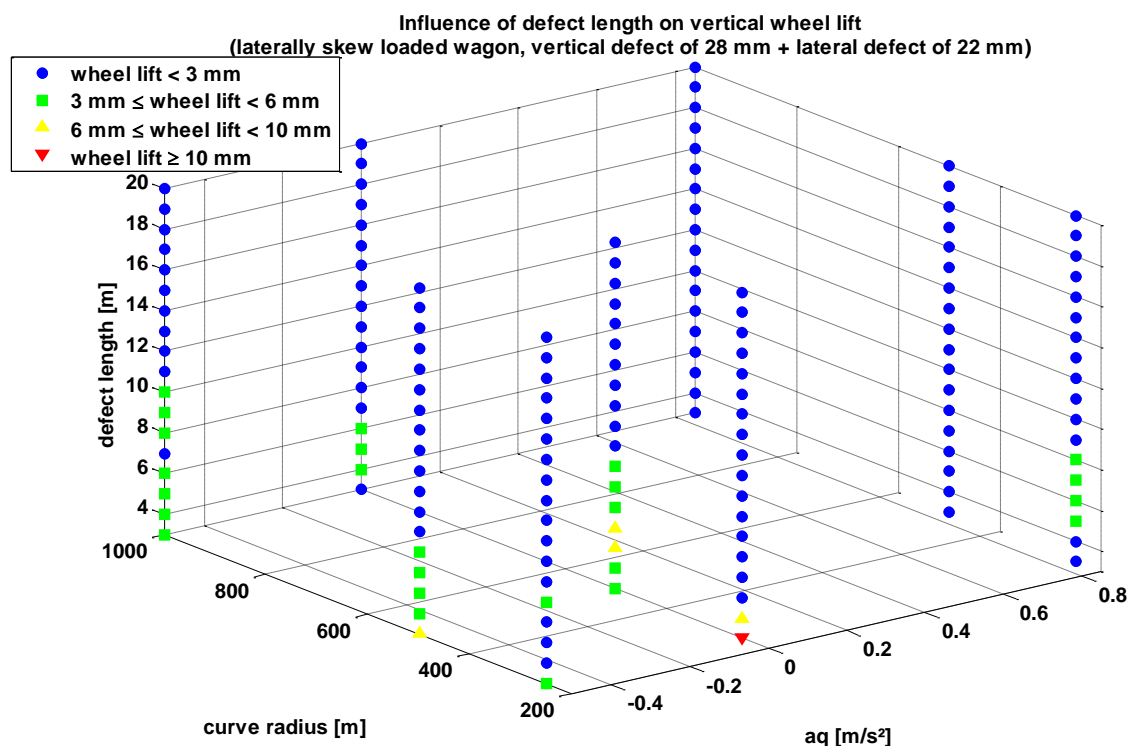


Figure 84 Maximum wheel lift in dependency on defect length and operational conditions (laterally skew loaded wagon with combined vertical and lateral excitation).

3.3.3 Conclusions – Isolated track defects

In the previous section the influence of isolated track defects in longitudinal level and lateral alignment in combination with tare and skew loaded vehicle state on the derailment risk is analysed where particular attention is paid to defect length and superposition of track parameters at the borderline of acceptable track geometry according to EN 13848.

The results of the preceding study on existing track defect amplitudes in dependence on the defect length confirm that it is very unlikely to reach the current Immediate Action Limits (IAL) as defined in EN 13848-5 at very short defect length. Based on the available track measuring data the relevant defect length was identified with about 18 m both for longitudinal and lateral track defects. However, the study is restricted to the available amount of measuring data and the results should be verified based on a significant larger sample including track of very poor geometric quality.

The MBS simulation results with artificial IAL track defects under varying operational conditions show significantly different behaviour of empty and skew loaded wagons. In tare state the most influencing parameter is the curve radius with the worst case at high cant deficiency in very small radius curves. Considerable wheel lift is observed only for pure lateral track defects of lengths below 8 m, which are supposed to be not relevant in railway practise. In case of skew loading with maximum permitted vertical unloading of the leading outer wheel the vertical track defects become more critical and the most important operational parameter regarding derailment is the cant deficiency. Here the worst case is a combination of cant excess and very small curve radius. Under these conditions also very long vertical defects of 20 m may lead to critical wheel lift of more than 6 mm even if there is no lateral track defect superposed. Hence, even if expected to be very unlikely, there exists a

theoretical derailment risk although the vehicle meets the UIC RIV loading guidelines and the track geometry complies with EN 13848-5.

Additional simulations with pure lateral skew loading – which is considered more critical than longitudinal load shift - and combined vertical and lateral track defects show considerably relaxed results with significant wheel lift only for defects shorter than 7 m.

Consequently it can be concluded that the IAL values of longitudinal level and lateral alignment in speed range $v \leq 80$ km/h according to EN 13848-5 are acceptable for 4-axle wagons provided that the defect length is not shorter than 8 m and the requirements of the UIC RIV loading guidelines are met. Thus, when assessing isolated track defects attention should be paid not only on their amplitude but also on the defect length. In addition, the railway freight operators have to ensure that the requirements regarding skew loading according to UIC RIV loading guidelines are respected whereby combinations of extensive lateral and longitudinal load asymmetry should be avoided. This can be checked by wayside wheel load measuring systems, for instance.

According to EN 13848-5 it is permitted to exceed the provided limit curves for track twist within a track length of up to 2 m. Thus for short wheelset bases as relevant for freight wagons considerably higher twist than that of the artificial track defects used in the previous investigation is accepted. Therefore, based on the obtained simulation results it is questionable if the requirements of EN 13848-5 concerning twist are appropriate.

Finally, further revisions of standards for vehicle acceptance should take into consideration that especially in loaded conditions with high centre of gravity cant excess can become more critical than high cant deficiency on which current evaluation procedures are mainly focussing.

3.4 Concluding remarks

3.4.1 Identified main affecting parameters

Limits to load imbalance

From the skew loading investigations based on simulation and measurement data, it is apparent that the UIC RIV limit for lateral load imbalance of 1:1.25 is appropriate, when applied to the overall imbalance of the vehicle. The skew loading cases simulated with lateral load imbalance in excess of this limit were likely to exceed the established $\Delta Q/Q$ and Y/Q limits imposed in EN 14363, especially when coupled with longitudinal load imbalance.

From the investigations regarding bogie yaw resistance it was also apparent that the UIC RIV load imbalance of 1:1.25 is appropriate. Skew loading cases with lateral load imbalance beyond this limit were found to generate bogie X-factors in excess of the 0.1 limit. The effect of the increase in yaw resistance was found to worsen when the lateral load imbalance was sufficient to bring one of the side bearer bumpstops in to contact.

Initial simulations suggest that a reduction in X-factor of up to 20% might be achieved by increasing the sidebearer vertical travel in these circumstances. The practical feasibility of this along with evaluation of the possible benefits require further investigation.

Comparison of the results from the EN 14363 and GM/RT 2141 low speed flange climb simulations suggest that either the assessment criteria stipulated in GM/RT 2141 are too severe, or that the EN 14363 criteria are too lenient. In contrast the other derailment limits used in the analysis ($\Delta Q/Q$, X-factor, RIV skew loading limits and EN 14363 Y/Q) seem well aligned to each other. It would therefore appear that a review of the low speed flange climb assessments used in the EN and GM/RT2141 would be a valuable exercise.

From investigating the influence of the maximum lateral axle imbalance on the skew laden vehicles it is apparent that the RIV limit of 1.25 provides a margin of safety in respect to the limits set for wheel unloading ($\Delta Q/Q$) and low speed flange climb (EN 14363 Y/Q and wheel lift). Analyses using the GMRT 2141 Y/Q test suit suggest that operating outside of the RIV limit of 1.25 increases the propensity for derailment. It must be recognised that the derailment assessments, measures and limits allow a margin of safety themselves, to account for unforeseen combinations of detrimental factors (although this is less the case for GM/RT 2141 Y/Q assessment which aims to combine a number of detrimental factors at once). Therefore it should not be expected that a vehicle slightly over the limiting value of Y/Q ratio (for example) will derail at the first opportunity. A number of other factors must also be present at the same time, the precise combination of which the vehicle may never see. Hence it may be observed that the vehicle is running safely, while it undoubtedly has a higher derailment risk than a vehicle within the limits.

For lateral axle imbalances outside the RIV limit, longitudinal vehicle imbalances greater than approximately 1.6 to 1.8 caused a significant increase in maximum axle imbalance. This suggests that the derailment risk could be reduced by applying a limit to the combined lateral and longitudinal imbalance.

The dynamic simulations with varying isolated track defects showed that a worst case scenario with combined lateral and longitudinal skew loading in very small radius curves may lead to critical wheel climbing even if the vehicle meets the UIC RIV loading guidelines and the track geometry complies with EN 13848-5. Consequently a combination of extensive lateral and longitudinal load imbalance should be avoided.

GB Gotcha data with respect to skew loading

The skew loading analysis of measured wheel loads from GB Gotcha data showed that nearly all bogied freight traffic (99.7%) were operating within the UIC RIV limits for loading imbalance, measured at vehicle level.

This suggests that load imbalance is generally well defined and as such could be more comprehensively included in Standards and formalised in the vehicle acceptance processes. Further analysis of a broader data set of measured wheel loads would help ensure that any limits would be relevant to current freight operations. The purpose of such limits would be to help minimise derailments caused by a minority of excessively skew laden vehicles.

A correlation was observed between high dynamic ratios (indicative of wheel defects) and high axle lateral imbalance and high vehicle skew loading. This appears to be due to the dynamic component of the measured force signal influencing the returned average wheel load. The reason for this cross-influence is not clear and requires further investigation.

A hypothetical alarm scenario was assessed based on axle lateral imbalance exceeding 1.70. It was found that between 0.24% and 0.94% (depending upon the distribution of offending axles across vehicles and consists) of freight trains would have been affected by an

immediate action alarm, when vehicles with dynamic ratios greater than 0.75 were omitted. The hypothetical scenario was repeated without omitting vehicles based on high dynamic ratios. In this case between 4.4% and 17% of freight trains would have been affected.

The integrity of the measurement data used to trigger an alarm is therefore paramount.

Bogie suspension variation

It was found that the transitional behaviour of the primary suspension system for part-laden vehicles is important and should be optimised at the vehicle design stage to maximise not only ride and gauging performance but also derailment resistance.

Consideration could be given to 3-stage stiffness transition in the primary suspension or adoption of rubber components to improve the derailment resistance for part-laden/inter-modal traffic.

It was found that in general, the bogie rotational resistance (X-factor) is not a critical derailment control measure for the friction type arrangements studied. However, the behaviour of the centrebowl arrangement can significantly influence the part-laden and laden X-factor values. This can lead to approximately a 10-20% increase in Y/Q values within the curves studied and exceedance of the 1.2 limit value. Therefore good maintenance practice in this area is recommended.

Suspension failure and faults

Several suspension failures and faults have been considered and their impact on vehicle derailment propensity assessed using simulation methods extracted from the GB standard GM/RT2141, such as, wheel unloading on twisted track ($\Delta Q/Q$), low speed flange climb (Y/Q) and vehicle body Acceleration Peak Counting over typical test track.

In the majority of the cases considered, the main effect of the failure mode on the vehicle was a change in the effective vehicle static wheel loads. Suspension failures or faults caused by bogie twist, failed primary spring or failed sidebearer resulted in a redistribution of load such that some wheel loads decreased and others increased. Changes in wheel load directly affect $\Delta Q/Q$ and Y/Q quotients. In the case of a failed lenoir link, the key change was a large reduction in primary damping and longitudinal link force.

The effect of a broken Lenoir link was demonstrated via vehicle body acceleration assessments. The effect on the measured accelerations was not critical in terms of derailment resistance. The accelerations were greater with a broken Lenoir link than the nominal case and exceeded the UK GM/RT2141 acceptance curve limit line, of the assessment used, in some cases on rough track. Assessment on higher speed track showed that there were no significant stability issues as a result of a broken Lenoir link. In summary a broken Lenoir link did not show a significant increase in derailment risk.

The fault with the largest effect on derailment propensity was a twisted bogie frame. Although the amount of twist modelled was an assumed value, it was demonstrated that any twist in the bogie frame can have a large effect on the vertical wheel loads. In the cases examined, a twisted frame resulted in up to 64% increase in $\Delta Q/Q$ and up to 30% increase in Y/Q. The modelling of bogie twist also represents incorrect bogie suspension setup for the cases where suspension heights are adjusted with packing. The results from the twisted

frame analysis highlight the importance of maintaining the correct bogie geometry in manufacture, assembly and maintenance.

Both a failed primary spring and a failed side bearer unit were also considered. Again, both $\Delta Q/Q$ and Y/Q increased as a result of the failures. The increase in $\Delta Q/Q$ was similar for both cases but the increase in Y/Q was marginal for the failed side bearer case: the latter observation being because the loss of a side bearer resulted in a reduced yaw torque on the bogie reducing the Y force on the wheel.

Analysis of the maximum axle imbalances for the suspension failure vehicle models showed that significant axle imbalances may result from suspension failures. The most significant failure modes were the failed tare spring and bogie twist, with the latter yielding axle imbalances as high as 1.87. All of the failure modes could lead to axle imbalance beyond the RIV limit of 1.25 if combined with another detrimental factor of modest amplitude (such as skew loading).

Isolated track defects

It was confirmed that not only the amplitude but also the length of isolated track defects has an important influence on the derailment risk. Especially in very small radius curves, track defects shorter than 8 m can become critical if the amplitude reaches the Immediate Action Limits according to EN 13848-5.

3.4.2 Recommendations

The following forms a summary of the key recommendations:

Skew loading

The UIC RIV loading ratio limits appear to be an effective measure in mitigating the risks of vehicle skew loading when applied to the overall imbalance of the vehicle. It is recommended these limit values are more clearly and universally mandated and monitored.

When the UIC RIV lateral imbalance is applied to the 'worst' axle on the skew laden vehicle a margin of safety is apparent, which varies according to the derailment metric used.

It is recommended that in-track measurement system data is used to establish the true population of offset loading levels. Based on analysis of this data and also cross-reference to skew loading levels of known derailed vehicles, alarm limits for skew loading should be defined.

However, operating experience and wheel load measurements show that there are many vehicles operating outside these limits which are not derailing. Further, to impose an immediate action limit at these thresholds would be significantly detrimental to the industry in terms of increased disruption, delays and costs. Consequently, from the data analysis the alarm limit should be set so as to only capture out-lying vehicles. By combining future wheel load/imbalance data and monitoring the impact of the control on the number of derailments the alarm limit can be further optimised to achieve the optimal balance between effectiveness and cost and convenience.

Suggested alarm limits for lateral and longitudinal skew loading are load ratios of 1:1.35 and 1:3. The warning limits could be put at 1:1.3 and 1:2.5 respectively. The alarm limit for

individual axles could be set to 1:1.7 which corresponds to the SBB limit which was found to be reasonable in simulations.

For tare state wagons it is recommended that a cross load ratio above 1:1.28 should result in a chassis inspection and that wagons with a cross load or axle imbalance ratio of 1:1.7 should be stopped as these ratios of load imbalance are on the derailment limit in simulations.

It is recommended that a system is put in place that can initially be run in an off-line mode; this will allow the alarm threshold to be adjusted to ensure that it does not overly impact railway operations. This could be augmented by also considering how the limit would have impacted past operations by including historical wheel load measurement data. Measurement of skew loading could be performed either at loading or mainline running but a demonstration system could be developed.

In response to an improved understanding of on-track skew loading levels, the governing railway acceptance standards should be reviewed and consideration given to the inclusion of a prescribed level of skew loading. The significant differences between the GB and EN low speed flange climb assessment methods should also be reviewed.

Bogie suspension variation

The UIC bogie sidebearer assembly is susceptible to bumpstop contact in response to lateral skew loading. This significantly increases x-factor values and ultimately Y/Q levels. It may be feasible to increase the clearance to the bumpstop and/or increase the spring rates to improve this issue. Any changes to the component would also require consideration of vehicle stability and gauging clearance (kinematic envelope).

Consideration could be given to the development of a Y-series bogie derivative with an improved tare to laden stiffness transition (smaller step change in stiffness). A 3-stage coil spring stiffness transition in the primary suspension or adoption of rubber components are possible options for inter-modal traffic.

3.5 References

- [1] 'Derailment at Dudderstons Junction', RAIB report 16/2008, July 2008. www.raib.gov.uk
- [2] RIV Loading Guidelines - Part 2: UIC, Paris, 01.01.1998
- [3] 'Derailment at Santon near Foreign Ore Branch Junction, Scunthorpe', RAIB report 10/2009, April 2009. www.raib.gov.uk
- [4] 'Angle of Repose of Various Materials', CAT Customer Support Documentation, www.catrental.net.au (Accessed May 2013)
- [5] EN 13848 - Railway applications - Testing for the acceptance of running characteristics of railway vehicles - Testing of running behaviour and stationary tests: CEN, Brussels, June 2005
- [6] EN 14363 - Railway applications - Track - Track geometry quality: CEN, Brussels, April 2010

4 Derailments in switches & crossings

4.1 Background

In all railway systems ‘switches and crossings’ (S&C) are an extremely crucial and sensitive component. To avoid derailments in S&C, significant efforts are employed by infrastructure providers to maintain correct geometry and controls at these locations. However, also the operational conditions of the passing vehicles will have a significant effect on the risk of derailment. Thus, if the vehicle conditions are not properly managed, there will continue to be a risk of derailment even for properly maintained S&C. This analysis investigates the combined effects of S&C conditions and vehicle characteristics on the risk of derailment. The complex geometry of the S&C together with the wide scatter in passing vehicle conditions introduces a multitude of influencing parameters.

As simulation models are very suitable for parameter studies, a “bottom-up” approach has been used to find the key parameters influencing derailment risk in turnouts. In total the sensitivity of 25 different parameters on derailment risk has been investigated. The parameters covered in the list of top derailment causes found in D1.1 are skew loading and excessive track twist. On the list is also spring & suspension failure. This category is not considered for traffic in turnouts, but the sensitivity of suspension parameters on derailment risk is investigated for a range of operational values.

4.2 Literature survey

4.2.1 Derailment in turnouts

The scientific literature was searched via Thomson Reuters Web of Science [7] which among an extensive amount of scientific publications covers relevant railway related journals such as *Vehicle System Dynamics*, *ImechE Part F—Journal of Rail and Rapid Transit* and *wear*.

A Search for articles including the keywords “derailment” and “switch” yielded a response of 112 articles. None covered simulation based parameter studies on derailment risks in turnouts.

A Search for articles including the keywords “derailment” and “crossing” yielded a response of 139 articles. None covered simulation based parameter studies on derailment risks in turnouts.

A Search for articles including the keywords “derailment” and “turnout” yielded a response of 9 articles. None covered simulation based parameter studies on derailment risks in turnouts.

Some articles found covered simulation of train-turnout interaction.

A special type of derailment risk in switches is covered in [8]. It is pointed out that the false flange of a hollow worn wheel might reach over the switch rail and interfere with the stock rail. This phenomenon can cause rail roll over if the force applied to the stock rail is mainly lateral.

4.2.2 Other literature

A review covering vehicle acceptance tests with focus on derailment [9] finds that the Y/Q limit of 0.8 is questionable as higher Y/Q-ratios have been recorded in traffic for freight wagons featuring Y25 bogies without derailment. The modelling of a freight wagon featuring Y25 bogies is covered in [10]. The article does not give much specific information such as parameter values, but stresses the importance of including track irregularities in simulations of friction damped freight vehicles to loosen up the friction surfaces for more realistic simulations.

4.2.3 Standards

Some standards of relevance for freight vehicles and turnouts are listed below.

- UIC 518. Appendix N covers tests in small radius turnouts for vehicle approval. The objective is to make sure that the switch rail loading caused by the vehicle is acceptable with regards to the fatigue strength of the switch rail
- UIC 716 R. Covers maximum permissible wear profiles for switches
- UIC 432. Wagons – Running speeds – Technical conditions to be observed
- EN 13232-X. Standards on turnout design
- EN 14363. Railway applications – Testing for the acceptance of running characteristics of railway vehicles – Testing of running behaviour and stationary tests

4.3 Studied derailment scenario

The derailment scenario studied for S&C in D-rail is flange climb derailment in switches. The traffic situation studied is traffic in the diverging route of a small radius ($R=190\text{m}$) right hand turnout for both the facing and the trailing move. This scenario is chosen because simulations and measurements show that the Y/Q-ratios for traffic in the diverging route are larger than those recorded for the through route [11]. Further, simulations show that traffic in a small radius turnout generates larger Y/Q-ratios than a turnout with larger radius for typical speed limits, see section 4.3.1 below. As the Y/Q-ratio correlates to the risk of derailment according to Nadal's criterion [12], the small radius turnout is considered to be the most critical case.

4.3.1 Motivation of derailment scenario

Train-turnout interaction has been simulated for switches of different radii (190, 300 and 760 m). The Y/Q-ratios for these switches have been compared to the Y/Q-ratios obtained for identical curves where the switch rail geometry has been replaced with a standard 60E1 rail profile. The Y/Q-ratios are post processed with a two metre sliding average window. The simulation results show that the largest Y/Q-ratio is obtained for a small radius switch and that the maximum Y/Q-ratio is larger in a curve with switch geometry compared to one with standard rails, see Figure 85. The velocity for each radius is set according to the DB standards which limit the speed in the diverging branch according to $v \leq 2.92\sqrt{R}$ where v is the vehicle speed in km/h and R the turnout radius in meters.

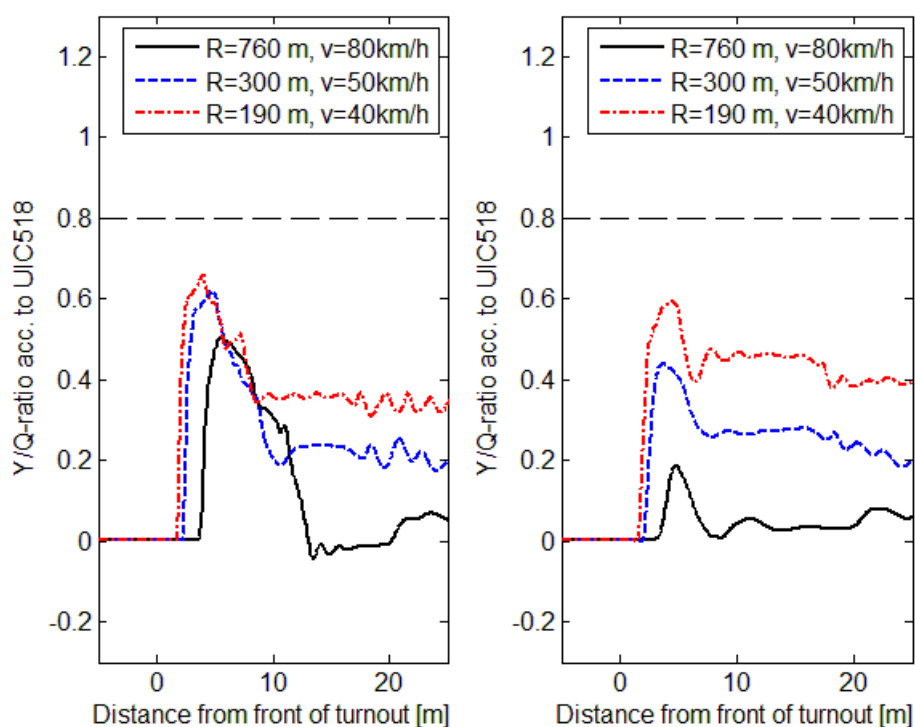


Figure 85. Y/Q comparison for switch (left) and standard (right) rail geometry. Results for leading outer wheel in the facing move. The wheel-rail friction coefficient is 0.5.

4.3.2 Delimitations

Multi Body System (MBS) simulations are suitable for the studies of a system's dynamic behaviour in situations with large rigid body displacement. To allow for fast simulation times, the wheel-rail contact problem is typically solved for in advance. It is then tabulated and used in the time domain simulations. As the rail profiles of the switch and crossing varies significantly and rapidly along the length of the switch, many sections are needed to describe the geometry. The contact properties between two sections are obtained by linear interpolation. This modelling approach for the wheel-rail contact is not suitable for the simulation of derailment risk due to localized rail damage such as rail breaks or large surface defects such as spalling/shelling. As these defects are obviously not beneficial to the smoothness of the vehicle-track interaction, they should be mitigated regardless, and it is not considered to be of interest to perform dedicated simulations for these types of damage in a derailment situation. MBS-simulations can however quantify the loads needed to perform damage evaluations for the rails in the turnout, such as the estimation of a crack propagation rate.

A similar way of reasoning can be applied to the crossing panel. As the crossing panel has a built in derailment guard in the form of a check rail, it is very unlikely that anything other than a component failure (or maybe actuation failure in the case of a moveable crossing nose) would cause a derailment in this area. It is not necessary to perform simulations to conclude that a broken or chipped crossing nose or a severely misaligned check rail are conditions that need mitigation measures. These issues are therefore considered to be more about monitoring and detection and the view for the S&C work within D-rail is that MBS-

simulations cannot add much information regarding the risk of derailment in the crossing panel.

4.4 Simulation Procedure

The simulation work flow for the defined derailment scenario has been divided into five sub-tasks.

4.4.1 Task 1 Sensitivity studies to find key influencing parameters

To find the influence of track and vehicle parameters on derailment risk, Design Of Experiments (DOE) studies have been performed for 25 different parameters. To make the simulation effort feasible, the parameters have been split into four separate investigations depending on parameter characteristics. Where available and applicable, current standards have been used to set parameter limits in the parameter investigations. One important aspect of this work is to find out if there are influential parameters which are not yet being monitored.

4.4.2 Task 2 Evaluation of current standards

Using the results from Task 1, a bad case scenario is defined by setting each parameter to its most detrimental value. This will answer the question whether current standards are sufficient (according to simulations) to prohibit derailments in S&C.

4.4.3 Task 3 Limit state as a function of key influencing parameters

Starting from the bad case scenario found in Task 2, a derailment surface is estimated in the most influencing parameters, or groups of parameters, as obtained by Task 1. This limit surface is associated with the parameter combinations that would cause derailment according to simulations.

4.4.4 Task 4 Comparison to standard rails

Here the derailment surface obtained for the switch rail geometry in Task 3 is compared to results where the rail geometry for a switch, i.e. switch rail and stock rail, have been replaced by a standard rail profile. The turnout then becomes a plain line curve without transition curve. This comparison is an attempt to quantify the increased risk of derailment in switches as compared to plain line.

4.4.5 Task 5 Vehicle parameter limits

Here a derailment limit surface is obtained as a function of the most influential vehicle parameters for traffic in a representative bad case switch. The track irregularity amplitudes for the switch are defined using the wave-length and amplitude relation obtained by DB from measured track irregularity data as presented in 3.3.1. Based on the obtained limit surface, limit values for the most influential vehicle parameters are discussed.

4.5 Numerical simulations

4.5.1 Simulation model

4.5.1.1 Vehicle

The vehicle configuration that defines the base design for the simulations within D-rail is described in Appendix. The simulation software environment used for the S&C work is GENSYS [13]. The above mentioned vehicle parameters have been implemented to an existing vehicle model of a freight car with Y25 bogies. In addition to the tare and fully loaded vehicle states defined for the benchmark vehicle, a partly loaded vehicle state is defined to investigate the influence of skew loading.

4.5.1.2 Track flexibility

The track flexibility model used for the switch simulations is similar to the model presented in Appendix and is also of the co-following type. The model employed has been tuned to turnout stiffness measurement data and should be more representative for the simulation case at hand.

The track flexibility model features a rigid track and individual vertical and lateral rail stiffnesses [11]. The simple track model is justified by the fact that low frequency dynamics (up to 20Hz) dominate the vehicle-turnout interaction for a nominal switch.

The current track model has the vertical stiffness of 60MN/m measured at the rail, and a viscous damping coefficient of 535kNs/m. The lateral rail stiffness and damping are set to half of the values in the vertical direction, i.e. the stiffness is 30MN/m at the rail and the damping coefficient is 270kNs/m. This relatively high lateral stiffness is motivated by the stiffer mounting of the rails in the switch and the fact that there are two rails next to each other. The composite rail profiles consisting of the stock rail and switch rail are modelled as one rigid part. The individual flexibilities of the rails are thus not accounted for.

4.5.1.3 Track geometry

Small amplitude track irregularities are always applied in simulations as background noise. The aim is to create a more realistic loading of the vehicle's many friction surfaces [10],[14] and avoid unrealistically locked friction surfaces. The track geometry references used to obtain track irregularity limits for parameter studies is EN 13848-5 and BVS 1523.004. The latter is issued by the Swedish transport administration (Trafikverket) and contains gauge tolerances for turnout maintenance.

4.5.1.4 Rail geometry

The switch rail geometry used in simulations is a nominal rail geometry that is based on 60E1 rails and 1:30 rail inclination.

4.5.1.5 Wheel profiles

To account for the different wear states of wheel profiles found in traffic, a sample of wheel profiles have been selected for use in simulations.

Based on a sample of 120 measured wheel profiles from freight wagons featuring Y25 bogies, wheel profiles have been selected based on their 3mm equivalent conicity value calculated

on 60E1 rails with 1:40 inclination [15] according to UIC 519. From this sample the wheel profiles with the lowest and largest equivalent conicities were chosen. As a worst-case reference, a hollow worn wheel profile provided by DB is included. The measured profiles are presented in Figure 86 where they are plotted normalised with respect to the nominal running circle. A nominal S1002 wheel profile is also included. The S1002 wheel profile is derailment critical in the sense that a wheel profile typically has its lowest flange height and smallest flange angle when it is new.

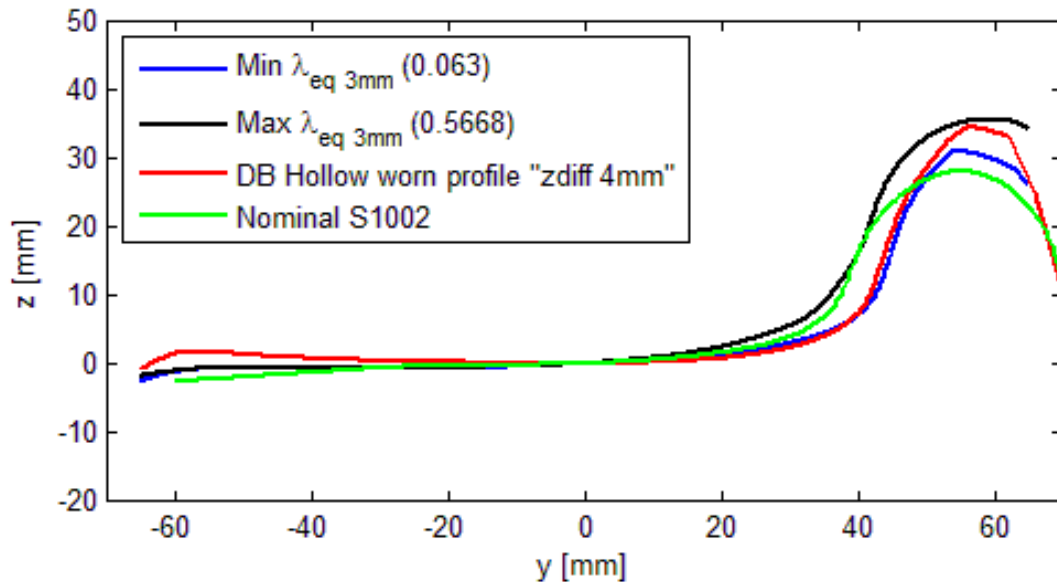


Figure 86. Measured and nominal S1002 wheel profiles

4.5.1.6 Validation

The simulation set-up used for the S&C simulations in D-rail has been validated in [11] against force measurement data from an instrumented wheelset.

4.5.2 Investigated parameters

Four different parameter studies are performed to evaluate a total of 25 track and vehicle parameters. All parameters are listed in Table 18. See Appendix for a description of the Y25 bogie.

Table 18 List of investigated parameters

Side bearer friction coefficient
Centre plate friction coefficient
Primary suspension friction coefficient
Side bearer play
Longitudinal play in primary suspension
Lateral play in primary suspension
Scale factor for vertical primary spring stiffness
Scale factor for horizontal primary spring stiffness
Bogie c-c distance
Axle c-c distance in bogie
Chassis torsional stiffness
Traffic move
Wheel polygonalization
Speed
Wheel-rail tread friction coefficient
Wheel-rail flange friction coefficient
Longitudinal load ratio for laden case
Lateral load ratio for laden case
Chassis twist
Car body vertical Centre of Mass (CoM) position
Lateral track irregularity amplitude
Vertical track irregularity amplitude
Track twist irregularity amplitude
Track gauge irregularity amplitude
Wheel profile

The major parameter group missing in these studies is parameters related to the switch rail geometry itself. Efforts have been made to create worn geometries based on Swedish maintenance templates, but it was found that a large number of assumptions were still needed regarding the actual shapes of the worn profiles. It is judged that a representative set of measured switch rail profiles on the maintenance limit would be needed to perform this task, and that has not been feasible within the D-rail project.

4.5.3 DOE methodology

Two different methods are used for evaluations in the performed parameter studies. The first is two level fractional factorial designs and the other is fitting of quadratic response surfaces to an evaluated parameter grid. For more information on the methods presented in this section, see for example [16].

4.5.3.1 Factorial designs

Factorial designs or design of experiments (DOE) can be used to obtain the sensitivity of a selected number of parameters on an objective of interest. They are suitable when the objective isn't available in closed form, but rather requires experiments or the evaluation of a black box function such as a numerical simulation of a complex system to be obtained. The benefit compared to varying one parameter at the time is that the parameter estimates become more robust and interactions between parameters can be detected.

In a two level factorial design, the parameters to be investigated are assigned one high and one low parameter level (typically denoted by +1 and -1). In a full two level factorial design all parameter combinations are investigated, which requires 2^n evaluations of the objective where n is the number of parameters. The sensitivity, or effect, for each parameter is obtained as the average objective when the parameter is at the high level subtracted by the average objective value when the parameter is at the low level. If a response value from an experiment is denoted y_i and an average response is denoted \bar{y} , an effect can be calculated as:

$$Effect = \sum_{i \in high\ level} \frac{y_i}{N/2} - \sum_{i \in low\ level} \frac{y_i}{N/2} = \bar{y}_{high} - \bar{y}_{low} \quad (6)$$

where N is the total number of runs. An example of a full factorial containing two parameters is presented in Table 19.

Table 19 Example of a two parameter full factorial design.

Run number	a	b	ab calculation	ab	Result, y
1	-1	-1	-1*-1	+1	$y_1=17$
2	+1	-1	+1*-1	-1	$y_2=26$
3	-1	+1	-1*+1	-1	$y_3=14$
4	+1	+1	+1*+1	+1	$y_4=19$

Columns two and three in this table present the parameter levels for all four parameter settings. Columns four and five present the calculation of and the resulting so called interaction. The interaction effect for two (or more) factors can be calculated in the same way as the first order effects. The first order effects, **a** and **b** in this case, are linearized estimates of the parameter influence and will capture linear trends such as those in Figure 87 (a). As the main effects measure linear trends, they cannot estimate pure quadratic effects, as shown in Figure 87 (b). To do this, higher order designs are needed as will be discussed

later. The interaction effect estimates cross influence. As the high level of the interaction effect **ab** is the sum of the objectives when the factors have equal signs and the low level consists of the runs where **a** and **b** have different signs, it captures objective function behaviour as that shown in Figure 87 (c). Such an objective function would result in main effects that are zero, while the interaction effect would be large. Even higher order interactions can be calculated for factorial designs with a larger number of parameters, but these can be hard to interpret and are less likely to be significant.

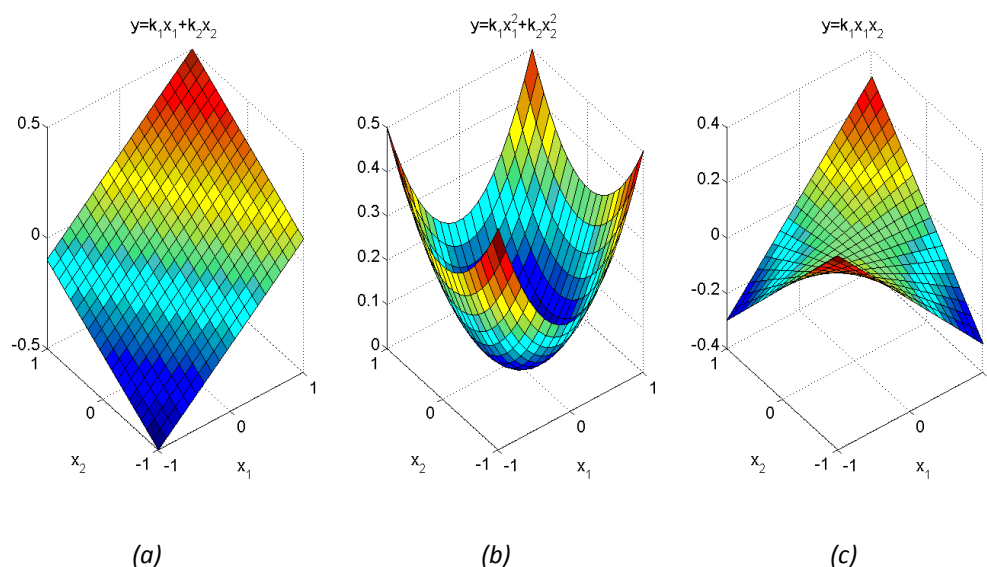


Figure 87 Illustrations of different objective function characteristics. Linear (a) quadratic (b) and cross term (c)

The **a** effect for the example DOE in Table 19 would be calculated as:

$$a = \bar{y}_{a+} - \bar{y}_{a-} = \frac{y_2 + y_4}{2} - \frac{y_1 + y_3}{2} = 7 \quad (7)$$

And for **ab** as:

$$ab = \bar{y}_{ab+} - \bar{y}_{ab-} = \frac{y_1 + y_4}{2} - \frac{y_2 + y_3}{2} = -2 \quad (8)$$

To summarise, the main effects and the interaction effects capture different characteristics of the objective function. Even if the interaction effects are zero, the main effects can still interact in the sense that they add to the objective function. For example a combined skew loading and a large track twist can combine to cause a derailment even if the interaction effect in a mathematical sense is zero. This is because the main effects of these parameters can add up to a Y/Q or wheel lift large enough to cause a derailment.

If a large number of parameters are to be investigated, the number of runs for a full factorial design might be unfeasible or unnecessary. By the creation of a so called fractional factorial

design the number of objective evaluations can be reduced at the cost of confounding between effects. The confounding means that you do not evaluate each effect individually but rather a sum of effects. For the DOEs used in this study, fractional factorial designs of resolution V (five) have been used. This means that first order effects are confounded with fourth order effects and second order effects are confounded with third order effects. As third order effects and higher are assumed to be insignificant, good resolution can be obtained anyhow in the DOEs with a significant reduction in the number of simulations required.

To capture higher order trends like quadratic effects, more than two levels are needed in the experimental set-up. A common way to evaluate these experiments is to fit a polynomial, or response surface, to the results using least squares or another regression method. For a two parameter case, a polynomial model can be expressed as:

$$y = K + A_1x_1 + A_2x_2 + B_{11}x_1^2 + B_{22}x_2^2 + B_{12}x_1x_2 \quad (9)$$

The estimated characteristics of the objective function can then be obtained from the magnitude of the coefficients. To estimate how well a second order polynomial fits to the observed objective values for the investigated parameter settings the R-squared quality measure can be used. It is defined as:

$$R^2 = 1 - \frac{SSE}{SST} = 1 - \frac{\sum_{i=1}^n (y_i - \hat{y}_i)^2}{\sum_{i=1}^n (y_i - \bar{y})^2} \quad (10)$$

where SSE is the sum of squares due to error calculated using the actual responses y_i and the objective estimate \hat{y}_i (from the polynomial) for each observation. SST is the squares about the mean and \bar{y} is thus a mean value for the actual responses. The R^2 can vary between zero and one. As can be seen from the expression, the R^2 is one if the agreement between the observations and the model is perfect and the SSE is zero. On the other end the fit is really poor if R^2 is closer to zero.

4.5.4 Objectives

For the DOEs, the objective is the maximum Y/Q_{2m} quotient recorded during one vehicle passage for any of the outside wheels in the diverging route of the turnout, i.e. those making the transition from stock rail to switch rail or vice versa. It is denoted $Y/Q_{2m,max}$. The 2m index means that the signal is post processed using a 2m sliding window average.

For the studies intended to detect an actual derailment event, wheel lift is used as the evaluation criteria. Also this quantity is post processed using a 2m sliding window average and denominated wl_{2m} .

4.5.5 Load Ratios

One of the most influential parameter categories of the present study is skew loading and the wheel load imbalances that result. This section defines and discuss different measures of skew-loading.

4.5.5.1 Nominal load ratios

Typical loading guidelines for freight vehicles such as those of UIC (RIV limits) [17] limit the longitudinal and lateral offset for payload centre of mass. The offset limits are determined through simple studies of static equilibria such as those presented in Figure 88 for a vehicle

with two bogies and four axles which is the vehicle type of interest for the present study. In the longitudinal direction the full vehicle is considered while in the lateral direction half a vehicle is considered.

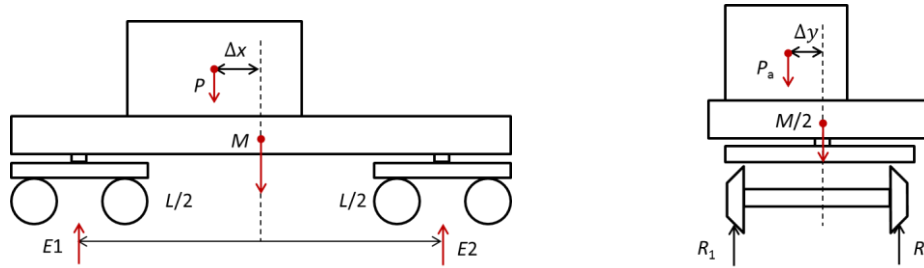


Figure 88 Illustrations of modelling for calculations of skew loading. Longitudinal (left) and lateral (right)

In Figure 88 the vehicle mass M is the mass of the tare state vehicle such that $M = E_1 + E_2 - P$. P is the full payload while P_a is the part of the payload for the studied half of the vehicle. $E_{1,2}$ are the bogie loads and $R_{1,2}$ the side loads for the studied half vehicle.

As there are only two unknown forces each in the studies of longitudinal and lateral load imbalance, the forces can be found using vertical force/load equilibrium and moment equilibrium. The UIC loading guidelines then state that

$$\varphi_{\text{long,nominal}} = \max \left[\frac{E_1}{E_2}, \frac{E_2}{E_1} \right] \leq 3 \quad (\leq 2 \text{ for two - axle vehicles}) \quad (11)$$

$$\varphi_{\text{lat,nominal}} = \max \left[\frac{R_1}{R_2}, \frac{R_2}{R_1} \right] \leq 1.25 \quad (12)$$

which imposes limits on the payload displacements Δx and Δy . As can be noted from the calculation set-up in Figure 88, only sums of wheel loads are included in the calculations as there isn't enough detail in the modelling to determine each individual wheel load. It can of course be assumed that the loads are distributed evenly, but such an approach doesn't account for e.g. non-linearities or compliance in the suspensions or any imperfections in chassis components that can be the case for real vehicles.

Especially for the lateral direction the observed lateral load imbalance in a bogie can be much larger than that predicted by the above model if there is a twist in the chassis which would apply a superimposed torque on the half-wagon model to the right in Figure 88. As long as any coupling torque between the vehicle halves isn't accounted for, it typically makes little difference for the offset limit whether the full or half vehicle is considered in the nominal calculations. If the payload is centred in the longitudinal direction it makes no difference. Also roll compliance in the suspension due to load offset can move the centre of mass of the vehicle and cause an increased load imbalance compared to the nominal.

It should therefore be recognised that even if a vehicle fulfils the nominal loading guidelines, it does not mean that the actual wheel loads that can be observed in track are also within those limits.

4.5.5.2 Observed load ratios

In this section vehicle load ratios for the longitudinal, lateral and diagonal direction will be defined. The ratios are based on observed vertical wheel loads that can come either from

simulation or axle load check points. The longitudinal load ratio is defined as the sum of all vertical wheel loads for the bogie carrying the largest load divided by the corresponding sum of the bogie carrying the smaller load. As it is difficult to know which bogie carries more load beforehand, both versions of the ratio are calculated and the maximum value is used. Mathematically this can be written as

$$\varphi_{\text{long,observed}} = \max \left[\frac{Q_{21l} + Q_{22l} + Q_{21r} + Q_{22r}}{Q_{11l} + Q_{12l} + Q_{11r} + Q_{12r}}, \frac{Q_{11l} + Q_{12l} + Q_{11r} + Q_{12r}}{Q_{21l} + Q_{22l} + Q_{21r} + Q_{22r}} \right] \quad (13)$$

where $Q_{xy\ l/r}$ are the estimated quasi static wheel loads, index x the bogie number and index y the wheelset number within a bogie. l/r means left or right.

In the same way a lateral load ratio can be defined as

$$\varphi_{\text{lat,observed}} = \max \left[\frac{Q_{11r} + Q_{12r} + Q_{21r} + Q_{22r}}{Q_{11l} + Q_{12l} + Q_{21l} + Q_{22l}}, \frac{Q_{11l} + Q_{12l} + Q_{21l} + Q_{22l}}{Q_{11r} + Q_{12r} + Q_{21r} + Q_{22r}} \right] \quad (14)$$

It can be noted that $\varphi_{\text{long,observed}}$ and $\varphi_{\text{lat,observed}}$ are statically determined in the sense that for a given centre of mass position of the vehicle, the sum of torques about the centre of mass must be zero in both the lateral and longitudinal direction for the vehicle to stay at rest. This means that the load ratios observed correspond to the actual load ratio of the vehicle within the tolerances that can be expected due to e.g. asymmetric contact point conditions that can affect the length of the vertical wheel load levers about the centre of mass. The centre of mass position of the vehicle itself isn't statically determined however as it depends on e.g. the suspension state.

For a mechanical system the term "statically determined" means that the forces and moments required for static equilibrium can be determined directly from static force and moment equilibrium equations. If the number of unknowns is larger, the deformation of the constituents of the system needs to be accounted for to obtain the equilibrium forces.

It should be noted that even if the sum of forces on each side of the vehicle and within each bogie of the vehicle are determined by the vehicle's load distribution, the individual wheel forces are not. Due to friction, suspension non-linearities, geometrical imperfections, load history etc the load distribution can differ between between the individual wheels between different measurements. This makes measurements of the vehicle load ratios necessary if skew loading is to be estimated. It is not sufficient to study the load ratio of individual axles to draw conclusions about the vehicle's load distribution.

In addition to the longitudinal and lateral load ratios, a diagonal load ratio which compares the sum of loads on the left front and right rear wheels to the loads on the right front and left rear wheels or vice versa is defined.

$$\varphi_{\text{diag,observed}} = \max \left[\frac{Q_{11r} + Q_{12r} + Q_{21l} + Q_{22l}}{Q_{11l} + Q_{12l} + Q_{21r} + Q_{22r}}, \frac{Q_{11l} + Q_{12l} + Q_{21r} + Q_{22r}}{Q_{11r} + Q_{12r} + Q_{21l} + Q_{22l}} \right] \quad (15)$$

The diagonal load ratio can be used to observe asymmetries in a vehicle such as a twisted chassis. The diagonal load ratio is statically undetermined and cannot be obtained directly from the payload distribution of the vehicle.

Even though it is difficult to draw conclusions about the exact skew loading state of a vehicle based on measured load ratios for individual axles, it is still a load imbalance measure that

can be highly relevant for detection of derailment propensity. The observed axle load imbalance can be defined as

$$\varphi_{\text{axle,observed}} = \max \left[\frac{Q_l}{Q_r}, \frac{Q_r}{Q_l} \right] \quad (16)$$

As there are several axles in a vehicle, it is also useful to define the maximum axle load imbalance as

$$\varphi_{\text{axle,observed,max}} = \max \left[\frac{Q_{11l}}{Q_{11r}}, \frac{Q_{11r}}{Q_{11l}}, \frac{Q_{12l}}{Q_{12r}}, \frac{Q_{12r}}{Q_{12l}}, \frac{Q_{21l}}{Q_{21r}}, \frac{Q_{21r}}{Q_{21l}}, \frac{Q_{22l}}{Q_{22r}}, \frac{Q_{22r}}{Q_{22l}} \right] \quad (17)$$

4.5.6 Overview of parameter study

First two two-level fractional factorial designs (DOE1&2) consisting of eight parameters each are evaluated. The resolution is V (five) which requires 64 runs for eight parameters. The parameters in these investigations are all symmetrical in the sense that the vehicle always maintains a symmetrical configuration when the parameters are varied. Thus, the same but mirrored response is expected if the vehicle travels in a left and right hand turn or if it travels forward or backward. These are also parameters where linear responses are expected to dominate, making it sufficient to use the two-level DOE for parameter screening. For example it is expected that the Y/Q-ratio will increase with an increasing wheel-rail friction coefficient. As the primary suspension of a Y25 bogie operates in different regimes depending on the payload, these DOEs are evaluated both for the laden and tare state vehicles.

DOE3 and DOE4 both focus on asymmetrical parameters. For these parameters, such as the vehicle's longitudinal and lateral load imbalance, it is more suitable to use three levels for each parameter as quadratic responses can be expected. For example it is expected that a vehicle with a nominal and perfectly symmetrical weight distribution will have a lower risk of derailment compared to versions of the vehicle where the load is skewed either to the front or the back of the vehicle.

The parameter levels and limits have as far as possible been selected according to current standards or are otherwise based on engineering judgement.

4.5.7 DOE 1

The variables and their levels for DOE1 are presented in Table 20.

Table 20. Parameter levels for DOE 1

Factor		Low	High
a	Side bearer friction coefficient [-]	0.2	0.5
b	Centre bowl friction coefficient [-]	0.2	0.5
c	Primary suspension friction coefficient [-]	0.2	0.5
d	Side bearer play [-]	0	1
e	Longitudinal play in primary suspension [-]	4	5
f	Lateral play in primary suspension [-]	10	12.5

g	Scale factor for vertical primary spring stiffness [-]	1	1.2
h	Scale factor for horizontal primary spring stiffness [-]	1	1.2

The resulting main effects for both load states as calculated according to Section 3.1.3 are presented in Figure 89.

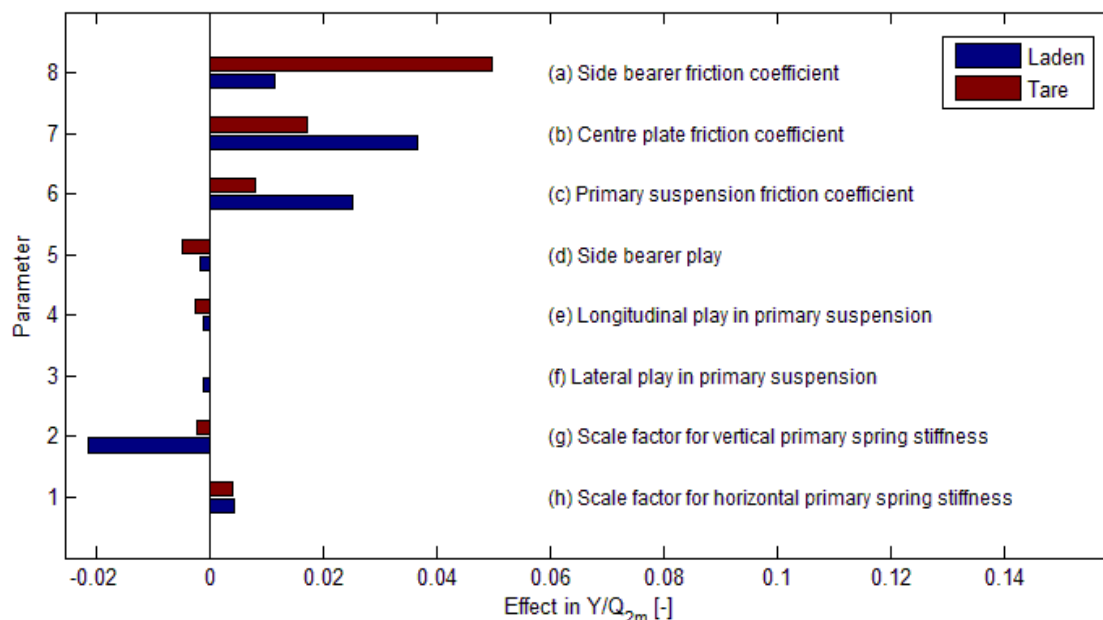


Figure 89 Y/Q effects for the laden and tare state vehicles and DOE1.

Comparing the two load states the load effect can be calculated from the mean objective values in the two DOEs. The average objective value for the laden case is $\bar{y}_{\text{laden}} = 0.648$ and for the tare case $\bar{y}_{\text{tare}} = 0.692$. The weight effect is then $E_{\text{load}} = \bar{y}_{\text{laden}} - \bar{y}_{\text{tare}} = -0.044$. The weight effect can also be calculated in percent as:

$$E_{\text{load},\%} = 100 \frac{(\bar{y}_{\text{laden}} - \bar{y}_{\text{tare}})}{\bar{y}_{\text{tare}}} = -6.3\% \quad (18)$$

The average Y/Q objective is thus 6.3% smaller in the loaded case compared to the tare case. The only interaction effect larger than 0.01 is (cg) for the laden case with the magnitude 0.02. It is considered realistic that there can be interaction effects between the stiffness and damping in the primary suspension. For the laden case, the maximum Y/Q-ratios were all obtained for the leading wheel.

For the tare case the maximum Y/Q-ratio was obtained for the leading wheel in 58 cases and for the leading wheel of the trailing bogie in 6 cases. No parameter setting resulted in wheel lift.

4.5.8 DOE 2

The parameters for DOE 2 are presented in Table 21. As the wheel-rail flange friction coefficient is one of the parameters in this DOE, it isn't straight forward to compare the $Y/Q_{2m,\text{max}}$ values from the different simulations as the derailment critical Y/Q-ratio is dependent on the wheel-rail flange friction coefficient according to Nadal's criterion.

To obtain a better estimate of the actual derailment propensity for the runs with a low flange friction coefficient in comparison to the runs with a high flange friction coefficient, all the objective values from runs with a w/r friction coefficient of 0.2 have been rescaled with the quotient between Nadal's limits for a w/r friction of 0.5 and 0.2. The scaling factor becomes:

$$K_{\text{Red},\mu=0.2} = \frac{Y/Q_{\text{Nadal},\mu=0.5,60^\circ}}{Y/Q_{\text{Nadal},\mu=0.2,60^\circ}} = \frac{0.66}{1.14} = 0.58 \quad (19)$$

Table 21 Parameter levels for DOE 2.

Factor		Low	High
a	Bogie semi spacing [m]	3.5	7.5
b	Axle semi spacing in bogie [m]	0.9	1
c	Chassis torsional stiffness [MNm/rad]	1.8 for tare state. 18.1 for laden state	rigid
d	Traffic move [-]	Facing	Trailing
e	Wheel polygonalization [mm]	0	3 waves on circumference. Amplitude 0.5
f	Speed [km/h]	40	45
g	W/r tread friction coefficient [-]	0.2	0.5
h	W/r flange friction coefficient [-]	0.2	0.5

The main effects for the tare and laden states are presented in Figure 90. It can be noted that both wheel-rail (w/r) friction coefficients have a large influence on the Y/Q -ratio. Without the rescaling of the objective for the runs with a low friction coefficient, the effect for the w/r flange friction coefficient would have been slightly negative. Therefore the Y/Q ratio actually decreases with an increasing w/r flange friction coefficient. However, according to Nadal, the propensity for derailment increases more than the reduction in Y/Q -ratio. The most significant interaction effects are presented in

Table 22.

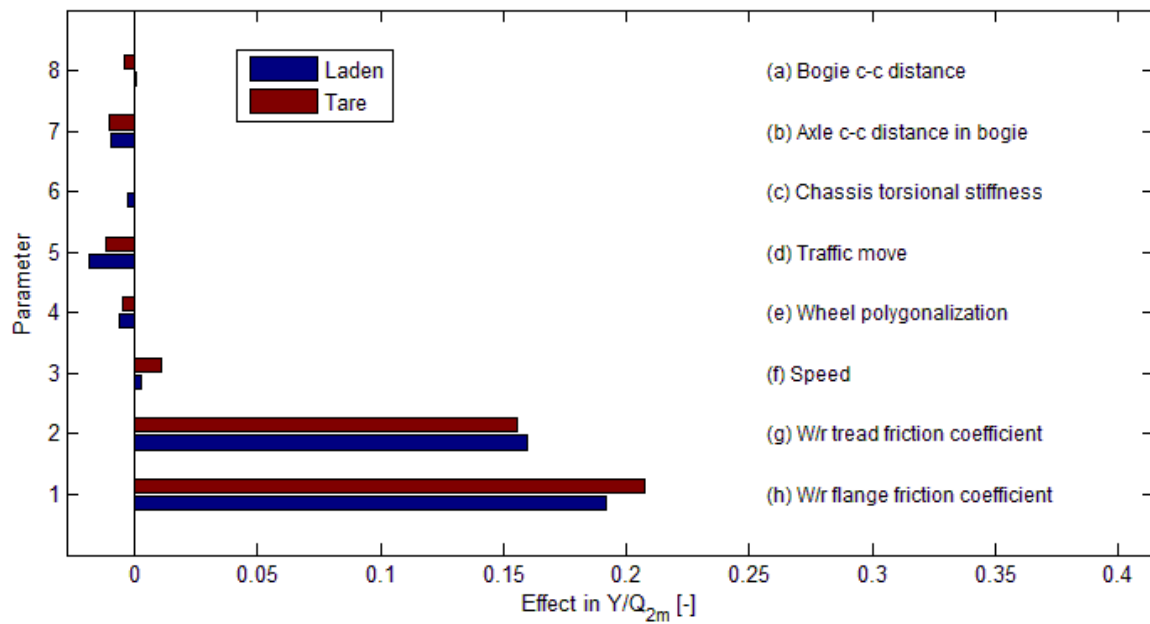


Figure 90 Y/Q effects for the laden and tare state vehicle.

Table 22 Interaction effects with a magnitude larger than 0.01 for laden and tare states

Interaction	Laden Y/Q [-]	Tare Y/Q [-]
ad	0.015	0.016
ag	0.012	0.011
dg	-0.013	magnitude smaller than 0.01
gh	0.033	0.032

Comparing the two load states the load effect can be calculated from the mean objective values in the two DOEs. The average objective value for the laden case is $\bar{y}_{\text{laden}} = 0.44$ and for the tare case $\bar{y}_{\text{tare}} = 0.478$. The weight effect is then $E_{\text{load}} = \bar{y}_{\text{laden}} - \bar{y}_{\text{tare}} = -0.038$. As the objective magnitudes vary between DOE 1 and DOE 2 due to the differences in w/r friction coefficient, the weight effect can be calculated in percentage as:

$$E_{\text{load},\%} = 100 \frac{(\bar{y}_{\text{laden}} - \bar{y}_{\text{tare}})}{\bar{y}_{\text{tare}}} = -7.9\% \quad (20)$$

The average Y/Q objective is thus 7.9% lower in the loaded case as compared to the tare case. For both the tare and the laden state, the highest Y/Q ratio was obtained for the leading wheelset for all runs in the facing move. For all runs in the trailing move, the highest Y/Q ratio was obtained for the leading wheelset in the trailing bogie. No parameter setting resulted in wheel lift.

4.5.9 DOE 3 skew loading

In this parameter study the influence of skew loading is investigated in combination with chassis twist. The parameters and levels are presented in Table 23. The chassis twist is positive when it unloads the vehicle's left front-rear right diagonal.

The longitudinal and lateral centre of mass (CoM) location for the car body as well as the chassis twist is asymmetrical in the sense that they will introduce asymmetric wheel loads. The results will therefore also depend on the direction which the parameter is varied. Different vehicle behaviour can for example be expected if the car body CoM is moved forward compared to backward in the running direction. It is therefore suitable to investigate these parameters using three parameter levels on a symmetrical interval around the default configuration. The vertical CoM for the carbody is also included as a parameter. As this is a symmetrical parameter, only two levels are used. All parameter combinations are evaluated, so the total number of runs is therefore $2 \cdot 3^3 = 54$.

Table 23 Asymmetrical vehicle parameters.

Factor		Low	Medium	High
A	Bogie load ratio. (front:rear)	3:1	1:1	1:3
B	Side load ratio. (left:right)	1.25:1	1:1	1:1.25
C	Chassis twist [mrad]	-21	0	21
D	Car body CoM Vert. [m]	1.69	N.A.	2.45

The CoM offset locations used are calculated in section 4.5.9.1 below according to the UIC loading guidelines (RIV-limits) [17]. (The actual work was performed using the public loading guidelines provided by Swedish freight company Green Cargo [18] which is based on the UIC-guidelines). See also 4.5.5 for a discussion on load ratios. According to these guidelines, the maximum allowed nominal bogie load ratio is 1:3 and the maximum left-right load ratio in a wheelset is 1:1.25. The measurements presented by DB and UoH in Section 3.1.3.3 show that these skew loading numbers are realistic but rare. The maximum allowed CoM position for the cargo load is 2.8m. To achieve the 1:3 bogie loading ratio without exceeding the axle load limit of 25T, the total car body mass is reduced to 58T.

4.5.9.1 Skew loading limits

The following limits apply to the longitudinal and lateral load imbalance and the vertical CoM position according to [18].

- For a bogie vehicle the maximum load ratio allowed between bogies in is 1:3.
- The axle load is not allowed to exceed the nominal value (here taken as 25T).
- The load ratio between wheels in a wheelset is 1: 1.25 maximum.
- The maximum vertical CoM position of the load is 2.8 m above top of rail.

If P is the load in tonnes and M the weight of the wagon (including bogies and wheels) in tonnes the bogie weights (2 times the axle load) $E1$ and $E2$ can be calculated using moment and force equilibrium. The bogie-bogie c-c distance is L . Using the axle load and load distribution constraints, the maximum allowed load P with a maximum longitudinal offset of Δx can be solved for.

With $M=22.6$ T and $P_A = 38.7$ T for the maximum allowed cargo weight on one bogie (it gives a 25 T axle load) it is obtained that $s_{max}=0.108$.

In the simulation model the chassis and the load are modelled as one car body. The allowed CoM deviations for this case can be obtained by setting M equal to the weight of the axles and bogies (in total 8.29T) and P to be the weight of the chassis frame and the cargo load (58.32T). Doing so the limits are obtained as $\Delta x_{ass} = 0.285L$ and $s_{max,ass} = 0.091$.

The vertical CoM position for the whole car body assembly can be calculated using the maximum allowed CoM for the cargo load of 2.8 m (z_{max}), The maximum load for the 1:3 bogieloading ratio $P=44$ T and the CoM ($z_c = 1.39$ m) and weight of the chassis frame ($m_c = 14.32$ T).

$$z_{max} = \frac{z_c m_c + z_{max} P}{P + m_c} = 2.45 \text{ m} \quad (28)$$

Those are thus the limits that are used in DOE 3.

4.5.9.2 Chassis twist

The chassis twist is implemented as an offset of the sidebearer stiffness curves. A 9mm offset on each side in opposite directions and on both bogies corresponds to a twist angle of

$$twist = 2 * \frac{2 * 9mm}{2 * 0.85} = 21 \text{ mrad} \quad (29)$$

where 0.85 is the side bearer semi spacing. This amount of twist correlates to a cross loading index (5) of about 0.085 for the wagon in its tare state (or a diagonal load ratio of about 1:1.2 according to (15)). This is a large but realistic value according to the results presented in Figure 37.

4.5.9.3 Results

The influence of the vertical CoM position for the car body is calculated as the difference between the average objective values when the CoM is at its high and low positions.

$$E_{CoMz} = \bar{y}_{CoMz,high} - \bar{y}_{CoMz,low} = 0.693 - 0.720 = -0.027 \quad (30)$$

The $Y/Q_{2m,max}$ is thus smaller on average when the CoM is located in the high position. This is most likely due to the fact that an increased CoM height increases the load transfer, the vertical load “moved” from the inside to the outside wheels due to the overturning moment caused by the centripetal acceleration in the curve. The increased vertical load causes a smaller $Y/Q_{2m,max}$ ratio. The rest of the evaluation will therefore focus on the asymmetric parameters for the runs with the low level vertical CoM position. All the objective values for these runs are plotted in Figure 92 as a function of one parameter at the time.

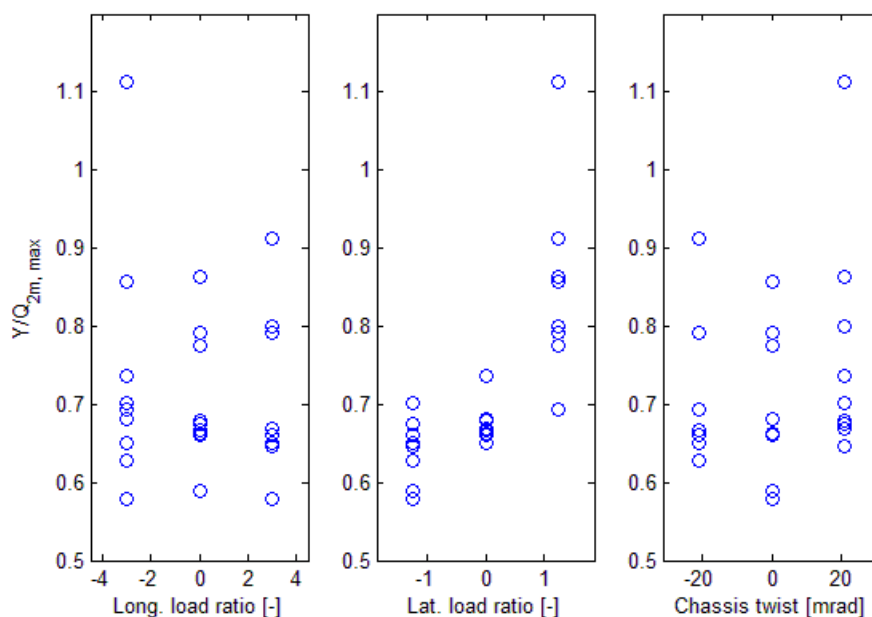


Figure 92 Objective values plotted as a function of one parameter at the time.

Some information can be obtained from Figure 92, but to better understand how the parameters interact, a more formal evaluation is performed where a second order polynomial is fitted to the 27 runs that constitute the full factorial for the three asymmetric parameters at the nominal CoM height. This task is performed using the Matlab [19] command *regstats*. The polynomial has the form

$$y = K + A_1x_1 + A_2x_2 + A_3x_3 + B_{11}x_1^2 + B_{22}x_2^2 + B_{33}x_3^2 + B_{12}x_1x_2 + B_{13}x_1x_3 + B_{23}x_2x_3 \quad (31)$$

where x_1 denotes longitudinal load distribution, x_2 lateral load distribution and x_3 the chassis twist. The polynomial is fitted in a non-dimensional form (variable ranges from -1 to 1). This makes it possible to directly compare the sensitivity of each parameter or interaction from the magnitude of the polynomial coefficients. The coefficient magnitudes are still dependent on the parameter levels used in the DOE.

The obtained numerical values for the coefficients are presented in Table 24. The R-squared quality index is 0.86.

Table 24 Regression coefficients for second order polynomial

Coefficient	K	A_1	A_2	A_3
Value	0.632	-0.016	0.105	0.032
Coefficient		B_{12}	B_{13}	B_{23}
Value		-0.011	-0.057	0.024
Coefficient		B_{11}	B_{22}	B_{33}
Value		0.015	0.067	0.047

Observing the magnitude of the coefficients, it can be concluded that the lateral load distribution is the most significant parameter followed by chassis twist and lastly the

longitudinal load distribution. It can especially be noted that the interaction between the longitudinal load distribution and the chassis twist (B_{13}) is quite large. The interpretation is that the parameters help to increase the objective when they both strive to unload the same wheels. E.g. if the longitudinal load distribution is positive (moved forward) and the twist is negative (unloads the front right-rear left diagonal) they both strive to reduce the vertical load for the outer wheels in the trailing bogie and interact also in a non-linear fashion to increase the Y/Q objective.

Using the obtained coefficients, the estimate of $Y/Q_{2m,max}$ as a function of the three parameters can be plotted for the parameter space in Figure 93. A positive longitudinal load ratio means load moved towards the front bogie, a positive lateral load ratio means increased weight on the inner wheels. A positive chassis twist means that the front left-right rear chassis diagonal has been unloaded. It is noted that the largest value is obtained when all three parameters interact, and when they all strive to unload the outer wheels of the leading bogie. i.e. moving the CoM backwards and inwards and twisting the chassis to unload the front left-rear right diagonal.

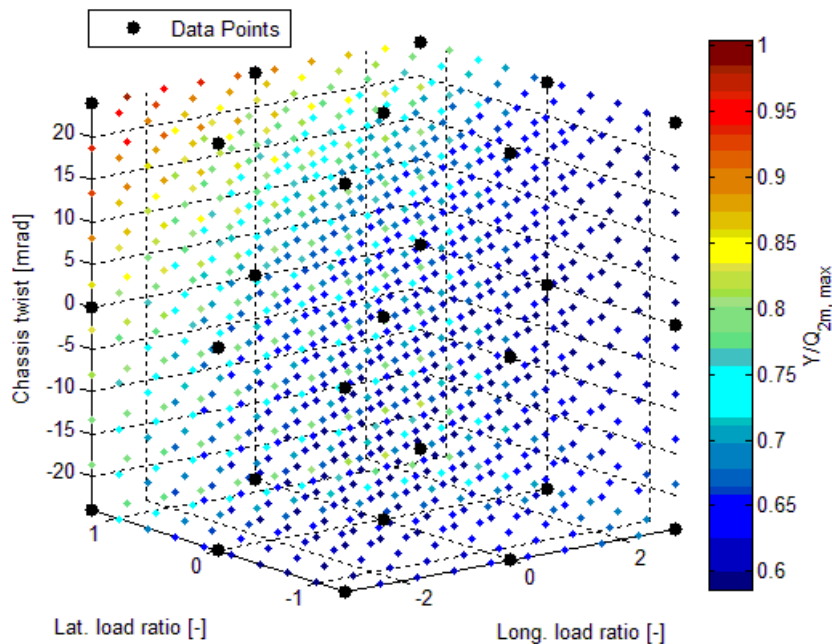


Figure 93 Contour of objective function estimate as a function of longitudinal and lateral load ratio as well as chassis twist. The black dots represent the actual simulated parameter combinations.

A clearer view of the shape of the objective function is obtained in Figure 94 where the response polynomial is plotted as a function of lateral load distribution and chassis twist when the longitudinal load offset is zero. The actual simulated values of the objective function are also included for comparison. The surface fit isn't very good as the R-square value indicates, but captures the overall trends.

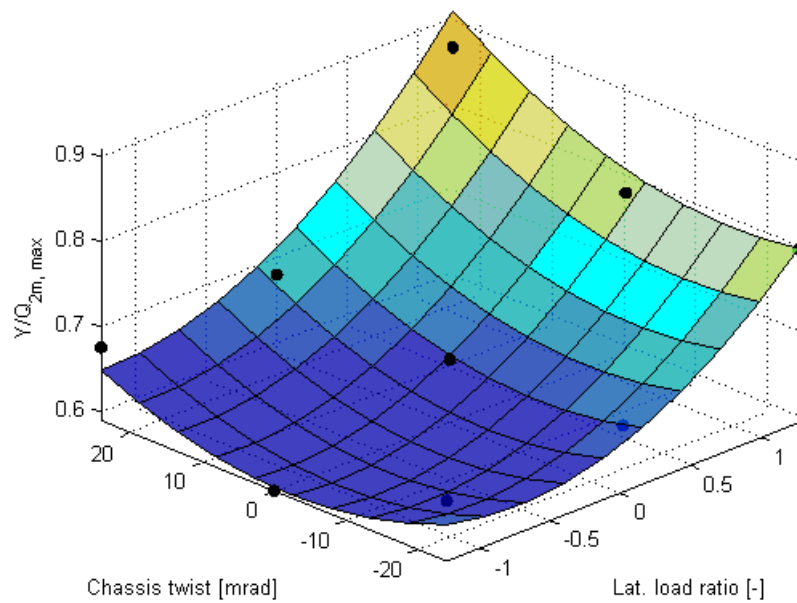


Figure 94 Estimated objective surface as a function of lateral load ratio and chassis twist. The black dots represent actual simulated results.

Of the 27 cases, the largest objective value is recorded for the leading wheel 18 times and for the leading wheel of the trailing bogie 9 times. The trailing bogie typically recorded the largest Y/Q ratio when the chassis twist was negative, i.e. when the front right-rear left diagonal is unloaded and increases the Y/Q ratio for the outer wheels of the rear bogie.

4.5.10 DOE 4 track irregularities

In this parameter study, the influence of isolated lateral, vertical, twist and gauge track irregularities are investigated in combination with four different wheel profiles.

The basis for the track irregularity investigation is the EN 13848-5 standard. The limits values for isolated defects in the wave length interval 1–25m are presented in Table 25.

Table 25 Maximum allowed isolated defects according to EN 13848-5 for D1 and $V \leq 80$ km/h

Irregularity	IL (intervention limit) Indicative	IAL (Immediate action limit)
Gauge max mm	+30	+35
Gauge min mm	-9	-11
Longitudinal level mm	+17-+21	+28
Alignment mm	+15-+17	+22
Twist mm/m	+5 (L=3)	+7 (L=3)

In Sweden, the standards for plain line also apply to turnouts but for gauge. Here the limits are -5 to +15 (Table 32 in BVS 1523.004) [20]. The track parameter amplitudes chosen for this study are the immediate action limit from EN13848-5 for all parameters but gauge, where the Swedish turnout limits are used.

For the simulations, the track irregularities, individual or in combination, are implemented using a sinusoidal basis function with a wavelength of six metres. The maximum amplitude is positioned in the area of largest Y/Q as recorded for a nominal geometry without any significant track irregularities. For the turnout studied in this work with a 190 m radius this is at a distance of 4m from the front of the turnout. The basis function used for the track irregularities is shown in Figure 95.

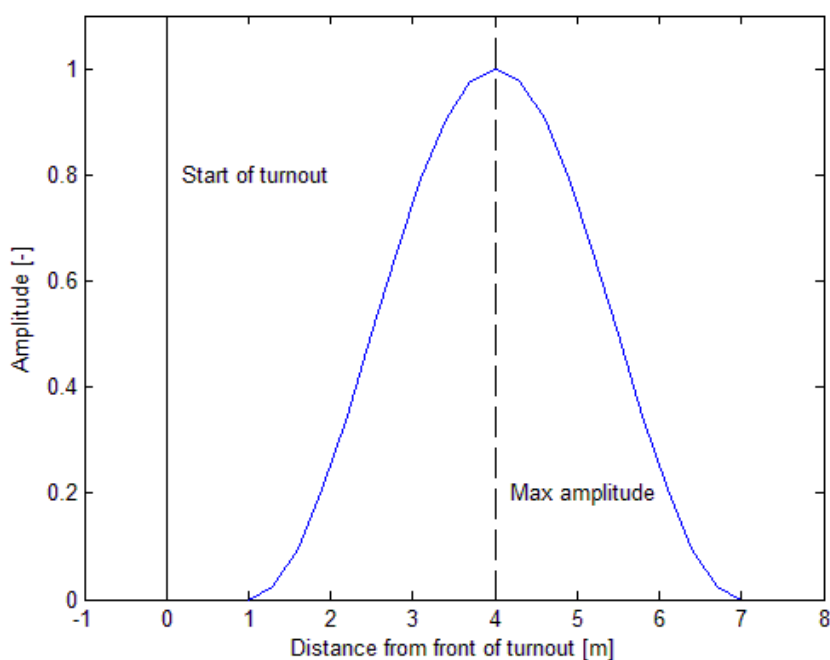


Figure 95. Basis function with 6 m wave-length for track irregularities.

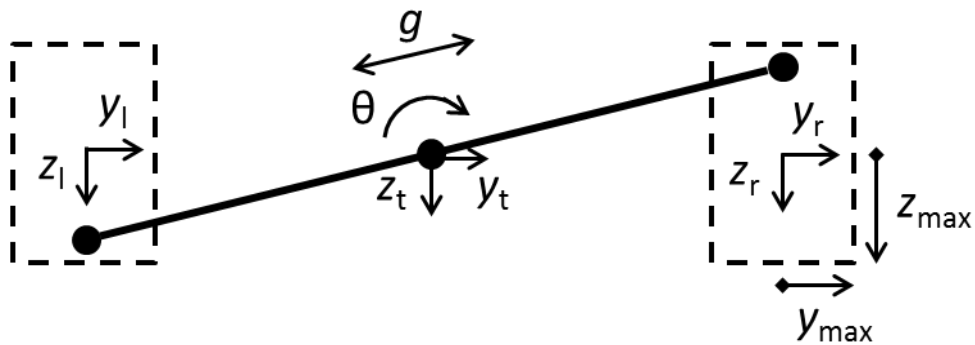


Figure 96 Track DOFs and rail position limits. The longitudinal x-position is directed into the paper.

The in-plane rail positions can be described using four track parameters. Two different parameterizations are shown in Figure 96. Either the vertical and lateral rail displacements on both rails or displacements of the track centre line in combination with inclination and gauge can be used. In this study the rail displacements will be used to parameterize the model and the more intuitive track parameters of the centre line will be used to interpret the results. The rail position limits can be formulated using linear constraints such as:

$$\begin{aligned}
 |z_l| &\leq z_{max} \\
 |z_r| &\leq z_{max} \\
 |y_l| &\leq y_{max} \\
 |y_r| &\leq y_{max} \\
 \frac{|z_r - z_l|}{L} &\leq \text{twist} \\
 y_r - y_l &\leq \Delta g_{max} \\
 y_r - y_l &\geq \Delta g_{min}
 \end{aligned} \tag{32}$$

here L is the longitudinal measurement basis for the twist. As the track irregularities are introduced as isolated defects, the horizontal level is the implicit starting point for twist measurements. These equations can be written as a linear constraint equation on matrix form.

$$\mathbf{B}\mathbf{x} \leq \mathbf{c} \tag{33}$$

This system of equations forms a convex polytope in four dimensions. Chosen from the immediate action limits of Table 25 and the maximum gauge narrowing according to Swedish turnout standards, the parameter limits for equation (32) are defined in

Table 26.

Table 26 Irregularity limits for Equation (32).

Parameter	value
z_{max}	28 mm
y_{max}	22 mm
$twist (L = 3)$	7 mm/m (total 21 mm)
Δg_{max}	15 mm
Δg_{min}	-5 mm

Using equation (32) and the limit values in

Table 26, an algorithm [21] is used to find all the extreme points of the polytope. The extreme points are the points on the polytope where the constraint hyper—planes intersect. This means that all the extreme parameter combinations that lie on the limiting corners that span the polytope can be investigated in simulations. The limiting polytope for (32) is presented in Figure 97. As there are four parameters, the polytope is plotted in three variables at the time while one is set to zero. There are therefore four polytope plots. The extreme points for each plot are the corner points where three surface planes intersect.

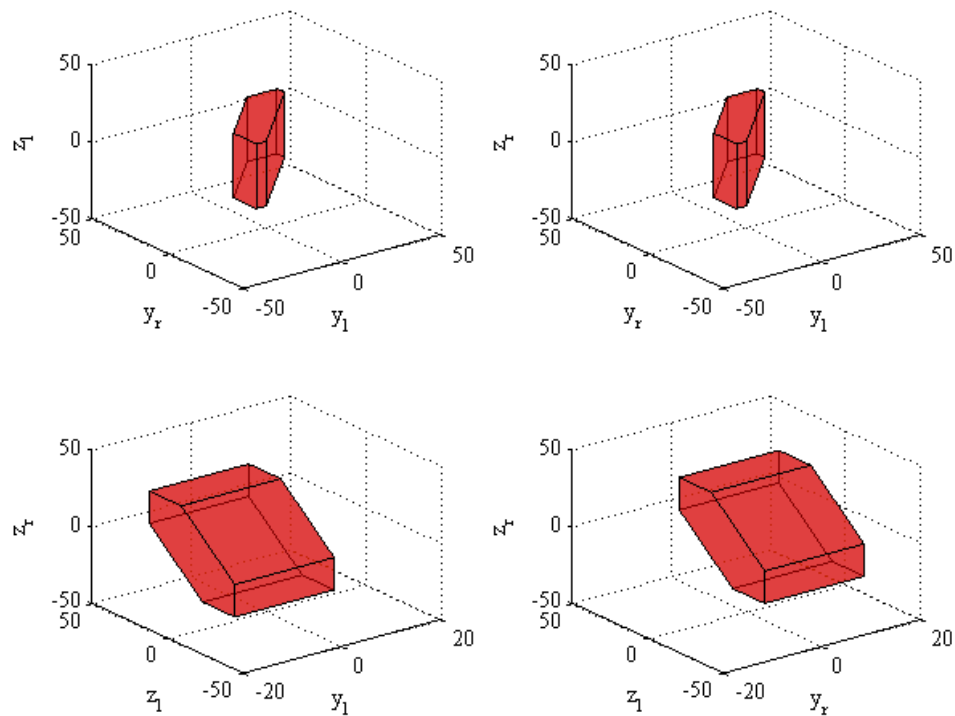


Figure 97 Limiting polytope for (32) using the limits of Table 26 plotted in three variables at the time

The set of polytope extreme points provide the most extreme feasible parameter combinations within the standards, but it does not provide neat parameter levels as in a three level DOE. To improve the resolution and make sure that there are runs that also include the zero level in the track's lateral and vertical dimensions, also the extreme points of the polytopes with the added constraints of $z_r + z_l = 0$ or $y_r + y_l = 0$ in equation (32) were added to the set of runs. In total 60 extreme points were found. In addition to the extreme points the origin is also evaluated which gives a total of 61 runs.

Each extreme point is evaluated for the four wheel profiles of Figure 86. The total number of runs is therefore 244 for one vehicle configuration. The study is performed for both the laden and tare state vehicle.

All vehicle parameters are according to the default configuration. All traffic is therefore in the facing move.

One important aspect of this parameter study is that it does not vary the irregularity wave length or phase, but it was considered to be too computationally demanding to also include them. A study on the relation between measured track irregularity amplitudes and wavelengths can be found in Section 3.3.1.

4.5.10.1 Results Laden State

All the objective values from the 244 runs are plotted along five different parameter dimensions in Figure 98 and Figure 99. In Figure 98 the objective values are sorted according to the wheel profile used in the simulation as indicated in the bottom of the figure. Each blue circle is the objective value of one run. The red squares mark the average objective value in each wheel profile category and the red lines connect the averages. It is noted that the

S1002 wheel profile is associated with both the highest maximum and average objective values of the wheel profiles investigated. In all cases but one it is the leading wheelset that records the highest Y/Q ratio.

In Figure 99 the objectives are plotted with respect to the four different track parameters. As the parameter settings are determined by the extreme points of the polytope, the spacing isn't uniform and the settings of the other parameters aren't the same for each parameter level. For example the low Y/Q obtained for the extreme settings of the track vertical position (top right figure) is most likely due to the fact that these settings do not allow for any track twist as both rails are at the maximum allowed vertical position at the same time. It can be seen in the twist plot (bottom right) that the variation and objective levels are quite low for all the cases where the track twist is zero. A positive track twist indicates a track inclination towards the inside of the turn. The conclusion from the figure is that the Y/Q-ratio is very sensitive to the track twist but not so sensitive to the other track parameters. This is because the difference in objective values between the zero—level and the non-zero levels is distinctly larger for the twist parameter.

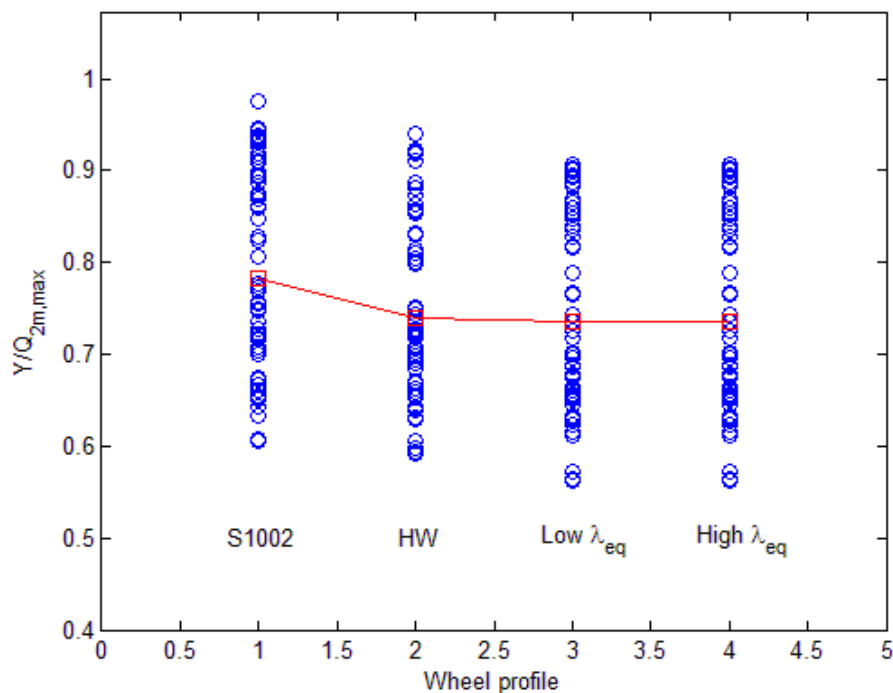


Figure 98 Damage objectives for four different wheel profiles in the laden state.

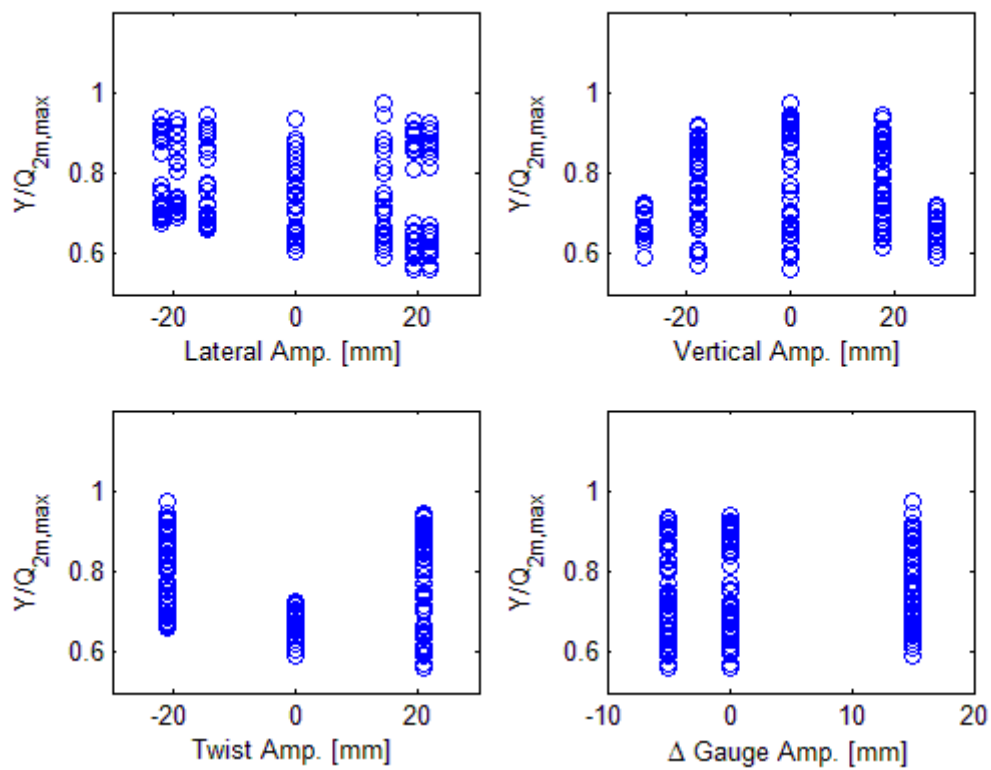


Figure 99 Objective values for all runs plotted in the four different track parameters.

Considering the Y/Q ratios for all evaluated wheels in Figure 100, it can be observed that the curves describe a characteristic “camel—back” double bump pattern around the maximum values. A closer investigation reveals that the location of the two peaks depend upon the direction of the track twist. If the track is twisted towards the outside of the turn the maximum Y/Q is recorded before the 4 m position. If the track is twisted towards the inside of the turn the maximum Y/Q is obtained after the 4 m coordinate.

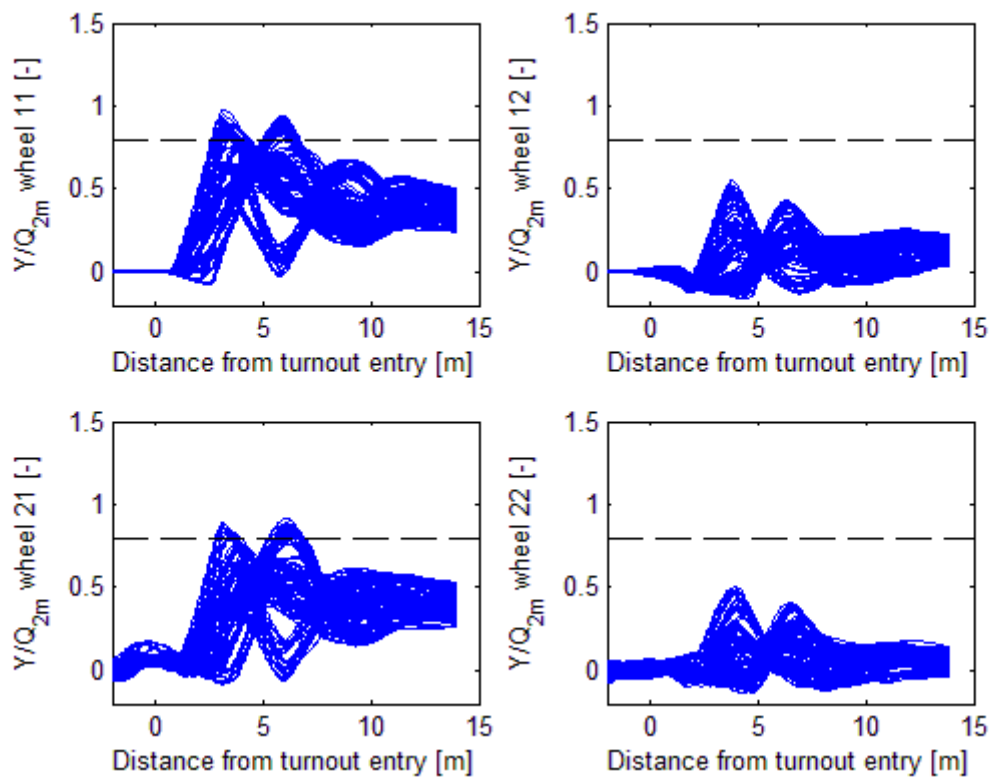


Figure 100 Y/Q evaluated as a 2m sliding average for the outer wheels. 11 is the leading wheelset. The dotted lines are $Y/Q=0.8$.

The reason for these phenomena is that in the first case the evaluated wheels are unloaded when they enter the dip. In the second case the wheels are unloaded first after they have passed over the top of the bump.

To better understand the influence of the different track irregularities and their combinations, a second order polynomial is fitted to the results. As the largest $Y/Q_{2m,max}$ value was recorded for the S1002 wheel profile, this curve fit will only be performed for the results associated with this wheel profile. The polynomial is on the same form as in DOE3, but this time for four variables where x_1 is for the lateral amplitude, x_2 the vertical, x_3 the track twist and x_4 the gauge change. The polynomial coefficients can be studied in Table 27. This polynomial expression is quite sufficient to fit the data as the R-squared value is 0.95. It can be observed that two coefficients are significantly larger than the others. These are the second order coefficient for the track twist, B_{33} and the interaction term between the lateral track position and twist B_{13} .

Table 27. Polynomial coefficients for track parameters. Lateral (1), vertical (2), twist (3) and gauge (4).

Coefficient	K	A_1	A_2	A_3	A_4		
Value	0.674	-0.041	0.005	-0.04	-0.018		
Coefficient		B_{11}	B_{22}	B_{33}	B_{44}		
Value		-0.003	-0.006	0.137	0.045		
Coefficient		B_{12}	B_{13}	B_{14}	B_{23}	B_{24}	B_{34}
Value		0.017	-0.116	0.015	-0.003	-0.005	0.023

To better understand how these parameters interact, the fitted polynomial is used to plot a response surface in only the normalised lateral track position and the normalised track twist. The result can be found in Figure 101. The graph suggest that the worst combinations of a lateral track fault and a twist is when either the lateral track deviation is directed inwards (positive amplitude) and the twist is leaning outwards (negative amplitude) in the switch—curve or vice versa. The interpretation of this relation connects to the results and discussion for Figure 100.

If the track is twisted outwards in the switch—curve, the outer wheels will start to unload vertically as soon as they enter the track irregularity zone as they will encounter a dip relative to the inner wheel. When the vertical force is reduced the best way to increase the Y/Q ratio even further is to increase the Y -force. As the results suggest, this is achieved if a lateral track deviation is applied towards the centre of the curve, pushing the wheel inwards. This mechanism thus causes a large Y/Q upon entering the track irregularity zone.

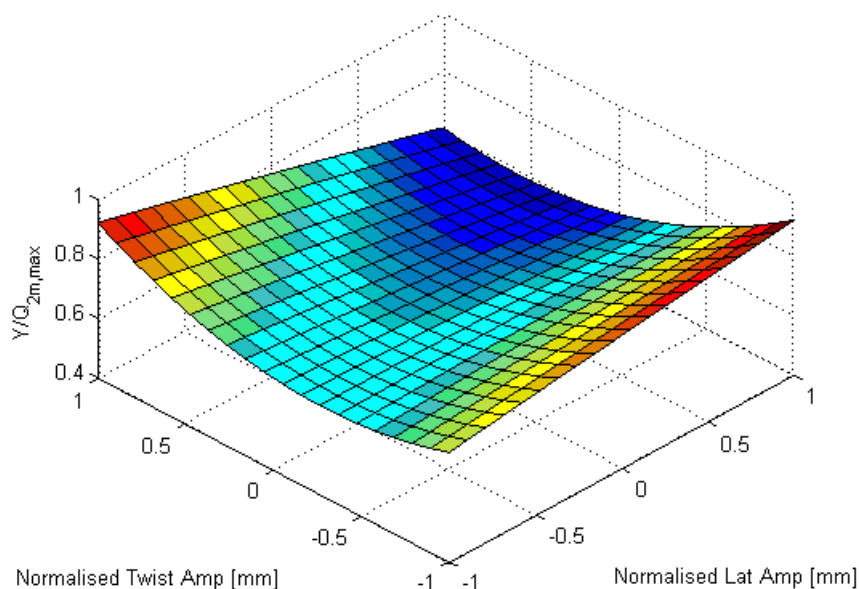


Figure 101 Objective function as a function of lateral and twist track irregularities.

When the signs are reversed, the largest Y/Q ratio is instead obtained further into the turnout. For this parameter combination the outer wheels are vertically unloaded first when they have passed the maximum twist amplitude as the track is now twisted inwards and

creates a bump for the outer wheel. Laterally the wheels are first unloaded when they enter the track irregularity zone as the lateral track irregularity is directed outwards. When the wheels have passed the point of maximum lateral track irregularity and the track error decreases, the wheel will be pushed laterally inwards relative to the track centre line at the same time as the wheel is vertically unloaded, thus causing a large Y/Q ratio.

The worst track parameter settings associated with these two irregularity modes which cause large Y/Q -ratios are presented in Table 28. It can be noted that a gauge change of zero doesn't exist in combination with the other parameters at these settings as it is not an extreme point on the polytope. The "twist outwards" case provides a slightly larger objective value than the "twist inwards" case.

Table 28 Worst case track irregularity parameters.

Case\Variable	Lateral [mm]	Vertical [mm]	Twist [mm]	Δ Gauge [mm]
Twist outwards	14.5	0	-21	15
Twist inwards	-14.5	0	21	15

Wheel lift of a few mm is present in some of the simulations for this parameter study. The magnitudes are small however, and are difficult to use for any evaluation purposes.

4.5.10.2 Results Tare State

The same graphs as presented for the laden case have been generated for the tare case to visualize the influence of the five different parameters as seen in Figure 102 and Figure 103. Also for the tare case the S1002 wheel profile records both the maximum objective and the largest average objective value. For the track parameters in Figure 103 the trends are very similar to the laden case.

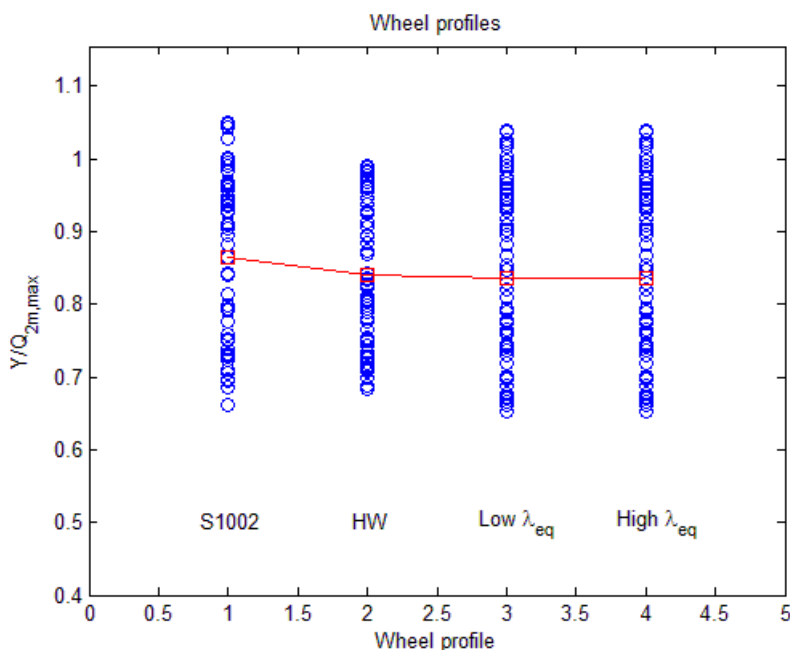


Figure 102 Damage objectives for four different wheel profiles in the tare state.

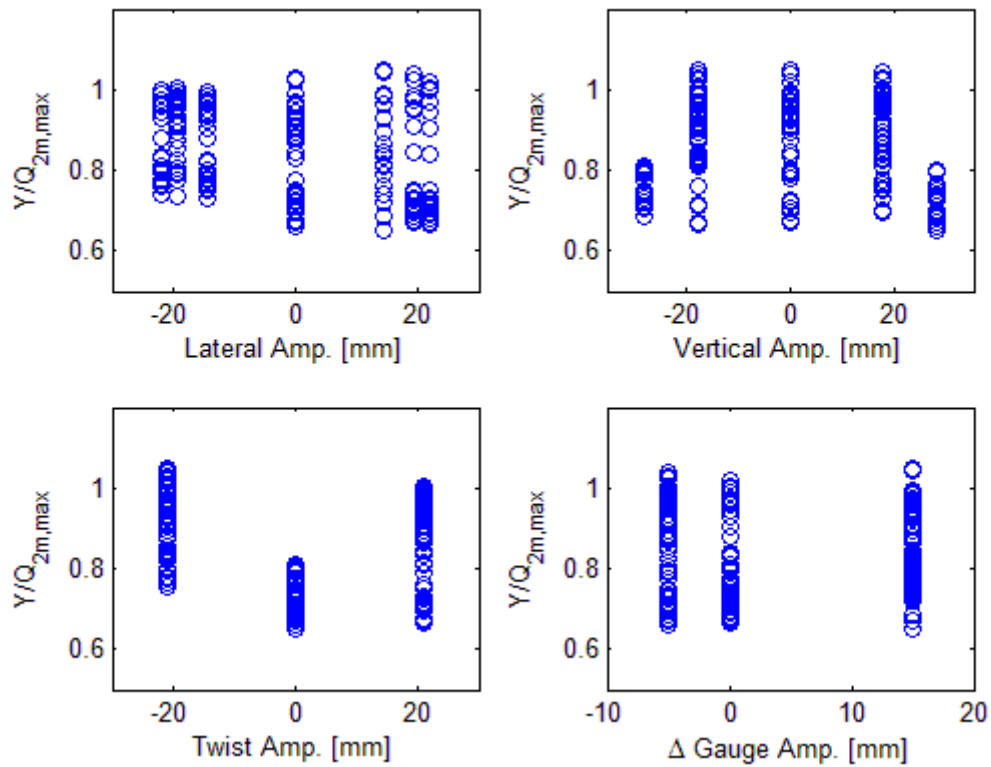


Figure 103 Objective values for all runs plotted in the four different track parameters.

Also for the tare case the two different twist directions show their significant signature in the Y/Q ratios. The parameter settings are shown in Table 29. Even though the parameter setting is not the same for the inward twist, the same general trend can be found as for the laden case.

Table 29 Bad case track parameter settings for different evaluation criteria and twist directions.

Case\Parameter	Lateral	Vertical	Twist	Δ Gauge
Twist outwards [mm]	14.5	0	-21	15
Twist inwards [mm]	-19.5	0	21	-5

Further support for the similarity with the laden case can be found in Table 30 which presents the polynomial coefficients for a polynomial of the same form as for the laden case. Comparing the two cases, the squared coefficient for the twist (B_{33}) is still very dominant while the lateral and twist interaction (B_{13}) is still the second largest coefficient.

Table 30 Polynomial coefficients for track irregularities.

Coefficient	K	A_1	A_2	A_3	A_4		
Value	0.72	-0.060	0.019	-0.038	-0.006		
Coefficient		B_{11}	B_{22}	B_{33}	B_{44}		
Value		-0.034	-0.024	0.195	0.025		
Coefficient		B_{12}	B_{13}	B_{14}	B_{23}	B_{24}	B_{34}

Value		0.002	-0.068	0.044	-0.038	-0.007	0.006
-------	--	-------	---------------	-------	--------	--------	-------

While very small wheel lift amplitudes were recorded for the laden case, wheel lift amplitudes starts to become significant in the tare case, even though for only a few parameter settings. The S1002 wheel profile records the largest wheel lift amplitude close to 5 mm calculated using a sliding 2m average.

4.5.10.3 The weight effect

Comparing the two load—states, the load effect can be calculated from the mean objective values in the two DOEs. The average objective value for the laden case is $\bar{y}_{\text{laden}} = 0.748$ and for the tare case $\bar{y}_{\text{tare}} = 0.844$. The weight effect can then be calculated as:

$$E_{\text{load}} = 100 \frac{(\bar{y}_{\text{laden}} - \bar{y}_{\text{tare}})}{\bar{y}_{\text{tare}}} = -11.4\% \quad (34)$$

The average $Y/Q_{2m,\max}$ objective is thus 11.4% smaller in the laden case compared to the tare case.

4.5.11 Summary of parameter studies

In total, the influence of 25 vehicle and track parameters on derailment risk has been investigated in four different parameter studies. The division of the parameters into several studies was considered necessary considering the large number of parameters and their different characteristics. The drawback is that possible interactions between parameters in different parameter studies cannot be detected. It is important to note though that parameters that have significant interactions typically also have significant first order effects and will be detected anyhow.

The overall summary of the parameter studies is that the most significant parameters are:

- Friction in all investigated locations

It is hardly surprising that the wheel—rail friction coefficients have a large influence on the derailment risk as this is a well-known phenomenon elegantly formulated in the Nadal criterion. It also comes as no surprise that increased friction in the primary and secondary suspension increases the Y/Q -ratio as they will contribute to increase the yaw stiffness. From a detection point of view, friction is a parameter that is difficult to monitor, even though it could be monitored indirectly through e.g. yaw stiffness tests. However, the simulations though highlight that wheel/rail friction modifiers could be used to decrease the derailment propensity. They also highlight that a well maintained suspension is a good way to reduce the derailment risk.

- Skew loading

It is shown that skew loading, and especially combined lateral and longitudinal skew loading, has a strong influence on the risk of derailment. The interaction between lateral skew loading and side bearer deformation is an area of interest for further studies. As soon as the side bearers are coil bound, the roll stiffness will be significantly increased and the vehicle will be much more sensitive to track irregularities as the load transfer between the wheels will be much more dramatic at the higher stiffness.

- Chassis twist

The chassis twist has been shown to have a significant influence on derailment risk. It also reduces the margin before the sidebearers are coil bound which can interact with the skew loading.

- Track irregularities

As expected the track twist came out as the most significant track parameter. What might be novel is that an interaction with the lateral track alignment was found. As stressed before, a severe limitation of this analysis is that the space of possible track irregularities is vast, and only a small subset of it has been explored.

4.5.12 Bad case

Based on DOE 1-4, it can be concluded that the tare state is worse than the laden state on average as evaluated by the difference in average $Y/Q_{2m,max}$. The factors that could make the laden case worse than the tare ditto are the skew loading parameters, as the tare state vehicle can't have any significant skew loading. According to Table 24, the coefficients associated with the longitudinal and lateral skew loading are sufficiently large to make the partly laden case the worst of the two for large amounts of skew loading. Therefore focus is mainly put on the laden vehicle, but also the tare state will be investigated.

The results from the four parameter studies will now be combined to a bad case based on the semi laden vehicle from DOE 3 with a total weight of 66.6T. This vehicle is chosen as it allows for the maximum longitudinal load ratio of 1:3 without exceeding an axle load of 25T.

For DOE1&2 it is easy to find the worst setting. As the effects measure the difference in objectives between a high and a low parameter level, the higher parameter value is worse if the effect is positive and the lower parameter level is worse if the effect is negative. As all parameter settings are evaluated in DOE 3, the parameter setting associated with the largest $Y/Q_{2m,max}$ ratio can be used directly.

Table 31 Bad case parameter setting compared to the nominal configuration. *Increased torsional stiffness had a negligible negative influence on the Y/Q ratio, but a rigid car body should be the most conservative option when wheel lift is considered.

<i>Parameter</i>	<i>Nominal</i>	<i>Bad Case</i>
Side bearer friction coefficient [-]	0.3	0.5
Centre plate friction coefficient [-]	0.3	0.5
Primary suspension friction coefficient [-]	0.4	0.5
Side bearer play [-]	1	0
Longitudinal play in primary suspension [-]	4	4
Lateral play in primary suspension [-]	10	10
Scale factor for vertical primary spring stiffness [-]	1	1
Scale factor for horizontal primary spring stiffness [-]	1	1.2
Bogie c-c distance [m]	5.89	3.5
Axle c-c distance in bogie [m]	0.9	0.9
Chassis torsional stiffness [MNm/rad]	rigid	rigid*
Traffic move [-]	facing	facing
Wheel polygonalization [mm]	0	0
Speed [km/h]	40	45
W/r tread friction coefficient [-]	0.5	0.5
W/r flange friction coefficient [-]	0.5	0.5
Longitudinal load ratio for laden case.	1:1	1:3

Lateral load ratio for laden case.	1:1	1:1.25
Chassis twist [mrad]	0	24
Car body Centre of Mass vertical. [m] (tare/laden)	1.39/1.69	1.39/1.69
Lateral track irregularity amplitude [mm]	0	14.5
Vertical track irregularity amplitude [mm]	0	0
Track twist irregularity amplitude [mm]	0	-21
Track gauge irregularity amplitude [mm]	0	15
Wheel profile	S1002	S1002

For the track parameters, all the extreme parameter combinations feasible within current standards are evaluated, so in this case the parameter setting associated with the largest objective value is taken. For the tare state the skew loading is zero as the cargo load is zero. The bad case is compiled and compared to the nominal parameter setting in *Table 31*.

As the same track parameter setting recorded the largest Y/Q with the S1002 wheel profile for both the tare and the laden state, this track geometry is used.

The following investigations starting from the assembled bad case are intended to answer the questions for Task 2-4 in Section 4.4.

4.5.12.1 Bad Case (Partly) Laden

The starting point for this investigation is the bad case defined in *Table 31* using the partly laden car body from DOE3 to allow for skew loading without exceeding the maximum axle load. The bad case is parameterized using scale factors multiplied to the parameters or parameter sets that were found to be the most influential. These are the worst combination of track parameters and skew loading as described by the longitudinal and lateral load offset and chassis twist. The friction coefficients were not included in this study to reduce the computational burden of the investigation. Also, friction is the variable in this setting which is the most difficult to monitor. It is therefore considered appropriate to keep the friction at a fixed bad case setting and study the influence of the more easily monitored parameters. The parameterized bad case is presented in *Table 32*. To parameterize the model more easily, the load ratios have been replaced by the corresponding CoM positions.

Table 32 Parameterization of selected parameters for bad case vehicle. #BB is the bogie-bogie c-c distance.

Lateral track irregularity amplitude [mm]	$14.5 * kTrack$
Vertical track irregularity amplitude [mm]	$0 * kTrack$
Track twist irregularity amplitude [mm]	$-21 * kTrack$
Track gauge irregularity amplitude [mm]	$15 * kTrack$
Longitudinal Car Body CoM	$0.285 * BB * kSkew\#$
Lateral Car Body CoM	$0.09 * kSkew$

Chassis twist [mrad]	21*kTwist
----------------------	-----------

The scale factors $kTrack$, $kSkew$ and $kTwist$ in Table 32 are each assigned the levels [0, 0.2, 0.4, 0.6, 0.8, 1, 1.2]. All combinations of the scale factors are evaluated resulting in $7^3 = 343$ simulations. The results for one such parameter study is presented in Figure 104. For each evaluated scale factor combination the resulting $wl_{2m,max}$ is categorized into three spans as indicated in Table 33.

Table 33 classification table for wheel lift

Range [mm]	Mark
$0 \leq wl_{2m,max} \leq 6$	Green circle
$6 < wl_{2m,max} \leq 20$	Yellow circle
$20 < wl_{2m,max}$	Red triangle

If the $wl_{2m,max}$ is smaller than 6mm it is assumed that no derailment will occur. If the $wl_{2m,max}$ is between 6 mm and 20 mm the train will not derail in simulation, but the large wheel lift amplitude indicate that it has entered an unstable region from which it might derail with a small disturbance. If the wheel lift exceeds 20 mm the flange will climb on top of the rail and the train derails in simulation. As can be observed in Figure 104, there are parameter combinations that lead to derailment. Therefore, according to these simulations, derailment can occur for a vehicle within standards if many parameters interact. From the plot it can also be noted that the most sensitive parameter sets are the track irregularities and skew loading while the chassis twist, at the selected amplitude, does not have an equally large influence.

To investigate the propensity for derailment in a switch as compared to a standard curve, the parameter study presented in Figure 104 has been performed for the case when the switch rail geometry has been replaced by a standard 60E1 rail profile with 1:30 inclination (which is the base profile also for the turnout geometry). The results are presented in Figure 105. Comparing Figure 104 and Figure 105, it can be concluded that there are more cases of derailment for the switch rail geometry than the standard rail case. To obtain the same risk of derailment in a switch as in a curve of the same geometry, the track irregularity amplitudes would thus have to be tightened for the switch. This investigation is not fair in the sense that switches already have tighter tolerances with regards to gauge (at least in Sweden) and for the complete picture the curve with standard rails should be investigated using the full set of parameter studies and with the appropriate gauge limit.

Another comparison to the results in Figure 104 can be found in Figure 106. In Figure 106 the bad case base configuration has been replaced by the nominal vehicle while the parameterized variables are the same. This means among other things lower friction in the suspension, lower velocity etc. as specified in Table 31. It can be noted that all the less significant parameters can make a substantial difference for the derailment propensity if they are all changed at the same time.

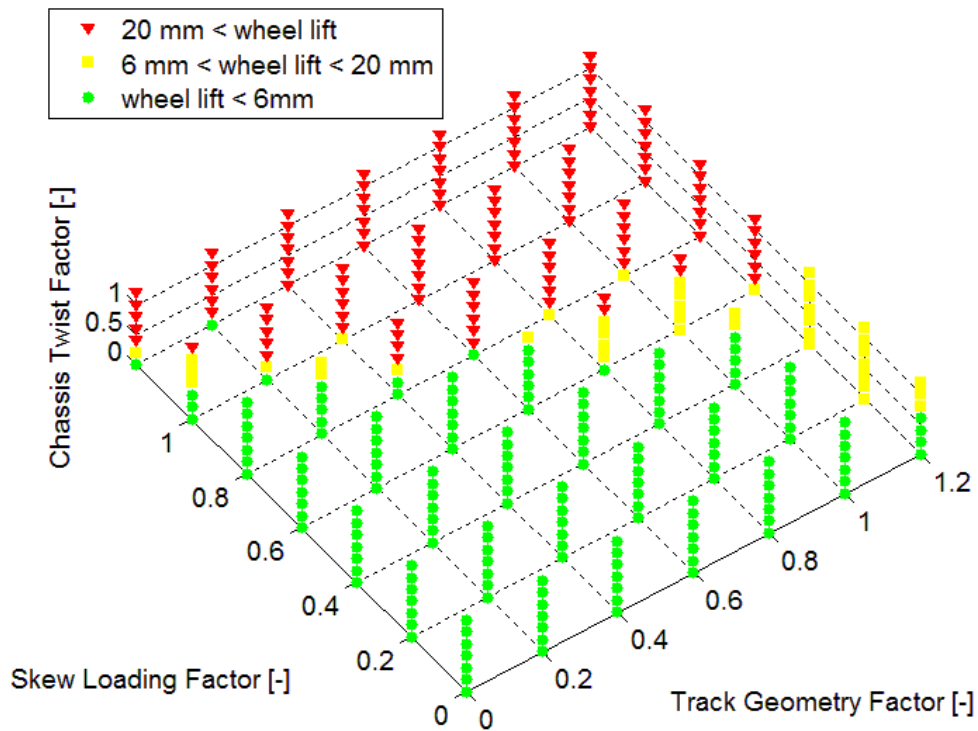


Figure 104 Maximum wheel lift as a function of normalised track irregularity, skew loading and chassis twist factors. Bad case vehicle and switch rail geometry

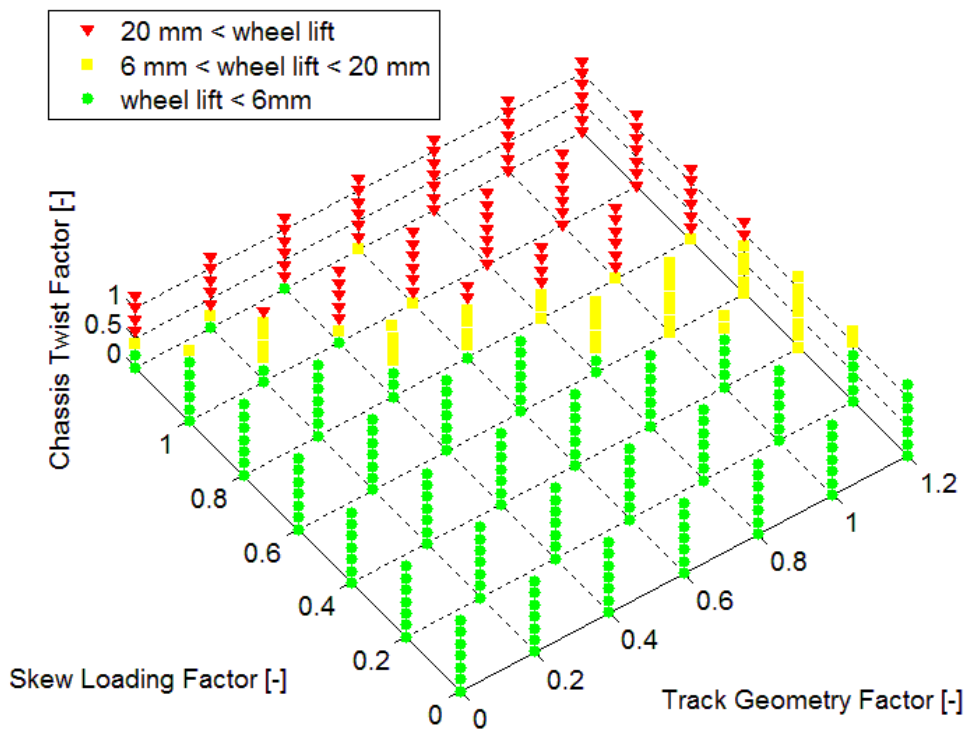


Figure 105 Maximum wheel lift as a function of normalised track irregularity, skew loading and chassis twist factors. Bad case vehicle and standard rail geometry.

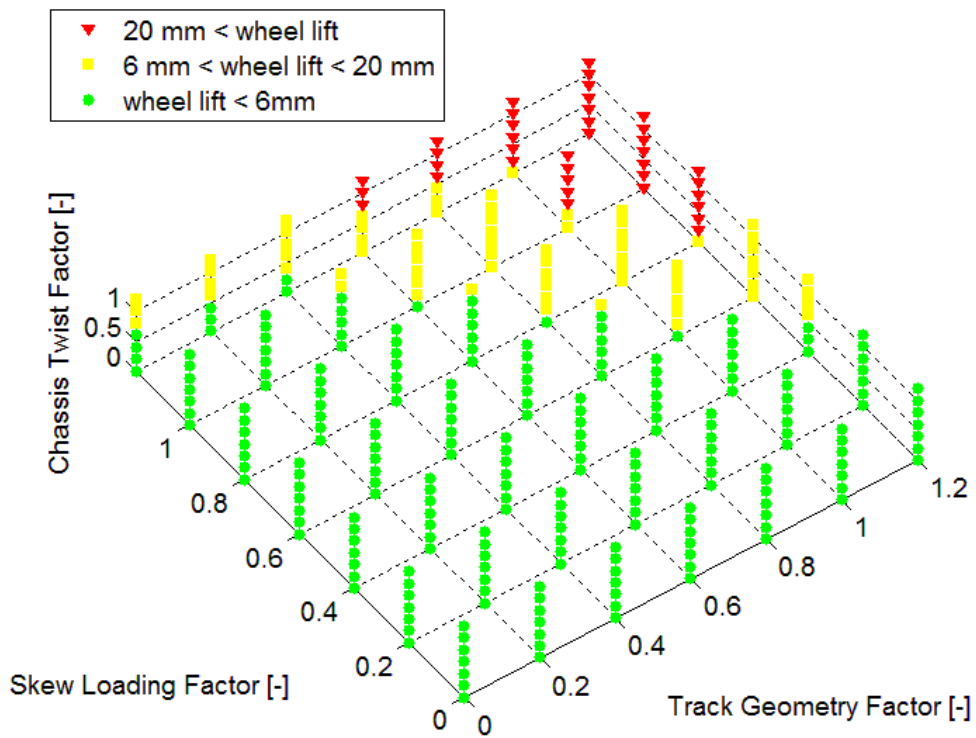


Figure 106 Maximum wheel lift as a function of normalised track irregularity, skew loading and chassis twist factors. Nominal vehicle and switch rail geometry.

4.5.12.2 Bad Case Tare

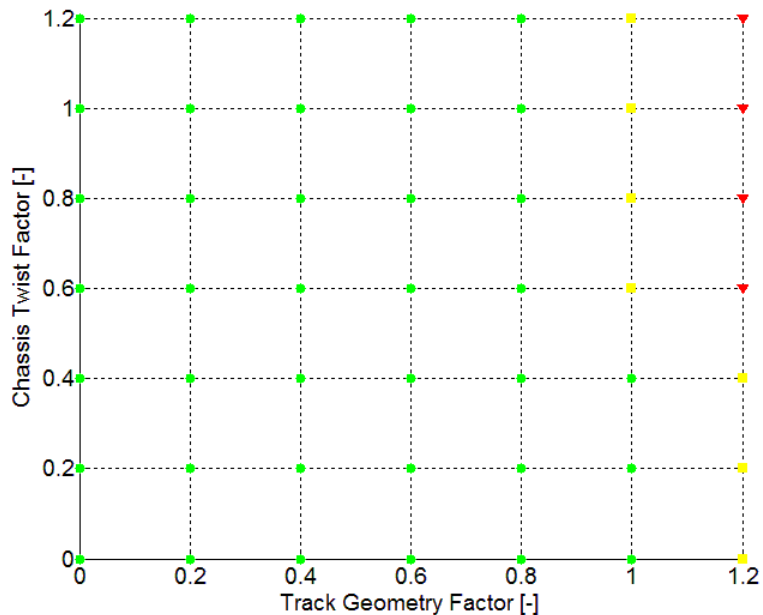


Figure 107 Maximum wheel lift as a function of normalised track irregularity and chassis twist factors. Bad case vehicle in tare state and switch rail geometry.

As skew loading isn't applicable for a tare state vehicle, the bad case parameter study is reduced to an investigation in two parameters; the track irregularities and chassis twist. The result from such a study is presented in Figure 107. Comparing these results to those of the laden case in Figure 104, it can be noted that they are similar to those of a partly laden vehicle with a skew loading scale factor of about 0.5. It can be concluded that the tare state vehicle, as indicated by the parameter studies, has a larger propensity for derailment unless a significant skew load is introduced for the laden vehicle. It should be pointed out that these simulations are for vehicles with rigid car bodies. Different torsional flexibilities might be expected for laden and tare state vehicles in a real traffic situation.

4.5.12.3 Discussion and conclusions for bad case

According to the limit surface of the parameterized bad case, the studied freight wagon can derail even if all parameters are within standards, assuming that the levels of the parameters not obtained from standards are reasonably estimated. There are however many indications that the parameter combinations that lead to derailment in these simulations are very unlikely.

- Considering the relation between track irregularity amplitude and irregularity wave length found by DB and shown in Section 3.3.1, a track scaling factor $kTrack$ of about 0.5 appears to be a realistic bad case in track.
- Considering the measured load distributions of Figure 33 and Figure 35, it can be observed that it is very unlikely that a vehicle features a skew loading combination which is close to both the lateral and the longitudinal limit.
- It is not very likely that all parameters are at their worst setting at the same time, and the derailment propensity can be significantly reduced if most of the parameters are at more normal levels as indicated by the difference between Figure 104 and Figure 106.

Just comparing switch rail geometry to standard rail geometry, the found bad case vehicle is more likely to derail in the switch case.

4.5.13 Vehicle parameter limits

In this section a derailment surface is presented as a function of skew loading and chassis twist for traffic through a bad case switch. The objective is to obtain tentative limits for these parameters to fulfill Task 5 defined in Section 4.4.5. The parameters are chosen as they have been found to be among the most influential vehicle parameters while still being possible to monitor using axle load check points. The friction coefficients were also found to be highly influential, but are considered to be much more difficult to monitor and are therefore excluded in this investigation.

The starting point for this study is once again the bad case vehicle-turnout parameter set defined in Table 31. What is considered to be a realistic bad case switch is created by setting the track irregularity scale factor $kTrack$ to 0.5. This value is motivated by the discussion in 4.5.12.3. Considering the distributions of the measured vehicle load imbalances of Figure 33 and Figure 35, it is highly relevant to perform a parameter study where the longitudinal and lateral skew loadings are varied independently. Therefore the $kSkew$ scale factor is replaced by $kSkewLong$ and $kSkewLat$ for the longitudinal and lateral load offset respectively. The parameterization is shown in Table 34 where $kTrack$ has been set to 0.5.

Table 34 Parameterization for derailment limit study as a function of skew loading and chassis twist. #BB is the bogie-bogie c-c distance

Lateral track irregularity amplitude [mm]	12.25
Vertical track irregularity amplitude [mm]	0
Track twist irregularity amplitude [mm]	-10.5
Track gauge irregularity amplitude [mm]	7.5
Longitudinal Car Body CoM	$0.285 * \text{BB} * k_{\text{SkewLong}} \#$
Lateral Car Body CoM	$0.09 * k_{\text{SkewLat}}$
Chassis twist [mrad]	$21 * k_{\text{Twist}}$

Using the scale factor range [0, 0.2, 0.4, 0.6, 0.8, 1, 1.2] for the three scale factors of Table 34, all $7^3=343$ combinations are evaluated. The categorized wheel lift results ($wl_{2m,max}$) for all parameter combinations are shown in Figure 108. As before, a skew loading scale factor of one corresponds to the nominal RIV limit of either a 1:3 load ratio longitudinally or 1:1.25 laterally. It is notable that actual simulated derailments occur when both the lateral and longitudinal skew loading are in their worst positions simultaneously. Fortunately, these combinations are rare in traffic as illustrated by Figure 33 and Figure 35. The appropriateness of the RIV limits can however be discussed as they provide a safety margin when the vehicle is skew loaded in only one direction, longitudinally or laterally, but are insufficient for significant combined skew loading according to these simulations. As before, an overlaid chassis twist can significantly reduce the derailment resistance.

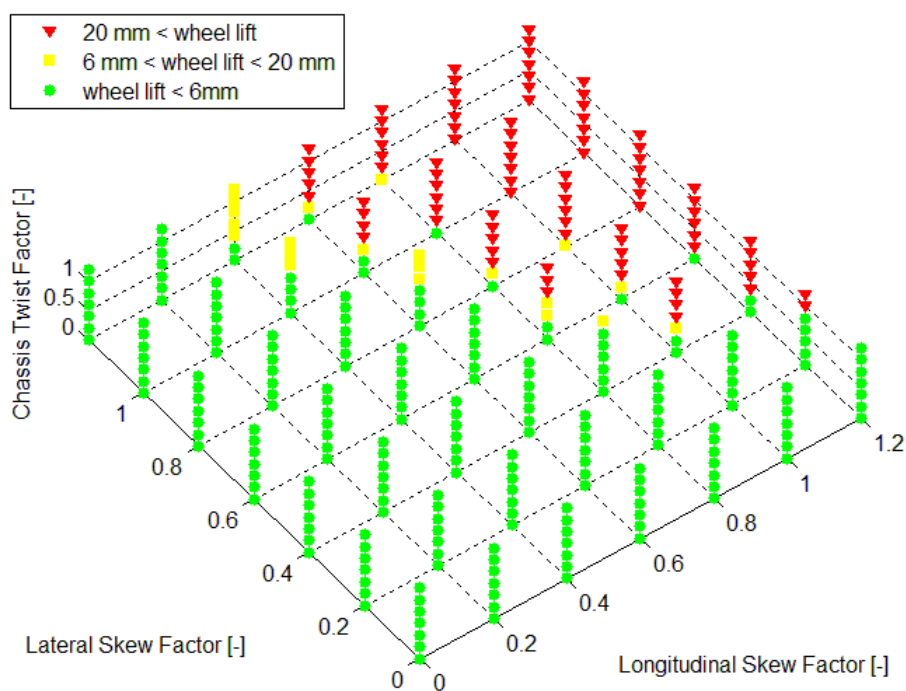


Figure 108 Derailment surface as a function of scale factors for longitudinal and lateral skew loading as well as chassis twist

4.5.14 Vehicle configuration and observed load imbalances

As influential parameters and detectable parameters are two different things, it is of interest to study the wheel load distribution that result from applied skew loading and chassis twist. The idea is that skew load and chassis twist can be estimated from wheel load data obtained from wheel load checkpoints. To obtain estimates of the quasi static wheel loads, simulations were performed over one kilometer of track with light track irregularities for all the 343 parameter combinations defined in section 4.5.13. Then the average vertical wheels loads were taken as the quasi static load distribution. The longitudinal, lateral and diagonal load imbalances were then calculated according to equations (13),(14) & (15)

The correlation between input and related output quantities can be studied in Figure 109. It can be noted that there is a very good correlation between the specified longitudinal CoM offset and the longitudinal load ratio. For a scale factor (*kSkewLong*) of one a longitudinal skew loading ratio of 1:3 is obtained. The relation between the two is not linear as the scale factor is applied to the CoM location and not the longitudinal load ratio itself.

For the relation between the lateral scale factor and the lateral load ratio the picture is a bit more blurred. The lateral skew loading varies somewhat and larger load ratios than expected are obtained. For a *kSkewLat* of one, the obtained lateral load ratio can be as high as 1:1.3 while the nominal static ratio is 1:1.25. This is because the lateral displacement of the carbody Centre of Mass can be significant due to suspension compliance induced by the lateral load imbalance. As the lateral load ratio is sensitive to small offsets, this can explain most of the deviation. Another uncertainty is that a significantly skew loaded vehicles doesn't necessarily run centred on the track. Unsymmetrical contact point locations on the left and right hand side wheels can affect the wheel loading and therefore the skew loading estimates. The variations are explained by the fact that the suspension of the Y25 bogie is highly non-linear. If e.g a side bearer becomes coil bound, the roll stiffness will increase. The same applies if the primary suspension makes the transition from one to two active springs. Therefore the chassis twist and longitudinal load ratio can affect the roll displacement for the same amount of lateral skew loading as the loads can be unevenly distributed in the suspension.

It can be seen that there exist a correlation between chassis twist and diagonal load ratio, but that the spread is large. This is due to the non-linearities of the Y25 suspension as discussed above that can cause unproportional wheel loading. If the objective is to get an accurate measure of a carbody twist, it is therefore better to use data from tare state wagons where the skew loading cannot be significant.

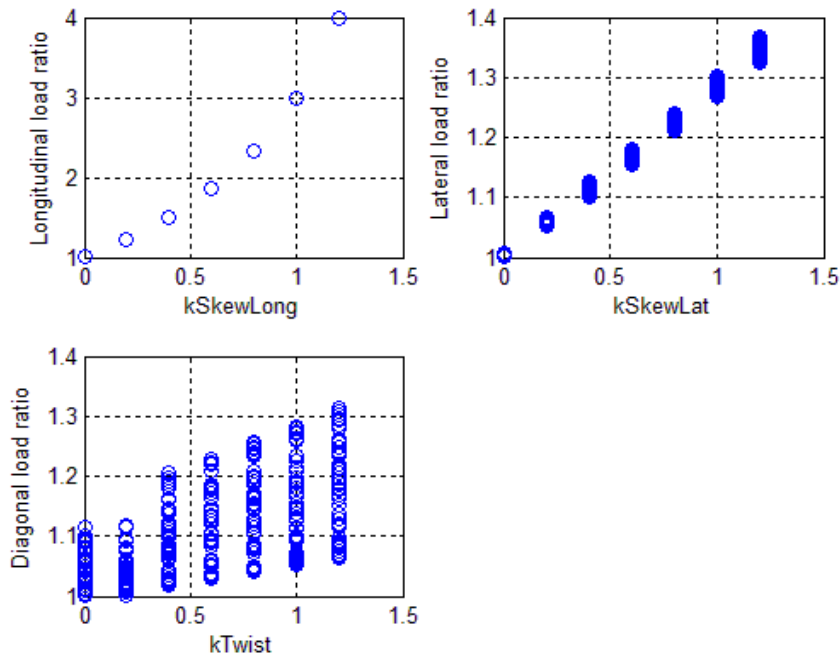


Figure 109 load distributions as a function of input scale factors.

Also histograms of the load imbalance quantities are presented in Figure 110.

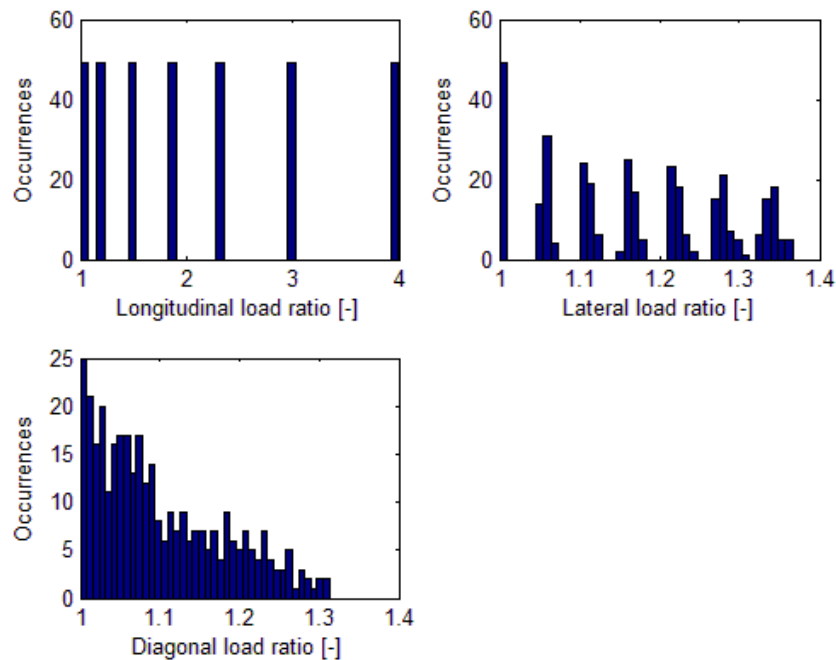


Figure 110 Histograms for load imbalance quantities. Results from simulations of 343 parameter combinations using the parameterization of Table 34

Another way to look at load imbalance is to study the load ratio between the right and left wheel on each axle (16). Histograms of the axle load imbalance for each axle corresponding to the parameter study of Table 34 are presented in Figure 111. As can be expected, the largest axle imbalances are recorded for the leading wheelsets as the parameterized case

strives to unload the front left wheels. In combinations with extreme parameter settings, the vertical load for these wheels can become very small and the axle load imbalances extreme.

To study the axle imbalance as a function of skew loading and chassis twist, the maximum axle imbalance in the wagon is plotted as a function of the longitudinal and lateral skew loading for four different levels of chassis twist in Figure 112. The contour plots are created by interpolation of the simulation data. The lateral and longitudinal load ratios are the actual imbalances calculated from simulation data while $kTwist$ determines the applied chassis twist. It can be noted that even for small levels of chassis twist, the maximum axle load imbalance can be large even for skew loading configurations that are within the RIV limits.

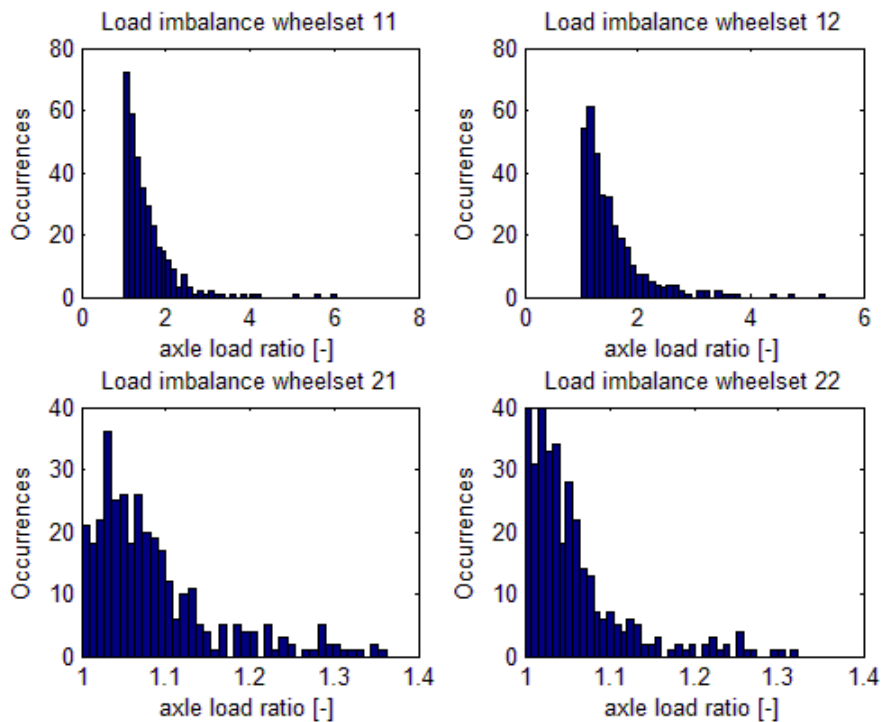


Figure 111 histograms for axle load imbalances. Results from simulations of 343 parameter combinations using the parameterization of Table 34

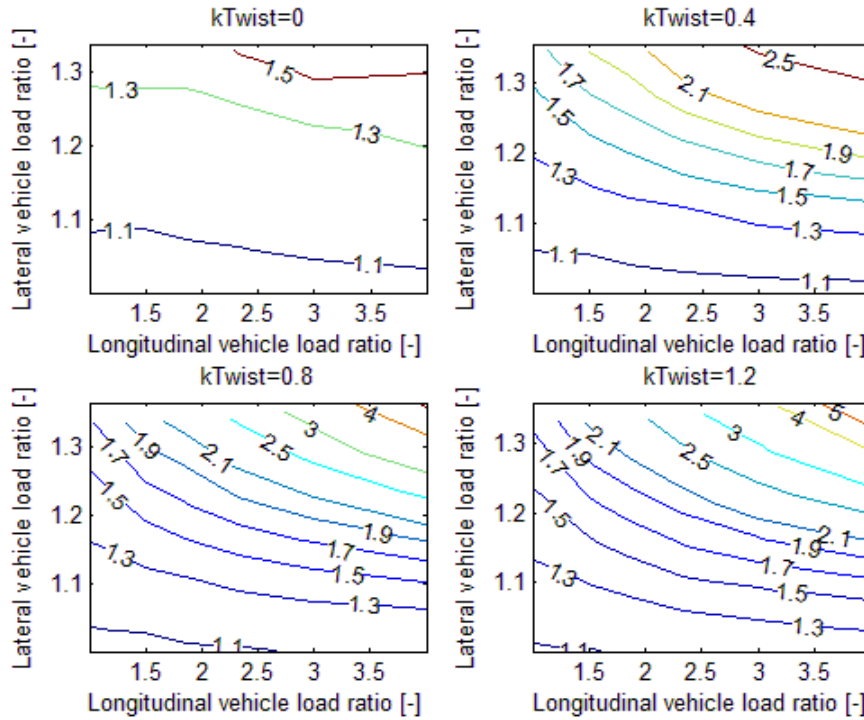


Figure 112 Contour plots of maximum axle imbalance in a wagon as a function of longitudinal and lateral skew loading for four different levels of chassis twist.

In order to study the derailment limit as function of load imbalance parameters that can be obtained via wheel loads (skew loading and diagonal load) the wheel lift results of Figure 108 are now plotted as a function of the observed load imbalance quantities of Figure 110. The resulting graph can be studied in Figure 113. Qualitatively the results are similar to those in Figure 108, but not as structured. Especially the span in the diagonal load imbalance increases significantly with an increased lateral load ratio.

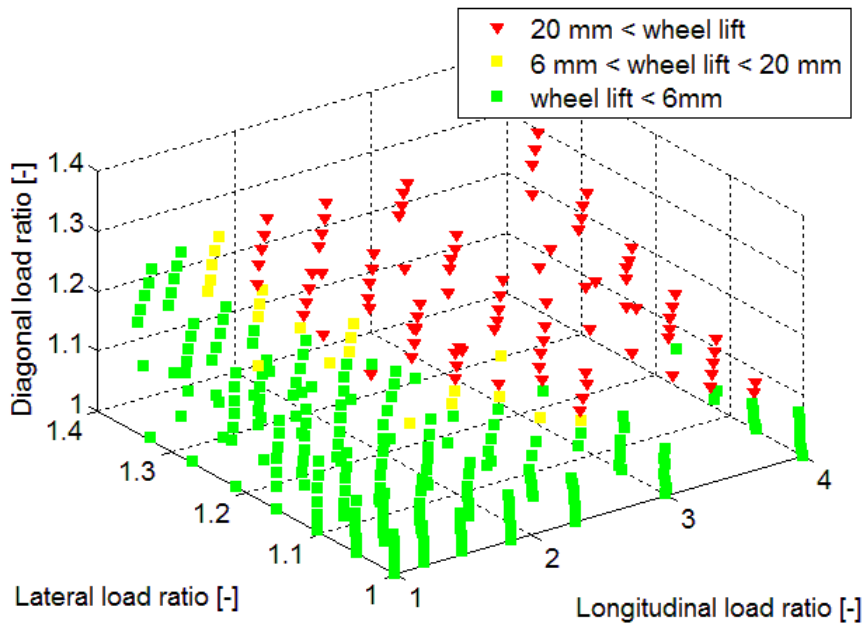


Figure 113 $w_{2m, \max}$ as a function of simulated load imbalance quantities

4.5.15 Load imbalance criteria

If a limit value is to be set for a monitored parameter, it is important that the parameter limit can, as clearly and distinctly as possible, discriminate between derailing and non-derailing vehicles. As a basis for the evaluation of different criteria, the scale factor range associated with Table 34 has been extended to get a better approximation of the derailment surface. The used scale factor ranges are:

$$kSkewLong = [0 \ 0.2 \ 0.4 \ 0.6 \ 0.8 \ 1.0 \ 1.2]$$

$$kSkewLat = [0 \ 0.2 \ 0.4 \ 0.6 \ 0.8 \ 1.0 \ 1.2 \ 1.4]$$

$$kTwist = [0 \ 0.2 \ 0.4 \ 0.6 \ 0.8 \ 1.0 \ 1.2 \ 1.4 \ 1.6 \ 1.8 \ 2.0 \ 2.2]$$

The resulting derailment surfaces as a function of scale factors and calculated load imbalances are shown in Figure 114 and Figure 115 which are thus extended versions of Figure 108 and Figure 113. Single- and multi-variable criteria will be evaluated using these data. The load imbalance (or ratio) quantities used are defined in Section 4.5.5.

It should be noted that the derailment surfaces presented here are evaluated using a cubic grid of input parameters. The actual probability for the different parameter combinations in traffic can differ by many orders of magnitude, and some may never happen at all. Therefore it is recommended that the accuracy of the criteria is also evaluated using data from vehicles in traffic.

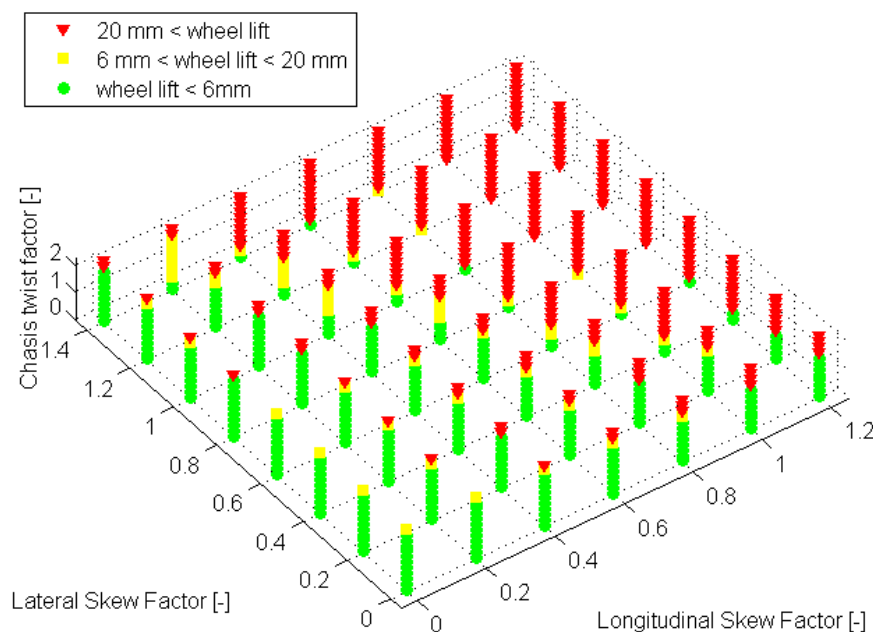


Figure 114 Extended derailment surface illustrated by $wl_{2m, \max}$ as a function of scale factors for longitudinal and lateral skew loading as well as chassis twist

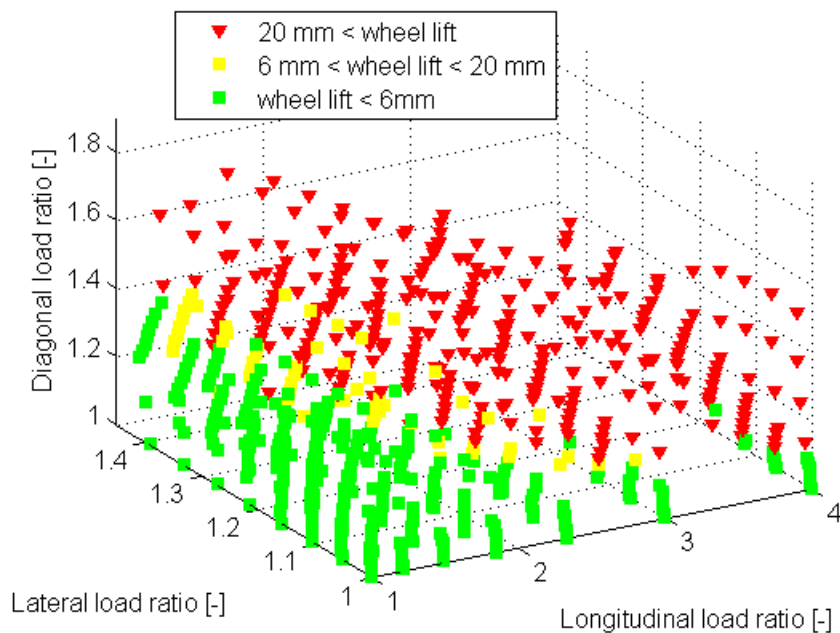


Figure 115 Extended derailment surface illustrated by $wl_{2m, \max}$ as a function of simulated load imbalance quantities

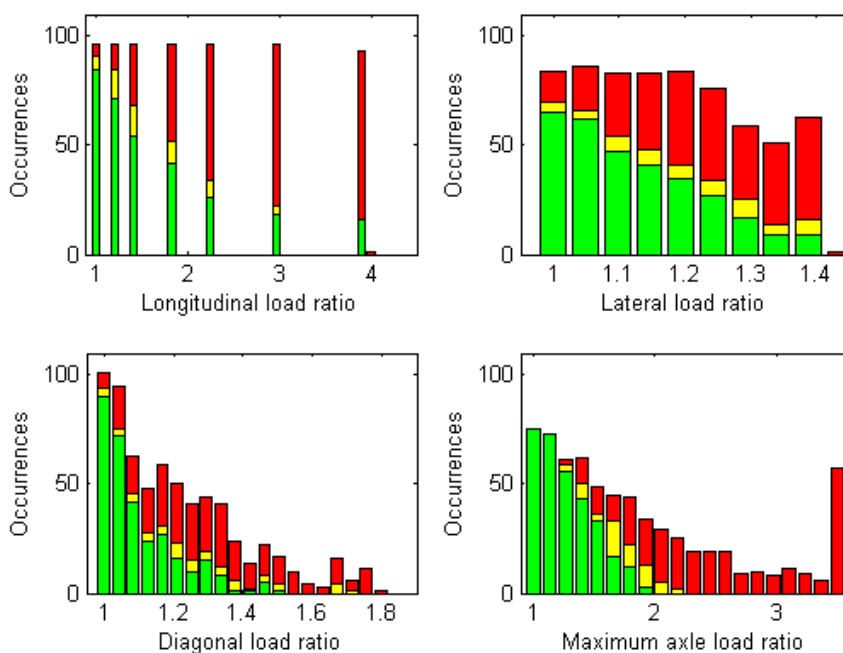


Figure 116 Stacked histograms of wheel lift results as a function of load imbalance parameters. The colour legend is the same as in Figure 114. The last bar in the maximum axle load ratio data represents all values that surpass 3.5.

4.5.15.1 Single parameter criteria

In order to study how well single parameter criteria can distinguish between derailing and non-derailing vehicles, the wheel lift results of Figure 114 are plotted in colour coded stacked histograms for one load ratio at the time in Figure 116. It is noted that the fraction of derailing vehicles increases with an increasing criterion in all four cases, but there is a

significant difference in the level of separation. It can be seen that the maximum axle load imbalance is the criteria that can best discriminate between the derailing and non-derailing vehicles.

4.5.15.2 Multi parameter criteria

Considering the shape of the derailment surface in Figure 115, it suggest that a criterion that can account for the risk of derailment as a function of all load imbalance measures can better discriminate between the derailing and non-derailing vehicles. Here three different criteria will be investigated. First two criteria based on three dimensional limit surfaces will be discussed and then a two dimensional line-based criterion.

Ellipsoidal criterion

The ellipsoidal criterion measures the normalised distance of a load imbalance state from the origin of Figure 113 [1,1,1] and is formulated as

$$q = \sqrt{\left(\frac{\varphi_{\text{long,observed}} - 1}{a_q - 1}\right)^2 + \left(\frac{\varphi_{\text{lat,observed}} - 1}{b_q - 1}\right)^2 + \left(\frac{\varphi_{\text{diag,observed}} - 1}{c_q - 1}\right)^2} \quad (35)$$

The suggested formula thus describes an ellipsoid surface with the semi axes $(a_q - 1)$, $(b_q - 1)$ & $(c_q - 1)$.

Planar criterion

A criterion based on the normalised distance for a point relative to a three dimensional plane defined by the points \mathbf{p}_a , \mathbf{p}_b & \mathbf{p}_c

$$\begin{aligned} \mathbf{p}_a &= [a_h, 1, 1]^T \\ \mathbf{p}_b &= [1, b_h, 1]^T \\ \mathbf{p}_c &= [1, 1, c_h]^T \end{aligned} \quad (36)$$

And the load ratio point \mathbf{r}

$$\mathbf{r} = [\varphi_{\text{long,observed}}, \varphi_{\text{lat,observed}}, \varphi_{\text{diag,observed}}]^T \quad (37)$$

can be calculated as follows. Using vector algebra, the intersection point between the plane and the line passing through the effective origin $[1,1,1]^T$ and \mathbf{r} can be calculated by solving the linear equation system

$$x(\mathbf{r} - [1,1,1]^T) = \mathbf{p}_a + s(\mathbf{p}_c - \mathbf{p}_a) + t(\mathbf{p}_b - \mathbf{p}_a) \quad (38)$$

where the left hand side is a scalar x times the vector from $[1,1,1]^T$ to \mathbf{r} and the right hand side is the equation for the plane defined by one point on the plane and direction vectors multiplied by parameters s & t . The system has three equations and three unknowns. After solving the system for one load ratio point the plane based derailment criteria h can be calculated as

$$h = 1/x \quad (39)$$

As x gives information about the magnitude which has to be multiplied to the $(\mathbf{r} - [1,1,1]^T)$ vector to create a scaled vector which ends in the plane, an x larger than one means that the load imbalance point lies between the plane and $[1,1,1]^T$ while an x smaller than one means that the load imbalance point is beyond the plane as measured from $[1,1,1]^T$. Therefore the inverse of x is used as the derailment criteria as the trend is that the propensity for derailment increases with an increasing distance between $[1,1,1]^T$ and \mathbf{r} .

Setting the constants for the ellipsoid criteria q to $a_q = 2.5$, $b_q = 1.35$, $c_q = 1.5$ and $q = 1$ and the constants for the plane criteria h to $a_h = 3.25$, $b_h = 1.45$, $c_h = 1.7$, the resulting surfaces are shown in Figure 117 together with the results from Figure 115.

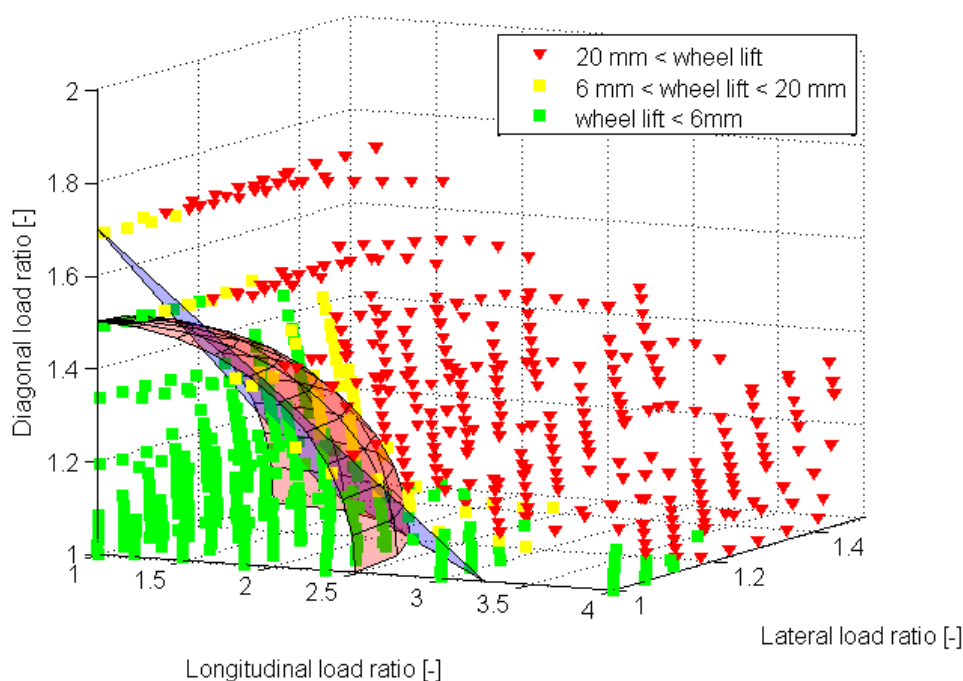


Figure 117. Ellipsoid and planar derailment surface approximations plotted together with data from Figure 115.

Line criterion

It can be observed in Figure 118 (a) that a good separation between derailing and non-derailing vehicle configurations is obtained if the derailment surface is plotted as a function of the longitudinal load ratio and the maximum axle load ratio. A separation line, or line criterion, is fitted to the results using two reference points. These can be written as

$$\begin{aligned} \mathbf{d}_1 &= \begin{bmatrix} \varphi_{\text{long,observed},1} \\ \varphi_{\text{axle,observed,max},1} \end{bmatrix}^T = [1, 1.8]^T \\ \mathbf{d}_2 &= \begin{bmatrix} \varphi_{\text{long,observed},2} \\ \varphi_{\text{axle,observed,max},2} \end{bmatrix}^T = [3, 1.3]^T \end{aligned} \quad (40)$$

The equation for a straight line in the plane of longitudinal load ratio and maximum axle load ratio can be written as

$$\varphi_{\text{axle,observed,max}} = k_l \varphi_{\text{long,observed}} + m_l \quad (41)$$

Using the reference points and the linear equation, a linear equation system is formed from which k_l and m_l can be solved for

$$\begin{bmatrix} \varphi_{\text{axle,observed,max},1} \\ \varphi_{\text{axle,observed,max},2} \end{bmatrix} = \begin{bmatrix} \varphi_{\text{long,observed},1} & 1 \\ \varphi_{\text{long,observed},2} & 1 \end{bmatrix} \begin{bmatrix} k_l \\ m_l \end{bmatrix} \quad (42)$$

Using the reference points of (40) it is obtained that $m_l = 2.05$ and $k_l = -0.25$. A derailment criterion can then be formulated by comparing the location of a measured load ratio point relative to the line. An observed load ratio state \mathbf{d} can be written as

$$\mathbf{d} = [\varphi_{\text{long,observed}}, \varphi_{\text{axle,observed,max}}]^T \quad (43)$$

The maximum axle load imbalance at the limit line for this particular longitudinal load imbalance then becomes

$$\varphi_{\text{axle,observed,max,limit}} = k_l \varphi_{\text{long,observed}} + m_l \quad (44)$$

and the line criterion l can be formulated as

$$l = \frac{\varphi_{\text{axle,observed,max}}}{\varphi_{\text{axle,observed,max,limit}}} \quad (45)$$

The criterion can be interpreted as such that if l is larger than 1, the observed load ratio state \mathbf{d} lies above the limiting line and below the line if the criterion is less than one.

Figure 118(b) highlights the poor correlation between the lateral load ratio on a vehicle level and the maximum axle load ratio when several parameters are varied at the same time. The agreement is good only when the lateral skew loading is purely lateral and there is no chassis twist.

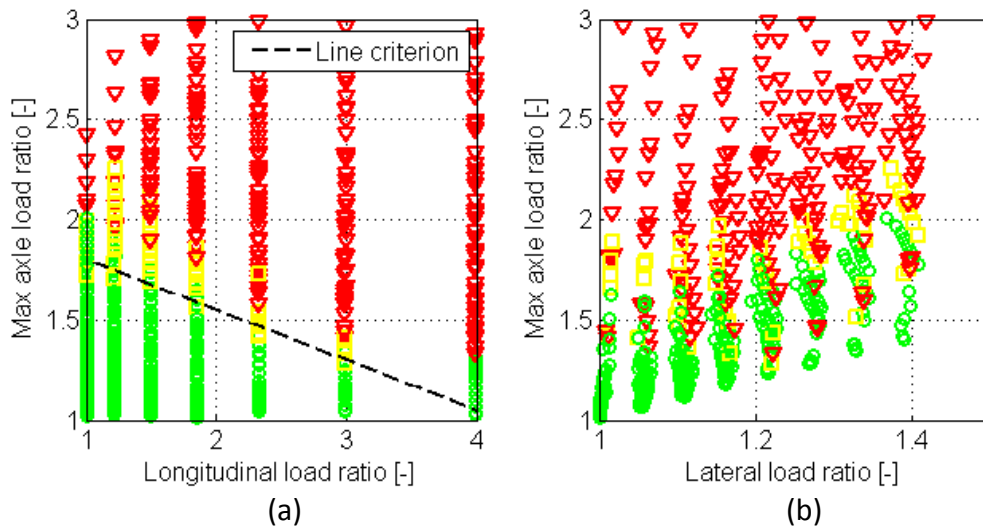


Figure 118. Extended derailment surface illustrated by $wl_{2m, \max}$ as a function of simulated load imbalance quantities. Maximum axle load imbalance ratios above three are not shown. The colour legend is the same as in Figure 117

Performance comparison

Histograms for q , h and l based on the results in Figure 117 and Figure 118 can be found in Figure 119. The fraction of runs with a green status which have a smaller criteria value than the smallest yellow status run is 53% for q , 65% for h and 81% for l . These numbers are intended to be a measure of the separation capability of the criteria. The corresponding number for the maximum axle load ratio (which was the best single parameter criteria) is 49%. It can thus be concluded that a derailment criterion that takes the full vehicle load imbalance status into account is better at separating the derailing from the non-derailing vehicles using this data set. Here the line criterion is the best at separating derailing from non-derailing vehicles while still being relatively easy to compute. The plane and line criteria also have the advantage over the ellipse criterion that they do not provide conservative limits if the criterion is applied to a single direction load imbalance. For example the limit for the longitudinal load imbalance is 1:2.5 in the ellipse criterion. The line criterion can be combined with an upper limit for the longitudinal load imbalance as it can be considered too lenient to allow for longitudinal load ratios of four, even if simulations suggest that it is feasible. The tolerance for other vehicle faults is most likely very low at this level of longitudinal load imbalance.

To get a better estimate of the discrimination success for the presented criteria, it would be necessary to consider the actual distribution of the different load ratio quantities for vehicles in traffic. As measurement data show that extreme skew loading both longitudinally and laterally is very rare, see Section 3.1.3.3, limits applied to the lateral and longitudinal skew loading separately (and probably also maximum axle load imbalances) should work better in practice than this investigation suggest.

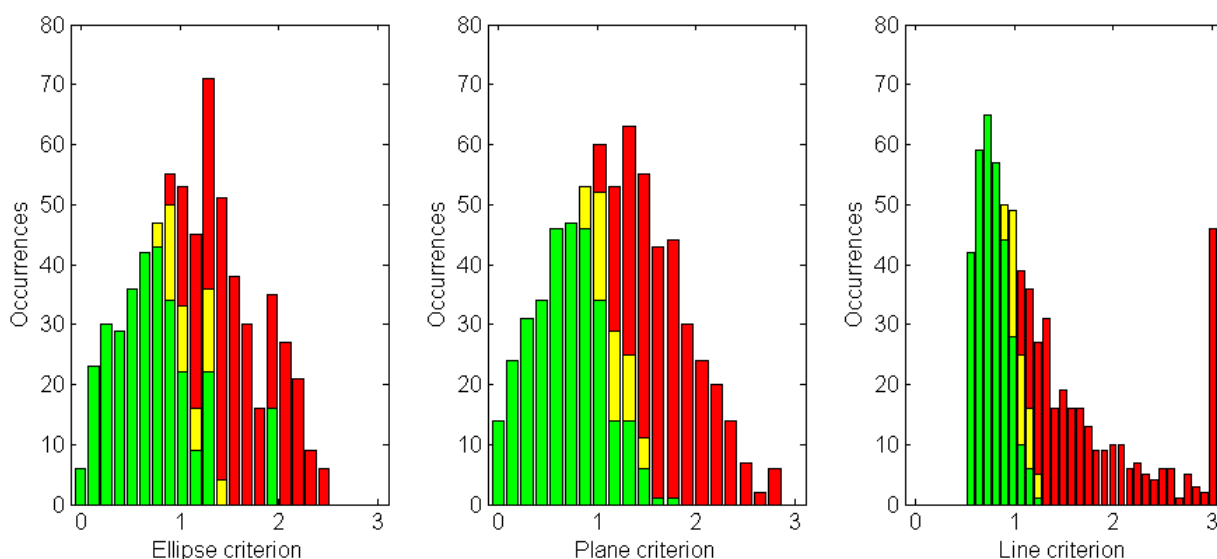


Figure 119 Categorized wheel lift results in a stacked histogram as a function of the ellipsoid derailment risk criteria (left) plane criteria (middle) line criteria (right). The rightmost bar in the line criterion plot represents all values larger than three. The colour legend is the same as in Figure 117

4.5.15.3 Diagonal load imbalance for tare state vehicles

In this section the relation between applied chassis twist, diagonal load imbalance and derailment limit is studied for a tare state vehicle. The simulation case is the same as for the previous vehicle limit investigation in Section 4.5.13, but the vehicle cargo load is removed and with it the parameters for skew loading. Therefore only the chassis twist parameter $kTwist$ remains. First the quasi static diagonal load ratio is obtained as a function of increasing levels of chassis twist. The result can be studied in the lower part of Figure 120. It can be seen that a transition point appears for a $kTwist$ factor of about 1.5 whereafter the diagonal load imbalance starts to increase at a faster rate. Simulating traffic through the representative bad case switch for increasing amounts of diagonal load imbalance, the results can be studied in the upper parts of Figure 120.

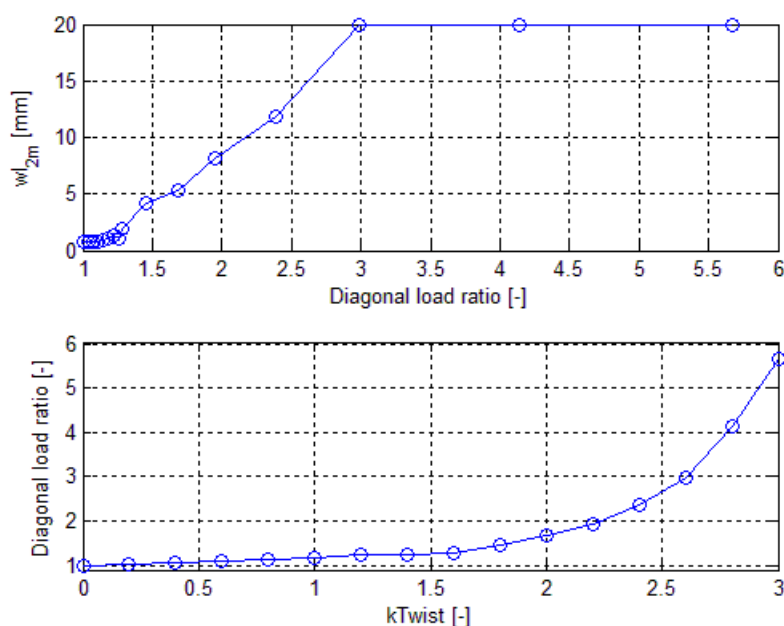


Figure 120 Diagonal load ratio for a tare state vehicle as a function of chassis twist (lower). Wheel lift as a function of the diagonal load ratio (upper)

It can be seen that significant wheel lift starts to appear over a diagonal load imbalance of about 1:1.3 (corresponding to a $kTwist$ value of about 1.5) and that the 6mm wheel lift limit is reached for a diagonal load imbalance of about 1:1.7.

4.5.16 Discussion and conclusions for vehicle parameter limits

The simulation results presented in 4.5.13 to 4.5.15 are aimed at providing the foundation for tentative limits on vehicle load imbalances as caused by skew loading and chassis twist. The investigation has been built around an estimated bad case scenario, and the parameter limits would thus depend on how representative this bad case is. It should also be noted that the criteria are fitted to the derailment surface without accounting for running direction or the direction of the diagonal loading. These are both set to their worst setting according to the performed parameter studies. On the other hand the derailment surface obtained could be used to set consistent limits in that it is shown roughly how critical one load imbalance is compared to another.

To be able to set well informed limits on load imbalance to be detected by wheel load check points, it is suggested that the following three tasks need to be carried out.

1. The derailment limit should be found as a function of the most influential vehicle parameters for a set of representative vehicle types and track cases using simulations
2. The joint probability distributions for the most influential vehicle parameters should be estimated using data from vehicles in traffic.
3. The accuracy of wheel loads obtained from wheel load check points needs to be known

Combining information from point one and two, the accuracy of different measures of derailment risk can be investigated. For example the criteria presented could be applied to measurement data and the number of vehicles that would surpass different thresholds could be estimated and compared to their respective simulated risk of derailment. This task is however difficult to perform with accuracy without the information from point 3. The work in D-rail WP3.2 has come a long way on points 1 and 2.

Even if there are a lot of uncertainties as discussed above, some tentative limits could be suggested based on the performed simulations.

4.5.16.1 Nominal and observed load imbalances

In order to set limits, distinction should first be made between nominal and observed vehicle and axle load imbalances as defined in Section 4.5.5. The nominal imbalances are of interest for loading guidelines while the observed load imbalances are relevant for the detection of derailment prone vehicles in track. Simulations show that a nominal lateral load imbalance (12) of 1:1.25 can correspond to an observed load imbalance for the vehicle (14) of up to 1:1.3 due to suspension compliance and other asymmetries that can arise when the vehicle is asymmetrically loaded in both the lateral and longitudinal direction. Longitudinal skew loading is less sensitive and a nominal load ratio (11) of 1:3 between bogies gives more or less the same result if calculated using observed wheel loads from simulation in (13).

For chassis twist the correlation between the applied twist and the diagonal load ratio (15) is good for a tare state vehicle. For a laden vehicle the correlation is poor as the diagonal load ratio can be affected by skew loading due to non-linearities in the suspension. The diagonal load ratio is dependent on the compliance properties of the specific wagon in question and is therefore not easily determined before the vehicle is loaded.

It has been shown that the maximum axle load imbalance (17) is a non-linear function of skew loading and chassis twist (Figure 112). It means that the observed axle load imbalances can be much higher than the nominal.

4.5.16.2 Limits for observed load imbalances

Studying the simulated derailment limit as a function of load imbalances (e.g. Figure 115), it seems that a limit of the observed lateral load ratio (14) of 1:1.35 and a limit of the observed longitudinal load ratio (13) of 1:3 could be reasonable for the enforcement of skew loading limits. With these limits there is still some margin to derailment in each individual direction such that some chassis twist and skew loading in the other direction could be accepted in combination with an extreme value in one direction. Individual limits for lateral and longitudinal skew loading should work reasonably well in practice as measurements (e.g.

Figure 33) indicates that cases of combined extreme skew loading are rare. It is recognised however that combined skew loading is the worst case and a loading situation which is not assessed with individual criteria for the longitudinal and lateral direction.

Considering limits on the maximum axle load imbalance (17), the derailment surface study shows that all parameter combinations with an associated axle load imbalance above 1:2 derail for the given simulation set-up. In the light of these results, the SBB axle load imbalance limit of 1:1.7 is definitely reasonable as most vehicles with a maximum axle load imbalance above this limit derail. It is therefore suggested as a tentative axle load imbalance limit.

The load imbalance limits on vehicle and axle level are complementary. Sometimes the axle load imbalance is stricter than the imbalance on vehicle level and vice versa. It is therefore recommended that both limit types are used to detect derailment prone vehicles. Especially the maximum axle load imbalance and the longitudinal vehicle load imbalance have been found to be complementary in this study. The lateral load imbalance on the vehicle level is almost rudimentary if the axle load imbalance is also in place (with the proposed limits). The axle load imbalance criterion was shown to be the better single parameter criterion in this study as it is better at separating the derailing vehicles from the non-derailing vehicles for the investigated parameter space.

Limits are also proposed in a more implicit fashion by the multi-parameter criteria. The line and also the plane criteria show promising results in the above investigation. Therefore these criteria as demonstrated in Figure 117 and Figure 118(a) are also proposed as limits.

4.5.16.3 Limits for nominal load imbalances

The simulations show that the RIV loading guidelines are appropriate, but it is a problem that they do not account for (extensive) combined skew loading which was found to be critical in simulations. It is therefore recommended that the loading guidelines are updated such that they also limit the amount of combined skew loading allowed. The planar derailment criteria of Section 4.5.15 could be a starting point for such a discussion. It can be simplified into two dimensional criteria that is a function of longitudinal and lateral skew loading only. This creates a rhombic loading limit surface instead of the rectangular which is the result of the RIV-limits.

4.5.16.4 Chassis twist

It is recommended that tare state vehicles with a diagonal load ratio (15) above 1:1.3 should be inspected for chassis twist. To reach this level of diagonal load ratio a chassis twist of 32 [mrad] was applied to a chassis modelled as rigid. If the diagonal load ratio is as high as 1:1.7, the wagon is estimated to be on the derailment limit and should be stopped then if not earlier. As there is no significant skew loading for a tare state vehicle, the stated diagonal load ratios correspond to the average axle load imbalance in each bogie. This means that an axle load imbalance of about 1:1.7 corresponds to the derailment limit for a tare state vehicle in this study.

4.6 References

- [7] www.webofknowledge.com/
- [8] S. Iwnicki (editor), *Handbook of Railway Vehicle Dynamics*, CRC Press, Taylor & Francis group, Boca Raton, Florida, 2006
- [9] N. Wilson et al. *Assessment of safety against derailment using simulations and vehicle acceptance test: a worldwide comparison of state-of-the-art assessment methods*, Veh. Syst. Dyn. 49(7) (2011), pp. 1113-1157
- [10] J.R. Evans, P.J Rogers, *Validation of dynamic simulations of rail vehicles with friction damped Y25 bogies*, Veh.Sys. Dyn., 29(S1) (2007), pp. 219-233
- [11] B. Pålsson, *Towards optimization of railway turnouts*, Licentiate Thesis, Department of Applied Mechanics, Chalmers University of Technology, Göteborg, Sweden, 2011
- [12] UIC Code 716 R
- [13] www.gensys.se
- [14] J. Evans & M. Berg, *Challenges in simulation of rail vehicle dynamics*, Veh.Sys.Dyn. 47(8) (2009), pp. 1023-1048
- [15] B.A. Palsson & J.C.O. Nielsen, *Wheel-rail interaction and damage in switches and crossings*, Veh.Sys.Dyn. 50(1) (2012), pp. 43-58
- [16] G.E.P Box et. al. *Statistics for experimenters 2nd Edition*, John Wiley & Sons Inc., Hoboken, New Jersey, 2005
- [17] RIV Loading Guidelines - Part 2: UIC, Paris, 01.01.1998
- [18] H. Sjöström, *Riktlinjer för lastning av järnvägsfordon*, Policy document A 83-01, Green cargo. http://www.greencargo.com/Global/Kundservice%20jvg/Lastningsinfo/a_83-01%20riktlinjer.pdf
- [19] www.mathworks.com
- [20] *Spårväxel-Normalvärden och toleranser*, Standard BVS 1523.004, Trafikverket (Swedish Railway Administration), Sweden, 2010
- [21] <http://control.ee.ethz.ch/~mpt/>

5 Derailments due to sloshing

This section analyses the effects of a wagon partially loaded with liquids on the dynamics of a freight train: motion of the liquid, excited by the tank motion is referred to as sloshing. While this phenomenon was proven to have an important influence on road vehicles, no detailed research has been developed for railway vehicles, even if an accident may have a very large impact, especially if hazardous liquids are transported. A computational fluid dynamic (CFD) model is developed in order to understand the motion of a liquid inside a tank, subject to an imposed motion and acceleration field. Then, based on the CFD simulations, an equivalent mechanical model is identified in order to have a simplified representation of the sloshing liquid; such model is then imported in a multi-body model of the freight wagon, which is used to simulate the dynamics of a railway tank with partial filling for a variety of tracks, train speeds and fill levels. In conclusion, derailment and rollover risks are evaluated and, in particular, the most critical conditions for running safety are defined. Results show that, if sloshing is neglected, a significant error affects the evaluation of the rollover risk.

5.1 Background

5.1.1 Literature survey

Sloshing in railway vehicles has been investigated much less than for other means of transportation and only recently some numerical simulations have analysed the phenomenon in detail.

In [22] a pendulum model is used to evaluate sloshing- induced vibrations and it shows that the presence of liquid motion increases horizontal and vertical accelerations of the tank, producing a worse dynamic behaviour. In order to define the equivalent model's parameters, the liquid system is modelled using an analytical method, based on a bounded-value problem; experimental tests show good accordance with the numerical simulations, when a motion is imposed on the vehicle and forces are measured. The main limit of this research is that the equivalent pendulum is highly simplified (only one 3-D model is used for the whole volume of liquid, or two planar ones are used as an alternative) and thus it is impossible to reproduce any different motion between the front and rear portions of the liquid. Moreover, vehicle dynamics are highly simplified, both in the internal elements (primary and secondary suspensions, as well as friction elements are all represented by linear models) and in the wheel-rail contact (modelled as equivalent springs and dampers).

In [23] a similar mechanical model is used in order to study a particular aspect of the vehicle dynamics: effects of sloshing on the coupling screws are studied by means of multi-body simulations that consider four wagons. As a result, sloshing is experienced when the train undergoes curves or braking manoeuvres, with no risk for the train's running safety. However, the unused coupling screws get into resonance, that makes them release from their hangers. Anyway, this undesired phenomenon is not hazardous. From a methodological point of view, the equivalent pendulum is identified by means of a CFD analysis, that demonstrates that modes of vibration, forces and moments are in good agreement between the two models. A limit of the model is that many simplifications are needed in order to

reduce the computational time (for instance, the four wagons are modelled with only 79 DOFs instead of the expected 124, decided in advance; moreover, no friction elements are considered in the suspensions). Another limit is that lateral sloshing is modelled by only one pendulum per wagon and cannot reproduce the different motion of the fluid at the front and rear position on the wagon.

In [24] the particular situation of an Iranian track is studied, since two accidents occurred there. Sloshing is modelled with an equivalent mass-spring system, identified using a simplified, analytical model of the fluid (no CFD is performed); multi-body simulations are performed with the commercial software ADAMS, simulating different fill levels, train speeds and properties of the liquid. As a conclusion, it was shown that ignoring the sloshing phenomenon may lead to an error of up to 25% in calculating the unload ratio $\Delta Q/Q_0$ (defined as the variation of the vertical force applied on the wheel with respect to the static load). Moreover, fluids with different densities were compared (e.g. water and sulphuric acid) and it was concluded that the denser ones show lower potential for derailment. In this case, while the multi-body model of the vehicle is very detailed (for example, frictional forces on the Lenoir link are computed with a non-linear system), the equivalent mass-spring model is defined by means of results published in past research. Moreover, as in the other articles, the different motion of the fluid at front and rear positions on the wagon are not considered.

5.2 CFD analysis

The equivalent mechanical model is a fundamental part of the final multi-body model of the freight train, since it represents the dynamics of the liquid volume. In order to define such model, it is fundamental to have a preliminary understanding of the fluid dynamics of the liquid inside the tank, that is subject to a centrifugal acceleration, as well as the gravitational one. Aim of this subsection is to develop numerical simulations that not only allow a deep comprehension of the sloshing phenomenon, but also provide the base for the following identification of the equivalent mechanical model.

Sloshing is a very complex phenomenon, because it depends on the motion of two fluids (gasoline and air, whose behaviour is modelled by Navier-Stokes equations) and the interaction between them; moreover, two body forces have to be considered (centrifugal and gravitational accelerations). Therefore no exact analytical solution is available and a numerical approximated solution is sought. As reported in [25], numerical simulations give precise results for small-amplitude sloshing.

5.2.1 Description of the model of the fluid

Main characteristics of the model are:

- the model is unsteady, in the sense that Navier-Stokes equation are solved by means of an unsteady Reynolds-averaged approach;
- it is assumed that, when the train approaches a curve, the main forces exerted on the fluid are in the lateral direction, along which sloshing occurs. Thus, a sectional 2D model in the vertical plane is considered. This simplification allows a significant reduction of the required computing time, that leads to the possibility to use a dense discretization of the geometry and a shorter time step for numerical integration. On the other hand, no longitudinal motion of the fluid is considered: this may introduce

an approximation in the computation of the forces acting on the tank, and also in the evaluation of de-railing/overturning risk; anyway, assuming the train is traveling at constant speed, the lateral forces have a higher influence on derailment/overturning, rather than the longitudinal ones;

- to simulate the interaction between the two fluid phases, the Volume-Of-Fluid model (VOF) is used: this is the standard choice for free-surface flows. In such a model, the different (two or more) phases are present at the same time in any cell; it is assumed that these phases are not interpenetrating. For each cell, all variables and properties are defined as volume-averaged values: such values are representative of the mixture of gasoline and air. As a consequence, continuity equation and Navier-Stokes equations can be written and solved numerically;
- a moving mesh is used in order to simulate the train negotiating curves. The effects of a curve on the fluid content is to generate a body force. This force is reproduced in the CFD simulations by imposing a lateral motion on the mesh, where the velocity of the tank centre is obtained by integrating the acceleration. For instance, the typical trapezoidal shape of the lateral acceleration measured on the carbody corresponding to the sequence of entry curve transition, full curve and exit curve transition can be modelled in the numerical simulations by applying a time history of velocity;
- main outputs of the simulation are forces and moments exerted by the fluid on the walls of the tank. They can be computed as the integral sum along the cells adjacent to the wall of the contributions due to pressure and viscous components;
- the position of the centre of gravity (CoG) of the liquid is also computed from the simulations, in order to understand the sloshing motion.

5.2.2 Results

Different railway curves are simulated, characterised by different lengths of the full curve and transitions, and train velocity is computed in order to reproduce a cant deficiency equal to 92 mm for any simulation.

Therefore the velocity function imposed to the tank changes its shape and magnitude accordingly. Of course, vehicle dynamics are not considered at this stage, so the tank is moved according to the quasi-static lateral acceleration defined as function of curve geometry and speed (with no oscillations due to elasticity and damping on the roll plane of the train). Different fill levels are considered: 25%, 50% and 75%.

For the sake of brevity results referred only to a particular curve are reported (with length of the circular curve equal to 200 m and transition length equal to 100 m), but similar comments apply for the other ones.

Forces transmitted to the tank are shown in Figure 121. Note that:

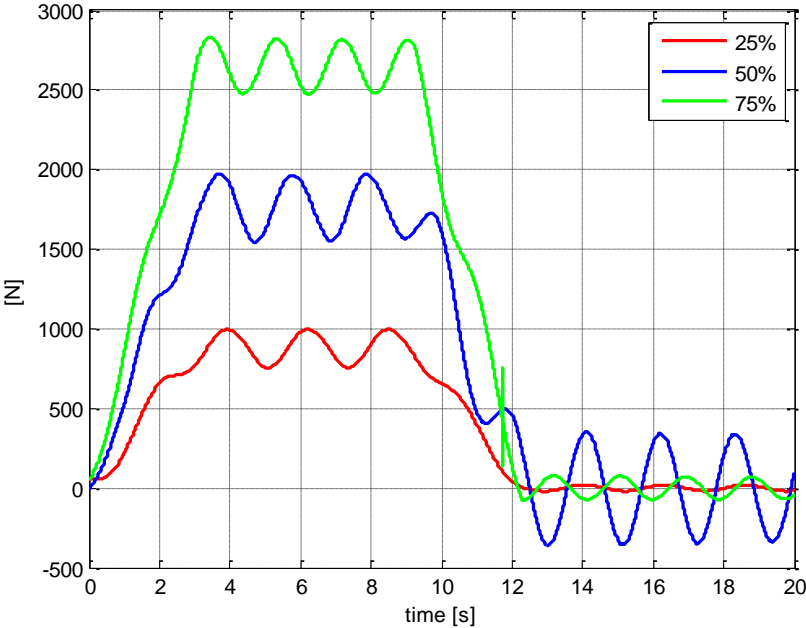
- vertical forces are almost constant in time. As expected, they have a mean value equal to the gasoline weight;
- lateral forces show the effects of sloshing: in fact, it is possible to recognize two components. The centrifugal acceleration causes a quasi-steady force, with a trapezoidal shape, that disappears after about 12 s, when the train exits the curve. Moreover, an oscillatory force is superimposed: it is due to the oscillations of the

free-surface of fluid,. The fluid motion that appears in the numerical simulations is very similar to the one that can be obtained analytically, as described in Table 35. The oscillatory forces have a high magnitude, if compared to the quasi-static ones; considering also that they are applied at the geometrical centre of the tank, they could strongly affect the risk of rollover of the carbody;

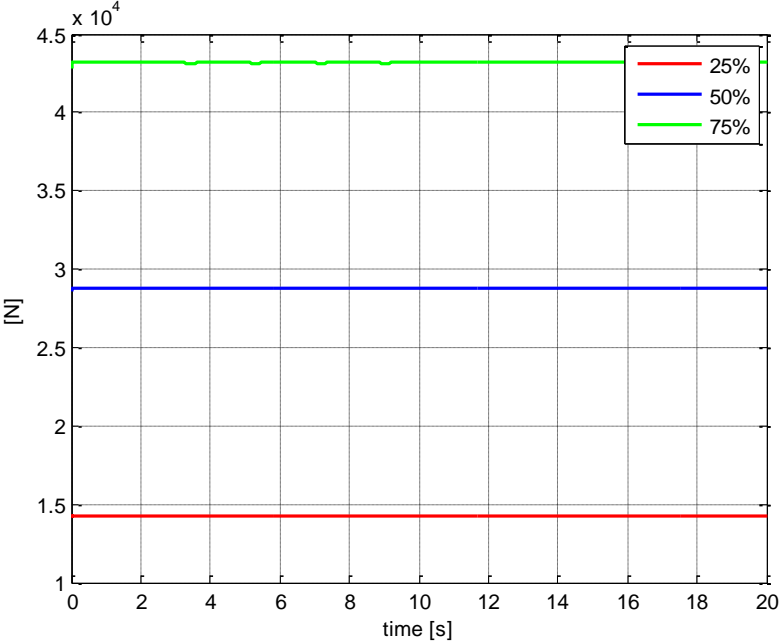
Table 35 Comparison between analytical and numerical values of the sloshing frequencies.

Fill level χ	Numerical simulation	Analytical
25%	0.42 Hz	0.43 Hz
50%	0.47 Hz	0.47 Hz
75%	0.54 Hz	0.53 Hz

- the roll moment generated on the tank has a very low magnitude, if compared for example with the lateral force; for instance, for $\chi = 50\%$, it reaches a maximum value of about 0.15 Nm. This is an expected result: in fact, the moment is expected to be very low, if compared to the other forces. From a physical point of view, because of the circular geometry of the tank, only viscous effects create a moment around the tank's centre.
- Also the position of the centre of mass is considered: this information is useful to understand the motion and shape assumed by the fluid volume. Figure 122 shows that the motion primarily happens in the horizontal direction; this is the reason why lateral forces are the ones characterized by the largest oscillatory amplitudes.
- It is also interesting to note that, for $\chi=75\%$ the motion of the centre of mass is very small, both during the curve and during the straight path. The largest oscillations are experienced after the curve, for $\chi =50\%$; the same happens during the curve, for $\chi=25\%$. This difference is due to the different frequencies associated to the waves generated on the free-surface of the fluid (Table 35). This implies that a variation in the centrifugal acceleration (e.g. when the train enters or exits the curve) can create a different perturbation, depending on position and shape of the wave in the free-surface.

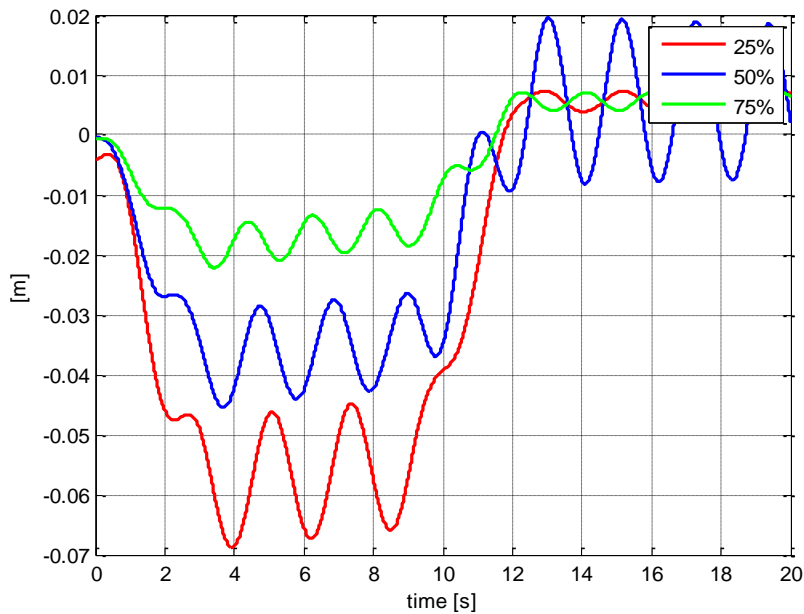


a) lateral

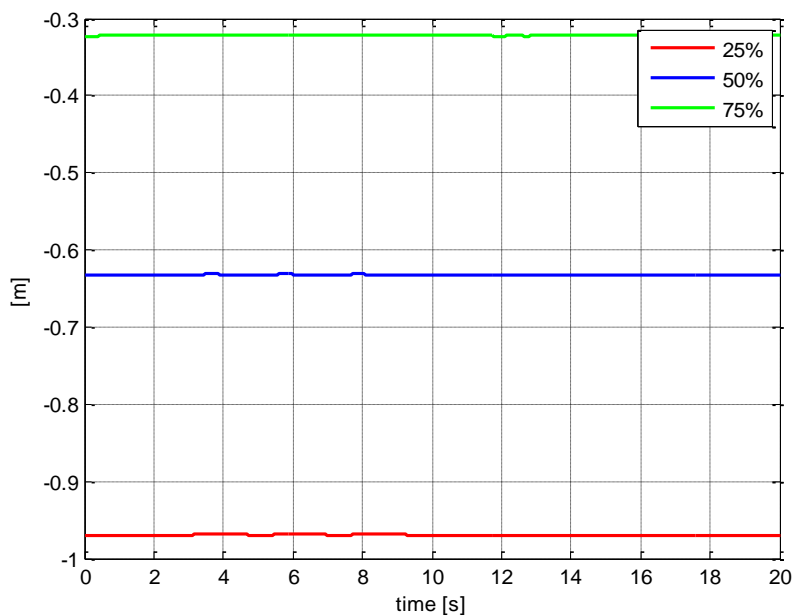


b) vertical

Figure 121 Forces on the tank due to fluid sloshing simulated with different fill levels.



a) lateral



b) vertical

Figure 122 Motion of the centre of mass simulated with different fill levels.

As a conclusion, the forces generated by a sloshing fluid in a railway tank car include quasi-static forces, associated to the centrifugal acceleration, directly proportional to the fluid mass and sloshing forces, associated to the oscillations of the free-surface of the fluid, that are strongly related to the relation between the natural frequencies of the fluid and the imposed changes in centrifugal acceleration.

5.2.3 Damping

As a general observation, all simulations show that after the curve no significant decay of the oscillations (forces and motion of the centre of mass) is experienced: the liquid is characterized by a very low damping. Even if a similar result was experienced in literature, a better understanding is required because it strongly affects the dynamics margin of the whole vehicle.

The natural damping of the liquid volume depends on its viscosity, that dissipates kinetic energy into heat; no analytical solution can help to determine fluid damping. Therefore, the CFD analyses are used. In particular, an initial condition is given to the fluid, by imposing the negotiation of the curve to the different fill levels; simulations are run for a total duration of 63 s and the lateral motion of the centre of mass is studied. At about 13s, the tank exits the curve and therefore no external forces are generated on the fluid: it follows its free motion with an initial condition due to the previous forcing. Considering that the oscillations only show one frequency, thanks to the methodology of the logarithmic decay, it is possible to evaluate the natural damping of the system.

As an example, Figure 123 reports the time histories of the CFD analysis, for $\chi=50\%$, compared with the exponential function. As a result, for $\chi=50\%$, a non-dimensional damping $h = 0.0036$ is computed. This result confirms that damping associated to the viscosity of the gasoline is very low.

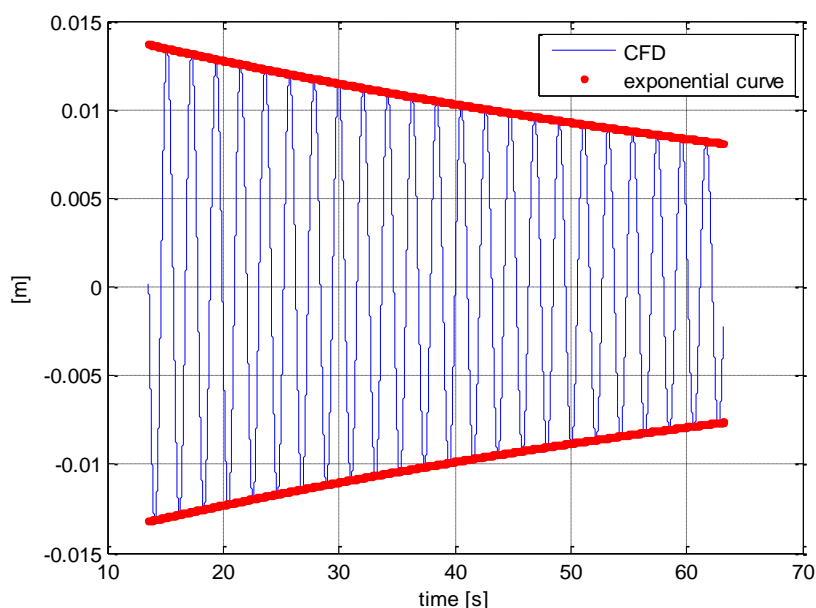


Figure 123 Results of the logarithmic decay method, used to evaluate the natural damping, for $\chi=50\%$.

A similar procedure is developed for the other fill levels, with similar results: Table 36 reports the evaluated non-dimensional damping, for different fill levels.

Table 36 Identified non-dimensional damping, for different fill levels.

χ	h
25%	0.0010

50%	0.0036
75%	0.0025

5.3 Equivalent mechanical model

A mechanical model is developed in order to reproduce the sloshing motion of the fluid. The model is considered optimal if it gives the same output as the CFD simulations, in any simulated condition (different curves and different fill levels). Anyway, since the mechanical model is a simplification of the problem, its output is affected by an error; therefore, the objective of the identification is to minimize this error.

As a general methodology, the following procedure is used:

1. definition of the model. A mechanical model is chosen, according to studies in literature; equations of motion are written in a general form that depends on a set of mechanical parameters ξ (e.g. mass, stiffness, length...);
2. identification of the parameters. Parameters required to define the model are obtained with an iterative procedure:
 - starting from an initial guess ξ_0 , the motion of the equivalent model is computed by integrating the equations of motion, imposing the motion of the tank. The lateral force generated on the tank is also computed;
 - an error function $e(\xi)$ is calculated. This function is very important in this procedure, since the whole method is based on its minimization. Since the lateral force is the most important to understand the risk of train rollover and since it is the most representative of the sloshing phenomenon (it shows the biggest oscillatory amplitudes), it is chosen as an indicator of the accuracy of the mechanical model. This force has an important dependence on time and the error function is therefore defined as an RMS – error;
 - parameters ξ_j are updated to new values ξ_{j+1} , according to the gradient of the error;
 - iteration is repeated until convergence to a minimum is reached;
3. qualitative comparison. The choice of the above-defined error function is very critical.

For instance, there is no control on the vertical forces (therefore, it is not guaranteed that the total mass of the mechanical model is equal to the mass of the CFD model); moreover, minimizing an RMS-error does not guarantee that the peak values of the lateral forces will coincide in the mechanical model and in the CFD. A qualitative comparison is performed: in particular, the whole time history of all forces is evaluated. Finally, in the iterative procedure no constraints are imposed on the parameters ξ : after the optimization, the correctness of the result has to be checked (e.g. masses cannot be negative). If results are not satisfactory, the initial guess ξ_0 is changed and the iteration is repeated: this helps to avoid the risk of obtaining a solution that is local minimum and not a global one. If no improvements are obtained, the mechanical model has to be changed.

An equivalent pendulum model, shown in Figure 124, was analysed and it was found that results are not satisfactory.

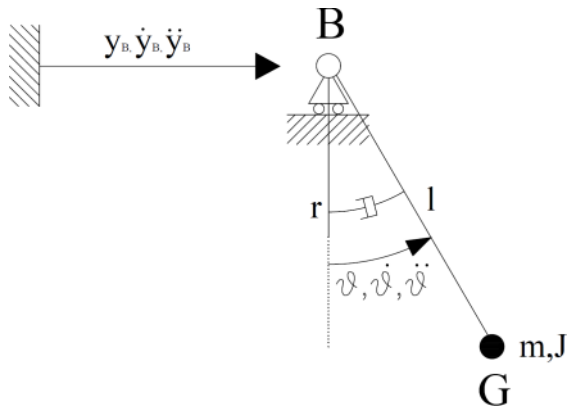
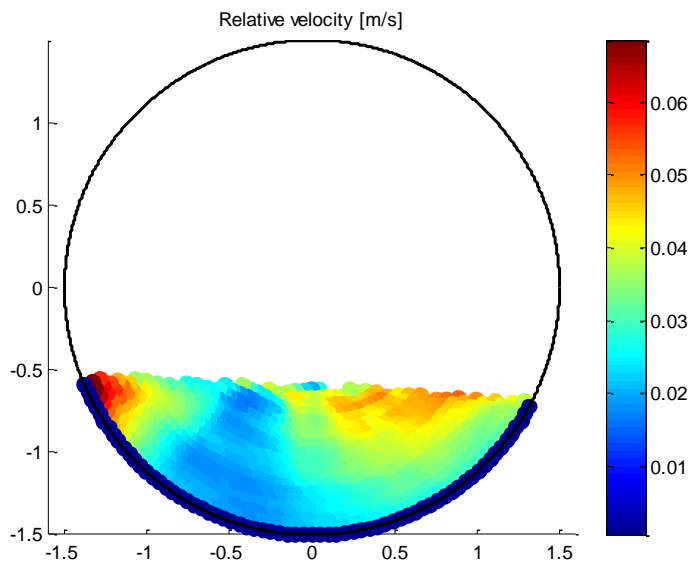


Figure 124 Equivalent pendulum model.

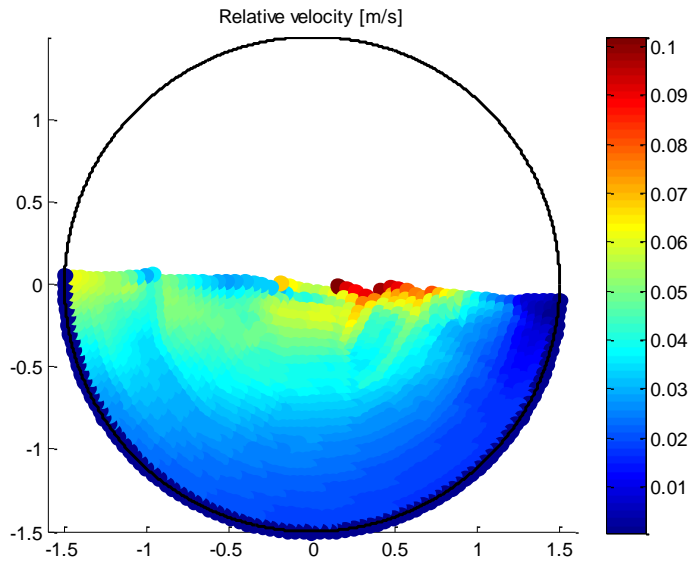
In particular lateral forces are much higher than those computed by the CFD analysis, both during the curve and during a straight path (the oscillatory amplitude is higher than the expected value by about 50%).

Analysing the velocity field obtained in the CFD simulations, it is possible to note that part of the liquid does not move significantly with respect to the tank. Figure 125 shows that the central part of the fluid has higher velocities with respect to the outer part: this zone is, in fact, affected by the prescribed stick condition (on the wall) and therefore its motion is inhibited. Moreover, the velocity distribution is not symmetric around the centre of the tank.

These observations imply that the pendulum model is not appropriate.



$\chi = 25\%$



$\chi = 50\%$

Figure 125 Distribution of the velocity magnitude at the end of curve transition, for different fill levels.

With the aim of better reproducing the forces generated by the sloshing fluid, a modified pendulum model is introduced, as represented in Figure 126.

The following model is considered a more sophisticated representation of the sloshing phenomenon because:

- it considers that part of the liquid volume (m_0) does not move significantly and therefore does not produce any oscillation;
- a wave in the free-surface can be simulated by the motion of the pendulum ($m_1 - l_1$).

Thus, parameters m_0 and m_1 are directly linked to the static and oscillatory components of the lateral force F_y , respectively.

Some disadvantages of this model include:

- the model's parameters have no precise physical meaning and cannot be computed analytically;
- no damping is considered.

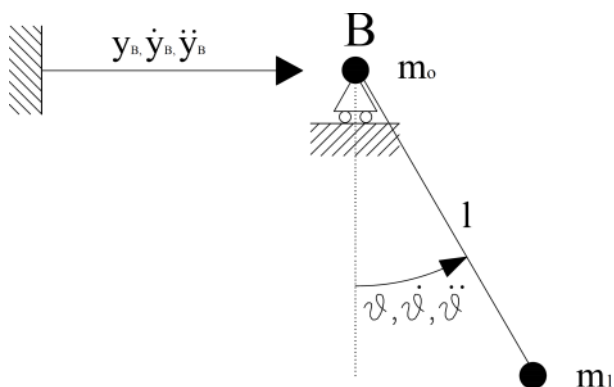


Figure 126 Modified pendulum model.

Considering that the CFD simulations show small oscillations of the liquid, the equivalent model can be linearized, resulting in an $m - k$ system, as shown in Figure 127. In this case, vertical forces have no oscillatory components, but they are always equal to the fluid's weight; the CFD anyway shows that this approximation is accurate (Figure 121).

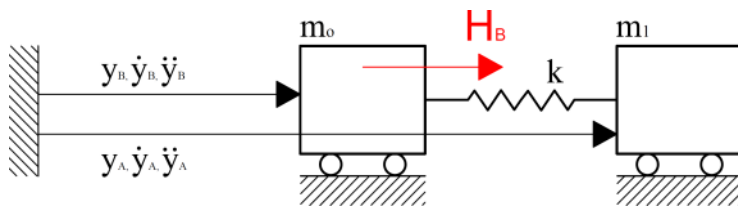


Figure 127 Linearization of the pendulum model.

Literature reports that many studies considered this model in order to simulate the sloshing:

- [26] introduces the model for low-gravity systems and identifies the parameters in order to correctly reproduce the natural frequencies of the fluid;
- [27] applies the same model for longitudinal sloshing on a tank vehicle;
- [28] explains that, for small sloshing oscillations, the equivalent spring-mass model is an accurate description of the phenomenon.

As already explained, no analytical formulation is available to understand which volume fraction contributes to the sloshing motion or moves in a rigid way: therefore, the initial guesses are chosen arbitrarily: being m_{total} the total liquid mass, $m_{0,0}$ and $m_{1,0}$ are set to half the total liquid mass m_{total} . Stiffness k_0 is instead calculated to reproduce the first sloshing frequency $f_{sloshing}$.

Anyway, these initial guesses are changed during the identification procedure, in order to verify its robustness and to avoid the risk of local minima.

Results of the tuning, obtained for $\chi = 50\%$ are plotted in Figure 128.

The tuning algorithm works properly, since the tuned curve is closer to the CFD simulation, than the one obtained with the initial guess. The algorithm is also very robust: even if different ξ_0 are used, the optimization always gives the same result; this means that no local minima are encountered.

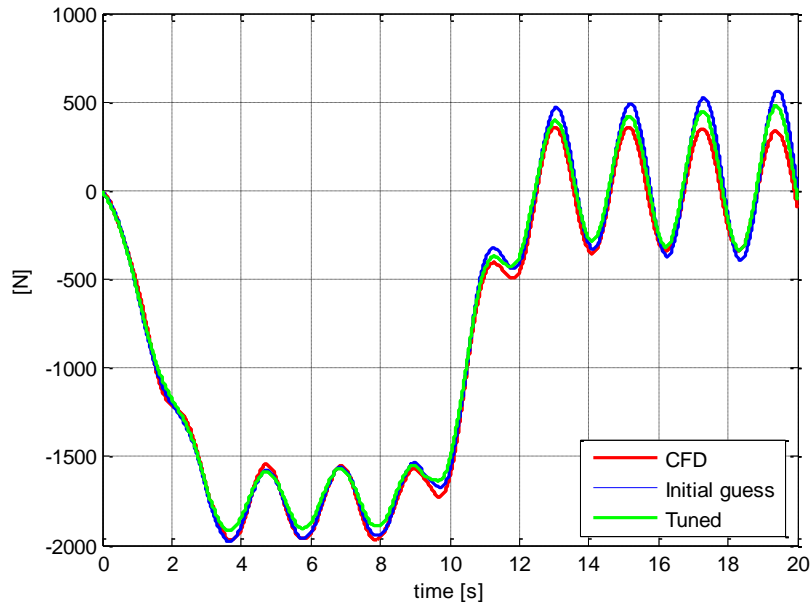
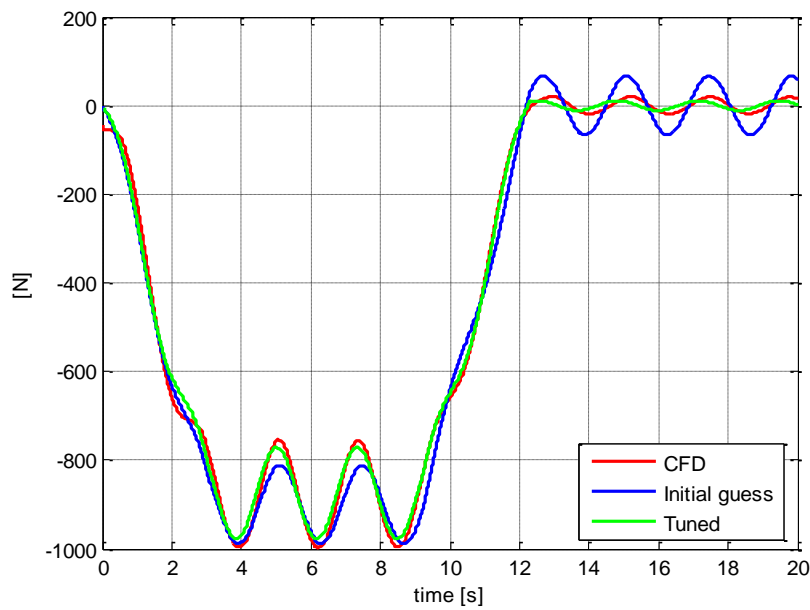
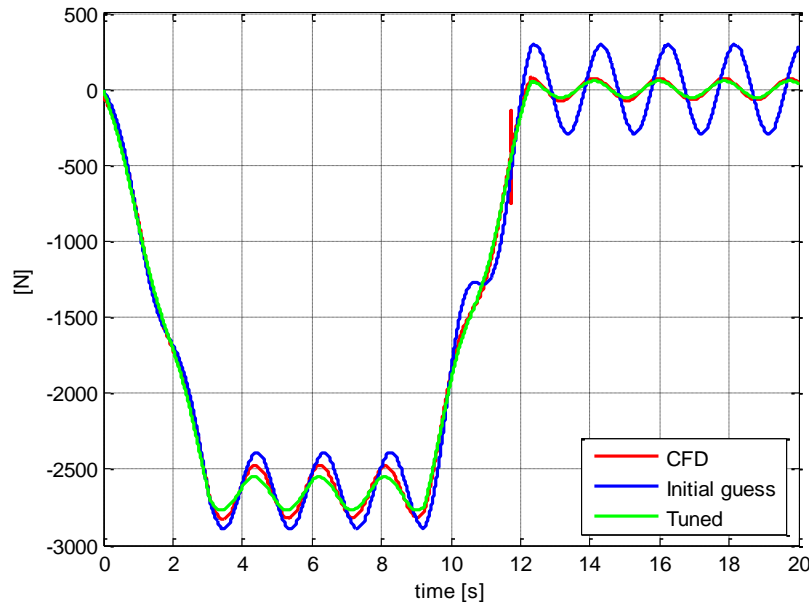


Figure 128 Lateral force: comparison between CFD simulations and the mass-spring model, at $\chi=50\%$.

The same observations are valid for $\chi=25\%$ and $\chi=75\%$ (Figure 129).



a) $\chi=25\%$



b) $\chi=75\%$

Figure 129 Lateral force: comparison between CFD simulations and the mass-spring model, at $\chi=25\%$ and $\chi=75\%$.

Table 37 reports the optimal parameters, obtained with the identification algorithm. Note that ratio m_1/m_0 decreases with the fill level because of the velocity distributions (as shown by the CFD analyses). For instance, for $\chi=50\%$, the volume fraction that shows a low velocity (lower than 0.04 m/s) is about 60%: this fraction is almost equal to $m_0/(m_0 + m_1)$. If the same reasoning is applied to the simulation with $\chi=25\%$, the ratio between non-moving and total mass is about 40%, which is coherent with the identified parameters.

Table 37 Tuned parameters of the mass-spring model. Masses m_0 and m_1 are expressed for unitary length of the tank.

Parameter	$\chi = 25\%$	$\chi = 50\%$	$\chi = 75\%$	Units
m_0	620	1430	3398	kg
m_1	846	1544	1022	kg
k	6150	13351	11600	N/m

Also the motion of the centre of mass needs to be considered in order to assess the validity of the equivalent mechanical model. CFD simulations show that the centre of gravity does not move significantly on the vertical axis and thus if the equivalent mechanical model is set at a height equal to that of the liquid centre of mass, the two systems are equivalent. On the horizontal axis instead oscillations are relevant and the correctness of the equivalent model has to be verified. A comparison between the curves generated by the CFD model and the equivalent mechanical system shows that there is good accordance between the two. Figure 130 reports, for example, the simulations for a fill level of 50%: the results are qualitatively equal (same shape and frequency), while the maximum amplitudes differ of less than 20%

and the equivalent model is therefore validated. Similar observations can be made for the other fill levels and simulated curves.

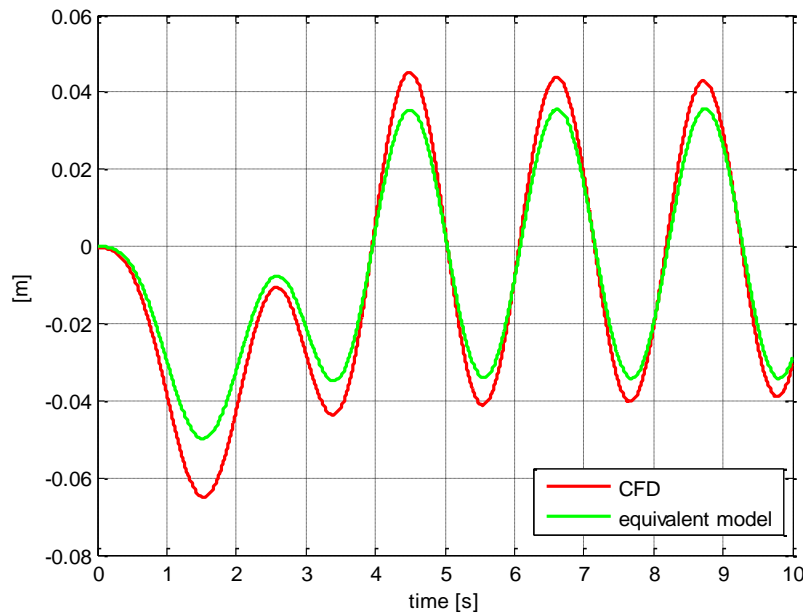


Figure 130 Lateral motion of the centre of mass: comparison between CFD simulations and the mass-spring model, at $\chi=50\%$.

In conclusion, the choice of the equivalent model and the tuning algorithm are adequate to represent the sloshing motion because:

- total mass $m_{total} = m_0 + m_1$ is equal to the liquid mass of the CFD simulation. Note that this outcome is not obvious, since the tuning algorithm does not consider the total weight of the fluid in its error function: the model anyway converges to the correct total mass;
- ratios between m_0 and m_1 are coherent with the velocities distribution (Figure 125);
- the natural frequency of the mechanical model is equal to that of the fluid;
- even changing the formulation of the error function $e(\xi)$, the optimal result remains the same.

Finally, it is necessary to define the positions, on the vertical axis, of m_0 and m_1 , indicated with $h_{0,COM}$ and h_1 , respectively. Considering that both masses have a precise physical meaning (they represent the non-moving and moving portion of liquid), it is possible to define their position according to the velocity fields obtained in the CFD analysis. As shown for example in Figure 125, the non-moving mass represents the lowest part of the liquid, while the moving one is close to the free-surface. Therefore, it is assumed that the liquid volume can be divided horizontally in two parts, whose dimensions respect the mass ratio m_1/m_0 , as reported in Figure 131.

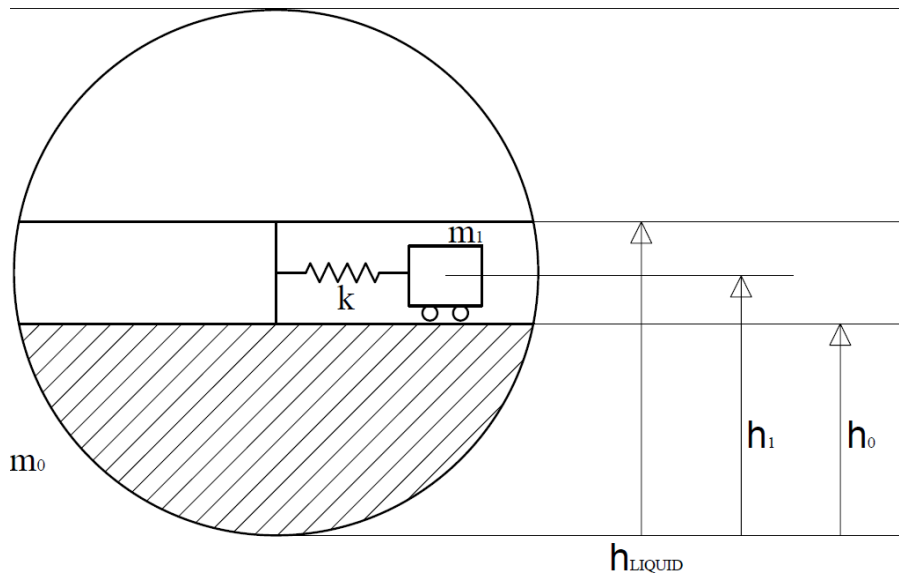


Figure 131 Schematic 2-D representation of the mechanical model, used to model the sloshing fluid, for $\chi=60\%$.

By simple geometric considerations $h_{0,COM}$ is computed, while it is assumed that m_1 can be approximated to a rectangular shape and, consequently, its centre of mass is at half of its height. Note that the CoG of the whole volume of fluid is preserved in this model.

In order to check the correctness of this approach, the moment generated on the tank, in the rolling plane is computed for both the CFD simulation and the equivalent mechanical model. Figure 132 shows, for instance, the comparison for $\chi=50\%$; the moment is computed with respect to the lowest point of the circular section.

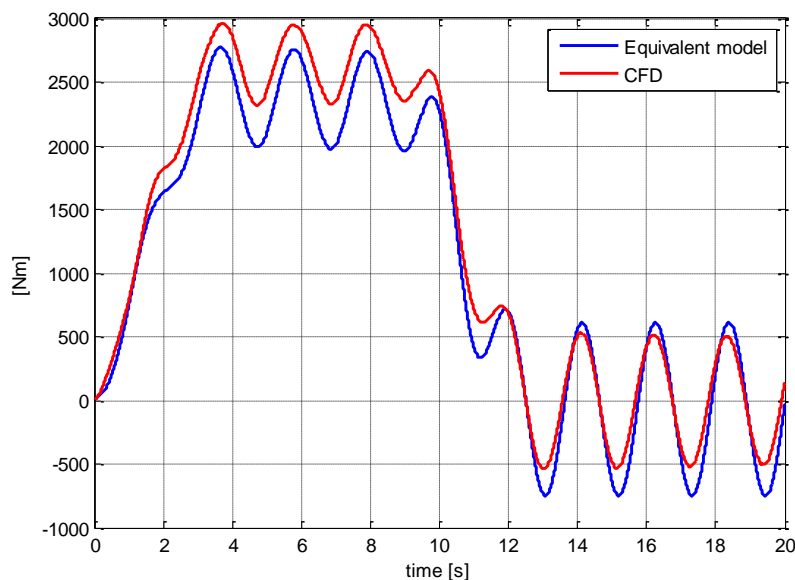


Figure 132 Moment generated on the tank, in the rolling plane, by the sloshing liquid: comparison between CFD and equivalent model ($\chi=50\%$).

Following the same methodology, other fill rates are studied in order to identify the mechanical parameters required for the multi-body simulations. In particular, fill rates between 40% and 60% are considered: CFD simulations are performed and then the identification algorithm is executed.

Similarly to what was observed in the previous analyses, for every fill level, the total mass converges to the expected one, as does also the natural frequency.

Figure 133 and Figure 134 report, respectively, the identified masses and their relative weight, in comparison with the total mass. As a general observation, it is possible to note that, when the fill level increases, both of the masses increase their absolute value, but the moving one (m_1) decreases its relative importance.

In order to check also the correctness of the identified stiffness k , the associated natural frequency is computed and reported in Figure 135, for the different fill levels. A comparison with the analytical values shows a good accordance with the identified natural frequencies.

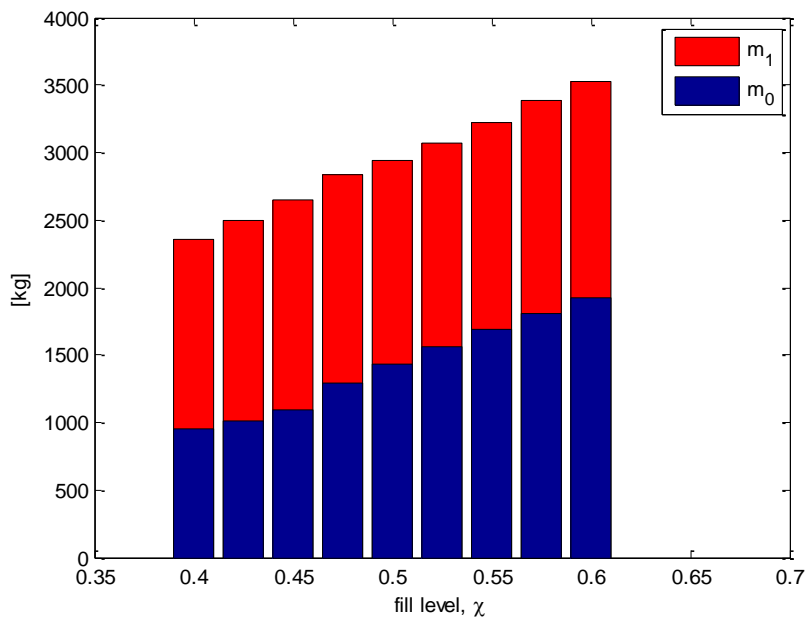


Figure 133 Identified masses m_0 and m_1 , for different fill levels χ .

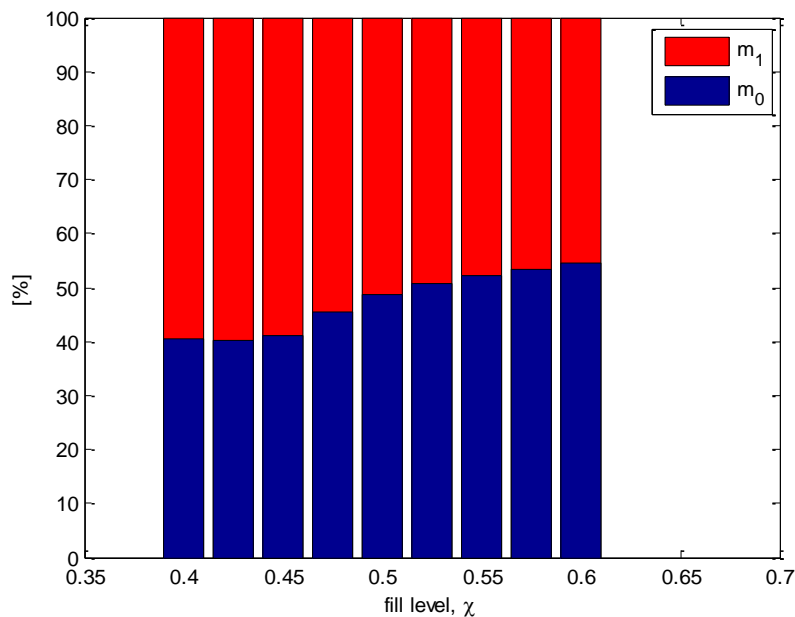


Figure 134 Relative weight of the identified masses m_0 and m_1 , for different fill levels χ .

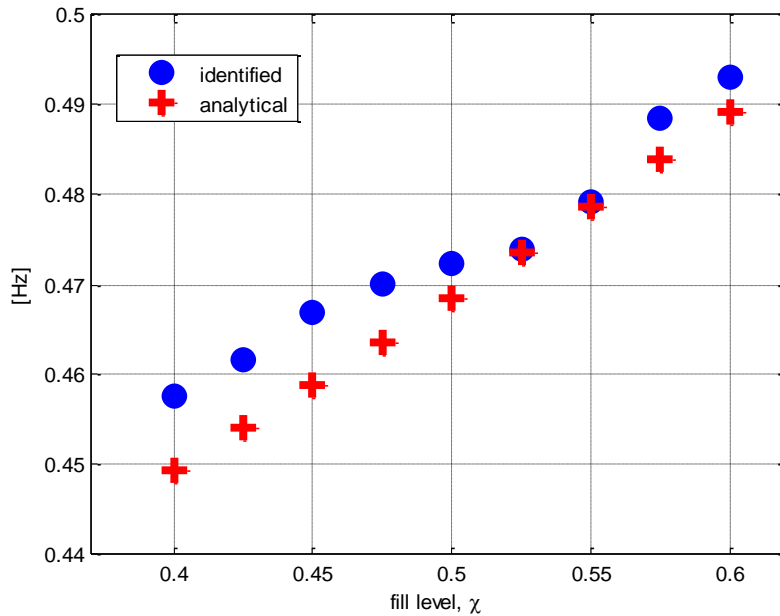


Figure 135 Identified natural frequencies, compared with the analytical ones.

5.4 Multi-body model of the tank vehicle

In this subsection a brief description of the multi-body model of the tank vehicle is provided. The vehicle is supposed to transport a partial load of liquid. Specifications of the wagon are obtained from a real model, a Zagkks wagon [29] which is a 4-axle vehicle equipped with Y25 bogies, common in Europe; the sloshing model is instead defined by means of the equivalent mechanical model, previously described.

The liquid content of the tank is modelled by a series of equivalent mechanical models, in order to represent the different portions of fluid, along the longitudinal direction, that move in the lateral direction.

All of these models have the same mechanical characteristics (m_0 , m_1 and k), but are located at different longitudinal positions along the carbody.

The equivalent models are fully defined by the following mechanical properties:

- m_1 and k have been defined by means of the identification algorithm, as explained in the previous subsection. Note that, since the equivalent models have only a translational DOF, there is no need to define their shape (and therefore their moments of inertia);
- also the non-moving mass m_0 has been previously identified. Since it represents a liquid portion that rigidly moves with the tank, it is also necessary to define its 3-D shape and identify the moments of inertia;
- longitudinal positions of the equivalent models are obtained by dividing the total length of the carbody into segments having the same length (Figure 136).

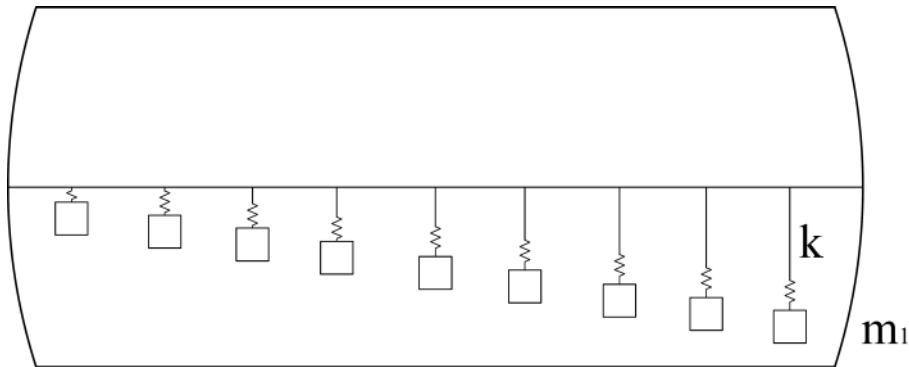


Figure 136 Longitudinal distribution of the equivalent models in the carbody (seen from the top).

After defining the properties of the equivalent models, it is necessary to decide how many models are required in order to accurately reproduce the sloshing motion. Two main aspects have to be considered:

- generally speaking, the free-surface of the liquid is not horizontal in the longitudinal direction, since the front and rear fractions of fluid can undergo different motions. As a consequence, the multi-body system should include a high number of equivalent models, so that the three-dimensionality of the sloshing phenomenon is approximately reproduced;
- since the identification of the equivalent models was based on a 2-D model, the interaction between different sections is not defined: the motion of a section does not influence that of the neighbouring ones (in a real case, viscous forces would reduce the relative motion between them). A high number of equivalent models would cause a high under-estimation of the forces acting between two sections, causing an inaccurate representation of the free-surface and therefore, of the transmitted forces as well.

A trade-off between these two aspects has to be found.

Articles in literature do not report any detailed analysis on how to decide the number of equivalent models and, therefore different possibilities are simulated and results are compared. In particular different multi-body models are created, with 1, 5, 9 and 13 equivalent models, respectively; an s-curve with radius $R=250\text{m}$ is run at a speed of 12.5 m/s , corresponding to a lateral acceleration on the track plane of 0.63 m/s^2 .

For the four simulations, the most significant variables for the effects of the sloshing are analysed: the motion of the equivalent models (evaluated as the average lateral motion of the masses), the yaw angle of the carbody and the vertical forces on the third wheelset (defined as the maximum force unload between left and right wheel). The third wheelset is chosen because it is the one that experiences the highest unload ratios.

Figure 137 shows that the simulated sloshing motion does not depend on the number of equivalent models, during the s-curve (between 4s and 9.4s); on the other hand, in the final straight (after 9.4s) the model with only one mass shows a significant deviation from the others.

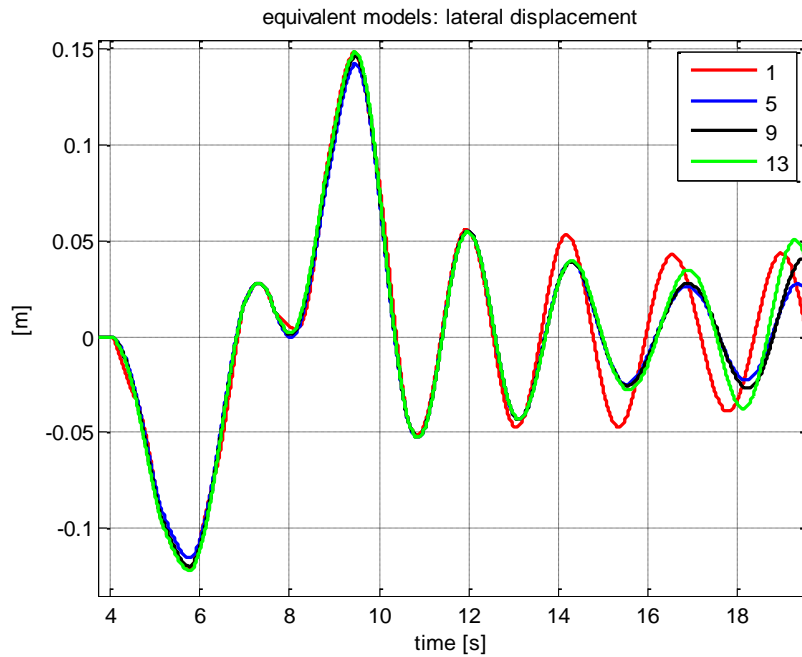


Figure 137 Average lateral motion of the $m-k$ systems, for a different number of equivalent models.

Similar observations can be made for the carbody yaw angle (Figure 138), that shows a deviation between the different simulations only in the final straight; the differences are mainly due to a phase-shifting between the motion of the $m-k$ models that, if considered as a whole, also show an oscillation on the yaw angle that forces the carbody to rotate. This oscillation is apparent when a high number of equivalent models is used and its physical meaning is strictly related to the possibility of the fluid to deform in the 3D space. Note that an initial straight was included in the simulations, but is not present in the reported time histories.

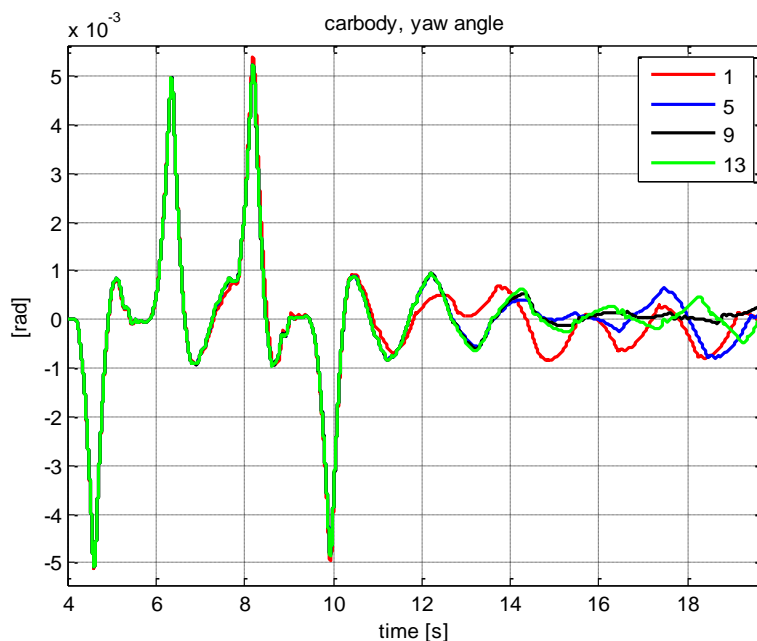


Figure 138 Yaw angle of the carbody, for a different number of equivalent models.

Table 38 reports the maximum vertical unload on the third wheelset and the corresponding unload ratio: it is possible to observe that all simulations give similar results and, as the number of equivalent models increases, forces tend to converge to the same value.

Table 38 Comparison between different numbers of sloshing models: vertical forces on the third wheelset.

equivalent models	vertical forces unloading [N]	unload ratio [—]
1	40392	0.432
5	40018	0.428
9	39925	0.427
13	39904	0.427

As a conclusion, comparing the different simulations it is possible to state that 9 equivalent models are an adequate representation of the sloshing liquid. Therefore parametric analysis is performed using a multi-body model having 9 additional DOFs in order to account for sloshing effects of the fluid.

A preliminary analysis is performed considering an s-shaped curve. The aim of this simulation is to understand the multi-body dynamics of the system and, in particular, to examine the contribution of the sloshing liquid on the system dynamics.

The following methodology will be used:

- Derailment and rollover risk are evaluated by means of two indicators: Y/Q and $\Delta Q/Q_0$, defined respectively as the ratio between the lateral (Y) and vertical forces (Q) and the ratio between the force unload ($Q_0 - Q$) and the static load (Q_0) (unload ratio), for any wheel. By means of the multi-body simulations, time histories can be obtained and then, according to the European standards, they are filtered using a fourth-order Butterworth filter, at 20Hz. Finally, the maximum value across the eight wheels and the whole time histories is computed, in order to represent the derailment and rollover risks with only two, non-dimensional indicators. Limit values are normally set to 0.8 (for Y/Q) and 0.6 (for $\Delta Q/Q_0$): if higher values are experienced, the wagon is considered to be not safe with respect to derailment or rollover.
- Two multi-body systems are used for every simulation: *mk* and *rigid*. The first one is inclusive of the sloshing model, while the second one assumes that the whole liquid volume moves rigidly with the carbody. Comparison between the two allows to understand the relevance of the sloshing motion on the dynamics of the wagon.

The s-shaped curve is chosen since it is expected that sloshing have higher dynamics effects, than in the case of a full curve. In particular, the physical intuition is that, when the vehicle enters the first curve (to the left), the liquid load moves to the right and starts an oscillatory motion; when the vehicle enters the second curve (to the right), the centrifugal acceleration, together with the free motion of the fluid, can give rise to dynamic effects that increase the sloshing motion and, eventually, cause a high unload of the internal wheel.

The track geometry represented in Figure 139 is imposed with the following parameters: $L_{C1} = L_{C2} = 22.9$ m, $L_I = 22.0$ m, $R = 250$ m. Note that no curve transitions are present and the cant

is null (this geometry can be similar to a turnout geometry); therefore, since the curve is run at 12.5 m/s, the maximum lateral acceleration on the track plane is 0.6 m/s^2 , which is the maximum allowed for this kind of vehicle.

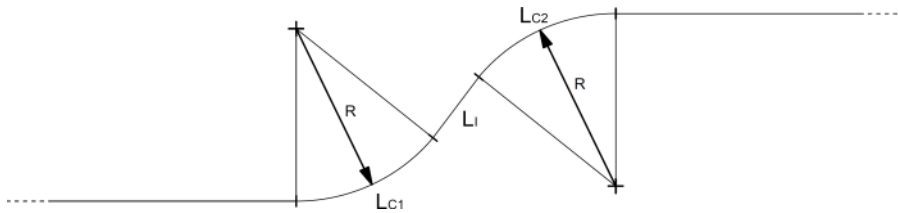


Figure 139 Schematic representation of the s-curve.

Results show that in this case, vehicle dynamics are strongly affected by the sloshing phenomenon (for example, Figure 140 reports the vertical forces on the third wheelset):

- in the second curve, the two models (*mk* and *rigid*) show relevant differences both in the shape of the time histories and in the maximum values. In particular, the *mk* model reaches the peak values before the *rigid* one and, moreover, two local maxima are experienced. As a consequence, the vehicle with partial liquid load is affected by a larger unload;
- in the *rigid* model, time histories on the inner and outer wheels are repeated symmetrically in the first and second curve. If, instead sloshing is considered, the second curve is characterized by a different behaviour of the vehicle with respect to the first one, because of the dynamic effects associated to the liquid content. A direct consequence of this phenomenon is the difference between the vertical forces experienced in the first and second curve by the *mk* model.

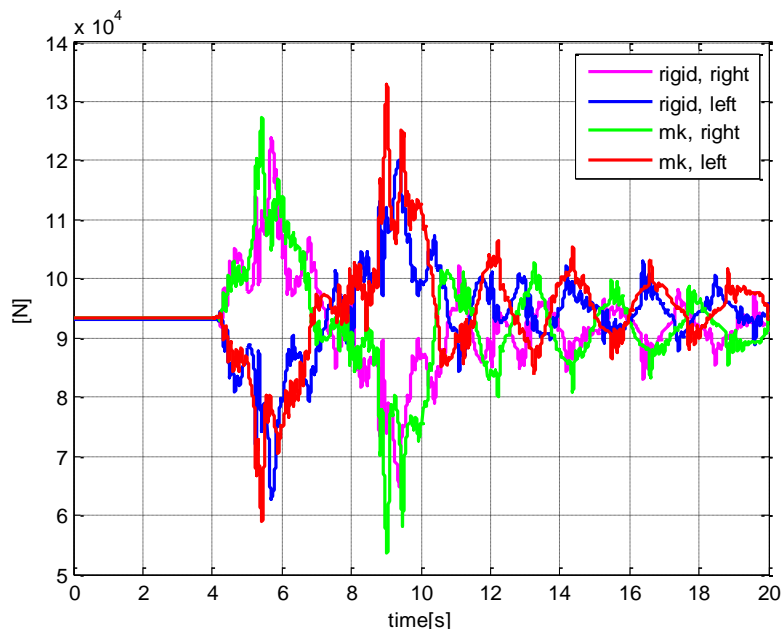


Figure 140 S-curve, $v=12.5 \text{ m/s}$: vertical forces on the third wheelset.

Table 39 reports the maximum values of Y/Q and $\Delta Q/Q_0$ for this simulation. It is possible to note that sloshing has almost no effect on the derailment risk, while it increases significantly

the rollover risk: neglecting the sloshing effects would cause an under-estimation of the unload ratio of about 20%.

Table 39 S-curve: maximum values of Y/Q and $\Delta Q/Q_0$.

	<i>mk</i> (wheelset)	<i>rigid</i> (wheelset)
Y/Q	0.62 (1)	0.63 (1)
$\Delta Q/Q_0$	0.43 (3)	0.35 (2)

Figure 141 shows that the highest unload ratio is experienced when the equivalent models are close to their maximum displacement, which occurs at the end of the second curve. Also note that this oscillatory motion increases when the wagon enters the second curve, because of the combination of the free-motion of the 9 masses with the change in the centrifugal acceleration: this combination amplifies the sloshing motion if the vehicle enters the counter-curve (to the right) when the equivalent models are close to their extreme position to the right.

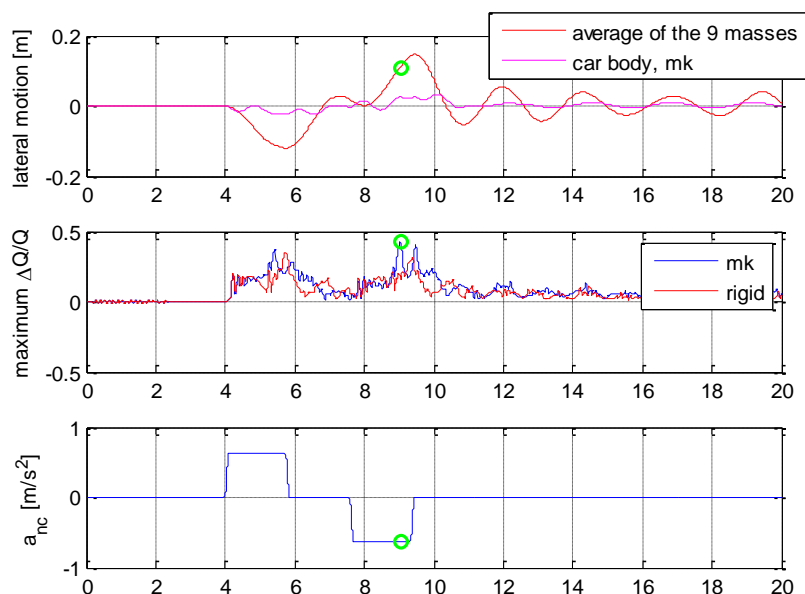


Figure 141 S-curve: lateral motion of the equivalent models and of the carbody (above), maximum $\Delta Q/Q_0$ and lateral acceleration (below). The green circle represents the instant when the maximum $\Delta Q/Q_0$ is experienced.

Figure 142 shows the different contributions to rollover and, therefore, to $\Delta Q/Q_0$: for each of the reported forces, the equivalent unload on the inside wheel is computed using D'Alembert's principle, assuming the unloading to be uniformly distributed on the four axles of the vehicle. Equations **Error! Reference source not found.** report the gravitational and inertial contributions, respectively (m is a generic mass, y its lateral displacement, h its height from the ground and a_{nc} the lateral acceleration on the track plane).

$$\begin{aligned} \Delta Q_{\text{gravitational}} &= \frac{mgy}{2s} \\ \Delta Q_{\text{inertial}} &= \frac{m(\ddot{y} + a_{nc})h}{2s} \end{aligned} \quad (46)$$

Note that this is only an approximation, but gives an idea of the prevailing terms.

In general, it is possible to observe that the most important contribution to rollover is associated to the carbody acceleration: this rigid body is in fact located at a high height above the ground and it has the largest mass. Its dynamics is of course coupled with that of the equivalent models. By comparing the *mk* and *rigid* models, it is possible to state that, in this simulation, sloshing causes an increased motion of the carbody that, together with the motion of the equivalent models, causes higher maximum unload ratios.

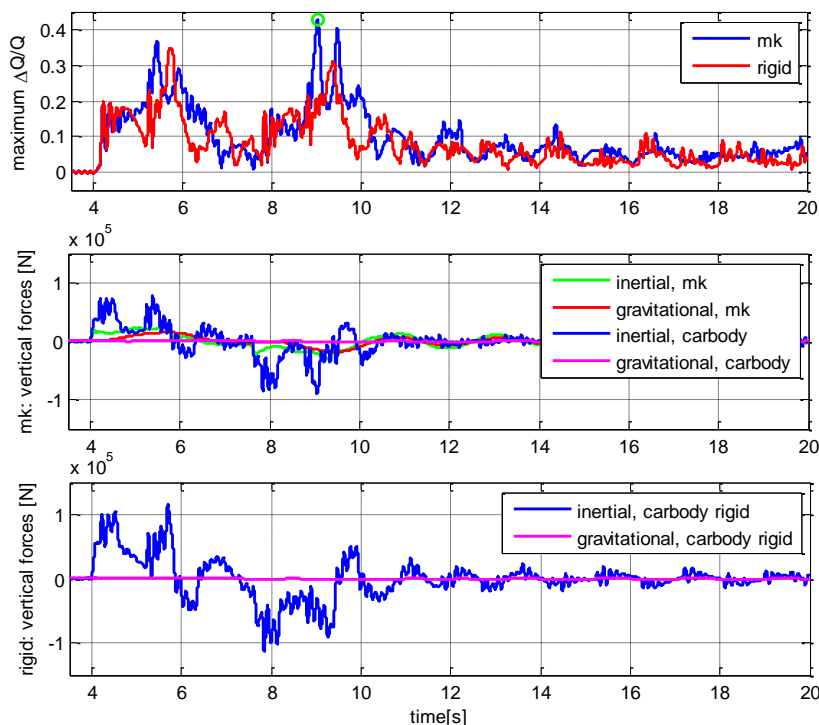


Figure 142 Maximum $\Delta Q / Q_0$ (above) and the different components of the internal-wheel unload (middle and below).

In conclusion:

- the s-curve geometry magnifies the effects of sloshing on vehicle dynamics. While flange climbing risk is not affected, the rollover risk is increased significantly;
- sloshing effects are associated to an increased motion of the liquid volume, due to the non-compensated acceleration imposed by the curve and counter-curve.

In order to understand when this excitation is dangerous for the vehicle's running safety, a parametric study will be performed to identify the effects of different variables on the multi-body dynamics.

5.5 Results of the parametric analysis

In this section, the multi-body model previously defined is used to run a variety of simulation cases, whose main goal is to understand which are the most important parameters that affect the rollover risk associated to the liquid sloshing. Variables under analysis are related both to the vehicle (fill level χ and velocity v) and the track.

The unload ratio $\Delta Q/Q_0$ will be considered in order to evaluate the rollover risk. Moreover, the difference in terms of $\Delta Q/Q_0$ between the *mk* and *rigid* models is evaluated in order to assess the effects of sloshing, in comparison with a model considering the fluid as a rigid load. Such difference is evaluated based on the sensitivity parameter δ_Q , defined in Equation **Error! Reference source not found.**: a high value of δ_Q indicates that the sloshing causes a significant increase in the unload ratio and therefore a higher risk of rollover, with respect to the rigid case. If considered from a different point of view, δ_Q can be interpreted as the error one would incur when evaluating the rollover risk, if the effects of the motion of liquid are neglected.

$$\delta_Q = (\Delta Q / Q_0)_{mk} - (\Delta Q / Q_0)_{rigid} \quad (47)$$

In order to make the analysis as general as possible, a mathematical relation between the most important parameters will be defined and in particular the sensitivity parameter δ_Q will be expressed as a function of other non-dimensional variables. In the following subsection this non dimensional relation will be defined and applied to different conditions, in order to check its validity.

5.5.1 Non-dimensional relation

In the following simulations, the multi-body model travels at different velocities (ranging from 3.0 m/s to 17.0 m/s, with steps of 0.5 m/s), along the s-curve defined in Figure 139. Main objective is to understand if there is a velocity range in which the sloshing motion has stronger effects on the vehicle dynamics.

Figure 143 reports the maximum value of $\Delta Q/Q_0$, evaluated over all wheels in the vehicle, both for the *mk* and *rigid* models, as a function of the train velocity; note that $v=12.5$ m/s corresponds to a non-compensated lateral acceleration $a_{nc}=0.6$ m/s² and, therefore should be considered as an upper limit (typically, 0.6 m/s² is considered the maximum acceptable non-compensated acceleration, for normal operating conditions of freight trains). Based on this result, it is possible to observe that:

- unless the non-compensated acceleration is above the limits (i.e. when $v > 13$ m/s), the unload ratio never exceeds 0.6 (considered as a threshold value) and thus no rollover risk is encountered;
- the unload ratio increases, as the velocity increases. This is due to the centrifugal effects, that increases quadratically with speed, causing higher quasi-static lateral forces and the consequent wheel unload; moreover, all of the vehicle's parts show larger oscillations and therefore higher forces are generated;
- for low velocities (between 3.0 m/s and 9.0 m/s), *mk* and *rigid* models provide very similar unload ratios, because fluid dynamics effects are rarely significant. On the contrary, at higher velocities (above 9.0 m/s) it is possible to note some differences between the two models. Such differences are due to the different dynamic

properties of the two models: the *mk* model has eigenfrequencies and eigenmodes such that, when it moves with a velocity between 12 m/s and 15 m/s, its dynamics cause a higher unload on the inner wheel. A similar behaviour is shown by the rigid model, for velocities between 9 m/s and 12 m/s. Note that, if the effects of sloshing are neglected, the unload ratio can be significantly under-estimated: for instance, an error of 0.08 ($\approx 23\%$) on $\Delta Q/Q_0$ would be experienced when $v=12.5\text{m/s}$.

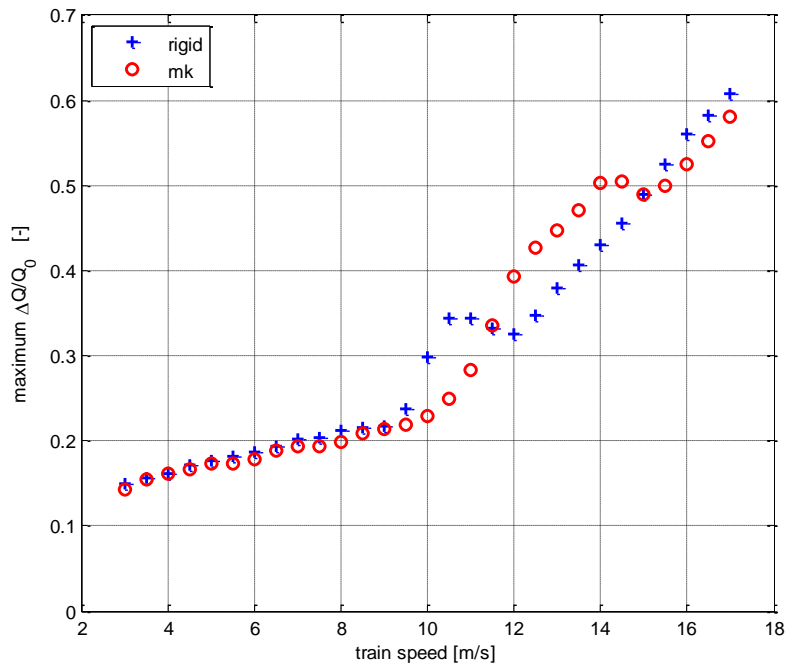


Figure 143 $\Delta Q/Q_0$ as a function of the velocity of the vehicle.

It is possible to explain the results in Figure 143 based on the definition of a non-dimensional variable called hereafter reduced frequency, as described below.

1. First, it is observed that when the vehicle enters the first curve, the equivalent models start to move, under effects of the centrifugal force, towards the external part of the track. After a time T_{init} after entering the curve, the liquid reaches its maximum lateral displacement. Generally speaking, this initial time depends on the properties of the liquid (including the fill level), the curve geometry and the non-compensated acceleration as well. However, simulations show that no significant variations are experienced, for different velocities, a value of $T_{init} \approx 1.6$ s is obtained for all the cases (as in Figure 144). Amplitude of this first oscillation is increasing with the train speed.

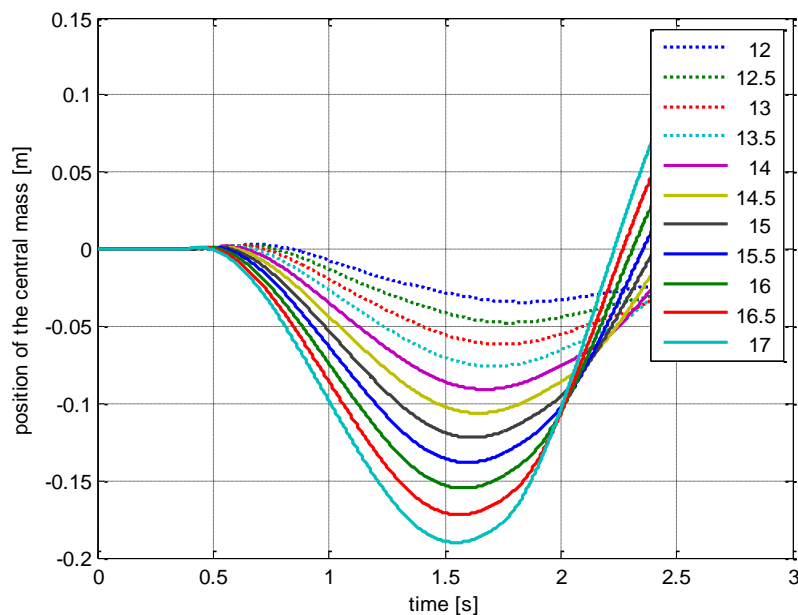


Figure 144 Curve entry: lateral motion of the central mass, for different train velocities.

2. Since the equivalent models are characterized by a very small damping, they continue their free oscillation, under the effect of the centrifugal force. When the vehicle exits the first curve and travels along the intermediate straight path, the oscillatory motion continues undisturbed following the natural sloshing frequency.
3. When the vehicle enters the counter-curve, the equivalent models begin to be excited by the centrifugal acceleration, that forces them to move towards the external part of the track. If this excitation is in phase with the free oscillation of the models, it can lead to an increased oscillation in the counter-curve. This happens when the equivalent models undergo an integer number of oscillations, from their beginning to the entry into the second curve: in other cases, the combination of the centrifugal forces with the free motion of the masses reduces the oscillation. As a consequence, also the carbody motion can be increased and, eventually the combination of all these effects may lead to an increased wheel unload.

Based on this physical interpretation, it appears that the vehicle dynamics can be analysed as a function of the non-dimensional parameter f^* (reduced frequency), as defined in Equation **Error! Reference source not found.**, where T_{slosh} is the first natural sloshing period (it can be obtained for instance by means of a CFD analysis, as in Table 35) and vT_{init} represents the length run by the vehicle while the sloshing motion begins its first oscillation.

$$f^* = \frac{L_{C1} - vT_{init} + L_I}{vT_{slosh}} \quad (48)$$

Note that if $f^*=1$, the equivalent masses are expected to undergo, between the two curves, exactly one complete oscillation period and enter the second curve with a lateral displacement towards the right; therefore, when the non-compensated acceleration forces them to move to the left, it combines with the free oscillation and causes an increased motion of the masses themselves. Similar considerations can be made for any integer value of f^* , in correspondence to which the highest effects of sloshing should be experienced.

Figure 145 reports $\delta_Q(f^*)$. As predicted, the maximum effects of sloshing are experienced when $f^* \approx 1$: in particular, a zone with high sloshing effects can be defined for f^* between 0.7 and 1.1. If instead f^* is between 1.1 and 1.6, the dynamics of the *rigid* model, combined with the curve geometry, causes higher unloads than the *mk* model: for instance, Figure 145 shows that, at $v=10.5\text{m/s}$ ($f^*=1.3$), the dynamic behaviour of the *rigid* model causes higher accelerations of the carbody and therefore a higher $\Delta Q/Q_0$, whereas in the *mk* model, the equivalent masses approach the second curve in counter-phase, with respect to the imposed centrifugal force and, thus their oscillations are not amplified.

A similar behaviour would be expected for $f^* \approx 2$ and $f^* \approx 3$, but the low corresponding velocities cause an insufficient initial oscillation of the equivalent models: dynamic effects are not large enough to cause a significant deviation between the *mk* and *rigid* models. In fact, for example Table 40 reports the lateral displacements of the central mass, for the different reduced frequencies, associated to its first oscillation.

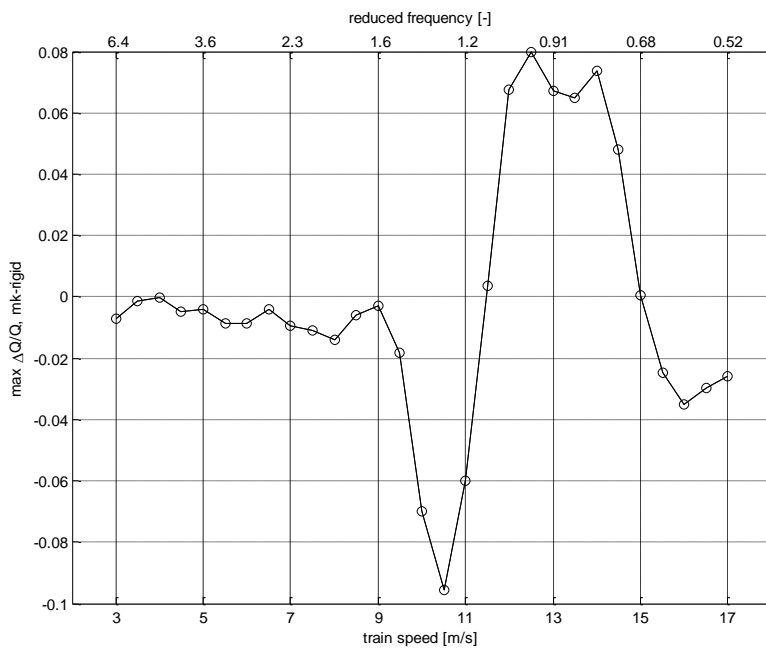


Figure 145 δ_Q as a function of the velocity of the vehicle and of the respective reduced frequency, f^* .

Table 40 Maximum lateral motion of the central equivalent model, during the first oscillation, for different reduced frequencies.

f^*	v [m/s]	a_{nc} [m/s^2]	$y_{\text{centralmass}}$ [mm]
0.97	12.5	0.63	120
1.94	8.0	0.26	35
3.16	5.5	0.12	20

5.5.2 Effect of the length of the intermediate straight

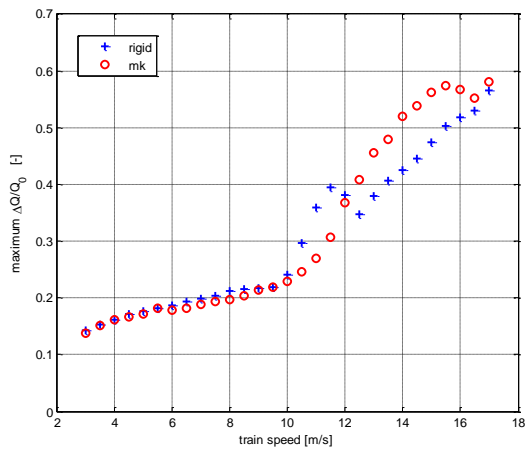
The influence of the length of the intermediate straight (L_I) is investigated. In particular, simulations with $L_I=26.0\text{ m}$ and $L_I=30.0\text{ m}$ will be performed, as well as $L_I=14.0\text{ m}$ and

$L_I=50.0$ m; in order to evaluate the validity of the non-dimensional relation $\delta_Q(f^*)$ different velocities will be simulated.

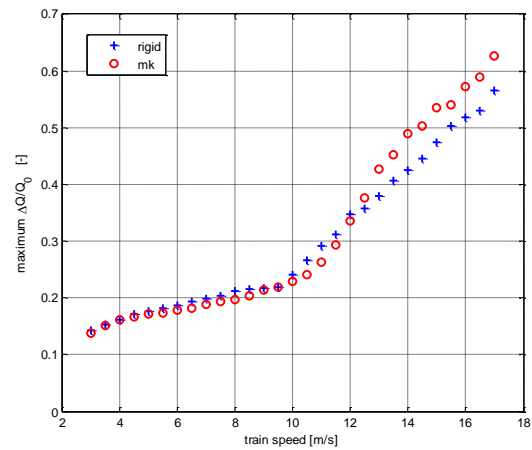
5.5.2.1 $L_I=26.0$ m and $L_I=30.0$ m

Figure 146 shows that, for $L_I=26.0$ m and $L_I=30.0$ m, curve $\Delta Q/Q_0(v)$ has a similar shape to the one obtained with $L_I=22.0$ m; the same considerations previously made can be applied also to these cases.

Moreover, it is possible to note that, as L_I increases, the effects of sloshing become significant only at higher velocities. This result is coherent with the previously determined non-dimensional relation, since, in order to have $f^*\approx 1$, a higher velocity is required if L_I is increased. Figure 147 reports the comparison between functions $\delta_Q(f^*)$, obtained with different L_I : the good accordance demonstrates that the non-dimensional analysis is valid in all the three cases.



(a) $L_I=26.0$ m



(b) $L_I=30.0$ m

Figure 146 $\Delta Q/Q_0(v)$, for different lengths of the intermediate straight.

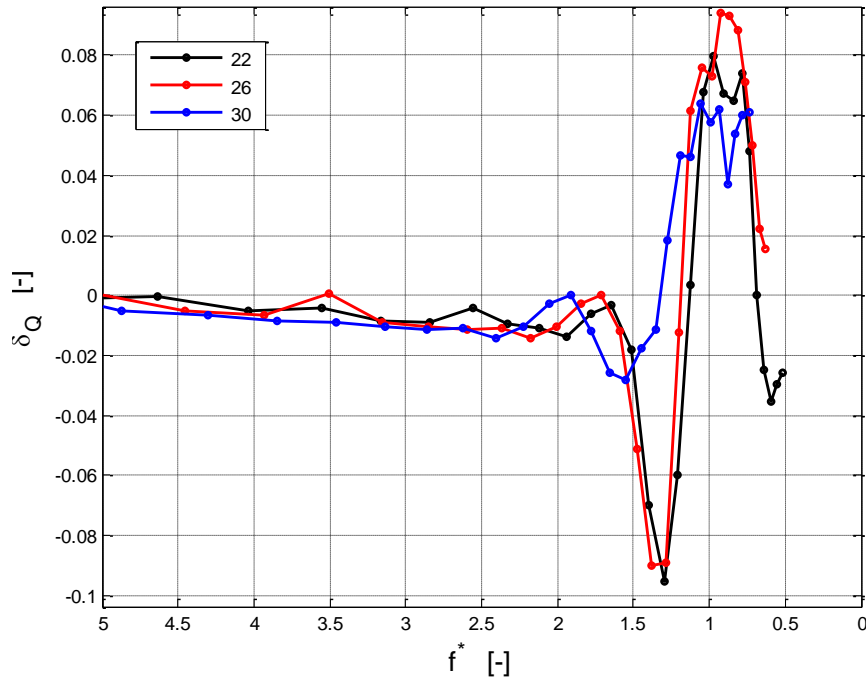


Figure 147 $\delta_Q(f^*)$, obtained for different values of L_1 [m].

5.5.2.2 $L_1=14.0$ m

The same simulation is run for $L_1=14.0$ m; as shown in Figure 148, in this case only minor effects of sloshing are experienced. According to the above-defined non-dimensional model, a reduced frequency $f^*=1$ occurs for $v \approx 10$ m/s ($a_{nc}=0.4$ m/s²): as previously explained, this velocity (and the corresponding non-compensated acceleration) is not sufficient to induce a large oscillation of the equivalent masses (that reach an initial amplitude of about 60 mm) and therefore sloshing does not significantly affect the overall system.

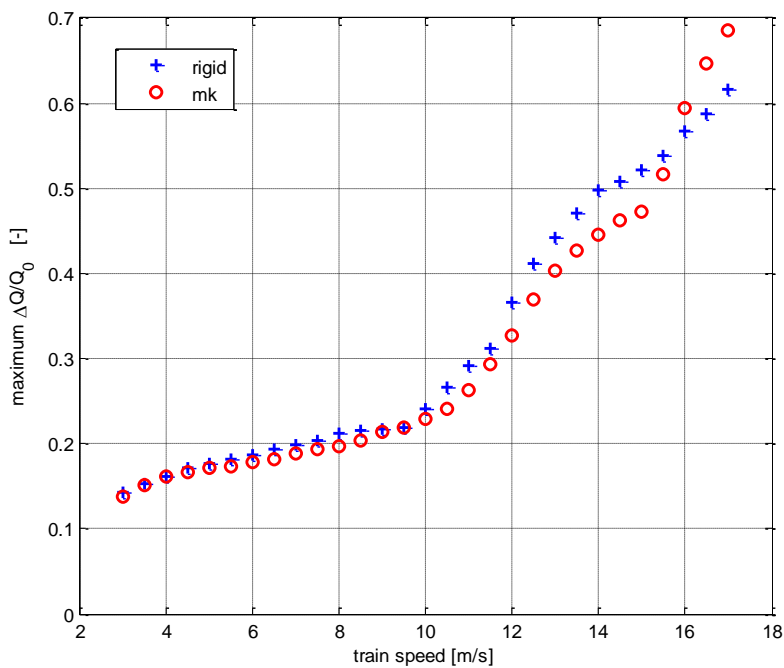
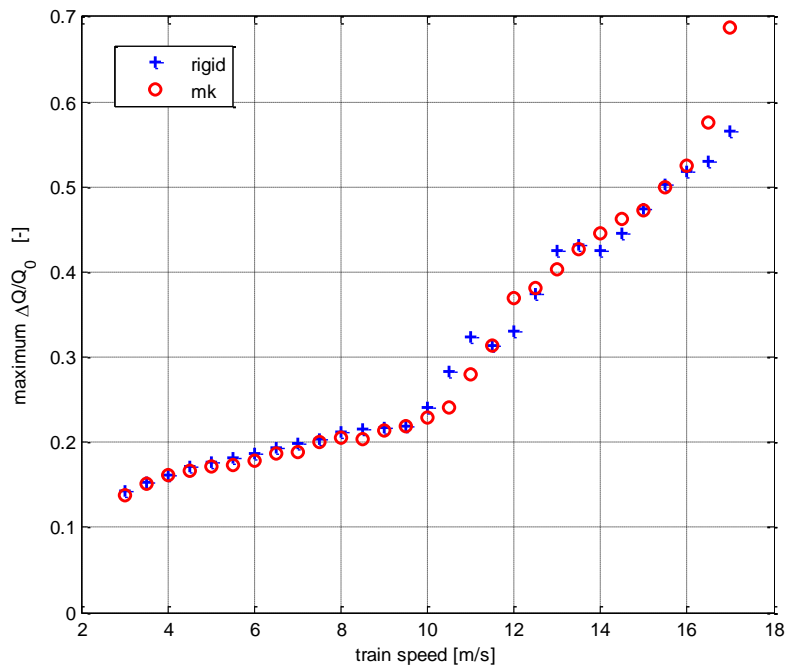


Figure 148 $\Delta Q/Q_0(v)$, obtained for $L_i=14.0$ m.

5.5.2.3 $L_i=50.0$ m

As in the previous case with $L_i=14$ m/s, $\Delta Q/Q_0(v)$ does not show relevant differences between the *mk* and *rigid* models. In this case, $f^*=1$ corresponds to a velocity well above the limits on the non-compensated acceleration, while $f^*=2$ corresponds to $v=12.5$ m/s: therefore, if the train velocity is close to this value, sloshing would be expected to have relevant effects on the unload ratio. Anyway, the simulations show small differences between the two models (Figure 149).

Figure 149 $\Delta Q/Q_0(v)$, obtained for $L_i=50.0$ m.

A possible explanation lies in the overall damping of the multi-body system: during the intermediate straight (that is crossed in 4 s, when the train travels at 12.5 m/s), the wagon dissipates part of its energy and, in particular, the carbody reduces its oscillatory motion. As a consequence, when the wagon enters the counter-curve, the combination of the centrifugal forces with the free oscillation of the multi-body system do not cause a significant amplification of the sloshing motion (and of the unloaded forces, as well). Figure 150 shows that the carbody motion is damped during the intermediate straight and, therefore, the counter-curve shows a similar behaviour to the first curve.

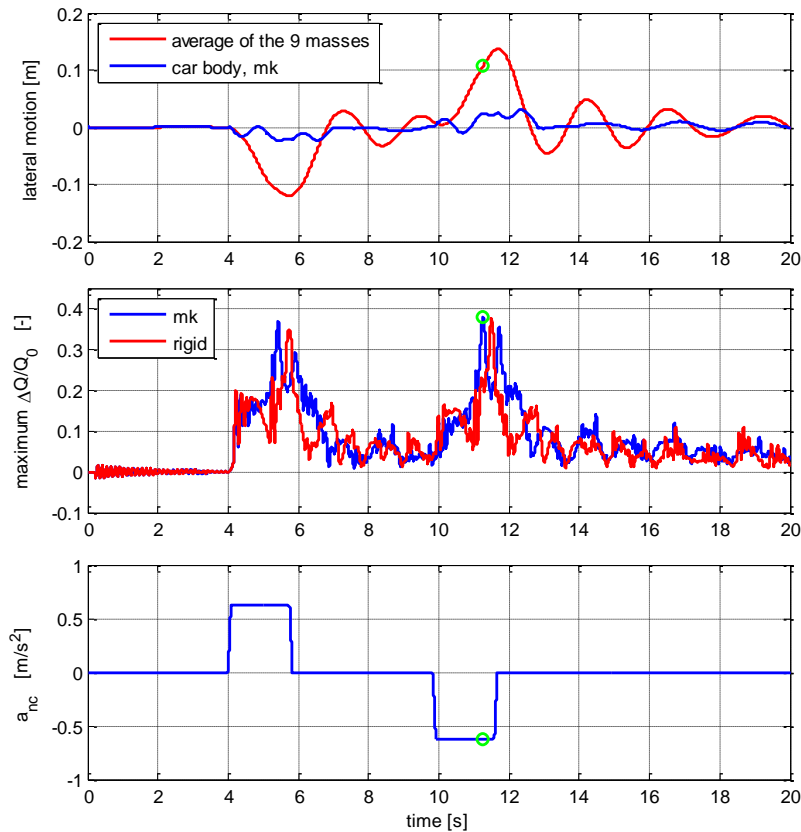


Figure 150 Lateral motion of the equivalent models and of the carbody (above), maximum $\Delta Q/Q_0$ (middle) and lateral non-compensated acceleration (below), obtained for $L_1=50.0$ m and $v=12.5$ m/s.

5.5.3 Effect of the curve radius

The effect of the curve radius is investigated as well. The parameters of the simulations used in order to investigate the influence of the curve radius are reported in Table 41.

Table 41 Parameters of the simulations.

R [m]	L_{C1} [m]	L_1 [m]	L_{C2} [m]	velocities [m/s]
375	27.0	28.0	27.0	[7.0:21.0]
170	20.3	15.0	20.3	[3.0:17.0]

When curve radius is increased to 375m, results are similar to those obtained with $R=250$ m, both in terms of $\Delta Q/Q_0(v)$ (Figure 151) and of $\delta_Q(f^*)$ (Figure 152).

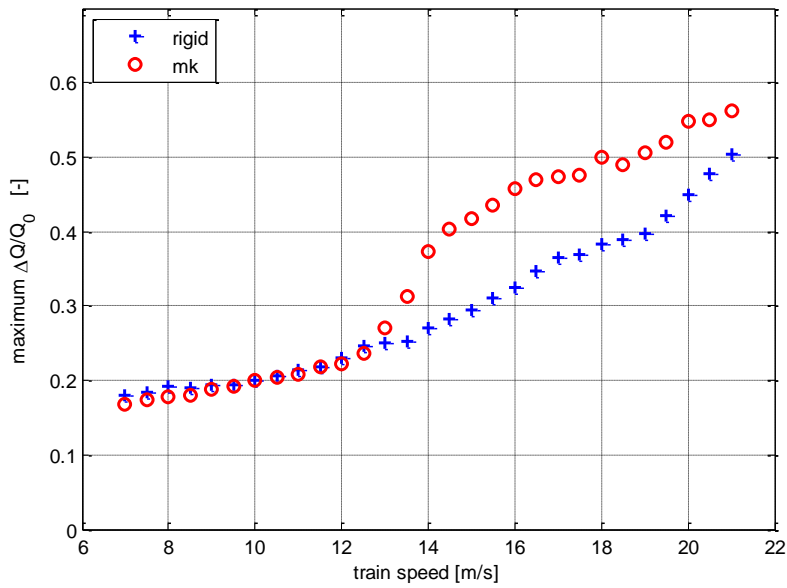


Figure 151 $\Delta Q/Q_0(v)$, for $R=375$ m.

Note that the range of reduced frequencies in which sloshing causes a significant increase in $\Delta Q/Q_0$ is similar to the one observed for $R=250$ m (f^* between 0.7 and 1.1): this finding qualitatively validates the general validity of the non-dimensional analysis. Moreover, $\delta_Q(f^*)$ in this range of reduced frequencies generally assumes values between 0.08 and 0.11.

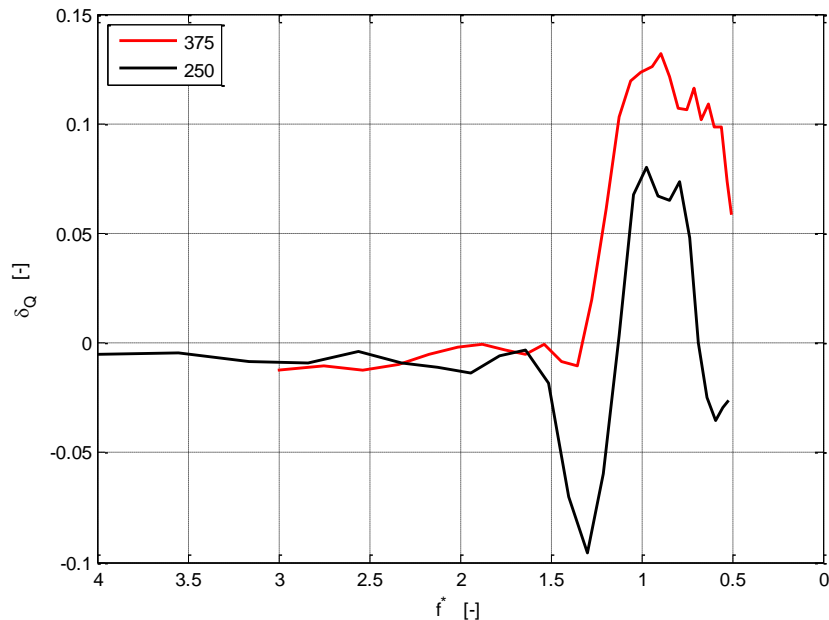


Figure 152 $\delta_Q(f^*)$, for different values of R [m].

Figure 6.12 reports $\Delta Q/Q_0(v)$, for $R=170$ m: in this case, $f^*=1$ corresponds to $v \approx 10$ m/s and $a_{nc} = 0.6$ m/s². The main difference with respect to the previous cases is that, for velocities around 10 m/s, the dynamics of the rigid model induce higher values for $\Delta Q/Q_0$. Note that the reduced frequency f^* does not consider any characteristic of the rigid model and, as a

consequence, cannot be used to predict this situations; anyway, for the sake of simplicity, no further variables will be introduced in the analyses.

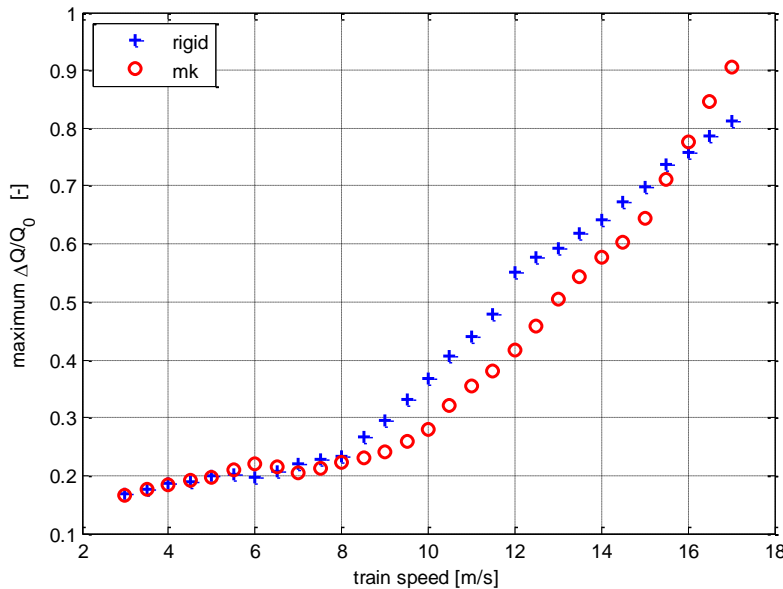


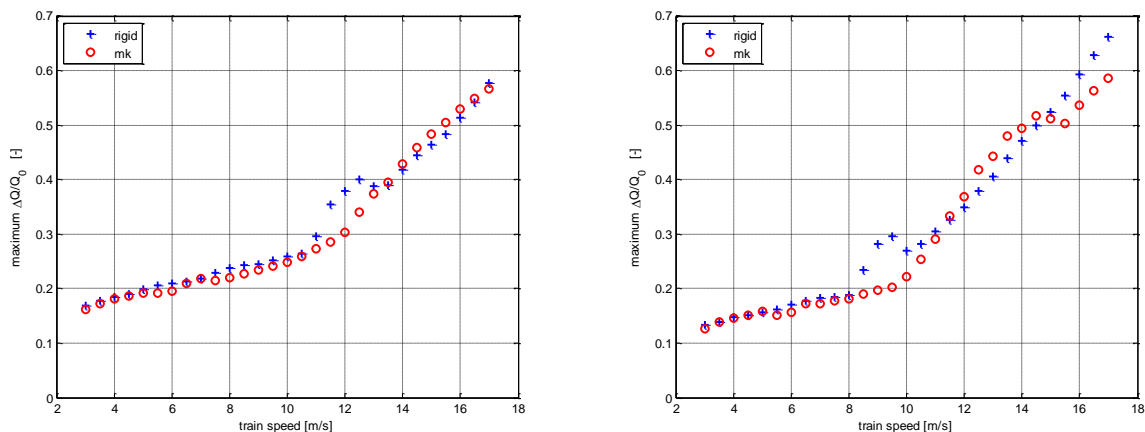
Figure 153 $\Delta Q/Q_0(v)$, for R=170 m.

In both cases (R=170m and R=375m), in order to compute the reduced frequency f^* , time histories of the lateral displacement of the equivalent models were studied; as a result, T_{init} is found to be again 1.6 s, in any case.

5.5.4 Effect of the fill level

The identification procedure shown in subsection 5.3 is used to define the multi-body models that correspond to fill levels $\chi=40\%$ and $\chi=60\%$ (in normal operating conditions, the maximum load per axle does not exceed 22 t and therefore a fill level of 60% is considered as a maximum). These fill levels are chosen for the multibody simulations because the first one is characterized by the largest m_1/m_0 ratio and the latter one has the largest m_0 , m_1 and height of the CoG therefore, both of them may increase the rollover risk of the vehicle.

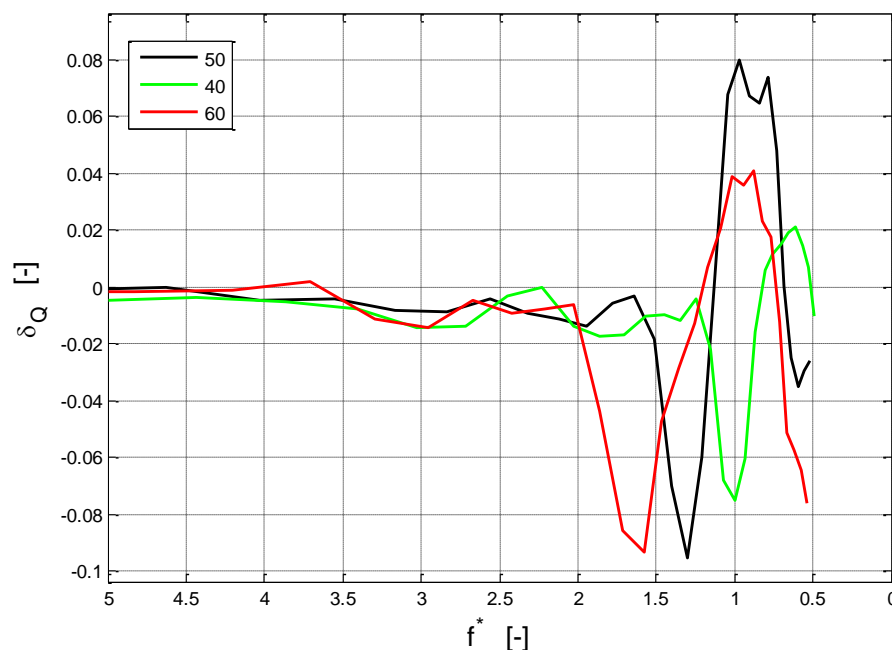
Figure 154 shows that curves $\Delta Q/Q_0(v)$ are qualitatively similar to the one obtained for $\chi=50\%$, even though there are some quantitative differences.



(a) $\chi=40\%$ (b) $\chi=60\%$ Figure 154 $\Delta Q/Q_0(v)$, for different fill levels.

The non-dimensional analysis (reported in Figure 155) shows that, for both $\chi=50\%$ and 60% , and the maximum δ_Q corresponds to reduced frequencies f^* between 0.7 and 1.1. In the case of $\chi=40\%$, the obtained curve is qualitatively similar to the other ones, but maximum values of δ_Q are lower and do not correspond to the expected reduced frequencies. This is probably due to the lower height of the CoG of the equivalent models, that reduces the effects of sloshing on the roll-plane vehicle dynamics; therefore, sloshing has lower effects on the rollover risk.

The highest effects of sloshing (highest δ_Q) are obtained for the fill level $\chi=50\%$.

Figure 155 $\delta_Q(f^*)$, for different values of the fill level χ [%].

Note that a preliminary analysis allowed to determine again $T_{init}=1.6s$.

5.5.5 Effect of the length of the counter-curve

This section investigate the effect of the length of the counter curve L_{C2} : in particular, the main objective is to understand in which position, along the counter-curve, the vehicle experiences the maximum $\Delta Q/Q_0$. Therefore, length of the second counter-curve is increased to 150.0m, in order to have a longer observation time for the multi-body dynamics.

The same curve described in Figure 139 is used, where only L_{C2} is changed; as an example, Figure 156 reports the corresponding time histories, for $v=12.5$ m/s. Note that the maximum $\Delta Q/Q_0$, in the *mk* model, is experienced at the beginning of the counter-curve, similarly to the case with $L_{C2}=22.9$ m (Figure 156). After this moment, the sloshing motion (represented by the 9 equivalent models) continues with almost no damping, while the oscillations of the carbody decrease; therefore, the following peaks in $\Delta Q/Q_0$ are lower. Note that, as expected

also values of the maximum $\Delta Q/Q_0$, for both the *rigid* and *mk* model, are the same as in Figure 141. As a conclusion, it is possible to state that, since the overall damping of the multi-body system reduces its free oscillations, the maximum unload ratios are experienced at the beginning of the counter-curve and, thus, an increase of L_{C2} has no effects on $\Delta Q/Q_0$.

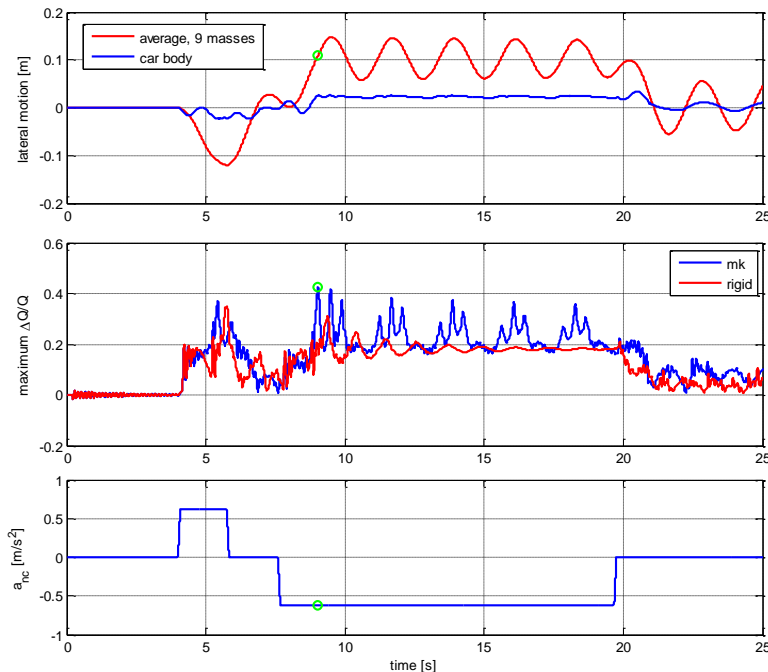


Figure 156 Lateral motion of the equivalent models and of the carbody (above), maximum $\Delta Q/Q_0$ (middle) and non-compensated acceleration (below), obtained for $L_{C2}=150.0$ m.

Figure 157 reports a comparison between the non-dimensional analyses, performed for both $L_{C2}=22.9$ m and $L_{C2}=150.0$ m: a good accordance between the two curves confirms that results have a weak dependence on L_{C2} .

The same comparison is then performed for all of the above-defined simulations, that are repeated with the same parameters, except for L_{C2} that is set to 150.0m. Every case shows that L_{C2} has no influence on the final results ($\Delta Q/Q_0(v)$ and $\delta_Q(f^*)$).

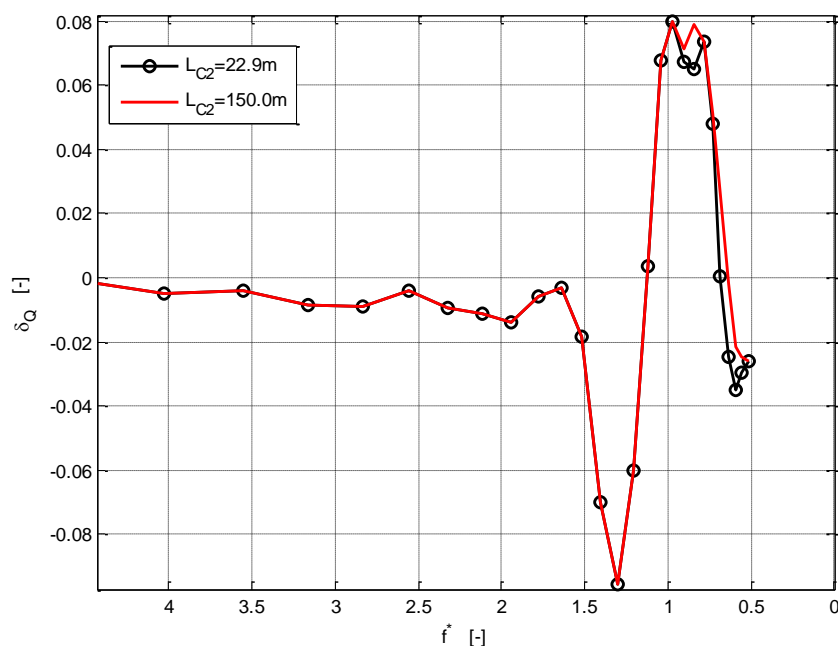


Figure 157 $\delta_Q(f^*)$, for different values of L_{C2} .

5.6 Concluding remarks

A dynamic model of the coupled dynamics between a tank vehicle and its fluid content was used in a variety of simulations, with the main objective of understanding the dynamic behaviour of a railway wagon that carries a liquid load under partial filling condition. In particular, the effects of train velocity, curve geometry and fill level were investigated. From a general point of view, the derailment quotient Y/Q is only marginally affected by the sloshing motion and is always below the safety limits. On the other hand, the rollover ratio $\Delta Q/Q_0$ can be significantly increased by the liquid motion and, in extreme cases, it can reach values close to the safety limit (0.6). In particular, while a full curve is not found to be critical, sloshing effects are strongly experienced in s-curves, in which the liquid motion can be increased by the centrifugal forces if, in the counter-curve, the free oscillation of the liquid and the external forcing are in phase.

A non-dimensional analysis allowed to identify, as an important variable, the reduced frequency f^* , defined as the number of sloshing periods that occur from the first oscillation of the liquid (in the first curve) to the entrance into the counter-curve. By comparing different simulations, it was shown that, if f^* is between 0.7 and 1.1, the unload ratio $\Delta Q/Q_0$ is increased by the sloshing effects, if compared with an equivalent wagon with rigid cargo. This relation was found to be valid only if the wagon is subject to high lateral non-compensated accelerations ($>0.4 \text{ m/s}^2$). Neglecting sloshing effect would cause an underestimation of the maximum $\Delta Q/Q_0$ of about 20%, in the bad case.

5.6.1 Identified main affecting parameters

In the analysis it has been shown that sloshing effects can be significant if the vehicle negotiates an s-curve.

The fill level of the tank also influences the vertical unload.

5.6.2 Estimation of commercial impact of preventive measures

The presented analysis has shown a possible increase of the rollover risk of tank vehicles when negotiating a s-curve. With respect to the commercial impact it can be pointed out that the speed of tank vehicles should be monitored in order to avoid the synchronisation of the sloshing phenomenon with the curve negotiation, thus avoiding to obtain a value of the reduced frequency f^* close to 1.

Additional on account of the low damping of the sloshing phenomenon it can increase the fatigue of the components of the running stock, thus reducing their life.

5.7 References

- [22] G.I. Bogomaz, O.M. Markova, and YU.G. Chernomashentseva. Mathematical cargo mobility. International Journal of Vehicle Mechanics and Mobility, 2007.
- [23] C. Vera, J. Paulin, B. Suarez, and M. Gutierrez. Simulation of freight trains equipped with partially filled tank containers and related resonance phenomenon. Proceedings of the Institution of Mechanical Engineers, Part F: Journal of Rail and Rapid Transit, 2005.
- [24] I.H. Ashtiani, D. Younesian, M. Abedi, and E. Esmailzadeh. Effects of partially-filled containers in dynamic behavior of tanker trains traveling on curved tracks. Proceedings of the ASME, 2008.
- [25] Dongming Liu and Pengzhi Lin. A numerical study of three-dimensional liquid sloshing in tanks. Journal of Computational Physics, 2008.
- [26] M. Utsumi. A mechanical model for low-gravity sloshing in an axisymmetric tank. 2004.
- [27] L. Dai, L. Xu, and B. Setiawan. A new non-linear approach to analysing the dynamic behaviour of tank vehicles subjected to liquid sloshing. Proceedings of the Institution of Mechanical Engineers, Part K: Journal of Multi-body Dynamics, 2004.
- [28] Raouf A. Ibrahim. Liquid Sloshing Dynamics, Theory and Applications. Cambridge, 2005.
- [29] 2011/314/EU: TSI Operation and traffic management. Brussels: EU; 2011.

6 Derailments due to wheel failures

In deliverable D1.1 it is stated that: “Solid wheel ruptures occur as a result of braking effects, unexpected loads (greater than design loads) or the metallurgical properties of steel (old wheels). Rupture of solid wheels is directly linked to wheel technology (cast wheels in North America and forged and laminated wheels in Europe).” With this as a starting point, typical freight wheels as found on the on European market are studied. This mean that the wheel failures are studies for solid forged wheels but not cast wheels (as used in North America) or laminated (build-up wheels as used for passenger traffic).

6.1 Derailment scenarios

Generally, wheel failures are at risk when a railway wheel is subjected to thermal or mechanical loads that are more severe than the ones which for it was designed, see deliverable D1.1 [1]. The types of wheel failures that are studied have in common that the integrity of the wheelset is degraded in a way that it no longer can keep the wheel in the rail or the train on the track.

One reason for this can be that the wheel-to-axle interface cannot support the forces acting on the wheel tread causing the wheel to slip along the axle with the result that the tread can no longer find support on the rail. This can result from radial cracking of a wheel, from rim to hub, or the wheel being lifted off the axle by a thermal loading on the wheel.

Another reason for loss of integrity of the wheelset can be that the wheel itself cracks, either circumferential along the web of the wheel or that a crack grows in a mixed radial circumferential mode. The circumferential crack ultimately makes the outer part of the web and rim to break away from the wheel hub and centre while the mixed radial-circumferential crack causes a section of the wheel to break off.

Thermal loads and mechanical loads can each cause fatigue damage and cracks to grow in wheels. Basically three scenarios for derailment have been analysed in D-RAIL:

1. Wheel failure due to (excessive) tread braking
2. Wheel failure due to (excessive) wheel-rail contact forces
3. Wheel failure due to combined damage from tread braking and wheel-rail contact

In addition to the above three scenarios, also the risk of derailment caused by rolling contact fatigue is addressed. Moreover, a study on the influence of track brakes is included. Risk of fatigue and fracture will be assessed for two generic wheel designs where one represents the classical freight wheel with a slightly S-shaped web and where one is a so-called low-stress wheel specifically designed for high thermal loads with a more elaborate shape of the wheel web. The wheel designs will be studied for new and for fully worn down rims.

The aim is to find limiting parameters for both the loading of the wheels and for allowable cracks in wheels. The studied wheel designs (described above) have been chosen with aim to cover most wheels that are in use in Europe.

6.2 Studied wheel designs

Influence from wheel design is studied by analysing two generic geometries:

1. classically S-shaped web (similar to ORE-wheel)
2. low-stress type for severe tread braking (approved according to EN13979-1 / UIC510-5, see references [2] and [3])

Finding the characteristics of design (1) and design (2), with a quite different behaviour with respect to thermomechanical performance will give results that are meaningful for derailments of a major part of the wheels that are in use today.

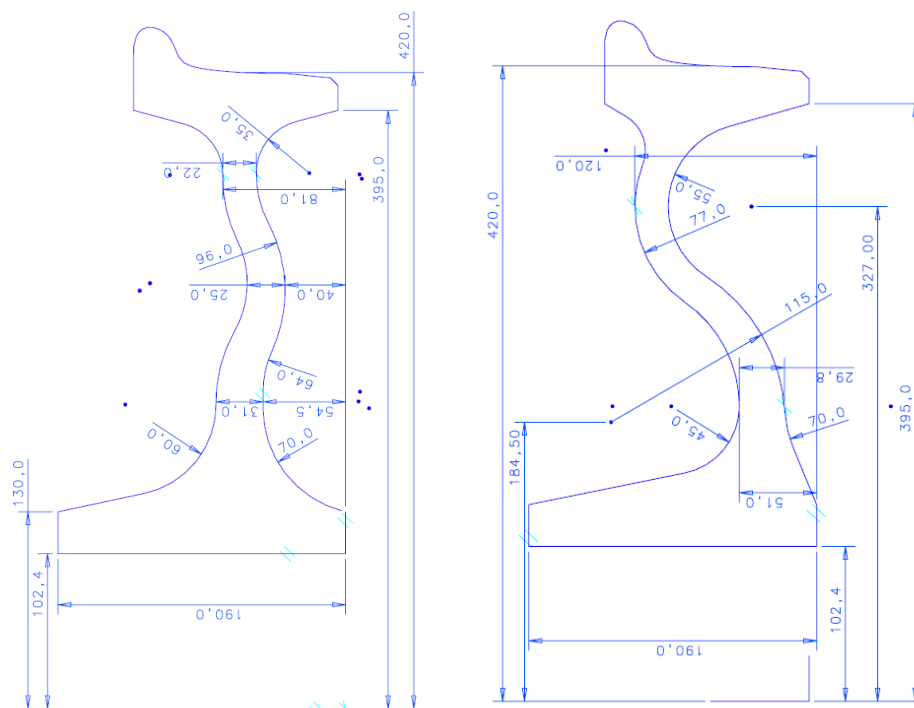


Figure 158 Cross sections of studied wheel designs at minimum wheel diameter. Left sketch shows the S-shaped wheel design and Right sketch shows the Low-stress wheel design.

6.3 Numerical simulations

Two basically different types of simulations will be utilised to impact from 1) mechanical loads from wheel-rail contact and 2) thermal loads from tread braking. The impact from the mechanical loading will be assessed by establishing a 3D-model of the wheel on which the wheel-rail contact forces are acting on the wheel rim. Magnitudes and positions of the loads will be varied to simulate standard loading situations but also cases when tread damage is present, which will influence the mechanical loads. One type of damage is such that it causes substantially increased vertical loads on the wheels, which is the case for e.g. a wheel flat or for significant spalling/shelling. Another type of damage is such that it causes significantly increased lateral loads on the wheels, which e.g. could be expected for a bogie with bad curving properties or for a when the treads of the wheels have equivalent conicity problems that causes hunting. Additionally, loading on wheels as induced by so-called track brakes as utilised on shunting yards are studied. The track brakes can induce a new type of loading on

the wheel rim that can be detrimental to the wheel life, which has not been considered at the design stage of the wheels.

The effects from tread braking will be assessed by using axisymmetric models of the wheels where heat partitioning of the braking power between wheel, brake blocks and rail is accounted for. Wheel rim displacements and build-up of stresses are studied by use of a two material models, one traditionally used linear kinematic model and one novel material model specially developed and calibrated for wheel steels at elevated temperatures as found during a severe braking incident.

The combined damage in the webs of the wheels from tread braking and wheel-rail contact forces is assessed using a Coffin-Manson approach together with Palmgren-Miner damage accumulation. Brake loads are varied to find main influencing parameters. Web lives are studied when also track brake loading cases are included.

6.3.1 Numerical models

6.3.1.1 Mechanical loading from conventional wheel-rail contact

The evaluation of fatigue in the wheel web due to loads induced at the wheel-rail contact basically follows the standard EN 13979-1. In the standard, a set of fatigue loads are given and a method for assessing fatigue due to the stresses induced by the loads. The fatigue loads simulate the train in three different situations:

Load case

1. The train travels on a straight track
2. The train passes a curve
3. The train passes a switch or a crossing

Application points for the forces representing these loads are visualised in Figure 159. The range of the principal stresses in the web of the wheel must not at any point exceed 360 MPa when considering all the three load cases. For a certain material point in the web, this range is calculated as the difference between the *maximum principal stress* and the *minimum normal stress in the direction of the maximum principal stress* for all three load cases. The forces corresponding to the three load cases are given in Table 42, for the loads specified in EN13979-1. The loads are based on the maximum static wheel load P on the rail. It is enough to study half a wheel (due to symmetry) and the material points in the web for calculating the maximum range of stress in the wheel. The effect of wheel rotation on the stress range is not included since they do not have an influence principal stress range.

The influence from the different types of damage as described above are studied by increasing the magnitudes of the vertical and the lateral loads as outlined in load cases 1-3 to levels higher than given in by the EN standard.

Table 42 Load cases according to EN13979-1 used in fatigue analyses, where P is maximum static wheel load. Note that the lower load level for lateral loads F_{Y2} and F_{Y3} correspond to non-guiding wheelsets while the upper level corresponds to guiding wheelsets.

Load case	F_{Z1}	F_{Y1}	F_{Z2}	F_{Y2}	F_{Z3}	F_{Y3}
LC 1	$1.25P$	-	-	-	-	-
LC 2	-	-	$1.25P$	$0.6P / 0.7P$	-	-
LC 3	-	-	-	-	$1.25P$	$0.36P / 0.42P$

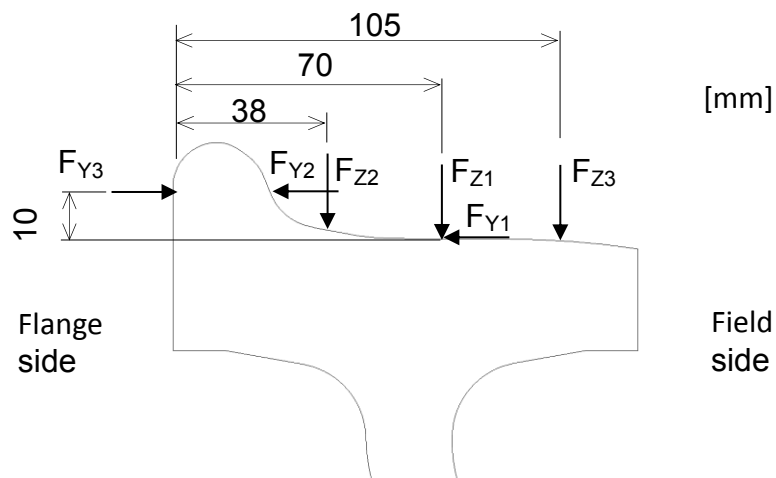


Figure 159 Definition of loads used in fatigue analyses.

6.3.1.2 Thermomechanical loading from tread braking

A thermal model of railway tread braking developed within CHARMEC¹ is utilised for calculations of wheel and brake block temperatures. Block(s) and wheel are coupled via a contact interface that controls the heat generation and also the heat partitioning between block and wheel. Heat transfer from the rolling wheel into the rail is accounted for. The thermal model has been calibrated using results from field studies. The temperature field in a wheel during braking causes axial deflection of the wheel rim (in relation to the hub), which may cause a permanent change of the gauge of the wheelset. It can also induce high tensile residual stresses in the wheel rim after braking and cooling that may lead to initiation and growth of transverse cracks in the wheel rim.

A sequentially coupled thermal-stress analysis is performed by first solving the pure heat transfer problem and then the temperature solution is used in the stress analysis as a predefined field.

The model developed for simulating thermal interaction of wheel, blocks and rail during braking and after braking at cooling down was developed as part of the doctoral dissertation [4] and a short review is given here. An axisymmetric finite element model of wheel and brake blocks is used to achieve short calculation times allowing for analyses of wheel and block temperatures of a train in revenue service. The heat input at the wheel-block interface is calculated, prior to analysis, from train data. The heat partitioning between wheel and block(s), is controlled by introducing thermal resistances at the contact interface, and the heat transfer from wheel to rail is controlled by introducing a thermal conductance at the contact, see Figure 160. The heat flux generated at the interface q^{brake} is partitioned between the wheel, q_w , and the block, q_b , as

¹ Chalmers Railway Mechanics

$$q_w = \frac{T_b^{\text{cont}} - T_w^{\text{cont}}}{R_w + R_b} + \frac{R_b}{R_w + R_b} q^{\text{brake}} \quad (49)$$

$$q_b = \frac{T_w^{\text{cont}} - T_b^{\text{cont}}}{R_w + R_b} + \frac{R_w}{R_w + R_b} q^{\text{brake}} \quad (50)$$

Here T_b^{cont} and T_w^{cont} [°C] are contact temperatures of block and wheel, respectively, and R_b and R_w [°C/(W/m²)] are heat resistances at contact. Heat transfer from wheel to rail can be analysed assuming perfect thermal wheel-rail contact. For rolling contact and the same thermal material properties in wheel and rail, the heat Q_{wr}^{perfect} [W] transferred from wheel to rail is then taken as

$$Q_{wr}^{\text{perfect}} \approx -6.99 \frac{b\lambda}{\sqrt{\kappa}} (T_{w0} - T_{r0}) \sqrt{\frac{av}{8\pi}} \quad (51)$$

Here a and b [m] are semi-axes of the contact patch (a is in direction of rolling), λ [W/m °C] thermal conductivity, κ [m²/s] thermal diffusivity, v [m/s] train speed, T_{w0} [°C] wheel tread temperature and T_{r0} rail temperature. This expression gives an upper limit for the heat transferred from wheel to rail. The heat transfer for constant wheel and rail temperatures may be calculated numerically by integrating the heat flux over the contact area, see example in Figure 161. The rail chill is implemented in the FE-models via the rail chill parameter $Q_{wr}/\Delta T$ (thermal power transferred from wheel to rail per unit difference in surface temperature) which is transformed to convection cooling applied to the area of wheel-rail contact.

Cooling by convection and cooling by radiation are modelled using the classical formulae. For the wheel, a convection model is here employed that accounts for radial variation of the heat transfer.

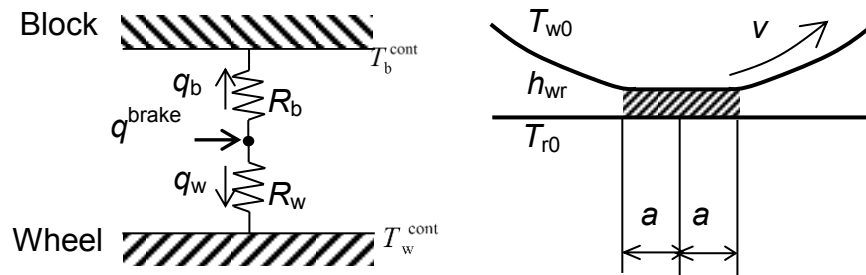


Figure 160 Thermal resistances at wheel and block contact are used to partition heat between wheel and block (left). Contact between wheel and rail-wheel with film (thermal conductance) at contact (right).

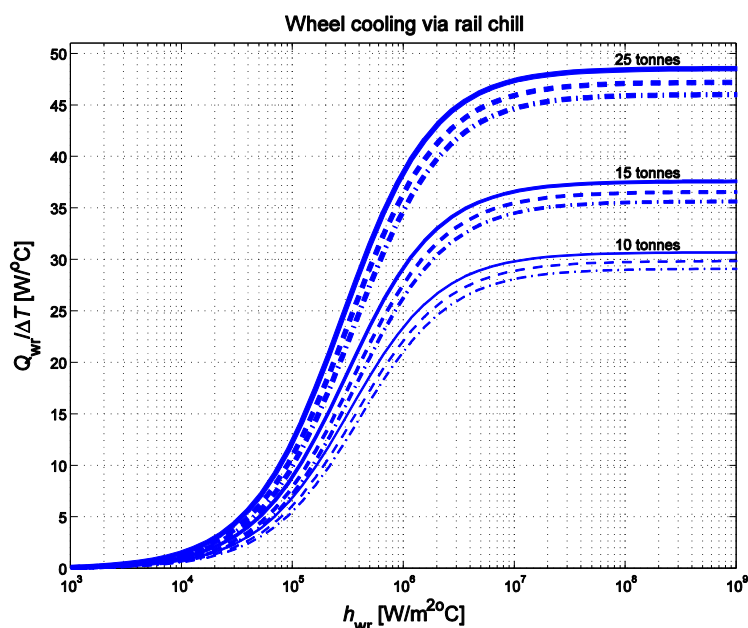


Figure 161 Calculated thermal power transferred from wheel to rail per unit difference in surface temperature as function of thermal contact conductance. Three axle loads and three wheel diameters are considered. Full line corresponds to wheel diameter 1.5 m, dashed line to 0.92 m, and dash-dotted line to 0.65 m. Rail head radius 0.30 m is assumed.

For the mechanical analysis that follows the thermal analysis, the nodes of the hub that would be in contact with an axle are clamped. For the wheel, one set of material parameters were firstly implemented that have previously been utilised by SNCF [5] for assessment of wheels at dynamometer testing. This material model is of linear kinematic hardening type with temperature dependent material parameters. At a later stage also a more advanced material model of viscoplasticity type with a combination of nonlinear isotropic and kinematic hardening was implemented [6]. The viscous response of the model is primarily obtained from a Norton type of overstress function which has been included in order to be able to capture the observed relaxation of the material at elevated temperatures. The overstress function is defined in terms of von Mises equivalent stress taking into account the hardening variables. The nonlinear kinematic hardening has been tuned to fit the cyclic hardening (the Bauschinger effect) of the material. Furthermore, the nonlinear hardening relations have been extended to also include time recovery effects in order to capture slow processes (diffusion dominated) in the material leading to a decreased hardening. The model has been calibrated at temperatures from 300 °C to 650 °C by use of tensile testing with controlled cyclic strains but also including time periods where the largest compressive strains were held to reveal relaxation effects. At the implementation of this model, also variations of yield stress in the wheel as induced at manufacturing by rim hardening was implemented. These variations were taken as decreasing the yield stress by 0.25% per mm depth below the wheel tread of the new wheel down to a depth of 50 mm [7] after which no change was assumed. The wheels are assumed stress free at the start of analyses (residual stresses from manufacturing are neglected).

The wheel behaviour is assessed as given by EN13979-1. Hence, the axial displacement of the rim during braking and after cooling down is calculated for a point on the flange side of the rim on a diameter equal to the wear limit of the wheel. Further, the residual stresses in the wheel rim are calculated after the wheel has cooled down to ambient temperature.

6.3.1.3 Wheel web fatigue due to track brakes

A recent accident at Neufchateau in France 2010 [8] put the attention on the use of so-called track brakes, see Figure 162, which are used on shunting yards. At this accident, the wheel web failed close to the rim, which in the analyses after the accident was hypothetically induced by the track brakes. Interaction between the loads from the track brakes and the fluid inside the tank wagon produced substantial unbalance loads acting on the wheels that in a detrimental way could contributed to the wheel failure. The track brakes in question were of two types, where the first acted on both wheels of the wheelset (Primary track brake) at a somewhat higher speed than the following track brake which acts on only one wheel in the wheelset (Secondary track brake).



Figure 162 Example of secondary track brake <http://www.foudurail.org/belge/atelier3.html>

The fatigue of the wheel web is assessed for sets of conventional loads (wheel-rail contact forces as stipulated in EN13979-1), braking loads and the un-conventional loads given by the track brakes. The life of the web is assessed using a Coffin-Manson fatigue criterion and Palmgren-Miner damage accumulation. It should be noted that only one wheel design is simulated for this case, due to the complexity of the load cases. In fact, it is the actual wheel design that was involved in the accident (the ORE wheel at diameter 908 mm) that is analysed, which has a web shape that is similar to the one of the S-shaped wheel. The analyses shown were performed as part of a PhD course in Advanced Fatigue Design by Shahab Teimourimanesh at Chalmers University of Technology [9].

The conventional mechanical loads are here based on the axle load 22.5 tonnes. The three sets of fatigue loads given in the standard EN13979-1 are used for assessing the web fatigue, see Table 42. In the present analyses, the stresses were calculated separately for each set of loads LC1 to LC3 separately, thus considering the stress variations for a material point on the wheel web during wheel rotation. Stress variations were calculated in the direction of the largest principal stress at all nodes on the field and flange sides of the wheel web (nodes with the same radial and axial position on web were used to assess the stresses for one rotation of the wheel). The effect of centrifugal stresses due to wheel rotation on the stress range is not included. The axial load cases were prescribed for a non-guiding wheelset.

The unconventional loading of the wheel as induced by the track brakes in combination with the unbalance loads from the fluid in the tank is presented in Figure 163 and in Table 43 and Table 44. Note that the loads acting on the wheels when passing a Primary track brake acts on both wheels in the wheelset while the loads from the Secondary track brake only acts on one wheel. Stress

variations on points in the wheel web were calculated for one revolution of the wheel as for the conventional loading.

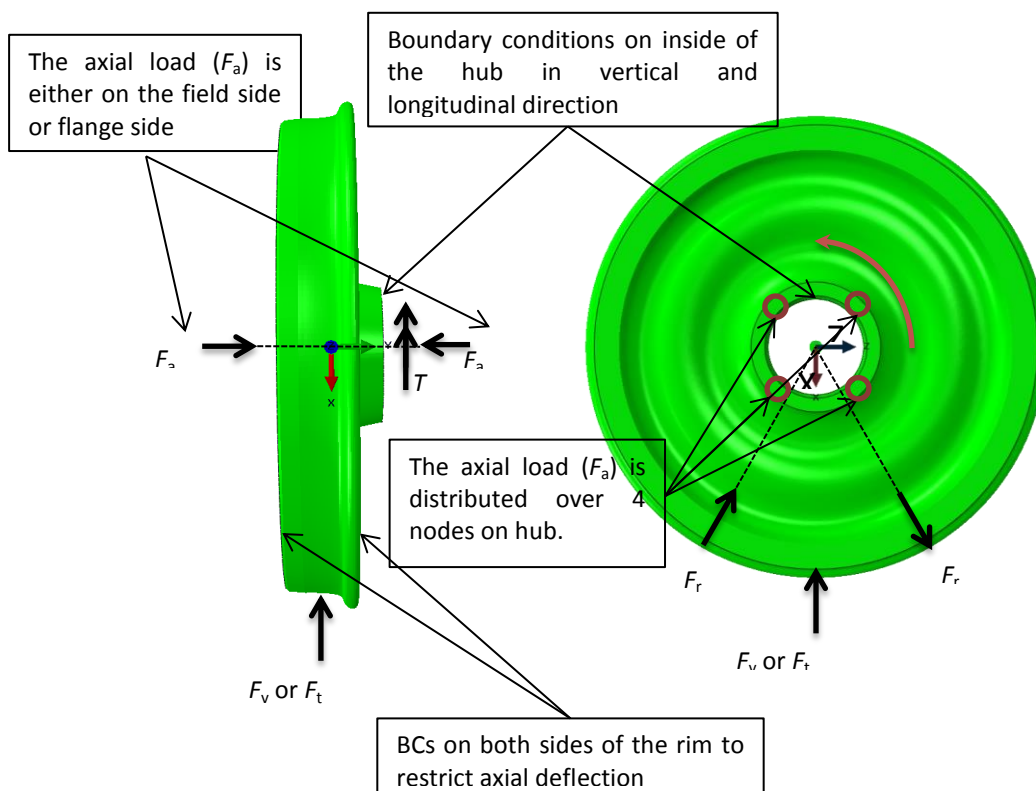


Figure 163 Schematics of loads and boundary conditions for wheel when passing Primary and Secondary track brake. Note that when passing Secondary track brake the torque T is added (implemented as point forces on hub)

Table 43 Load cases LC4 when passing Primary track brake

	Load (kN)	Scenario 1	Scenario 2
Vertical load (F_v)	138 + 40	Applied	Not Applied
Radial loads (F_r)	50	Applied	Applied
One side axial load on the hub (F_a)	41	Applied	Applied
Vertical load from transversal unbalance load of fluid (F_t)	220	Not Applied	Applied

Table 44 Load cases LC5 when passing Secondary track brake

	Load (kN)	Scenario 1	Scenario 2
Vertical load (F_v)	138 + 40	Applied	Not Applied
Radial loads (F_r)	33	Applied	Applied
One side axial load on the hub (F_a)	41	Applied	Applied
Vertical load from transversal	220	Not Applied	Applied

unbalance load of fluid (F_t)			
Torque T (kNm)	31	Applied	Applied

Thermomechanical loading from tread braking was assessed for drag braking and stop braking. The drag braking application was modelled as braking at power 35kW during 45 min at constant speed 60 km/h and then allowing for cooling down to ambient temperature. The stop braking load case consisted of *three* sequential emergency brake cycles and each stop was composed of two steps: (1) braking from an initial braking power, which is linearly ramped down as function of time to the standstill and (2) accelerating up to constant speed. The emergency stop corresponds to an axle load of 22.5 tonnes, initial speed 100 km/h and retardation 1.0 m/s^2 . This means an initial power of about 313 kW being ramped down to zero in about 27.8 s. The data used are given in Table 45. The drag braking load case is defined LC6 and the stop braking load case is defined LC7. Drag braking and stop braking were repeated (after a prolonged cooling period) to reach a steady cyclic state of stress and strain that were used in the fatigue analysis. It is assumed about 90% of the braking heat enters the wheel [5] (organic composite brake blocks).

In the thermal analysis, the convection of exterior surfaces was assumed for three major surfaces, *i e* web, rim and tread surfaces, see Figure 164. The heat transfer coefficients were assumed constant for these surfaces.

Table 45: Drag and stop braking load cases. Drag braking (load case LC6) speed is 60 km/h. Stop braking (load case LC7) has maximum speed 100 km/h.

Axle load	$2m = 22.5 \text{ tonnes}$	Initial wheel temperature	$T_{w0} = 20 \text{ }^\circ\text{C}$
Retardation	$a = 1.00 \text{ m/s}^2$	Drag braking constant power	35 kW
Block configuration	2Bg	Period of drag braking	45 minutes
Block material	Organic composite	Stop braking initial power	312.5 kW

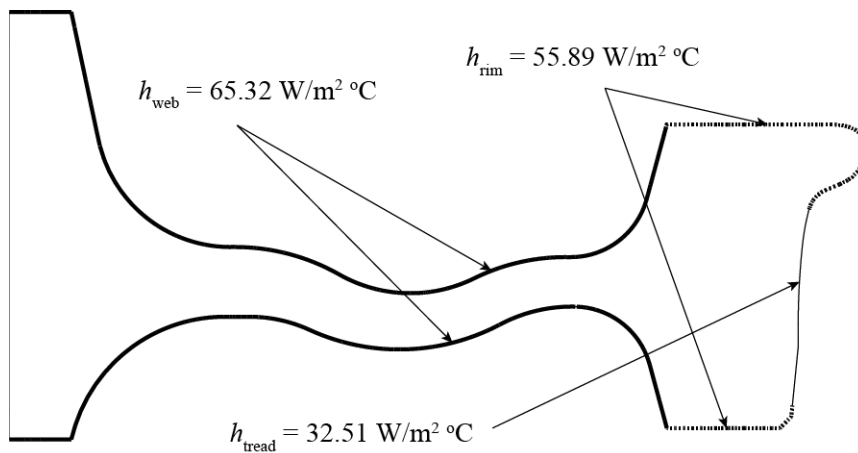


Figure 164: The convection boundary conditions for the thermal model [5]. The heat transfer coefficients from the surfaces are given. Note that the thick solid line shows the web surfaces, the dashed line is the rim surfaces and the thin solid line is showing the tread.

The damage resulting from the stresses and strains in the wheel is for each load case assessed using the Coffin-Manson relationship to produce life estimates. The static analyses have been performed with respect to the conventional load cases, see Table 42, and unconventional loads, see Table 43 and Table 44. In order to establish stress ranges and mean stresses the maximum and minimum stresses are calculated for nodes around the

circumference of the web. The wheel behaviour at one revolution of the wheel is thus analysed. The Coffin-Manson relationship was implemented considering the influence of mean stress on fatigue life

$$\varepsilon_a = \left(\frac{\sigma_f' - \sigma_m}{E} \right) \cdot (2N_f)^b + \varepsilon_f' (2N_f)^c \quad (52)$$

where parameters utilised by SNCF [5] have been implemented.

The fatigue lives N_i for the different load cases were determined and the damage was calculated by applying the Miner cumulative damage rule using a predefined number of occurrences for the load cases n_i . The fatigue life was then calculated by

$$N_t = 1 / \sum (n_i / N_i) \quad (53)$$

The number of cycles for the cumulative damage rule was introduced for different sets of combinations of load cases [8]. The cycles are given in Table 46. The fatigue life was calculated according to the percentages of the loading life which is spent at a certain stress level with respect to load cases. For the conventional load case it is assumed 94% of the life is running on straight track (LC1), 5% is travelling in curves (LC2) and 1% is negotiation of points / crossings (LC3). Passage of Track brakes (LC4-5) are assumed every 300 km. For the thermomechanical loading of the wheels, it is assumed that one stop brake occurs every 30 km and one (severe) drag brake every 30 000 km.

Table 46: Number of estimated loading cycles for the actually failed wheel (300×10^3 km).

Load cases	Number of cycles
Conventional (LC1-3)	105454085
Nonconventional (LC4-5)	1000
Drag braking (LC6)	10
Stop braking (LC7)	10×10^3

6.3.1.4 Wheel web fatigue due to combined mechanical and thermomechanical loading

A more detailed analysis of fatigue damage for the wheel web has been performed for the combined mechanical wheel/rail contact forces (as specified by the EN 13979-1) and by thermomechanical loading induced by drag braking and stop braking (as described in Section 6.3.1.2). Here, the mechanical load cases consider only the conventional load cases according to EN13979-1, see Table 42. It should be noted that here also a Rainflow counting procedure [10, 11] has been implemented to consider the variations in stresses for the mechanical loading history.

The damage is evaluated using a Coffin-Manson approach together with Palmgren-Miner damage accumulation. The damage from braking load cases is based on the stress-strain cycles during the fourth simulated brake cycle not to consider the non-typical variations during the first brake cycle. The calculated lives of the wheels are determined for assumedly fully loaded wagons and for some given drag and stop braking load cases. For the conventional load case it is assumed 94% of the life is running on straight track (LC1), 5% is travelling in curves (LC2) and 1% is negotiation of points / crossings (LC3). For the thermomechanical loading of the wheels, it is assumed that one stop brake occurs every 30 km and one (severe) drag brake every 30 000 km. These assumptions on frequency of loads have been carried over from Section 6.3.2.3 (evaluation of track brakes). Positions of critical points with respect to life are determined and the partial damage contributions from

the different loading cases are studied. Moreover, in order to study the influence from an assumed deteriorated web surface as caused by e.g. severe corrosion or a surface scratch, it has been assumed that the fatigue limit is reduced. This reduction affects the assumed high cycle fatigue life, leaving the low cycle fatigue life unaffected.

6.3.1.5 Cracking of wheel web and wheel rim

The fatigue strength of the wheel material may be reduced by material defects and by corrosion and surface damage. Although the fatigue life may be reduced in order to roughly account for effects of surface roughness, corrosion etc, the safe-life approach taken in EN13979-1 implicitly assumes that no further damage that may reduce the life of the wheel web is inflicted during service. When freight train speeds and loads increase in the future, the stresses in the wheels will also increase. This means that the wheels could be susceptible to crack growth. Circumferential cracks in the wheel web due to mechanical loading are here primarily studied but also radial cracking of wheel rim and web as induced by tread braking.

In order to analyse crack initiation and propagation, semi-elliptical surface cracks in the web and rim are studied. Handbook solutions [12] of stress intensity factors for finite surface cracks in a plate are used to calculate the Mode I stress intensity factors (normally denoted K_I , here denoted K) as

$$K = \sqrt{\pi a} \sum_{i=0}^5 \sigma_i f_i \left(\frac{a}{t}, \frac{2c}{a} \right) \quad (54)$$

where σ_i ($i=0$ to 5) are components which define the stress state σ according to

$$\sigma = \sigma(u) = \sum_{i=0}^5 \sigma_i \left(\frac{u}{a} \right)^i \quad (55)$$

and f is a dimensionless geometric factor. The crack propagation is predicted from the stress intensity factors K_A and K_C at points A and C in Figure 165, which represent circumferential and radial growth, respectively. It should be noted that the handbook solution is valid for a plane crack in a plate, whereas the crack in the wheel is curved and the back surface is possibly not in parallel with the cracked surface. However, for small cracks the solutions will still give sufficient accuracy of stress intensity factors. For large cracks having depth larger than 0.8 times the web thickness, there are no values available for the geometry factor f .

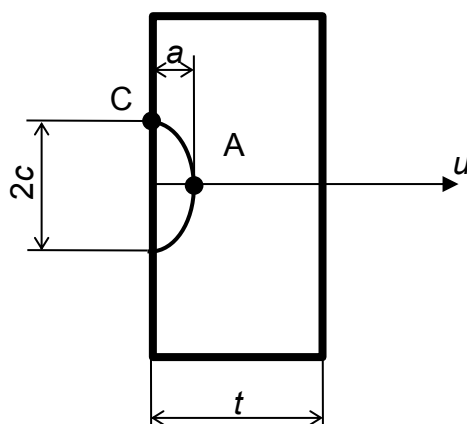


Figure 165 Schematic illustration of handbook solution for finite surface crack in plate used for assessing stress intensity factor in wheel web.

Crack propagation for a crack with known dimensions is studied. The stress intensities in the two positions A and C in Figure 165 can be related to crack propagation through Paris' law

$$\frac{da}{dN} = C \left(\frac{\Delta K}{1-R} \right)^n \quad (56)$$

where a is crack size (depth or length), N the number of loading cycles (i.e., number of revolutions of the wheelset) and $R = K_{\min} / K_{\max}$. Here K_{\min} and K_{\max} are the algebraically largest and smallest values of the stress intensity factor during a loading cycle. The stress intensity range $\Delta K = K_{\max} - K_{\min}$ also includes negative values of K_{\min} . However, the denominator "1-R" means that negative values of K_{\min} do not contribute. Material parameters $C = 5.0 \times 10^{-9}$ and $n = 3.04$ for ENR7 according to Reference [13] are employed, requiring ΔK to be expressed in the unit [MPam^{1/2}] and da / dN in [mm / cycle].

Crack propagation is assumed to take place according to equation (56) only if the stress intensity range $\Delta K / (1-R)$ exceeds the threshold value $\Delta K = 7.1 \text{ MPam}^{1/2}$ taken from Reference [13].

The growth of a crack could be evaluated using spectrum loads representing a typical operational loading. Ideally, such spectrum loads should be measured for conditions closely corresponding to the real application. Complications here are unknown running conditions, climatic conditions, maintenance status etc. However, no load spectra for freight wheel loading are available for use in the present study and hence standardized spectra are employed. For this reason, a "synthetic spectrum" is utilized, originally developed for study of crack growth in axles [14] in a situation when data are not available, see Figure 166. The method is adapted to wheels such that the wheel-rail contact forces correspond to the three load cases corresponding to EN13979-1 (straight track, curving and points/crossings). The stresses in the wheel web as caused by vertical only loading of the wheel when running on straight track (σ_s) together with the stresses in the wheel web for when running with additional maximum lateral loading (σ_E) are used for defining the load spectrum with assumed number of cycles (N_s and N_E). Further, to account for the different lateral load directions at curves and points/crossings a ratio between the occurrences of these load types is presumed.

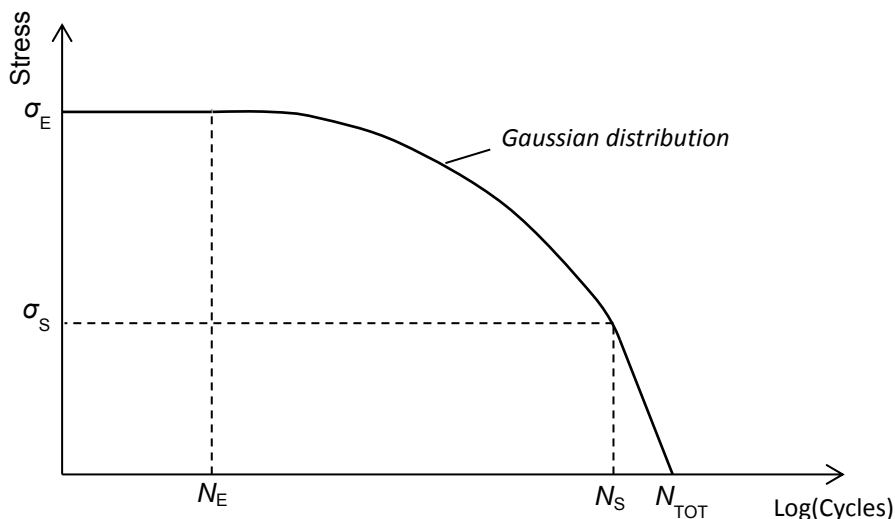


Figure 166 Illustration of synthetic load spectrum for assessing crack growth in wheels. Loads corresponding to straight run correspond to load case CEN 1 in Section 6.3.2.1 and the extreme loading correspond to load case CEN2 and CEN3 respectively for curving and negotiation of point or crossing.

The calculation of crack propagation is performed by dividing the load spectrum into a discrete number of load levels. A multiplication factor is then implemented to evaluate the number of cycles for each discrete load level of the spectrum. An automatic routine has been developed to calculate the multiplication factor both for achieving significant crack growth per partial spectrum and for limiting the largest resulting crack growth for each partial spectrum.

6.3.2 Parametric studies

The influence from loading conditions are generally studied for the two wheel designs with wheels in new condition (diameter 920 mm) and in fully worn down condition (diameter 820 mm). However, for the track brake study, only one wheel is studied as described above.

6.3.2.1 Mechanical loading from conventional wheel-rail contact

Both wheels are assessed for an axle load of 25 tonnes. Firstly, the influence of an increased vertical loading is investigated under the assumption that the vertical load is increased only at the rolling circle (as caused by e.g. a localized wheel flat), keeping the vertical and lateral loading at curving and points/crossing negotiations unchanged. Secondly it is assumed that the increase in the vertical load also affects the vertical loading acting in combination with lateral loads during curving and negotiation of points and crossings. This implies a tread damage that covers the full width of the tread. Thirdly, the influence of increased lateral loading is studied. Lateral loads for negotiation of curves (F_{Y2}) and passage of switch or crossings (F_{Y3}) are than assumed to increase proportionally.

6.3.2.2 Thermomechanical loading from tread braking

Results are in general presented for both the linear kinematic hardening model (by SCNF) and for the advanced viscoplastic model. Drag braking for 45 min is studied at brake power levels from 30 kW to 80 kW for single brake cycles. Moreover, for the same brake load cases, ten sequential drag braking cycles with intermediate cooling to ambient temperature are assessed using the viscoplastic model. The influence from the cooling of the wheel by the

rolling contact with the rail is studied by assessing two axle loads, 5 tonnes and 25 tonnes and two speeds 60km /h and 160 km/h.

6.3.2.3 Wheel web fatigue due to track brakes

The influence from the track brakes on calculated wheel life is assessed by evaluating eight different combinations of the considered load cases (conventional mechanical, unconventional mechanical, stop braking and drag braking). The wheel lives are calculated with respect to two positions on the wheel web, one towards the hub and one towards the rim. The life is calculated for all positions on the web field and flange sides, from hub to rim.

6.3.2.4 Wheel web fatigue due to combined mechanical and thermomechanical loading

The mechanical loads correspond to 25 tonnes axle load. The magnitudes of the stop and drag braking cycles during the life of the wheels are varied while maintaining the frequency of the brakings. Wheel lives are calculated for mechanical loads and drag cycles ranging from 30 kW up to 70 kW and stops from 100 km/h and 120 km/h with decelerations 0.6 m/s^2 , 0.8 m/s^2 and 1.0 m/s^2 . It is generally assumed that the wheels cool down between brake cycles. To study the influence from consecutive stop brake cycles, also a braking load case is assessed that consists of two consecutive stops with time in-between only to allow for train acceleration. Results are in general presented for both the linear kinematic hardening model (by SCNF) and for the advanced viscoplastic model.

6.3.2.5 Cracking of wheel web and wheel rim

Stress intensity factors are evaluated for loads according to EN13979-1 (axle load 25 tonnes) and a crack with a depth of $a = 2 \text{ mm}$ and half-width $c = 6 \text{ mm}$ located at *all* positions on the wheel web. The case of an increased vertical loading is also analysed by assuming a vertical load factor of $3P$ (the standard prescribes $1.25P$) to study sensitivity to tread damage. The growth of cracks in the wheel web under spectrum loading is studied where the loads consists of combined vertical and lateral loading according to EN 13979-1. Additionally, a more severe spectrum has been utilised where the vertical loading has been increased to two times the static axle load. The crack growth is analysed for two initial crack geometries, both having depth $a = 2 \text{ mm}$ and one having half-width $c = 2 \text{ mm}$ and one with $c = 6 \text{ mm}$. Crack growth is evaluated at two positions on the web: one towards the hub and one at a central position on the web.

6.4 Results

6.4.1 Mechanical loading from wheel-rail contact

Resulting fatigue stress ranges for the Low-stress wheel and S-shaped wheel in new and worn conditions are shown in Figure 167 and Figure 168, respectively. Both wheels are here assessed for an assumed axle load 25 tonnes. The stresses for the Low-stress wheel are by a good margin within the allowed range (360 MPa according to EN13979-1); while the S-shaped wheel in worn condition is slightly outside the allowed range with stress range 364 MPa as compared to the allowed stress range of 360 MPa. Nevertheless, even though the highest stress is marginally higher than the allowed stress range, the changes in stresses due assumed increased loads are still very much indicative of the wheel type behaviour. Both wheels show three local maxima in the calculated stress ranges, one towards the hub at small radii, one towards the rim at large radii and one in-between at intermediate radii. The

S-shaped wheel has distinctly the largest maximum towards the hub in both new and worn state, whereas the Low-stress wheel is more balanced with approximately equal stresses at the three maxima (at least in worn state).

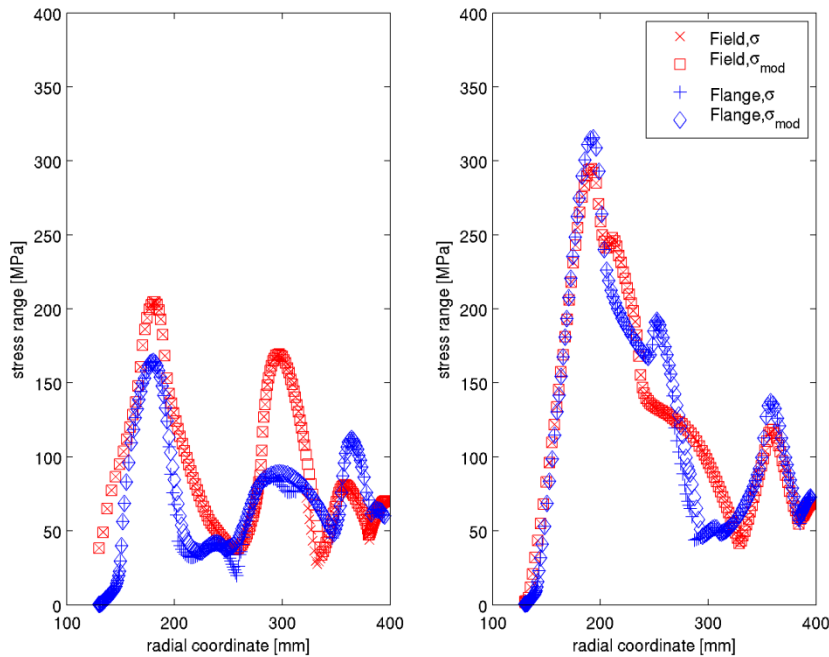


Figure 167 New wheels and default CEN loads for non-guiding wheelsets: Principal stress range as function of radius for field and flange side of web. Results for Low-stress wheel to the left and S-shaped wheel to the right.

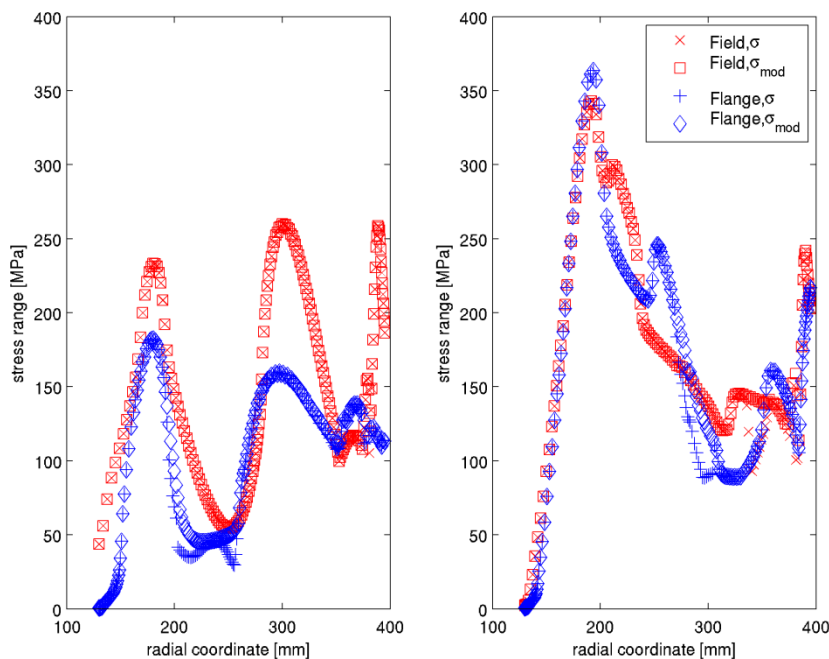


Figure 168 Worn wheels and default CEN loads for non-guiding wheelsets: Principal stress range as function of radius for field and flange side of web. Results for Low-stress wheel to the left and S-shaped wheel to the right.

The influence from increased vertical loading has been investigated, assuming that the vertical load is increased at the rolling circle only (as caused by e.g. a localized wheel flat), keeping the vertical and lateral loading at curving and passing of points/crossing unchanged.

The results are visualised in Figure 169 and Figure 170 for field and flange side of web respectively. The results show that the maximum stress range of the S-shaped wheel is not sensitive to increased vertical loading. For the worn wheel, which is always dimensioning, an increase in the maximum stress is not found until reaching very high load factors corresponding to between $5P$ and $6P$. On the other hand that the Low-stress wheel show an increase in the maximum stress already at about $3P$. For both wheel designs, the reason for the increase in maximum stress is that the stresses at the intermediate part of the web increases. Evidently, the design of the Low-stress wheel is more sensitive to increased vertical loading than the S-shaped wheel and already at $2P$ the stress range in the web towards the rim can be seen to increase. For future wheel designs, this could be a risk if wheels are stress optimized only regarding the load cases given in the norms, hence making the wheels sensitive to tread damage.

The influence of increased lateral loading is analysed in Figure 171 and Figure 172. The behaviour is quite similar for both wheel designs, with stresses in the wheels increasing almost linearly with the increased lateral loading. No differences between the behaviour of the two wheel designs are found.

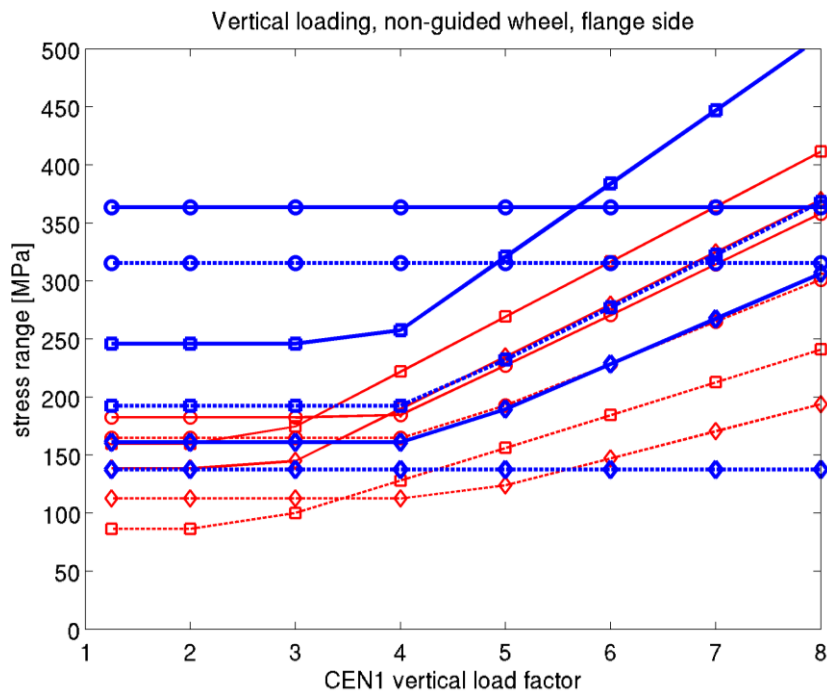


Figure 169 Calculated stress ranges for flange side of web and standard CEN load case for non-guided wheelsets, modified with increased vertical loading at the rolling circle of the wheel (load case CEN1, tangent track). Thick (blue) lines are for S-shaped wheel and thin (red) lines are for Low-stress wheel. Solid lines and dashed lines represent worn and new wheels, respectively. The symbols indicate the three local maxima found along the radius: “o” is near hub, “□” is intermediate and “◇” is close to rim.

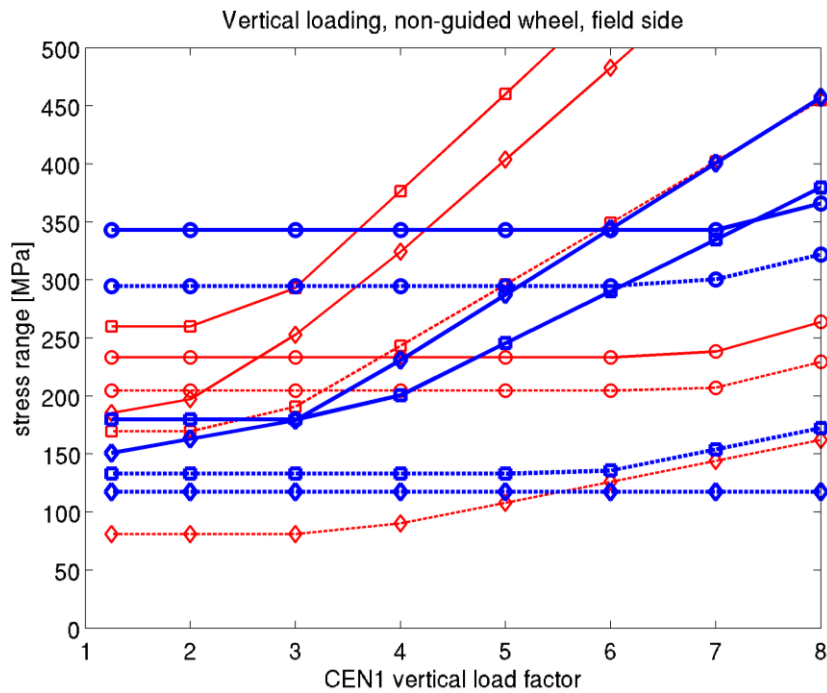


Figure 170 Calculated stress ranges for field side of web and standard CEN load case for non-guided wheelsets, modified with increased vertical loading at the rolling circle of the wheel (load case CEN1, tangent track). Thick (blue) lines are for S-shaped wheel and thin (red) lines are for Low-stress wheel. Solid lines and dashed lines represent worn and new wheels, respectively. The symbols indicate the three local maxima found along the radius: “o” is near hub, “□” is intermediate and “◇” is close to rim.

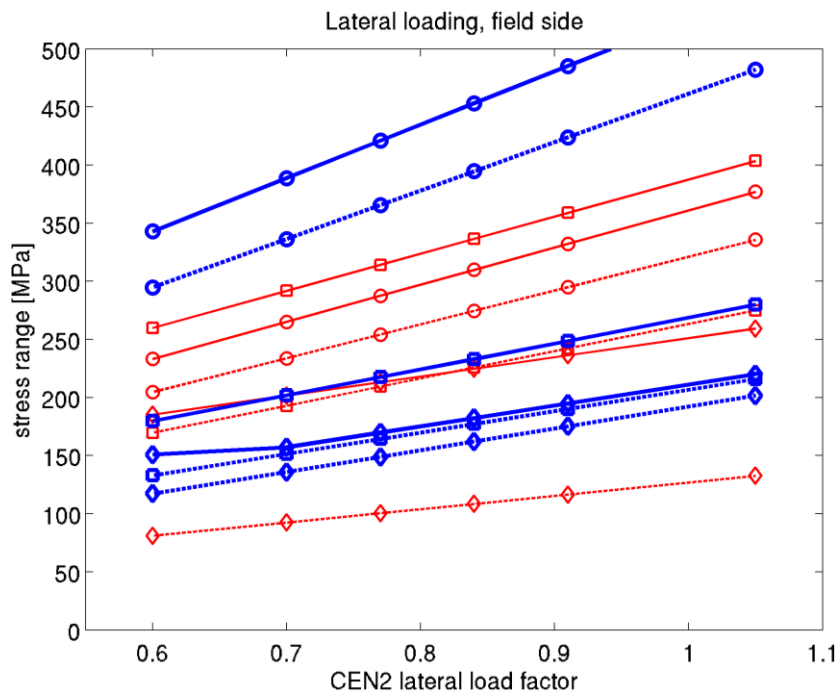


Figure 171 Calculated stress ranges for flange side of web and standard CEN load case for non-guided wheelsets, modified with increased lateral loading. Given is lateral load factor for load case CEN2, but load case CEN3 is assumed to increase proportionally. The vertical load is unchanged. Thick (blue) lines are for S-shaped wheel and thin (red) lines are for Low-stress wheel. Solid lines and dashed lines represent worn and new wheels, respectively. The symbols indicate the three local maxima found along the radius: “o” is near hub, “□” is intermediate and “◇” is close to rim.

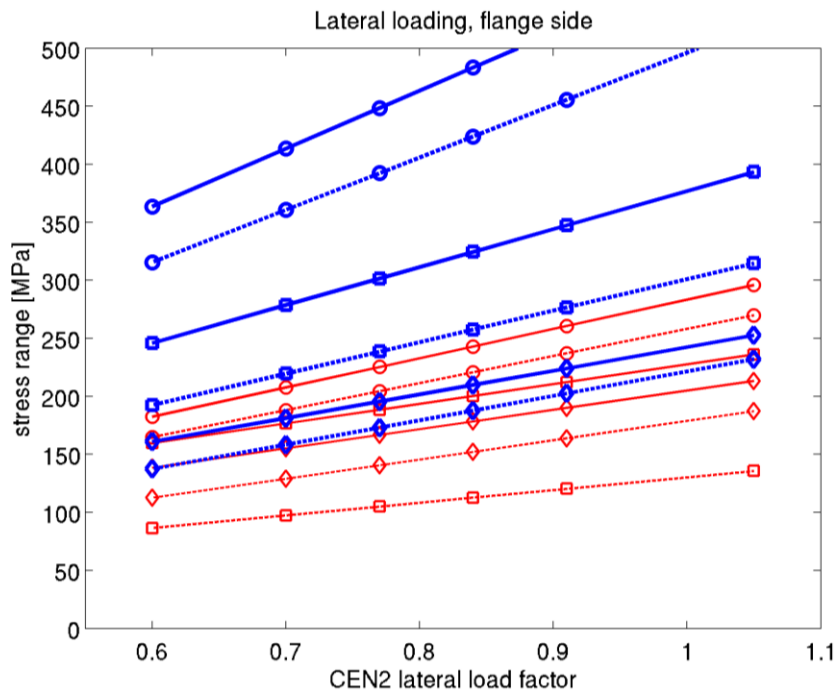


Figure 172 Calculated stress ranges for field side of web and standard CEN load case for non-guided wheelsets, modified with increased lateral loading. Given is lateral load factor for load case CEN2, but load case CEN3 is assumed to increase proportionally. The vertical load is unchanged. Thick (blue) lines are for S-shaped wheel and thin (red) lines are for Low-stress wheel. Solid lines and dashed lines represent worn and new wheels, respectively. The symbols indicate the three local maxima found along the radius: “o” is near hub, “□” is intermediate and “◇” is close to rim.

A different situation is found, if it is assumed that the increase in the vertical load also affects the vertical loading that interacts with the lateral loads at curving and negotiation of points and crossings. This would mean tread damage that covers the width of the tread. In Figure 173 and Figure 174 a quite substantially increase in the fatigue stresses can be seen at the transition between web and rim for the Low-stress wheel.

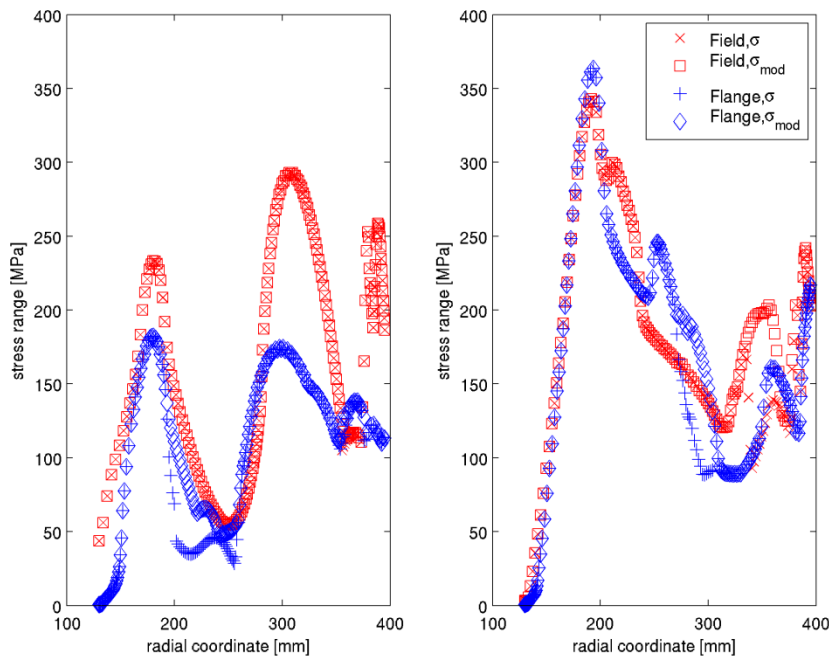


Figure 173 Worn wheels and CEN loads for non-guiding wheelsets with increased vertical component for travel on straight track (2P instead of 1.25P): Principal stress range as function of radius for field and flange side of web. Results for Low-stress wheel to the left and S-shaped wheel to the right.

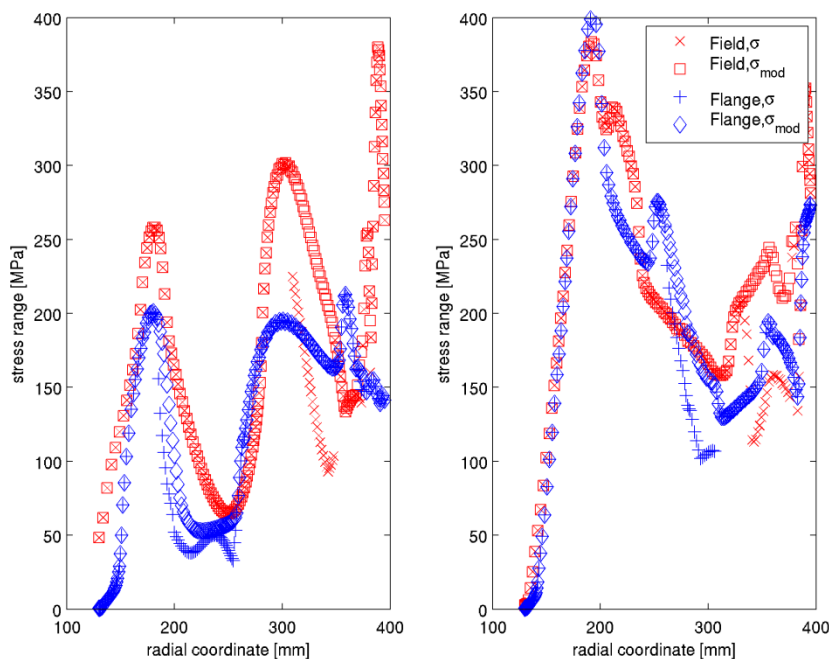


Figure 174 Worn wheels and CEN loads for non-guiding wheelsets with increased vertical component for all load cases (3P instead of 1.25P): Principal stress range as function of radius for field and flange side of web. Results for Low-stress wheel to the left and S-shaped wheel to the right.

6.4.2 Thermomechanical loading from tread braking

The results from a parametric study on drag braking are summarized in Figure 175, showing wheel rim temperature², axial flange deflection during braking, axial flange deflection after

² Point inside wheel rim, 10 mm below rolling circle of worn wheel.

cooling down and residual stresses in the wheel rim. These results concern analyses using the linear kinematic hardening material model. The considered braking load case is 50 kW, 60 kW, 70 kW and 80 kW constant power during 45 min. It should be noted that the wheels are assumed to be braked using organic composite blocks in 2Bg configuration at speed 60 km/h assuming rail chill based on 5 tonne axle load. Brake blocks made from cast iron or sinter material would lower the wheel temperatures. Moreover, the low speed and the low axle load mean that the cooling of the wheel is low.

The calculated temperatures of the Low-stress wheel and the S-shaped wheel are very similar, with significantly higher (bulk rim) temperatures for the worn wheels than for the new wheels. However, the results show that there are substantial differences between wheels with a straight wheel web, similar to the S-shaped wheel, and a wheel with a more curved web, similar to the Low-stress wheel. The allowed hot axial rim displacement is in the interval -1 and +3 mm, residual axial rim displacement in the interval -0.5 and +1.5 mm and residual stress below 200 MPa for the new wheel or below 275 MPa for the worn wheel. All wheels have axial displacements even at the highest studied power level (80 kW) that are within requirements. When considering the residual axial displacements after braking, it is only the worn Low-stress wheel that shows too large values at the highest power level (2.2 mm as compared to allowed 1.5 mm). On the other hand, the Low-stress wheel shows residual stresses that are within the regulations, both for the new and the worn wheels for all power levels. The worn S-shaped wheel shows too large stresses that can result in global wheel fracture already at a power level of 60 kW for the worn wheel. The S-shaped wheel in new condition shows too large stresses (>200 MPa) for the highest power level only (80 kW).

Results from the same parametric study after implementing the advanced viscoplastic material model are summarized in Figure 176. These results are rather similar to the ones generated using the linear kinematic hardening material (considering limits for approval). However, the Low-stress wheel shows larger displacements during braking for the intermediate power levels (60 kW and 70 kW) and also larger residual displacements after cooling down (for all power levels). The results show that the residual axial rim displacements for power level 60 kW now is slightly outside of the requirements for approval (allowed +1.5 mm). For the S-shaped wheel, a slight change is that the new wheel will show too large residual stresses at power level 70 kW (80 kW with the linear kinematic hardening material model).

In order to further investigate the behaviour of the wheels during drag braking, a sequence of ten drag braking cycles (with intermediate cooling to ambient temperature) were simulated using the advanced viscoplastic material model. Results for evolution of residual axial flange deflections are given in Figure 177 and residual stresses in the wheel rim after the ten cycles are given in Figure 178. These results show that the Low-stress wheel in worn condition exhibits a ratchetting behaviour with respect to residual axial displacements for power levels 60 kW and 70 kW. For each brake cycle at these power levels, the incremental increase of residual axial flange deflection will cause an increase in the gauge between the two wheels in a wheelset. This behaviour means that the gauge possibly can reach levels that substantially increase the risk of a derailment. The calculated residual stresses in the wheel rims are found to be somewhat larger than after one brake cycle but no changes are found with respect to limit for approval.

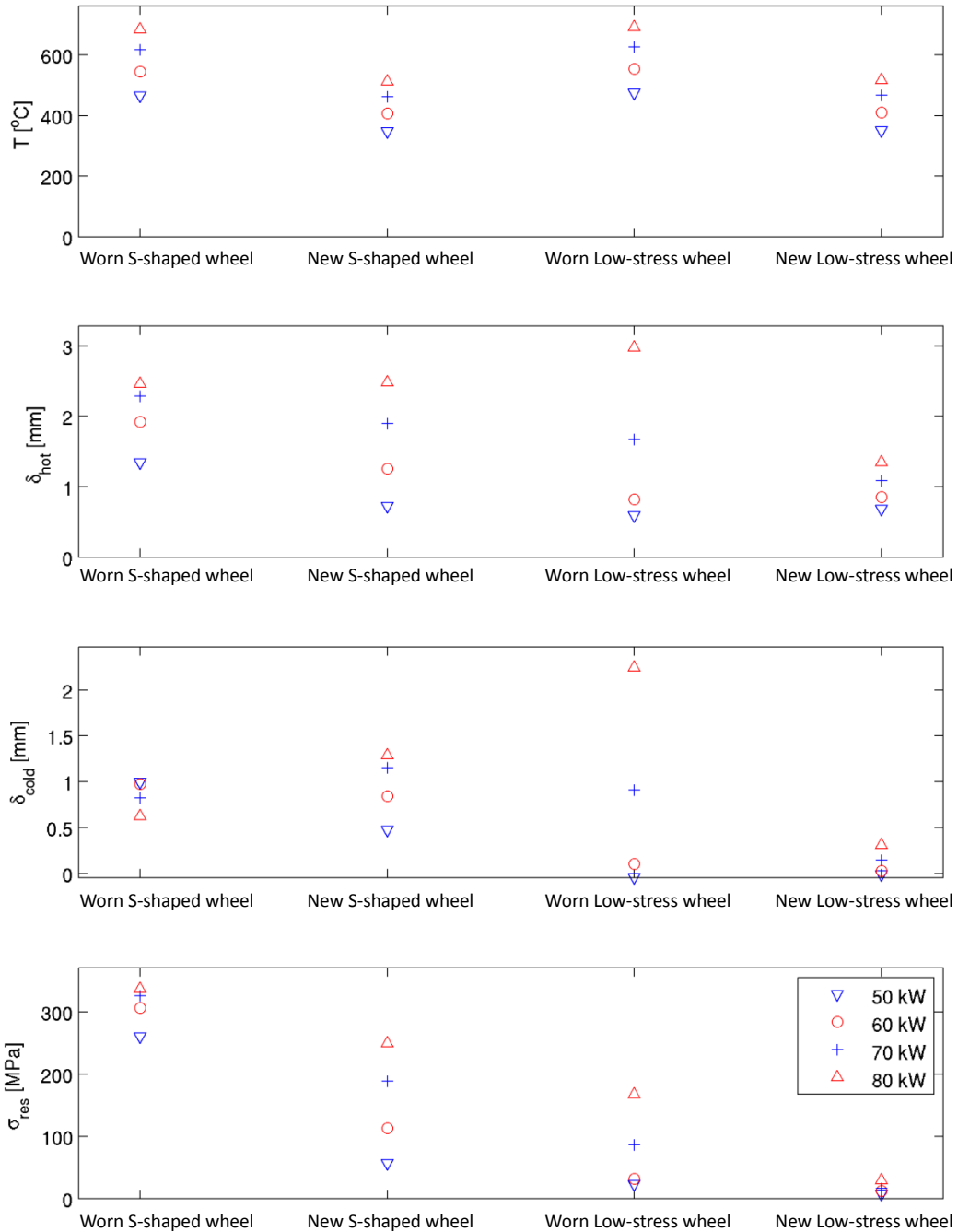


Figure 175 Results from parametric study of wheel behaviour at tread braking during 45 min at constant power level as indicated. Simulations using the linear kinematic hardening material model. Upper graph shows wheel temperature at a point inside the wheel rim at end of drag cycle, second upper shows largest axial flange deflection during braking, second lower shows residual axial flange deflection after cooling down and lower figure shows average residual rim stresses. Braking with organic composite brake blocks (2Bg) with convection cooling for in-field conditions and rail chill based on axle load 5 tonnes.

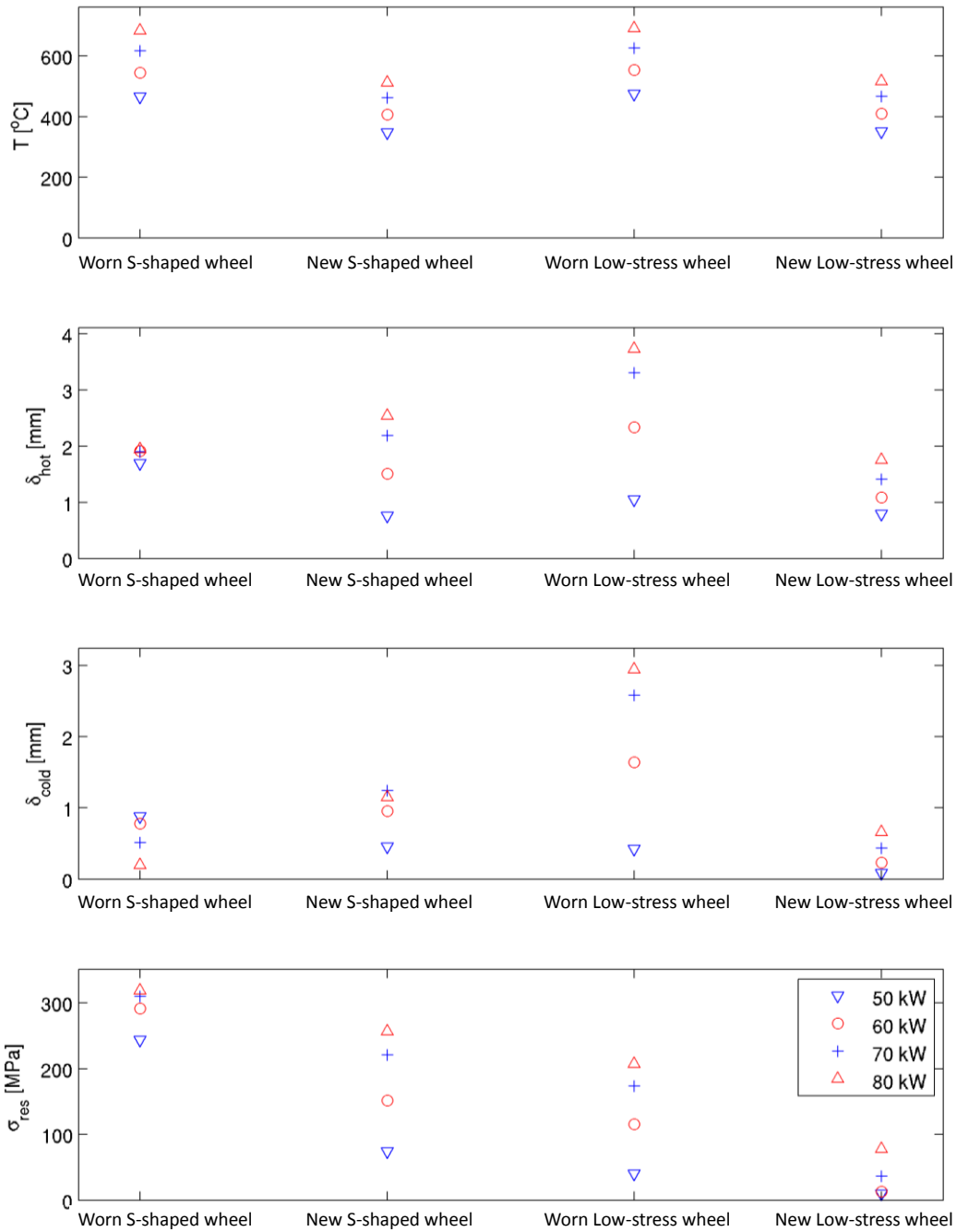


Figure 176 Results from parametric study of wheel behaviour at tread braking during 45 min at constant power level as indicated. Simulations using the advanced viscoplastic material model. Upper graph shows residual axial flange deflection after cooling down and lower figure shows average residual rim stresses. Braking with organic composite brake blocks (2Bg) with convection cooling for in-field conditions and rail chill based on axle load 5 tonnes.

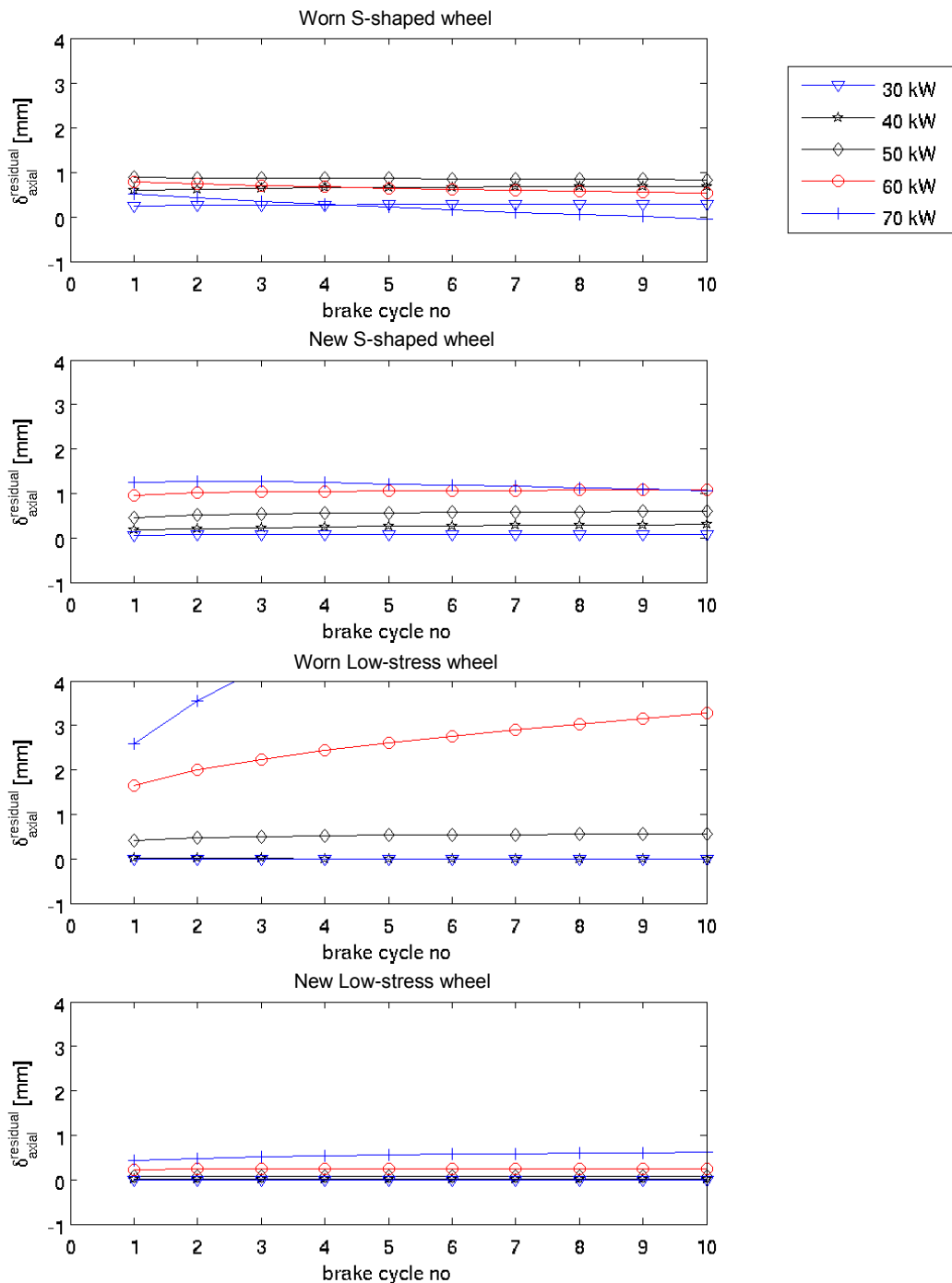


Figure 177 Results from parametric study of wheel behaviour at tread braking during 45 min at constant power level as indicated. The results are after 10 drag braking cycles. Simulations using the advanced viscoplastic material model. Evolution of residual axial flange deflection after cooling down after each brake cycle is shown. Braking with organic composite brake blocks (2Bg) with convection cooling for in-field conditions and rail chill based on axle load 5 tonnes

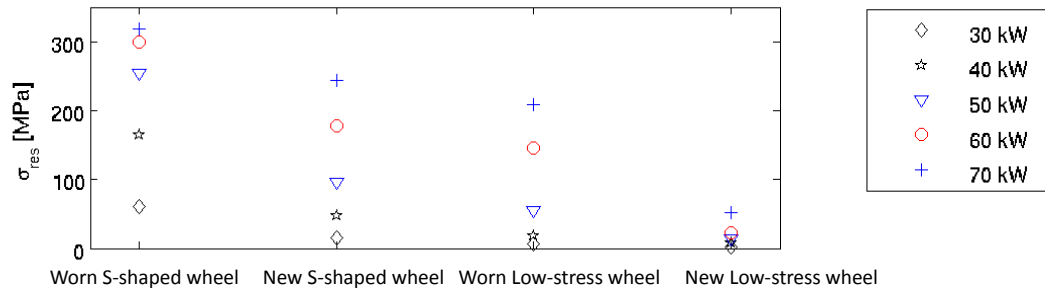


Figure 178 Results from parametric study of wheel behaviour at tread braking during 45 min at constant power level as indicated. The results are after 10 drag braking cycles. Simulations using the advanced viscoplastic material model. Graph shows average residual rim stresses after 10 cycles. Braking with organic composite brake blocks (2Bg) with convection cooling for in-field conditions and rail chill based on axle load 5 tonnes.

In order to investigate the sensitivity of the wheels to differences in cooling conditions, a parametric study has been performed when also the train speed and axle load have been varied. For all cases, braking with organic composite brake blocks (2Bg) and convection cooling corresponding to in-field conditions are considered and the brake power is constant during the considered braking time 45 minutes. A summary of the results are given in below, with maximum wheel temperatures in Figure 179, maximum axial flange deflection in Figure 180, residual axial flange deflection in Figure 181 and residual stresses in Figure 182. The results show the lowering of the wheel temperatures as given by the increased cooling (by increasing train speed and/or by increasing the axle load), give a corresponding decrease in axial deflections and residual stresses. Both the maximum and residual axial rim displacements can be seen to decrease to allowed levels for the studied power levels by the increased cooling from higher speed or axle load. However, the residual stresses of the S-shaped wheel in worn state can be seen to be higher than the allowed limit when the axle load or the speed is increased, but it's below the limit considering both increased axle load *and* speed.

The sensitivity to the cooling conditions have also been analysed using the viscoplastic model and the results are summarized in Figure 183, Figure 184 and Figure 185. The main difference as compared to the analysis using the linear kinematic hardening material model is (as previously pointed out) that the axial flange deflections for the worn Low-stress wheel increase to not allowed levels already at the power level 60 kW.

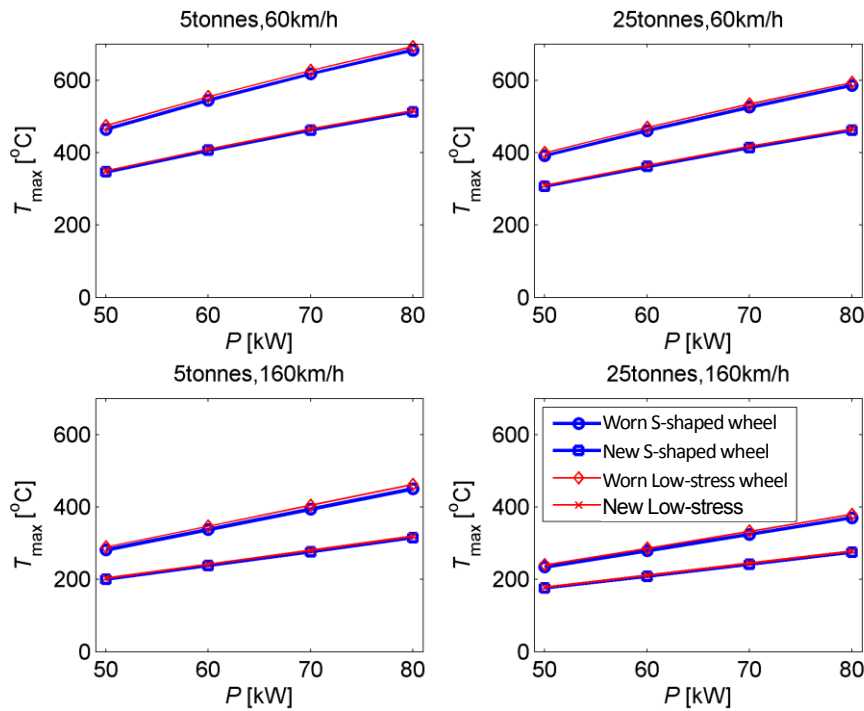


Figure 179 Maximum wheel temperatures are given for varying brake power and cooling conditions, considering rail chill for 5 and 25 tonnes axle load and forced convection cooling for 60 and 160 km/h.

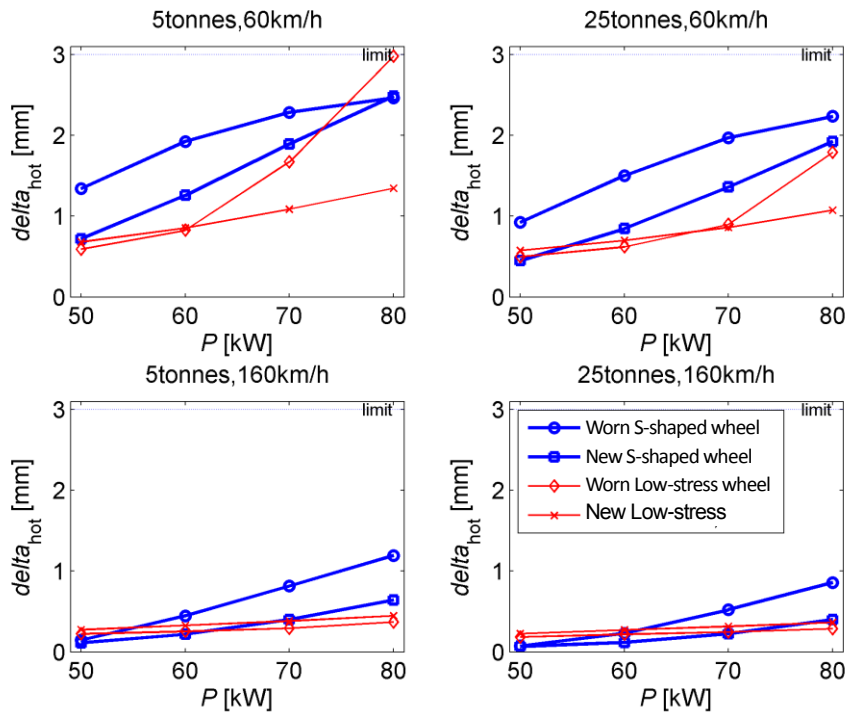


Figure 180 Maximum axial flange deflections during braking are given for varying brake power and cooling conditions, considering rail chill for 5 and 25 tonnes axle load and forced convection cooling for 60 and 160 km/h. Simulations using the linear kinematic hardening material model.

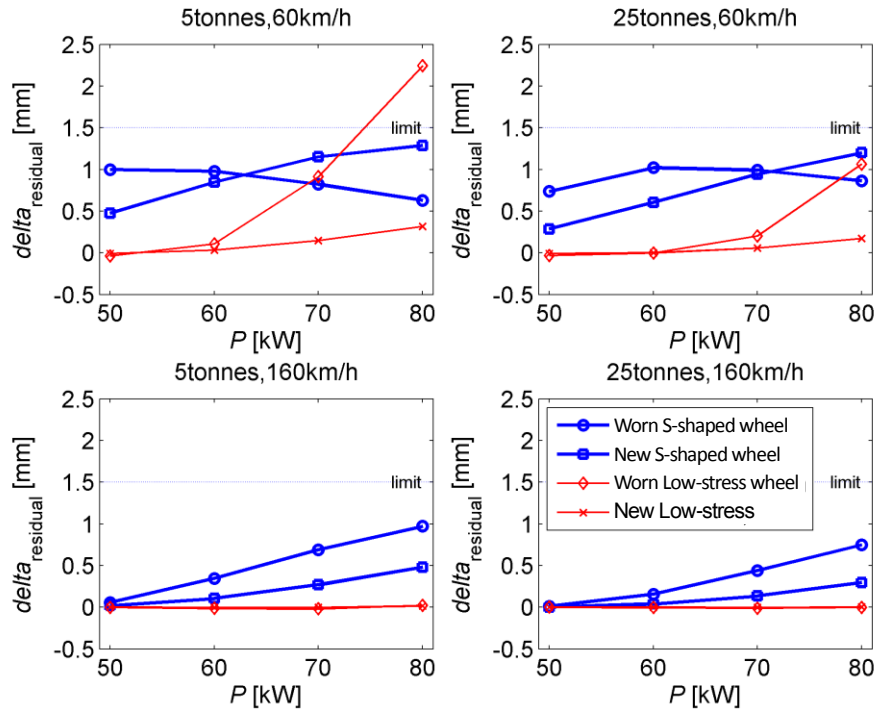


Figure 181 Maximum residual axial flange deflections are given for varying brake power and cooling conditions, considering rail chill for 5 and 25 tonnes axle load and forced convection cooling for 60 and 160 km/h. Simulations using the linear kinematic hardening material model.

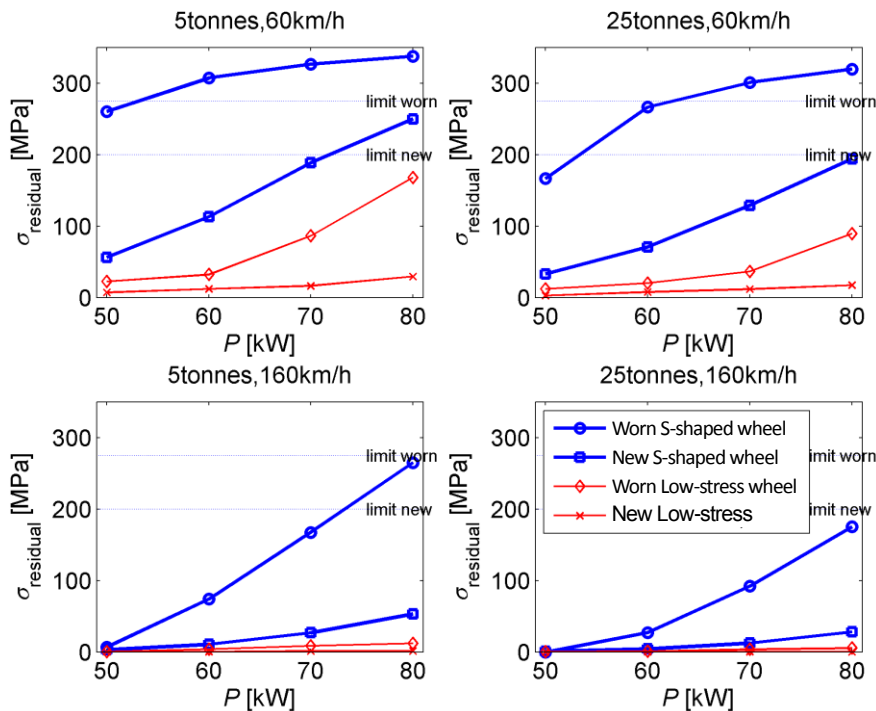


Figure 182 Maximum (average) residual rim stress are given for varying brake power and cooling conditions, considering rail chill for 5 and 25 tonnes axle load and forced convection cooling for 60 and 160 km/h. Simulations using the linear kinematic hardening material model.

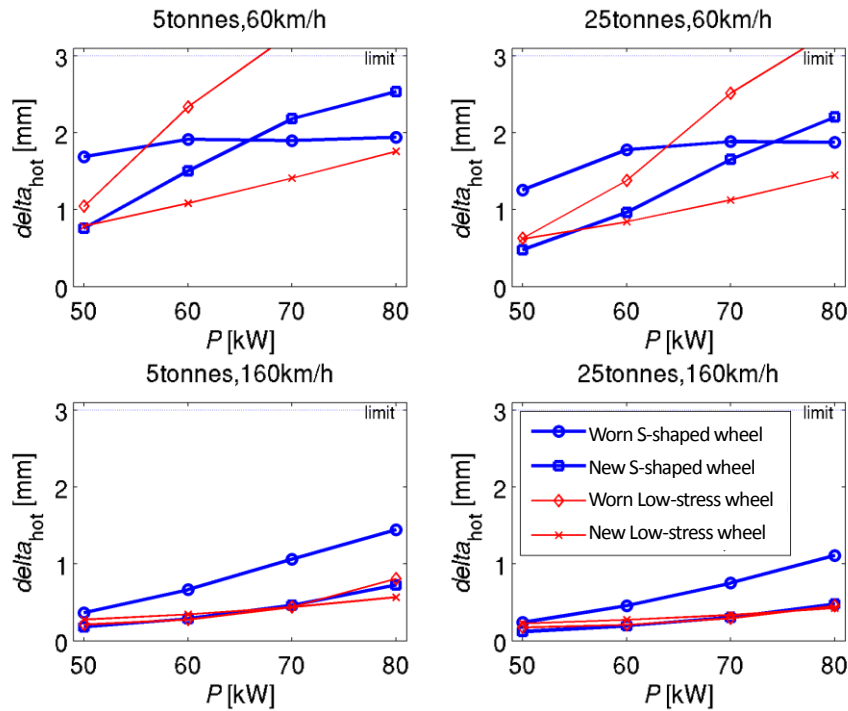


Figure 183 Maximum axial flange deflections during braking are given for varying brake power and cooling conditions, considering rail chill for 5 and 25 tonnes axle load and forced convection cooling for 60 and 160 km/h. Simulations using the advanced viscoplastic material model.

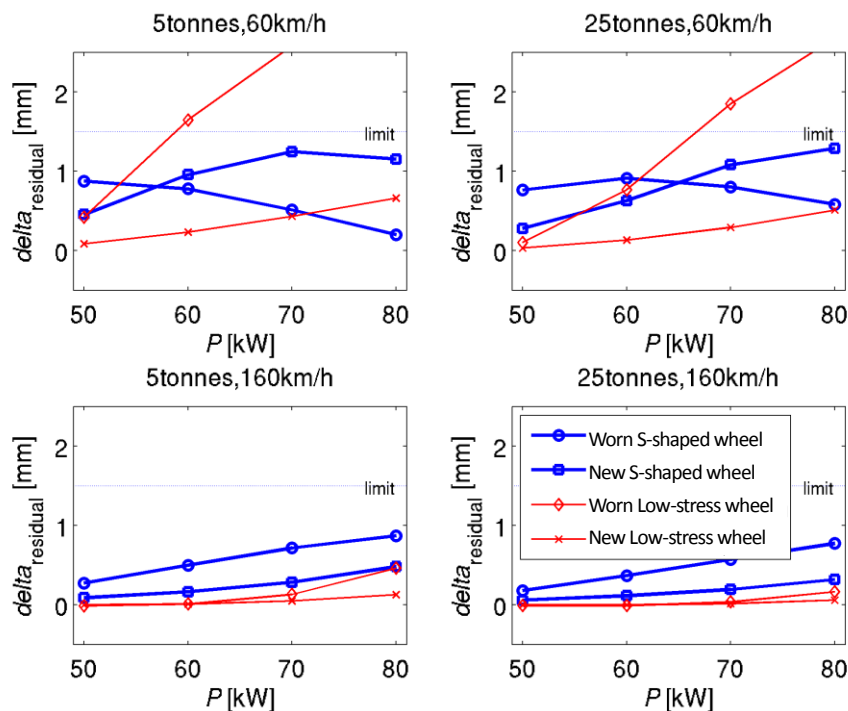


Figure 184 Maximum residual axial flange deflections are given for varying brake power and cooling conditions, considering rail chill for 5 and 25 tonnes axle load and forced convection cooling for 60 and 160 km/h. Simulations using the advanced viscoplastic material model.

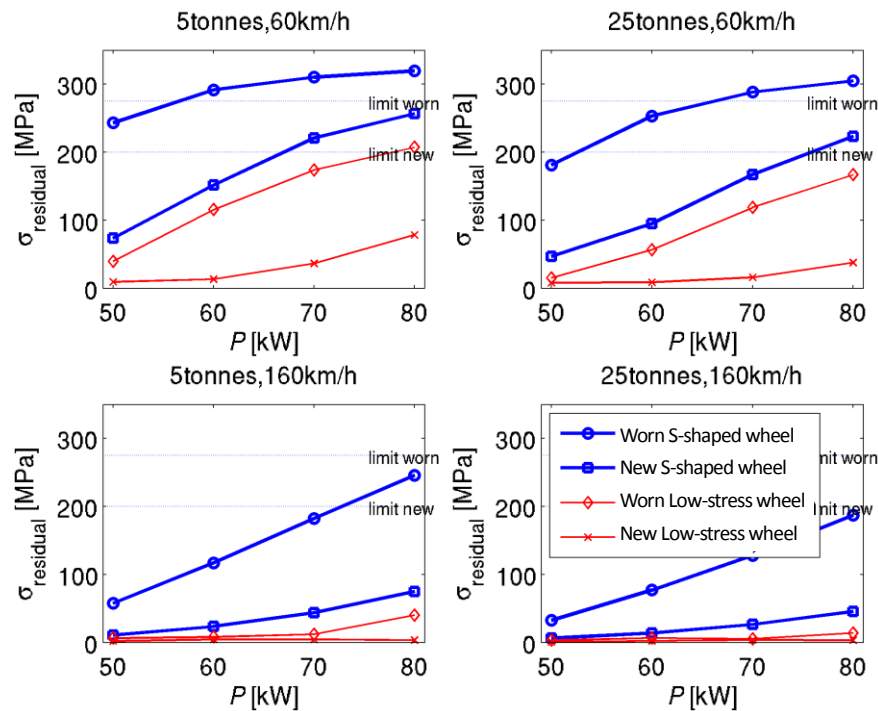


Figure 185 Maximum (average) residual rim stress are given for varying brake power and cooling conditions, considering rail chill for 5 and 25 tonnes axle load and forced convection cooling for 60 and 160 km/h. Simulations using the advanced viscoplastic material model.

The rim temperatures and power levels when the allowed residual stresses in the S-shaped wheel are equal to the allowed limit can be determined from the above figures. It is found that power levels of about 52 kW can be allowed with resulting rim temperatures of about 470 °C when considering the linear kinematic hardening material model (slightly higher power and temperatures can be allowed using the viscoplastic model). For the Low-stress wheel, the linear kinematic hardening material model gives a limiting power of about 74 kW and a rim temperature of 640 °C, while the viscoplastic material model gives a highest allowed power of 59 kW and a rim temperature of 550 °C. These wheel temperatures can be compared to the temperature requirements given by the TSI legislation regarding homologated brake blocks. Such brake blocks are required to act as a “thermal fuse” to protect the wheel (testing with fixed brakes) and should hence give very high wear at extreme wheel temperatures. The requirements give that, according to UIC leaflet 541-4, long-term wheel tread temperatures of up to 600°C can be produced by such brake blocks. The calculated temperatures given in this section are bulk rim temperatures which are lower than the temperatures at the tread. Temperatures of the wheel tread are shown in Figure 186 for drag braking during 45 min, showing both average tread temperatures and maximum tread temperatures. The temperatures of the wheel tread that corresponds to the above allowed power levels is for the worn S-shape wheel a maximum tread temperature of 590 °C or an average tread temperature of 535 °C, whereas the worn Low-stress wheel shows maximum tread temperature of 685 °C or average tread temperature of 612 °C. According to these tentative findings, the use of homologated brake blocks (that limits tread temperatures to a maximum of 600 °C) *can not* be used as a guarantee to avoid excessive and potentially detrimental residual stresses in wheels of the S-shaped wheels, while the blocks do give protection to the Low-stress wheels.

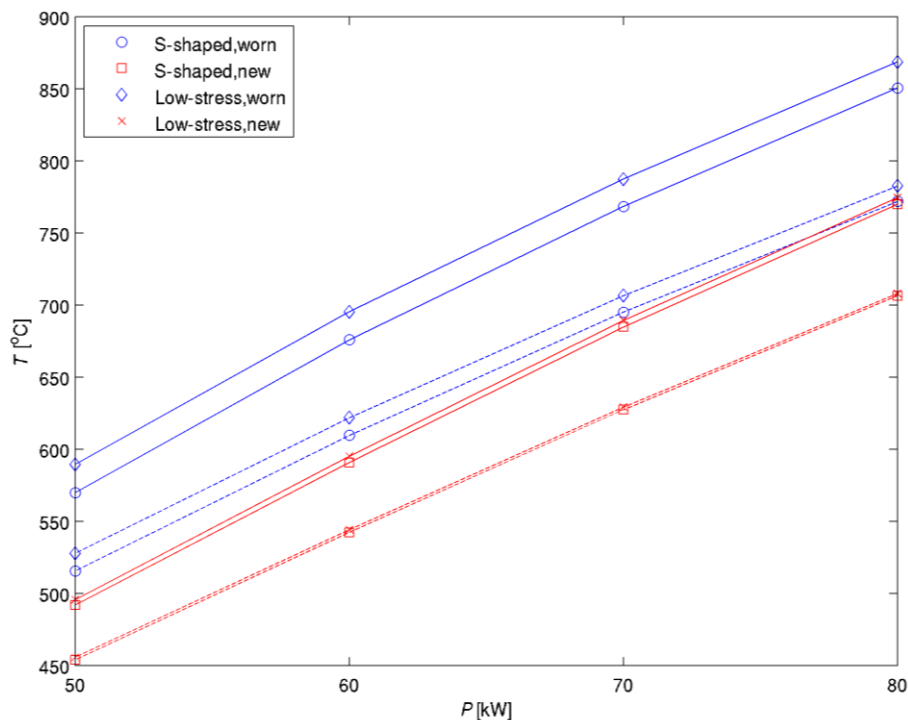


Figure 186 Wheel temperatures after 45 min drag braking at varying brake power, considering rail chill for 5 tonnes axle load and forced convection cooling for 60 km/h. Solid lines are maximum tread temperatures and dashed are average tread temperatures.

6.4.3 Wheel web fatigue due to track brakes

The results are illustrated in Figure 187 to Figure 190 for different load scenarios, see Table 47. The results are shown for the flange side and field side of the web and for the cases when the axial load F_a is applied either on the field side or flange side of the hub.

The fatigue analyses for different combinations of loading show that the importance of the different loading cases. Apparently, tread braking has the most significant influence on the fatigue life of the wheel web. This is best shown by the relatively short lives given in bars number 9 and 10 in the figures, having a mix between conventional mechanical loads and brakings, and long life given by bar number 4 with only conventional mechanical loading. The three consecutive stop brakings have the most negative effects on the fatigue life. For this case it should be noted that the strain amplitude for this case is almost three times as large as for a single stop. This loading case might be considered as too conservative for a general assessment of freight wheels. It is also found that the nonconventional loads have a negligible effect on the fatigue life (compare bar 10 with bars 11 and 12). The minor influence on the calculated wheel web life from the track brakes is the reason for not making a complete survey on all wheel designs³.

³ Instead of performing a parametric study for these load cases, the detailed parametric study on combined conventional loading and thermomechanical loading is given in the following Section.

Table 47: Loading alternatives for estimating fatigue failure of wheel web.

Load case	Bar chart identification number	
Conventional loads (CEN)	LC1 (100%)	1
	LC1 + LC2 (50% + 50%)	2
	LC1 + LC3 (50% + 50%)	3
	LC1 + LC2 + LC3 (94% + 5% + 1%)	4
Unconventional load	LC4-S1 ¹	5
	LC4-S2	6
	LC5-S1	7
	LC5-S2	8
Conventional + drag braking	LC1 + LC2 + LC3 + LC6 ²	9
Conventional + stop braking	LC1 + LC2 + LC3 + LC7	10
Conventional + unconventional (S1)+ stop braking	LC1 + LC2 + LC3 + LC4 + LC5 + LC7	11
Conventional + unconventional (S2)+ stop braking	LC1 + LC2 + LC3 + LC4 + LC5 + LC7	12

1) LC4 and LC5 show the load cases from primary and secondary track brakes, respectively. S1 and S2 show the first and second scenario when the vertical load is different, see Section 6.3.2.3.

2) LC6 and LC7 show the drag and stop braking load cases respectively.

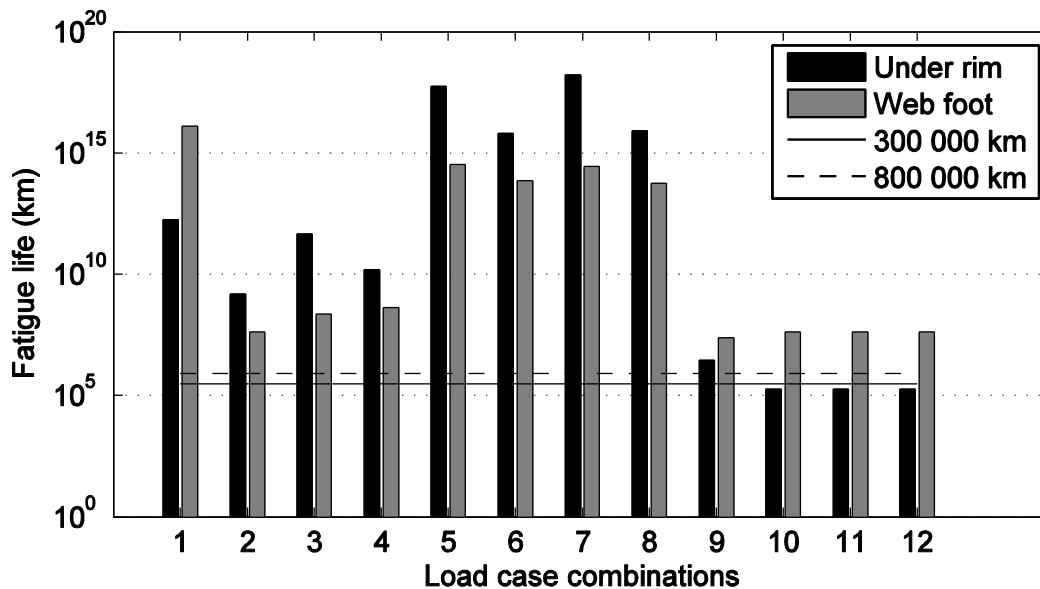


Figure 187 Fatigue lives for the nodes on the field side of the web when the axial load F_a is applied on the field side⁴.

⁴ Note that the calculated fatigue lives are unrealistic large for some cases. The longest calculated lives correspond to several light years (1 light year is about 1E13 km). The lives are shown nevertheless to indicate the relative importance of the different load cases.

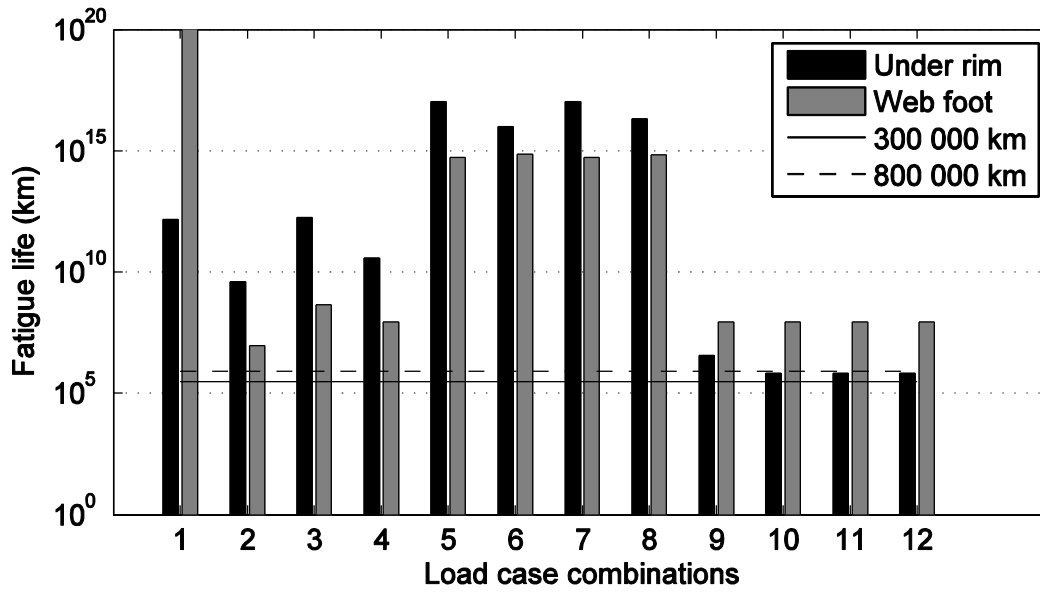


Figure 188 Fatigue lives for the nodes on the flange side of the web when the axial load F_a is applied on the field side.

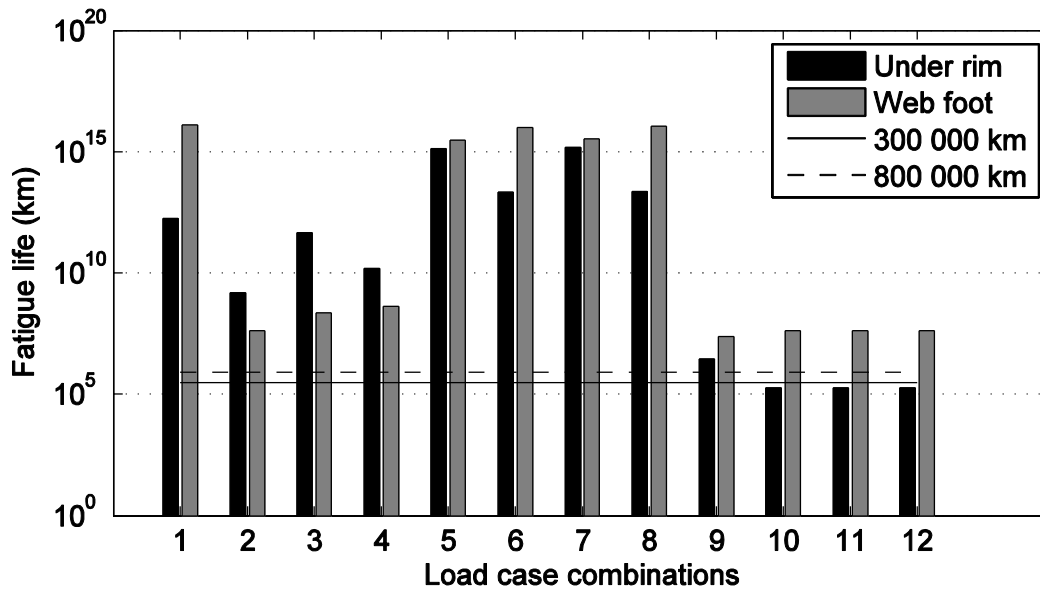


Figure 189 Fatigue lives for the nodes on the field side of the web when the axial load F_a is applied on the flange side.

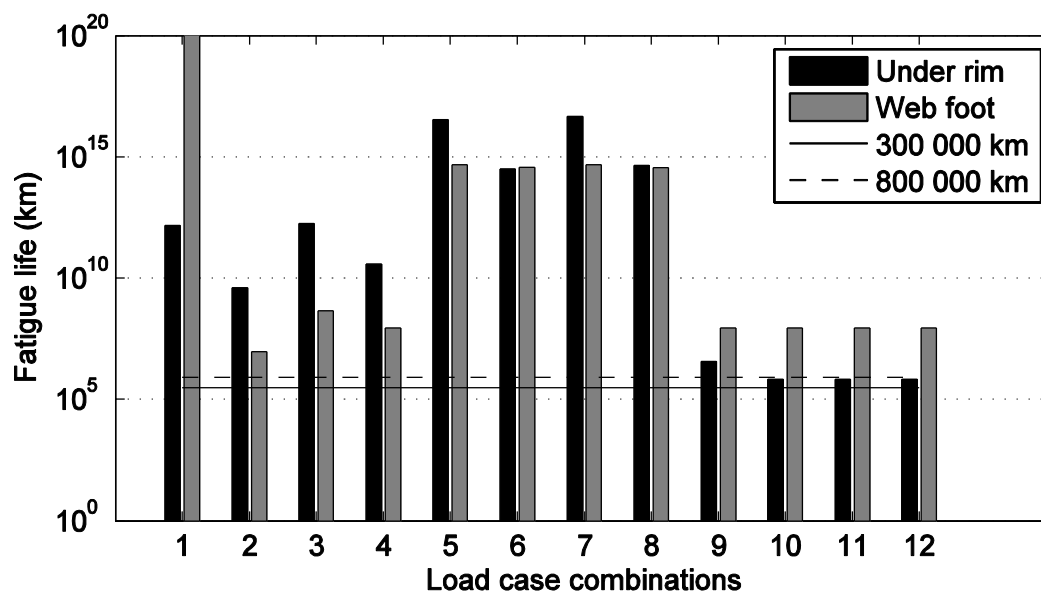


Figure 190 Fatigue lives for the nodes on the flange side of the web when the axial load F_a is applied on the flange side.

6.4.4 Wheel web fatigue due to combined mechanical and thermomechanical loading

Calculated web lives for S-shaped wheel and Low-stress wheel are given in Figure 191 for simulations using the advanced viscoplastic material model. The lives of the new wheels can be seen to be independent of the studied brake loads. This fact, combined with a more detailed analysis of the contributions to the calculated damage from the different loadings, reveal that the web lives are controlled by the mechanical loading of the wheels. For the cases when the mechanical loading is the main contributor to the damage, the critical location on the wheel web is close to the hub (corresponding to the location of the maximum stress range in Section 6.4.1). The calculated lives of the webs are more than 10 million km for both wheel designs and such long lives cannot be considered as limiting for the use of the wheels. For the worn wheels, the calculated lives are found to be depending on the considered braking loads. However, for the worn S-shaped wheel, it is only the most severe braking cycle (braking from 120 km/h at 1 m/s² with 25 tonnes axle load) that gives a minor reduction in the web fatigue life. For other less severe braking cases, wheel life is limited by the mechanical loading to 6.9 million km, with the critical point (with highest total damage) towards the hub. For the most severe stop braking cycles in combination with the drag cycles, the lives reduced to a minimum of 6.5 million km, with a critical point towards the rim. For the worn Low-stress wheel, the lives are larger than 9 million km for all combinations of load cases. The results again show that the lives are to a lesser degree influenced by the severity of the drag cycles and to a higher degree controlled by the stop loadings. Here, the largest damage occurs at a point towards the rim of the wheel. The analysis of the causes of the damage is here more complicated. When braking from 100 km/h (all accelerations) the generated damage to a high degree comes from the mechanical load cases, ranging from 78 % to 93 % of the total damage and the remainder of the damage is contributed by both drag braking and stop braking. For the stops from 120 km/h, the lives can be seen to drop quite substantially as compared to stopping from the lower speed. The damage is here to a lesser degree controlled by damage from mechanical

loadings (40 % to 60 %) and the stops now contribute to the total damage in a substantial way (40 % to 60 %). A minor part of the damage comes from drag braking.

The web lives have also been analysed using the alternative material model denoted linear kinematic hardening. The lives calculated using this material model are close to the ones calculated using the viscoplastic model when braking controls the lives (the calculated lives are, of course, identical if the mechanical loading controls the lives). The maximum difference is found for the most severe stop cycles when the calculated lives are up to 10 % longer for the linear kinematic hardening model than for the viscoplastic model. It can be concluded that the calculated lives and the associated strain cycling at the critical points in the web are relatively in-sensitive to the choice of material model (for the here two considered models). Moreover, since more conservative estimates of web lives are found from the viscoplastic material model, only results analysed using this model are presented in the following.

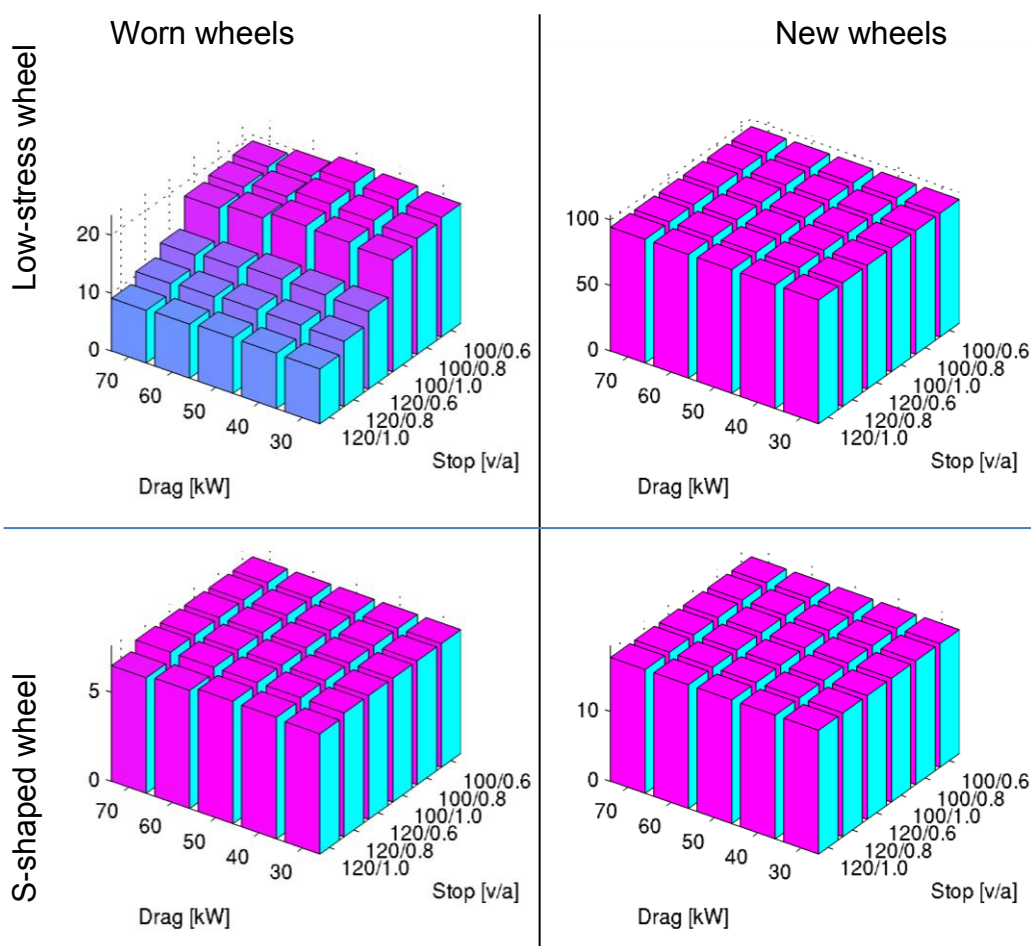


Figure 191 Calculated fatigue lives in million km ($\text{km} \times 10^6$) for combined mechanical and thermomechanical load cases. Drag braking power in kW and stop braking initial speeds v (km/h) and deceleration a (m/s^2) are indicated. Left column is for worn wheels and right column is new wheels. Upper row is for Low-stress wheel and lower row is for S-shaped wheel. Note the different scales of the lives in the graphs

The more severe cases when assuming two consecutive stop brake cycles have also been analysed when combined with drag braking and mechanical loading, see Figure 192. Thus, for each stopping event (one in 30 km), two stops are considered with only time for train

acceleration between stops. This renders strain ranges that are almost twice as large as when considering only single stops (with cooling to ambient before next brake cycle). Comparison with the case of single stops, see Figure 191, clearly shows that the lives for the new wheels are not affected at all by the double stops. The reason is that the lives are still being controlled by the mechanical load cases. However, the lives for the worn wheels are clearly reduced by the more severe stopping events. Nevertheless, the calculated lives are still larger than one million km for both wheels (Low-stress wheel $> 1.6 \times 10^6$ km and S-shaped wheel $> 1.0 \times 10^6$ km). It can be concluded that performing double stops on wheels do shorten the lives of the wheels if they are worn, but the calculated lives are still sufficiently large not to risk failure of the wheels during their service lives.

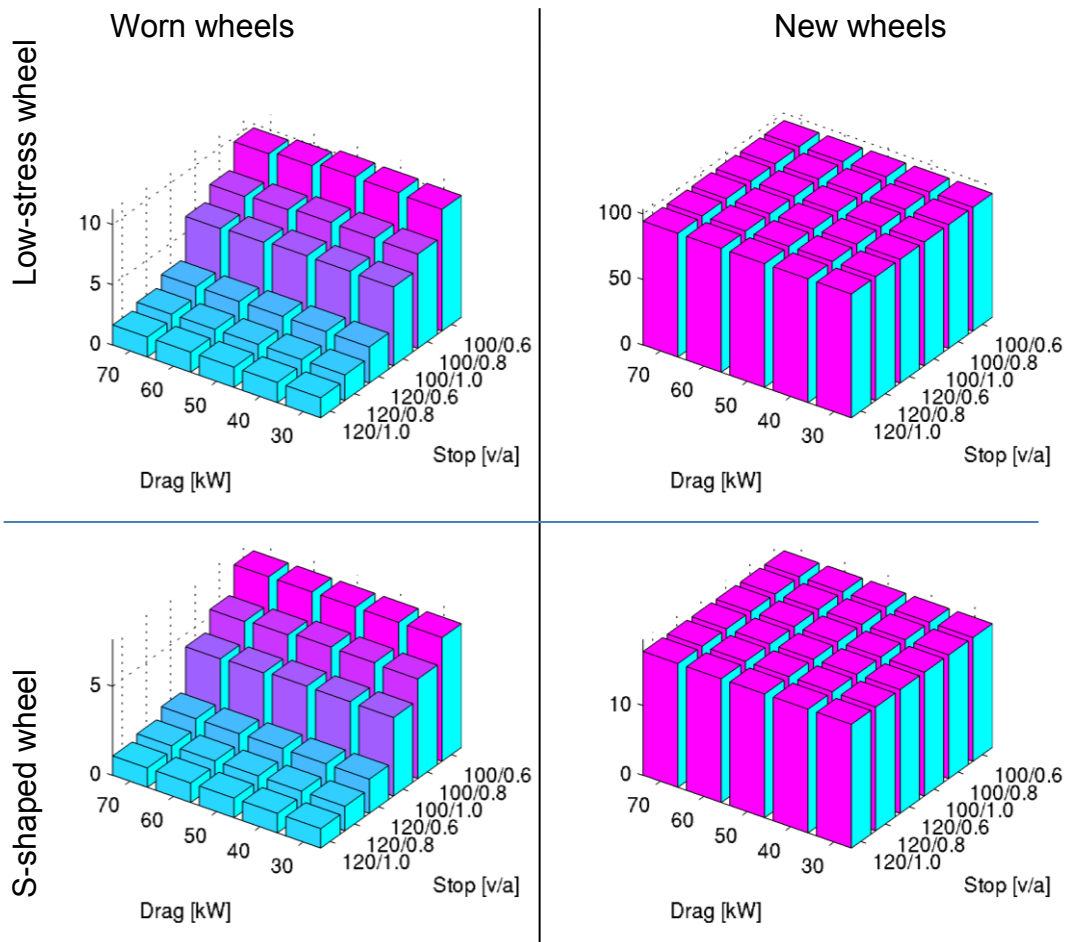


Figure 192 Calculated fatigue lives in million km ($\text{km} \times 10^6$) for combined mechanical and thermomechanical load cases. Note that two consecutive stops are considered for each stopping event. Drag braking power in kW and stop braking initial speeds v (km/h) and deceleration a (m/s^2) are indicated. Left column is for worn wheels and right column is new wheels. Upper row is for Low-stress wheel and lower row is for S-shaped wheel. Note the different scales of the lives in the graphs

The influence from an assumed deteriorated web surface as caused by e.g. severe corrosion or a surface scratch, has been studied by assumed that the fatigue limit is reduced. This reduction affects the assumed high cycle fatigue life, leaving the low cycle fatigue life unaffected. This has here been implemented by modification of the σ_f parameter in Equation (52). Two cases of assumed deteriorated web surfaces (severe corrosion or surface scratch) that lead to fatigue limit reductions have been studied. In the first case a reduction by 25% is studied (corresponding e.g. to a change in surface roughness $R_a=6.3 \mu\text{m}$ to $40 \mu\text{m}$)

and in the second case a reduction by 50% is studied (corresponding e.g. to a change in surface roughness $R_a=6.3 \mu\text{m}$ to a non-machined forged surface appearance). The results are presented in Figure 193 and Figure 194. The results show a dramatic reduction in calculated wheel lives. For the 25% reduction, the calculated wheel lives are still longer than about 800 000 km. For the 50% reduction, the wheel lives now range from 90 000 km up to 150 000 km for all studied geometries. Such short lives are *not* sufficient for avoiding problems in revenue traffic. For both reduction cases it can be found that a larger part of the damage now comes from the mechanical loading than for the analyses with no reduction. In detail, for both the 25% reduction and the 50% reduction, all of the damage for the new wheels and for the worn S-shaped wheel comes from the mechanical loading. For the worn Low-stress wheel the damage from mechanical loading is responsible for more than 78% of the total damage for the 25% reduction and more than 94% for the 50% reduction. It can be concluded that the surface finish of the web is of utmost importance for wheel lives. Moreover, in the future, when stress optimized wheels will be more common these results indicate that wheel webs should be checked regularly at maintenance to avoid surface deterioration that substantially lowers the fatigue limit. An intact wheel web paint system for the duration of the wheel life is hence essential not to increase the risk of fatigue damage.

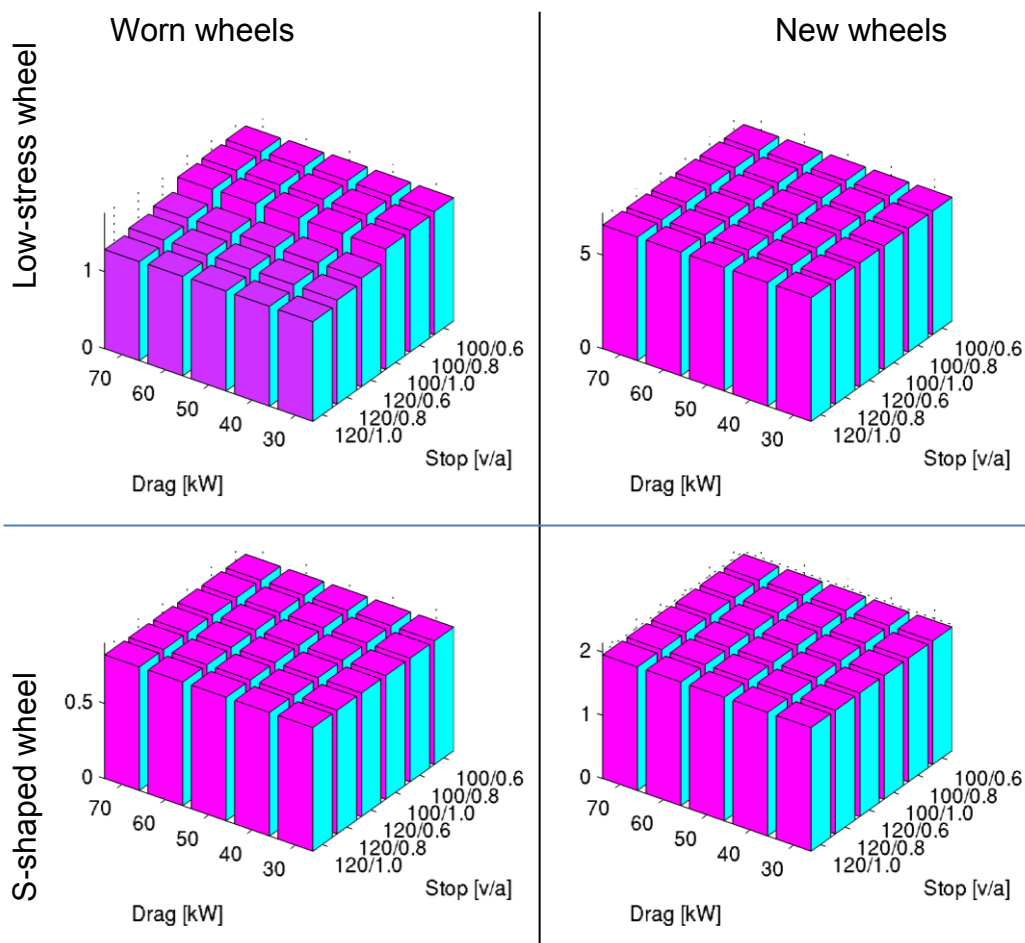


Figure 193 Calculated fatigue lives in million km ($\text{km} \times 10^6$) for combined mechanical and thermomechanical load cases. Fatigue criterion modified for an assumed reduction in high cycle fatigue life of 25%. Drag braking power in kW and stop braking initial speeds v (km/h) and deceleration a (m/s^2) are indicated. Left column is for worn wheels and right column is new wheels. Upper row is for Low-stress wheel and lower row is for S-shaped wheel. Note the different scales of the lives in the graphs

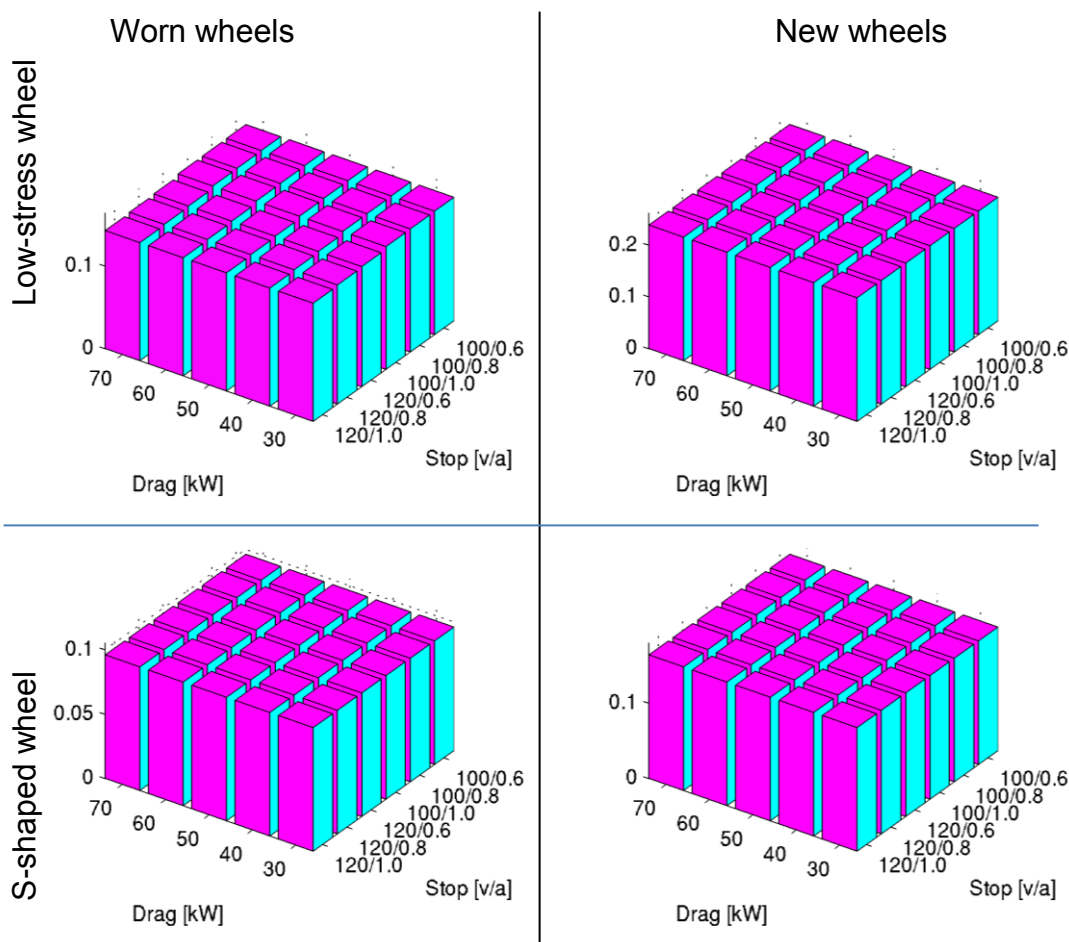


Figure 194 Calculated fatigue lives in million km ($\text{km} \times 10^6$) for combined mechanical and thermomechanical load cases. Fatigue criterion modified for an assumed reduction in high cycle fatigue life of 50%. Drag braking power in kW and stop braking initial speeds v (km/h) and deceleration a (m/s^2) are indicated. Left column is for worn wheels and right column is new wheels. Upper row is for Low-stress wheel and lower row is for S-shaped wheel. Note the different scales of the lives in the graphs

6.4.5 Cracks in wheel rim and web

It is first studied assumed that an initial crack exists in the wheel web. In a first step, the stress intensity factor at the deepest point of the crack is studied for the default three mechanical load cases according to EN 13979-1 with loads based on an axle load of 25 tonnes. To study the sensitivity to extreme vertical loading (as generated by e.g. a large wheel flat), a modified load case is studied where the vertical load component of the three load cases has been increased from $1.25P$ to $3.0P$.

Stress intensity factors were calculated for a range of crack depths and widths. The results for loads according to EN13979-1 when assuming a crack with depth 2 mm and half-width 6 mm located at different positions on the wheel web are presented in Figure 195 for S-shaped wheel when the wheel is at its minimum diameter. The maximum stress intensities for field side and flange side for the three load cases are summarized in Figure 196. The maximum stress intensities for field side and flange side for the three load cases when considering an increased vertical load $3P$ are summarized in Figure 197. Summaries of the corresponding stress intensities for the Low-stress wheel are given in Figure 198 and Figure 199.

The stress intensities for the both studies wheel types are higher than the threshold value ($K_{\text{th}}=7.1 \text{ MPam}^{\frac{1}{2}}$) for the wheel in worn state for the studied crack, with maximum values of 12-15 $\text{MPam}^{\frac{1}{2}}$. This means that cracks of this size will start to grow.

From this study it can also be concluded that the crack intensities not are very sensitive to an increase in vertical loading. For the S-shaped wheel design an increase of the vertical load component from $1.25P$ to $3P$ means that the magnitude of the largest stress intensity for the field side is almost unaffected (about $12 \text{ MPam}^{\frac{1}{2}}$), but that the position of the maximum is shifted from near to the hub to near the mid radius of the web. When the vertical loading increases, the flange side shows an increase from 9.5 to $12 \text{ MPam}^{\frac{1}{2}}$, with the maximum positioned at the hub for both cases. For the Low-stress wheel design, an increase in the maximum stress intensity can be found for both field and flange side of the web, from 9 to $12.5 \text{ MPam}^{\frac{1}{2}}$ for field side and from 8.5 to $17 \text{ MPam}^{\frac{1}{2}}$ for flange side. The position of the maximum stress intensities is located near the hub for the field side while it is positioned at about mid radius for the flange side, with no shifts in position with increased vertical loading.

From this study it can be concluded that the S-shaped wheel has a minor sensitivity to increase in the maximum stress intensity factor with increasing vertical load while the Low-stress wheel has a more pronounced sensitivity.

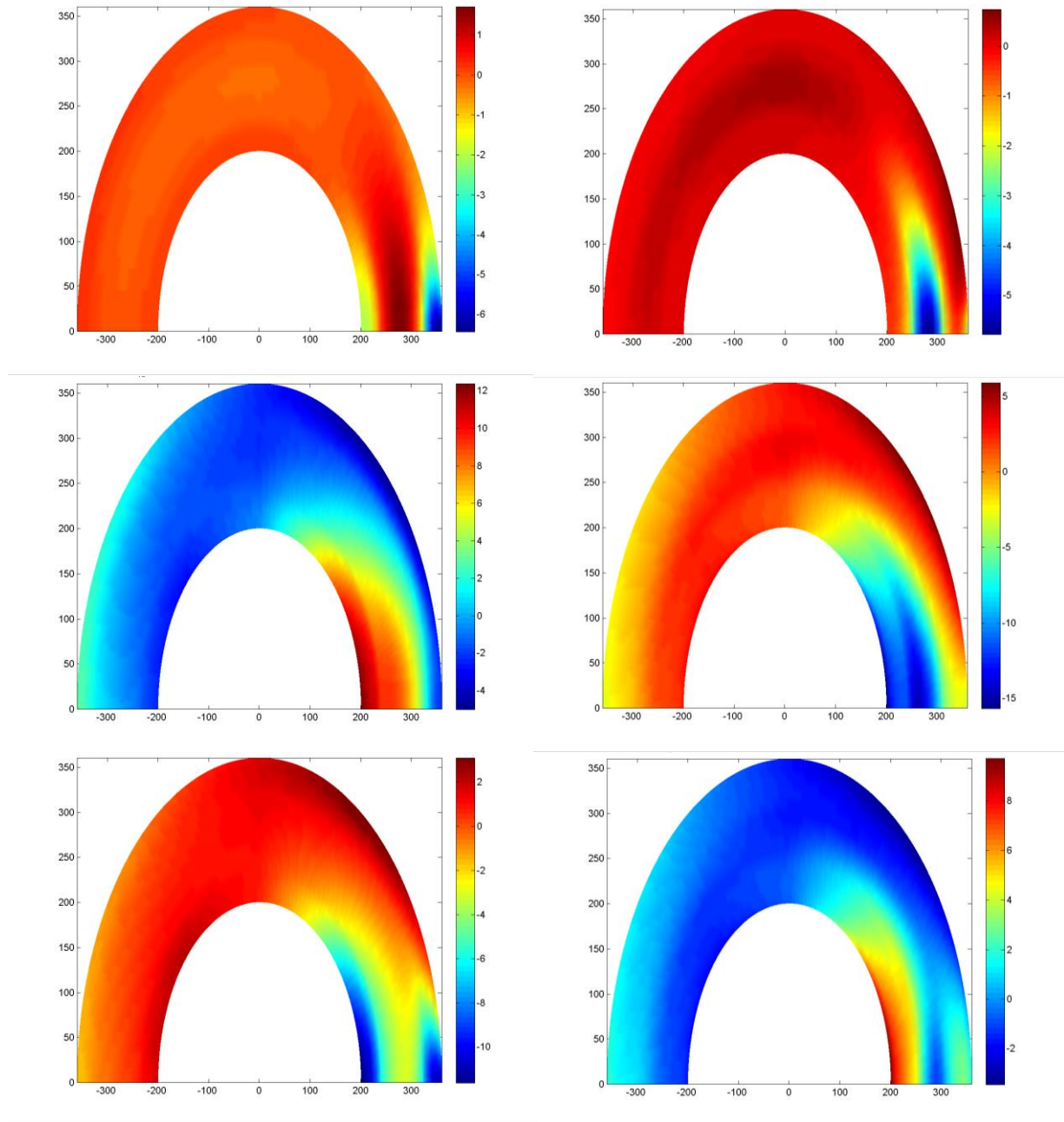


Figure 195 S-shaped wheel: Calculated stress intensity factors for different assumed positions on the wheel web when loads CEN1-3 are applied on the rim to the right. Results for field side and flange side of web are given in left and right columns, respectively. Upper row shows results for load case CEN1 (straight track), mid row shows CEN2 (curving) and lower row shows CEN3 (points and crossings).

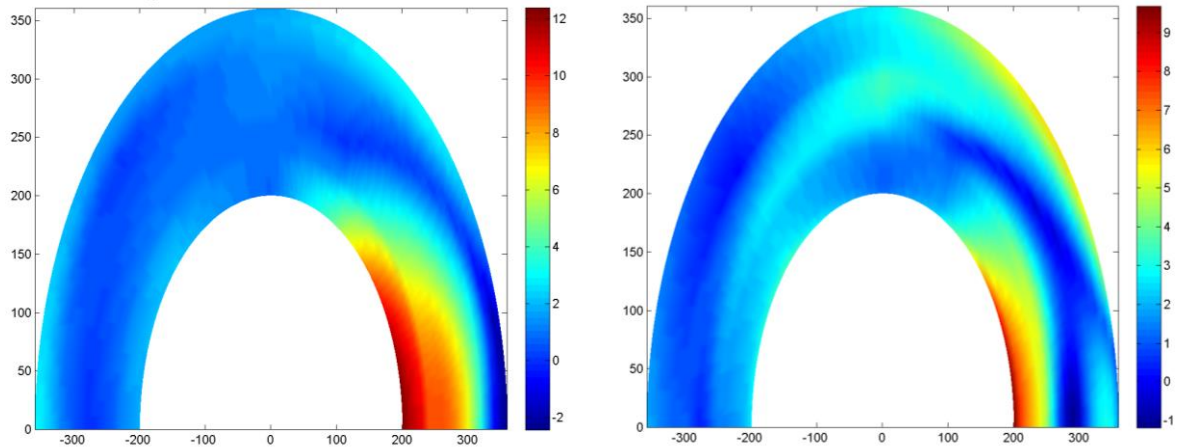


Figure 196 S-shaped wheel: Maximum of calculated stress intensity factors for different assumed positions on the wheel web when loads CEN1-3 are applied on the rim to the right. Results for field side and flange side of web are given to left and right, respectively.

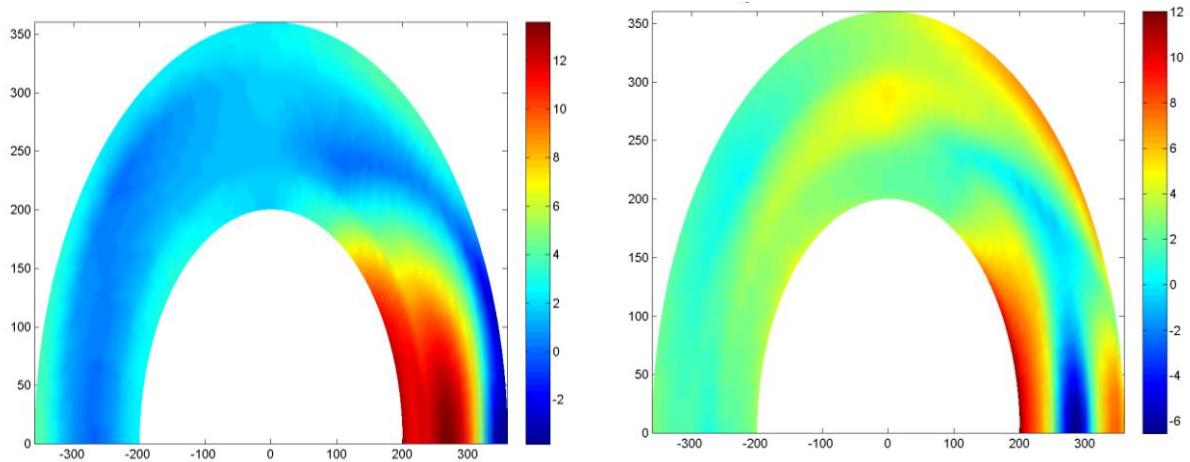


Figure 197 S-shaped wheel: Maximum of calculated stress intensity factors for different assumed positions on the wheel web when loads CEN1-3, with an increased vertical load component 3P, are applied on the rim to the right. Results for field side and flange side of web are given to left and right, respectively.

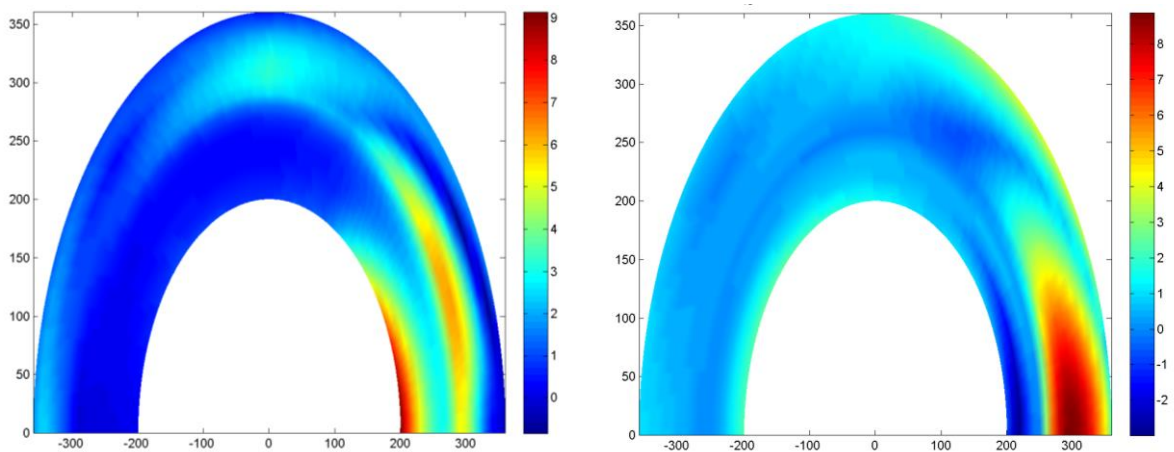


Figure 198 Low-stress wheel: Maximum of calculated stress intensity factors for different assumed positions on the wheel web when loads CEN1-3 are applied on the rim to the right. Results for field side and flange side of web are given to left and right, respectively.

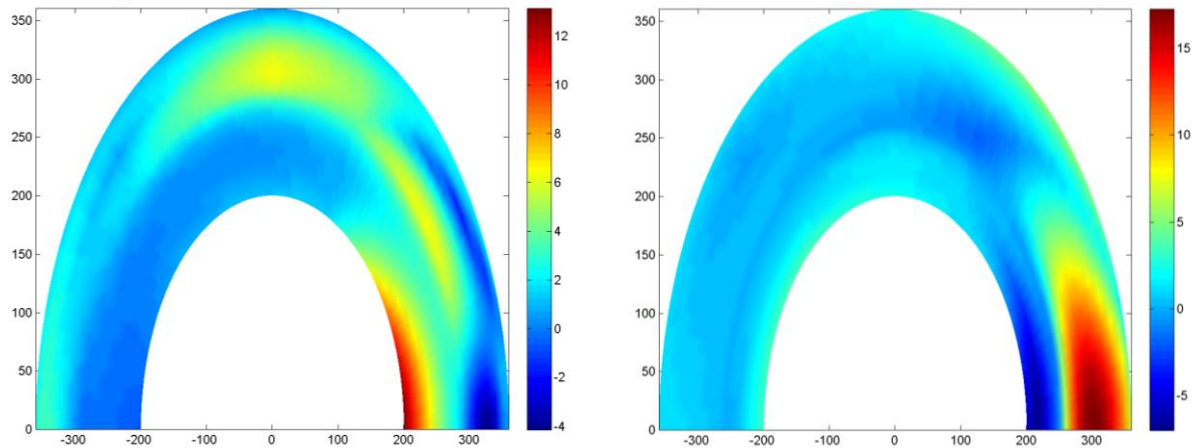


Figure 199 Low-stress wheel: Maximum of calculated stress intensity factors for different assumed positions on the wheel web when loads CEN1-3, with an increased vertical load component $3P$, are applied on the rim to the right. Results for field side and flange side of web are given to left and right, respectively.

The growth of cracks in the wheel web is studied by use of spectrum loading. The loading is characterized by having a high stress level σ_E for 10^{-6} out of the total number of cycles which is given by the vertical and lateral loading according to EN 13979-1. The number of points and crossing has been assumed to be 10% of the number of curves. Running on straight track causing stress σ_S with maximum axle load is assumed for half the life. Additionally two more severe spectra has been utilised where the vertical loading has been increased to two and three times the static axle load.

An example of crack growth for a assumed initial crack with depth 2 mm and half-width 6 mm located at the middle of the web of the worn Low-stress wheel is given in Figure 200. From this example, it can be seen that the crack grows very slowly in the depth direction. Moreover, it is clear that for the crack to grow in the depth direction at all, it requires a crack that becomes very shallow in its shape. It is the increasing width that induces the growth of the crack through the web thickness. Three different stopping criteria for the crack growth have been used at the analyses: Firstly if the critical stress intensity is reached, secondly if the crack has grown though more than 80% of the web thickness and thirdly of the crack width is larger than $\frac{1}{4}$ of the web circumference. In the example, the crack growth analysis has been stopped for violating the crack width criterion.

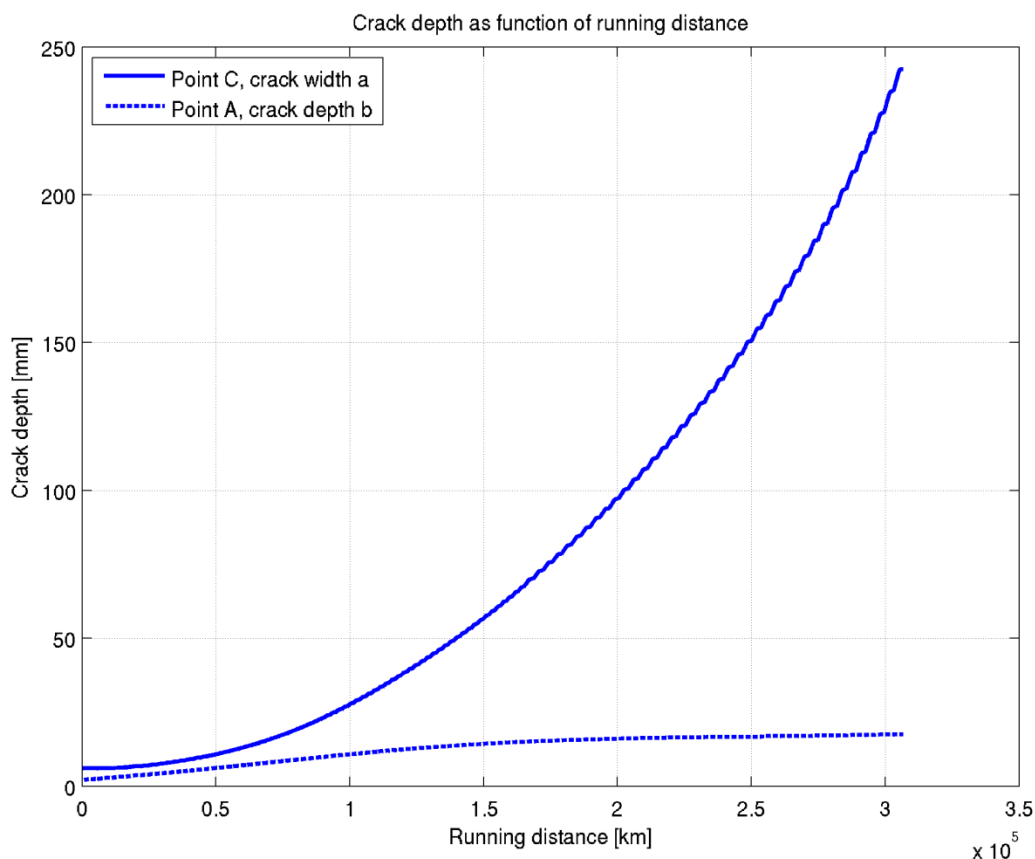


Figure 200 Example of crack growth from an initial crack with depth 2 mm and half-width 6 mm using a load spectrum based on vertical loading based on vertical load 1.25 times the static wheel load.

An overview of results for crack life in this web crack study is given in Table 48. An initial crack depth of 2 mm has been assumed and the crack half-width is 2 or 6 mm. Two spectra have been evaluated where spectrum A has $1.25P$ vertical load component and while spectrum B has $2P$ vertical load. Two positions have been evaluated, one towards the hub and one having a central position on the web. One main conclusion is that the Low-stress wheel is more sensitive to web cracking than the S-shaped wheel. The reason for this can (of course) be found in the higher stress intensities for the web of the Low-stress wheel. Assuming that the vertical loading in the spectra is based on vertical loading $1.25P$ (as in the standard EN13979-1) and cracks having initial depth 2 mm, both wheel designs seem to have sufficient crack life with a lowest life of 310 000 km for an initial crack width of 12 mm (half-width 6 mm). However, assuming that the vertical loading is increased due to excessive tread damage to $2P$ show calculated crack lives that are (again) sufficient of the S-shaped wheel for all cases whereas for the Low-stress wheel, cracks at a mid-web position give cracks lives as low as 61 thousand km. It can be concluded that the Low-stress wheel design has a larger sensitivity to web cracking than the S-shaped wheels and that the maintenance of the tread of the wheels for avoiding e.g. wheel flats become more important than for the S-shaped wheel design.

Table 48 Calculated crack life [km] for initial crack depth 2 mm and indicated crack half-width. Spectrum load A has 1.25P vertical load component and spectrum B has 2P vertical load. Two positions have been evaluated one towards the hub and having a central position on web.

Spectrum	Initial crack half-width	Low-stress wheel - worn		S-shaped wheel – worn	
		Hub	Mid web	Hub	Mid web
A	2	1.2E9	1.1E9	1.5E9	7.9E9
	6	7.2E8	3.1E5	1.3E9	6.eE9
B	2	2.6E8	7.1E4	1.6E9	3.8E9
	6	9.9E7	6.1E4	1.3E9	3.1E9

Analyses have also been performed for a case where a small crack starts to grow from the threshold value for crack growth for the web material. These analyses all very slow initial crack growth and yielding a typically life of 10^9 km.

Cracking of the wheel rim can also be studied using the above techniques to find influence from the thermomechanical loading of the wheel at tread braking. In Reference [15], two-dimensional FE-simulations of elastoplastic thermomechanical stresses during heating and cooling have been combined with using similar analytical evaluations as used above for resulting stress intensities for thermal cracks. For heavy haul conditions, the results imply that fully functional brake systems on are not likely to induce thermal crack propagation in the wheel tread under normal stop braking since the operational speed is too low. On the other hand, severe drag braking due to malfunctioning brakes may cause very deep cracking. The analysis also concludes that thermal cracking is a static phenomenon related to the most severe brake cycle. The material model utilised for producing the results for the thermomechanical load cases accounts for temperature dependent linear kinematic hardening.

6.5 Derailments caused by mechanical wheel tread cracking

6.5.1 Studied derailment scenarios

The focus of the section is derailment caused by cracks formed (mainly) by rolling contact fatigue (RCF), propagated to cause a fracture where part of the tread is broken off.

There are basically two RCF forming mechanisms: Initiation at the surface due to high interfacial wheel–rail shear, and initiation below the surface due to a combination of high vertical wheel loads and material defects.

Surface initiated RCF cracks may grow deep, especially if promoted also by thermal loading, see Figure 201. Although this may result in very high vertical load magnitudes, the result is seldom a derailment due to a wheel fracture (it may instead cause rail breaks and/or break down of gear boxes with related derailments caused by axle failures).



Figure 201 Deep pitting caused by surface initiated rolling contact fatigue cracking.

In the context of derailment due to mechanical wheel tread cracking, it is instead the subsurface initiated RCF cracks that are a potential hazard.

Such cracks are rather rare and typically form at depths 4 to 25 mm below the surface. The cracks eventually branches towards the wheel surface or towards the hub. Examples of a failure owing to subsurface initiated rolling contact fatigue are presented in Figure 202.



Figure 202 Subsurface initiated rolling contact fatigue cracks. From [1] (left) and [17] (right)

6.5.2 Influencing parameters

The risk of subsurface RCF initiation can be quantified by the fatigue index FI_{sub} [18]:

$$FI_{\text{sub}} = \frac{F_z}{4\pi ab} (1 + f^2) + c_{\text{dv}} \sigma_{\text{h,res}}$$

where F_z is the normal contact load, a and b the semi-axes of the contact patch, f the traction coefficient, c_{dv} a material parameter and $\sigma_{\text{h,res}}$ the hydrostatic part of the residual stress. Note that FI_{sub} relates to the largest (elastic) shear stress located some millimetres below the running surface. For RCF initiated deeper down the stress magnitude will be lower and there will be less influence of the contact patch size.

Fatigue is presumed $F_{l,sub} \geq \tau_{fl,red}$, with $\tau_{fl,red} \approx \tau_{fl}(d/d_0)^{1/6}$. Here $\tau_{fl,red}$ is the reduced fatigue limit in shear of a material containing a defect of size d . Further d_0 is the defect size corresponding to fatigue initiation at the unreduced fatigue limit in shear τ_{fl} .

It can also be noted that the risk of subsurface initiated RCF increases significantly at contact close to the field edge of the wheel.

Thus from the brief overview above it can be noted that the most important parameters are:

- vertical load magnitude
- contact patch size – monitored as profile geometries of wheel and rail
- material defect size
- contact close to field side – monitored as track gauge (accounting for rail head wear)

Much more details may be found in references [18–22].

6.5.3 Prevention of wheel breaks caused by RCF

Limiting vertical load magnitudes as caused by wheel flats *etc* has been dealt with in section 7. In addition also increased vertical loading caused by rail irregularities – in particular rail corrugation – is an important issue. It is here important to notice that also the high frequency content (up to, and above 1000 Hz) of the load is of importance as it will have a significant contribution to the total load level. Two ways of monitoring the influence of rail defects is by hand-driven trolleys, or by high-frequency measurements, see [16].

The wheel and rail geometries can either be measured with high precision e.g. using MiniProof. Alternatively, faster, but less precise measurements featuring laser scanning can be employed.

The material defect size is assessed during manufacturing. In addition also continuous measurements featuring ultra-sonics can be performed. These are however costly. Also the efficiency of such measurements can be questioned, see [23].

Contact close to the field side is monitored and ensured through standard track geometry measurements.

Knowing this input, limiting conditions where subsurface initiated RCF can be an issue may be identified using simulation of high-frequency, vertical train–track interaction combined with an RCF assessment. Details of how such an analysis can be performed (and also account for noise emission) is presented along with results for selected cases in ??

6.6 Concluding remarks

Fatigue at mechanical loading has been studied for the two wheel designs. An assumed increase of the vertical loading (from $1.25P$ to $2P$ or $3P$) when the train is rolling on straight track, results in a minor increase of the fatigue stresses in the wheel web. However, if it is assumed that the increase in the vertical load also affects the vertical loading that interacts with the lateral loads at curving and negotiation of points and crossings, a quite substantially increase in the fatigue stresses can be seen at the transition between web and rim for the Low-stress wheel.

For the thermomechanical load case it is shown that there is a substantial difference between wheels with a slightly S-shaped web and a low-stress wheel. For single brake cycles at high power, all wheels have axial displacements even that are within requirements at the highest studied power level (80 kW). Moreover, for the residual axial displacements after braking, too high values are only obtained for the worn low-stress wheel. On the other hand, the low-stress wheel shows residual stresses that are within the regulations also for the worn wheel, whereas the slightly S-shaped shows too large stresses that can result in global wheel fracture. When analysing single brake cycles using the more advanced viscoplastic material model, it is found that all wheels except the worn slightly S-shaped wheel has axial rim displacements that are in line with the standards. However, the worn low-stress wheel shows too high residual displacements of the wheel rim for powers higher than 60 kW. Similar to the analyses with the linear kinematic model, the slightly S-shaped wheel has residual stresses in the rim that are lower than required by the standards also at the highest studied power level of 80 kW. The worn low-stress wheel shows too high residual stresses in the wheel rim already at 60 kW.

The wheels have also been assessed for multiple brake cycles (with intermediate cooling to ambient temperature) using the viscoplastic material model. These analyses confirm the results from the single brake cycle with respect to residual stresses after braking; the slightly S-shaped wheel does not fulfil the requirements at 60 kW while the low-stress wheel fulfils the requirements also at the highest tested brake power (80 kW). When it comes to the residual axial flange deflection, it is found that the low-stress wheel shows a substantial global ratchetting behaviour in the axial direction for power levels of 60 kW and higher. For each brake cycle, an additional displacement increment is then added to the total axial flange deflection. This makes the wheel rim gradually move outside of allowed limits (towards the field side). At the same time, the stresses in the wheel rim increase, but are kept within the allowed limits. For the slightly S-shaped wheel the assumptions made after single brake cycles still hold with only minor differences (in residual stress levels and displacements) as compared to when analysing single cycles.

The analyses of wheel web life with respect to combined mechanical loads and loads from tread braking generally show long lives (several millions of kilometres) for the assumed loading. The loading spectrum of the wheels is based on a train running for 300 000 km with 94% straight track, 5% curves and 1% switches / crossings, with additionally 10 high power drag cycles and 10 000 stops (one stop every 30 km). It is found that the lives of the low-stress wheel and the slightly S-shaped wheel are limited by mechanical fatigue. The largest damage levels occur in the web close to the hub. However, worn slightly S-shaped wheels are limited in life by a combination of damage originating from mechanical fatigue and thermomechanical fatigue from braking. The largest damage is then found to occur towards the wheel rim. Depending on the assumed braking load cases, thermomechanical fatigue (from braking) contributes with up to 65% of the total damage. It should here be noted that the braking load cases have been considered to occur separately (i.e. intermediate cooling to ambient temperature) but assuming severe braking load cases (drag braking up to 70 kW and stop braking as severe as resulting from braking 25 tonnes axle load at 1 m/s² from 120 km/h). In conclusion, the analyses of damage for combined mechanical loads (with forces in accordance with the standard EN 13979-1) and thermomechanical loads from braking are not restricting for wheel lives even when considering severe stop braking. Even

the calculated lives of the worn wheels are higher than the expected total maximum service life of freight wheels (then having diameters ranging from new down to worn state).

Two cases of assumed deteriorated web surface (severe corrosion or surface scratch) that lead to fatigue limit reductions have been studied. In the first case a reduction by 25% is studied (corresponding e.g. to a change in surface roughness $R_a=6.3 \mu\text{m}$ to $40 \mu\text{m}$) and in the second case a reduction by 50% is studied (corresponding e.g. to a change in surface roughness $R_a=6.3 \mu\text{m}$ to a non-machined forged surface appearance). These reductions are presumed to modify the high cycle fatigue life, while leaving the low cycle fatigue life mainly unaffected. The result is a dramatic reduction in calculated wheel lives. For the 25 % reduction, the calculated wheel lives are still longer than about 800 000 km. For the 50 % reduction, the wheel lives now range from 90 000 km up to 150 000 km for all studied geometries. It can be concluded that the surface finish / appearance of the web is of utmost importance for wheel lives. Moreover, in the future, when stress optimized wheels will be more common these results indicate that wheel webs should be checked regularly at maintenance to avoid surface deterioration that substantially lowers the fatigue limit. An intact wheel web paint system for the duration of the wheel life is hence essential not to increase the risk of fatigue damage.

The wheel web life has also been analysed when assuming that each stopping event consists of two consecutive stop brake cycles (time between for train acceleration only) at each stop-braking event in the load spectrum. For this case, the resulting strain amplitude in the web is almost twice the one given by a separate stop. For this (degenerate) case it is found that the lives of the new wheels still are controlled by the mechanical fatigue, but that the lives of both wheel designs in the worn states are controlled by predominantly stop braking damage. However, even when considering double stops, the calculated lives of the wheels are still more than one million km.

The analyses of the wheel life when also considering loads from track brakes show that the wheel lives are controlled by a combination of mechanical fatigue from conventional load cases and thermomechanical fatigue induced by tread braking. The lives are only to a negligible degree controlled by the non-conventional mechanical loading cases that are induced by the track brakes. These findings indicate that there is no need to add loads from track brakes to the design load cases specified in standards.

The study of cracks in the web of the wheels indicates that for normal running conditions, the crack growth is very slow, only marginally larger than the threshold for crack growth. When a crack continues to grow, the speed of the growth remain low and a substantial widening of the crack (in circumferential direction) is required to for the crack too grow deeper into the web. Furthermore, for future assumed increasing vertical and lateral loading it has been found that the cracking of the wheel web is not particularly sensitive to such a development

The main derailment hazard related to rolling contact fatigue (RCF) of the wheel tread has been identified as subsurface initiated RCF. Influencing parameters, monitoring and prediction possibilities are indicated in the report.

6.7 References

1. **Delivery D1.1: Summary report and database of derailments incidents**, *D-RAIL*, 2012, 71 pp + 1 annex (3 pp).
2. **European Standard, Railway applications – Wheelsets and bogies – Wheels – Technical approval procedure – Part 1: Forged and rolled wheels**, *CEN*, EN 13979-1:2004+A2:2011 E, Brussels, BE, March 2011, 50 pp.
3. Technical approval of monobloc wheels – Application document for standard EN 13979-1, *International union of railways (UIC)*, UIC code 510-5, 2nd edition, Paris, FR, May 2007, 72 pp.
4. Tore Vernersson, **Tread braking of railway wheels – noise-related tread roughness and dimensioning wheel temperatures: field tests, rig measurements and numerical simulations**, Doctoral Dissertation, *Chalmers Applied Mechanics*, Gothenburg 2006, 136 pp (introduction, summary and six appended papers)
5. Pascal Tomasin, SNCF, private communication.
6. Tore Vernersson, Johan Ahlström and Magnus Ekh, Viscoplastic material model for railway wheel materials at high temperatures, *Chalmers Applied Mechanics*, November 2013 (availability restricted).
7. Niklas Köppen, **Deformation behaviour of near fully pearlitic steels during monotonic and cyclic loading**, Licentiate Thesis, *Chalmers Materials and Manufacturing Technology*, Gothenburg 2006, 66 pp (introduction, summary and two appended papers).
8. Reports available through BEA-TT: <http://www.bea-tt.developpement-durable.gouv.fr/neufchateau-r136.html>
9. [Shahab Teimourimanesh, **Fatigue analysis of Neufchâteau accident**, *Chalmers Applied Mechanics*, Göteborg 2013, 25 pp.](#)
10. ASTM E 1049-85 (Reapproved 1997), *Standard practices for cycle counting in fatigue analysis*, in: Annual Book of ASTM Standards, Vol. 03.01, Philadelphia 1999, pp. 710-718
11. NIEŚŁONY A., *Determination of fragments of multiaxial service loading strongly influencing the fatigue of machine components*, Mechanical Systems and Signal Processing, Vol. 23(8), 2009, pp. 2712-2721
12. S. Al Laham, **Stress Intensity Factor and Limit Load Handbook**, Report EPD/GEN/REP/0316/98, *British Energy Generation Ltd*, Issue 2, April 1998
13. A. Ghidini, M. Diener, A. Gianni and J. Scheider, **SUPERLOS – Innovative steel by Lucchini RS for high-speed wheel application**, LRS-TECHNO Series 5, *Lucchini RS*, Lovere Italy, 2012
14. Roger Lundén, Tore Vernersson and Anders Ekberg, **Railway axle design – to be based on fatigue initiation or crack propagation?**, *IMechE Journal of Rail and Rapid Transit*, vol 224, no F5, 2010, pp 445-453
15. Sara Caprioli, **Thermal cracking of a railway wheel tread due to tread braking – the mechanical influence of repeated thermal cycles**, IHHA 2011 conference (Special Technical Session), Calgary Canada, 19-22 June 2011
16. Per Gullers, Paul Dreik, Jens C O Nielsen, Anders Ekberg & Lars Andersson, **Track condition analyser – detection of track irregularities based on instrumented wheelset measurements**, *IMechE Journal of Rail and Rapid Transit*, vol 225, no 1, pp 1--13, 2011

17. Anders Ekberg & Johan Marais, **Effects of imperfections on fatigue initiation in railway wheels**, *IMEchE Journal of Rail and Rapid Transit*, vol 214, no F1, pp 45--54, 2000
18. Anders Ekberg, Elena Kabo & Hans Andersson, **An engineering model for rolling contact fatigue**, *Fatigue & Fracture of Engineering Materials & Structures*, vol 25, no 10, pp 899--909, 2002
19. Anders Ekberg & Elena Kabo, **Fatigue of railway wheels and rails under rolling contact and thermal loading – an overview**, *Wear*, vol 258 no 7--8, pp 1288--1300, 2005
20. Elena Kabo, **Material defects in rolling contact fatigue – influence of overloads and defect clusters**, *International Journal of Fatigue*, vol 24, no 8, Pages 887-894, 2002
21. Elena Kabo & Anders Ekberg, **Material defects in rolling contact fatigue of railway wheels – the influence of defect size**, *Wear*, vol 258 no 7--8, pp 1194--1200, 2005
22. Anders Ekberg, Bengt Åkesson & Elena Kabo, **Wheel/rail rolling contact fatigue – probe, predict, prevent**, *Proceedings of the 9th International Conference on Contact Mechanics and Wear of Rail/Wheel Systems (CM2012)*, August 27 – 30, Chengdu, China, pp 29–41, 2012
23. Johan Sandström, Jacques de Maré, **Probability of subsurface fatigue initiation in rolling contact**, *Wear*, Volume 271, Issues 1–2, Pages 143-147, 2011
24. Jens C O Nielsen & Anders Ekberg, **Acceptance criterion for rail roughness level spectrum based on assessment of rolling contact fatigue and rolling noise**, *Wear*, vol 271, no 1–2, pp 319–327, 2011

7 Derailments due to rail failures

7.1 Studied derailment scenarios

The study focuses on rail breaks. Primarily rail breaks owing to cracks originating from the gauge corner of the railhead (head checks) and from the edge of the rail foot have been investigated. The main conclusions should however (perhaps with some additional analyses) be roughly transferable to other types of cracks in the railhead (e.g. squats) and the rail foot (centre cracks).

As for other rail cracks (see e.g. [1]), such as cracks emanating at the rail web, from bolt holes at insulated joints, from welds etc, caution should be taken. The reason is that such defects are strongly related to local conditions (e.g. the run-down of a joint, the quality of a weld etc). Thus, the formation and growth of these cracks will depend more on these local conditions, then on global conditions (wheel impact load, track stiffness etc).

The analysis has set out from the presumption that:

- A rather large initial crack exists either in the rail head or the rail foot
- The crack is sufficiently large so that global bending (and uniform tension due to global thermal loading) will be the dominating crack driving force.
- Linear elastic fracture mechanics is valid, i.e. fracture is presumed when $K_I \geq K_{Ic}$, where K_I is the stress intensity owing to rail bending and uniform thermal loading and K_{Ic} is the fracture toughness of the rail. Further, crack propagation can be predicted in accordance with Paris law.

7.2 Numerical simulations

Further details on numerical models for analyses of dynamic train-track interaction, crack growth and fracture may be found in [[31], [32], [33]].

7.2.1 Model for numerical analysis of dynamic interaction between wheel and rail

The analysis focuses on vertical wheel/rail interaction. The primary output from the simulations are bending moments in the rail. Wheel flat impact loads are to be included in the analysis, which imposes demands to account for high frequency loading. To this end the in-house code DIFF [[34]] has been employed.

7.2.1.1 Global track model

The track structure and applied loads are assumed to be symmetric with respect to the track centre. Thus, one rail and half of each sleeper is modelled. The discretely supported 60E1 rail is modelled by eight undamped Rayleigh–Timoshenko beam finite elements (FE) per sleeper bay, with bending stiffness $EI = 6.4 \text{ MN}\cdot\text{m}^2$, shear stiffness $kGA = 250 \text{ MN}$, mass per unit element length $m = 60 \text{ kg/m}$ and rotational inertia per unit element length $mr^2 = 0.24 \text{ kg}\cdot\text{m}$. The (half) sleepers are treated as rigid with mass $M_s = 125 \text{ kg}$. Each rail pad is modelled by

three spring-damper sets with each set containing one spring and one viscous damper coupled in parallel (Kelvin element). The three spring-damper sets connect three adjacent FE nodes on the rail with the single FE node on the sleeper below. Sleeper rotation with respect to the length axis of the sleeper is neglected. The ballast and subgrade under each half sleeper is modelled by one Kelvin element with spring stiffness k_b and viscous damping c_b . If not otherwise stated, the resilient rail pad has total vertical stiffness $k_p = 80$ MN/m and total damping $c_p = 16$ kNs/m. The length of the track model is 70 sleeper bays with sleeper spacing L and clamped boundaries at the two rail ends.

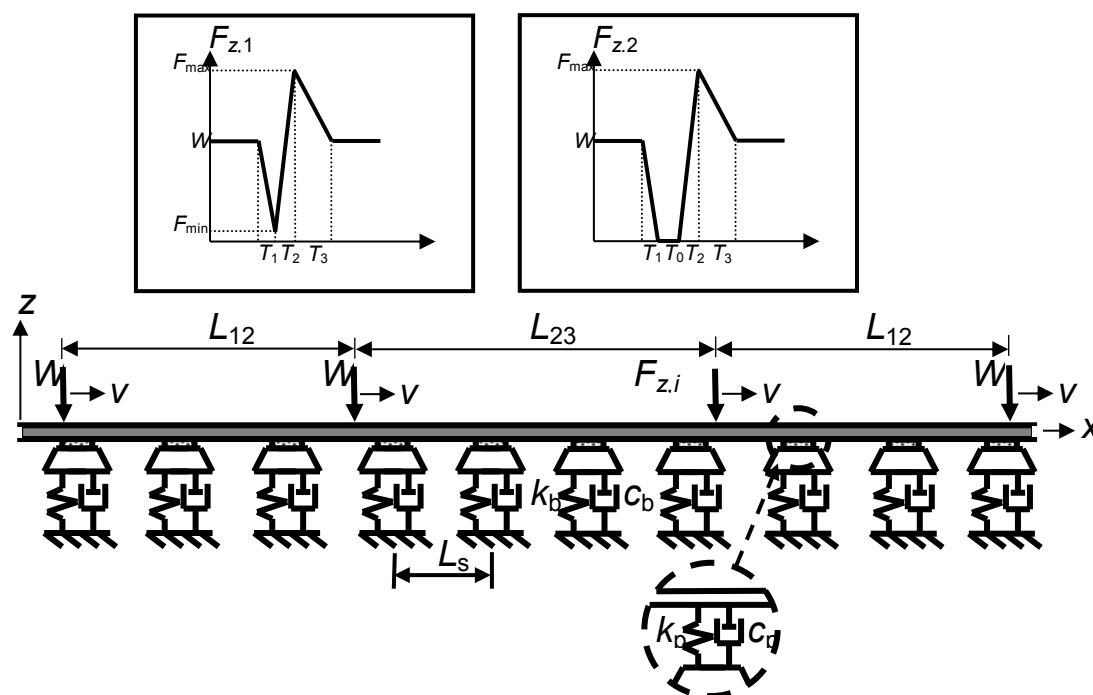


Figure 203 Principal sketch of part of track model in DIFF, from [[32]]. The track model is loaded by four prescribed point loads moving with a constant speed v . The second point load (in the order the loads enter the track model from the left) has a time history either according to time history 1 ($F_{z,1}$, left) or time history 2 ($F_{z,2}$, right). Other loads are constant with a magnitude corresponding to the nominal wheel load W .

7.2.1.2 Load model

Three vehicle types considered to potentially impose severe loading maximum and minimum bending moments generated in the rail were identified. These are (A) a heavy haul vehicle with axle load 30 tonnes and speed 60 km/h, (B) a freight vehicle with axle load 25 tonnes and speed 100 km/h, and (C) a passenger vehicle with axle load 21 tonnes and speed 200 km/h. Each vehicle type was modelled according to Figure 203. However, in order to cover the possibility that the minimum rail bending moment occurs halfway between the last and the first bogie of two adjacent cars, the full vehicle model accounts for eight moving point loads corresponding to eight adjacent wheel loads on one rail, see Figure 204. Input data for the vehicle models, including axle distances, are summarised in Table 49.

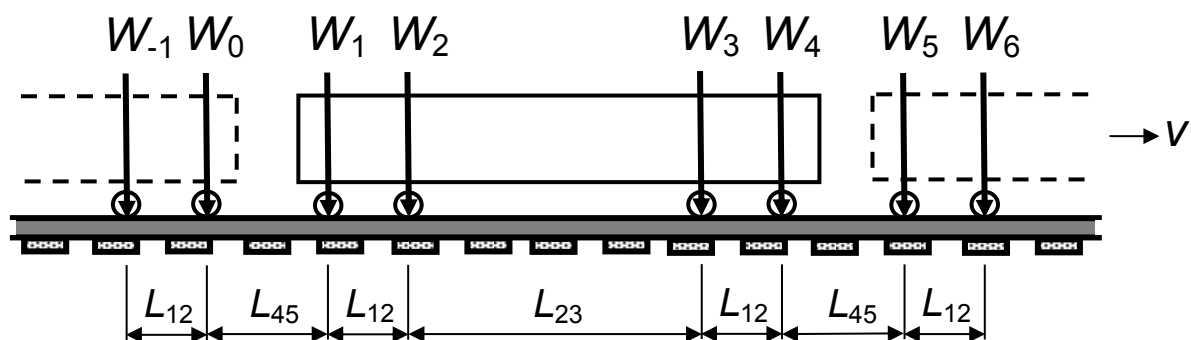


Figure 204 Configuration of wheel loads in parametric study, from [[32]].

Table 49 Input data for vehicle models in parametric study

Train type	Axle load W [tonnes]	Speed v [km/h]	Axle distance L_{12} [m]	Axle distance L_{23} [m]	Axle distance L_{45} [m]
A Heavy Haul	30.0	60	1.78	4.40	1.77
B Freight	25.0	100	1.80	7.00	3.20
C Passenger	21.4	200	2.50	17.5	6.40

To establish a worst-case load scenario in terms of the time history of a wheel flat impact, time intervals T_0 , T_1 , T_2 and T_3 in Figure 203 that results in the highest rail bending moments were identified. The analysis showed [[32]] that the influence of ballast stiffness was significant. For the different ballast stiffnesses considered (5, 10, 30 and 100 MN/m per half sleeper), the worst time evolution (with limiting magnitudes of the time intervals estimated from field measurements) were employed.

For a given combination of vehicle model, time history and track model input data, increasing peak load magnitude, F_{max} , leads to a proportional increase in maximum rail bending moment since the adopted track model is linear. Expressions linking peak impact load, F_{max} , to maximum (tensile stresses in rail foot) and minimum (tensile stresses in rail head) bending moments have been established for the three vehicle types and four ballast stiffnesses considered.

7.2.1.3 Validation of results

Measured impact loads and rail bending moments, see [[35]] have been employed to calibrate and validate numerical predictions. Details of these analyses are presented in [[32]]. In Figure 205 and Figure 206 examples of measured and predicted bending moments are presented. In these examples, the applied impact load consisted of a time series according to $F_{z,2}$ in Figure 203 with time instants matched to the measured impact load evolution with $F_{max} = 193$ kN preceded by a minimum load of 7 kN.

Wheel-rail contact forces were measured by a strain-gauge based wheel impact load detector, while bending moments in the rail were determined based on strain gauge measurements on the rail foot above sleepers. The sampling frequency was 6.0 kHz. The measurements presented in Figure 205 and Figure 206 feature a freight train with measured

wheel loads of [143 127 142 119 137 123 117 135] kN for the eight wheels, and a speed of 100 km/h.

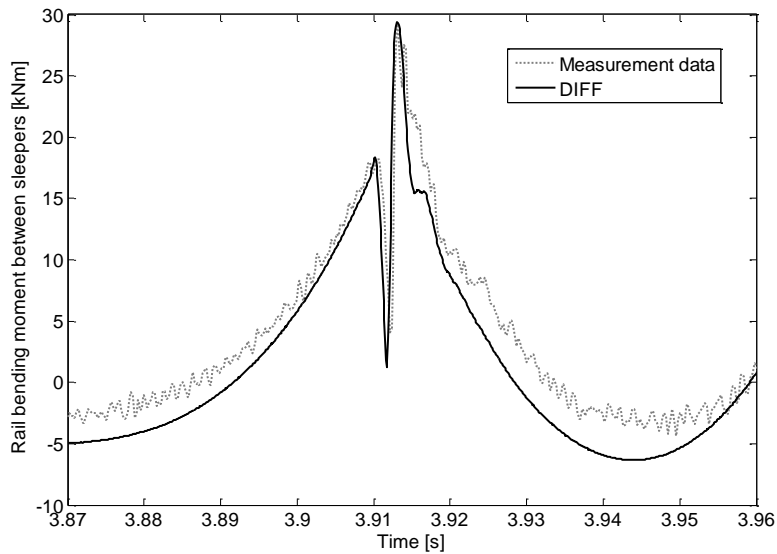


Figure 205 Measured (dotted line) and calculated (solid line) bending moments (in the rail between two sleepers) at the impact position of the wheel flat, from [[32]].

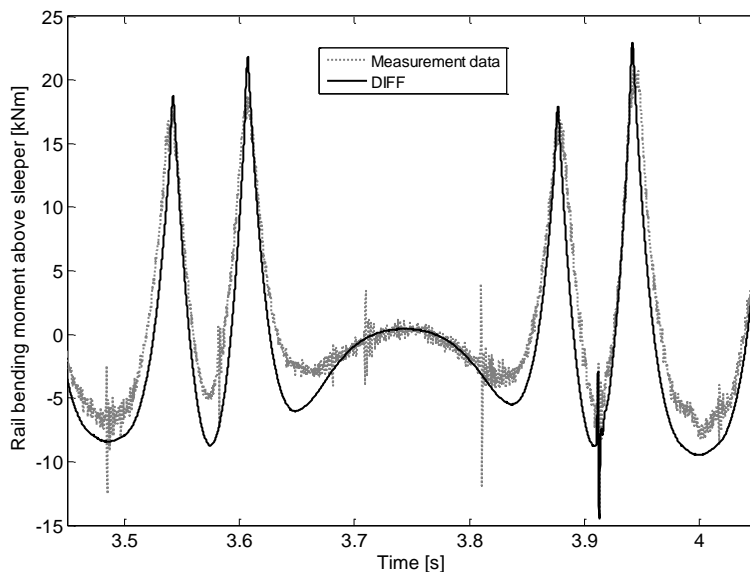


Figure 206 Measured (dotted line) and calculated (solid line) bending moments in the rail above the sleeper that was located 1.5 sleeper distances away from the impact position of the wheel flat, from [[32]]. In the model, wheel flat impact was only applied at time 3.91 s.

7.2.1.4 Hanging sleepers

Insufficiently supported (hanging) sleepers may increase the bending moment in the loaded rails. To analyse this influence, numerical simulations were carried out. In these simulations up to six hanging sleepers have been considered. A configuration with four hanging sleepers (sleeper no $j-2$, $j-1$, $j+1$ and $j+2$) is presented in Figure 207.

Hanging sleepers are modelled with a gap, δ , towards the ballast such that when a wheel load is approaching an unsupported sleeper, the rail and the sleeper are displaced vertically and the sleeper eventually reaches contact with the ballast with stiffness k_b and damping c_b . In the study bed $\delta = 2$ mm has been employed.

Numerically, this is achieved by the introduction of a counter-directional load $F_{s,j}$

$$F_{s,j} = \begin{cases} k_b (z_{s,j} - d) + c_b \dot{z}_{s,j} & \text{for } z_{s,j} \geq d \\ 0 & \text{else} \end{cases} \quad (1)$$

Further details on numerical implementation can be found in [[36]].

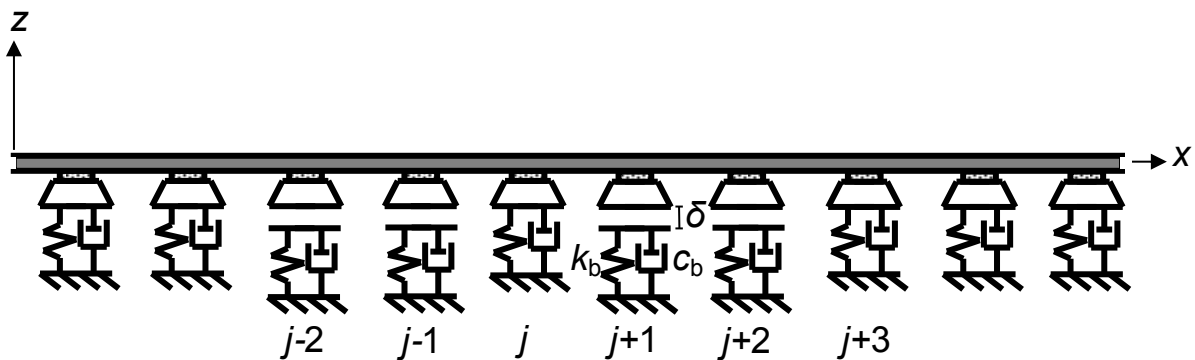


Figure 207 Example of unloaded track model with unsupported sleepers $j-2$, $j-1$, $j+1$ and $j+2$, from [[32]]. The vertical distance between unsupported sleepers and ballast is δ . From [[32]].

7.2.2 Model for numerical analysis of crack loading, risk of fracture and crack growth

7.2.2.1 Stress intensity factors

The current study considers rail foot cracks emanating from the side of the rail foot and rail head cracks stemming from head check cracks. All geometric constants are taken as corresponding to a nominal 60E1 profile.

The geometries of these two cracks are defined by the crack lengths a_f and a_h , as defined in Figure 208.

The cracks are presumed to be loaded normal stresses in the longitudinal rail direction due to (vertical) rail bending

$$S_b = \frac{M_y}{I_y} h \quad (2)$$

where h are h_f and h_h (see Figure 208) for foot and head cracks, respectively.

In addition to rail bending an all-welded rail is also subjected to a tensile stress due to restricted thermal contraction. The resulting normal stress may be evaluated as

$$S_t = \alpha E \Delta T \quad (3)$$

Here $\alpha = 11.5 \cdot 10^{-6}$ [$^{\circ}\text{C}^{-1}$] is the thermal expansion coefficient, $E = 210$ [GPa] is the elasticity modulus and $\Delta T = T_0 - T$ where T is the current and T_0 the stress free temperature.

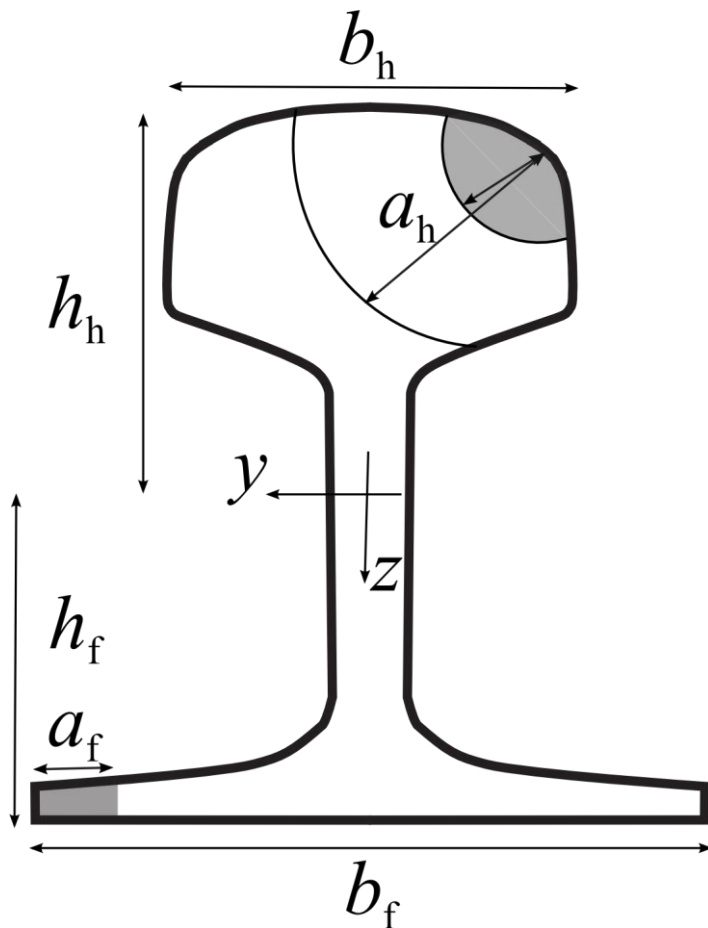


Figure 208 Definition of the crack geometry of studied rail foot and rail head cracks. The crack size is defined by the crack lengths a .

Stress intensity factors corresponding to mode I loading are expressed as

$$K_I(a, b) = f(a, b) \times S \sqrt{\rho a} \quad (4)$$

The geometric factor is for bending and uniform tensile loading of rail foot cracks approximated as that of an edge crack in a plate, e.g.

$$f(a, b) = \sqrt{\frac{2b_f \tan \frac{\rho a_f}{2b_f}}{\rho a_f}} \times \left[0.752 + 2.02 \frac{a_f}{b_f} + 0.37 \left(1 - \sin \frac{\rho a_f}{2b_f} \right)^3 \right] \quad (5)$$

For rail head cracks, the geometry factor is approximated, see [[37]], for bending as

$$f_b(a, b) = 2.6 \frac{a_h}{b_h} - 0.97 \frac{a_h}{b_h} + 0.70 \quad (6)$$

and for uniform tension as

$$f_t(a, b) = 1.4 \frac{a_h}{b_h} - 0.16 \frac{a_h}{b_h} + 0.72 \quad (7)$$

7.2.2.2 Fracture criterion

For rail head and rail foot cracks, the fracture criterion is expressed as

$$\max_t \{K_I\}^3 K_{Ic} \quad (8)$$

Here max is taken over the time t corresponding to a load passage, and K_{Ic} is the rail fracture toughness. In the following taken as $K_{Ic} = 40 \text{ MPa}\sqrt{\text{m}}$. Note that LEFM is presumed to be valid, a presumption that is less strong due to the cyclic loading.

A fracture criterion for the combined bending and thermal loading (both loading the crack in mode I) can thus be expressed as

$$\max_t \{K_{Ib} + K_{It}\}^3 K_{Ic} \quad (9)$$

Since the thermal loading is presumed to be constant during a wheel passage, equation (9) can be reformulated as

$$\max_t \{K_{Ib}\}^3 K_{Ic} - K_{It} \quad (10)$$

In the current study the influence of temperatures $\Delta T = 0^\circ\text{C}$, 20°C and 40°C have been investigated. Examples of results are given in Figure 209 and Figure 210 for a foot crack of $a_f = 5 \text{ mm}$, and a head crack of $a_h = 25 \text{ mm}$, respectively. Note that any temperature influence on material properties (e.g. in terms of decreased fracture toughness at low temperatures) is not considered.

Vehicle types and ballast stiffness are indicated by colour:

- Vehicle type A (iron ore) – black
- Vehicle type B (high speed freight) – blue
- Vehicle type C (passenger) – red

and line types:

- $k_b = 5 \text{ MN/m}$ – dotted
- $k_b = 10 \text{ MN/m}$ – dashed-dotted
- $k_b = 30 \text{ MN/m}$ – dashed
- $k_b = 100 \text{ MN/m}$ – solid

Fracture according to the fracture criterion in equation (10) corresponding to crossing of the horizontal lines for the different temperatures considered.

It is seen in this case that the influence of thermal load is highest for the foot crack.

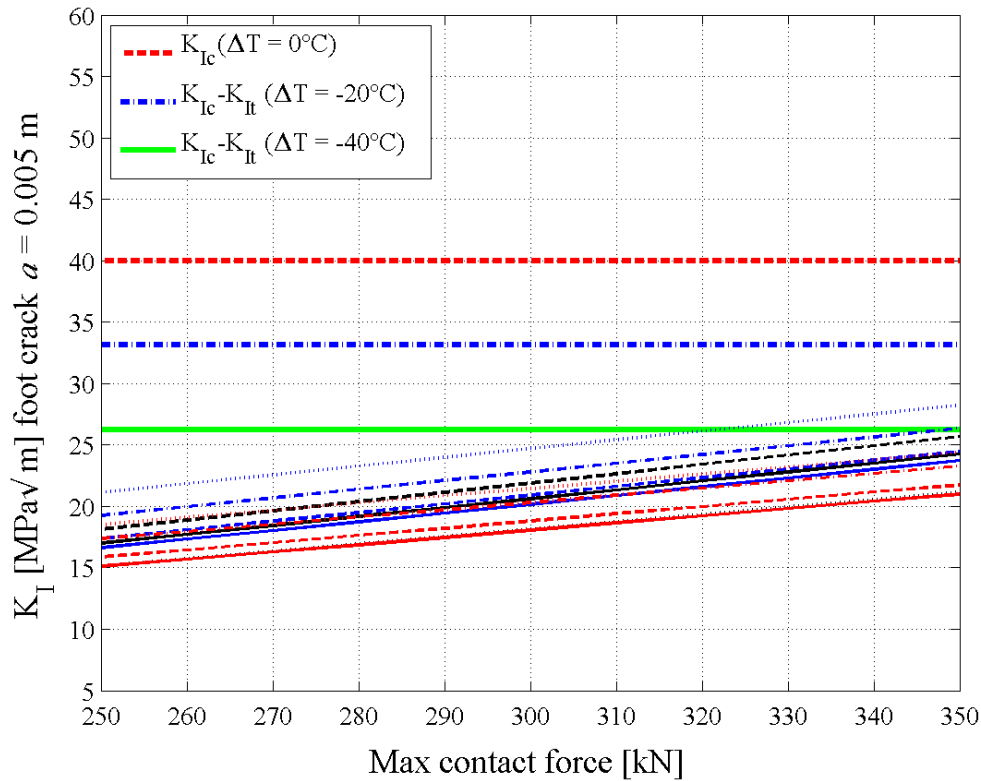


Figure 209 Stress intensity factors for a 5 mm foot crack in a 60E1 rail due to impact loads of varying magnitudes. Vehicle type is indicated by colour, and ballast stiffness by line type. The horizontal lines indicate fracture toughness reduced by thermal stresses according to equation (10).

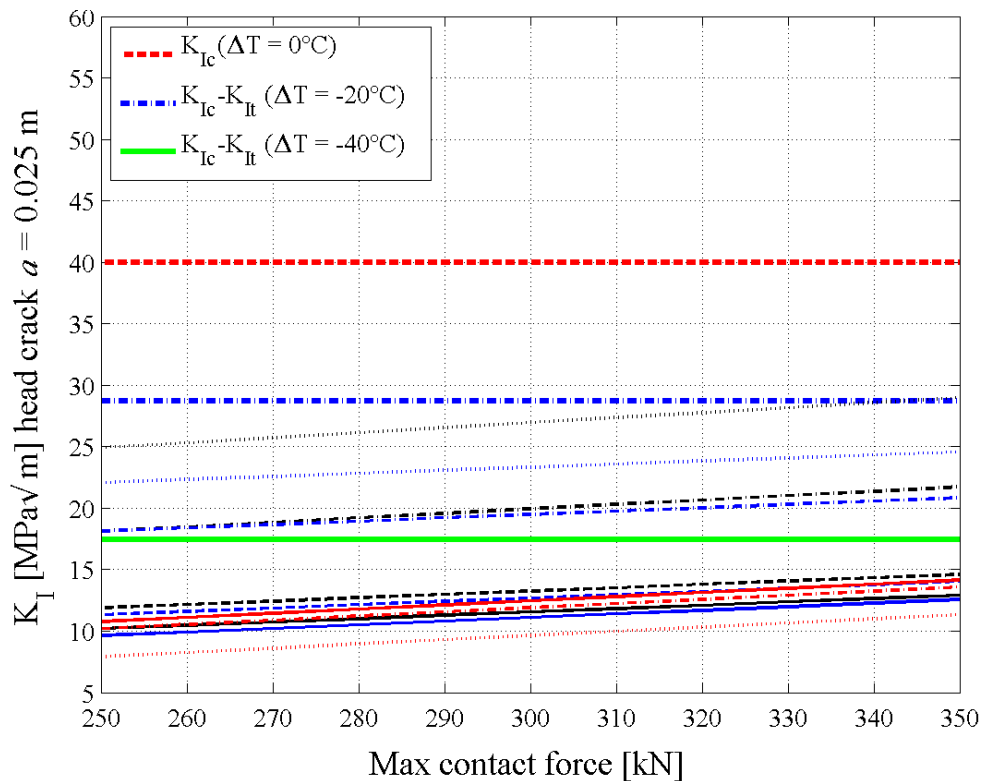


Figure 210 Stress intensity factors for a 25 mm head crack in a 60E1 rail due to impact loads of varying magnitudes. Vehicle type is indicated by colour, and ballast stiffness by line type. The horizontal lines indicate fracture toughness reduced by thermal stresses according to equation (10).

7.2.2.3 Crack growth criterion

To quantify crack growth a fracture mechanics approach has been taken in which Paris law is presumed to be valid, i.e.

$$\frac{da}{dN} = C(\Delta K_I)^n \quad (11)$$

Here da/dN is crack growth per load cycle, and material parameters taken as $C = 2.47 \cdot 10^{-9}$ and $n = 3.33$ for da/dN in mm/cycle and $\Delta K_I = \max_t\{K_I(t)\} - \max\{\min_t\{K_I(t), 0\}$ in MPa \sqrt{m} .

Crack propagation under a load spectrum can be evaluated using a cycle-by-cycle integration. Alternatively, an equivalent stress intensity factor range, see [[38]], can be introduced to decrease computational demands. Such an equivalent stress intensity is evaluated as

$$DS_q = \left[\left(\sum_{j=1}^N (DS_j)^n \right) / N \right]^{1/n} \quad (12)$$

Here N is the number of load cycles in repeating sequence. Note that mid stress effects (except those directly influencing magnitudes of $\Delta\sigma$ (and thus ΔK) through preventing crack closure) have not been accounted for.

7.2.3 Influence of main parameters – definition of a “bad case scenario”

Below the influence of different operational parameters is scrutinized with the aim of defining a “bad case scenario”. This corresponds to severe, but not unrealistically severe, operational conditions that can be employed for an analysis of allowed wheel loads and pertinent derailment mitigation actions.

It has been shown below that the vehicle type will influence the response (in terms of bending moments in the rail). This relation is complex and relates to axle loads, vehicle speed, wheel base distance *etc*, see [[32]] for further details. A “bad case scenario” cannot neglect this influence and realistically has to account for the worst vehicle configuration.

The track stiffness (in terms of the ballast stiffness, k_b , has been shown to have a significant influence. However in this case it may be realistic to exclude the softest tracks (i.e. $k_b = 5$ MN/m and $k_b = 10$ MN/m) from consideration. A reason for this is that such soft tracks are likely in need of strengthening. One may also note that hanging sleepers will have less of an influence in such soft tracks as shown below.

Temperatures down to 40 degrees below stress free temperature are plausible. As an example they will correspond to some -20°C in southern and mid Sweden, which occurs regularly. Thus, such temperatures need to be considered. The significant effects on stress intensity factor magnitudes at these low temperatures can however be compensated for to some extent by decreasing allowed wheel load magnitudes at these low temperatures.

Regarding allowed crack sizes this is a balance: The larger the cracks that are allowed, the lower the maximum wheel loads that can be allowed and the shorter the feasible inspection intervals. This issue is studied further in the HRMS project that is run by the UIC.

Based on the discussion above and extensive analysis of simulation results etc, a tentative “bad case scenario” has been established as follows:

- A worst-case vehicle (of the analysed cases) has been considered together with a worst-case load evolution corresponding to a wheel flat impact

- Results corresponding to ballast stiffness below 30 MN/m have been excluded
- Tentatively a 5 mm foot and a 25 mm head crack have been considered as limiting crack sizes

7.3 Operational conditions resulting in high risk of rail breaks

7.3.1 Nominal track conditions

Maximum and minimum bending moments in the rail corresponding to the defined “bad case scenario” can be established as

$$\max_t \{M_y(t)\} = 48 + 50 \frac{\partial F_{\max}}{\partial 250} - 1 \frac{\ddot{\theta}}{\theta} \quad (13)$$

$$\min_t \{M_y(t)\} = -21 - 12 \frac{\partial F_{\max}}{\partial 250} - 1 \frac{\ddot{\theta}}{\theta} \quad (14)$$

with M_y in kNm and F_{\max} in kN.

Corresponding stress intensity factors for a 5 mm foot crack and a 25 mm head crack are presented in Figure 211 and Figure 212. It can be noted that for a 5 mm foot crack, fracture is presumed at an impact load of 350 kN at a rail temperature of $\Delta T = 40^\circ\text{C}$, see Figure 211. For a 25 mm head crack, fracture is predicted for an impact load of 450 kN at a rail temperature of $\Delta T = 40^\circ\text{C}$, see Figure 212.

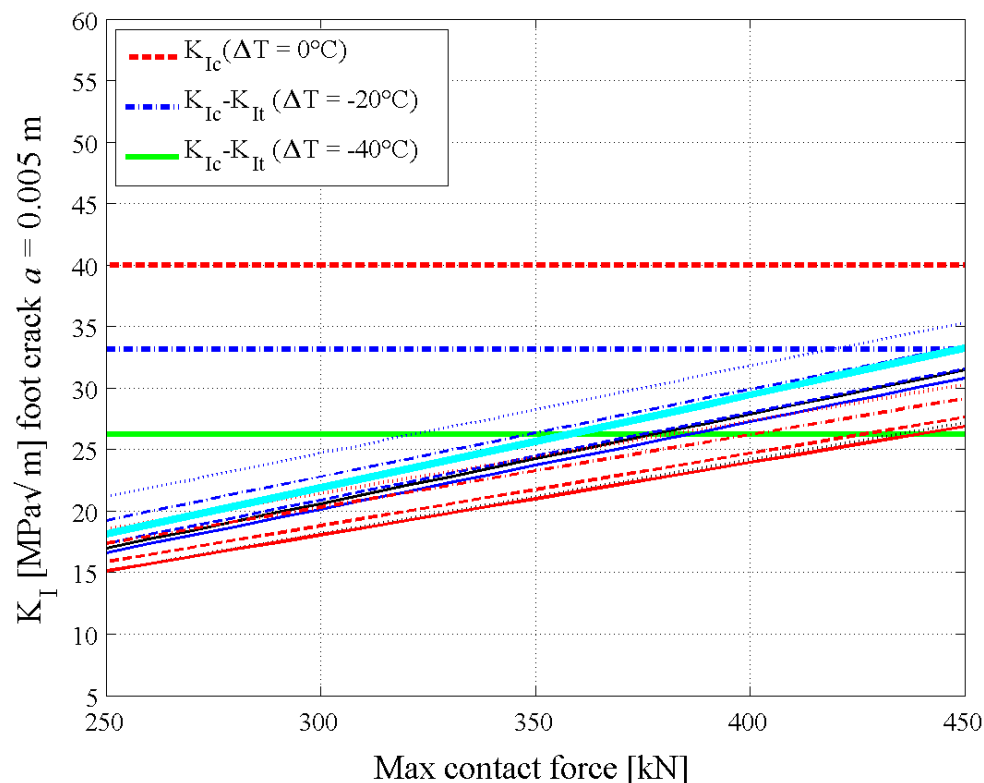


Figure 211 Stress intensity factors for a 5 mm foot due to impact loads of varying. The thick magenta coloured line indicates a nominal “bad case scenario”.

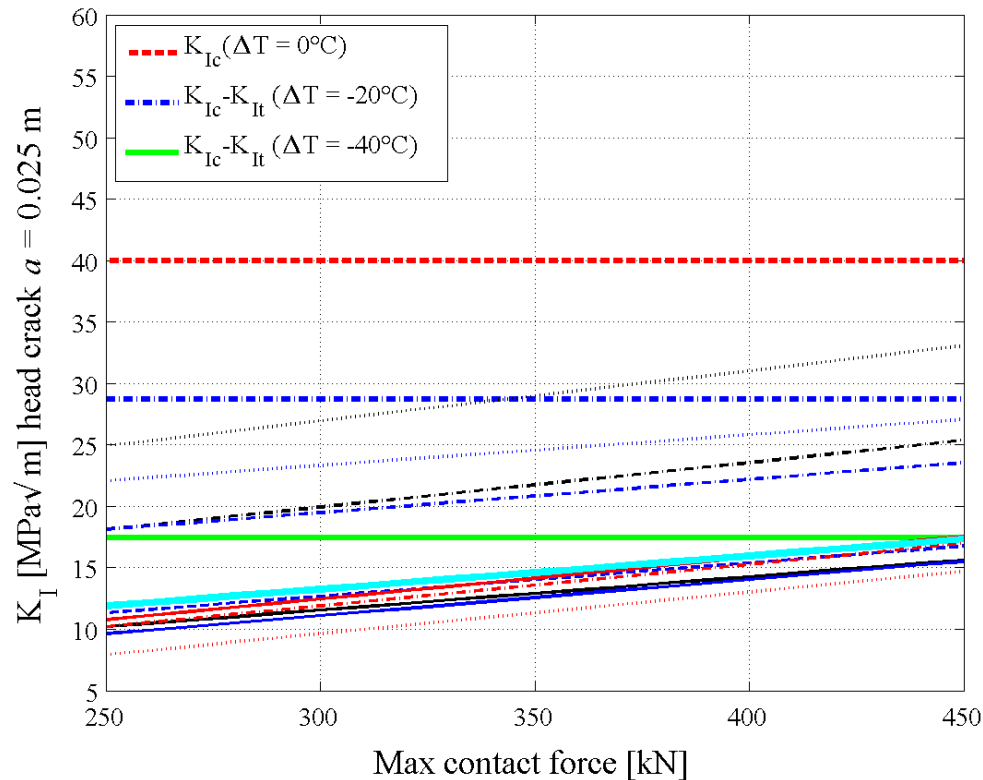


Figure 212 Stress intensity factors for a 25 mm head crack due to impact loads of varying magnitudes. The thick magenta coloured line indicates a nominal “bad case scenario”.

7.3.2 Influence of hanging sleepers

If hanging sleepers are considered, peak bending moments in the rail will increase. In general terms, the increase will be the largest for hard track beds. Compensating for the increase in bending moments corresponding to a worst-case configuration of hanging sleepers (as discussed above), maximum and minimum bending moments in the rail corresponding to a “bad case scenario” can be estimated as

$$\max_t \{M_y(t)\} = \frac{\pi}{6} 46 + 48 \frac{\pi}{6} \frac{F_{\max}}{250} - 1 \frac{\pi}{6} \times 1.33 \quad (15)$$

$$\min_t \{M_y(t)\} = \frac{\pi}{6} 19 - 15 \frac{\pi}{6} \frac{F_{\max}}{250} - 1 \frac{\pi}{6} \times 1.68 \quad (16)$$

Corresponding stress intensity factors for a 5 mm foot crack and a 25 mm head crack are presented in Figure 213 and Figure 214. It can be noted that for a 5 mm foot crack, fracture is presumed at an impact load of 280 kN at a rail temperature of $\Delta T = 40^\circ\text{C}$, see Figure 213. For a 25 mm head crack, fracture is predicted for an impact load of 250 kN at a rail temperature of $\Delta T = 40^\circ\text{C}$, see Figure 214.

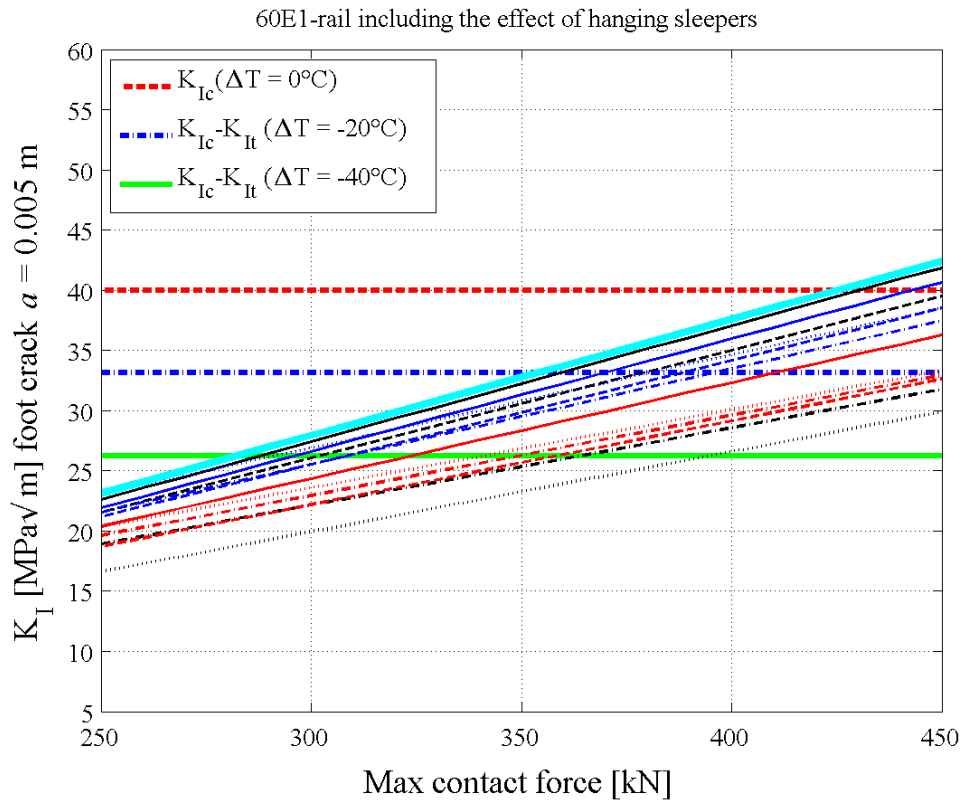


Figure 213 Stress intensity factors for a 5 mm foot crack due to impact loads of varying magnitudes. Hanging sleepers are accounted for. A thick magenta line indicates the “bad case scenario”.

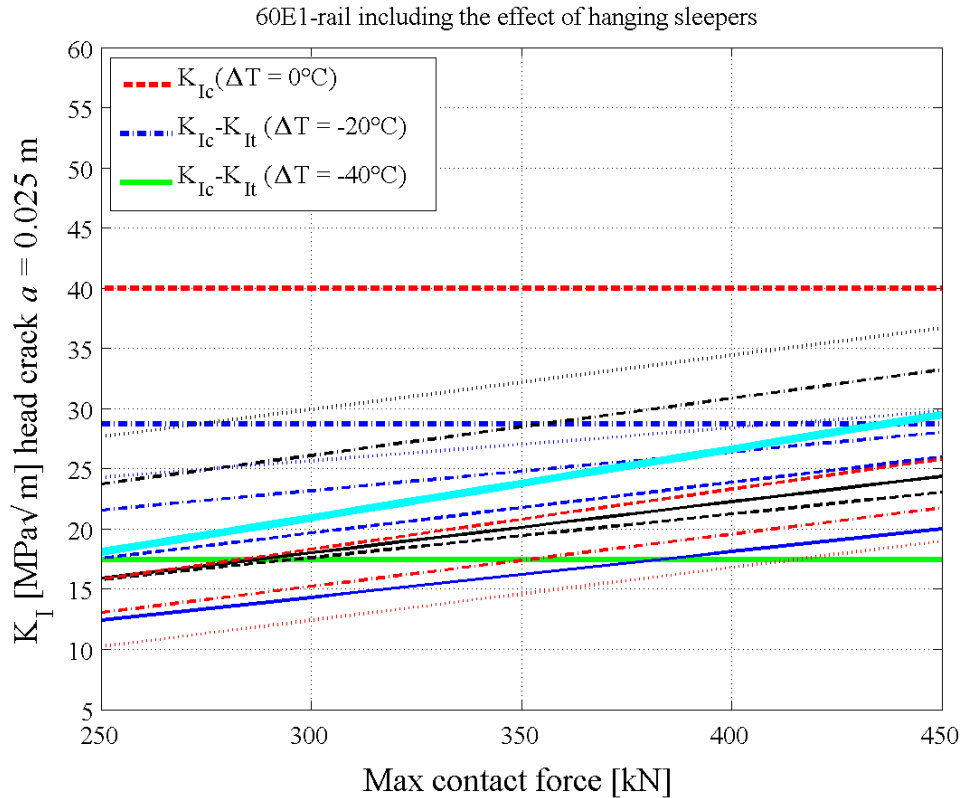


Figure 214 Stress intensity factors for a 25 mm head crack due to impact loads of varying magnitudes. Hanging sleepers are accounted for. A thick magenta line indicates the “bad case scenario”.

7.3.3 Influence of lateral rail bending

Lateral loading of the rail will result in torsion, warping and lateral bending of the rail. The latter may be an issue for rail foot cracks if it induces a sufficiently high normal stress along the rail.

The first issue in evaluating if lateral bending is an issue of importance is to establish the magnitude of the normal stress due to the lateral bending. This is far from trivial: As mentioned a lateral load will result in torsion, warping and lateral bending of the rail. The relative magnitude of each of these depends on the stiffness of the rail, the fastening and rail pad characteristics, the ballast resistance *etc.* Several of these parameters are not linear and their magnitude may vary significantly. To further investigate the issue, tentative numerical simulations have been carried out. An example of results is presented in Figure 215. These investigations are foreseen to be continued and combined with field tests in D-Rail WP6.

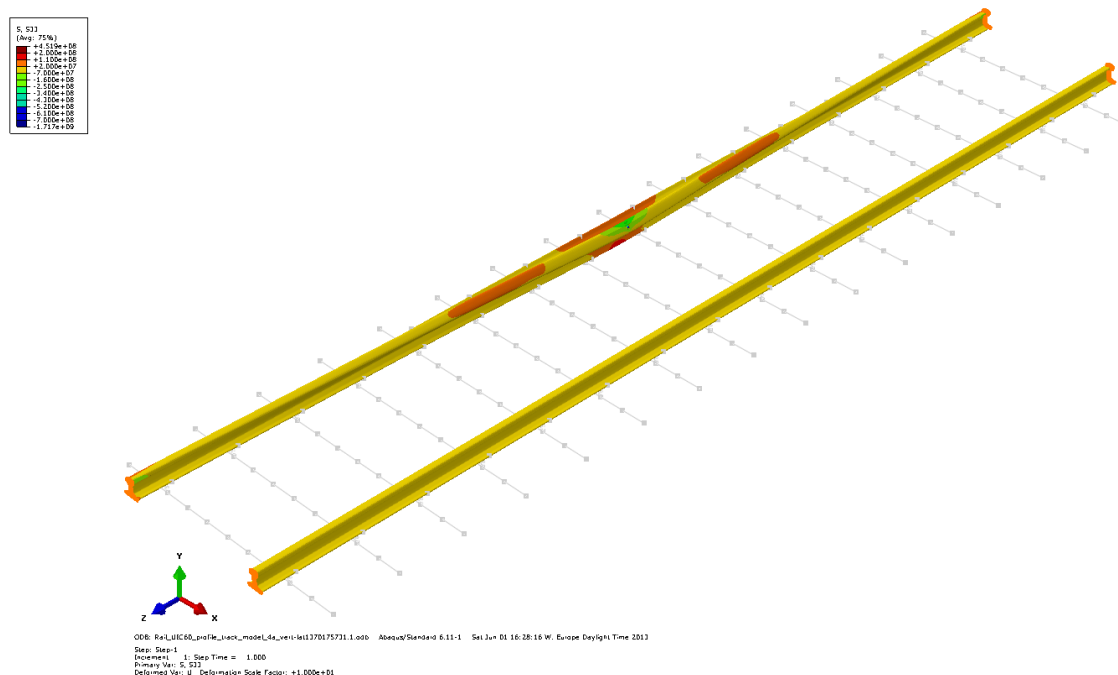


Figure 215 Example of results from FE-analyses of lateral rail bending. The upper rail is subjected to a vertical and a lateral load applied in a mid-span position.

Lateral bending will appear in combination with vertical bending (owing to the vertical load). However to employ a normal stress due to a full impact load in combination with a maximum lateral load would be conservative. The reason is that the decrease in vertical load magnitude before wheel flat impact (see Figure 203) will decrease the lateral loading. It will then take time to build up a full lateral loading when the wheel flat impacts. The exception is a case with flange contact. However due to flange friction, the lateral displacement of the wheel and the (likely) reduced speed, it is unlikely that a vertical impact load corresponding to the worst-case scenario presented in section 7.2.1 would occur.

7.4 Crack growth and pertinent inspection intervals

Crack growth prediction has been implemented according to the procedure outlined in section 7.2.2.3 above. An example of predicted crack growth is presented for foot cracks in Figure 216 and Figure 217.

The loading consists of forces measured at a track based wheel load detector. Both predictions based on average and peak loads are presented. Predictions based on the average load are somewhat non-conservative, since the crack growth rate does not scale linearly with stress range. On the other hand crack growth predictions based on peak loads are highly conservative since this would imply that all passing wheels impact in the worst position (in the case of a foot crack directly above a crack located mid span). It further implies that the same load impacts at a position corresponding to the largest negative stress at the position of the foot crack. A more refined crack growth prediction based on a statistical analysis is possible, but would require an analysis of wheel load time series.

The red lines in Figure 216 and Figure 217 indicate predictions featuring the equivalent stress range defined in equation 12. For the cases studied, these are

Nominal “bad case scenario”:

- For average vertical load, left rail: $\Delta\sigma_{q,va} = 81.2$ MPa
- For average vertical load, right rail: $\Delta\sigma_{q,va} = 81.5$ MPa
- For maximum vertical load, left rail: $\Delta\sigma_{q,vm} = 87.6$ MPa
- For maximum vertical load, right rail: $\Delta\sigma_{q,rm} = 88.9$ MPa

“Bad case scenario” with hanging sleepers:

- For average vertical load, left rail: $\Delta\sigma_{q,va} = 95.0$ MPa
- For average vertical load, right rail: $\Delta\sigma_{q,va} = 95.5$ MPa
- For maximum vertical load, left rail: $\Delta\sigma_{q,vm} = 103.2$ MPa
- For maximum vertical load, right rail: $\Delta\sigma_{q,rm} = 104.8$ MPa

Crack growth predictions for head cracks are presented in Figure 218 and Figure 219. It can be noted that these do not feature predictions based on equivalent stress ranges. The reason is that the stress is here composed of a component related to bending and a component related to temperature loading. Since these influence the crack differently (through the geometrical factors defined in equations 6 and 7, respectively) a combined stress range is not suitable.

7.4.1 Influence of temperature

The predictions presented in Figure 216 to Figure 219 employ a constant temperature (15 degrees below stress free temperature). If temperature is measured along the line (or at the detector), it is straight-forward to include temperature variations in the predictions. Examples of such simulations featuring the synthetic temperature variation of Figure 220 are shown for foot cracks in Figure 221, and for head cracks in Figure 222. It is clear that the temperature will have a significant influence on crack growth rates.

7.4.2 Influence of crack geometry

It can be noted that the initial size of the foot cracks in the examples are very low. The reason is the conservative presumption of a through-thickness foot crack, see Figure 208. This (and the approximation of the bending stress as constant over the rail foot thickness) generally simplifies the analysis, and is needed if equivalent stress ranges should be used. On the other

hand, it results in the need for short initial crack sizes if realistic results should be obtained. This is a bit cumbersome since linear elastic fracture mechanics is not fully valid for such small crack sizes. Thus, in some sense the initial crack size can be seen as an equivalent initial crack that reflects the growth characteristics of a “real” foot crack as in Figure 223.

A refined analysis would set out from a more realistic initial crack geometry, e.g. a small corner crack as in Figure 223. The propagation of this crack is then predicted in the same way as described above for the through-thickness crack. There are complications with this approach that does not make it suitable for use in operational prediction. A more useful approach would be to adopt such an analysis (in combination with empirical knowledge of occurring rail breaks setting out from foot cracks) to establish a suitable size of an equivalent initial through-thickness foot crack.

For the head crack, the situation is a bit different: The initial crack size employed is large enough so that linear elastic fracture mechanics can be employed. The complication here is rather that for shorter cracks the contact stress field may have an influence. The contact stress field favours growth in a different direction than the transversal path promoted by rail bending. A first indication of the crack depths at which the contact stress field can be ignored is provided by the crack morphology. From the fracture surface in Figure 224 it is seen that an initial crack length of 10 mm should be sufficiently large.

7.4.3 Load cycles for head crack growth prediction

The predictions of crack growth presume a load cycle per passing wheel. For a foot crack, this is fully plausible. For a head crack the presumption is more doubtful. In Figure 206 it is seen how the four wheels of (one side of the) wagon induces five negative stress peaks (tension in head). It should however be noted that some peaks (in Figure 206 the peaks between the bogies) are smaller. The “bad case scenario” considers the largest of these and the corresponding largest compressive peaks. Thus the error in considering four cycles instead of the five should be relatively small. However, if a (very) conservative prediction is ought for, crack growth rates may be increased by 25%. Red lines in Figure 218 and Figure 219 indicate the results of such predictions.

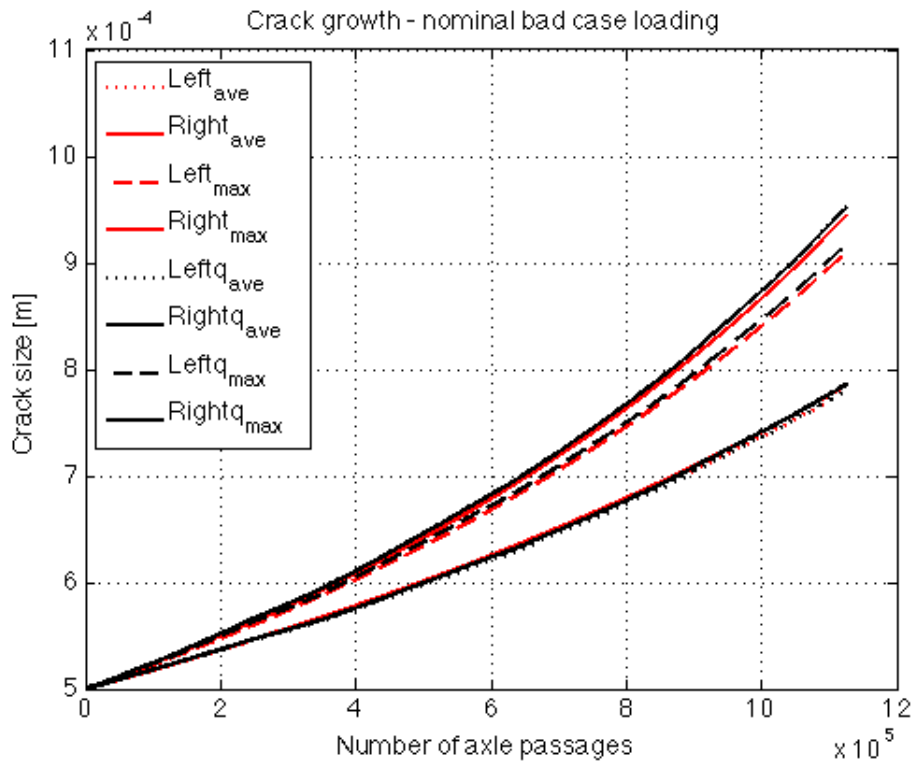


Figure 216 Predicted foot crack growth for a measured spectrum of some 1.1 million passing axles. The crack growth has been evaluated for a “bad case scenario” as outlined above. The crack growth prediction has been based on detected average loads (non-conservative) or measured peak loads (very conservative) on left and right wheels. Temperature has been taken as 15 degrees below stress free temperature.

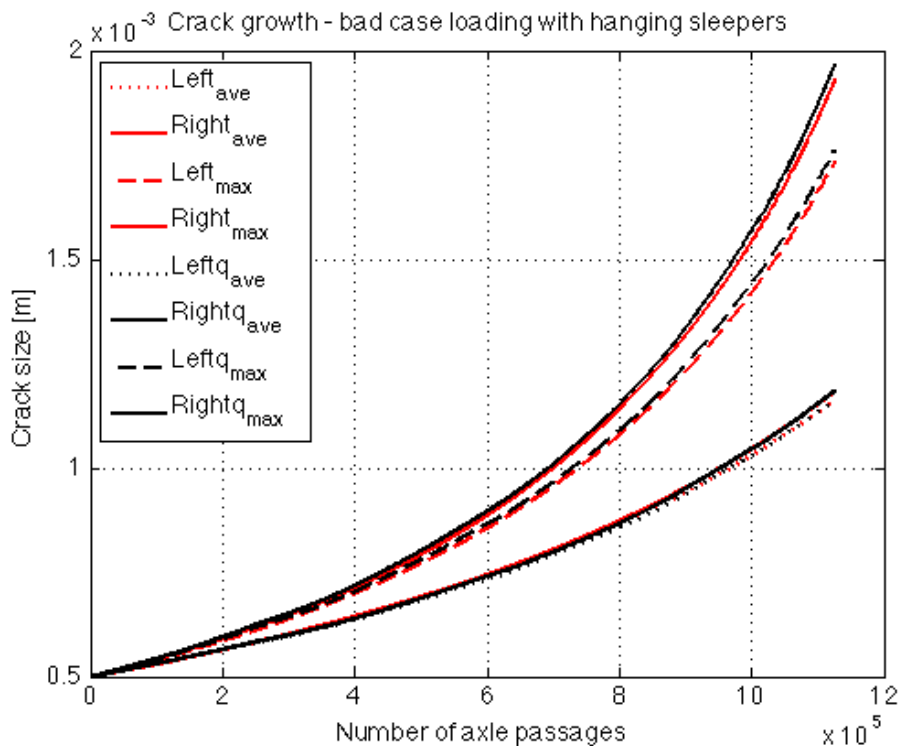


Figure 217 Predicted foot crack growth for a “bad case scenario” including hanging sleepers.

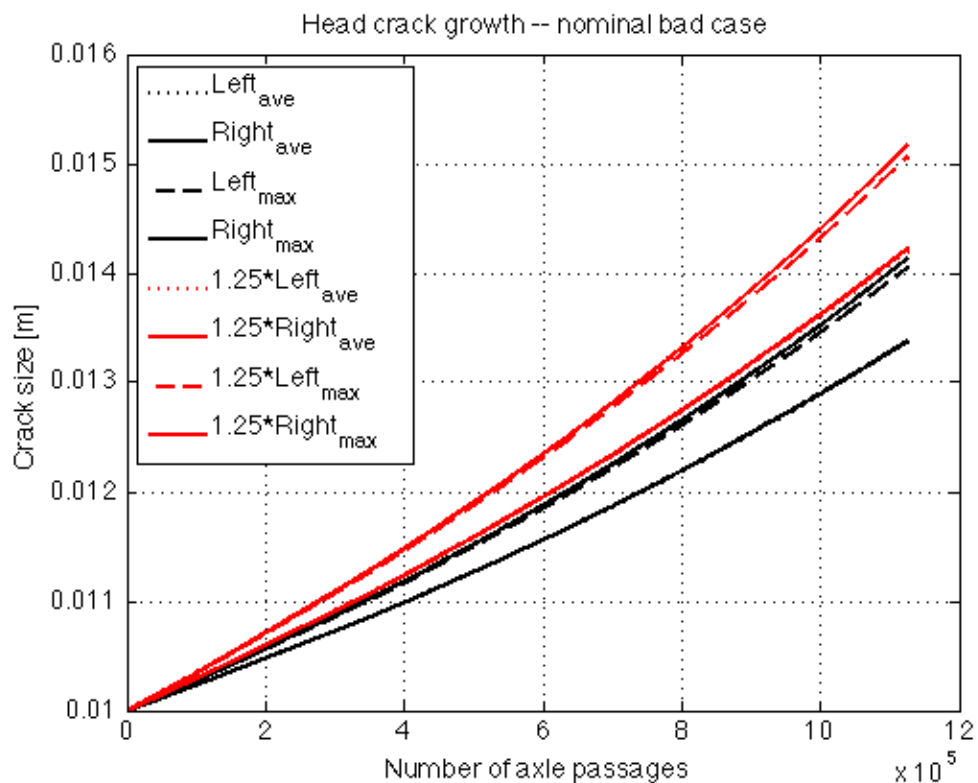


Figure 218 Predicted head crack growth for a nominal “bad case scenario”. The crack growth prediction has been based on detected average loads (non-conservative) or measured peak loads (very conservative). Red curves are for a 25% increase in crack growth rates (conservative).

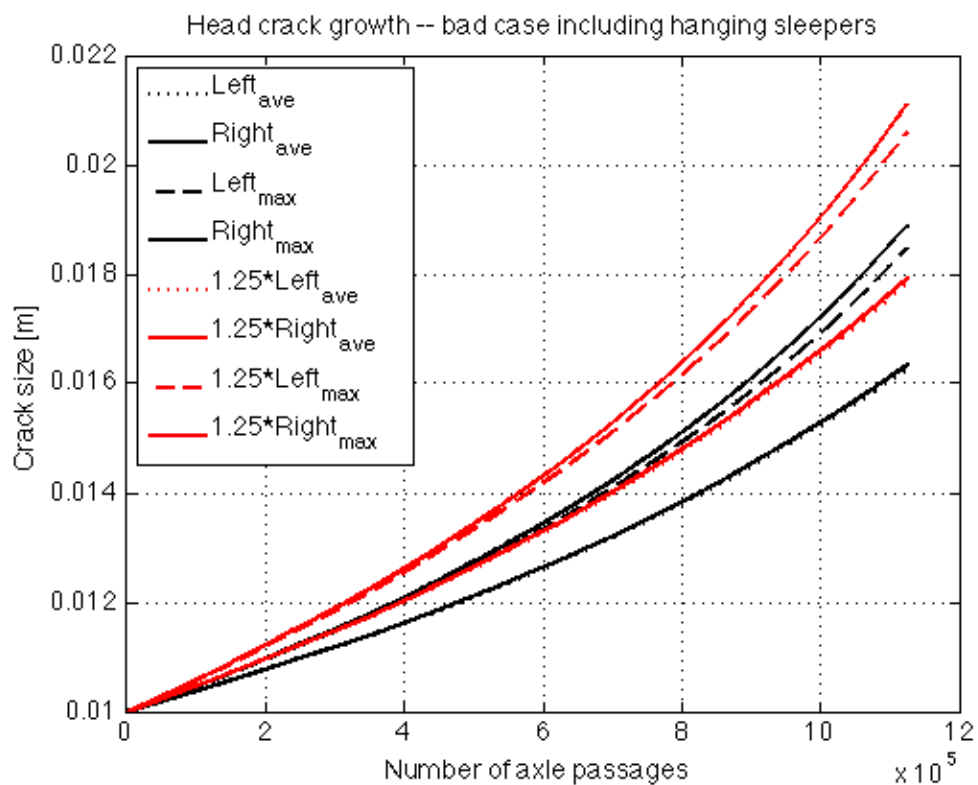


Figure 219 Predicted head crack growth for a “bad case scenario” including hanging sleepers.

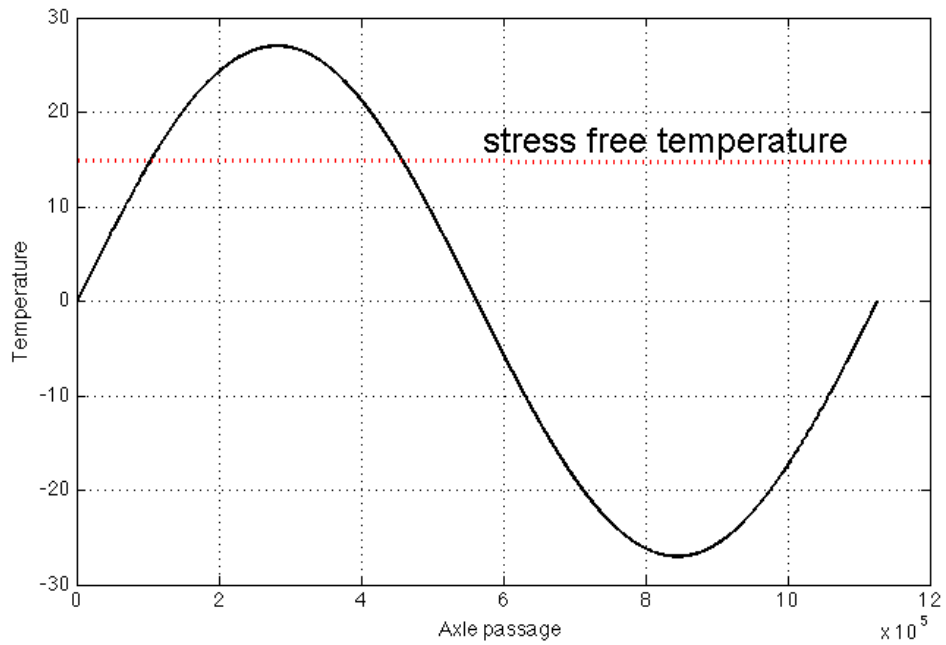


Figure 220 Synthetic temperature variations employed in the temperature dependent simulations. The stress free temperature is taken as 15°C (indicated as a red dotted line).

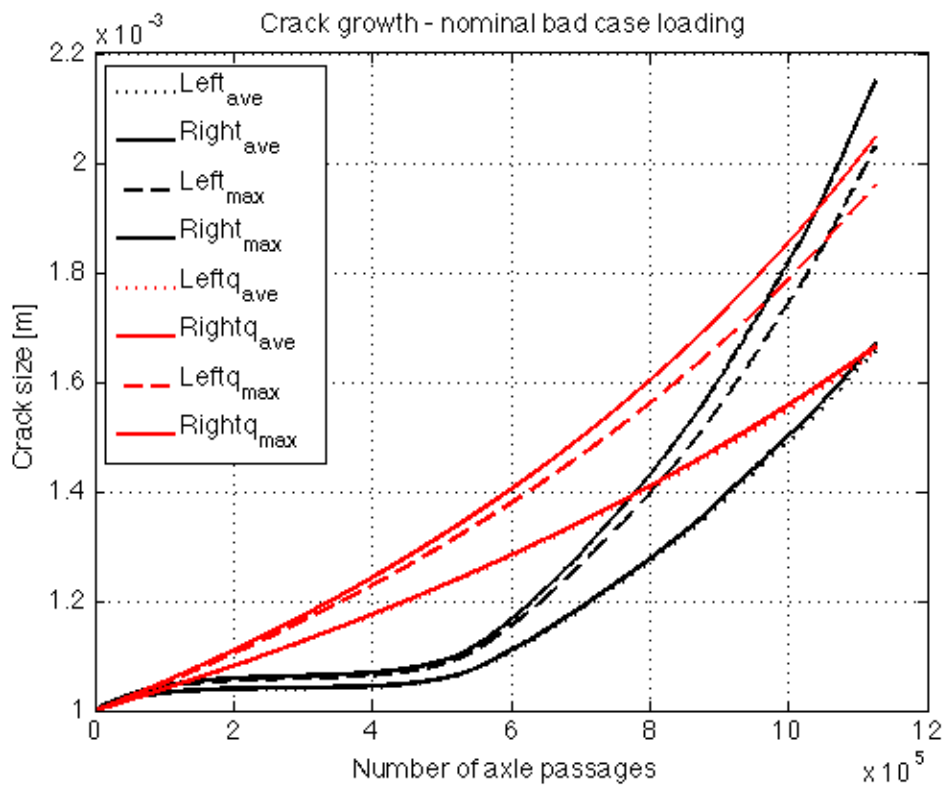


Figure 221 Predicted foot crack growth for a nominal “bad case scenario” including temperature dependence according to Figure 220. The red curves indicate predictions featuring an equivalent stress range.

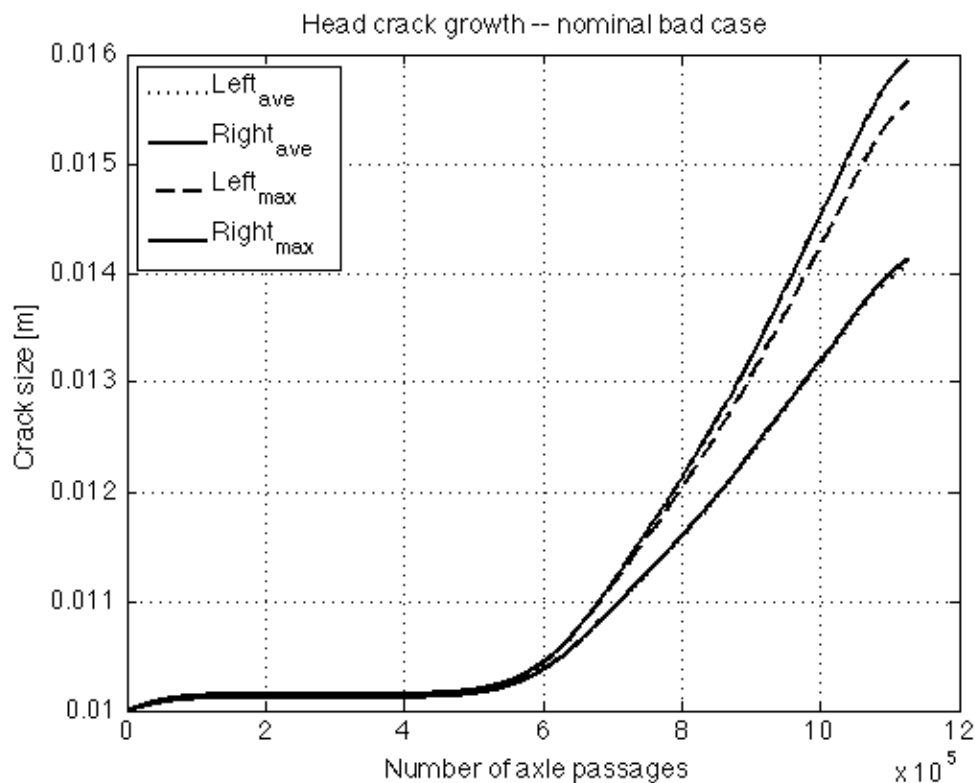


Figure 222 Predicted head crack growth for a nominal “bad case scenario” including temperature dependence according to Figure 220.

7.5 Wöhler curve based prediction

A different approach to predict the progress of deterioration of rails would be to base it on an evaluation of damage accumulation. In short, such an approach would evaluate the fatigue damage related to a passing axle based from a Wöhler curve (also called an SN-curve). The input is the stress range (and optionally the mid stress) and the output is the damage for the studied load cycle. Damage is then accumulated linearly (according to the Palmgren–Miner rule) and fracture is presumed when the accumulated damage reaches a prescribed level (theoretically one).

Such an approach would be straight-forward to implement. It will however have drawbacks such as uncertainties in the establishment of the Wöhler curve (especially in the presence of pre-existing defects) and the lack of relationship between evaluated damage and crack length. Still it may be a useful complement, in particular with respect to foot cracks.

7.6 Validation of predictions

An indication of the validity of the numerical simulations is given from operationally occurring rail breaks. In Figure 223 and Figure 224 rail breaks originating at rail foot and rail head cracks are shown. It is seen that the critical crack sizes are larger than what is predicted for a “bad case scenario” including a temperature of $\Delta T = 40^\circ\text{C}$ if the rail break is presumed to occur at wheel loads levels in the order of 300 kN. This observation indicates that the “bad case scenario” is on the safe side.

Some possible reasons may be:

- Better support conditions than presumed (likely since a “bad case” including hanging sleepers has been presumed)
- Not as high loads as presumed (likely)
- Higher fracture toughness than presumed
- Not as cold as presumed

Note also that the rail is 50E3, and not 60E1, which gives somewhat different predictions, see [[33]] for details. However, it is important to note that extra safety (in reasonably magnitudes) is desirable e.g. since crack growth accelerates before failure



Figure 223 Operational rail break stemming from a foot edge crack. (Picture courtesy Anders Frick, Trafikverket). Note that the rail is of 50E3 type.

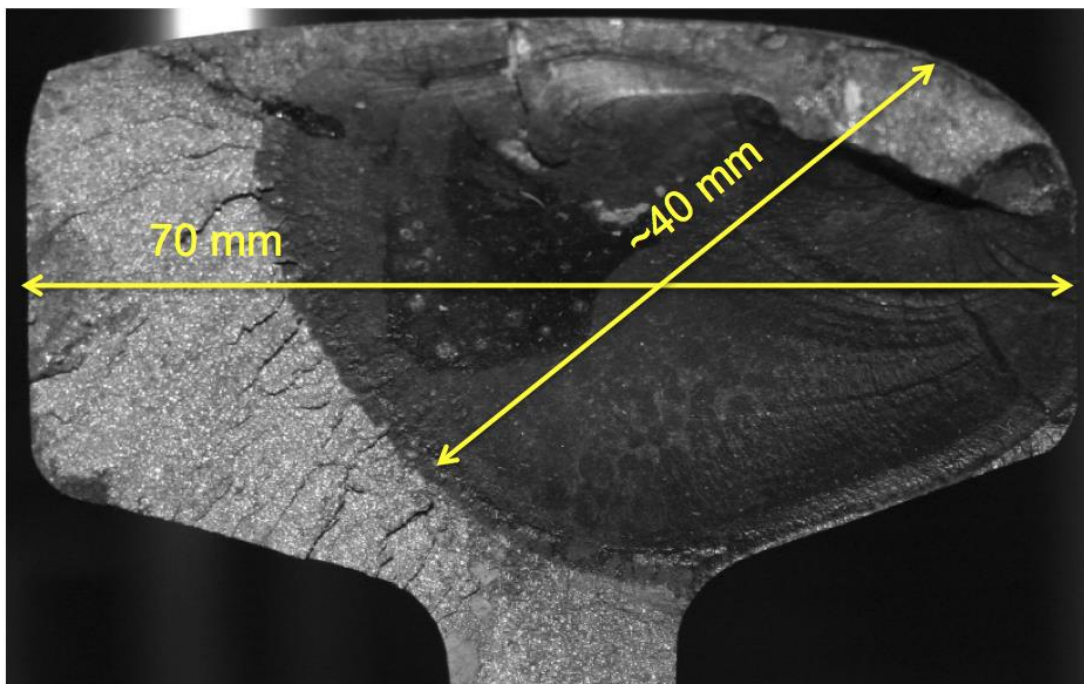


Figure 224 Operational rail break stemming from a head check crack. Note that the rail is of 50E3 type.

7.7 Other rail break mechanisms

Local conditions may cause increased load magnitudes and/or stress concentrations. Three examples of such local conditions are:

Insulated joints, which are discontinuities in the track that cause increased load magnitudes. If the joints are run-down the load increase may be substantial, see [[42]]. In addition insulated joints contain stress concentrations, both at the insulating layer and at bolt holes. Thus caution must be taken in manufacturing, maintenance and inspections of insulated joints.

Welds may also cause increased loads if they alter the rail geometry. In addition welds may contain impurities and tensile residual stresses may have formed during the welding process. Both of these phenomena increase the risk of fatigue crack initiation.

Transition zones are somewhat similar to hanging sleepers in that track stiffness discontinuities will lead to higher loads and/or bending moments in the rail. The topic was examined in detail in the EU-project INNOTRACK, see [[43]].

7.8 Concluding remarks

7.8.1 Identified main affecting parameters

The chapter has outlined how bending moments and stress intensity factors in rails containing foot and head cracks are influenced by operational conditions. Numerical simulations have been employed and validated towards field measurements. A “worst case” wheel flat load evolution has been identified, the influence of ballast stiffness, rail temperature and vehicle configuration has been examined. As a first analysis, a “bad case scenario” has been established and employed to identify combinations of load magnitudes and crack sizes that will lead to rail breaks. In addition, it has been shown how hanging sleepers will have a significant effect on wheel loads/crack sizes that can be sustained.

Inspection intervals can be established through analyses of crack growth. This procedure has been outlined and exemplified in the report. It is seen how crack growth rates increase significantly in cold climate and in the presence of hanging sleepers. Further, it is clear that a reliable identification of small cracks will have significant consequences in allowing for longer inspection intervals.

Lateral bending may occur due to lateral loading in curves and may impose an additional loading on rail foot cracks. Tentative analyses have been made. Due to the major uncertainty in parameters affecting the influence of lateral loading, it is foreseen that these studies continues in WP6 and are accompanied by field-testing.

Finally, the results from the analysis need to be considered in an overall risk analysis. In this context it may be recalled that rail head cracks continuously form due to the frictional contact between wheel and rail in moderately sharp curves (sharp enough to cause the formation of rolling contact fatigue cracks, but shallow enough to keep wear at moderate levels). On the other hand rail foot cracks do not show this continuous formation. Instead they occur more sporadically initiated by corrugation and/or operationally induced scratch marks and/or locally increased load magnitudes. Since the risk of derailment is significantly increased in the occurrence of multiple rail breaks at a rather short track section (*cf* the

Hatfield accident), foot cracks should pose a less severe risk in causing derailments. This topic will be dealt with more in detail in the HRMS project.

7.8.2 Estimation of commercial impact of preventive measures

Regarding potential reductions in derailment costs, please refer to [39], [40]. Potential mitigating actions are outlined in D-Rail deliverable D3.1.

In general, preventive measures in the form of e.g. wheel load detectors have additional value in that they can be used for operational monitoring (e.g. of amounts of transported cargo), vehicle maintenance planning *etc.* Also track stiffness measurements have synergy effects in that data can be used for maintenance planning. Temperature measurements can be employed also for other types of meteorological prognoses. This should be considered when LCC evaluations are carried out.

Further, the commercial impact can be divided in two parts: The first is better use of current equipment and routines. For this part there are minor investments needed and the output is expected to be substantial. As an example, focusing non-destructive of rails on locations and time periods where it is needed the most based on crack growth predictions has potential benefit in reducing needs for inspections (and facilitating coordination with other inspections), decreasing the number of derailments, and decrease operational disturbances (both those due to inspections and those due to occurring rail breaks).

7.9 References

- [30] UIC, UIC Code 712R: Rail defects, 4th Edition, January 2002.
- [31] Elena Kabo, Anders Ekberg & Jens C O Nielsen, Analysis of static fractures of rails due to wheel flats, Chalmers Applied Mechanics, Research report 2009:01, 22 pp, 2009
- [32] Jens C O Nielsen, Elena Kabo & Anders Ekberg, Alarm limits for wheel–rail impact loads – part 1: rail bending moments generated by wheel flats, Chalmers Applied Mechanics, Research report 2009:02, 35 pp, 2009
- [33] Anders Ekberg, Elena Kabo & Jens C O Nielsen, Alarm limits for wheel–rail impact loads – part 2: analysis of crack growth and fracture, Chalmers Applied Mechanics, Research report 2009:03, 53 pp, 2009
- [34] Jens C O Nielsen & Annika Igeland, Vertical dynamic interaction between train and track – influence of wheel and track imperfections, Journal of Sound and Vibration, vol 187, no 5, pp 825-839, 1995
- [35] Anders Johansson & Jens C O Nielsen, Out-of-round railway wheels – wheel-rail contact forces and track response derived from field tests and numerical simulations, IMechE Journal of Rail and Rapid Transit, vol 217, pp 135-146, 2003
- [36] Jens C O Nielsen & Johan Oscarsson, Simulation of dynamic train–track interaction with state-dependent track properties, IMechE Journal of Sound and Vibration, vol 275, no 3–5, pp 515-532, 2004
- [37] Johan Sandström & Anders Ekberg, Predicting crack growth and risks of rail breaks due to wheel flat impacts in heavy haul operations, IMechE Journal of Rail and Rapid Transit, vol 223, no 2, pp 153--161, 2009
- [38] Norman E Dowling, Mechanical behaviour of materials, Pearson Prentice Hall, ISBN 0-13-186312-6, 912 pp, 2007

- [39] D-RAIL, D1.1: Summary report and database of derailments incidents, 71 pp + 1 annex (3 pp), 2012
- [40] D-RAIL, D1.2: Report on derailment economic impact assessment, 27 pp + 3 annexes (3+1+2 pp), 2012
- [41] D-RAIL, D3.3: Guidelines on derailment analysis and prevention, in preparation, 2013
- [42] Elena Kabo, Jens Nielsen & Anders Ekberg, Prediction of dynamic train--track interaction and subsequent material deterioration in the presence of insulated rail joints, Vehicle System Dynamics, vol 44, no S1, pp 718 -- 729, 2006
- [43] Anders Ekberg & Björn Paulsson (eds), INNOTRACK--Concluding technical report, International Union of Railways (UIC), ISBN 978-2-7461-1850-8, 288 pp, 2010

8 Conclusions

The analysis has shown that there are a number of influencing parameters and that their importance on derailment depends on the considered scenario. The following is a list of the conclusions and recommendations drawn in each chapter.

8.1 Derailment due to flange climbing in line operations

8.1.1 Limits to lateral load imbalance

From the skew loading investigations based on simulation and measurement data, it is apparent that the UIC RIV limit for lateral load imbalance of 1:1.25 is appropriate. The skew loading cases simulated with lateral load imbalance in excess of this limit were likely to exceed the established $\Delta Q/Q$ and Y/Q limits imposed in EN 14363, especially when coupled with longitudinal load imbalance.

From the investigations regarding bogie yaw resistance it was also apparent that the UIC RIV load imbalance of 1:1.25 is appropriate. Skew loading cases with lateral load imbalance beyond this limit were found to generate bogie X-factors in excess of the 0.1 limit. The effect of the increase in yaw resistance was found to worsen when the lateral load imbalance was sufficient to bring one of the side bearer bumpstops in to contact.

Initial simulations suggest that a reduction in X-factor of up to 20% might be achieved by increasing the sidebearer vertical travel in these circumstances. The practical feasibility of this along with evaluation of the possible benefits require further investigation.

The dynamic simulations with varying isolated track defects showed that a worst case scenario with combined lateral and longitudinal skew loading in very small radius curves may lead to critical wheel climbing even if the vehicle meets the UIC RIV loading guidelines and the track geometry complies with EN 13848-5. Consequently a combination of extensive lateral and longitudinal load imbalance should be avoided.

Comparison of the results from the EN 14363 and GM/RT 2141 low speed flange climb simulations suggest that either the assessment criteria stipulated in GM/RT 2141 are too severe, or that the EN 14363 criteria are too lenient. In contrast the other derailment limits used in the analysis ($\Delta Q/Q$, X-factor, RIV skew loading limits and EN 14363 Y/Q) seem well aligned to each other.

It would appear that a review of the low speed flange climb assessments used in the EN and GM/RT2141 would be a valuable exercise.

The skew loading analysis of measured wheel loads from GB Gotcha data showed that nearly all bogied freight traffic (99.8%) were operating within the UIC RIV limits for loading imbalance.

This suggests that load imbalance is generally well defined and as such could be more comprehensively included in Standards and formalised in the vehicle acceptance processes. Further analysis of a broader data set of measured wheel loads would help ensure that any limits would be relevant to current freight operations. The purpose of such limits would be to help minimise derailments caused by a minority of excessively skew laden vehicles.

It is recommended further studies are carried out to investigate possible alarm levels for skew load detection using in-track measurement systems. This work should also form part of a review of the low speed flange climb assessments within the EN and GB acceptance standards.

The UIC RIV loading ratio limits appear to be an effective measure in mitigating the risks of vehicle skew loading. It is recommended these limit values are more clearly and universally mandated and monitored.

It is recommended that in-track measurement system data is used to establish the true population of offset loading levels. Based on analysis of this data and also cross-reference to skew loading levels of known derailed vehicles, alarm limits for skew loading should be defined. Based on the data analysis, the alarm limit value should capture only out-lying vehicles. It is recommended that a system is put in place that can initially be run in an off-line mode; this will allow the alarm threshold to be adjusted to ensure that it does not overly impact railway operations. Measurement of skew loading could be performed either at loading or mainline running but a demonstration system could be developed.

In response to an improved understanding of on-track skew loading levels, the governing railway acceptance standards should be reviewed and consideration given to the inclusion of a prescribed level of skew loading. The significant differences between the GB and EN low speed flange climb assessment methods should also be reviewed.

8.1.2 Bogie suspension variation

It was found that the transitional behaviour of the primary suspension system for part-laden vehicles is important and should be optimised at the vehicle design stage to maximise not only ride and gauging performance but also derailment resistance.

Consideration could be given to 3-stage stiffness transition in the primary suspension or adoption of rubber components to improve increase the derailment resistance for part-laden/inter-modal traffic.

It was found that in general, the bogie rotational resistance (X-factor) is not a critical derailment control measure for the friction type arrangements studied. However, the behaviour of the centrebowl arrangement can significantly influence the part-laden and laden X-factor values. This can lead to approximately a 10-20% increase in Y/Q values within the curves studied and exceedance of the 1.2 limit value. Therefore good maintenance practice in this area is recommended.

The UIC sidebearer assembly is susceptible to bumpstop contact in response to lateral skew loading. This significantly increases x-factor values and ultimately Y/Q levels. It may be feasible to increase the clearance to the bumpstop and/or increase the spring rates to improve this issue. Any changes to the component would also require consideration of vehicle stability and gauging clearance (kinematic envelope).

Consideration could be given to the development of a Y-series bogie derivative with an improved tare to laden stiffness transition (smaller step change in stiffness). A 3-stage coil spring stiffness transition in the primary suspension or adoption of rubber components are possible options for inter-modal traffic.

8.1.3 Suspension failure and faults

Several suspension failures and faults have been considered and their impact on vehicle derailment propensity assessed using suitable simulation methods from the GB standard GM/RT2141 such as wheel unloading on twisted track ($\Delta Q/Q$), low speed flange climb (Y/Q) and on-track ride Acceleration Peak Counting.

The effect of a broken Lenoir link was also considered. It was shown that the loss of a Lenoir link has an effect on the measured accelerations but the effect was not critical in terms of derailment resistance. The accelerations were greater with a broken Lenoir link than the nominal case and exceed the limit line in some cases on rough track. Assessment on higher speed track showed that there were no stability issues as a result of a broken Lenoir link. In summary a broken Lenoir link did not show a significant increase in derailment risk.

The fault with the largest effect on derailment propensity was a twisted bogie frame. Any twist in the bogie frame has a large effect on the vertical wheel loads with a lower wheel load posing a greater derailment risk. In the cases examined, a twisted frame resulted in up to 64% increase in $\Delta Q/Q$ and up to 30% increase in Y/Q . The results from the twisted frame analysis highlight the importance of maintaining the correct bogie geometry in manufacture, assembly and maintenance.

The investigation which considered the influence of vehicle parameters on derailment resistance revealed that lateral wheel load imbalance was a key factor. Wheel load imbalance may be a consequence of asymmetrical loading (affecting the imbalance at a vehicle level) or a suspension defect (which may only affect the imbalance of one given axle). By combining simulation results with GB wheel load measurement data and experience from current alarm interventions in use in Europe, the work recommended that a wheel load measurement system, combined with an alarm limit for axle imbalance, could be used to remove excessively high risk vehicles from traffic. Running a trial system in 'offline' mode, combined with historical wheel load measurement data, would allow a limit to be set which optimises the balance between effectiveness, cost and convenience.

It was also observed that a poorly selected alarm limit and/or the use of wheel load data of limited integrity could be significantly detrimental to rail freight.

8.1.4 Isolated track defects

It was confirmed that not only the amplitude but also the length of isolated track defects has an important influence on the derailment risk. It is shown that, especially in very small radius curves, track defects shorter than 8 m can become critical if the amplitude reaches the Immediate Action Limits according to EN 13848-5. Therefore future track geometry assessment rules should take this into account for instance by limiting the defect amplitude in dependence on the defect length.

8.2 Derailments in switches & crossings

In the S&C part of WP3.2 the risk of derailment has been studied for traffic in the diverging route of a small radius switch ($R=190$). The study has investigated the influence of 25 parameters on derailment risk as evaluated by $Y/Q_{2m,max}$. This has been a screening activity to find the most influential parameters. Based on the parameter studies, a bad case vehicle-turnout set-up was formulated. By parameterization of the bad case, the derailment limit

was found as a function of the most influential parameters from which tentative conclusions about limit values were drawn.

8.2.1 The most influential parameters

The most influential parameter categories were found to be

- Friction. The wheel rail friction coefficient is the most important (as can be expected from Nadal's criterion) but also the friction coefficients in the primary and secondary suspensions. The magnitude of influence for the different friction coefficient depends on the load state of the vehicle.
- Skew loading, especially combined lateral and longitudinal skew loading.
- Chassis twist. It was also found that chassis twist and skew loading can interact in a non-linear fashion when they both strive to unload the same wheels. According to DB measurements, cross loading for tare state wagons in traffic can be large which indicates the existence of chassis twist among wagons in traffic at levels that can significantly increase the risk of derailment.
- Track irregularities, especially track twist. A strong interaction was found between track twist and lateral alignment. If the track twist unloads the outer wheel (reduced Q) and the lateral alignment pushes the same wheel inwards (increased Y) the resulting increase in Y/Q is larger than what can be expected from the sum of the contributions from these parameters when they are applied one at the time.

Also, the facing move was found to record the largest Y/Q ratios and therefore the derailment risk is expected to be largest for this direction of travel. The exact magnitude of the influence for each parameter on the Y/Q-ratio can be found in the result sections.

8.2.2 Bad vehicle-turnout case

Based on the parameter screening, a bad case vehicle-turnout combination was defined where all parameters were set to their worst setting. By introducing a parameterization of the model in the most influential parameters (but friction) it was possible to estimate a derailment limit surface as a function of these parameters (see Figure 104). The results suggest that a vehicle can derail within current standards if all parameters are set in their worst or close to worst position.

However, considering the studies presented in Chapter 3 on measured wagon skew loading and the relation between track irregularity amplitudes and wave lengths, it should be noted that the parameter combinations leading to derailment in simulations are very unlikely in practice even if they are theoretically feasible within standards. Also, some of the variable levels used are based on engineering judgement.

Simulations suggest that the risk of derailment is larger in a curve featuring switch rail geometry compared to a plain line curve, everything else being equal. This is illustrated in comparison between Figure 104 and Figure 105. It is therefore suggested that the maintenance tolerances for track irregularities in switches should be tighter than those for plain line.

Studying the influence of load state, it was concluded that a tare state wagon generates larger Y/Q ratios than a laden wagon where the payload is centred. If the skew loading is

large, a laden vehicle can generate larger Y/Q ratios than a tare state vehicle. The derailment limits for laden and tare state vehicles can be compared more closely using Figure 104 and Figure 107.

8.2.3 Vehicle parameter limits

The simulation results presented in 4.5.13 to 4.5.15 are aimed at providing the foundation for tentative limits on vehicle load imbalances as caused by skew loading and chassis twist. The investigation has been built around an estimated bad case scenario, and the parameter limits would thus depend on how representative this bad case is. It should also be noted that the criteria are fitted to the derailment surface without accounting for running direction or the direction of the diagonal loading. These are both set to their worst setting according to the performed parameter studies. On the other hand the derailment surface obtained could be used to set consistent limits in that it is shown roughly how critical one load imbalance is compared to another.

To be able to set well informed limits on load imbalance to be detected by wheel load check points, it is suggested that the following three tasks need to be carried out.

1. The derailment limit should be found as a function of the most influential vehicle parameters for a set of representative vehicle types and track cases using simulations
2. The joint probability distributions for the most influential vehicle parameters should be estimated using data from vehicles in traffic.
3. The accuracy of wheel loads obtained from wheel load check points needs to be known

Combining information from point one and two, the accuracy of different measures of derailment risk can be investigated. For example the criteria presented could be applied to measurement data and the number of vehicles that would surpass different thresholds could be estimated and compared to their respective simulated risk of derailment. This task is however difficult to perform with accuracy without the information from point 3. The work in D-rail WP3.2 has come a long way on points 1 and 2.

Even if there are a lot of uncertainties as discussed above, some tentative limits could be suggested based on the performed simulations.

8.2.3.1 Nominal and observed load imbalances

In order to set limits, distinction should first be made between nominal and observed vehicle and axle load imbalances as defined in Section 4.5.5. The nominal imbalances are of interest for loading guidelines while the observed load imbalances are relevant for the detection of derailment prone vehicles in track. Simulations show that a nominal lateral load imbalance (12) of 1:1.25 can correspond to an observed load imbalance for the vehicle (14) of up to 1:1.3 due to suspension compliance and other asymmetries that can arise when the vehicle is asymmetrically loaded in both the lateral and longitudinal direction. Longitudinal skew loading is less sensitive and a nominal load ratio (11) of 1:3 between bogies gives more or less the same result if calculated using observed wheel loads from simulation in (13).

For chassis twist the correlation between the applied twist and the diagonal load ratio (15) is good for a tare state vehicle. For a laden vehicle the correlation is poor as the diagonal load ratio can be affected by skew loading due to non-linearities in the suspension. The diagonal

load ratio is dependent on the compliance properties of the specific wagon in question and is therefore not easily determined before the vehicle is loaded.

It has been shown that the maximum axle load imbalance (17) is a non-linear function of skew loading and chassis twist (Figure 112). It means that the observed axle load imbalances can be much higher than the nominal.

8.2.3.2 Limits for observed load imbalances

Studying the simulated derailment limit as a function of load imbalances (e.g. Figure 115), it seems that a limit of the observed lateral load ratio (14) of 1:1.35 and a limit of the observed longitudinal load ratio (13) of 1:3 could be reasonable for the enforcement of skew loading limits. With these limits there is still some margin to derailment in each individual direction such that some chassis twist and skew loading in the other direction could be accepted in combination with an extreme value in one direction. Individual limits for lateral and longitudinal skew loading should work reasonably well in practice as measurements (e.g. Figure 33) indicates that cases of combined extreme skew loading are rare. It is recognised however that combined skew loading is the worst case and a loading situation which is not assessed with individual criteria for the longitudinal and lateral direction.

Considering limits on the maximum axle load imbalance (17), the derailment surface study shows that all parameter combinations with an associated axle load imbalance above 1:2 derail for the given simulation set-up. In the light of these results, the SBB axle load imbalance limit of 1:1.7 is definitely reasonable as most vehicles with a maximum axle load imbalance above this limit derail. It is therefore suggested as a tentative axle load imbalance limit.

The load imbalance limits on vehicle and axle level are complementary. Sometimes the axle load imbalance is stricter than the imbalance on vehicle level and vice versa. It is therefore recommended that both limit types are used to detect derailment prone vehicles. Especially the maximum axle load imbalance and the longitudinal vehicle load imbalance have been found to be complementary in this study. The lateral load imbalance on the vehicle level is almost rudimentary if the axle load imbalance is also in place (with the proposed limits). The axle load imbalance criterion was shown to be the better single parameter criterion in this study as it is better at separating the derailing vehicles from the non-derailing vehicles for the investigated parameter space.

Limits are also proposed in a more implicit fashion by the multi-parameter criteria. The line and also the plane criteria show promising results in the above investigation. Therefore these criteria as demonstrated in Figure 117 and Figure 118(a) are also proposed as limits.

8.2.3.3 Limits for nominal load imbalances

The simulations show that the RIV loading guidelines are appropriate, but it is a problem that they do not account for (extensive) combined skew loading which was found to be critical in simulations. It is therefore recommended that the loading guidelines are updated such that they also limit the amount of combined skew loading allowed. The planar derailment criteria of Section 4.5.15 could be a starting point for such a discussion. It can be simplified into two dimensional criteria that is a function of longitudinal and lateral skew loading only. This creates a rhombic loading limit surface instead of the rectangular which is the result of the RIV-limits.

8.2.3.4 Chassis twist

It is recommended that tare state vehicles with a diagonal load ratio (15) above 1:1.3 should be inspected for chassis twist. To reach this level of diagonal load ratio a chassis twist of 32 [mrad] was applied to a chassis modelled as rigid. If the diagonal load ratio is as high as 1:1.7, the wagon is estimated to be on the derailment limit and should be stopped then if not earlier. As there is no significant skew loading for a tare state vehicle, the stated diagonal load ratios correspond to the average axle load imbalance in each bogie. This means that an axle load imbalance of about 1:1.7 corresponds to the derailment limit for a tare state vehicle in this study.

8.2.4 Implementation strategy

As this work has shown, the derailment limit is a function of all the influencing parameters which makes it difficult to set limits for each parameter separately. The suggested approach for derailment mitigation is that high limits that would stop only a very small part of the vehicle fleet are implemented and enforced for skew and diagonal loading on vehicles in traffic. Through investigation of the stopped vehicles, more information can be obtained about the correlation between vehicle wheel load status and the vehicle condition and limits could then be tightened in steps if the stopped vehicles are in a very poor condition. Different levels of the limits could also be applied. E.g. above a certain threshold the vehicle isn't stopped but has to be inspected within a specified time period. The objective in mind must be to increase the overall safety and efficiency of the railway freight sector, not to obstruct it.

8.3 Derailments due to sloshing

A dynamic model of the coupled dynamics between a tank vehicle and its fluid content was used in a variety of simulations, with the main objective of understanding the dynamic behaviour of a railway wagon that carries a liquid load under partial filling condition. In particular, the effects of train velocity, curve geometry and fill level were investigated. From a general point of view, the derailment quotient Y/Q is only marginally affected by the sloshing motion and is always below the safety limits. On the other hand, the rollover ratio $\Delta Q/Q_0$ can be significantly increased by the liquid motion and, in extreme cases, it can reach values close to the safety limit (0.6). In particular, while a full curve is not found to be critical, sloshing effects are strongly experienced in s-curves, in which the liquid motion can be increased by the centrifugal forces if, in the counter-curve, the free oscillation of the liquid and the external forcing are in phase.

A non-dimensional analysis allowed to identify, as an important variable, the reduced frequency f^* , defined as the number of sloshing periods that occur from the first oscillation of the liquid (in the first curve) to the entrance into the counter-curve. By comparing different simulations, it was shown that, if f^* is between 0.7 and 1.1, the unload ratio $\Delta Q/Q_0$ is increased by the sloshing effects, if compared with an equivalent wagon with rigid cargo. This relation was found to be valid only if the wagon is subject to high lateral non-compensated accelerations ($>0.4 \text{ m/s}^2$). Neglecting sloshing effect would cause an underestimation of the maximum $\Delta Q/Q_0$ of about 20%, in the worst case.

8.4 Derailments due to wheel failures

Fatigue at mechanical loading has been studied for the two wheel designs. An assumed increase of the vertical loading (from $1.25P$ to $2P$ or $3P$) when the train is rolling on straight track, results in a minor increase of the fatigue stresses in the wheel web. However, if it is assumed that the increase in the vertical load also affects the vertical loading that interacts with the lateral loads at curving and negotiation of points and crossings, a quite substantially increase in the fatigue stresses can be seen at the transition between web and rim for the Low-stress wheel. In detail, an assumed increase in vertical loading at the rolling circle of the two wheel designs does not increase the maximum fatigue stresses until the load is higher than three times the static wheel load.

For the thermomechanical load case it is shown that there is a substantial difference between wheels with a straight wheel web, similar to the S-shaped wheel, and a wheel with a more curved web, similar to the Low-stress wheel. All wheels have axial displacements even at the highest studied power level (80 kW) that are within requirements. For the residual axial displacements after braking, it is only the worn Low-stress wheel that show somewhat to large values. On the other side, the Low-stress wheel show residual stresses that are within the regulations also for the worn wheel, whereas the worn S-shaped wheel show too large stresses that can result in global wheel fracture.

The analyses of wheel web life with respect to combined mechanical loads and loads from tread braking generally show long lives (several millions of kilometres) for the assumed loading. Even the calculated lives of the worn wheels are higher than the expected total maximum service life of freight wheels (then having diameters ranging from new down to worn state). Two cases of assumed deteriorated web surface (severe corrosion or surface scratch) that lead to fatigue limit reductions have been studied. For a 25 % reduction (corresponding e.g. to a change in surface roughness $R_a=6.3 \mu\text{m}$ to $40 \mu\text{m}$), the calculated wheel lives are still longer than about 800 000 km. For a 50 % reduction (corresponding e.g. to a change in surface roughness $R_a=6.3 \mu\text{m}$ to a non-machined forged surface appearance), the wheel lives now range from 90 000 km up to 150 000 km for all studied geometries. It can be concluded that the surface finish / appearance of the web is of high importance for wheel lives. Moreover, in the future, when stress optimized wheels will be more common these results indicate that wheel webs should be checked regularly at maintenance to avoid surface deterioration that substantially lowers the fatigue limit. An intact wheel web paint system for the duration of the wheel life is hence essential not to increase the risk of fatigue damage.

The analyses of the wheel life when also considering loads from track brakes show that the wheel lives are controlled by a combination of mechanical fatigue from conventional load cases and thermomechanical fatigue induced by tread braking. The track brakes have a minor influence on calculated lives.

The study of cracks in the web of the wheels indicates that for normal running conditions, the crack growth is very slow, only marginally larger than the threshold for crack growth. When a crack continues to grow, the speed of the growth remain low and a substantial widening of the crack (in circumferential direction) is required to for the crack to grow deeper into the web. Furthermore, for future assumed increasing vertical and lateral loading it has been found that the cracking of the wheel web is not particularly sensitive to such a development

The main derailment hazard related to rolling contact fatigue (RCF) of the wheel tread has been identified as subsurface initiated RCF. Influencing parameters, monitoring and prediction possibilities are indicated in the report.

8.4.1 Identified main affecting parameters

Concerning increased vertical loading at a lateral position corresponding to the rolling circle the risk of mechanical fatigue is low. However, the low-stress wheel design is sensitivity to large tread damage resulting in high vertical loads with an application point towards the sides of the wheel tread. For such a case fatigue of the wheel web could be an issue. However, to limit such loads more than vertical loads as generated at the rolling circle seem unrealistic. In general, no further limitations are required for such vertical loads than what is required for the safety of the rail. In detail, an assumed increase in vertical loading at the rolling circle of the two wheel designs does not increase the maximum fatigue stresses until the load is higher than three times the static wheel load.

Analyses of severe drag braking (power levels up to 80 kW with a duration of 45 min) show that displacements during and after braking and build-up of residual stresses can be limiting for the wheels. The two studied different wheel designs have different types of response to high power drag braking. For worn slightly S-shaped wheel too high residual tensile stresses occur for power levels larger than 60 kW. For the low-stress wheel residual displacements become too high at power levels 60 kW and higher. For this case, the analyses also indicate incremental growth of the axial flange deflection of the wheel rim, while residual stress levels are still within allowed limits.

For subsurface initiated RCF fractures, the main affecting parameters are vertical load magnitude (with a high influence also of high frequency content), contact geometry, material defects, and contact close to the field side.

8.4.2 Estimation of commercial impact of preventive measures

Regarding vertical mechanical loading of wheels, no further limitations are required for such vertical loads than what is required for the safety of the rail. An assumed increase in vertical loading at the rolling circle of the two wheel designs does not increase the maximum fatigue stresses until the load is higher than three times the static wheel load. For an axle load of 25 tonnes, a vertical load of three times the static axle load corresponds to 370 kN, which is higher than the maximum allowed vertical load proposed for avoiding rail damage of 350 kN (or even down to 250 kN at very cold conditions), see Section 8.5. The measuring of wheel-rail contact forces seem to be an adequate method reduces risks of derailments due to high impact forces. This method is already used at an increasing number of sites on the European network.

Limitation of braking power or excessive wheel temperatures cannot be handled by way-side monitoring since the brake cycle can be of relatively short duration. Hence, on-wagon monitoring is required to assess problems with build-up of too high residual stresses (S-shaped wheel design) or too high residual axial displacements of the wheel rim (low-stress wheel design). The two studied designs have the same limiting brake power and hence also the same limiting temperature level. Classification of wheels according to their handling of different time-temperature scenarios could be a way forward. In the present study, the power limits for a 45 min braking duration have been assessed and for this case a bulk rim temperature limit of 550 °C corresponds to the limiting power level 60 kW. For a specific

location of wheel temperature detection appropriate temperature limits can be defined. These wheel temperature limits might alternatively be “translated” into brake block temperatures for a specific block material. These wheel temperatures can be compared to the temperature requirements given by the TSI legislation regarding homologated brake blocks. Such brake blocks are required to act as a “thermal fuse” to protect the wheel (testing with fixed brakes) and should hence give very high wear at extreme wheel temperatures. According to these tentative findings, the use of homologated brake blocks (that limits tread temperatures to a maximum of 600 °C) *can not* be used as a guarantee to avoid excessive and potentially detrimental residual stresses in wheels of the S-shaped wheels, while the blocks do give protection to the Low-stress wheels.

Regarding RCF-related fractures, the proposed monitoring actions are rather expensive. However some are already employed for other reasons (e.g. track geometry measurements, defect detection of new wheels, some wheel load measurements, profile measurements in workshops and during rail grinding). Further monitoring actions will of course carry an additional cost. However the benefits are not confined to derailment prevention. As an example corrugation identification from measurements of high-frequency contact loads will aid also in combating noise pollution. Further, there is a major commercial impact in that the study aids in applying physically sound limit values e.g. on corrugation magnitudes. This will lead to savings in finding a better balance between decreasing risk of derailment (and deterioration, noise pollution etc) and the maintenance cost.

8.5 Derailments due to rail failures

8.5.1 Identified main affecting parameters

The report has outlined how bending moments and stress intensity factors in rails containing foot and head cracks are influenced by operational conditions. Numerical simulations have been employed and validated towards field measurements. A “worst case” wheel flat load evolution has been identified, the influence of ballast stiffness, rail temperature and vehicle configuration has been examined. A “bad case scenario” has been established and employed to identify combinations of load magnitudes and crack sizes that will lead to rail breaks. In addition, it has been shown how hanging sleepers will have a significant effect on wheel loads/crack sizes that can be sustained.

The main focus of the study is on how inspection intervals can be established through analyses of crack growth. This procedure has been outlined and exemplified in the report. The simulations clearly show that crack growth rates increase significantly in cold climate and in the presence of hanging sleepers. Further, it is clear that a reliable identification of small cracks will have significant consequences in allowing for longer inspection intervals.

Operational applications of the research findings is foreseen as follows:

- The work in WPs 4 and 5 in combination of empirical knowledge from the field is employed to establish realistic initial crack sizes. Note that these may vary depending on the status (operational, maintenance, inspection etc) of the studied line.
- Crack growth predictions are then employed to evaluate theoretical crack growth from measured wheel loads.

- Suitable inspection intervals are prescribed in order to identify and mitigate cracks before they grow long enough to pose a risk of rail breaks. Note that to obtain reasonable safety margins this implies that several inspections should be carried out in the predicted time to grow an initial crack to fracture.
- Inspection intervals should also consider local stress raisers such as welds, insulated joints etc. This is not different from the current practices of having specific inspections for such components.

It is further advised that identification of conditions that promote crack growth (e.g. hanging sleepers, transition zones, mechanical damage to the rails *etc*) should call for additional inspections of cracks at the identified locations.

Initial studies on the influence of lateral bending of the rail have been carried out. Lateral bending may occur due to lateral loading in curves and may impose an additional loading on rail foot cracks. Further analyses are needed to quantify the effect. This is foreseen as a combination of numerical simulations and field-testing in WP6.

Finally, a brief risk analysis has been made. In this context it was recalled that rail head cracks continuously form due to the frictional contact between wheel and rail in moderately sharp curves (sharp enough to cause the formation of rolling contact fatigue cracks, but shallow enough to keep wear at moderate levels). On the other hand rail foot cracks do not show this continuous formation. Instead they occur more sporadically initiated by corrugation and/or operationally induced scratch marks and/or locally increased load magnitudes. Since the risk of derailment is significantly increased in the occurrence of multiple rail breaks at a rather short track section (*cf* the Hatfield accident), foot cracks should pose a less severe risk in causing derailments.

8.5.2 Estimation of commercial impact of preventive measures

Regarding potential reductions in derailment costs, please refer to D-Rail deliverables D1.1 and D1.2. Potential monitoring and mitigating actions are outlined in D-Rail deliverables D3.1 and D3.3. In general preventive measures have additional value in that they can be used for operational monitoring. As an example wheel load detectors can be employed to monitor the amount of transported cargo, to facilitate vehicle maintenance planning *etc*. As further examples track stiffness measurements also have spill-over effects in that data can be used for maintenance planning; temperature measurements can be employed also for other types of meteorological prognoses *etc*.

In general the potential impact is high, not only in preventing rail break related disturbances and derailments, but also (and perhaps even more) in supporting the development of more optimised monitoring and inspection routines.

Appendices

This section contains the appendices associated with the major report modules

Common model for WP3.2

Vehicle Parameters of the Benchmark Y25 Box Wagon

Tare Box Wagon Body Details E02B-WS00602A

Bogie pivot spacing/mm	11,780
Mass/kg	14,320
Roll inertia/kgm ²	15,504
Pitch inertia/kgm ²	387,915
Yaw inertia/kgm ²	378,015
CoG Height ARL/mm	1,390
Body torsional stiffness	∞

Laden Box Wagon Body Details

Mass/kg	80,600
Roll inertia/kgm ²	58,192
Pitch inertia/kgm ²	1,768,358
Yaw inertia/kgm ²	1,734,523
CoG Height ARL/mm	1,691
Body torsional stiffness	∞

Bogie

Bogie Mass /kg	1,635
Roll inertia/kgm ²	1,025
Pitch inertia/kgm ²	875
Yaw inertia/kgm ²	1,823
CoG Height (ARL)/mm	593

Wheelset

Unsprung Mass (wset + axlebox) /kg	1,254
Wset roll and yaw inertia kgm ²	688
Pitch inertia not available	

Wheelbase/mm	1,800
Wheel diameter/mm	920
Primary Suspension	
Primary tare spring stiffnesses per axlebox	
Vertical /MN/m	0.997
Lateral and Longitudinal (Shear)/ MN/m	0.786
Primary laden spring stiffnesses per axlebox	
Vertical /MN/m	1.557
Lateral and Longitudinal (Shear) / MN/m	0.894
Clearance to laden spring at 20t (5t axle load)/mm	14
Primary vertical bumpstop clearance at 20t (5t axle load) /mm	66
Primary longitudinal pusher clearance to stop/mm*	+4
Primary lateral bumpstop clearance/mm	+10
Primary friction face coefficient	0.4
Secondary Suspension	
Sidebearer vertical stiffness /MN/m	0.572
Sidebearer long. stiffness /MN/m	0.116
Vertical sidebearer bumpstop clearance /mm	12
Longitudinal sidebearer bumpstop clearance /mm**	+1
Sidebearer vertical pre-load on underbody /kN	15.97
Sidebearer friction coefficient to underbody	0.3
Centre bowl friction coefficient	0.3
Centre bowl effective radius/m	0.16

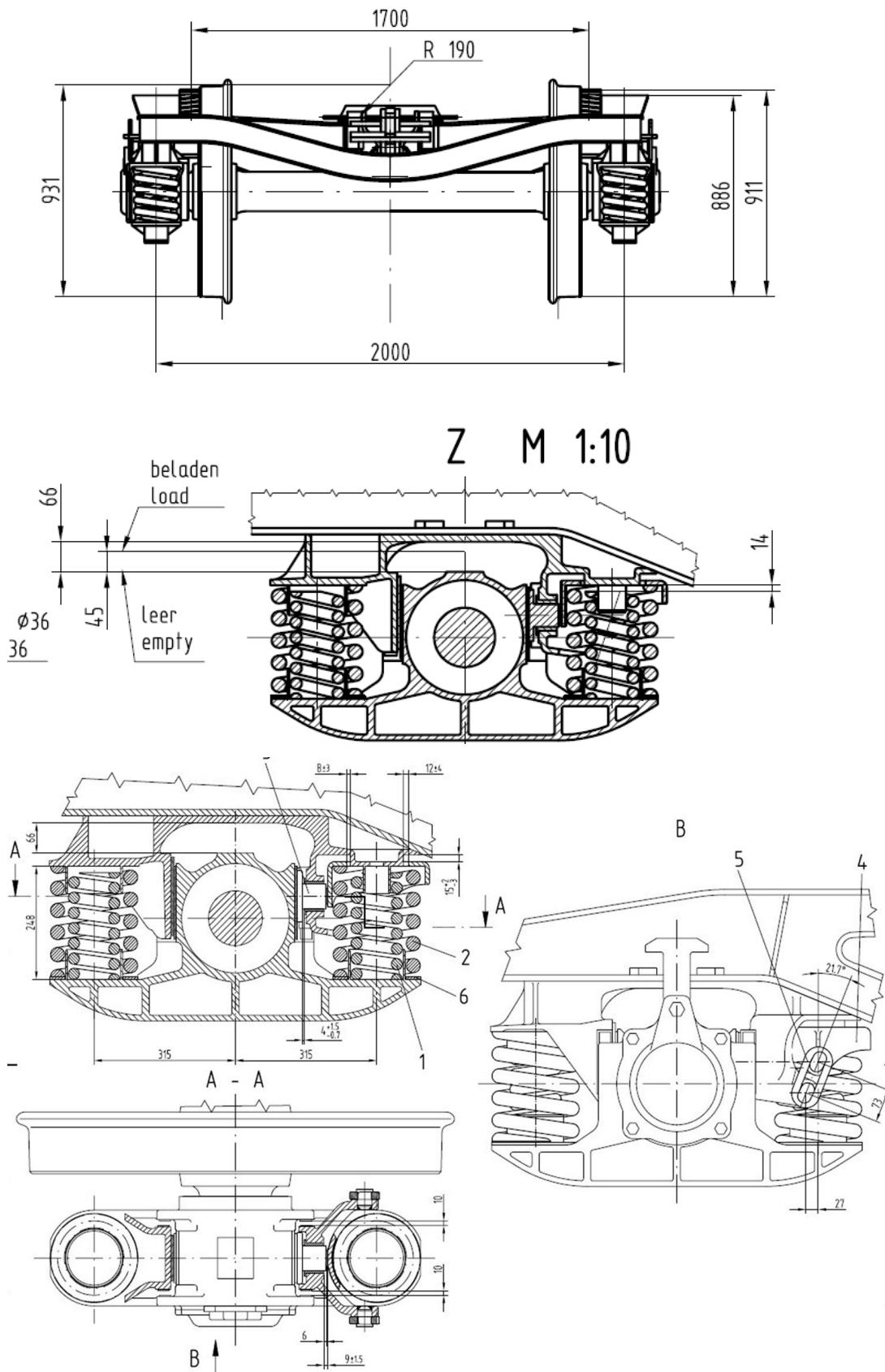


Figure A1.1 Benchmark Primary Suspension Clearances under 5t Axleload

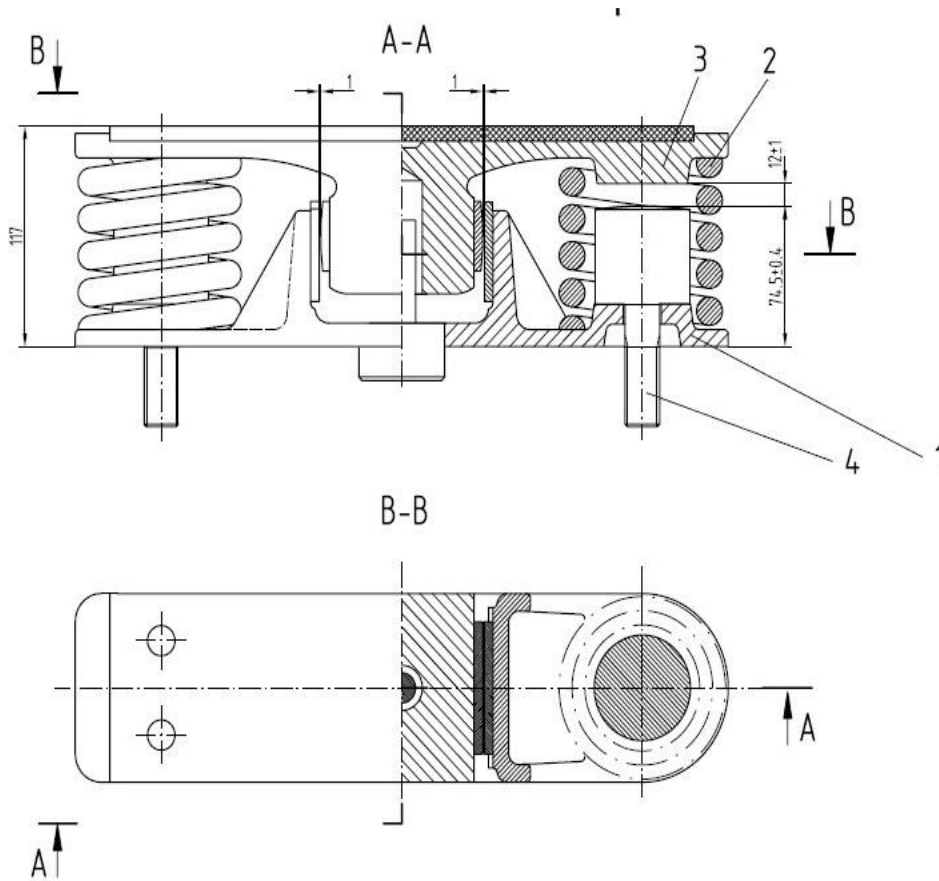


Figure A1.2 Benchmark Sidebearer Arrangement

Track Parameters

The track model used in the simulations can have a significant effect on the simulation results. For plain line simulations (not S&C), the following simplified track model and associated parameters should be adopted. Track stiffness, based on a single layer track model as shown in Figure 3 below.

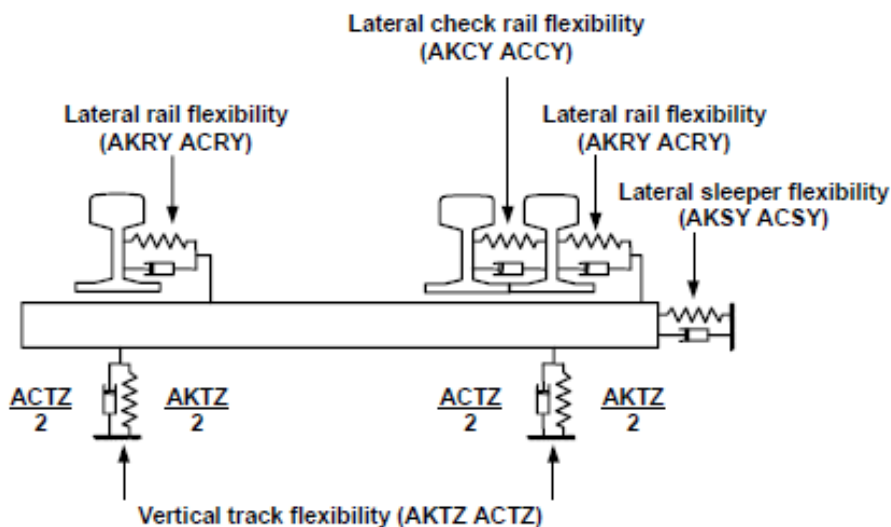


Figure A1.3 Generic Track Model

Default track model values to be adopted:

- "AKTZ" Track Vertical Stiffness 100MN/m
- "ACTZ" Track Vertical Damping 0.2 MNs/m
- "AKRY" Rail–sleeper Lateral Stiffness 43.0 MN/m
- "ACRY" Rail–sleeper Lateral Damping 0.24 MNs/m
- "AKSY" Sleeper – ground Lateral Stiffness 37.0 MN/m
- "ACSY" Sleeper–ground Lateral Damping 0.24 MNs/m
- "AKCY" Check Rail–rail Lateral Stiffness 500.0 MN/m
- "ACCY" Check Rail–rail Lateral Damping 0.75 MNs/m

If the software package has a multi-layer track model then stiffness parameters other than rail to ground should be made as stiff as possible in order to approximate towards the simple single layer model or the model should be reduced (simplified).

Dynamic Simulation Environment

Wheel-rail contact

Wheel profiles to be new S1002

Rail profiles to be new 60E1 inclined at 1:40

Wheel-rail friction coefficient must be 0.45 tread and flange for benchmark simulation

For the purpose when lubrication is simulated, the friction coefficient for the above profiles should change from 0.50 to 0.1 at a contact angle of 69.4 degrees (6.7mm lateral shift) – Values based on Vampire output.

Nominal axleload for contact data generation = 100kN

Wheel Flangeback spacing must be 1360 mm

Track gauge must nominally be 1435 mm

Simulation settings

Integration timestep should be selected to produce stable contact forces – these should be checked for instabilities or 'spikes'.

Simulation output should be at a constant rate of 200 Hz (0.005 s) prior to any filtering

Required Output

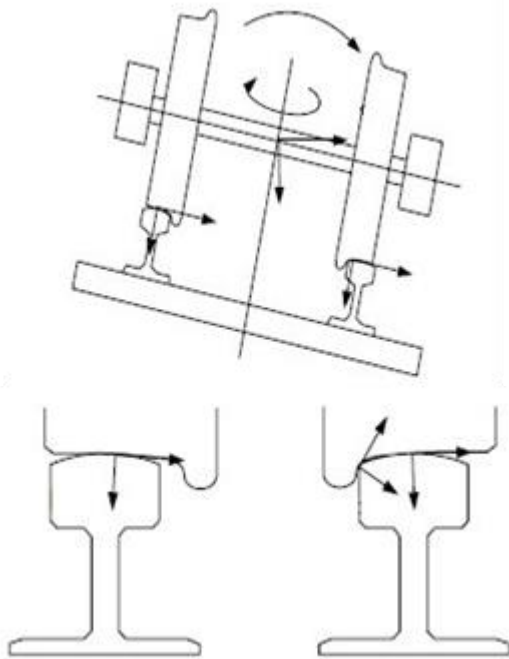


Figure A1.4 Definition of wheel-rail force axes

Simulation result reporting should include a definition of the mnemonics which describe the axes system of the wheel-rail forces. Likely outputs and their definitions are described below:

- Vehicle static axleload, (kN)
- Speed, (kph)
- Y_i force (kN), the lateral force at a wheel Q_i force (kN), the vertical force at a wheel.
- Y_i/Q_i , ratio of lateral to vertical force at a wheel (this should be processed with 2m sliding average)
- $\Delta Q_i/Q_i$, ratio of change in vertical wheel load over the static wheel load
- Wheel lift (mm), the vertical lift of the wheel from the nominal position of the wheelset in the track centreline (see Figure 2)
- Angle of attack (mrad), the yaw angle of the wheelset relative to the track. A positive angle indicates the wheelset steering away from the centre of the curve

Limit Values

- Y/Q limit to be set for governing friction and flange angle (typically limit ≈ 1.2)
- $\Delta Q/Q$ limit = 0.6

- Derailment indicated by wheel lift value $\geq 6\text{mm}$ (this will be reviewed following benchmark simulations)

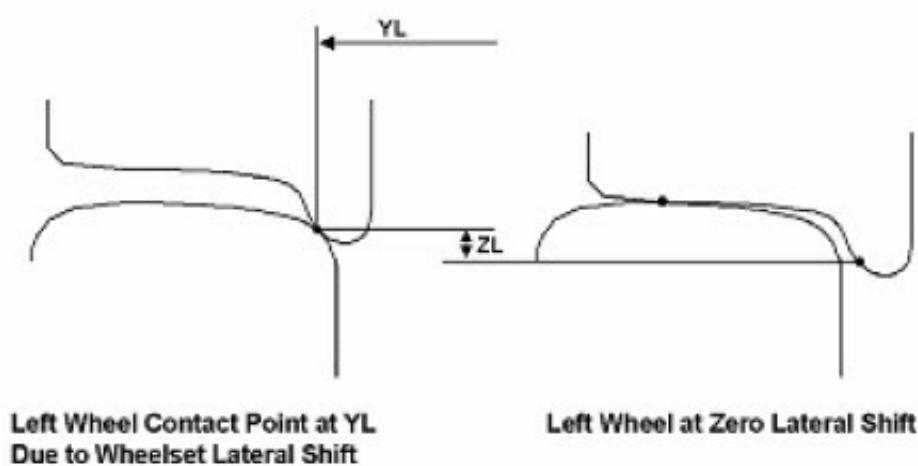


Figure A1.5 Definition of Wheel Lift

Results table for influence of vehicle parameters on derailment resistance

Vehicle ID	Sprung Mass (t)	Lateral Imbalance	Longitudinal Imbalance	Tare Spring Rate (MN/m)	Laden Spring Rate (MN/m)	Clearance (mm)	Centre Bowl mu	Side Bearer mu	GM/RT 2141 DQQ	EN 14363 DQQ	GM/RT 2141 YQ	EN 14363 YQ	XFac
V-01	17.59	1.00	1.00	0.50	0.78	11.00	0.30	0.30	0.41	0.44	1.26	0.91	0.10
V-02	83.87	1.00	1.00	0.50	0.78	11.00	0.30	0.30	0.26	0.26	0.93	0.68	0.07
V-03	67.57	1.00	1.00	0.50	0.78	11.00	0.30	0.30	0.29	0.29	1.08	0.75	0.08
V-04	56.07	1.00	1.37	0.50	0.78	11.00	0.30	0.30	0.41	0.44	1.40	0.87	0.08
V-05	46.07	1.00	1.96	0.50	0.78	11.00	0.30	0.30	0.48	0.50	1.52	1.10	0.09
V-06	42.87	1.00	2.34	0.50	0.78	11.00	0.30	0.30	0.50	0.53	1.53	1.09	0.09
V-07	67.57	1.10	1.00	0.50	0.78	11.00	0.30	0.30	0.34	0.35	1.28	0.87	0.08
V-08	56.07	1.10	1.37	0.50	0.78	11.00	0.30	0.30	0.47	0.49	1.48	1.04	0.08
V-09	46.07	1.09	1.96	0.50	0.78	11.00	0.30	0.30	0.49	0.53	1.59	1.19	0.09
V-10	42.87	1.08	2.34	0.50	0.78	11.00	0.30	0.30	0.56	0.59	1.61	1.20	0.09
V-11	67.57	1.21	1.00	0.50	0.78	11.00	0.30	0.30	0.40	0.41	1.39	1.01	0.09
V-12	56.07	1.20	1.37	0.50	0.78	11.00	0.30	0.30	0.51	0.53	1.52	1.17	0.09
V-13	46.07	1.17	1.96	0.50	0.78	11.00	0.30	0.30	0.50	0.53	1.61	1.20	0.09
V-14	42.87	1.17	2.35	0.50	0.78	11.00	0.30	0.30	0.55	0.58	1.56	1.20	0.10
V-15	67.57	1.36	1.00	0.50	0.78	11.00	0.30	0.30	0.50	0.48	1.51	1.20	0.10
V-16	56.07	1.33	1.37	0.50	0.78	11.00	0.30	0.30	0.56	0.57	1.64	1.23	0.10
V-17	46.07	1.29	1.96	0.50	0.78	11.00	0.30	0.30	0.79	0.81	29.60	1.23	0.11
V-18	42.87	1.28	2.35	0.50	0.78	11.00	0.30	0.30	0.86	0.89	29.13	1.27	0.11
V-19	67.57	1.87	1.00	0.50	0.78	11.00	0.30	0.30	0.77	0.75	6.29	1.23	0.14
V-20	56.07	1.78	1.37	0.50	0.78	11.00	0.30	0.30	0.76	0.76	14.61	1.22	0.13
V-21	46.07	1.68	1.96	0.50	0.78	11.00	0.30	0.30	1.00	1.00	47.26	5.11	0.14
V-22	42.87	1.64	2.35	0.50	0.78	11.00	0.30	0.30	1.00	1.00	55.06	8.29	0.15
V-23	67.57	2.22	1.00	0.50	0.78	11.00	0.30	0.30	0.87	0.86	70.63	1.24	0.16

Vehicle ID	Sprung Mass (t)	Lateral Imbalance	Longitudinal Imbalance	Tare Spring Rate (MN/m)	Laden Spring Rate (MN/m)	Clearance (mm)	Centre Bowl mu	Side Bearer mu	GM/RT 2141 DQQ	EN 14363 DQQ	GM/RT 2141 YQ	EN 14363 YQ	XFac
V-24	56.07	2.08	1.37	0.50	0.78	11.00	0.30	0.30	0.91	0.92	69.19	1.40	0.15
V-25	46.07	1.93	1.96	0.50	0.78	11.00	0.30	0.30	1.00	1.00	51.44	11.16	0.16
V-26	42.87	1.86	2.35	0.50	0.78	11.00	0.30	0.30	1.00	1.00	66.01	33.24	0.17
V-27	94.07	1.00	1.00	0.50	0.78	11.00	0.30	0.30	0.21	0.24	0.97	0.66	0.07
V-28	94.07	1.28	1.00	0.50	0.78	11.00	0.30	0.30	0.42	0.40	1.47	0.99	0.09
V-29	94.07	1.27	1.04	0.50	0.78	11.00	0.30	0.30	0.41	0.39	1.46	1.01	0.09
V-30	76.67	1.01	1.00	0.50	0.78	11.00	0.30	0.30	0.27	0.27	1.06	0.71	0.07
V-31	76.67	1.25	1.04	0.50	0.78	11.00	0.30	0.30	0.40	0.40	1.46	1.00	0.09
V-32	67.57	1.00	1.00	0.50	0.78	11.00	0.10	0.10	0.30	0.29	0.91	0.67	0.03
V-33	67.57	1.00	1.00	0.50	0.78	11.00	0.10	0.30	0.30	0.29	0.90	0.67	0.04
V-34	67.57	1.00	1.00	0.50	0.78	11.00	0.10	0.50	0.30	0.29	0.96	0.70	0.06
V-35	67.57	1.00	1.00	0.50	0.78	11.00	0.30	0.10	0.29	0.29	0.98	0.73	0.06
V-36	67.57	1.00	1.00	0.50	0.78	11.00	0.30	0.30	0.29	0.29	1.08	0.75	0.08
V-37	67.57	1.00	1.00	0.50	0.78	11.00	0.30	0.50	0.29	0.29	1.21	0.74	0.09
V-38	67.57	1.00	1.00	0.50	0.78	11.00	0.50	0.10	0.31	0.33	1.28	0.76	0.09
V-39	67.57	1.00	1.00	0.50	0.78	11.00	0.50	0.30	0.31	0.33	1.32	0.77	0.11
V-40	67.57	1.00	1.00	0.50	0.78	11.00	0.50	0.50	0.31	0.33	1.32	0.78	0.13
V-41	40.57	1.00	1.00	0.50	0.78	11.00	0.10	0.10	0.45	0.49	1.34	0.85	0.03
V-42	40.57	1.00	1.00	0.50	0.78	11.00	0.10	0.30	0.45	0.49	1.35	0.84	0.05
V-43	40.57	1.00	1.00	0.50	0.78	11.00	0.10	0.50	0.45	0.49	1.36	0.83	0.08
V-44	40.57	1.00	1.00	0.50	0.78	11.00	0.30	0.10	0.46	0.49	1.34	0.86	0.06
V-45	40.57	1.00	1.00	0.50	0.78	11.00	0.30	0.30	0.46	0.49	1.38	0.89	0.08
V-46	40.57	1.00	1.00	0.50	0.78	11.00	0.30	0.50	0.46	0.49	1.41	0.93	0.11
V-47	40.57	1.00	1.00	0.50	0.78	11.00	0.50	0.10	0.46	0.48	1.39	0.93	0.08
V-48	40.57	1.00	1.00	0.50	0.78	11.00	0.50	0.30	0.46	0.48	1.41	0.95	0.11

Vehicle ID	Sprung Mass (t)	Lateral Imbalance	Longitudinal Imbalance	Tare Spring Rate (MN/m)	Laden Spring Rate (MN/m)	Clearance (mm)	Centre Bowl mu	Side Bearer mu	GM/RT 2141 DQQ	EN 14363 DQQ	GM/RT 2141 YQ	EN 14363 YQ	XFac
V-49	40.57	1.00	1.00	0.50	0.78	11.00	0.50	0.50	0.46	0.48	1.39	0.97	0.14
V-50	21.07	1.00	1.00	0.50	0.78	11.00	0.10	0.10	0.40	0.42	1.06	0.86	0.03
V-51	21.07	1.00	1.00	0.50	0.78	11.00	0.10	0.30	0.40	0.42	1.13	0.89	0.08
V-52	21.07	1.00	1.00	0.50	0.78	11.00	0.10	0.50	0.40	0.42	1.34	0.92	0.13
V-53	21.07	1.00	1.00	0.50	0.78	11.00	0.30	0.10	0.38	0.42	1.10	0.88	0.05
V-54	21.07	1.00	1.00	0.50	0.78	11.00	0.30	0.30	0.38	0.42	1.32	0.90	0.10
V-55	21.07	1.00	1.00	0.50	0.78	11.00	0.30	0.50	0.38	0.42	1.34	0.94	0.14
V-56	21.07	1.00	1.00	0.50	0.78	11.00	0.50	0.10	0.40	0.41	1.08	0.87	0.07
V-57	21.07	1.00	1.00	0.50	0.78	11.00	0.50	0.30	0.40	0.41	1.35	0.91	0.12
V-58	21.07	1.00	1.00	0.50	0.78	11.00	0.50	0.50	0.40	0.41	1.34	0.94	0.16
V-62	17.50	1.00	1.00	0.50	0.78	11.00	0.30	0.30	0.42	0.45	1.37	0.94	0.10
V-63	26.40	1.00	1.00	0.50	0.78	11.00	0.30	0.30	0.40	0.43	1.37	0.96	0.09
V-64	83.90	1.00	1.00	0.50	0.78	11.00	0.30	0.30	0.25	0.26	0.93	0.70	0.07
V-65	17.50	1.00	1.00	0.40	0.62	8.80	0.30	0.30	0.35	0.38	1.29	0.89	0.10
V-66	26.40	1.00	1.00	0.40	0.62	8.80	0.30	0.30	0.41	0.43	1.34	0.92	0.09
V-67	83.90	1.00	1.00	0.40	0.62	8.80	0.30	0.30	0.22	0.21	0.89	0.65	0.07
V-68	17.50	1.00	1.00	0.62	0.62	8.80	0.30	0.30	0.51	0.54	1.47	1.01	0.10
V-69	26.40	1.00	1.00	0.62	0.62	8.80	0.30	0.30	0.45	0.48	1.43	0.99	0.09
V-70	83.90	1.00	1.00	0.62	0.62	8.80	0.30	0.30	0.26	0.28	0.94	0.72	0.07
V-71	17.50	1.00	1.00	0.40	0.97	8.80	0.30	0.30	0.35	0.38	1.29	0.89	0.10
V-72	26.40	1.00	1.00	0.40	0.97	8.80	0.30	0.30	0.44	0.46	1.39	0.99	0.09
V-73	83.90	1.00	1.00	0.40	0.97	8.80	0.30	0.30	0.25	0.25	0.92	0.68	0.07
V-74	17.50	1.00	1.00	0.62	0.97	8.80	0.30	0.30	0.51	0.54	1.47	1.01	0.10
V-75	26.40	1.00	1.00	0.62	0.97	8.80	0.30	0.30	0.48	0.50	1.49	1.01	0.09
V-76	83.90	1.00	1.00	0.62	0.97	8.80	0.30	0.30	0.29	0.31	0.98	0.73	0.07

Vehicle ID	Sprung Mass (t)	Lateral Imbalance	Longitudinal Imbalance	Tare Spring Rate (MN/m)	Laden Spring Rate (MN/m)	Clearance (mm)	Centre Bowl mu	Side Bearer mu	GM/RT 2141 DQQ	EN 14363 DQQ	GM/RT 2141 YQ	EN 14363 YQ	XFac
V-77	17.50	1.00	1.00	0.40	0.62	13.75	0.30	0.30	0.35	0.38	1.28	0.89	0.10
V-78	26.40	1.00	1.00	0.40	0.62	13.75	0.30	0.30	0.36	0.36	1.28	0.91	0.09
V-79	83.90	1.00	1.00	0.40	0.62	13.75	0.30	0.30	0.22	0.22	0.89	0.65	0.07
V-80	17.50	1.00	1.00	0.62	0.62	13.75	0.30	0.30	0.51	0.54	1.47	1.01	0.10
V-81	26.40	1.00	1.00	0.62	0.62	13.75	0.30	0.30	0.40	0.43	1.35	0.90	0.09
V-82	83.90	1.00	1.00	0.62	0.62	13.75	0.30	0.30	0.27	0.29	0.95	0.72	0.07
V-83	17.50	1.00	1.00	0.40	0.97	13.75	0.30	0.30	0.35	0.38	1.28	0.89	0.10
V-84	26.40	1.00	1.00	0.40	0.97	13.75	0.30	0.30	0.36	0.37	1.32	0.94	0.09
V-85	83.90	1.00	1.00	0.40	0.97	13.75	0.30	0.30	0.25	0.25	0.93	0.68	0.07
V-86	17.50	1.00	1.00	0.62	0.97	13.75	0.30	0.30	0.51	0.54	1.47	1.01	0.10
V-87	26.40	1.00	1.00	0.62	0.97	13.75	0.30	0.30	0.40	0.43	1.36	0.90	0.09
V-88	83.90	1.00	1.00	0.62	0.97	13.75	0.30	0.30	0.30	0.32	0.99	0.74	0.07



Comparison of EN 14363 and GM/RT 2141 – with respect to resistance to derailment, in the context of D-Rail simulation cases.

The Euro Norm EN 14363:2005 and the GB Railway Group Standard GM/RT 2141 both detail requirements for demonstrating that a vehicle has an acceptable resistance to derailment. The comparison made here specifically considers the 'flange climb' derailment mechanism.

Overview of the methods

The two standards each present three separate methods of proving a vehicle's derailment resistance, which are summarised briefly below.

GM/RT 2141

Method 1 – Laboratory test rigs and on track tests

- Static or quasi-static measurement of wheel unloading on twisted track
- Measurement of bogie rotational resistance
- On-track ride tests

Method 2 – Simulations and on track tests

- Computer simulations designed to examine whether the vehicle has an acceptable resistance to flange climb derailment at low speed
- On-track ride tests

Method 3 – On track tests

- On-track dynamic measurement of Y/Q ratio and analysis of the results

EN 14363

Method 1 – Twisted test track

- Measurement of the safety against derailment by running through a twisted test track.

Method 2 – Twist test rig and flat test track

- Measurement of the minimum wheel force $Q_{a,min}$ on a vehicle test rig;
- Measurement of the guiding force Y_a on an appropriate test track;
- Calculation of the ratio $(Y/Q)_a$.

Method 3 – Twist test rig and yaw test rig

- Measurement of the minimum wheel force $Q_{a,min}$ on a vehicle test rig
- Measurement of wheel forces and the torque required to rotate (yaw) the bogie in a small radius curve.

Equivalents between the standards

There are some similarities between the philosophies of the methods from the two standards.

Table 50 EN 14363 equivalents to GM/RT 2141 Methods

GM/RT 2141	EN 14363 Equivalent	Notes
Method 1	Method 3	EN 14363 does not stipulate ride tests in the relevant derailment resistance section; however similar tests are included in the standard elsewhere.
Method 2	Method 1	In GM/RT 2141 a numerical simulation is acceptable, whereas for EN 14363 the demonstration must be undertaken on a test track. EN 14363 does not stipulate ride tests in the relevant derailment resistance section; however similar tests are included in the standard elsewhere.
Method 3	No equivalent	EN 14363 does not allow for the proving of safety against derailment through on-track tests as GM/RT 2141 does. However a Y/Q assessment from on-track tests is required to prove running safety elsewhere in the standard. In that context a Y/Q quotient limit of 0.8 is set, while at the same time recognising that the absolute limit of 1.2 (or as defined by Nadal's equation) specified in the section regarding the resistance to derailment still stands.

Table 51 GM/RT 2141 equivalents to EN 14363 Methods

EN 14363	GM/RT 2141 Equivalent	Notes
Method 1	Method 2	In GM/RT 2141 a numerical simulation is acceptable, whereas for EN 14363 the demonstration must be undertaken on a test track.
Method 2	Method 2	In EN 14363 Method 2 the Y and Q values are measured using separate tests (test rig and test track) and are combined to provide the Y/Q quotient. GM/RT 2141 permits a numerical simulation to be undertaken to evaluate the Y/Q quotient. EN 14363 does not stipulate ride tests in the relevant derailment resistance section; however similar tests are included in the standard elsewhere.
Method 3	Method 1	EN 14363 does not stipulate ride tests in the relevant derailment resistance section; however similar tests are included in the standard elsewhere.

Differences between the equivalent methods

The following sections detail the differences between the equivalent methods (as per Table 50 and Table 51).

GM/RT 2141 Method 1 versus EN 14363 Method 3

$\Delta Q/Q$ Limit

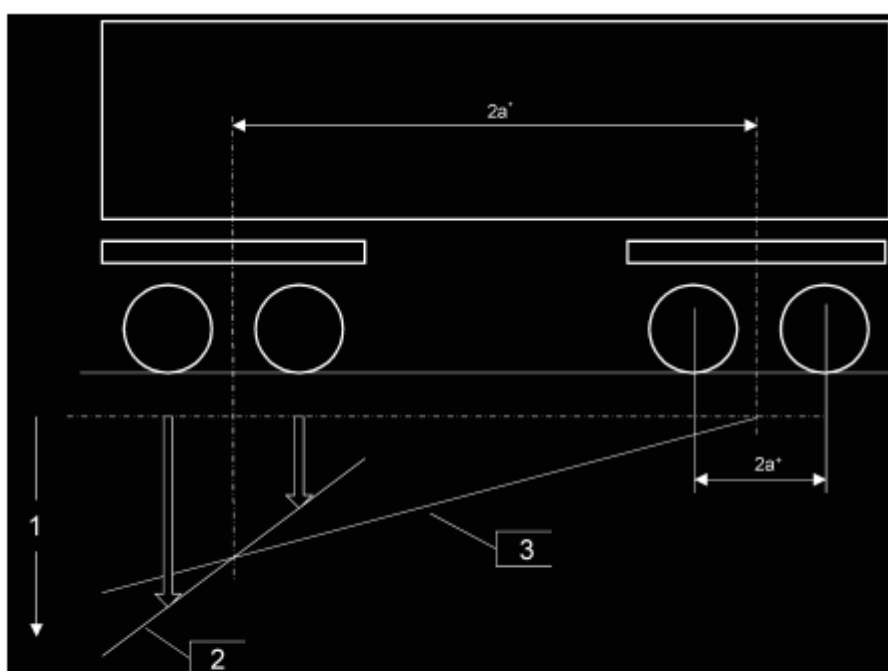
Both standards use the same limit of 0.6

In order to evaluate the maximum $\Delta Q/Q$ quotient EN 14363 specifies a twist along the bogie length, superimposed over a twist along the vehicle length. The location of the short wavelength fault is stipulated. In the context of D-Rail simulations which are concerned with Y-series bogied freight vehicles the two twists can be specified as:

Bogie twist = 0.7%

Body twist = 0.44% (based on a 14 m bogie centre pivot spacing)

The net result of the EN 14363 specification is to have the bogie centres on a gradient of 0.44%, while the leading bogie is on a gradient of 0.7%. The actual track gradient on the approach to the short wavelength fault must therefore be shallower than 0.44%.



Key

- 1 vertical displacement
- 2 bogie test twist
- 3 vehicle body test twist

Figure 2 — Combination of bogie and vehicle body test twist

Similarly GM/RT 2141 specifies a short wavelength irregularity superimposed over a long wavelength irregularity. The location of the short wavelength twist (or dip) is not prescribed, and should be positioned so as to produce the worst unloading case. The twists are specified as:

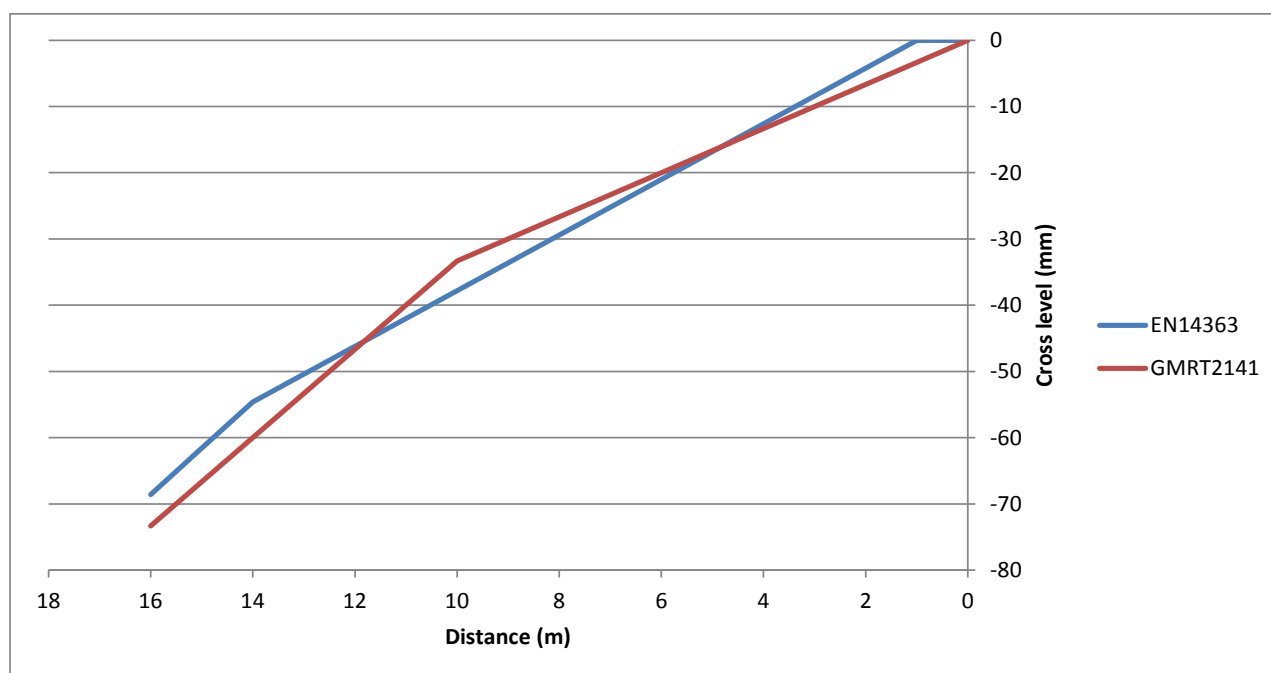
Long wavelength twist = 1:300 inclination (0.33%)

Short wavelength dip = 1:150 inclination (0.67%) (from horizontal)

Semi-span of short wavelength dip = 6 m

The net result of the GM/RT 2141 specification is a twist of 1:300 with a 20 mm dip over 12 m.

Theoretical crosslevels required to produce both cases is shown in the figure below. The leading wheelset of the vehicle would be at 16 m, the second wheelset at 14 m, the third at 2 m and the trailing wheelset at 0 m. The plot shows that the conditions in GM/RT 2141 produce a greater twist along the vehicle length and that the twist along the leading bogie is similar. Note that the short wavelength irregularity in the GM/RT 2141 data has been positioned so the centre of the dip coincides with the leading wheelset, but it could be placed anywhere.



X-factor Limit

For passenger vehicles and locomotives both standards set a limit of 0.1. For freight vehicles both standards use the same non-linear function, except that as EN 14363 specifies the axle load in kN and in GM/RT 2141 the axle load is one-tenth of that in EN 14363 but specified in tonnes, the two functions disagree by a factor of 9.81/10 (1.9%).

The function defined in GM/RT 2141 is shown in Figure 225 for reference.

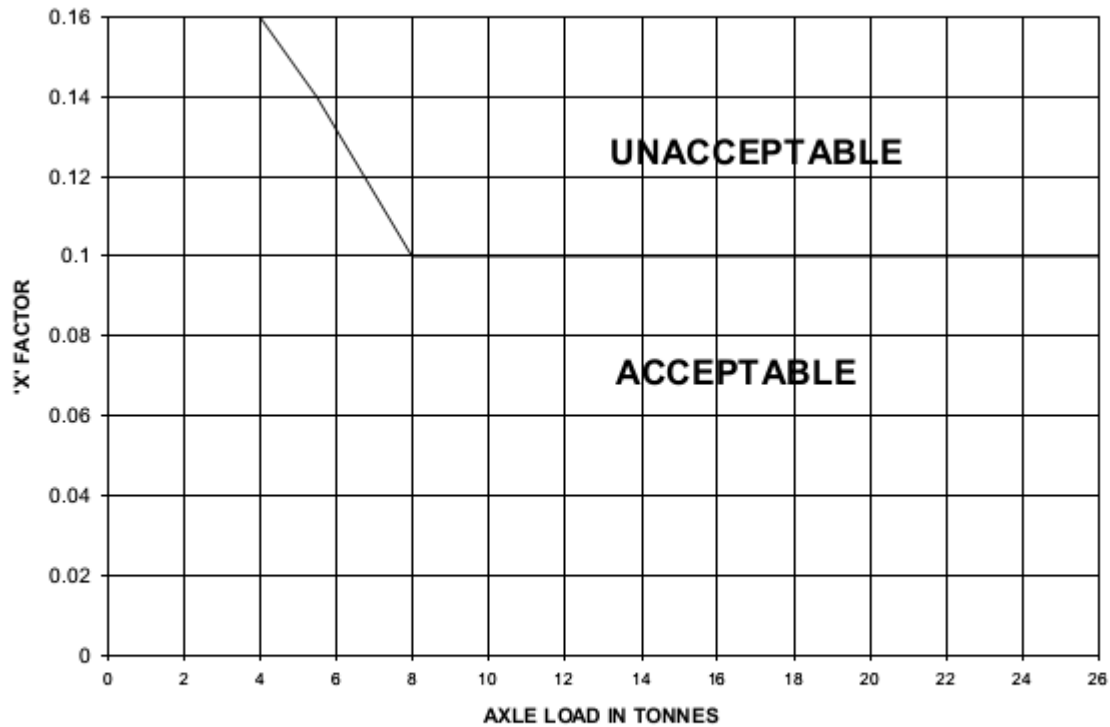


Figure B.1 Maximum permissible freight vehicle X - factor as a function of axle load

Figure 225 Figure B.1 from GM/RT 2141

GM/RT 2141 Method 2 versus EN 14363 Method 1 and Method 2

In the context of applying the derailment resistance measurement methods to the D-Rail dynamic simulations the difference between the simulation environment (allowable in GM/RT 2141) and the real test environment (specified in EN 14363) shall be ignored. The discussion here will focus on the difference in the parameters for the cases only.

Y/Q limit

EN 14363 states a Y/Q limit of 1.2 for a flange angle of 70°. For other flange angles Nadal's equation should be applied, with $\mu = 0.36$.

GM/RT 2141 states a Y/Q limit of 1.2 for a flange angle of 68°. For other flange angles Nadal's equation should be applied with $\mu = 0.32$.

The Y/Q limits are essentially the same, however due to the differing coefficients of friction used there is approximately a 7.5% deviation between the two standards (around the contact angle range of interest), with GM/RT 2141 providing the higher limit.

Track specification

EN 14363 Method 1 specifies a curve of 150 m radius with a twist of 0.3% through the body of the curve. The test track should otherwise be representative of typical conditions (gauge, profiles, etc.). The coefficient of friction during the test should be within the ranges specified in § 4.1.2.2.5 of the standard, that is within 80% of a value between 0.42 and 0.49 (approximately) depending upon axle load.

An alternative method presented in EN 14363 as Method 2, involves the measuring of the $\Delta Q/Q$ quotient on a test rig (in a similar fashion to EN 14363 Method 3, but with different twist values) and measuring the lateral force of the leading outer wheel on a curved test track of 150 m installed without cant or twist. The separation of the two measures is not necessary in the simulation environment to be used in D-Rail, and therefore EN 14363 Method 1 would be used in preference.

GM/RT 2141 specifies a curve with entry and exit transitions of 1:300 gradient. A 20 mm dip with

6 m semi-span is positioned to create the most unfavourable conditions on the exit transition. Gauge widening is also specified for ranges of curve radii along with maximum levels of cant. The wheel-rail coefficient of friction is specified as 0.32. Further, the effects of the bogie-body yaw stiffness is brought into play by either including a lateral irregularity or artificial force/torque applied to the bogie, in such a way as to promote derailment of the critical wheel. A range of curve radii should be used in order to identify the worst case conditions.

The difference in the track cases specified by the two standards suggests that different conclusions may be found in some circumstances.

GM/RT 2141 Method 3

This method stipulates on-track measurement of the Y/Q ratio, and is intended for cases where the other methods might not be expected to provide reliable results (such as for novel vehicle designs). This type of testing is not necessary for the D-Rail simulation cases, as they feature conventional vehicle designs.

Methods relevant to D-Rail

The following methods were identified as being relevant to D-Rail vehicle simulations:

GM/RT 2141 Method 1

GM/RT 2141 Method 2

EN 14363 Method 1

EN 14363 Method 3

GM/RT 2141 Method 1 and EN 14363 Method 3 are both designed to be undertaken in laboratory conditions and are not ideally suited to a transient analysis. Indeed the relevant limit values stated may not be valid if the approach to the test conditions is not as it would be in a laboratory (e.g. hysteresis in friction components would be different).

It is however possible to artificially replicate laboratory conditions in a transient simulation.

GM/RT 2141 Method 2 requires a number of different combinations of curvature, cant, dip position and gauge to be analysed, in order to ensure that the worst case conditions are identified. This would need to be the case for D-Rail simulations to ensure a change in vehicle parameters (for example) doesn't merely move the derailment risk to a different set of conditions.

A set of track cases to satisfy this method could be created and treated as a single test case.

EN 14363 Method 1 is the simplest of the cases to run in a dynamic simulation and all relevant factors are specifically prescribed by the standard.

It is probable that relying on this one set of track parameters alone would lead to misguided conclusions regarding the influence of varying other parameters on the derailment resistance, as the key worst case conditions may not be identified.